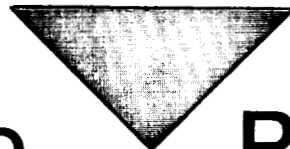
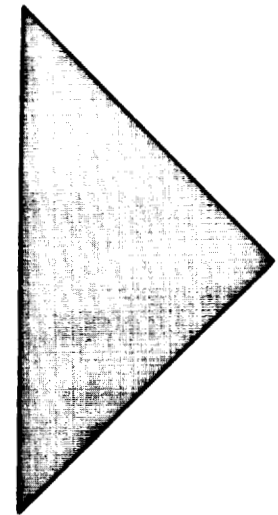
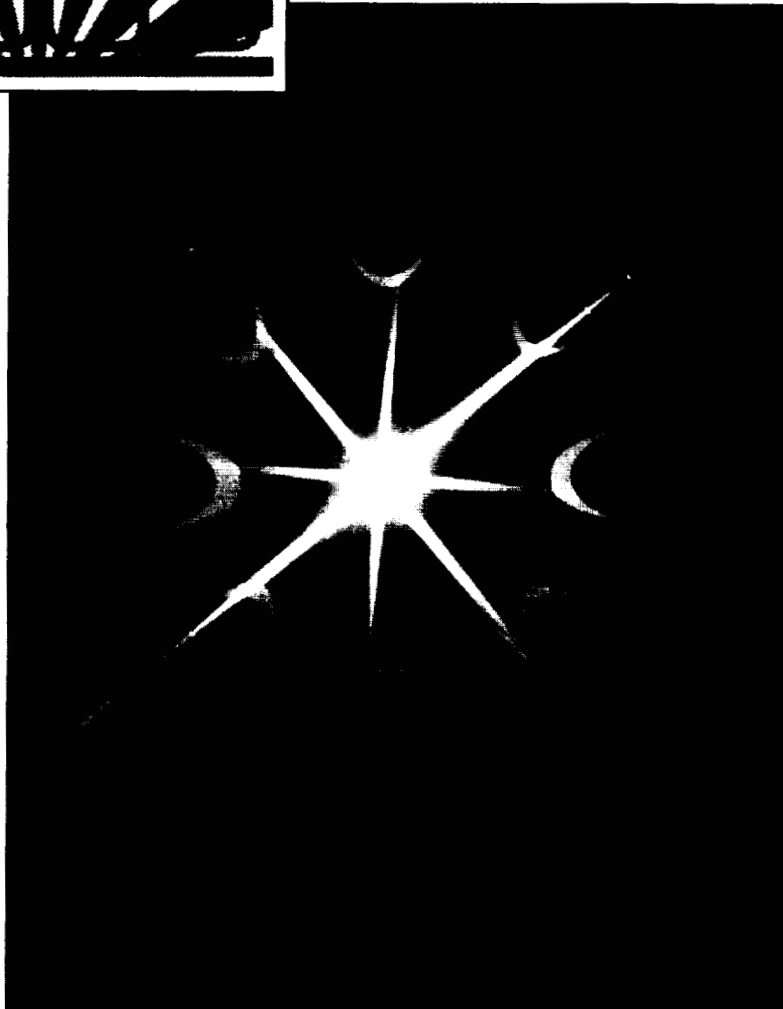
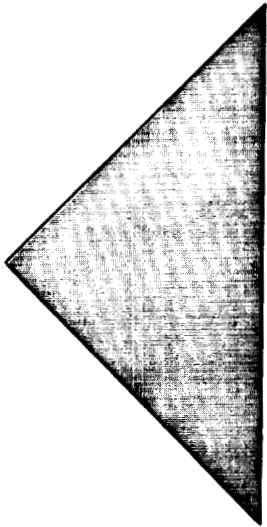
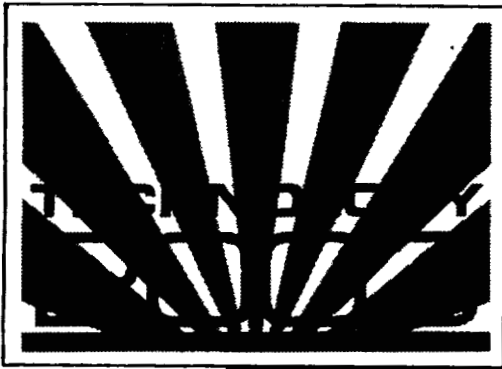


*NASA Conference Publication 3249 - Vol-1
Volume One*



Conference Proceedings

The Fourth National Technology Transfer Conference & Exposition
December 7-9, 1993 • Anaheim, CA

*Sponsored by NASA, NASA Tech Briefs Magazine
and the Technology Utilization Foundation*



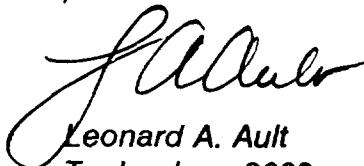
FOREWORD

Technology 2003, the fourth national technology transfer conference and exposition, was held December 7-9, 1993 at the Anaheim, California, Convention Center. As the centerpiece for the second annual "National Technology Transfer Week," Technology 2003 shared the spotlight with the Technology Transfer Society's annual meeting (Dec. 6-7) and a one-day symposia sponsored by the Society for Photogrammetry and Remote Sensing (Dec. 8).

Begun in 1990, the Technology 2000 series of conferences has promoted and facilitated the transferral of Federally-developed technologies by putting people directly in touch with the leading technology developers and technology transfer experts from government, industry and universities. This year, attendees were able to visit over 230 exhibits, covering 80,000 square feet, that showcased the latest technologies and products available for sale or license. A symposia that featured 100 presentations by researchers from throughout the Federal R&D base focused attention on commercially-promising technologies in areas critical to domestic and world growth markets. Through workshops and special sessions, current trends affecting areas such as international technology transfer and partnering, new precision casting techniques for the next century, and how to successfully market to the Federal government were addressed.

Of particular interest was Defense Conversion and the Technology Reinvestment Project. Both Tuesday's opening Plenary Session and Wednesday's Plenary Workshop provided close examination from the perspectives of government and industry. Distinguished speakers included Robert Paster of the Rocketdyne Division of Rockwell International; Greg Reck, from NASA's Office of Advanced Concepts and Technology; Dr. Steve Wax of the Advanced Research Projects Agency; Kevin Carr, from the National Institute of Standards and Technology; Michael Long of the Department of Energy; and, Frank Penaranda, from NASA's Technology Transfer Program.

We are pleased to provide their remarks in this year's Conference Proceedings, in addition to the 100 papers presented. The Proceedings are published in two volumes. Volume One contains transcripts of the opening Plenary Session and the Plenary Workshop, plus papers presented in the categories of Advanced Manufacturing, Biotechnology/Medical Technology, Environmental Technology, Materials Science and Power and Energy. Volume Two contains all other symposia presentations.



Leonard A. Ault
Technology 2003
Conference Program Chairman

TABLE OF CONTENTS

National Technology Transfer Week	vi
Opening Plenary Session: Defense Conversion and Technology Reinvestment – New Opportunities for Industry	vii
Plenary Workshop: How to do Business with the Federal Government – the Technology Reinvestment Project	xxiii
Symposia:	
Advanced Manufacturing	1
A Force-Controllable Macro-Micro Manipulator and its Application to Medical Robotics	3
The Use of Interactive Computer Vision and Robot Hand Controllers for Enhancing Manufacturing Safety	17
Programmable Automated Welding System (PAWS): Control of Welding Through Software and Hardware	32
Sensing The Gas Metal Arc Welding Process	38
A Combined Electron Beam/Optical Lithography Process Step for the Fabrication of Sub-Half-Micron-Gate-Length MMIC Chips	54
Metafusion: A Breakthrough in Metallurgy	60
Near-Net-Shape Manufacturing: Spray-Formed Metal Matrix Composites and Tooling	64
Composite Hot Drap Forming	74
Precision and Manufacturing at Lawrence Livermore National Laboratory	81
Potential Capabilities of Reynolds Stress Turbulence Model in the COMMIX-RSM Code	90
An Improved Plating Process	100
The Universal Applications of Microtubes and Microtube Composites	108
Biotechnology/Medical Technology	115
Microencapsulation of Anti-Tumor, Antibiotic and Thrombolytic Drugs in Microgravity	117
Cubanes: Super Explosives and Potential Pharmaceutical Intermediates	127
Dual Use of Image-Based Tracking Techniques: Laser Eye Surgery and Low Vision Prosthesis	131
Analysis and an Image Recovery Algorithm for Ultrasonic Tomography System	138
Composite Redesign of Obstetrical Forceps	146
Development of the NASA/Baylor Left Ventricle Assist Device (LVAD)	151
A Fuzzy Logic Controller for Hormone Administration Using an Implantable Pump	158
Monitor for <i>Status Epilepticus</i> Seizures	168
Environment Technology	177
Seed Viability Detection Using Computerized False-Color Radiographic Image Enhancement	179
A Commercialized, Continuous Flow Fiber-Optic Sensor for Trichloroethylene and Haloforms	188
Computerized <i>In Vitro</i> Test for Chemical Toxicity Based on <i>Tetrahymena</i> Swimming Patterns	196
A Modular Approach for Automated Sample Preparation and Chemical Analysis	209

TABLE OF CONTENTS

Environmental Technology (continued)

Photovoltaic Power Without Batteries for Continuous Cathodic Protection	219
Nonaqueous Cleaning Solvent Substitution	223
Supersonic Gas-Liquid Cleaning System	232
Regenerating Used Aqueous Cleaners with Ozone and Electrolysis	241
Gas Stream Purifier	248
Using Spacecraft Trace Contaminant Control Systems to Cure Sick Building Syndrome	258
A New Material for Removing Heavy Metals From Waste Water	266
Dewatering of Contaminated River Sediments	273

Materials Science

Bench-Scale Synthesis of Nanoscale Materials	285
Synthesis and Characterization of Advanced Materials for Navy Applications	294
Deposition of Tantalum Carbide Coatings on Graphite by Laser Interactions	307
Development of a Unique Polyurethane Primer/Topcoat	312
High Elongation Elastomers	318
Solventless, Curable, Fluid Oligomeric Systems for High-Performance Microwave, Acoustical and Mechanical Applications	337
Plasma Treatment of Polymer Dielectric Films to Improve Capacitive Energy Storage	344
Development of Radiation Resistant Cable Insulations	352
Advances in Carbon-Carbon Materials Technology	361
Casting of Weldable Graphite/Magnesium Metal Matrix Composites with Built-In Metallic Inserts	371
Design and Analysis of Composite Isogrid for Bridge Construction	377
Improved Construction Materials for Polar Regions Using Microcellular Thermoplastic Foams	385

Power and Energy

Use of Magnetic Compression to Support Turbine Engine Rotors	395
Full Wave Analysis of Passive Microwave Monolithic Integrated Circuit Devices Using a Generalized Finite Difference Time Domain (GFDTD) Algorithm	402
A Future, Intense Source of Negative Hydrogen Ions	411
Fiber Optical Solar Simulator (FOSS)	421

Acknowledgments

For information regarding additional copies of the
Technology 2003 Conference Proceedings, please contact:

The Technology Utilization Foundation
41 East 42nd Street, Suite 921
New York, NY 10017
ph.: 212/490-3999; fax: 212/986-7864

NATIONAL TECHNOLOGY TRANSFER WEEK

National Technology Transfer Week • December 5-11, 1993

"Working To Keep America Strong"

Three events came together with the single goal of helping businesses increase their competitiveness and productivity through the transferral of leading-edge technologies.

Technology 2003

**The Fourth National Technology Transfer Conference and Exposition
December 7-9, 1993**

The leading technology transfer showcase once again proved to be a vital business resource for those seeking engineering solutions, new product ideas, improved processes, and prospective partnerships. The opening plenary session examined defense conversion and technology reinvestment, while Wednesday's plenary workshop discussed the Technology Reinvestment Project in greater detail. This 3-day event featured 100 symposia presentations in areas critical to domestic and world growth markets. Workshops were also conducted on how to successfully market to the Federal government, international technology transfer and partnering, and new precision casting techniques. Attendees were also able to tour an 80,000 square feet of exhibits which showcased the latest technologies available for sale or license.

Technology Transfer Society Annual Meeting "How to Make Money in Technology Transfer" December 6, 1993

The annual meeting of the leading society for individuals and firms engaged in technology transfer featured a "how to" approach in addressing "the business of technology transfer." Case studies in the areas of licensing, technology brokering, technology transfer contracts, spinoffs and financing were examined. Other workshops focused on today's "hot" opportunities afforded by technology commercialization and State of California initiatives, and commercialization relationships through strategic partnering and industry associations.

The American Society for Photogrammetry and Remote Sensing "Capitalizing Geographic Information Technology: Market and Finance Opportunities in GIS and Remote Sensing" December 8, 1993

This one-day symposium spotlighted emerging business and financial opportunities in remote sensing, Geographic Information System (GIS), and Global Positioning System (GPS) technologies. The program examined specific industry R&D efforts in these rapidly-growing, economically-critical areas, such as new and emerging markets, new technologies, and market and finance. The meeting concluded with a look at NASA's Commercial Remote Sensing program.

OPENING PLENARY SESSION

DEFENSE CONVERSION AND TECHNOLOGY REINVESTMENT: NEW OPPORTUNITIES FOR INDUSTRY

Introduction by J.R. Thompson

Good morning, my name is J.R. Thompson. I'm the General Chairman of the Technology 2003 Conference. It's certainly my pleasure to welcome you to the world's largest technology transfer conference. It's sponsored by the Technology Utilization Foundation, NASA, and *NASA Tech Briefs*. Four years ago this month the Technology 2000 Conference, with some 2300 attendees in Washington, D.C., embarked on a mission of showcasing America's technology. During these next several days, over 8000 attendees are expected in the exhibit hall, seeing what America does best.

This year we are also joined by a dozen Federal agencies, representing over 100 national laboratories, some 230 exhibitors, and technologists that are presenting over 100 papers. We are also pleased to have with us at the conference this year -- which, by the way, with this week being National Technology Transfer Week -- the Technology Transfer Society, the Federal Laboratory Consortium, and the American Society for Photogrammetry and Remote Sensing.

As you all know, the theme of this year's conference is Defense Conversion and Technology Reinvestment. This theme is both timely and critical in today's changing economic environment. During this conference you're going to hear and discuss the scope of the administration's Technology Reinvestment Project. It is the cornerstone of what the President's Defense Reinvestment and Conversion Initiative is all about. It's a national program supported by the White House and the Congress with budgets this fiscal year of some \$460M-plus and increasing for FY94, our current fiscal year. This initiative, I think, is less about what we are converting from and more about where we are going and what we are converting to, where we as a nation are indeed headed.

Today, with the end of the cold war, national security takes on a totally different meaning and context. Increasingly, we equate prospects for our future economic prosperity more with national security. And there is no more certain road map for achieving this goal than through emerging technologies and technology transfer of our nation's know-how. That's really what this conference here in California in 1993 is all about, is where we point and where we're headed in 10 years from now, the year 2003.

Today we've got three distinguished speakers.

It's my pleasure now to introduce an old friend, Bob Paster, who is the President of Rocketdyne Division of Rockwell International in Canoga Park, CA. Bob joined Rocketdyne back in 1962. His career has taken him through the Gemini and Apollo programs and a lot of America's early missile defense projects. Prior to becoming Rocketdyne's president, Bob led the NASA Shuttle Main Engine Project Team, which has now sent some 157 engines into orbit safely, each engine providing about a half-million pounds of thrust, and there have been no problems and no failures en route. Collectively, the Space Shuttle to date has put up some 2 million pounds of payload, and Bob's team at Rocketdyne has been fundamentally responsible for a lot of that.

Rocketdyne, I think and as you know out here in California, is a world leader in technology. The high visibility programs certainly include not only the Space Shuttle, but also the Space Station, where it provides the electrical power. Bob today is real technologist and leader of one of America's most talented and innovative engineering companies. Please join me in welcoming Bob Paster to the podium this morning.

OPENING PLENARY SESSION

Bob Paster:

It's a pleasure to join all of you this morning at Technology 2003, as you pursue the opportunities in technology transfer and reinvestment. *Pro-active technology transfer*, both as policy and as a reality, is now in full swing, and it's gratifying to see this new dynamic at work.

As you know, all of this has been a long time in coming, in large measure because of overriding policies that restricted cooperative development of dual-use technologies and limited usage in commercial applications. Ignoring, ironically, that much was to be gained through a cooperative effort. Ignoring the fact that other nations were reaping enormous benefits -- and advantage -- through a matching of resources of every kind.

In 1989, that state of affairs in America was fundamentally changed through the National Competitiveness Technology Transfer Act, which followed several years of legislative actions aimed at releasing defense related technologies. Now the transfer of technologies to the private sector and defense reinvestment is not only policy, it has been structured for access and implementation -- with the Technology Reinvestment Project, under the Department of Defense, which will be funded at about \$500 million each fiscal year through 1998 and with CRADAs, funded through federal laboratories.

Similarly, NASA is engaged in moving technologies into the commercial arena with ambitious new efforts and an ever-expanding outreach program. I'd like to take a few moments to expand briefly on NASA technology transfer efforts and how recent technologies originated in the aerospace program are now finding their way into the commercial marketplace -- technologies that have definitely involved Rockwell, and very likely most of you.

Then I'll comment on TRP -- without stealing Steve Wax's thunder, who will be offering an in-depth view of this very important program a little later on -- and CRADAs . . . and the impact of both on the mix. Included in those comments will be an assessment of some of the changes and mechanisms that characterize the new thinking in defense conversion and reinvestment and some of the reasons for our optimism and support.

First, a brief overview of the NASA effort. By charter, NASA has been mandated to promote and encourage technology transfer since its inception nearly forty years ago . . . and continues to be a leading and driving force, both nationally and internationally.

NASA addresses the technology transfer issue in several ways: with *NASA Tech Briefs*, which I'm sure many of you are familiar with; and on a local basis, where area businesses are urged to bring technical problems to regional NASA offices for resolution, ranging from straight-forward problems to highly technical challenges. As an example, the Marshall Space Flight Center in Huntsville, Alabama works with small and large concerns over a seven-state area to great success. And, of course, there's NASA's ambitious outreach program, an energetic, comprehensive effort to bring NASA's enormous range of research and technology expertise to industry for new, "spinoff" creations in both dual-use scenarios and commercial applications.

Just how effective that outreach program has been to date has been reported many times before. Some recent examples you may not be aware of are emerging from the Space Station program and the NASA/DOD National Aero-Space Plane program.

From the electrical power system that is being developed for the space station have come novel elements for electrical contractors that are being marketed commercially by Kilovac, Inc., a small

OPENING PLENARY SESSION

company in Carpinteria, CA. Kilovac is now supplying power contactors based on the Space Station power system design to Lockheed for inclusion in the F-22; and to Boeing/Sikorsky for inclusion in the Army's Commanche helicopter. Kilovac's power contactors are also being used in General Motors/Delco's prototype electric car and Allison's prototype electric bus.

Technology from the National Aerospace Plane -- where materials development is a major part of the challenge -- is also appearing in new applications in other aerospace projects and in unrelated venues such as the automotive, computer, chemical, electrical and medical industries. From those new materials have come an impressive and diverse array of new products, including artificial limbs and joints, computer actuator arms, catalytic converter foils, camera shutters and piston rings, to name just a few. Just five of the NASP program's 800-plus subcontractors anticipate marketing new products that should be worth \$4 billion in sales over the next two decades -- all capitalizing on materials that did not exist prior to NASP.

These and a host of other applications in new venues are being aggressively pursued by NASA, with remarkable results, underscoring not only the value of dual-use technologies but the double value accorded tax dollars. Similar performance can be expected with the Technology Reinvestment Project, which is now well under way.

Last Friday, the Secretary of Defense Les Aspin announced the third round of winning selections in the Project. These selections -- some 66, involving more than 400 organizations -- are in addition to 96 selections previously announced. Together, the winning organizations will be receiving nearly \$415 million in matching funds for their work from the fiscal 1993 budget allotment.

Here are brief synopses of three of the winning proposals from the first two releases.

- A consortium that includes GM Hughes Electronics, IBM, Micromodule Systems, Microchip, Polycon (a small business), and Texas Instruments have joined with Sandia National Laboratories to develop a new method of interconnecting integrated circuits on a common substrate, which recently has become the key to increased performance and reduced size and cost in the microelectronics industry.
- Power One Incorporated has proposed a program to develop an affordable manufacturing process for aerocapacitors -- an inexpensive super capacitor that offers a ten-fold increase in energy density over current capacitors. Included on the team is Rockwell International, Polystor Corp., Airojet and Lawrence Livermore Laboratories.
- TRW Space and Electronics Group has proposed a project to develop precision laser machine tools for drilling, cutting, welding and heat-treating a variety of mechanical and composite parts on manufacturing assembly lines.

In last Friday's announcements, Rockwell-led teams were named in three awards:

- Rockwell's Command and Control division and the Rockwell Science Center will combine with Texas Instruments, AT&T Bell Laboratories/NCR, and the Uniformed Services University of the Health Sciences to develop a trauma care information system.
- Rockwell's Rocketdyne Division and the Rockwell Science Center are leading a team that includes LaSen, INRAD, Wahlico and an advisory panel consisting of industry, national laboratories, NASA, state regulatory agencies and the military to develop "ECOSCAN," a

OPENING PLENARY SESSION

portable environmental monitor that will be able to remotely identify low concentrations of hazardous chemicals.

- A team made up of Rockwell's North American Aviation Division, Caterpillar, Moog, and the Air Force/Wright Laboratory will design and develop electromechanical actuators, electrohydraulic actuators and direct drive valves for industrial and automotive use.

And that's only a sampling. The other awardees present a wide spectrum of technologies and applications. Further, all of the teams conform to a fairly consistent profile: A typical team has a mix of six to seven different entities, often with three companies -- with one or two of them defense contractors, small businesses, universities and government agencies -- Federal, state and local.

That profile parallels the one offered by the Ohio Aerospace Institute, a non-profit organization I have been associated with that was established to promote collaborative research and the adaptation of advanced technology for industry. OAI combines nine major universities with six aerospace companies and two government-operated laboratories and has used the TRP philosophy of collaboration among federal laboratories, academia and industry. OAI is focusing on identifying the technology of end users in industry by finding the underlying technologies that match those needs, as well as supporting research in those areas.

In 1993, OAI has secured or begun a half-dozen contracts in technology development. Included is a contract from ARPA to create a feature-based automatic target recognition system. OAI is also seeking a grant to examine image processing technologies used in target recognition to enhance the readings of mammograms or to detect heart defects. In short, OAI is a stellar example of what collaborative technology development is all about.

And finally, from "what's new": Cooperative Research and Development Agreements -- CRADAs -- which bring leading edge technology from federal laboratories to a host of industrial and commercial needs and requirements.

The Clinton Administration has called for the budgets of all federal laboratories to earmark 15-20% toward commercial projects and applications. While the sheer numbers of CRADAs now reach into the hundreds, let me point to a Rockwell example of technology newly enabled through this mechanism.

Rockwell and DOE have been developing molten salt oxidation technology for environmental cleanup for a number of years. Now Rockwell is negotiating CRADAs with the Department of Energy's national laboratories to commercialize MSO technology. By enabling Rockwell and DOE to pool their resources, these agreements serve DOE's needs. And by securing Rockwell's right to intellectual property developed during the course of its MSO work, the CRADAs serve the national goal of transferring technologies from DOE facilities to industry so that industry can commercialize those technologies and contribute to U.S. competitiveness. This amounts to a mutually beneficial opportunity to leverage resources. And they can help both DOE and Rockwell move faster toward realizing the benefits of this technology.

Integral to all of this -- and consistent with new policies toward the business/government relationship -- is the matter of cost-sharing. In 1960, the Defense Department permitted contractors to consider independent research as allowable. However, costs of development were strictly limited to product lines for which the government had contracts. The government also consistently maintained that costs incurred in co-sponsored projects should be unallowable. In the 1970s, internal research and

OPENING PLENARY SESSION

development concepts were developed. However, companies had to demonstrate the relationship between the cost and the particular military function are operational. Arbitrary cost ceilings were imposed by Congress in the 1980s resulting in inconsistencies and inequities throughout the industry. Concurrent with this stifling treatment of research costs, the government was also very protective of non-recurring funds expended on new products. A recoupment charge required the contractor to make payments to the U.S. Government when the contractor made a commercial sale or other transfer of products or technology. Contrast these regulations with the current climate . . .

At the very end of 1991, DOD announced that IR&D costs incurred by defense contractors will qualify as in-kind contributions made under cooperative agreements. Furthermore, DOD indicated that the resulting contracts were not the type of contract anticipated under the Federal Acquisition Regulations (FARs).

CRADAs were another step in the development of user-friendly instruments to initiate and define a program of cooperative research between industry participants and government laboratories. While CRADAs took a large step to promote technology transfer, there were still difficult issues to be resolved in the areas of intellectual property, liability, publication and non-disclosure terms.

More progress was made in the summer of 1993 when the FAR recoupment provisions were withdrawn, and the Technology Reinvestment Project was established where the recently renamed agency, ARPA, was given statutory authority to award funds for research projects on user-friendly terms. The fundamental principal announced by ARPA is that government contract regulations would not apply. This means: (1) FAR does not apply; (2) Intellectual property terms are negotiable; and (3) DCAA is not a participant. Once again, you should view all of this as a watershed change from business -- and government -- as usual. The rules have changed, and you can expect very different results from the experience of the near past. What was once a restrictive -- not to say exclusive -- arrangement has become a working -- and growing -- cooperative, with benefits to both industry and government -- benefits that are well beyond our most optimistic expectations.

And the bottom line for you here today is that it represents an extraordinary opportunity. On the one hand, to combine your expertise with related and needed skills from another source; and on the other, to access resources that you may need but could not heretofore get to. So I urge you to make the most of it. This is a matchless opportunity, and one that has not been available before. In fact, it might even be said that this is something of an obligation, as well. Because if you don't find a ready match for what your company or agency can do, important environmental or transportation -- or any of a thousand human needs answerable through technology -- could go wanting unnecessarily.

Again, the broadest possible involvement will ensure the greatest possible success. The Latin phrase that you've seen on t-shirts everywhere definitely applies here: "Carpe diem . . . seize the day"... or less literally, "seize the moment." I highly recommend you do it. Together, we can beat a few swords into plowshares... and make America a better place to live in the process.

Thank you.

J.R. Thompson:

Our next speaker is a longtime associate of mine at NASA, Greg Reck. He's now the Associate Administrator of the Office of Advanced Concepts and Technology. Greg received his degree in aerospace engineering from the University of Cincinnati in Ohio and has been with NASA some 28 years, starting with the Lewis Research Center, starting there as a student trainee, and has certainly

OPENING PLENARY SESSION

come up through the ranks. Since then, he's held various positions in research and management in combustion, fuels, environmental monitoring and overall propulsion systems. Greg then moved to the Langley Research Center as head of the Aero-Space Plane technology office, and then in 1987 went to NASA Headquarters and served as the Director of Propulsion Power and Energy. Greg is currently responsible for advanced technology throughout NASA, tech transfer and the commercialization of the technology spinoffs programs. Greg is a major player in promoting and supporting this conference. Please join me in welcoming Greg Reck to the podium.

Greg Reck:

Good morning. It's a real pleasure to be here and I really welcome the opportunity to come out here and meet with all of you. Of course, we're all disappointed, to some extent, that (NASA Administrator) Dan Goldin couldn't join us. He certainly looked forward to coming out, and as late as this past weekend he planned to be here. But unfortunately the activities associated with the Hubble Space Telescope repair mission and, to a large extent, an awful lot of activity that's taking place in the agency right now that's associated with the Space Station and our cooperation with Russia and Russian activities in that which will culminate in another trip to Russia in the very near future are really demanding far too much of his time and he felt he just couldn't dedicate the time it would take to come out here. However, he had worked on the remarks he planned to give here today, and with his permission, I expect to go through those.

But before I get to that, though, I do want to offer my congratulations and thanks to our co-sponsors of Technology 2003. That includes *NASA Tech Briefs*, the Technology Utilization Foundation, the other agencies and universities, and the U.S. companies that have supported this activity over the years, and once again this year, and I think we're looking forward to an even bigger and better program over the next several days, and so I'm very pleased. I think it's a superb job and it's a very important activity from our perspective, not just for NASA and the other agencies, but for the country as well.

We work in a fascinating and frustrating business, you and I. We can do so much for our society, yet it frequently may seem that we are under-appreciated. By that I mean under-utilized, under-challenged, and of course, under-appropriated. I have found that much of the job involves telling that story -- that we have done and we are doing great things, but more importantly that we have an unlimited potential for future greatness.

But, let's be honest with ourselves. The companies, industries, and institutions which are responsible for what we call "modern technology," which have grown and prospered with success, have in some cases also become bureaucratic, ponderous, unresponsive, and tied to old ideas and methods. At NASA, we pride ourselves on having dragged the world into the Space Age. But we are also guilty of having developed, with age, some hardened arteries. We understand now that it is our obligation to take the lead again in revitalizing the R&D community to increase its relevance to today's society.

By way of illustration, let me recall one of our past triumphs in technology transfer. It harkens to the very beginning, when NASA was developing Project Mercury. We needed to test the capsule's ablative heat shield, but we couldn't generate the temperatures necessary to simulate re-entry heating. The solution came in the form of a plasma torch in which gas is ionized by a high-voltage power supply, producing a superheated exit stream with temperatures as high as 10,000 degrees Fahrenheit. For 25 years this technology was not exploited for commercial use. Finally, when U.S. industries and foundries were all but eliminated by international competition and environmental constraints, plasma torch technology re-emerged. Presently, plasma melters are in widespread use, making U.S. industry more competitive, clean, efficient, and cost-effective.

OPENING PLENARY SESSION

However, this is a success story that invites the question, "Where were we for the quarter-century between development of the technology, and its application by industry?" During that interval, how much had we needlessly polluted the environment, how many jobs had been lost, how much profit had been missed, how much energy had we wasted? It is this kind of lost opportunity that we must organize ourselves against. This is why we are gathered here in Anaheim for this fourth annual celebration of good ideas. It is precisely this sort of interchange -- a discussion of what we can provide for each other -- that will re-assert and redefine the role of commercial technology on society.

The difference between being reactive and pro-active is at the root of what the Administration means by re-inventing government, and more particularly, re-inventing NASA. As with the example of the plasma torch, it is the difference in getting out in front of an issue, or reacting in desperation at the eleventh hour, or when it may already be too late.

What do I mean by "too late?" Regrettably, examples abound of where we have lost the competitive edge in the aerospace industry -- in general aviation, in the passenger plane business, in satellite delivery -- I could go on and on. We can re-claim that edge and our leadership in the world marketplace by introducing a new paradigm -- a new way of doing business. The need is self-evident. For if we can agree on ANYTHING, we can surely agree that the existing method of doing business is a failure. It has uniformly failed in all agencies, in the unanimous opinion of practitioners inside and outside of government, and in the opinion of the Congress, the White House, and the general public. It is a systemic failure, not attributable to negligent individuals. Simply put, our current system of safeguards does not prevent bad behavior, and we are not getting the product we are paying for.

These are the principle thrusts of President Clinton's program to improve U.S. industrial competitiveness and the nation's economy. In his Report on Technology for Economic Growth, the President flatly stated that "...leadership in the use and commercialization of technology provides the foundation for America's status as an economic and military superpower."

That is a strong and specific statement. Is it backed up by action? You bet! The President has made technology policy a key element of his economic strategy. In the first nine months of this administration, tax incentives were provided for investments in R&D and new businesses; export controls were liberalized; federal resources were shifted toward basic research and civilian technology; investments were made in worker skills; and defense conversion has been aggressively promoted. Time and again, the Administration has asserted its dedication to a new partnership between government, labor, industry, and academia -- to tearing down the walls that have inhibited meaningful cooperation in the past.

NASA is fortunate to be a key player and contributor in this initiative. Our immediate challenge is to address our internal organization. Last year Mr. Goldin chartered a Special Initiatives Team on Technology Transfer to investigate how we relate to other government agencies, industry, the economy, and society. The findings showed that NASA employees often do not consider tech transfer to be part of the agency's mission. Perhaps as a consequence, our successes in tech transfer are modest compared to the amount of technology we generate and the potential that exists.

Furthermore, we must increase our awareness of NASA as a customer for commercial technology. We do not always employ the proper initiative in soliciting new technology from the private sector. As a consequence of these findings, we are re-tooling our mental sets to acknowledge technology transfer in both directions as a fundamental mission -- on equal footing with any NASA mission. Subsequently Mr. Goldin issued a directive to all NASA field center directors and to officials-in-charge of all headquarters offices, placing technology transfer at the top of their agendas. They were told to

OPENING PLENARY SESSION

consider this new emphasis as a major initiative in NASA, and that technology transfer will become a way of life.

I'd like to discuss a number of proactive steps we are taking to improve the way NASA approaches technology transfer and the commercialization of its technology. First, we are going beyond technology transfer to a more appropriate paradigm for our time – a technology super-highway that links us to you through our Commercial Technology Network.

A critical and immediate challenge in bringing this network into reality is to streamline our internal organization to facilitate quick response to the needs of industry, and pave the way for developing a new way of doing business. We intend to develop a new way of doing business that is built on a commitment to industry: partnerships, dual use technology development, regional alliances, small business development, commercial technology acquisition, and fast-track mechanisms. Six elements that we're going to focus on as we develop and strengthen our own internal capabilities.

Toward this objective, NASA's Strategic Plan has been re-structured around a core of business enterprise units. Rather than relying on serendipity to insert technologies developed specifically for NASA missions into the private sector, we now require that research focus on providing useful technology to industry, to the same extent that it focuses on accomplishing our traditional mission. This does not mean that half of our programs will be mission-oriented, and half dedicated to other national needs. We will conduct programs in a way that accomplishes our mission AND makes maximum contribution to the American economy and quality of life.

Let me describe some of the specific areas in which we are applying these initiatives: Our traditional expertise and capability across a wide range of technologies, from lightweight materials to high-temperature electronics, has application to a variety of sectors such as the automotive industry. We are presently actively pursuing this route. We are discussing joint development of super-plastic forming technology for the production of aluminum automobile parts. Weight reductions of up to 30% can be achieved, and may translate into significant fuel savings. At the same time, this is a dual-use technology, and the products of this research can apply not only to the automotive industry, but the models, techniques and methods we developed can lead to new and improved structures and materials for aerospace applications.

We have initiated an Advanced Small Spacecraft Technology program to develop and apply advanced miniaturization technology for spacecraft design and instrumentation. This program will greatly reduce the cost of space missions. Industry-led Integrated Product Development teams will be used to define, plan, and implement the detailed program content. This will allow the integration of industry, universities, and small businesses into effective teams that fully develop the best ideas and concepts. The high level of industry involvement in this program provides a mechanism for effective technology transfer, and will lead to the development of commercial products.

We will also begin the Industry Technology Program, which is focused on pre-competitive technologies and innovative applications. This program will also use industry-led teams to develop and apply new technology. It will support high-risk research and applications with strong potential for commercial benefits. Priorities will be established by technical and business merit. Cost-sharing by industry will be a prominent element of this effort, to ensure a vested interest in successful and timely commercialization.

NASA's Office of Aeronautics is developing a new level of interdependence, communication, and partnership with other government agencies, with industry, and with universities. The aim is to enable

OPENING PLENARY SESSION

research and technology development to be shaped by and to influence the design, product development, manufacturing, and certification. In addition to the collaborative aspects of the High Speed Research, Advanced Subsonic Technology, and High Performance Computing and Communications programs, NASA Aeronautics is currently involved in more than 400 cooperative programs with industry and government users.

Twenty-one partners from industry and twenty-five from universities are involved with NASA's Advanced Communications Technology Satellite. Over the next two years, more than 50 experiments are scheduled in areas ranging from business communications to supercomputer networking to remote delivery of health care services.

In the area of micro-electro-mechanical systems, or computer-chip-sized machines, NASA is in the process of finalizing eleven cooperative agreements with industry. Efforts such as these will help us build bridges between NASA and industry, as well as between aerospace and non-aerospace markets. Our objective is to leverage our resources and provide benefits to numerous sectors of the U.S. economy. And we plan to monitor our success by establishing clear and sensible metrics to measure results. These metrics will focus on areas such as new products to market, and new jobs created.

I hope this illustrates to you that the NASA headquarters and field centers are getting organized to serve you better. The NASA Commercial Technology Network directly commits our senior management to this new way of doing business. We have elevated Commercial Technology to the same level of importance that we give to mission programs. The Commercial Technology Network leverages our people with state-of-the-art brainpower, located across the field centers. This technology superhighway is to be our delivery system to meet your needs on a timely basis following commercial norms -- not prolonged government bureaucratic response. The field centers will be authorized, delegated and empowered to enter into innovative agreements, with the necessary discretion to fund commercial technology applications development.

And more changes are on tap. First, during 1994, NASA R&D activities will include plans for partnership arrangements with the commercial sector. The goal is to devote 10-20% of NASA's budget to these partnerships. Second, our contractors will be required to identify commercial applications of the technology they develop for us. A part of their performance and their proposal evaluations will be based on the plans that they submit for commercial applications.

Third, as part of our commercial technology network, we are establishing at each field center, an organization to link individual entrepreneurs, small, and large businesses with NASA technology. A number of centers have already established new commercial technology organization reporting directly to the Center Director. We'll define our success as having achieved our commercial technology metrics in each enterprise area. We'll know we're succeeding in helping the national competitiveness if we are successful together into pulling our resources, our know-how, and our experience in a winning alliance. It's already well beyond the eleventh hour. There's a sense of urgency at NASA and our culture is poised for change. We're ready to work with you to create jobs, to create new businesses and to help strengthen your competitiveness. Our partnership is the key to ensuring an American future of restored, renewed and redoubled prosperity. We welcome your business and invite you to call on us and count on us.

Those were the remarks that Dan had prepared to give. We, of course, have been working very closely with him in undertaking the kind of changes and efforts described. We do expect and anticipate that over the next few months and year that we are going to be taking a very critical and

OPENING PLENARY SESSION

close look at the Technology Utilization and Applications Programs within NASA. The aspects and elements described here are parts of that proposal. We're going to be re-examining all of the components of our system. We're going to be looking at how we utilize the National Technology Transfer Network that's in place and how we utilize all of the existing structures. Where they are working, we'll reinforce them; where they need change, we'll change them; and where we need new mechanisms, we'll put those in place. It's going to be a very rigorous and a very dynamic period, and we're committed to making the kinds of changes that this administration expects NASA to make. It's absolutely essential that if NASA is going to continue as an agency that we succeed not only in the traditional NASA missions, but that we also demonstrate to the Congress and to the public our relevance to the economic well-being of this nation.

I appreciate your attention. Thank you.

J.R. Thompson:

President Clinton was out in California last week talking about the Technology Reinvestment Project and what it's all about and what it can do for California. This morning, our next speaker is the man with the money, Dr. Steve Wax, who's the Chief of Staff who serves with Lee Buchanan and runs the TRP. Steve oversees a staff responsible for running this program, which includes the evaluation, selection process, etc., as well as the interagency coordination that's involved. Steve is an active-duty Air Force Lt. Colonel. He's on loan to ARPA from the Office of the Secretary of the Air Force. He has some 18-plus years in defense R&D projects and technology, serving more recently as a program manager at ARPA and a program manager for the Air Force Office of Scientific Research. He graduated from the University of Massachusetts, University of Illinois, and he received his Ph.D. from the Georgia Institute of Technology. Please join me in welcoming Steve Wax to the podium.

Steve Wax:

Thank you. Thanks to NASA and the other hosts for inviting Lee Buchanan. He sends his regrets he was unable to attend. I'd also like to congratulate Bob Paster for both winning awards and speaking so eloquently about TRP.

People think of TRP as an inter-agency solicitation. Let me mention the agencies, because the cooperation in this program has been exceptional. Of course, ARPA leads the Department of Defense, but it's a joint-agency program: National Science Foundation (NSF), National Institute of Standards and Technology (NIST), Department of Energy Defense Programs, the Department of Transportation, which newly joined this summer, and of course, NASA. Greg Reck is, in fact, the NASA representative for TRP. What I want to talk about is, of course, TRP, but I also want to put in perspective in terms of this whole idea of technology reinvestment, especially from the Department of Defense side.

It's quite clear that DOD is committed to maintaining a strong national defense, and spends a lot of money, something like \$37B in R&D funds, to that end. Defense, despite the draw down, is still a major player in the Federal government's, and the nation's, R&D arena. What's changed from an administration point of view is an admission that what's also important, probably most important for defense, is having a strong industrial base. TRP is the beginning cornerstone, the recognition that in order to have a strong defense you need a strong commercial base and you can no longer keep the two separate. Defense, in the past has been accused of, and in fact has, developed its own technology for its own purposes. When spinoffs occurred, and there have been many, it was most serendipitous. However, that is changing. Now what you're seeing is a concerted effort by defense to

OPENING PLENARY SESSION

conduct their R&D with the industrial base in mind. We can no longer afford this separate defense base, first of all because we have declining defense resources and secondly because commercial technology in many cases now leads defense technology. To not make use of that industrial base would be foolish. So what we see in the components of defense are really two aspects: defense will do what it needs to develop systems that it needs for defense of the nation, and when there are dual-use or industrial based spinoffs, that is great. But what we're seeing is a growing sector of defense R&D where dual-use technologies integrated in the industrial base is the main thrust, and where you needed that benefit is a requirement. And that really is what TRP is all about. Not only TRP, but, as most of you are aware since tech transfer is the theme here, this whole concept of dual-use is pervasive throughout defense and throughout the Federal government. TRP is really the beginning of this integration of the industrial base. The solicitation is really just part of an ongoing thrust, one we expect to continue of this integration.

The three areas of TRP are:

- **Technology Development:** is the development of the dual use technologies, the spinoff technologies that most people are familiar with. That, of course, is one of the key aspects of TRP and the projects that Bob Paster described earlier come from that section.
- **Technology Deployment:** is much closer to the tech transfer theme of this conference. In this area, extension services and other tech transfer mechanisms are established to take technology either from Federal technology sources and transfer it to small and medium-sized businesses, or to provide those businesses the links and help they need to be vibrant in this changing world. One of the keys here for defense is when you help small and medium-sized businesses anywhere in this nation, you are essentially helping the defense base since the overlay of defense contractors and the small and medium-sized businesses is almost one-to-one. The defense industry is pervasive and helping these businesses is critical.
- **Manufacturing Education and Training:** is longer term, but in some ways most interesting. TRP is trying to change the way manufacturing is taught in our institutions of higher education, creating new curricula that go cross-campus, or in many cases, cross-universities, and make manufacturing much more of a, shall we say, respectable academic pursuit rather than taking engineers with engineering degrees and thrusting them without experience into the manufacturing arena. That is an extremely interesting arm of TRP.

The foundation of TRP, and the reason it represents major thrusts is because this really is a joint effort and a joint philosophy of both this administration and Congress.

When President Clinton talks about \$1.8B in defense conversion funds, he's talking about the Defense Conversion, Reinvestment and Transition Act. This is the program that will be \$20B over the next several years. The defense TRP is a part of that program. Last year it was about \$470M worth of that program, with the other parts going toward base closures, personnel assistance, etc. So it's not the entire \$1.8B, but the technology reinvestment portion which is funded by eight different congressional programs. That is basically the technology cornerstone of defense conversion for this administration and as mentioned before, led by ARPA but with the full cooperation of the other five agencies.

The key requirements for TRP, although the solicitation is over, are still in the statutes and are indicative of a trend in the way the Federal government is going to relate to industry. The first statement, Competitive Award, is something that, for TRP in particular, was very important. I can

OPENING PLENARY SESSION

assure you that of all the things TRP can be accused of, we should never be accused of not selecting something strictly on the merits as we evaluated it. This was a full and honest competition. More to the point in terms of how we deal with industry, the theme really is partnerships. The first point -- the statutes, TRP and other dual-use activities -- require partnerships, require the proposing industries to form partnerships: partnerships with universities, partnerships with Federal laboratories, partnerships with state and local governments. That's a requirement and an essential part to get good teams proposing, to get good teams interested in this technology reinvestment. The second partnership is one between the Federal government and the proposers, and the ultimate winners, we hope.

The requirement in statutes, the requirement for TRP is cost-sharing. No longer will the Federal government, no longer will DOD strictly say, "Here's what we need, here's your money, go do it for us." In order to get to an integrated military and commercial industrial base, we need a partnership between the Defense Department and industry. The end product of these efforts have to be end products that are beneficial both to DOD and to the proposers. The cost-sharing requirement of putting something real on the table by the proposer is an essential part of that. For those familiar with the ATP Program at NIST and other similar programs, you'll find that's a theme throughout the Federal government. For TRP, that's not a requirement that it be cash. In fact IRAD, as was discussed earlier, is a more than acceptable form of cost-share. Incoming services, salaries of personnel, fair-market rental value, there are lots of ways that proposers can and did come up with to meet these requirements. But the important thing is, it's a partnership. Proposers that won really made that clear, that they had a partnership with the Federal government.

Defense emphasis is a defense program, but the real emphasis in defense is on making sure that the products and processes that come out of this program are beneficial to defense and dual-use nature. That really describes the common requirements and is really the theme of TRP.

Starting with the March 12th announcement by the President at Westinghouse, through a multitude of discussions, through solicitations, with proposals due July 23rd, we are now in the final phase of the FY93 TRP Program. The key is the five agencies plus the military departments. Those are the executors of these efforts. That really has two benefits. One is, with ARPA being involved in all of them because they are in charge of the money, but in fact the agencies will go out and execute these. What that does is it spreads the TRP efforts across the Federal government.

The philosophy of TRP, which came in many ways from the philosophy from ARPA, is that these agreements with proposers need to be mutually beneficial. TRP has very liberal views in terms of patent rights -- basically, it's negotiable between the partnership and the Federal government. IRAD is accepted. There are a lot of things ARPA does by its other transaction mechanism that, people who have worked with it make it a very nice instrument to be a partnership between the Federal government and the proposer. By having these efforts distributed across the Federal government, one of the real benefits is that other Federal organizations which tend not, at least in the past, to have been as forward-looking as ARPA, are beginning to really get there. NASA for one, DOE and others have come right along with these cooperative agreements and are beginning to pick up this philosophy of really making this partnership work. We think that's a very constructive point for the cooperation.

This program was clearly oversubscribed. We received over 2800 proposals, worth about \$8.5B. We have about \$460M ourselves. We were very pleased on one hand, of course, but the percentage of winners will be very small just by the nature of the solicitation, and that is a downside. We saw a very diverse array of participants: small businesses, universities, foreign-owned companies, foreign

OPENING PLENARY SESSION

companies. We thought that was very good. We have just completed a very elaborate, multi-tiered selection process. We had over 300 technical evaluators from the six agencies. It was a very competitive process and we really believe that the proposals that won were the best that we saw. To date, we've announced 162 proposals, about 85% of the funds. President Clinton made the first announcement on October 22nd in a press conference with Vice President Gore. Both did, and continue to, speak well of the program, as do Congress, so we in fact have complete agreement, in this program at least, between the administration and Congress about value, where it's going and what it needs to do.

There are several myths that TRP had. The diverse array of winning proposals we've announced to date, I think, set many of those myths aside. We've talked to defense contractors who've said this program is not for us, this doesn't help us get anywhere. In fact, a multitude of defense contractors won awards. We talked to non-defense contractors who said that clearly this is just geared for defense contractors. That wasn't true either in proposing or in winning. Apple Computer and others that you don't think of as traditional defense contractors were awardees.

People told us up front that we were only going to make large awards when in fact we've had awards as small as \$80,000 and as large as the \$20M range, so there's quite a wide variety. Again, there was no bias other than, "Did you put in a good proposal?"

We saw small business represented. On the winning proposals in technology development, for example, of the 46 announced to date, 22 of those had at least one of the participants being a small business. Does small business lead a lot of proposals and take this over single-handedly? No. The cost-share, I think, was too tough for them. Did small business participate? The answer is yes, and in many cases they were paid for by the larger corporations, so that they would be present -- larger corporations picked up some of their cost-share.

The same is true of universities. Universities were extremely well-represented in the technology development and in most cases, they did not put up the full 50% cost-sharing. In fact, the industry teams helped the universities. What that says to us is that industry wanted that university with them because they needed that capability and they were willing to pay for it. We think that's an extremely good feature.

Just to show you some diversity, you should be aware, we'll say this a million times, regional bias was not part of TRP selection process. What we see now is the array of cumulative of all the participants. People won in areas where there was a lot of technology capability, like California. There were a lot of California participants. In general, what you see is a very wide display of winners. We biased our selection process toward no one.

In a preliminary assessment of TRP, we are still in the process of trying to see what we got and develop lessons learned from this particular solicitation. The first one really doesn't need much more analysis. The cooperation among the multiple Federal agencies was outstanding! If nothing else, it was certainly a lesson on Federal cooperation, that it can be done if the people at high levels are willing to make it happen.

We also saw a surprisingly robust response to what in truth was a very complicated solicitation. For those who proposed, it's quite clear we had a multi-faceted solicitation with three different areas. We got lots and lots and lots of excellent proposals, far more than we're able to fund, which is, again, the downside. We saw some meaningful and unique collaborations, some large well-integrated teams, both horizontal and vertical teams. We saw government-industry-university teams, the inclusion of

OPENING PLENARY SESSION

small business. I will say, there were clearly some teams that were just paper teams. I think that's to be expected with this large a solicitation. There were some reports on certain site visits of team members introducing themselves to one another. That's probably not the first time you ought to meet if you're writing a proposal.

On the other hand, I think, overall, judging from the proposals and having read many, many more than I wanted to, the teams were in fact very solid and well organized. We saw lots of participation by the state and local governments. I think that was good as some of the statutes on regional technology alliances required that. States like California, for example, actually had matching funds. In terms of matching funds, most of the teams also put real matching funds on the table. We saw some that were, shall we say, less real than others. But in fact, most of the time, the proposals included things of real value by the proposer, and that's what we're looking for. Remember, there's a requirement to have a commitment by the partnership alongside the Federal government.

Finally, although it is a bit early, I think we have a promising start to this concept of military/commercial integration. We saw some very innovative dual use programs. Workforce retraining in the education field was very good. In the deployment, there's an awful lot of infrastructure support that's now being established that we think will be very helpful. We saw a lot of anecdotal evidence of impact. Of course, it's hard to assess, but we've heard cases of where teams formed to do the proposal and, win or lose, feel they are now better off and ready to do something of value.

Obviously, the final assessment of this whole issue of how you judge this, the final assessment is years away. This is a long-term program, this isn't a short-term program. This doesn't solve immediate base closing issues. It really goes to the longer term of addressing the overall economic base. So to assess as to how these programs are working in any meaningful way will take some time.

Where do we go from here? One thing is clear: the TRP statutes appear to be well funded. That's certainly true for development, less true for the area of deployment. There's also some additional funding in FY94 for education. So, in terms of technology development, the statutes are extremely well funded for FY94. Once again, they still require collaboration, they still require partnerships, cost-sharing is still an issue. There are some breaks included in the authorization language for small businesses. But, in general, again, we are asking partners to share.

The real question is "What do we do in FY94?" Right now, there is no official position about what DOD will do in FY94. Let me say, however, having heard this enough times from enough high-level officials, I would be extremely surprised if we did not use some of the FY94 funds to fund some of the very good FY93 proposals we received that would be un-funded otherwise. We clearly received a lot of good proposals, a lot more than we could fund. We understand and are sympathetic to the amount of time and effort it takes to put one of these proposals together, and I think, from all the discussions I've had, it's clear that TRP will do some of that. What isn't known is how much of the FY94 money will be used that way and what the plan is for the other. There are some options, no commitments. It's possible to do a limited FY94 competition where you focus on some key areas. It's also possible to do a larger competition, again, taking lessons learned and implementing them in FY94, may be even in conjunction with FY95. That's pretty much all I can say and all that's known right now about the future.

The FY94 appropriations, and what's interesting to note is that the \$324M was the President's budget in the appropriation. Congress added \$150M, which is kind of unheard of, to this area. The statutes that are funded, as I mentioned before, do not include technology deployment statutes. The TRP

OPENING PLENARY SESSION

statutes, that's \$404M, most of that is in technology development. So, from a technology development point of view in the appropriations bill, there's a very heavy emphasis, and in fact a significant increase, in the technology development area. I think there are some issues still being worked on about the difference between the House and the Senate -- stay tuned for other fiscal information. But at a minimum, technology development is well funded.

What good does \$470M do in billions of dollars worth of down-sizing? It's quite clear, and I'd be lying to you if I said, that TRP is not going to convert the defense industry. There's not enough money, and for those of you who work in the defense arena, you'll probably agree that acquisition reform is probably much more beneficial to any immediate changes in the way defense does its business. But what I think TRP really does, and what this whole concept of technology reinvestment does is it, first of all, allows specific participants to capitalize on underutilized technical capabilities. We expect that to be magnified and grow. We expect that as new products and processes come out, this will have long term benefits -- remember, not short term benefits.

Finally, and really last but not least, TRP really is providing a model for a long term structural change in both defense R&D and, I think, Federal R&D. This concept of partnership between the proposers, between industry, partnerships between the Federal government, I think that's here to stay. I think that's a benefit to defense. I think that's also a benefit to corporations, universities, etc.

Thank you very much.



PLENARY WORKSHOP

HOW TO DO BUSINESS WITH THE FEDERAL GOVERNMENT: THE TECHNOLOGY REINVESTMENT PROJECT

Introduction by Frank Penaranda

We have a special treat for you today, under the umbrella of "How to Do Business with the Federal Government." We are going to emphasize the recent Technology Reinvestment Project, brought under the Defense Conversion Act, the process that took place over the past year. We initiated this conversation yesterday morning and there was such a good response that we decided to focus this morning's session on that process. We are very privileged to have some senior folks from the four major agencies that participated in TRP and that are participating in the broad technology transfer movement of the Federal government. My name is Frank Penaranda, and I'm Director of Technology Transfer for NASA, and one of your hosts.

With me this morning is Steve Wax from the Advanced Research Project Agency (ARPA) of DOD. Steve is going to provide an overview of TRP, of which he was a major architect and certainly participant. Next to him is Kevin Carr from the National Institute of Standards and Technology (NIST), which is also one of the architect agencies of TRP. Mike Long, from the Department of Energy, is next to him.

Our approach is for Steve to make his presentation and then for each of the other agencies to speak about their programs: how they have participated in TRP, what their involvement is, and then some broad areas of information about how you can reach those agencies to meet your tech transfer needs.

Steve Wax:

Thanks Frank. Apologies to those who were here yesterday. Obviously, by the nature of the project, some of the discussion will have to be the same on TRP. What we'll try to do this morning is give it a slightly different focus, maybe a more personal and informal focus. I will do the overview, trying to put more emphasis on what we saw, what we liked, what we didn't like in terms of proposals, after a briefer background on TRP itself. We have representatives from other agencies who will pick up both from their agencies perspective of TRP and into other opportunities that are similar or spinoffs or related in some other way to the idea of idea of technology reinvestment and defense conversion.

Just a reminder of where TRP fits into this whole concept of technology reinvestment, defense in its downturn is looking at new opportunities, and in this administration, is convinced that an integrated military/commercial/industrial base is essential. And this integrated base is what this whole concept of dual use and defense conversion from a technology point of view is really aiming for. Defense can no longer afford to maintain its own R&D for its own products uniquely. That's because of two reasons: one, because with limited resources that becomes very difficult; and, in many cases, commercial technologies lead defense technologies, so it would be silly of defense not to make full use of an integrated base. TRP is really one of the key administration programs. It's a multi-agency program. NASA, of course, Department of Energy, National Science Foundation, NIST, Department of Transportation, as well as the Department of Defense are involved.

There are three arms of this project: development, deployment, and manufacturing education training. Technology Development is primarily dual use technologies trying to foster that integrated base from a technology point of view. Technology Deployment is really trying to assist small and medium-sized businesses, make the best use of technologies, capabilities and practices that already exist that they may not have access to. Kevin Carr from NIST will spend some time talking about deployment in

PLENARY WORKSHOP

particular and how that might assist any of you who are small and medium-sized businesses trying to get technology transferred to you from, for example, Federal laboratories. Manufacturing, Education and Training involves trying to reform the educational structure, obviously university-led programs, but the requirement of this program was to have industrial participation as well. Successful proposers did have industrial participation, to really make manufacturing a more substantial part of universities and higher education curriculum.

The funding comes from eight different programs within the defense conversion overview. Of the \$1.8B in defense conversion for FY93, approximately \$470M of that was set aside for technology reinvestment falling in these eight different statutes. The first four relate primarily to development, except for regional technology alliances, which is also deployment. The next two are extension programs and the last two are education programs. So you see, within the appropriations, there was sort of a Congressional distribution of how the emphasis should be between or among development, deployment and education.

You'll also note that we took out 1.5% of this program for small business, so we, in fact, have under TRP a separate Small Business Initiative. That solicitation was later than the TRP main solicitation. It was more focused in that it was only on technology development, it only allowed 11 technology areas. Also, the criteria for that were the same criteria used for all of the SBIR programs. Although this was TRP, although this is being evaluated jointly, even as we speak, by the six agencies, the SBIR part of TRP was extremely similar to all of the SBIR programs throughout the Federal government. There was \$7M set aside; in fact, ARPA has added another \$7M to the Phase I, so we will double the awards to approximately 150 Phase I awards. They should be announced early next year (1994). So that's an opportunity that we've added to. I expect that to be an additional part of TRP efforts and additional dual use efforts, as I see this as a particularly successful way to reach the small business community.

Again, briefly, the common requirements for the main TRP program are that everything is competitive, the emphasis is on partnerships, and that partnership includes both who participates and the fiscal partnership between the Federal government and the proposers. There's a requirement that at least half of the money comes from the proposers. We think that's extremely important since that commits the proposer to the project. If the proposer can't put real commitment in the form of real cash or real valuable assets on the table, then obviously that is not a proposal that we will accept or award. Finally, defense emphasis, the money is defense money, and this concept of dual use for defense, of course, in an integrated industrial base is required.

I'll spend a little more time on the update parts and where we're going and try to provide some views into both the evaluation process and what we thought were good and bad in the proposals we received. Comments will be general in nature. Our plan is to formalize this and get back out to the community with what we thought were the shortcomings. One of the issues we want to hear are what were the shortcomings of our solicitation and request as well. We received over 2800 proposals from a very diverse array of participants.

If you look at Technology Development, which is what people traditionally think of when they think of ARPA, for the approximately \$200M that we have available we received requests for approximately \$6.4B from the proposers. Oversubscribed is probably an understatement in that case, and we are extremely sensitive to the hard work that went into those 1900 proposals and the fact that we are going to be able to fund very few of those. Of the things we kept track of, about 2% were historically black colleges, universities and minority institutions; 13% of the participants were small business; 1% were small disadvantaged business; 1% were foreign-owned business; and the rest, approximately 83% were other standard eligible proposers. That's for the participants. I will say that small business

PLENARY WORKSHOP

was better represented on individual proposals than as participants at large. That is, one of every three proposals had a small business on it. We think, therefore, that small business was involved more than this 13% indicates.

We had a multi-tiered selection process. To take some of the mystery out of "how do you handle 2800 proposals," the first thing we did was to clearly divide the proposals by the three technology areas, so we basically had three separate, parallel evaluations going on: one for technology evaluation, one for technology deployment and one for education. In each of those, there were five tiers of evaluation and review. The first two tiers were made up of over 300 evaluators from across the agencies that took these proposals through, evaluated them against the criteria, made some decisions about whether those proposals should be funded or not based on a quantitative scoring approach against the criteria, moved it up to the next panels, which focused the technologies, focused the groups a bit, did their thing with the proposals that came up to them, passed on their recommendations to the next level -- in fact there was a final review level which looked at all three areas together to make sure that they all matched, that TRP was presenting a unified program. That was presented then to the key members of each of the agencies who, I will add, approved the recommended program without alteration. So, there was a very formal process, a very well-documented process that every proposal went through, and that was truly a joint process across all agencies, dominated by no one agency. We are, of all things, proudest of the evaluation process that we put in place to ensure these would be fairly selected.

The selections themselves, as I said, we've announced 85%. The Office of Secretary of Defense Public Affairs has a number through which they will send out the complete list of TRP winners. So if you are interested, it's (703) 697-5737. What you'll receive is a list of all the participants and a single paragraph on each of the awardees. The paragraphs in there are vague on purpose. Keep in mind that the 162 proposals that have been announced really have been announced for negotiation. Until the government and the proposers come to agreement about what the terms of that project are going to be, everything in there is really still owned by the proposer. So, we've tried not to provide a lot of information. It's really up to the proposer to decide if they want to provide some information to the press or to whomever. Most of the winners have been very willing to discuss, but it's really not our position to provide that information.

What was good and bad in some of the proposals? As I said, the winners included companies that we don't think of traditionally as defense contractors. Johnson and Johnson, Apple, Rio Grande Medical, which is a small company that won one of our first awards. Of course, people will say it's not for defense contractors, which is not true. Yesterday we had someone from Rocketdyne who was a winner. Rockwell won, Hughes, GE also won. TRP is not for small business? Although only 10% of the winning participants were small businesses, 38% of the winning proposals had a small business on it. 47% of the technology development proposals had at least one of their participants a small business. What that says to us, and what we thought was good about this process, was small businesses and universities were carried by major corporations as part of their teams. And in many cases, carried fiscally as well as just being on the proposal. As I said, universities were well represented as well.

We were told that the way we structured the solicitation made it very difficult for national labs to participate. I think that proved to not be true and I think in the first awards, Sandia did very well. All of the organizations got their labs very involved. The other thing that people said was, "Do I propose a big project with lots of people? Do I propose a small project with just a few people? Where is your bias?" We had no bias. We were only interested in what you were proposing and how well it met the criteria.

PLENARY WORKSHOP

Consequently, we had a very large range of numbers of participants on proposals and dollar values for the proposals. I don't know what the largest winner was in terms of number of participants, but I'm sure it was over 20 or 30. We had some winners with just a couple of participants. We had dollar ranges that went anywhere from \$80,000 up to over \$20M. I think you can see there was really no way to game this, and that's what we intended. It was really good ideas and good plans that were successful. We didn't bias this at all by region. It just came out however it came out.

I need to stress this every time I speak: the cooperation among agencies was outstanding. One myth that was debunked is that you can't get six Federal agencies to work together. Not only can you, but we did, and I think it was exceptional. And also, we had a very good response to a very complicated solicitation. One of the issues that we are aware of is that we need to provide feedback, and get feedback, from proposers about the process itself.

We saw some very meaningful and unique collaborations. Let me tell you we saw some that weren't so meaningful or unique, and as I mentioned yesterday, there were examples on site visits of partners introducing themselves to one another, and that is not what we mean by a meaningful relationship. In many cases it was clear that proposers had worked together and established a very good proposal together. In many cases it was clear that participants were just "stuck on." That's obvious from the proposal when a participant isn't really fitting into a plan. It shows up. When one proposes to these kinds of things, when you put partnerships together, if they are not real partnerships, it will show up in your proposal. It's very hard to hide that.

We saw a lot of participation by state and local governments. The states many times put up matching funds. I will tell you, and we've told the states this as well, the fact that a state backs a proposal does not help that proposal in the evaluation process. The value that a state can add to a proposal is by making that proposal viable at all. For example, if you are a small business and cannot come up with the matching funds and the state can help you with that, the state has made your proposal possible, and you'll win or lose on the merit. States and other support can enable proposals to come through in the technology development area, for example, but they were not considered part of the criteria. A letter from California saying you had won the California TRP did not give you any advantage in the proposal evaluations.

Now, in technology deployment, where state and local governments really needed to play a large role in extension services, then the role of those was more critical. But in technology development, for example, the role of the state was not critical in terms of its support with the exception of regional technology alliances. That was a statute that was set up to develop regional technology areas or regional extension services specifically to service a state or local region. In that case, a state or local government had to be involved. As we said yesterday, it's a promising start, but we need to see how this goes.

This whole idea of cost-share and cost-match -- let me give you some feedback on this whole issue of what's a good cost-share, what's a good cost-match, what looked good in proposals, what didn't look good in proposals. The whole concept of having proposers put up 50% is to show that the proposer really cares that they're getting to the end. The Federal government is putting up some money, obviously the Federal government has to want to be there. But the proposer has to show that they want to get to the end product just as badly as the Federal government wants to get there. That's kind of unique, certainly for DOD, which in general just pays somebody to get where defense wants to go. In this case it's a true partnership.

PLENARY WORKSHOP

One of the criteria for technology development was commitment of the proposer, and one of the surest forms of commitment was to put some real value on the table in terms of your cost-share. Most of the proposers did that. I will tell you that there were some things that clearly were not good cost-match. There were clearly cases where what was put up were things that the proposer had done a long time ago without really a lot of thought to what the real value to this project is. There were also cases where the proposer had an ongoing program off here to the side and said we're going to count as it moves along as part of our match. But it wasn't tied in any way to the program they had proposed. The thing to keep in mind, and one of the feedback we hope to get out to proposers is what are we really looking for in this way of cost-match, of business plan. If there was any difficulty the proposers had, and I guess we would expect this, it's the business side of the TRP proposals. Technically, people did fairly well. I think where people failed, in general, was on the business side. Coming up with a good plan, a good plan to get to a product and coming up with some decent cost-matching.

What's next from our point of view? The FY93 selections have been made. We are waiting for the final round of announcements. We have about \$50M more to provide. We are also trying to make some decisions about what we're doing with FY94. Our plan over the next several weeks is to send out letters to proposers who have no opportunity for either FY93 or FY94 funds. Just looking at the numbers, it's going to be a lot of proposers. It doesn't mean necessarily that the proposal was bad, just that there are limited resources and we received a lot of proposals. The first letter that proposers receive will be from ARPA, the TRP saying sorry you weren't selected.

Our plan is to follow that with some help. Depending on what activity area you were in -- development, deployment, training -- we'll tailor the next correspondence to that area. We will try to, in the case of development, provide some feedback as to how you did in the evaluation process. Deployment is actually planning to have specific workshops to work with proposers. Education will be closer to development. So the plan is to try to provide as much feedback as we can. I will also tell you that with 2800 proposers we will not be able to do one-on-one debriefings. I'm sure you can imagine the time frame that would take. Probably not useful to anybody. But we are going to try to provide as much feedback as we can given the time and the number of proposers to the process. We also are going to entertain feedback in the other direction. We're very sympathetic to the fact this was a large solicitation that cost people a lot of money to put in proposals and we're going to try to make sure we understand all the issues.

Finally, what's going on in '94? The statutes, again, are well funded, certainly in the technology development area. We expect, again, collaboration, partnerships, cost-sharing. The authorization language had some breaks for small business that allowed them to count some of the money they get from the Federal government under certain programs as part of their match. So there will be some breaks for small business in the next incarnation of TRP, but still that cost-sharing requirement will be there, as will partnerships.

It's almost certain -- as certain as we can be without an official position -- that we will be spending some '94 money on '93 proposals. Otherwise, we're not really sure what the next '94 competition will be. Will it be limited in scope? Will it be as broad as this one? One thing is sure is that we want to make sure we have feedback and interaction. With that, I'll turn it over to Kevin Carr from NIST. Kevin will expand a bit on the deployment side. Even if you aren't a winner, but need some help in manufacturing, this is a good opportunity.

PLENARY WORKSHOP

Kevin Carr:

Good morning. I am going to talk just a little bit about TRP and in particular this morning deployment. If I could emphasize, I was listening to Steve as he was talking about how closely the six agencies work together. We hosted the deployment selection panel out at NIST, and the accommodations were basically trailer offices where we packed at least five or six people so the closeness was real. Technology Deployment really was broken down into four different areas. Manufacturing Extension Service providers is the first area, which focuses on establishing extension centers -- extension systems in some cases -- and industrial extension infrastructures that are based at universities and some cases based at states. The principle purpose of these extension services or systems or centers is to work with small/medium-sized manufacturing firms helping them to adopt newer, more advanced manufacturing methods and technologies. So that was the first category of TRP -- deployment.

The second category -- it's called Extension Enabling Services -- dealt mainly with the infrastructure that needs to be put in place as you establish these extension centers and extension systems throughout the U.S. There's a layer of integration services that need to be provided for these centers so that they can link themselves together, share resources, leverage off of each other. Within the context of extension enabling we were looking for programs and projects that looked at electronic communications among the centers, that looked at a national evaluation system for the center's activities and that also looked at training. As we establish extension systems and extension centers throughout the U.S., there is a need for training engineers and scientists and MBAs in the process of extending services to small/medium-sized firms. So extension enabling services really focused on that layer of support infrastructure that would be put in place for the extension services.

The third category, Technology Accessed Services, really dealt with the extracting and packaging of technology that you might find in the federal laboratory systems -- particularly the technologies that you may find in the DOD and DOE laboratories. There is an understanding out there that a lot of this technology exists in its rawest form and could be put to use and help make these businesses more competitive if it was made available to the small/medium-sized firms.

So proposals in the category of Technology Accessed Services focused on taking a technology-oriented problem and marrying it with a technology solution from the laboratories. And in some cases that solution may not be hard technology, it may just be processed information and it also may be expertise that's in the laboratory system.

The last category was Alternative Deployment Pilot Projects. That was sort of a catchall that was set up for the extension areas to say that if you are not an extension center or system, if you are not an access service, if you are not an enabling service, if you are not any one of these models that we think we have already figured out, perhaps you fit into this category. We got some very creative proposals in this category, but we also got some very innovative proposals in this category that were funded. The types of proposals we were looking for, and a lot of what we got, focused on the area of supplier chains: improving the relationship between major OEMs and their suppliers throughout the tier levels. Also, programs which focus on electronic commerce. So they were the four basic TRP areas in the area of deployment that were put together for the process, and that seemed to work out pretty well.

I am going to talk to you a little bit about what is going on at NIST, where I work at NIST, how this TRP process -- in particular deployment -- relates to the things that we are doing at NIST.

PLENARY WORKSHOP

At NIST I work on a program called the Manufacturing Extension Partnership. As you can see from the view graph here, we have been tasked by the administration -- in particular the President through the Secretary of Commerce -- to establish a network of over 100 manufacturing extension-type centers throughout the U.S. The plan is to have that network in place by 1997. The objective of the centers, as I mentioned earlier, was to assist small/medium-sized manufacturing firms. We are building on top of a foundation that we have had in place for about four and a half years now at NIST. two programs. One, the Manufacturing Technology Centers Program, which you can imagine, by title, the purpose of which is to establish large technology centers. They are funded at a level of \$3M Federal matched typically with \$3M of state or local funds. They work with 6,000-8,000 manufacturing firms in a given area. Since 1988-89, we have established seven Manufacturing Technology Centers throughout the U.S. So as you see, our challenge of 100 centers by 1997 is indeed going to be a challenge.

We are working very closely with TRP because the TRP projects and the TRP activities focusing in deployment help build this network. A lot of the activities that we are working with ARPA on and working, I guess, for ARPA on, will be activities that we hope in the long run we can pick up and maintain through Department of Commerce funds. A center that might be established under TRP may remain in place after a few years of DOD funding and may remain in place for the long term with the Department of Commerce funds, so we have an active interest in this. Things that were created in technology deployment that are extension center-like or are extension enabling-like help us build our system.

The strategy of our program, and Steve mentioned this a bit, is to build on local strengths of technology infrastructure. The Federal government cannot guess which model for technology extension or technology deployment would work in a given area. Different states operate in different ways, different industries operate in different ways -- it all depends on the region. We have a center in Cleveland which serves principally 87,000 small/medium-sized manufacturing firms which are within a one hour drive of that center. And that is contrasted with the center that we have in Kansas that serves about 4,000 manufacturers in a four-state area. So as you can imagine you cannot propose a model or develop a model and hope to impose that on all the state participants. We need to work very closely with the programs that are in place at the local level. We need our program to be put together within their culture and within the context of their environment.

The second strategy of MEP deals mainly with building a national framework of inner connection, access to data, performance evaluation, tool development and field agent training. Now this is a major strategic area within Manufacturing Extension Partnership and if you looked at TRP it would read basically "Extension Enabling Services." So our strategies matched one-to-one with the strategy of the TRP. So you can see how TRP has been an opportunity for NIST.

A third strategy of the Manufacturing Extension Partnership is to establish linkages with sources of technology to provide access by the extension centers. Again, our extension centers, while the work very closely with the small/medium-sized firms, and they develop very strong relationships, they also have the technology supply problem. For the most part, a lot of the technology solutions for small/medium-sized firms is on the shelf. But in instances where there is a particular expertise needed, it's often very difficult to find. So we are trying to put systems in place where a technology extension field agent in Kansas, for example, is working with an aerospace manufacturer who needs some assistance in the area of machining a certain alloy, could find the expertise that perhaps might exist in Oak Ridge National Laboratory. So what we need to do is build a system that marries that technology source together with the delivery agent and ultimately with the small/medium-sized firm.

PLENARY WORKSHOP

The fourth strategy of the Manufacturing Extension Partnership is to establish linkages with sources of central related services, and this has become a real important strategic element to us. When we started our program at NIST four years ago the focus was on technology, technology, technology -- let's transfer technology and everybody will be okay. Something we learned along the way was that technology in and of itself was not a solution. In many cases the small/medium sized businesses need assistance in the area of marketing and in the area of business planning. In many cases when you are introducing a new technology they need assistance in the area of training. In some cases, it's all three and more.

What we are trying to do at NIST is to put together an infrastructure but not put together the entire solution under one roof in terms of a federal agency. We have established very strong linkages with the Small Business Administration, and we are in process now of co-locating Small Business Development Centers with manufacturing technology centers that were created under NIST.

We also have a very strong relationship developing with the Environmental Protection Agency. There's a real need out there in terms of the small/medium sized manufacturer for assistance in the area of conforming to the various environmental regulations that are being imposed upon them. The EPA was very interested in developing an extension service, but sees the opportunity to work with us at NIST as a way of implementing and delivering their program through this existing system that is already being created.

We have similar relationships with the Department of Labor in the area of workforce training, and also one developing with the Department of Education in the area of skills development. We just had a round table about a month ago with all the DOE national labs, and we are trying to figure our way through the process of how do we tap those resources within the labs -- the expertise, the information the technology -- and make it available to the centers.

So basically what we are trying to do is to put into place an infrastructure for working with small/medium sized manufacturers. And we see our role in the creation, development and integration of that infrastructure, but we see it as an infrastructure that should work with the entire Federal government and all Federal agencies.

I will just give you a quick overview of the four components that make up the Manufacturing Extension Partnership. After hearing Steve's talk on technology deployment, you can see some of the integration. Our system of 100 centers will be comprised mainly of about 25 Manufacturing Technology Centers. These are large centers operating at \$6M budgets and serving basically a region of 6,000-8,000 manufacturing firms. Those are just rough numbers, that's not cast in concrete.

One of the things that we developed as part of our strategies is something called a Manufacturing Outreach Center. This gets back to that model when I was talking about Cleveland and Kansas. There are a lot of areas in the country that could be served by a very big, very large fully-funded center, and they are very densely populated industrial regions. But there are also a number of areas that could never justify a center of that size. So what we have proposed developing is something which is a smaller MTC which may be linked to manufacturing technology centers or may even be stand alone centers that would serve lower concentrations of industries: probably about 600-800 manufacturing firms, probably operating a budget of \$1M-\$2M. We see about 75 of these centers being created. So in this composition of 100 centers, 25 of the really big ones, which we would see in areas like a Detroit and a Cleveland and probably a Philadelphia some day, and also 75 of the smaller ones, which we are seeing more and more of a need for in the more rural areas of the country.

PLENARY WORKSHOP

A critical component to our program which we will be working on a lot this year, at least with DOC funds in anticipation of Round Two for TRP, is the State Technology Expansion Program. Really, what that program does is provide funding to states and local governments to help them with the planning process of coordinating a state-wide technology infrastructure. A lot of these programs in the category of deployment require a very strong state partner. What we do under STEP is provide some up-front money to states to help them put together a plan. The money is not enough to put together a system or a center, but mainly to get a number of people in the room and talking together. We have places -- and I will pick on Pennsylvania -- that in the past, and even today, operate three and four different extension programs. Pennsylvania has an industrial resource center system, it has the Ben Franklin system, it has a PENNTAP system. What STEP does is go in and work with the state in trying to integrate those extension services and as well integrate them with local sources of technology: universities, laboratories and such.

So we envision that in order to get 100 centers we are going to have to do a lot of up-front outreach and a lot of up-front planning. We did get very strong proposals under TRP and we are funding a lot of new programs; but if we are to get to 100 centers by 1997, we need to do some more up-front work because there may be a supply problem come 1996-1997 in terms of the high quality and very competent proposers.

The last category is Links. I pretty much talked to this already, but it's an integral part of our strategy that deals with the national infrastructure; this layer of support services; this dealing with communication among the centers, electronic principally; data systems; and evaluation, which is a critical component and will be a critical component as a TRP process. We will be spending a lot of the Federal government's money. Was it worth it? Did we cause a shift? Are manufacturers more competitive? Are there more or less jobs because of this activity? So that is a critical component to MEP as well as TRP.

Field agent training. As we develop 100 centers, again, there is going to be a supply problem. Where do you find a field agent? For the most part there are people with 10 - 15 years of industrial experience. Generally, if you are lucky, they have a MBA degree with a technical undergraduate; but still they need to be trained in the process of assessing a company, going in and performing an evaluation of their system, and recommending solutions. They also need to be trained in understanding the critical aspects of operating a small business.

Tool development is another key factor, and we saw a lot of that in TRP. Some very good tools were proposed and some winners announced. One tool in particular is a project called a "Quick View" that was proposed by the New York State Science and Technology Foundation. Quick View is a one-day assessment instrument where you can go into a company and make an assessment of their process. So there will be more and more tools. There is no point in creating these assessment tools a hundred times over, creating these client tracking systems a hundred times over, so there is going to be some more funding in tool development and some more activity along the lines of sharing those tools. And, again, linkages with technology sources.

As I mentioned earlier we are working very closely right now with DOE. Tomorrow I go to a director's meeting of our Manufacturing Technology Centers where we will have presentations by the DOE Head for State and Local Programs as well as the DOE Program Lead for Programs with Small Businesses. So we are trying to work those relationships. And that's about all I have for now.

PLENARY WORKSHOP

Michael Long:

I had a bit of a flashback here when I came up on stage. Back in April we did a number of these kinds of sessions all across the country and became known as the "TRP Roadshow." This is very reminiscent of that time. Apparently, we did a pretty good job of it because we ended up with 28 hundred plus proposals and some very good ones. Hopefully, some of the information that you get today will be useful not only to TRP, if we have another one or whatever form it takes, but for getting work with other agencies as well.

DOE has been involved in TRP since the very beginning, way back in December of last year, and throughout all efforts that have taken place thus far. We felt it was a very natural match for the kinds of activities that the Department is engaged in and some of the approaches are very similar. You have heard about deployment and Steve mentioned the other activities as well: manufacturing, education and development. The Department has been engaged in deployment-type activities through our national laboratories and through some of our program offices. Manufacturing is an area that we are heavily involved in from the weapons standpoint -- very detailed manufacturing -- so that was consistent with activities we were engaged in. And the biggest one -- development -- is one we are most familiar with. In TRP, the development was geared toward industry and partnerships, to take technologies that they had been working on or could acquire and move those technologies or special processes along to the point where they moved towards commercialization of a product or process. This, again, is something that DOE has participated in through programs with our laboratories and private industry, through CRADAs and other means.

We also provided direction and support. Through the evaluation process we had members -- technical experts, who supported the evaluation process. We have had personnel involved in the planning sessions of TRP and all other activities. TRP has helped to bring together some of the organizations within DOE and is also serving as a model for some of the activities that some of the program offices will start to undertake. And that is significant to note, if you expect or would like at some point to do business with DOE. Some of the program offices are beginning to use, as I said, TRP as a model for competition.

Our national laboratories -- we are pretty proud of our national laboratories. Kevin mentioned that they are a resource for technology -- some of the most advanced technology in the country, in fact. They were participants in many of the proposals that came into TRP, and they were also participants in some of the winning proposals. It is a case where they had something very unique to offer proposers. In fact, those were part of the requirements of TRP, that if a national lab or defense lab got involved they had to have something very special, and our labs did bring something special to the table in many cases.

In addition to TRP, there are other ways to acquire business from DOE. There are several exhibits out in the exhibit hall which will give you a very good idea of the types of activities the different program offices are interested in. And it is important to note that DOE has program offices and also field offices which, in some sense, set their own agenda for the types of technology and support they are looking for. That would be a good place for most of you to start to identify areas that you have expertise in and feel that you can make a contribution.

There are solicitations that are put out routinely in the *Commerce Business Daily* and the *Federal Register*. Those two documents should be reviewed by you periodically to see what is available. We also accept unsolicited proposals. To get more detailed information on the process and on mailing lists, I have made an agreement with the folks who routinely do that to take any business cards you

PLENARY WORKSHOP

may have back with me and we can get you some information packages.

TRP has been a very, very positive experience for us. It afforded us an opportunity not only to work closely with DOD in spending some of their money, but it also opened some new avenues of communication within the Department between program offices and other agencies who also participated in TRP.

Frank Penaranda:

As clean-up hitter, let me simply try to wrap all of this up and give you a quick glimpse of the mechanisms throughout the Federal government that have been implemented to assist the connecting of your needs with the Federal establishment. Let me remind you, again, that there are over 700 federal labs out there of which at least one to two hundred are very major R&D facilities across the many departments that make up the federal establishment.

NASA has a long history in Federal technology transfer. As part of our act, we were required to disseminate the technology that we developed for space use to the private sector. We have done that in the past through the traditional mechanisms of the print medium. We have tried to bring technology that has been coming out of the pipeline to you through publications such as *NASA Tech Briefs*, which are abstracts of these technologies, in as timely a fashion as we can.

Now the magazine, which is co-sponsoring this symposium and which many of you are familiar with, has in it not only the abstracts but also a road map indicating how you can then obtain the full report of abstracts that are of interest to you. After that, if you are further interested in some additional contacts with the source of this technology, how to get a hold of the NASA field labs that have provided this technology.

We realized from the very beginning, also, that simply the passive transfer of this technology through the print medium was not sufficient. We had to be much more proactive. As has been said very often, technology transfer is a contact sport and, in fact, we believe it is. We have to reach you individually, where you live, in order for you to feel comfortable that you have a ready-made and easy access point to Federal technology.

So we have established various outreach mechanisms. This symposium is one of them, of course. But more importantly, we established a network of agents -- non-Federal agents -- and that is very important. Some people may feel that Federal employees that have been in the private sector know nothing of how to sympathize and be sensitive to the needs of the industrial and the commercial community. And that is probably true in many respects. So we have employed a network of individuals who have a lot of experience in the business community, who have started businesses of their own, who are experts in not only technology, but the application of technology and in business development, capital acquisition and so forth.

We have structured these agents into six Regional Technology Transfer Centers that encompass the entire 50 states. Now, these centers are physically located in one particular spot, in some particular community in each of these six regions; but, their charter is to integrate and link every single community -- principle industrial community -- within their regions to the Federal laboratory system. I'm talking about all of the federal labs, not just the NASA labs.

These six Regional Technology Transfer Centers have now spent the first year of their existence trying to create these linkages with each of the state's governments, certainly, and with a lot of the major

PLENARY WORKSHOP

industrial or business communities through affiliates who are as close to each of you as a local telephone call or an "800" call. Rather than show a lot of maps where they are, I urge you to visit our exhibit. Where you see the big NASA sign, you will see the booths of these Regional Technology Transfer Centers, and you will become acquainted as to where the nearest one is to you and which is the affiliate in your community that can serve your needs.

The reason that we divided up the country into regions is that we realized that the communities, the culture, the industrial base of each of these regions may be quite different, and how to treat them and understand their particular problems may be different than if we did it centrally out of Washington, D.C. There is nothing more threatening than to say to somebody, "I'm from Washington, D.C. and I am here to help you." So we made sure that these centers were as local to you as the town in which you live.

One of the things that these people can do for you is to try to characterize your needs into technology solutions. Very often you may think your needs are technology -- probably they are not. They may be just money. It may assistance rather than a package technology. And that's very important because the Federal laboratories offer much more than shrink-wrapped technologies that you can run with and commercialize. They really offer capabilities that you, as individuals, cannot afford to build.

We are talking about experts: scientists, engineers, etc. We are certainly talking about very expensive, and very unique and exotic, facilities that are available to you. They are available to you through many mechanisms that we have set up. Some have been already alluded to by my colleagues. They can be very informal ways: a telephone call speaking to one of the engineers and asking some questions or as elaborate as a very intricate legal agreement that specifies what we are going to do for each other.

Most of the Federal labs -- I would say practically all of the Federal labs -- have an entry point which is the Technology Transfer Office. They call them ORTAs or they can call them TU offices. If you happen to live in a neighborhood, and you happen to know that your needs are technology driven, and you happen to understand that the Federal lab next to you has got the technology you want, by all means pick up the telephone and call that particular agent or entry way in that laboratory. More often than not, they may be near you, but they may not contain the technology you need, which is why we have these Regional Technology Transfer Centers with the agents who can help you no matter where the technology may exist anywhere in those 700 Federal labs.

It is also important to note that there is a National Technology Transfer Center that NASA sponsors. They may be physically located in West Virginia but, in fact, it's a virtual organization that offers or can offer the first entry point to any of you -- if you don't happen to remember or know what your regional center is or your affiliate next to you or the laboratory -- by calling, very simply, 1-800-678-NTTC. They can be your first contact point -- one single place. They are as local to you as that "800" number.

So we have, again, this network of agents that can help any of you acquire the facilities and capabilities of any of our agency's Federal laboratories. Become acquainted with them, talk to them, they can help you. I have just acquired technology that can help you secure capital, develop business plans, form alliances with other business establishments who may be seeking similar expertise or capability. And the technology, by the way, may not be resident in one of the federal laboratories it could be resident in another commercial organization. They have access to that information too and sometimes they can help you build these kinds of strategic alliances with -- it could be the IBMs of this world or it could be another small business.

PLENARY WORKSHOP

Since I am from NASA, I can tell you we have nine Federal laboratories and they are spread across the nation from Ohio in Cleveland, to Maryland, down in Florida, we have Alabama, we have Mississippi, we have Texas and we have two right here in the California area. One very close to you here at the Jet Propulsion Laboratory and one north of here at Moffett Field, near San Francisco and the bay area, Ames Research Center. These laboratories offer some very unique capabilities.

Let me leave you with another thought: the connection of NASA's technology transfer emphasis and TRP. As I mentioned, our emphasis in the past has been mostly to take the mature technology that has come out of NASA laboratories, or any of the Federal laboratories, and make them accessible to you, including the capabilities that I just mentioned. There is a new thrust, and clearly, this is a thrust that the entire administration is trying to emphasize: partnering. That's a key word I think you are going to hear a lot. I believe that is the way of the future. In order to ensure commitment from the commercial establishment it is believed that the best way to ensure that there is going to be some commercial product coming out of the end of the pipeline of any kind of endeavor or any kind of technology research is a partnership where the private firm is putting on the table something: it can be cash, it can be in-kind, labor, assets of any kind. TRP certainly has demonstrated that that's a very good vehicle to pursue. NASA is going to push very strongly dual use technology development, either with partners or without partners. That has been stated already by colleagues that addressed you yesterday.

The concept of devoting 10-20% of the Federal budget to more relevant use of federal assets and technology to the private sector is clearly a goal that we all want to achieve. One of the best ways to achieve that goal and leverage the entire budget of an agency such as NASA is to pursue the two objectives: the commercial objective as well as the mission objective of the agency from its very inception when the projects are being planned.

So we are going to do a very proactive task of reaching the industrial community, and seek your involvement from the time we dream up a planetary mission or even an aircraft mission, or whatever, so that we can have your inputs into our development plan and then we can seek and pursue it with a dual use or dual goal in mind. If you can partner with us, and bring your resources and leverage that into the synergistic effect of both and get more "bang for the buck," that's even better.

So we are jumping on the experience of TRP. We are looking at it very closely because we believe that is the way of the future.

Let me close by just making a personal observation about the TRP process and embellish on what Steve already said about how we went through the selection process. Each of us here at this table were intimately involved in the review and evaluation process. I, too, read many proposals and as we went through it, we realized that there was no formula for winning, but certainly there were some aspects we noted that can assure that that proposal will not be selected. Generally, the common fault that we found was that people who proposed did not read the solicitation carefully, particularly the selection criteria stipulated for each of the particular areas that were indicated. I'm not saying that if you left out your middle initial you were therefore disqualified. I'm talking about the fact that there were very specific selection criteria stated and those who followed them religiously had a leg up on those who simply went at it blindly. I can tell you that we did not deviate one iota from the selection criteria in evaluating each of the proposals. We have a tremendous order trail that can prove we did that, that we did not invent anything as we went along. So, please, if there is another solicitation be very careful and read the selection criteria adhered to them.

PLENARY WORKSHOP

Technology Reinvestment Project

Stimulate the transition to a growing integrated national industrial capability which provides the most advanced, affordable military systems and the most competitive commercial projects.

Three Avenues of Attack

I. Technology Development

- Stimulate commercialization of dual use technologies to foster integration of the defense and commercial industrial bases
- Provide for the national defense by promoting cutting-edge commercial and defense capabilities

II. Technology Deployment

- Assist new and established manufacturers to be globally competitive and achieve world class standards
- Coordinate Federal, state and local industries to improve and concentrate the flow of services to areas of opportunity

III. Manufacturing Education and Training

- Reform manufacturing engineering education to build the high skills manufacturing work force of the future
- Retrain defense engineers and technicians so they can contribute to the commercial and defense industries of today

Fiscal Year 1993 Title IV Appropriations for TRP Programs (\$ millions)

Defense Dual Use Critical Technology Partnerships	\$81.9
Commercial-Military Integration Partnerships	\$42.1
Regional Technology Alliances Assistance Program	\$90.5
Defense Advanced Manufacturing Technology Partnerships	\$23.5
Manufacturing Extension Programs	\$87.4
Defense Dual Use Assistance Extension Program	\$90.8
Manufacturing Engineering Education Grant Programming	\$43.6*
Manufacturing Experts in the Classroom	\$4.6
Small Business Innovative Research Program	\$7.2

TOTAL	\$471.6

* Including \$30M of FY 93 Funds

PLENARY WORKSHOP

Small Business Innovative Research (SBIR)

- Technology Reinvestment Project (TRP) SBIR solicitation released on 14 May 1993, proposals closed 16 September 1993
 - Proposals addressed 11 technology developed focus areas only
 - Procurement is based on Federal SBIR guidelines
- Cost sharing is permitted for TRP SBIR proposals, but is not required and will not be an evaluation factor
- Only Phase I proposals will be funded with this solicitation
 - Additional \$7M added to SBIR
 - \$100K, 6 month; anticipate 150 awards
- Out-year TRP activities are a natural SBIR Phase II follow-on

Common Requirements

Statutory Requirements Common to All TRP Programs:

1. **Competitive Award**
2. **Specific Participation (Emphasis on Partnerships)**
3. **Cost Sharing of at least fifty percent (50%)**
4. **Defense Emphasis -- 10 U.S.C. §2501**

TRP Update

- **Oversubscribed!**
 - Over 2800 proposal requesting \$8.5 billion
 - Diverse array of participants
- **Multi-tiered Selection Process Complete**
 - 300 evaluators from six agencies
- **162 Proposals Announced to date (85%)**
 - First announcements made by the President, 22 October
 - Additional announcements 24 November/4 December
- **Diverse Array of Winning Proposals**
 - Defense and non-defense contractors
 - Large range of award value
 - Small businesses, universities well represented

PLENARY WORKSHOP

TRP Proposal Summary			
<u>Activity Area</u>	<u># Prop</u>	<u>Request (\$M)</u>	<u>FY 93 (\$M)</u>
Technology Development	1916	6478	210
Technology Deployment	567	1515	210
Manufacturing Education & Training	361	507	45
TOTAL	2844	8500	465

TRP Participants by Type	
• Historically Black Colleges, Universities/Minorities	2%
• Small Businesses	13%
• Small Disadvantaged Businesses	1%
• Foreign Owned	1%
• Other	83%

TRP Preliminary Assessment	
• Cooperation Among Multiple Federal Agencies Outstanding!	
• Surprisingly Robust Response to Complex Solicitation	– Excellent proposals exceed available funding
• Meaningful and Unique Collaborations	– Large, well integrated teams (horizontal and vertical) – Government/industry/university teams – Inclusion of small businesses
• Active Participation by State and Local Governments	– Regional alliance – State funding
• Promising Start to Integration of Military Commercial Base	– Innovative dual use programs – Workforce retraining – Infrastructure support – Anecdotal evidence of impact
• Final Assessment Years Away!	

PLENARY WORKSHOP

TRP Myths Debunked

- **TRP is only for Defense Contractors**
 - Winners include many non-defense contractors: Johnson & Johnson, Apple, Rio Grande Medical
- **TRP is not for Defense Contractors**
 - Winners included many defense contractors: Rockwell, Hughes, GE
- **TRP is not for Small Businesses**
 - 10% of winning participants
 - 38% of winning proposals had small business participants
 - 47% in development
- **TRP Development is not for Universities**
 - Universities well represented among development winners
- **TRP is not for National Laboratories**
 - Played pivotal role in many successful proposals
- **TRP Discourages Participation by DOD Laboratories**
 - DOD laboratories well represented
- **TRP Will be Biased Against Small Dollar Proposals**
 - Large range of awards (\$80K to \$20M-plus)
- **TRP Will be Biased by Region**
 - Very diverse distribution of awards

TRP – What's Next

- **Dual Use, Defense Conversion Will Continue**
 - TRP statutes to be well funded in FY 94
- **Collaboration, Partnerships, Cost Sharing Still Required**
 - Some breaks for small businesses
- **TRP Options Available**
 - Some FY 94 funds for FY 93 proposals
 - Limited FY 94 Competition
 - Focused in Scope and Technology
 - Large Competition
 - FY 94 and/or FY 95

**ADVANCED
MANUFACTURING**



A Force-Controllable Macro-Micro Manipulator and its Application to Medical Robotics

Neville I. Marzwell
Jet Propulsion Laboratory
California Institute of Technology
4800 Oak Grove Drive
Pasadena, CA 91190

51-57
2437
P. 14

and

Darrin R. Uecker and Yulun Wang
Computer Motion, Inc.
Goleta, CA 93117

ABSTRACT

This paper describes an 8-degrees-of-freedom macro-micro robot. This robot is capable of performing tasks that require accurate force control, such as polishing, finishing, grinding, deburring, and cleaning. The design of the macro-micro mechanism, the control algorithms, and the hardware/software implementation of the algorithms are described in this paper. Initial experimental results are reported.

In addition, this paper includes a discussion of medical surgery and the role that force control may play. We introduce a new class of robotic systems collectively called Robotic Enhancement Technology (RET¹) [1]. RET systems introduce the combination of robotic manipulation with human control to perform manipulation tasks beyond the individual capability of either human or machine. The RET class of robotic systems offers new challenges in mechanism design, control-law development, and man/machine interface design. We believe force-controllable mechanisms such as the macro-micro structure we have developed are a necessary part of RET. Work in progress in the area of RET systems and their application to minimally invasive surgery is presented, along with future research directions.

1. INTRODUCTION

There are two main difficulties that have impeded the development of a high-precision, force-controlled robot. First, the execution of control strategies that enable precise force manipulation is difficult in real time because these algorithms have been too computationally complex for available controllers. Second, a robot mechanism that can quickly and precisely execute a force command and, at the same time, cover a large enough work-space for practical manufacturing applications is difficult to design. Actuation joints must be sufficiently stiff, frictionless, and lightweight so that desired torques can be accurately applied.

We have addressed the computational-complexity problem by building a high-performance, real-time, cost-effective multiprocessor system [2]. This system is highly modular in structure and was designed to support the needs of advanced robotic systems. Our robot mechanism uses a macro-micro design, which allows the end-effector to have the properties of a small and light robot, yet preserves the workspace capability of a large robot. The approach was to attach a small low-inertia, 3-degrees-of-freedom manipulator to the end of a larger and heavier 5-degrees-of-freedom manipulator.

¹RET is a registered trademark of Computer Motion Inc.

Clearly this robotic structure could have many applications, and, traditionally, robotic systems have been placed into one of two application categories: manufacturing robotic systems or teleoperated robotic systems. The commonality of tasks within each category dictates that in each category there will be general characteristics associated with a robot's design and its method of use or users interface. Manufacturing robotic systems have been characterized by repetitive tasks programmed by the user, usually through a computer console or teach pendant. These robots typically operate at high speeds and are very accurate. Task examples include pick-and-place, spray painting, and welding, just to name a few. Teleoperated robotic systems are different in that they are designed to imitate the exact actions of the user, usually through a master/slave interface. They are typically used in hazardous tasks such as bomb deployment and hazardous-waste cleanup. They can also be used to attenuate or amplify the actions of the user to perform delicate assembly or move large objects.

A new class of robotic systems is currently being developed that we have termed Robotic Enhancement Technology (RET) [1]. RET will be different from the traditional robotic systems described above in that it will combine robotic manipulation with human control to perform manipulation tasks beyond the individual capability of either human or machine. The fundamental difference is the cooperative interaction of the human and the robot; the interaction is under control of the human. This interaction gives the human greater ability to perform complex manipulation. In turn, it presents new challenges in robot-mechanism, robot-control and man/machine interface design, which together make up the different parts of RET.

We can apply RET to problems where one's mind can see a solution but performance is limited by one's physical capabilities. Computer Motion, Inc. has attacked one such application in minimally invasive surgery, or, more specifically, laparoscopy. Laparoscopic procedures make use of a camera, known as the laparoscope, which is typically held by an assistant while a surgeon performs an operation. Thus, the assistant has control of the surgeon's field of view. This is tantamount to somebody holding a flashlight for someone else trying to do very delicate work. From the surgeon's perspective, this is far from ideal; clearly he would like to be in control of the camera himself. With this in mind, we have developed the Automated Endoscopic System for Optimal Positioning (AESOP), which holds the laparoscope and is guided by the surgeon with a foot- and/or hand-controlled interface. Thus, the surgeon is able to gain control of his eyesight by coordination between himself and the robot. This is our first RET system in a medical application. We feel that RET systems will find their way into many more medical applications, and, furthermore, we believe the macro-micro force controllable manipulator concept will play an important role in future RET systems.

The macro-micro mechanism is described in Section 2, which is followed by a discussion of the control algorithms and their hardware/software implementation in Section 3. Initial experimental results are given in Section 4 and the medical applicability of the macro-micromechanism as used in the RET systems is covered in Section 5.

2. A FORCE-CONTROLLABLE MANIPULATOR

A manipulator capable of delicate interactions with its environment must be designed differently from today's position-controlled robots. It has been shown that a high-bandwidth, low-effective-inertia design is helpful for precise force control [3,4]. The approach we have taken is to attach a low-inertia small manipulator to the end of a larger and heavier manipulator. This macro-micro structure results in a combined structure with the low end-effector inertia of the micro robot and the large workspace of the macro robot. A photograph of the complete robot is shown in Figure 1.

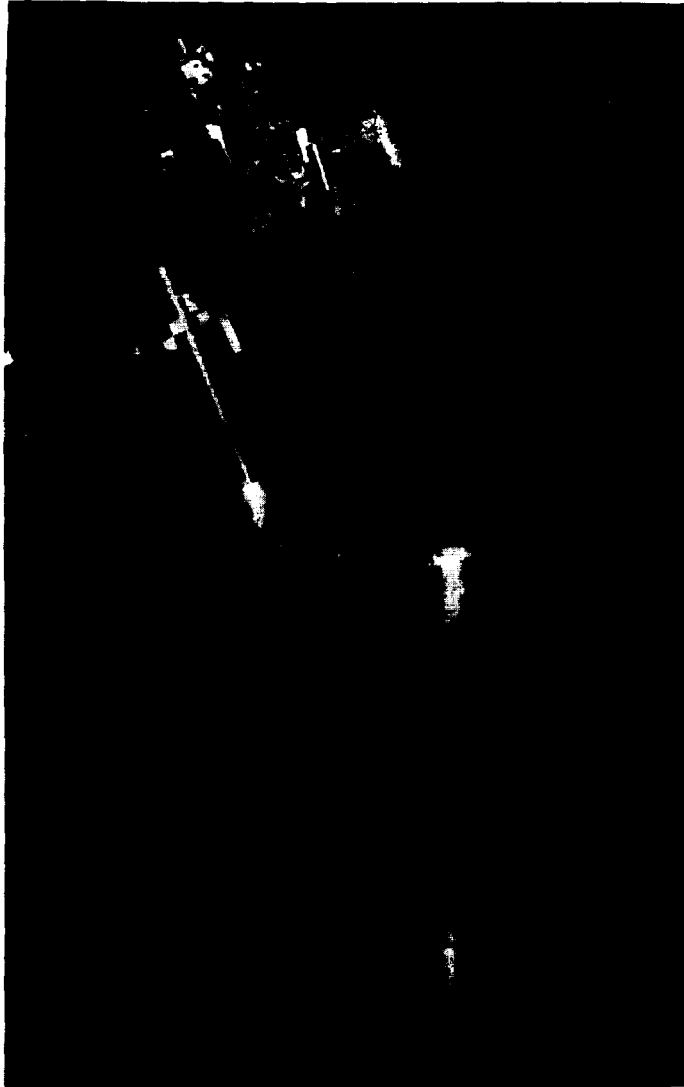


Figure 1. Photograph of the Macro-Micro Manipulator

The design strategy was to simplify the macro design by providing the micro robot with more capability. The main consequence of this decision is a large micro workspace, which allows less accuracy and performance capability in the macro. However, the micro's workspace volume directly influences the overall mass and size of the design considerably. In our design, reducing travel along each dimension by a factor of two roughly reduces the size and mass of the micro robot by roughly a factor of two.

The macro design is that of a 5-degrees-of-freedom articulated manipulator. This manipulator supports the weight and continuous force-exertion capability of the micro-manipulator throughout the workspace with 1-g acceleration. A 1-m reach was chosen as a reasonable workspace. The main features of this design are high mechanical rigidity, simple kinematics, large workspace volume, and cost effectiveness. The kinematic structure is very similar to that of the first five joints of a PUMA 560 robot [5]. A sixth joint is unnecessary because the tip of the micro robot spins continuously during grinding or polishing applications. We considered a variety of actuation methods, and after various optimization procedures, we decided on a harmonic drive/worm gear double-reduction scheme for the first three joints. The last two joints, which carry a much smaller load, use harmonic drives.

The macro-micro design couples a 3-degrees of freedom micro robot to the end of the 5-degrees of-freedom macro robot. A photograph of the micro design is shown in Figure 2. Motion along the x and y directions is actuated with parallel sets of 5-bar-link mechanisms, one attached to each of the two motor shafts. The z motion is actuated by a fixed motor oriented

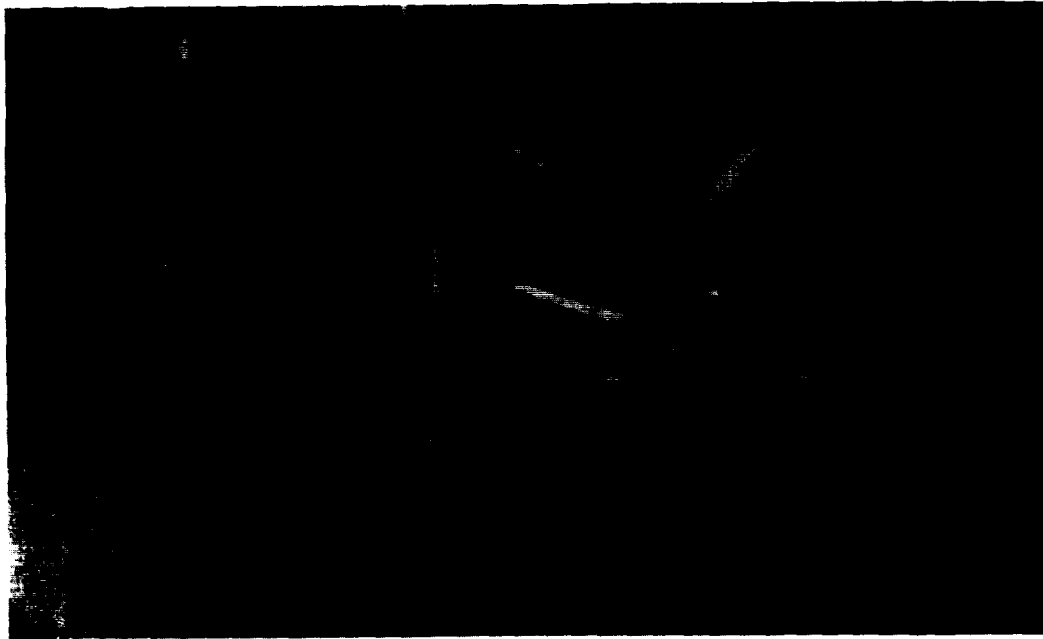


Figure 2. The Micro-Manipulator

perpendicularly to the x and y motors. This motor is attached to the parallel link mechanism through a pair of universal joints. The range of motion is 2 cm along each axis. A fourth pneumatic motor, located further from the tip than the other motors rotates the tip through a series of transmissions at a constant speed for polishing, finishing, and grinding applications.

The main objectives of the micro design were to minimize end-effector inertia, minimize joint friction, maintain tip orientation throughout the workspace, and support a maximum payload (i.e., force exertion) of 3 kg. The resulting tip inertia is roughly 250 gms. The joint friction was minimized by using direct-drive transmission and limited-angle flex bearings at the joints. Tip orientation is maintained by the parallel 5-bar-link structures.

The Secondary goals were to minimize the size and weight of the micro-manipulator. The final size is 35.5 by 19 by 17.8 cm, and the weight is 6.3 kg. Detailed analysis of the kinematics and dynamics of the micro-manipulator can be found in past publications [2,6].

3. REAL-TIME MACRO-MICRO FORCE CONTROL

A. Force-Control Algorithm

To control the macro-micro manipulator so that it will apply the desired force, we chose to use an impedance control method. The impedance-control method enables a robot to interact with its environment in a well controlled and precise manner [7]. The manipulator's end-effector reacts to environmental disturbances in the same manner as a linear mass-spring-damper does system. The mass, spring, and damper values are controlled electronically and can be different along different axes, and they can continuously change during a trajectory.

This method is different from hybrid position/force control [8], since particular forces or positions are never specified. The control variable is the equilibrium point of the mass-spring-damper system unaffected by external forces. The advantage of this methodology is that a single control variable and control algorithm can be used to guide a robot through interactions with the environment. Hybrid position/force control, on the other hand, requires a switch in control methods and control variables whenever the robot changes the configuration in which it interacts with its environment.

Figure 3 shows an example of a trajectory specified by the equilibrium path; in the trajectory, the manipulator comes into contact with a surface, slides across it, and then leaves the surface. Note that the nominal force exerted on the surface is proportional to the spring constant. By using the spring constant and surface location information, it is simple to calculate the equilibrium point's trajectory so as to produce a desired force across the surface. The force at the contact point will be influenced by contributions from the mass and damper as well. Consequently, if precise force control is important, the smaller the mass and damper values are, the better. The macro-micro design facilitates small mass values.

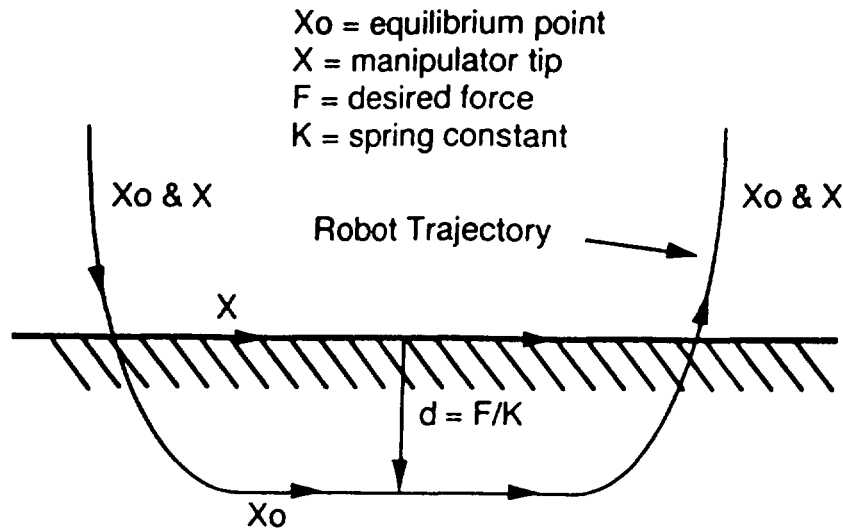


Figure 3. The Manipulator Trajectory Specified by the Equilibrium Point

The impedance equation can be written as follows:

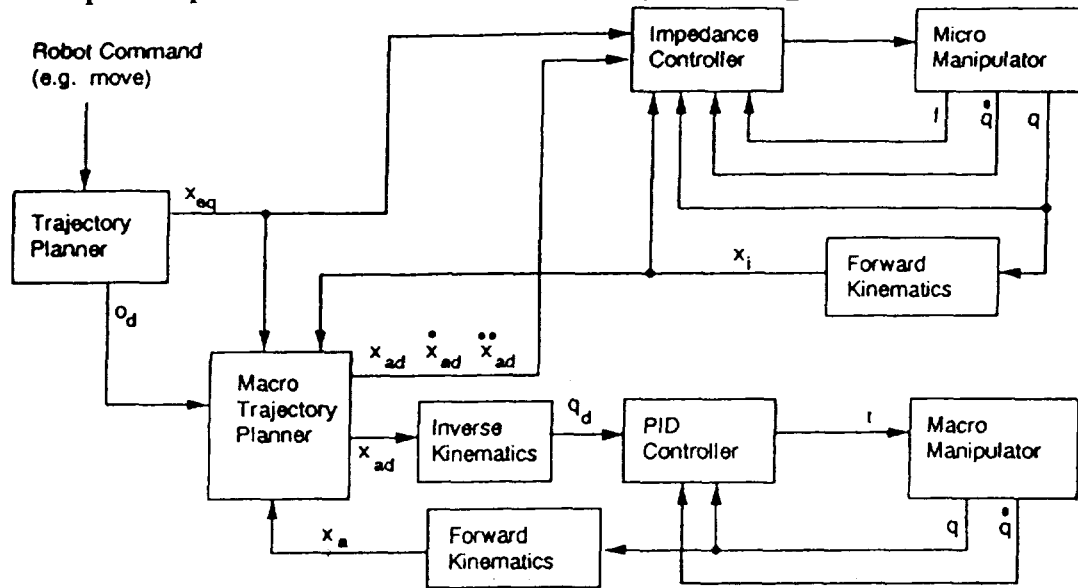
$$F_{ext} = M_s (\ddot{X}_R - \ddot{X}_o) + C_s (\dot{X}_R - \dot{X}_o) + K_s (X_R - X_o)$$

where

- F_{ext} = external force applied to robot tip
- X_R = tip position of macro-micro robot
- X_o = desired equilibrium point of macro-micro robot
- M_s = desired mass constant
- C_s = desired damper constant
- K_s = desired spring constant

Impedance control of a macro-micro design has the further complexity of managing the manipulator's redundancy so as to optimize force interactions, which is achieved by exploiting the micro robot's low tip inertia. In other words, the redundancy should be used to keep the micro robot from reaching its workspace limit, where one or more degrees of freedom would be lost. Our robot has 3 degrees of redundancy along the translational axes. Delicate interactions for translational motion are possible because of the micro robot. Orientation is left to the macro robot and is position controlled.

A block diagram of the control structure is shown in Figure 4. The impedance control law, which outputs torques to the micro robot, is derived by combining the desired impedance



- x_i - micro robot's actual tip position
- f - micro robot's force sensor readings
- x_a - macro robot's actual tip position
- o_d - desired orientation of macro-micro robot
- $x_{ad}, \dot{x}_{ad}, \ddot{x}_{ad}$ - desired tip position, velocity, and acceleration of macro robot
- q_d - desired joint position
- x_{eq} - equilibrium point
- q - actual joint position
- \dot{q} - actual joint velocity
- τ - torque

Figure 4. Impedance Control of Macro-Micro Manipulator

equation (stated above) with the equations of motion of the micro robot. Note that the servo-control law for all 5 joints of the macro robot is set by a simple position controller without feedback from the micro robot. However, feedback from the micro robot is input into a real-time trajectory generator for the macro robot. This trajectory generator uses the micro robot's redundant degrees of freedom to constantly update the macro robot's desired position, which is such that the micro robot is centered in the macro robot's workspace, and hence far from its workspace boundary. Consequently, the entire manipulator can respond to external disturbances with the quick reaction of the micro robot over the entire workspace of the macro robot.

B. The Control Computer

A high-performance multiprocessor system is used to satisfy the significant computational demands of controlling this robot. We designed this control system as a general-purpose high-performance controller with both hardware and software modularity as key features. The ability to easily rearrange and add other hardware and software modules to support different requirements for various tasks is particularly important in experimental projects such as this. Frequently, designs are unable to accommodate even minor modifications without a major impact to the existing system configuration.

The system is a VME-based system that is capable of using a number of compute, global-memory, and I/O modules. The compute modules are based on the TMS320C31 floating-point digital signal processor from Texas Instruments. This processor offers 33 MFLOPS of peak power. The global memory unit contains 2 Mbytes of memory for passing messages between compute units, for passing them to and from the host, and to store global variables shared by multiple compute units. The I/O modules are used to provide feedback for position, velocity, and force signals and as outputs for actuator commands.

Programs are developed in either C or C++ on the host computer and downloaded to the appropriate unit before run time. Several libraries are provided to support program development. Remote procedure calls were provided so that UNIX services, such as `printf()`, `scanf()`, `open()`, and `close()`, would be available for code development. Math functions, functions for accessing sensory data, and message-passing functions for multi processing are also provided.

4. EXPERIMENTAL RESULTS

The macro-micro robot has been fully assembled at Computer Motion, Inc., and we are in the early stages of experimentally verifying this design. At the time of this writing we have not reached the point of coordinated motion; however, we do have experimental results using the macro and the micro independently. These results follow.

The macro robot has been tested to verify that it will be capable of moving the micro robot throughout the macro's workspace without the need for torque control by the computer. To do this, the macro robot must be able to accurately move about the workspace with the load of the micro at the tip. The large gear reduction we have used should allow individual joints to have (PID) control of the manipulator. In Figure 5 we have plotted all five joints moving through different angular trajectories. The joints all move with very little trajectory-following error. The only joint that does have some tracking error is joint 5. This is mainly because of the load of the micro at this joint. This error is very small at the micro tip. We think that with some better tuning the tracking error will be reduced. The micro manipulator has been tested to insure that it has the characteristics described in Section 2. These initial experiments are with the micro detached from the macro, so we are primarily interested in their contact stability characteristics and disturbance-tolerance characteristics. These are the two areas in which traditional force-control mechanisms have experienced difficulties [4,7].

To test the contact stability, the equilibrium point of the micro was moved to a surface, in a configuration similar to the example in Figure 4. The results of this experiment are shown in Figure 6. Figure 6(a) shows the position along each axis, and Figure 6(b) shows the forces exerted on the tip. Initially, the tip is sitting at its equilibrium point without any contact forces (the forces seen are the results of gravity). At approximately 0.6 seconds, the tip equilibrium is moved +0.5 inches in the z-direction. The figure clearly shows the tip contacting the surface approximately 0.1 inch in that direction. The force in the z-direction quickly increases, with very little overshoot, and stabilizes at a constant force.

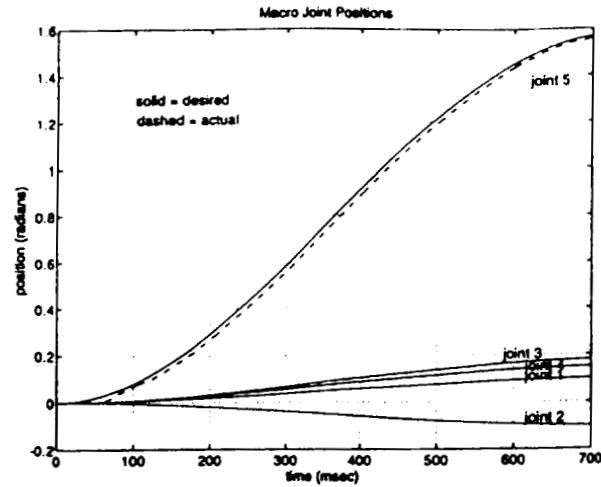


Figure 5. Macro-Manipulator Experimental Results

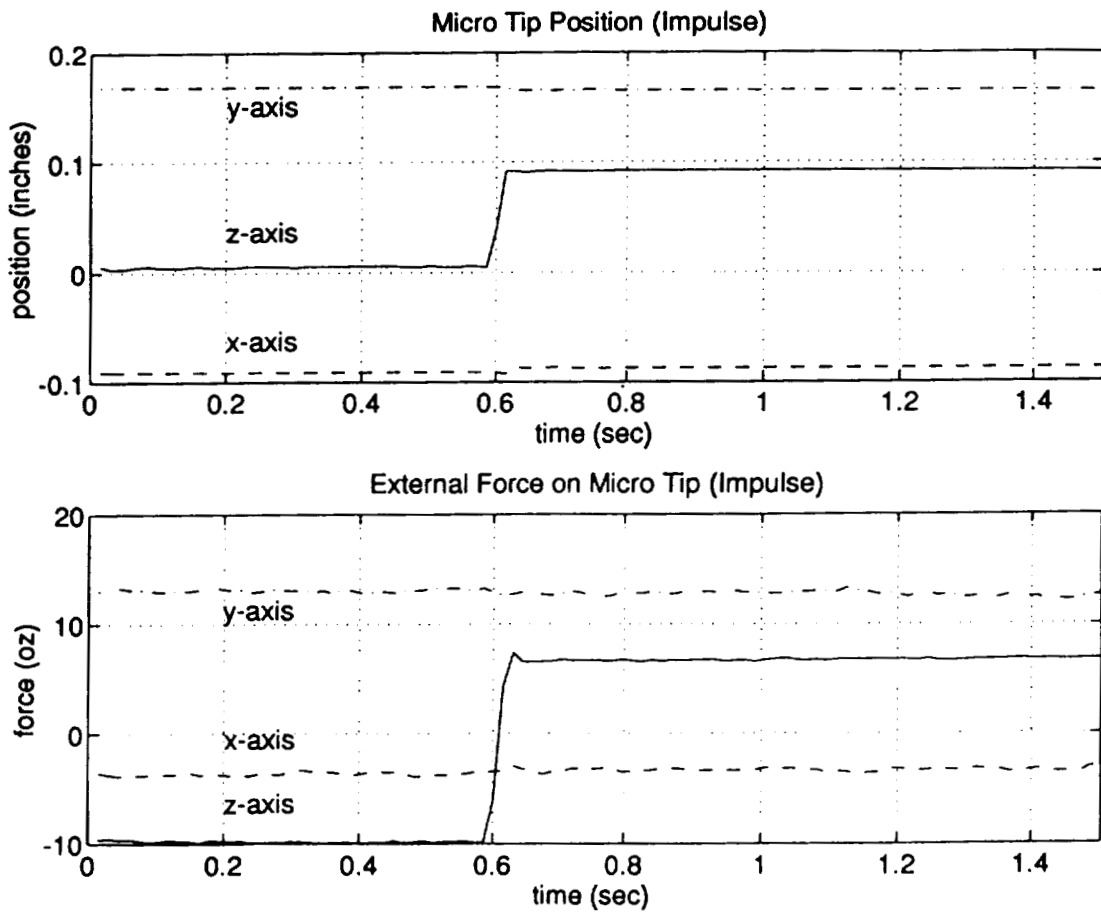


Figure 6. Contact Stability of the Micro: (a) Tip Position Data and (b) Force Data

The ability of the micro to tolerate disturbances while applying a constant force to a surface or object is demonstrated in Figure 7. In this experiment the entire micro is being moved in the y-direction while it is applying force in the z-direction. A disturbance is reached by the micro as it moves along the surface. The disturbance is shown graphically in Figure 7(a). Figure 7(b) and 7(c) show the position and the forces of the tip as it comes into contact with the disturbance. In this figure, one can see that the tip of the micro contacts the disturbance at approximately 0.8 seconds, and that the contact creates an increase in tip force in the z-direction. The tip moves along the disturbance and comes off of it approximately 4.5 seconds.

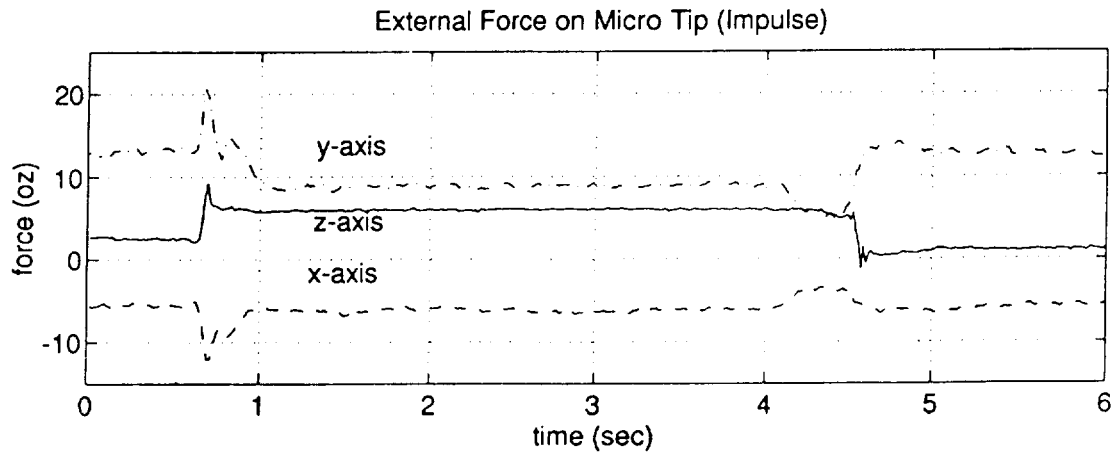
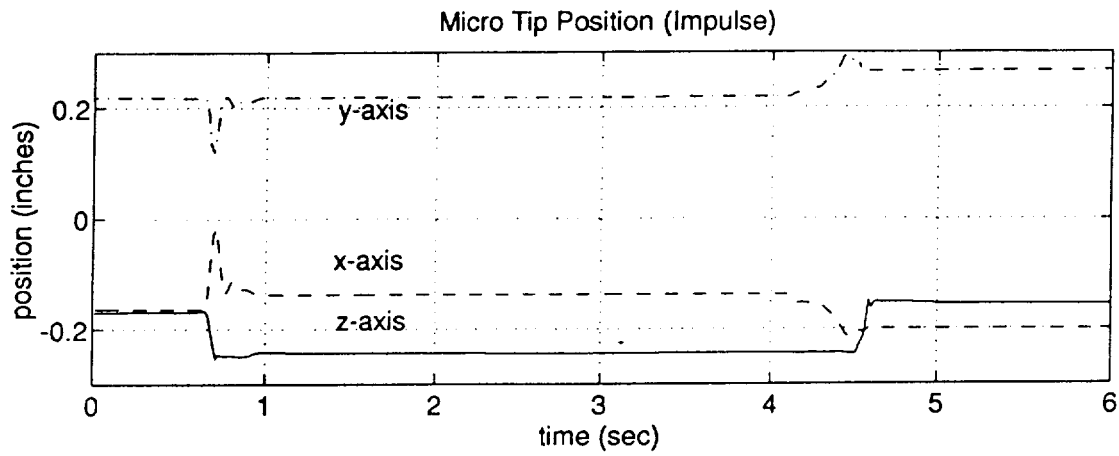
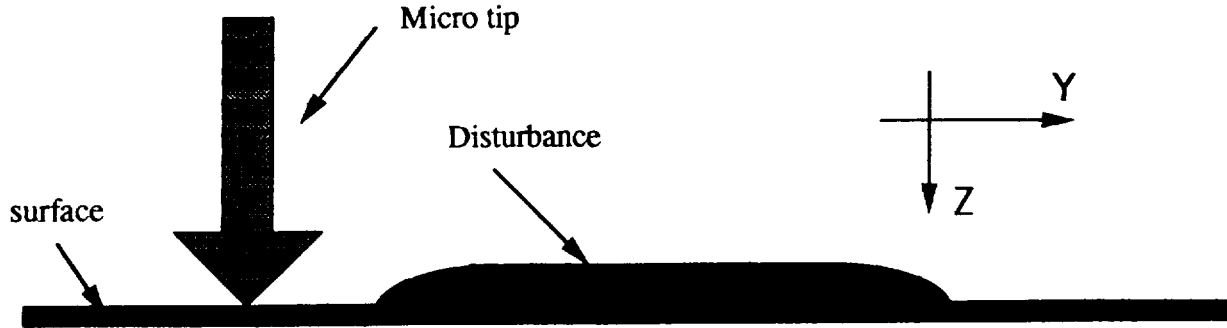


Figure 7. Disturbance Tolerance of the Micro: (a) Graphical Disturbance Model, (b) Position Data, and (c) Force Data

Transient forces are seen in the x and y directions at the beginning and end of the disturbance. The force in the y-direction along the disturbance is the result of friction. In the experiments described above we demonstrated the ability of the micro and the macro to perform their given tasks independently of each other. The next step, which we are currently working on, is the coordinated motion- and force-control of the two mechanisms.

5. MEDICAL APPLICATIONS FOR THE MACRO-MICRO FORCE-CONTROLLABLE MANIPULATOR

The macro-micro manipulator structure discussed above was conceived with manufacturing robotics in mind. However, we believe the structure will fit nicely in the RET framework. In this section we discuss current work at Computer Motion, Inc. in RET and the application of RET to laparoscopic surgery, as well as the potential application of the macro-micro force-controllable manipulator to this surgery.

A. The Automated Endoscopic System for Optimal Positioning (AESOP)

We have introduced the concept of RET into the surgical environment with the advent of AESOP, a robotic laparoscope holder for all forms of laparoscopic surgery [9]. Typical



Figure 8. Photograph of AESOP

procedures include gall bladder removal and hernia repair. There are three basic components which make up AESOP: the manipulator, the control computer, and the interface to the surgeon, which consists of a controller that can be operated by one's hand or foot. Figure 8 shows a photograph of AESOP and its components while Figure 9 shows a sketch of how AESOP would be incorporated into the operating environment.

The manipulator has 6 degrees-of-freedom, four actuated joints, and two passive joints. The structure of the manipulator is shown in Figure 10. The actuated joints are 1, 2, 3, and 6. Joints 1, 2, and 3 are used to control the tip of the manipulator, and hence the Cartesian location of the end of the laparoscope. Joint 6 is used to rotate the laparoscope for the correct orientation during movement. The passive joints, 4 and 5, are designed so that the laparoscope can rotate freely about the pivot-point constraint imposed by the cannula when the cannula is inserted through the patient's abdominal wall.

The fault-tolerant control computer translates the interface inputs from the surgeon into movements by the manipulator. The control computer includes a CPU and all of the digital, analog and encoder I/O needed for the feedback paths. The control computer begins running the control algorithms directly on power up, requiring no special boot up from the user.

The man/machine interface is composed of a controller that works by hand and a controller operated by one's foot.. Both controllers have the same functionality. This functionality consists of being able to move the laparoscope tip up/down, left/right, and zoom-in/zoom-out.

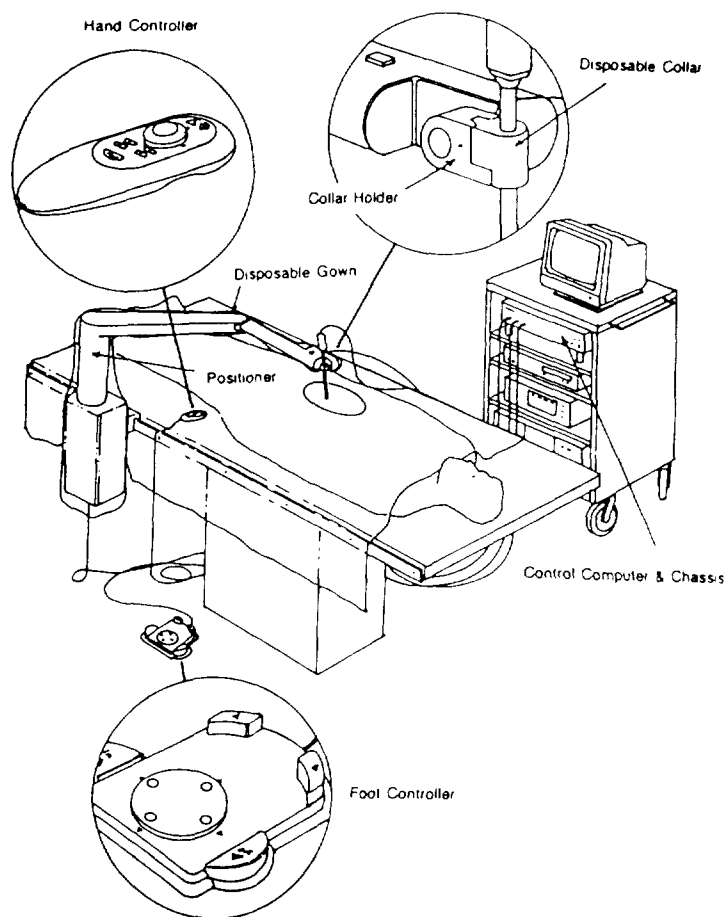


Figure 9. The AESOP System in the Surgical Environment

The surgeon merely watches the video image presented by the laparoscope and commands movements relative to the video images. AESOP is also capable of remembering past positions that were programmed by the surgeon and then returning to them on command from the surgeon. We call this function ReView, and it is a very valuable feature in our system.

AESOP represents the first generation of RET. Currently, the hand and foot controllers allow the surgeon to control the robot so as to enhance his or her overall performance. However, we feel these interfaces are just solutions for the immediate future. We are currently working on a natural-language interface and image-processing technology to create a more seamless interface between the surgeon and the robot.

B. Force Controllable Manipulators in Medical Robotics

As RET systems such as AESOP become accepted in surgical applications, their role in surgery will certainly become more active. The surgeon will become an "operating octopus" using many manipulators to aid in a variety of tasks. Clearly, this will not happen with mechanisms that are purely position controlled. RET systems will have to possess the ability to sense forces and react to them. Thus, force-controllable manipulators will have to play an integral part in RET. We feel the concept of the macro-micro manipulator we have described above can fill this need.

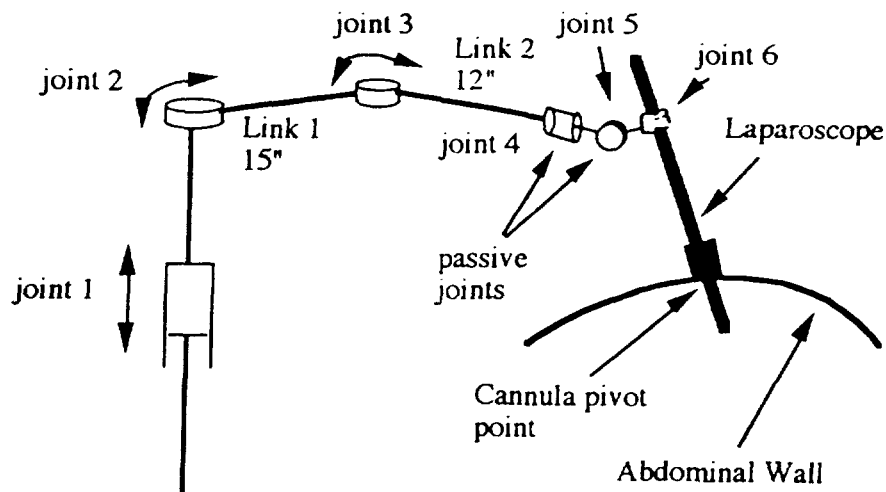


Figure 10. Schematic of AESOP as Used in Abdomen Surgery

An application that we have identified that requires a delicate interaction of forces is tissue approximation, or suturing. One of the key aspects of tissue approximation is tissue handling [10,11]. Tissue must be held steady with the proper tension and position so the surgeon can perform the appropriate suturing technique. Also, the tissue must be handled very delicately so as to avoid tearing or scarring, which can cause poorer overall recovery for the patient. One of the current problems is that tissue approximation usually involves long, leveraged instruments operated by less experienced than the surgeon assistants. Thus, this is another example where the surgeon would prefer to operate the machine if his or her hands were not already full. Static tissue holders can be used, but tissue is easily torn by any movement of the patient.

A force-controllable macro-micro manipulator would be the ideal mechanism to handle this problem. Modification of the impedance-force-control method may be needed for force regulation. With the proper interface, the surgeon would be able to set the correct force on the tissue, and then the macro-micro mechanism would always work to keep that force constant. The macro would be designed very much like AESOP, having a relatively large workspace and being stiff. The micro-manipulator would be small enough to actually enter the patient through one of the ports. The micro would work close to the tissue, keeping the appropriate forces applied at all times while the macro would be responsible for positioning the micro. Micro-mechanisms for laparoscopic surgery have recently been researched [12,13], although we are not aware of any force-controllable mechanisms.

One of the challenging design aspects of this RET system will be the man/machine interface. The surgeon will not know the exact quantitative forces that must be exerted on the tissue. Thus, for him or her to program numerically would be difficult and clearly not very intuitive. Part of the RET hypothesis requires a seamless man/machine interface. Thus, the surgeon should be able to "teach" the robot the required force through example, just as he or she would an assistant. The surgeon should be able to transfer some of his or her knowledge and experience directly to the RET system. The surgeon would then be operating with a robotic assistant that is acting like he or she would.

The design of the interface will drive the mechanism and control-law design. The interface will allow the surgeon to actually use the robot as an extension of his or her arm and feel the forces that are being exerted on the micro. When the surgeon has the proper hold on the tissue he or she will be able to let go of the manipulator and it will continue to regulate the forces to keep them as desired. A natural-language interface will also allow the surgeon to command minor in situ adjustments without interrupting the suturing process. Thus, the mechanism and control-law design must permit this type of interface.

6. CONCLUSION

An 8-degrees of freedom macro-micro manipulator has been described that can delicately interact with its environment. The mechanism includes a large macro that is mechanically stiff and has a large workspace, combined with a micro manipulator that has a low effective inertia with minimal friction and therefore a high mechanical bandwidth. A high-performance multiprocessor system was described that implements the impedance-control law for stable control and interaction with the environment. We have presented preliminary experimental results that validate this design. Further results will be obtained by the end of the year.

We have also discussed this macro-micro manipulator concept and its application to medical surgery. We introduced RET, a new class of robotic systems based on an interactive use of robots and humans. AESOP, the first RET system developed for minimally invasive laparoscopic surgery, was also introduced. Finally, we justified the need for force-controllable mechanisms in RET, as well as their application to tissue approximation. Computer Motion, Inc., plans to pursue developments in RET including medical applications.

7. ACKNOWLEDGMENTS

The authors would like to thank Amante Mangaser, Keith Laby, Steve Jordan, and Jeff Wilson of Computer Motion, Inc. for their efforts in designing and implementing this robot. We would also like to thank Professor Yoshihiko Nakamura of UCSB for his assistance in developing the control algorithm.

The research described in this paper was partially carried out by the Jet Propulsion Laboratory, California Institute of Technology, under a contract with the National Aeronautics and Space Administration, Office of Advanced Concepts and Technology. Computer Motion, Inc. funding from NASA/Jet Propulsion Laboratory under SBIR contract number NAS7-1149.

REFERENCES

- [1] Wang, Yulun "Introducing Robotic Enhancement's New Applications," Technical Note #1, Computer Motion, Inc., Goleta, Calif., 1993.
- [2] Marzwell, Neville, and Yulun Wang, "A Macro-Micro Robot for Precise Force Applications," *NASA Technology 2002*, Baltimore, Md., 1992.
- [3] Khatib, Oussama, "Augmented Object and Reduced Effective Inertia in Robot Systems," *Proc. of the American Control Conference*, Atlanta, Ga., June 1988.
- [4] Sharon, Andre, Neville Hogan, and David E. Hardt, "High Bandwidth Force Regulation and Inertia Reduction Using a Macro/Micro Manipulator System," *Proc. of the IEEE Conf. on Robotics and Automation*, Philadelphia, Penn., April 1988.
- [5] Leahy, M.B., et al., "Efficient Dynamics for the PUMA-600," *Proc. of the IEEE Conf. on Robotics and Automation*, San Francisco, Calif., 1986.
- [6] Wang, Yulun, Amante Mangaser, Keith Laby, Steve Jordan and Jeff Wilson "Design and Control of a Macro-Micro Robot for Precise Force Applications," *Proc. of the 5th NASA/NSF/DOD Workshop on Aerospace Computational Control*, 1993.
- [7] Hogan, Neville, "Stable Execution of Contact Tasks Using Impedance Control," *Proc. of the IEEE Int. Conf on Robotics and Automation*, Raleigh, N. C., 1987.
- [8] Raibert, M., and J. Craig, "Hybrid Position/Force Control of Manipulators," *Journal of Dynamic Systems, Measurement, and Control*, vol. 102, pp. 126-133.
- [9] Wang, Yulun, "AESOP: Automated Endoscope for Optimal Positioning," Technical Note #2, Computer Motion, Inc., Goleta, Calif., 1993.
- [10] Szabo, Zoltan, "Laparoscopic Suturing and Tissue Approximation," in *Minimally Invasive Surgery*, John G. Hunter and Jonathan M. Sackier (eds.), McGraw Hill Inc., 1993, pp. 141-155.
- [11] Nathansan, L. K., "The Sutured Laparoscopic Gastrointestinal Anastomosis, in *Minimally Invasive Surgery*, John G. Hunter and Jonathan M. Sackier (eds.), McGraw Hill Inc., 1993, pp. 157-170.
- [12] Rinisland, H. H., "Basics of Robotics and Manipulators in Endoscopic Surgery," *Endoscopic Surgery and Allied Technologies*, Vol. 1, No. 3, June 1993, pp. 154-159.
- [13] Mueglitz, A, G. Kunad, P. Dautzenberg, B. Neisius, and R. Trapp, "Kinematic Problems of Manipulators for Minimal Invasive Surgery," *Endoscopic Surgery and Allied Technologies*, Vol. 1, No. 3, June 1993, pp. 160-164.

**THE USE OF INTERACTIVE COMPUTER VISION
AND ROBOT HAND CONTROLLERS FOR
ENHANCING MANUFACTURING SAFETY**

52-37

2438

P. 15

Neville I. Marzwell
Jet Propulsion Laboratory
California Institute of Technology
4800 Oak Grove Drive
Pasadena, CA 91109

and

Charles J. Jacobus, Thomas M. Peurach, and Brian T. Mitchell
Cybernet Systems Corporation
1919 Green Rd.
Ann Arbor, MI 48105

ABSTRACT

Current available robotic systems provide limited support for CAD-based model-driven visualization, sensing algorithm development and integration, and automated graphical planning systems. This paper describes ongoing work which provides the functionality necessary to apply advanced robotics to automated manufacturing and assembly operations. An interface has been built which incorporates 6-DOF tactile manipulation, displays for three dimensional graphical models, and automated tracking functions which depend on automated machine vision. A set of tools for single and multiple focal plane sensor image processing and understanding has been demonstrated which utilizes object recognition models. The resulting tool will enable sensing and planning from computationally simple graphical objects.

A synergistic interplay between human and operator vision is thus created from a programmable feedback received from the controller. This approach can be used as the basis for implementing enhanced safety in automated robotics manufacturing, assembly, repair and inspection tasks in both ground and space applications. Thus an interactive capability has been developed to match the modeled environment to the real task environment for safe and predictable task execution.

IDENTIFYING MANUFACTURING PROBLEMS

In many manufacturing facilities, the Ergonomics Coordinator and Engineering Staff have in place routine reporting mechanisms for plant production problem reporting and OSHA compliance safety reporting. On a monthly basis, issues with product quality and injury incidence are accumulated and reviewed at the plant level (**Figure 1**). These problems have been ranked and potential near-term solutions are proposed for safe and efficient operator-robot interface.

A number of reported production and safety plant problems have no immediate solution with hard automation or changes in methodology or even workcell redesign. These applications are candidates for combined operator and robotic solutions. For such

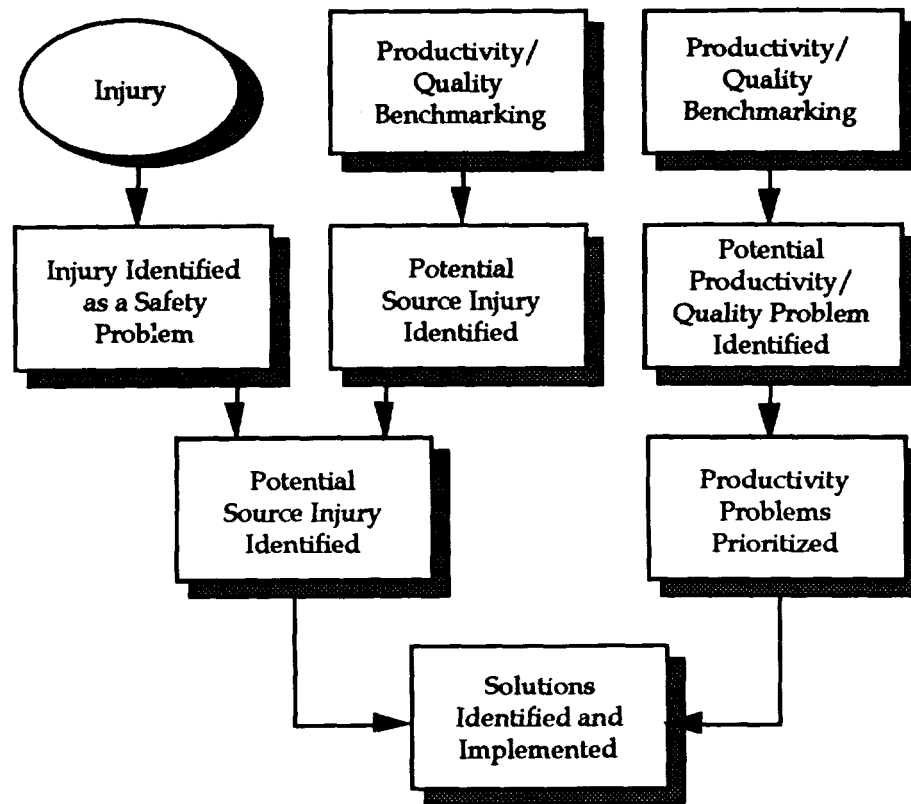


Figure 1. In-Plant Problem Identification Process

applications, a standard, rigorous methodology can be followed which consists of the following steps¹:

- (1) Identifying ergonomics problem areas which cannot be corrected through application of proven technology or job redesign -- this is performed through sanctioned plant reporting/ tracking processes outlined in Figure 1.
- (2) Scoping of the problem so estimated resources can be adequately weighed against the priority of the resulting solution to plant operation (i.e. preliminary cost benefit analysis).
- (3a) Analyzing relevant state of the art -- benchmarking the best of currently available job analysis/redesign methodology, automated system options, and mixed automation and human-in-the-loop methods.
- (3b) Detailing the current job methodology or process to act as a baseline for improvement benchmarking

¹This methodology is derived from the standard Ford Motor Company "Steps to Process Improvement."

- (4) Envisioning and implementing alternative teleoperated system concepts which maximize worker productivity (i.e. operation cycle times), and remain consistent with ergonomic principles.
- (5) Piloting in-plant testing of most cost effective and superior system concept proposed in (3) above.
- (6) Implementing the benchmarking of the system(s) pilot tested in (5) against prior manual practices as captured in step (3b). This benchmarking activity documents reduction in worker injury potential, documents any improvements in worker satisfaction and productivity, and documents any improvements in product quality if applicable.
- (7) Continuous improvement of commercialization of successful human-in-the-loop technology applications. Because (5) generates an unequivocal business case, commercialization can proceed expeditiously.

Through the above process applications have been identified that can benefit from telerobotic technology. These applications are focused on making the workplace more safe for the factory worker, and at the same time improve efficiency by enhanced human-robot interaction for task generation and environment calibration. This reduction of injury aspect of this form of automation is advantageous to both worker and management. The project development process used (Figure 2) has been effective in getting customers acceptance and support for this technology.

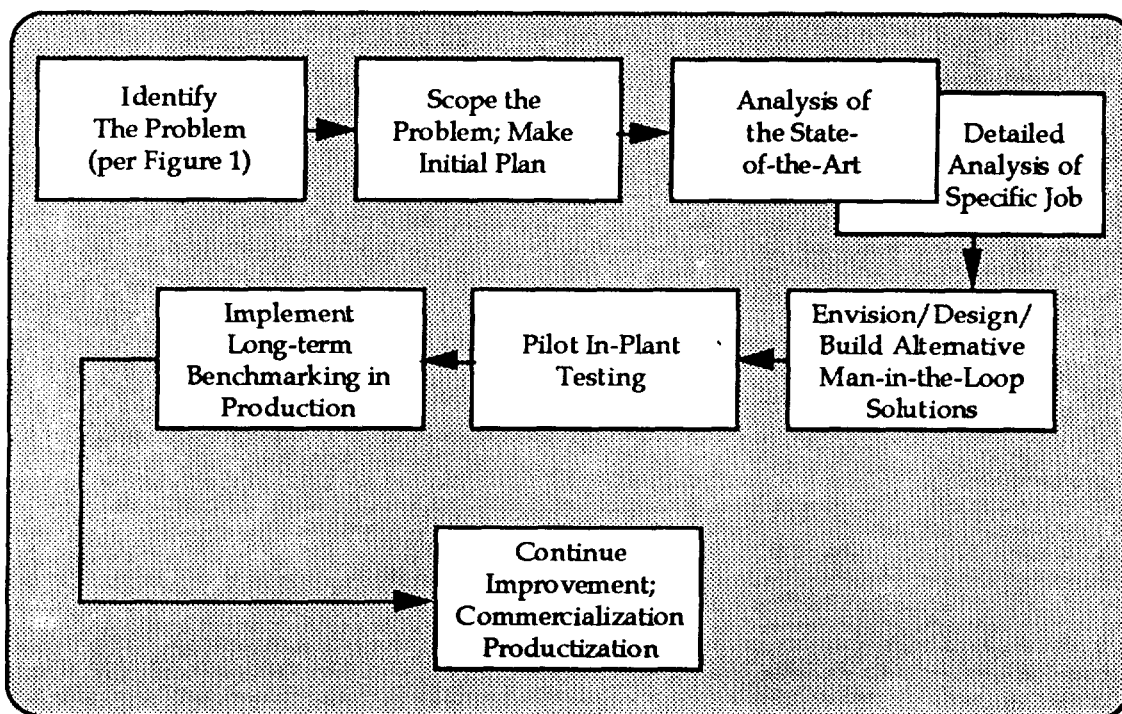


Figure 2. Technology Development Process

Telerobotics can remove a machine operator from hazardous environments by making it possible to understand, and tune operator's actions through the control interfaces to produce a specific effect at the remote machine. This added awareness is enhanced by combining computer generated visual or graphical cues with computer generated tactile/force feedback cues. Towards that goal an interactive computer vision-robot handcontroller for safe automated flexible manufacturing has been developed based on Cybernet 6-DOF force reflection handcontroller (see Figure 3), and advanced machine vision processing.

6 DOF HANDCONTROLLER

The PER-Force handcontroller manipulates robots or objects by "feel." Simulating a "sense of touch" by "force-reflection" with a wide motion range greatly enhances the efficiency of operations which require manipulation and dynamic control of objects in multidimensional spaces. The PER-Force handcontroller is a small backdrivable robot which moves in 6 degrees of freedom, 3 linear positions (x-, y-, z-) and 3 attitudes (roll, pitch, yaw) [1].

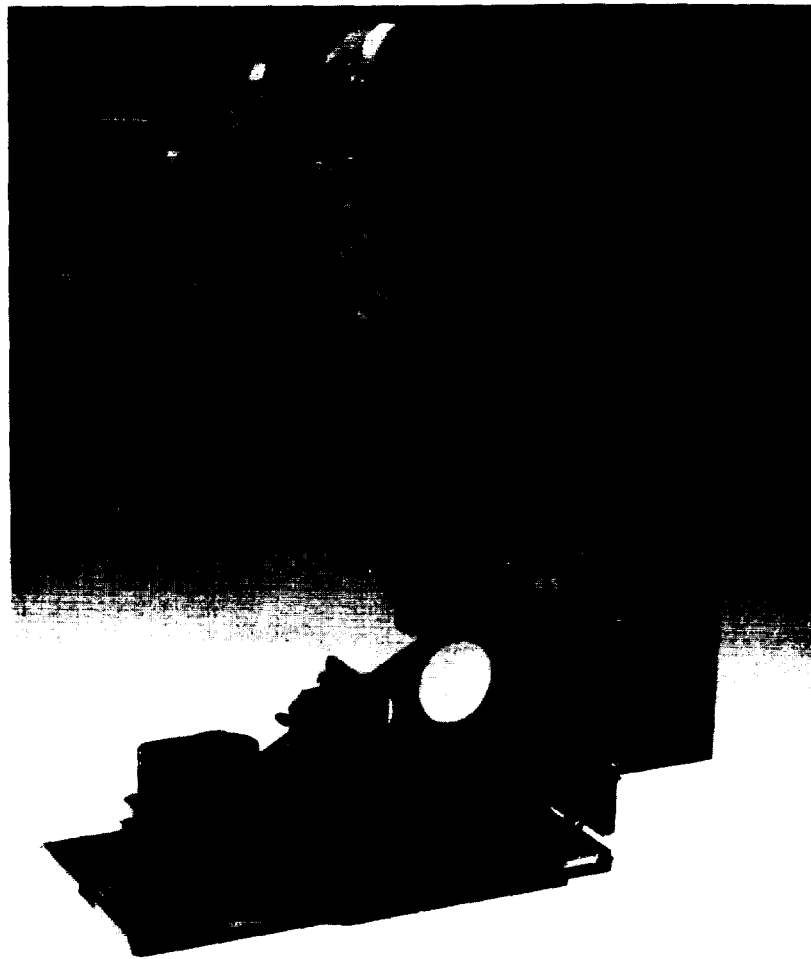


Figure 3. The Cybernet PER-Force 6 DOF Force Reflection Handcontroller

An operator can use this motorized handle to precisely position other robots or graphically displayed objects to a given location (x-, y-, z-) and tool angle (roll, pitch, yaw). This is done by a host computer or a robot control system that reads the handcontroller joint or transformed position, velocity, or force.

"Force-feedback" can be generated on each axis by the handcontroller through 6 small, brushless, DC servo motors. The six axis force-reflection output and six axis orientation and position control makes the manipulation and "feeling" of multidimensional objects or datasets extremely easy. The kinematic arrangement of the PER-Force stick is design for maximum simplicity and performance for both the electronic digital servo process and mechanical gravity compensation (**Figure 4**). The first two stages are a simple X-Y table (driven by a rack and pinion, and held in place by two parallel rails per stage). By convention X is side to side and Y is back and forth. Because these axes work parallel to gravity, no compensation is required.

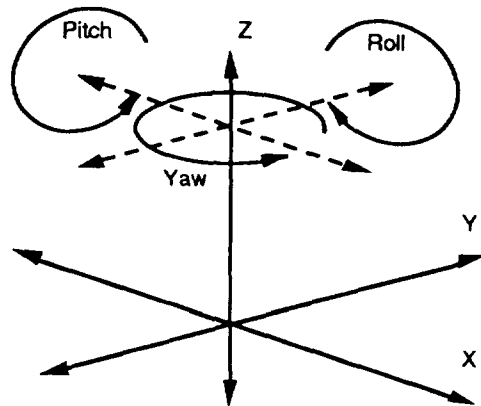


Figure 4. Handcontroller Kinematic Arrangement

The next stage is the Z axis, which is translated up and down. This axis levitates the yaw, pitch, and roll mechanisms, and the structures to which they attach. However, the Z motor and gear train themselves do not levitate (thus saving additional weight). The Z stage is gravity compensated by two constant force springs which are matched to the upper stage weight. The first revolute stage is yaw, which operates parallel to the base and therefore needs no gravity compensation. The next axis is pitch. The last axis is roll. All six axes of motion intersect at a point through the middle of the handle. We have found this to be the most comfortable pivot point for teleoperation.

The PER-Force Handcontroller is completely programmable including the time interval associated with the servo loop. Within the device, a servo shell process begins by initializing the interrupt loop data structures and linkages. After this is completed, the interrupt process runs every clock interval to provide the servo routines with a deterministic time base. In the PC-AT version, this clock interrupt is a re-programmed use of the system clock/timer.

The user initializes the desired time interval for the servo loop (shorter for crisper response -- longer to accommodate longer interrupt processing loops). The timer interrupt is skipped until enough ticks have been seen to represent this programmed interval. Then the interrupt level servo logic is executed. When the servo loop begins to run, it first collects each encoder value, computes estimates for velocity and acceleration, and then computes and option set of translations, scales, and rotations on the XYZ data and the pitch, roll, yaw data. This global transform allows the entire servo function space to be rotated, shifted, or scaled to create different force field "views".²

For a typical master-slave protocol, the input consists of slave positions or forces which are transformed from native slave coordinates to scaled master Cartesian coordinates (and then uses them to update gains, center locations, or forces in one or more interrupt level servo functions to create a force "feel"). Because the user actually installs pointers to their own control and/or command code, complete flexibility is available from the PER-Force servo structure (or course many useful controls are already included in the libraries). This flexibility enables the development of advanced user interfaces which use force feedback to implement new forms of machine-operator cooperative problem solving.

Towards integrating the 6-DOF handcontroller into the SGI environment, a stream module was written to generate handcontroller motion and button events for the SGI. The stream module converts a device specific data stream into an independent representation which the server interprets.

THE OPERATOR CONTROL STATION

The approach for the operator control station (OCS) is to develop a hybrid man/machine system, based on the competitive advantage of both the human and the computer, which will allow supervised control of a remote telerobot from an OCS which communicates with the telerobot over a communications channel that has a latency of several seconds and a thrupt limited to several megabits per second. The operator control station [2] represents the local site of a local-remote architecture telerobotic system for remote operations. The designed architecture supports multiple local-site operator control stations with a common remote site task execution system [3] as shown in Figure 5. The operator interface of the local operator control station has two primary parts: perception and manipulation. Perception provides an interactive means for modeling the remote site scene. Manipulation provides interactive task description, simulation, editing, and execution. Central to the operator interface is the knowledge base which holds information on the state of the local and remote site systems and manipulation and perception data. The methodology of the local-remote system is to build and simulate manipulation and sensing commands on the local site, using a model of the robot and its environment stored in the knowledge base, which has been updated and validated with feedback sensory data.

²This is analogous to changing the view port to a 3D model in model 3D graphics engines.

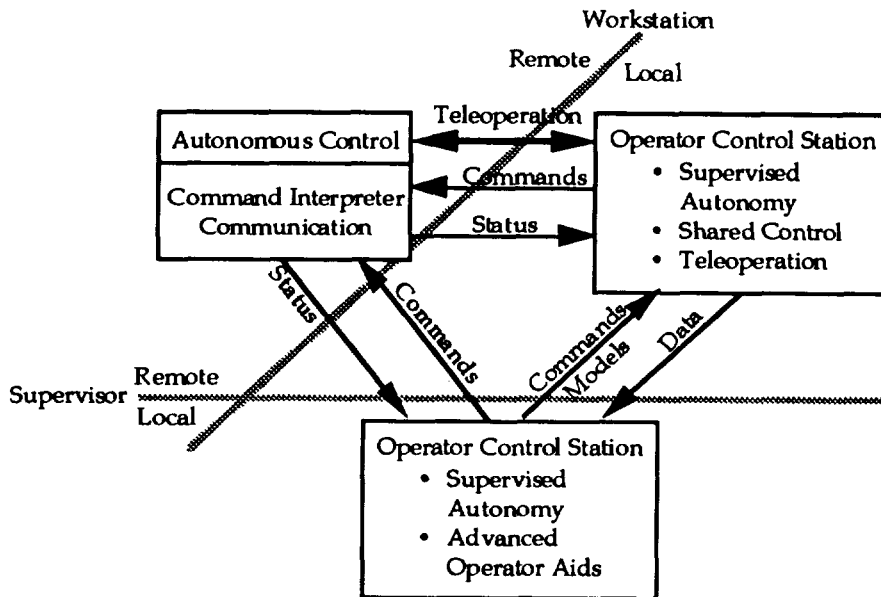


Figure 5. Local Remote Teleroobot Control Architecture

The control station is hosted on a Silicon Graphics IRIS 310 VGX Power Series workstation, equipped with a 6-axis "handcontroller" input device, and with LCD shuttered glasses for 3-D stereo viewing. The local site software is written in C, utilizing X Windows, Motif, the IRIS Inventor graphics product, and a small library of X resource manager extensions called the Widget Creation Library, developed at JPL.

The interactive perception module is designed to use a combination of operator input and machine vision to refine and calibrate the model of the task environment that resides in the knowledge base. Interactive perception utilizes computer power for precision measurement, and human perception for recognition, scene segmentation, and rough location designation, where reliable and efficient computer algorithms are unavailable. To aid human perception, the system provides views from multiple video cameras, including a stereo view for depth perception. 3-D graphics is overlaid onto both the stereo video views and the monocular video views in either wireframe, transparent, or solid. The three primary functions of perception are object localization, object model editing, and camera localization. In object localization, the operator translates and operates the graphics-overlay until reasonable registration has been achieved with video images of the object from multiple viewpoints. In camera localization, the operator uses the handcontroller to adjust the graphics overlay on a video image to best register the overlay against some visible objects whose position is accurately calibrated with respect to each other. For object model editing, the operator uses the handcontroller to move a 3-D cursor in order to designate the 3-D positions of vertices, and connect them graphically with edges..

The interactive task description capability is to make task description verification, and execution as simple as possible to the operator. This is achieved by providing the operator with a library of skills which the remote manipulators can perform. Skills are generic motion types, e.g., guarded-motion, move-to-touch, hinge, slide, screw, insert etc. When parameterized, a skill becomes a command which can be sent to the remote site for execution.

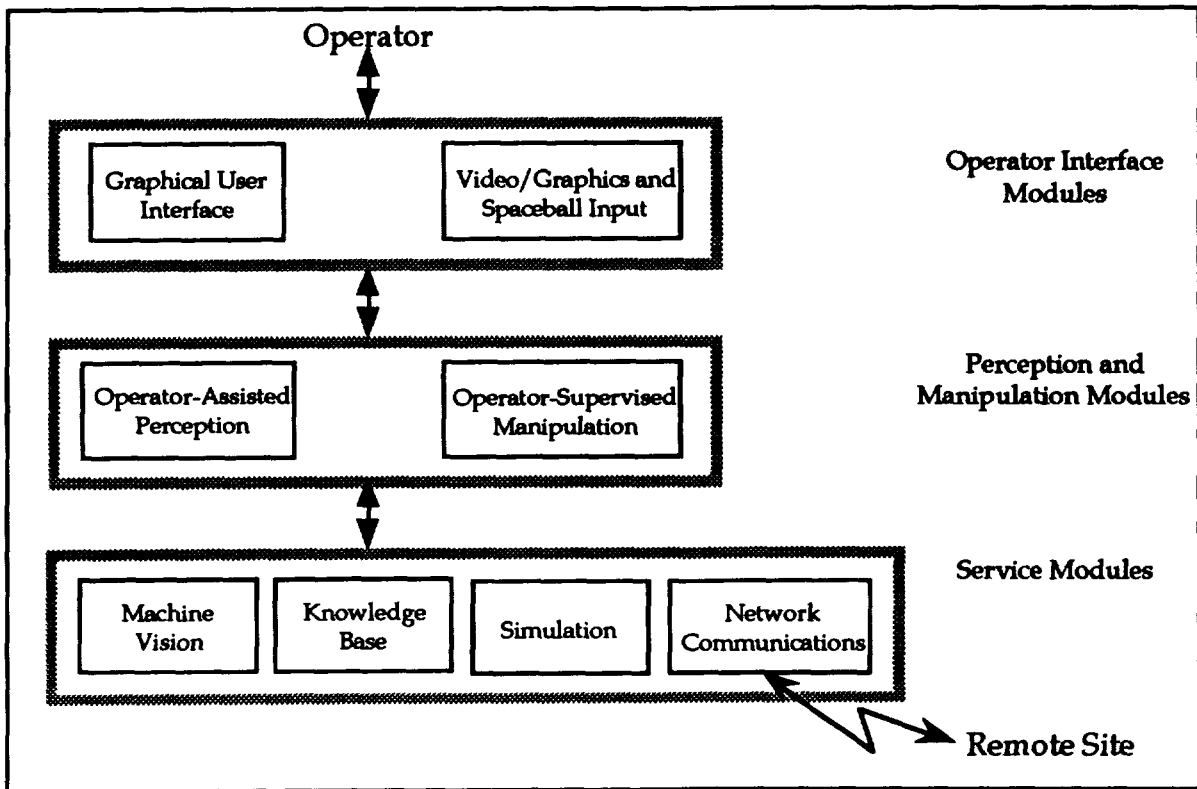


Figure 6. OCS Software Block Diagram

As shown in **Figure 6**, the software that implements the operator control station may be conceptualized in three levels. Operator interface modules directly interacting with the operator. The graphical user interface (GUI) allows the operator to command desired activities and provides high-level sequencing of subtasks, calling perception and manipulation modules as needed.

The current state of implementation of the local control station has enabled evaluation of the system's performance on several different tasks. It has been found to be an effective, convenient interface for controlling a telerobot in the presence of time delay in a semi-structured environment.

INTEGRATING THE TWO ENVIRONMENTS

The focus of our work has been directed at integrating the Per-Force into the OCS to enable rapid implementation of teleoperation environment within the manufacturing environment. Towards this end, we are developing an environment which features a 6 DOF force reflection handcontroller, contemporary CAD and graphics environments, image processing, and standardized robotic platform interfaces, to produce a 6 DOF robot controller (see **Figure 7**).

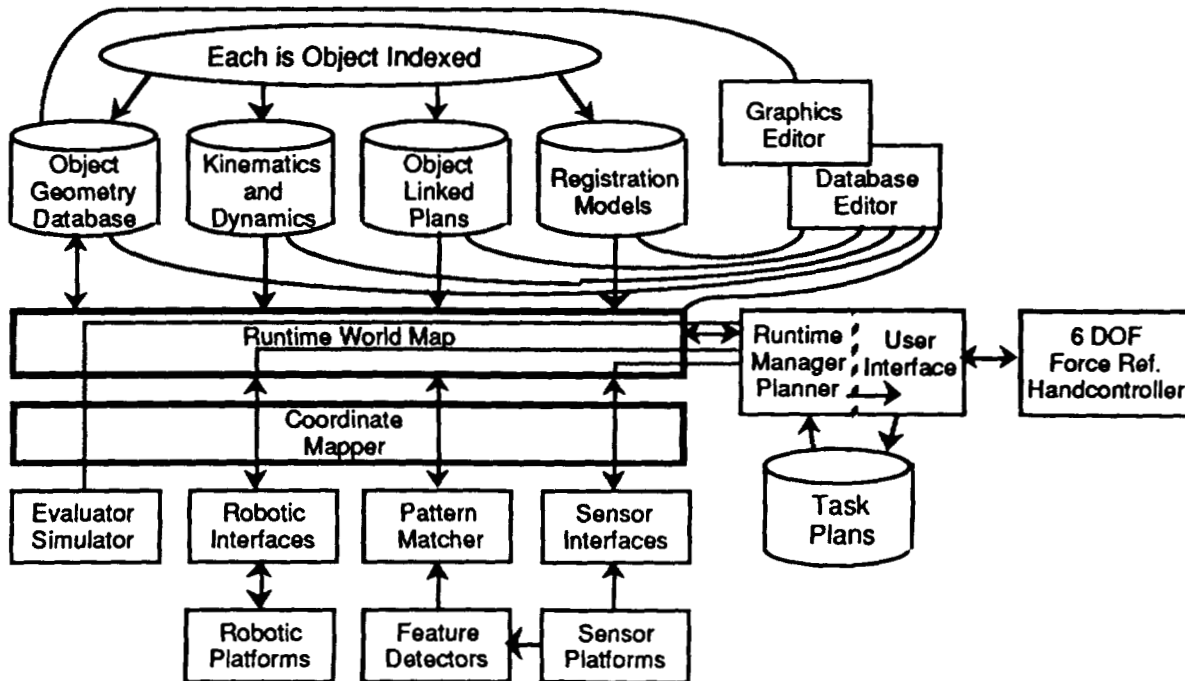


Figure 7. Combined Architecture

The development of such an environment is important because it facilitates more dynamic utilization of robots in manufacturing applications. It provides the operator with access to the geometry and physical properties of the parts to be manipulated. It bridges the gap between simulation and teleoperation. In doing so it provides an interesting vehicle for providing the human operator with supervision skills by combining human and machine vision capabilities. Within the system, object feature descriptions are linked back to the geometrical descriptions of parts (which link the feature locations to object locations and the object locations to gripping points) to enable machine vision registration of graphical part descriptions with physical sensed real-world information. Once this registration has been made, the operator can manipulate parts in a virtual reality which causes part placement within the real world.

APPLICATION TO MANUFACTURING

The process flow described above for identifying manufacturing applications has been used to identify manufacturing applications of the system under development. This process has identified several applications for this technology. One such application involves loading transmission cases within the Ford Motor Company. Currently transmission cases are delivered to the plant in large bins (nominally 4' x 4' x 7' in size - (Figure 8) in an unordered state and must be loaded onto kitting fixtures in a standard orientation. These cases weigh over 50 lbs and are now loaded manually, causing routine repetitive motion injuries. Standard manual lift assist devices are inconvenient and cumbersome enough that those performing this task have not adopted their consistent use.

This task is characteristic of one type of previously identified operation in which supervised teleoperation technology may be beneficial. That is, it is representative of tasks which require lifting heavier than safe loads. These tasks are still manually performed because part of the operation requires flexibility (i.e. rapid accommodation to

different transmission case types) and precision placement (placement in a standard orientation onto a standard kitting fixture for insertion onto the transfer line). This semi-structured bin-picking operation has been studied for full automation, usually by computer vision-guided robotics, for many years. This approach has resisted solution because of the complexity of part motion and computer vision program changeover for each successive new part (even relatively small part design changes dictate new computer vision recognition and part gripping strategies).

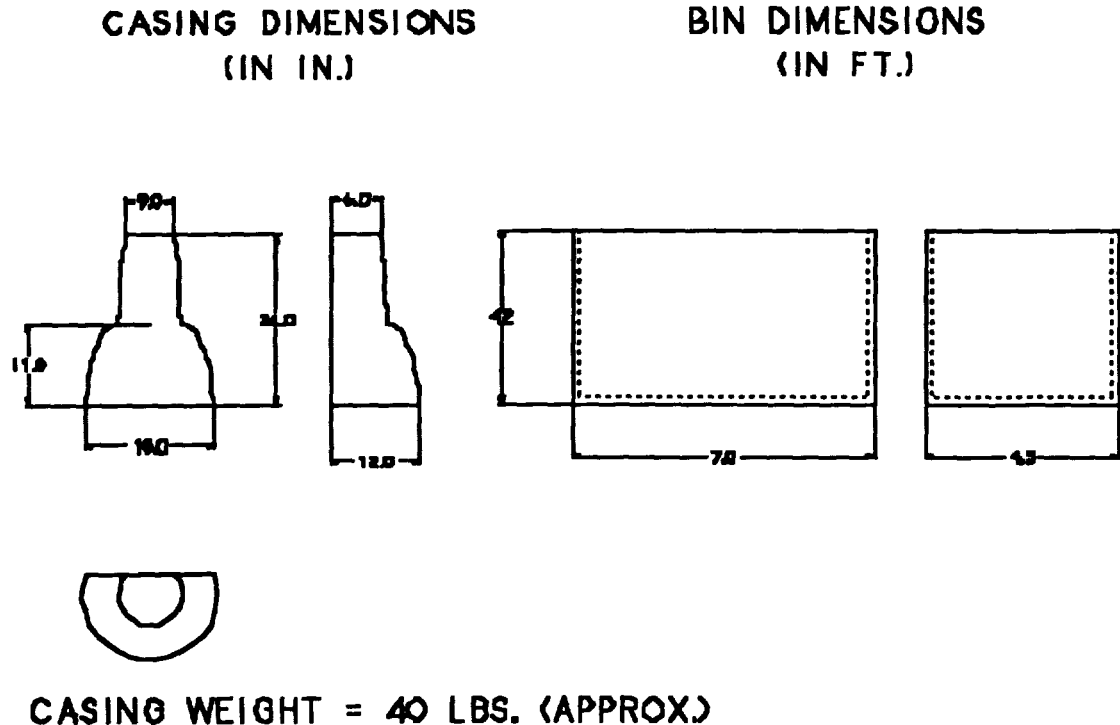


Figure 8. Transmission Cases and Their Transport Bins

Our approach combines an automated pick and place cycle robotics system with specific steps where an operator takes teleoperated control of the system. It includes an industrial robotic arm with an end effector capable of gripping and manipulating transmission cases. Control and manipulation is provided by a telerobotic force reflecting handcontroller electronically interfaced to the robot arm. Both teleoperated and automatic motions are supporting in the system to achieve both the flexibility of teleoperation coupled with the rapid cycle speed possible through automation. The alignment of transmission cases is enhanced through operator views provided by two cameras (and a graphics enhanced video viewing system). Transmission allotments are provided through a conveyor system. All moving parts/robotic elements are surrounded by safety fences. Figure 9 illustrates such a system.

Figure 10 shows the basic architecture of the design. The physical concept is shown in Figure 11a (top) and 11b (side). The unit consists of a conveyor subsystem for conveying work bins to the unloading site, a robot arm which is controlled to pick-up the transmission cases and place them on the assembly line conveyor system, and an operator control station from which operations are directed. The operator control station



Figure 9. Conceptual Layout of the Transmission Bin-Picking Cell

(Figure 9) consists of a telerobotic handcontroller for operator control of the robot system and a video viewing system, which allows transmission cases to be aligned for appropriate placement on the assembly transfer line.

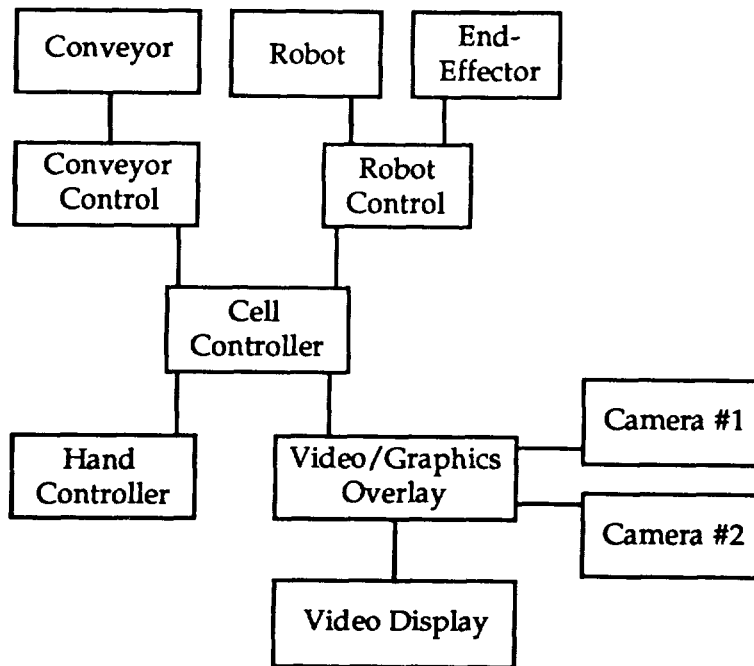


Figure 10. System architecture

As currently envisioned, a heavy duty conveyor system will be installed to convey the work bins into the work envelope. The conveyor must be designed to allow three full bins to be brought into the work envelope before the empty bins need to be removed. This system is gravity fed with safety brakes controlling the flow of the bins. The initial dimensions are estimated at 40 feet by 6.5 feet. Each bin is estimated to weigh 2000 lbs.

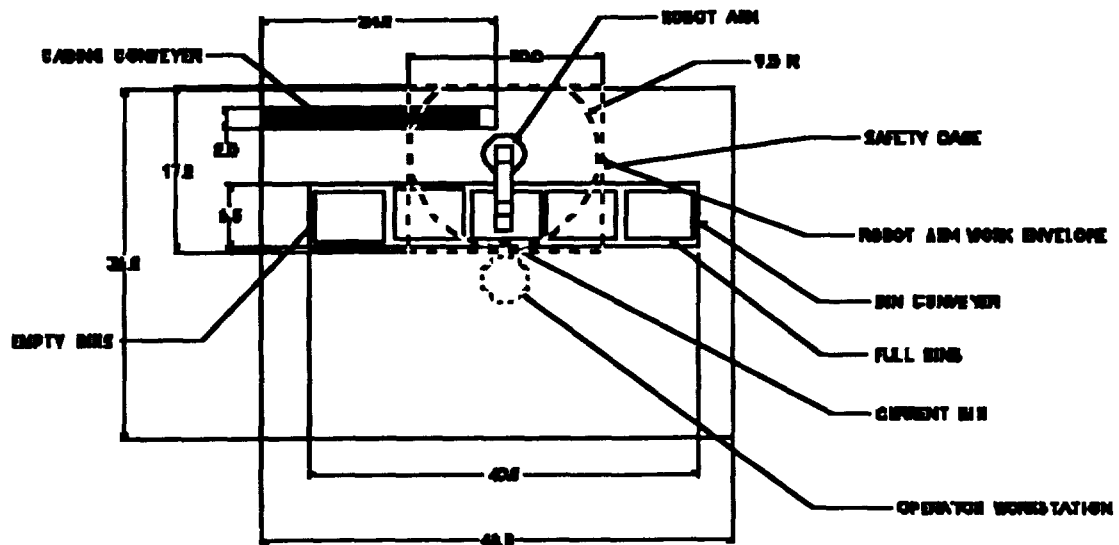


Figure 11a. Teleoperated Transmission Case Bin Picking Cell (Top)

The robotic arm which actually replaces manual lifting needs an envelope range of nominally eleven feet. A system in this size class has payload capacity of approximately 220 lbs. The arm is controlled by a combination of automated controls and a manually operated force reflecting telerobotic handcontroller. An appropriate transmission case-gripping end-effector is part of the robot system. The robot system is caged for operator safety.

The basic control interface to the operator is a telerobotic handcontroller with active force feedback. This allows the operator to have complete real-time control of the robot system position, orientation, and end-effector state (open/closed) and can allow the operator to feel robot-casing collisions and contacts. This handcontroller technology base also includes the technology of the robot system controller which acts as the cell control system, which drives conveyor, robot, and handcontroller actuators simultaneously.

A video viewing system is used to provide the operator with the visual cues necessary to properly align the transmission casing for the final placement. As currently envisioned, the operator cues the system to bring the case into a pre-specified location, within view of the video cameras, and performs manual alignment to a graphic overlaid on top of the casing video display. The cameras provide two orthogonal views which enhance the operator's ability to orient the casing prior to an automated step which places the case onto its suspension pins (on the carriers which transport the case to down stream assembly operations using the transmission conveyor system).

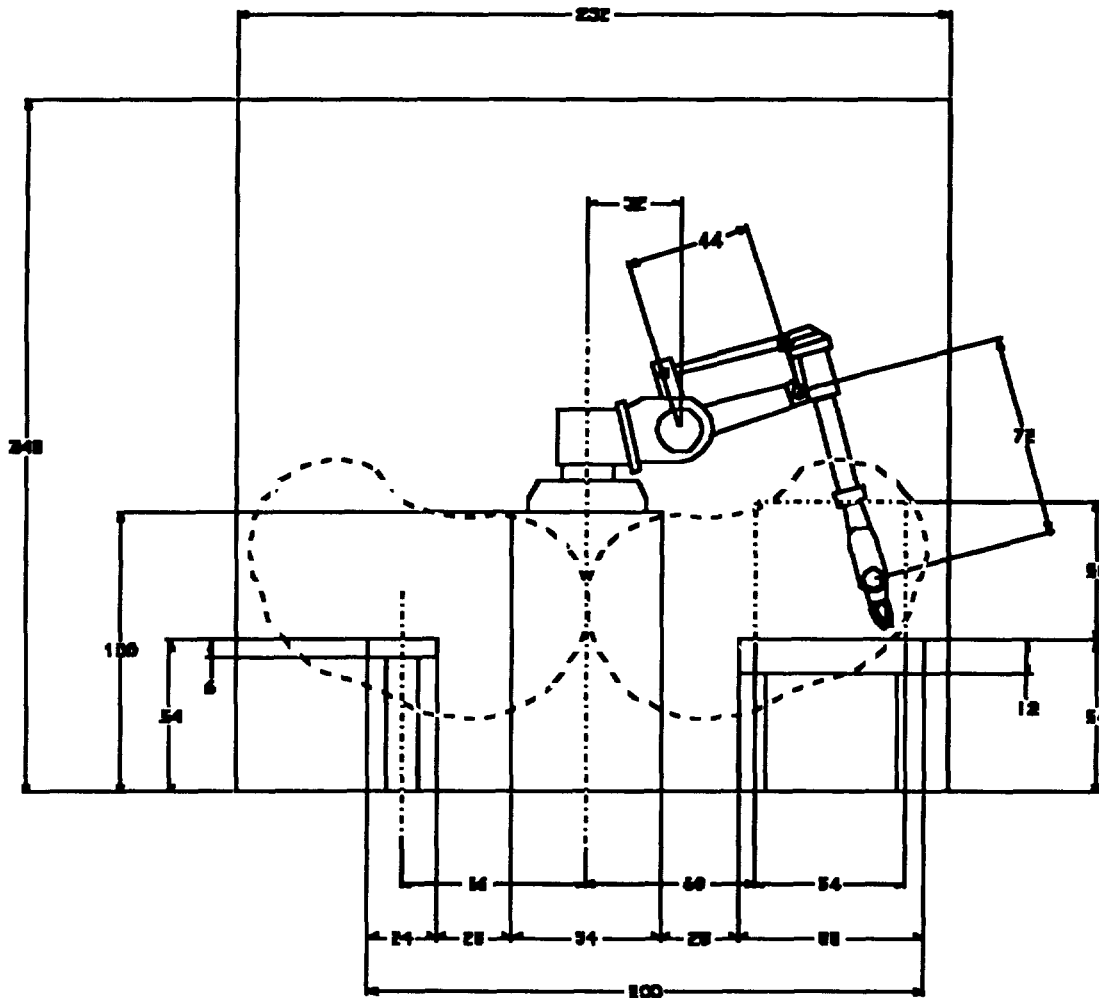


Figure 11b. Teleoperated Transmission Case Bin Picking Cell (Side)

Table 1 show a typical supervisor machine cycle for the conceptual teleoperated transmission bin-picking cell. The operator controls all actions of the robot arm through the use of a telerobotic handcontroller and control buttons. The operator is located slightly above the bin to provide direct visual contact for case grasping/gripping operations. Automation moves the robot to a location above the expected location of the next case within the bin (if this "guess" is incorrect the operator can control the robot to the correct location in the next step manually). Control is then passed to the operator (through the 6 axis handcontroller). The operator moves the robot arm to a casing using teleoperation (The operator controls the robot's end-effector by moving the handcontroller stick handle in the direction/orientation needed to mate the end-effector with the case; Tactile "feel" is provided by the stick to the operator's hand and visual cues are provide by direct viewing of the end-effector and the workpiece; End-effector grip is closed/opened through a trigger). Once the case is seized a control button is pressed which initiates a pre-programmed motion to move the transmission case to the alignment station (within view of alignment cameras). At the alignment station the operator visually aligns the case, using two cameras and a monitor (alignment is physically controlled by moving the force reflecting handcontroller to properly line up the video image of the unit with a graphics overlay target). After alignment has been

Table 1. Basic Machine Cycle: Diagram of Operations

Manual or Automated Operation	Operation Description	Operator Action Required
Automated	Robot moves to pick-up zone in bin	
Manual	If no case in the zone, operator cues system to next zone	Button Press
Automated	System passes robot control inside the zone to the operator (control is exercised through the handcontroller)	
Manual	Operator manipulates the handcontroller to place robot into gripping position around a case.	Hand Controller Operation
Manual	Operator cues end-effector gripping operation	Trigger Press
Automated	End-effector closes	
Manual	Operator cues re-grip (if grip operation failed) or automated move to the alignment viewing station (if grip is successful)	Trigger Release or Button Press
Automated	Cased is moved to the alignment viewing station	
Automated	System passes robot control to the operator for alignment	
Manual	Operator cues part flips	Button Press
Manual	Operator uses the handcontroller to make fine orientation adjustments (so that part image lines up with alignment graphics overlay)	Hand Controller Operation
Manual	Operator cues move to the transfer line conveyor fixturing	Button Press
Automated	Robot moves the case to the transfer line fixturing and places the case on the line	
Automated	Robot moves back to a pick-up zone in the bin -- operation cycles	

achieved, another switch depression initiates an automated action which places the casing on the transmission holder of the assembly line transfer conveyor.

Automated robotic pick-and-place operations can be much faster than the equivalent manual tasks, especially if the object to be manipulated is heavy for the operator. Thus, the cycle outlined decreases the loading operation time and at the same time retains manual flexibility to adapt to new transmission designs (assuming the hand-offs between man and machine are properly defined and tested).

Our system has the potential for implementing such solutions, and for quantifying capital cost and payback over an extended factory operational lifetime. The development of such applications and the verification of this payback is important to future human-in-the-loop manufacturing robotics technology.

ACKNOWLEDGMENTS

The authors wish to thank Dr. Paul Backes, John Beahan and Bruce Bon of the Jet Propulsion Laboratory for their research efforts. The research described in this paper was partially carried out by the Jet Propulsion Laboratory, California Institute of Technology, under a contract with the National Aeronautics and Space Administration, Office of Advanced Concepts and Technology. Cybernet Systems Corporation effort was funded from NASA/Jet Propulsion Laboratory under SBIR contract number NAS7-1189.

REFERENCES

Jacobus, H., Riggs, A. J., Jacobus, C. J., and Weinstein, Y. Implementation Issues for a Compact 6 Degree of Freedom Force Reflecting Handcontroller with Cueing of Modes. Human-Machine Interfaces for Teleoperators and Virtual Environments, Engineering Foundation, Santa Barbara, CA, March 4-9, 1990.

Bon, B., and Beahan, J., A graphics-based operator control station for local/remote telerobotics, SPIE Applications of Artificial Intelligence: Machine Vision and Robotics Conference, Orlando, FL, FL, April 1992.

Backes, P. G., Beahan, J., and Bon, B., Interactive Command Building and Sequencing for Supervised Autonomy, IEEE Int. Conf. Robotics and Automation, 1993.

53-37

N94- 30443

439

p. 6

**Programmable Automated Welding System (PAWS):
Control of Welding Through Software and Hardware**

**Martin D. Kline
Project Manager
Babcock & Wilcox
CIM Systems
Lynchburg, VA**

**Thomas E. Doyle
Technical Advisor
Babcock & Wilcox
Alliance Research Center
Alliance, OH**

Introduction

The first programmable control units for welding involved only the regulation of the welding power and travel speed usually performed by setting manual knobs and limit switches. The next generation of controllers then evolved as welding package extensions to commercial robot controllers. This second generation provides much greater capabilities such as, procedural language support (logic statements, sub-routine calls, etc.), control of complex manipulators, seam tracking, and the programmable control of the welding power supply. These controllers remain, however, hampered by complications with interfacing with other equipment (sensors, networks), limitations with processor performance, and a lack of flexibility. In addition, due to their nature, these controllers are more capable at the programming of the manipulator's motions than the integration of welding and motion attributes. This mode of operation provides adequate capabilities in medium- to large-batch operations where one of several pre-planned part programs are selected at the stand alone workcell.

The demands of very small batch operations and the need to integrate into a wider automation strategy have pushed the development of the present state-of-the-art controllers. These controllers address the integration of both off-line planning and real-time control activities. One such advanced welding control system is under development by Babcock & Wilcox. This system was initially developed as an Advanced Technology Development contract with the Naval Surface Warfare Center, Carderrock Division industrial transition is now being performed under a ManTech contract as part of the Navy Joining Center. This system, known as the Programmable Automated Welding System (PAWS), was created specifically to provide an automated means of planning, controlling, and evaluating critical welding situations to improve productivity and quality. The Navy was primarily concerned with the declining availability of skilled welders and increasingly difficult welding situations.

This system is capable of acquiring input from multiple process sensors and integrating this information to produce high quality welds with limited operator intervention. This challenge demanded a high-level of processing performance, a simple, yet flexible, operator interface, and a focus upon welding-specifics.

System Overview

PAWS consists of an Off-line Programming System (OLP) and an on-line, real-time controller. The OLP system provides a means to develop the plan for an entire automated welding operation, as well as the capability to manage existing plans. The OLP system provides an integrated platform for the motion and process planning functions. The Controller is capable of then implementing these plans during the actual welding process.

PAWS Off-line Programming System

The OLP system resides on a UNIX-based workstation and is comprised of a relational database, a motion planning module, a geometric modeling system, and a job builder module (refer to Figure 1). This system was developed following a client-server philosophy specifically to provide a decision support tool for the development, storage, and management of programs for the PAWS controller. The use of standards and the requirements of hardware portability have been highly stressed.

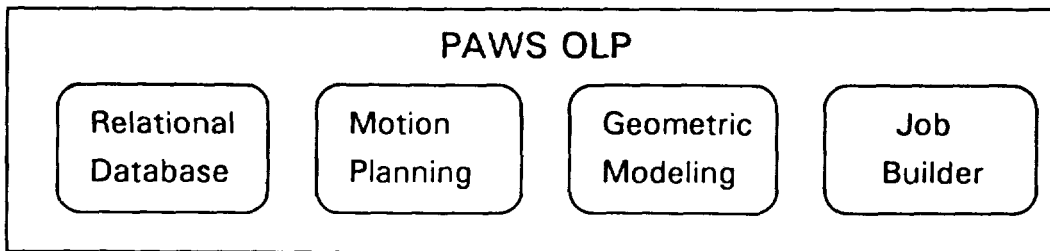


Figure 1: PAWS OLP

Relational Database This module provides a standard, user-friendly procedure for the generation and storage of strategies and information for performing the welding operation, these include welding process data, sensor fusion priorities, error resolution tactics, parameter logging plans, and I/O control actions. Storage of certified welding procedures in a standard database format allows for the maintenance and re-use of previously performed welding trails. This can significantly reduce the effort required to develop new certified weld procedures and weld schedules.

Motion Simulation The motion simulation module ties the motion of the manipulator to the process information. This module provides a graphical 3-D animation of the manipulator performing the welding operation with real-time collision detection. The interface for this process allows the operator to select joints for

welding, to assign to each joint a welding plan, to plan non-welding motion paths, to establish the orientation of the welding torch to the joint, to assign program attributes to physical part locations, and to re-plan motion in the event of a detected collision.

Geometric Modeling This module provides a convenient method for the modeling of parts, manipulators, end effectors, or physical environment constraints. This system also provides a means of importing CAD files of components and generating solid models from those files.

Job Builder The last subsystem, the job builder module, converts the plan into the PAWS controller-specific format to provide true off-line programming of the entire welding operation. This data is provided to the PAWS controller in the form of text files which are then converted to the real-time database format.

PAWS Controller

The PAWS controller consists of a VME Backplane with multi-tasking 68040 processor boards dedicated to welding and sensor control. In addition, a third 68040 processor provides the motion control, operator interface, and process coordination capabilities. On-bus resources provide the interface to the process equipment, including servo motion boards, as well as, digital, analog, and system I/O boards.

The PAWS controller accepts the plan from the PAWS OLP system and is capable of both on-line modification of this plan, as well as, the generation of an entirely new plan. The system uses a database structure to compartmentalize the process data. The controller is divided into modules which can be selectively employed to address the specific application (refer to Figure 2).

Process Coordinator The coordinator module utilizes a sequencer, to indicate the data which each process module should use for execution, and a rule-based expert system for exception handling. The sequence is built-up (either manually on the controller or automatically by the OLP's job builder module) as a series of statements specific to the welding process. These statements are English-like commands (e.g. START WELD ARC, STOP WELD ARC, MOVE ALONG, LOG DATA, etc..) which provide readable, high-level view of the job plan. During execution, the exception handler monitors the state of the on-going process and issues programmed responses when anomalous conditions occur. These responses can range from simple warnings to complex adaptive responses.

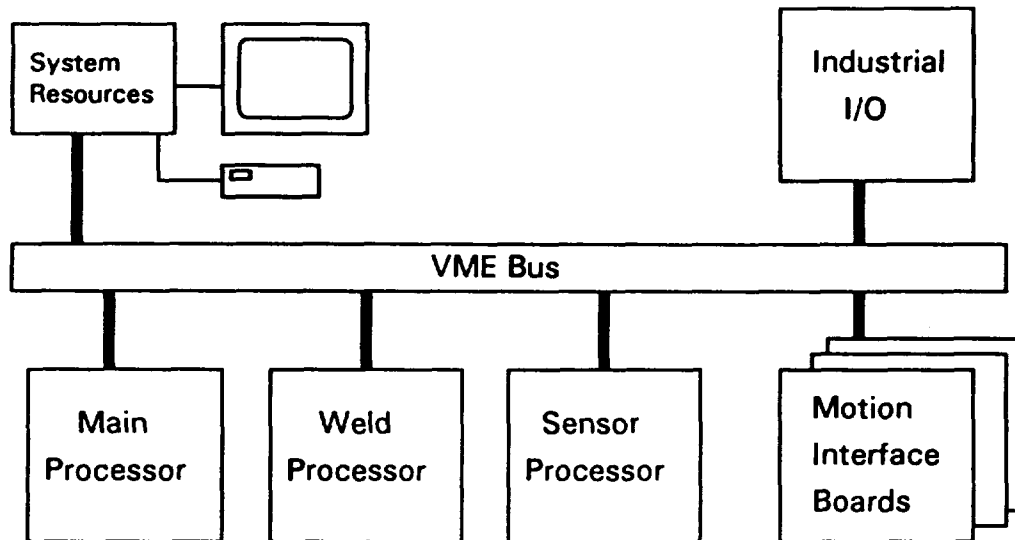


Figure 2: PAWS Controller Architecture

Motion Control The PAWS controller is capable of controlling a variety of manipulators, from a simple 3-axis tractor-type welding device up to multi-axis robotic manipulators. A total of three manipulators and 32-axis may be controlled from a single controller. The current demonstration system is based upon both a 6-axis PUMA 762 with a 7th oscillator axis and a separate 4-axis track device. The initial phase of the transition program will include the establishment of a teaching factory at a Babcock and Wilcox facility. This teaching factory is intended to include a gantry robot.

The motion control module incorporates the ability to perform path memorization, for the welding of passes which have been partially completed and are difficult to seam track. Additional features include: seamtracking, the ability to accept operator overrides of both cross seam and standoff distances, the ability to modify motion parameters (including oscillation parameters) for adaptive control, and the ability to perform touch sensing of the weld joint.

Weld Control The weld control module commands the power supply to control the weld process. The demonstration process is the synergic gas metal arc process (S-GMAW). The module commands the current and the voltage trim while monitoring a number of process parameters. Process parameters are prevented from exceeding the limits established in the weld procedure.

Parameter modifications are received from both the sensor control module and the operator interface and are implemented by the weld control module in a coordinated fashion. An embedded rules engine is employed for exception handling. Additional features include, consumable tracking and monitoring, user-definable I/O, and the expandability to other processes.

Operator Interface All interaction with the operator is performed through a menu-based graphical user interface. This interface provides both the run-time monitoring and reporting functions, as well as, the on-line teaching and planning features. Multiple window capabilities enable the viewing of data which is being logged, the monitoring of all system events, warnings, and errors, and the real-time monitoring of sensor data.

Parameter Logging The parameter logging module allows for the selective logging of data based upon time, path length, event-occurrence, or the reaching of an established threshold (e.g. heat input). Parameters can be also be averaged while being logged. Post-weld analysis capabilities allow logged data to be trend charted, as well as, the plotting of X-bar and R charts.

Sensor Control The last module to be discussed is the sensor control module. This module provides the corrective control algorithms for adaptive control and the fusion algorithms for dealing with the complicity of data provided by the numerous process sensors. The PAWS program incorporates the use of eight different sensors (see below). This module performs user-programmable data filtering, adaptive control of the welding process, and interfaces with the motion control module for joint finding and tracking. Exception handling is performed by an embedded rules engine. The current demonstration system performs communications with the various sensors through a dedicated serial port. Future implementations will incorporate a number of means including network protocols and backplane communications.

SENSOR	USAGE
Joint Vision Sensor	Seam Tracking Joint Volume Joint Shape
Integrated Optical Sensor	Pool Width Bead Height
Arc Element Sensor	Contamination in Arc (H ₂ , O ₂ , Fe)
Through-the-Arc Sensing	Seam Tracking
Touch Sensing	Joint Location
Arc Sensor Module	Arc Electrical Performance
Weld Acoustic Monitor	Arc Acoustical Performance
Plateborne Acoustic Emission Sensor	Defect Count Defect Type Defect Location

The Joint Vision Sensor is a commercially supplied sensor, whereas each other sensor has been developed within the PAWS program. The Idaho National Engineering Laboratory (INEL) developed and supplied the Integrated Optical Sensor. The National Institute of Standards and Technology (NIST) developed the Arc Sensor Module. The David Taylor Research Center developed the Weld Acoustic Monitor. Babcock & Wilcox has developed the Arc Hydrogen Sensor and the Plateborne Acoustic Emission Sensor.

The listed sensors cover a wide range of control areas including feedforward, feedback, and process monitoring. The PAWS controller is, however, capable of being configured to utilize only those sensors which are needed to perform the particular application. A typical application which is severely space-limited may use only through-the-arc tracking, whereas, an accessible component with critical process control criteria may utilize five or six different sensors.

Summary

The ATD phase of the PAWS program ended in November 1992 and the follow-on ManTech program was started in September 1993. The system will be industrially hardened during the first year of this program. Follow-on years will focus upon the transition into specific end-user sites. These implementations will also expand the system into other welding processes (e.g. FCAW, GTAW, PAW). In addition, the architecture is being developed for application to other non-welding robotic processes (e.g. inspection, surface finishing). Future development is anticipated to encompass hardening for extreme environments, expanded exception handling techniques, and application to a range of manipulators.

64-27
2440
P-16

SENSING THE GAS METAL ARC WELDING PROCESS

N. M. Carlson, J. A. Johnson, H. B. Smartt, A. D. Watkins,
E. D. Larsen, P. L. Taylor, and M. A. Waddoups

Idaho National Engineering Laboratory
P.O. Box 1625, Idaho Falls, ID 83415-2209

ABSTRACT

Control of gas metal arc welding (GMAW) requires real-time sensing of the process. Three sensing techniques for GMAW are being developed at the Idaho National Engineering Laboratory (INEL). These are (1) noncontacting ultrasonic sensing using a laser/EMAT (electromagnetic acoustic transducer) to detect defects in the solidified weld on a pass-by-pass basis, (2) integrated optical sensing using a CCD camera and a laser stripe to obtain cooling rate and weld bead geometry information, and (3) monitoring fluctuations in digitized welding voltage data to detect the mode of metal droplet transfer and assure that the desired mass input is achieved.

NONCONTACTING ULTRASONIC SENSOR SYSTEM

The ultrasonic sensor detects defects in the solidified weld metal on a pass-by-pass basis [1,2,3,4] for a multipass, pulsed GMAW process on thick section (31.8 to 41.3 mm, 1.25 to 1.625 in.) welds. The sensor is being developed under the Programmable Automated Welding System (PAWS) project. The noncontacting sensor system [5] has two sensor components, an ultrasound generating source and an ultrasound detector, as well as a remotely located computer data acquisition and processing unit.

The ultrasound is generated by a short duration, 11 ns, light pulse from an Nd:YAG laser with an exit beam power of 56 mJ/pulse. The 1 mm laser spot is delivered at a 20 Hz rate to the solidified top surface of the weld several inches behind the electrode using focusing optics mounted on the laser head [6,7]. The ultrasonic detector is an EMAT and amplifier designed and fabricated for PAWS at the National Institute of Standards and Technology in Boulder, Colorado [8]. The permanent magnet EMAT induces a magnetic field in the weld sample. The sound generated by the laser pulse interacts with the magnetic field, changing an associated electrical field. This interaction is detected by a pickup coil. The signal is then evaluated as an ultrasonic A scan. The ultrasonic system includes the hardware and software necessary to monitor the condition of the solidified weld metal while receiving and sending information to the weld controller about the quality of the solidified weld bead.

Pulsed Laser Sound Generation

A first step in devising a noncontacting technique for sensing defect generation in the welding process is to develop a method for generating sound waves in the material. In this system, ultrasound is generated by a focused, 1 mm (0.039 in.) diameter laser spot from a pulsed Nd:YAG laser operating at 1064 nm. The short duration, 11 ns, laser pulse has a peak intensity of 10^7 W/cm² and generates high frequency, broadband ultrasound in the solidified weld metal by surface ablation. The sound waves arrive at the top surface of the weld sample, where they are received by the EMAT, after reflecting or mode converting at the bottom surface of the sample.

For the PAWS demonstration, the compact laser head is mounted on a weld head. The laser head is 533 x 178 x 127 mm (21 x 7 x 5 in.) and 7.7 kg (17 lbs). The rugged laser head design provides optics sealed from the environment. To assure safe operation of the laser, the shutter and the high voltage supply are disabled by either computer or manual control. The laser head is connected to the laser power supply by an umbilical that supplies power and cooling to the laser head. A focusing optics fixture that houses a 50-50 beamsplitter, optional neutral density filters, and a 300 mm (11.8 in.) focusing lens is mounted in front of the laser to form the 1 mm (0.039 in.) spot size on the solidified weld bead.

EMAT Receiver

The basic components of an EMAT are a magnet, a conducting pickup coil, and amplifying electronics. The EMAT sensor assembly is 105 x 68.6 x 157 mm (4.13 x 2.70 x 6.18 in.). The height includes the cable to the associated electronics. The overall length increases to 163.5 mm (6.44 in.) with the addition of wheels to facilitate the movement of the EMAT down the weld sample. In Figure 1 the laser and EMAT are shown mounted to the carriage of a sidebeam welder. In the demonstration system, the components will be mounted on the weld head of a crawler; the detection approach is the same for both fixturings of the sensor components.

The EMAT produces a magnetic field in the sample using a neodymium-iron-boron permanent magnet. A magnetic pole-piece is placed between the permanent magnet and the pickup coil to intensify the magnetic field at the EMAT coil. The arriving laser-generated sound field causes the charges in the metal to move in the magnetic field, which generates a secondary field that is detected by a small pickup coil. The conducting pickup coil is a 25-turn counter wound, center tapped, coil mounted behind a stainless steel plate. The entire unit is designed to be sensitive to incident shear waves arriving at 45° with a frequency range of 0.5 to 2.0 MHz. The EMAT is sensitive to a minimum flaw size of 1 mm (0.039 in.) in the plane of the ultrasonic wave perpendicular to the direction of weld travel.

Effective operation of the EMAT also requires amplification of the received signal; this is accomplished by a preamplifier and a narrowband amplifier. The high gain, low noise preamplifier consists of two electronic circuit boards, located in the EMAT assembly, that provide common mode rejection and signal amplification of approximately 60 dB. The narrowband amplifier is located near the sensor computer away from the EMAT assembly and welder. This amplifier rejects electromagnetic interference picked up by the EMAT assembly and the 6.7 m (22 ft) signal cable, amplifies the signal by 20 dB, filters noise outside the signal bandpass, and outputs a signal to a 50 ohm load.

For the EMAT assembly to operate effectively on a weld sample, the pickup coil needs to be ~ 0.16 mm (6 mil) or less above the sample. To achieve this standoff distance and to allow the EMAT to move easily over the part being inspected, the EMAT is equipped with wheels. The wheels are electrically isolated from the weld sample using nonconducting shaft sleeves to avoid electrical interference from the welder. The EMAT assembly is attached to the welding head by a mounting fixture; the weight of the EMAT is supported by weld sample. The path that the laser and the EMAT follow is dictated by the path of the crawler weld head; the sensor components are positioned at the start of the welding pass and not relocated during the pass. Thus, for the demonstration system, the sensor is used on linear welds with the EMAT and laser moving parallel to the weld centerline. With the addition of servo motors, it would be possible for the EMAT and laser to inspect nonlinear weld parts.

Because the EMAT assembly is close to the preheated weld sample, external cooling is required to keep the magnet well below its Curie temperature and to cool the electronics enclosed in the EMAT assembly. The EMAT is currently designed to be placed on a plate preheated up to 93°C (200°F). Dry nitrogen or argon at -4°C and 6.9×10^4 Pa (25°F and 10 psi) is used as



Figure 1. Ultrasonic sensor components mounted on sidebeam welder.

the cooling medium. The cooling line is attached to a 6.35 mm (0.25 in.) electrically isolated line tube located on the top of the EMAT assembly.

Computer System

The computer system for the ultrasonic sensor acquires and processes information from the EMAT and determines if the weld is of acceptable quality. Information about unacceptable weld is sent to the weld controller. The central processing unit of the ultrasonic sensor is a full-featured 80486 based PC/AT compatible with a clock speed of 25 MHz. The CPU board has 4 megabytes of RAM memory, on chip memory cache, math co-processor, small computer systems interface and floppy controllers, and keyboard and VGA monitor ports. When the system is powered up, the watch-dog timer assures the successful start or restart of the system. The keyboard and monitor are necessary during the system integration and debugging phases. For the demonstration, the system operates without the keyboard or monitor.

A read-only solid state disk emulator and a read/write daughter board are used for storage of the operating system and data acquisition and processing software, and for temporary file storage of calibration and initialization values. The solid state disk emulator is equipped with an onboard PROM programmer. Utility software is available to copy files and programs onto the solid state disk emulator via a floppy disk.

A watch-dog timer/communication port card is used to reboot the sensor when the system crashes or hangs up due to an unexpected event. The watch-dog timer is equipped with a variable timer that is set by the sensor software. Before the end of each period the sensor software sets a bit in the register of the card. However, if the bit is not set before the end of the set period, the card provides a low-going TTL signal that is used to reset the CPU using auto restart routines. A card is also provided on the receiver and transmit lines to protect the computer from high-level common mode voltage spikes.

An RS-422 interface is used to communicate with the weld controller. If unacceptable weld is detected, the ultrasonic sensor system computer streams data packets about this condition to the controller via the RS-422 interface. Throughout the welding operation, data packets are communicated over the interface between the sensor and the controller.

A waveform analyzer board analyzes the incoming EMAT signals. The board is externally triggered by a synchronization pulse from the laser. The board, operating in the peak detection mode, detects the presence of signals in two calculated time windows. The presence or absence of the signals in the selected time windows indicates the quality of the weld and the health of the sensor system, as explained below.

The laser exit beam is controlled by the computer to ensure that the beam is only present when required for calibration and data acquisition. The signals to open the shutter and enable the high voltage creating the exit beam are sent to the laser from the digital I/O board. The status of the enable and disable of the beam on the digital I/O board is under the control of the ultrasonic sensor system's CPU. The CPU card, back plane, and necessary boards are housed in an industrial chassis in an environmental rack.

Defect Detection Approach

Ultrasound data are acquired and processed by the ultrasonic sensor system to determine the quality of the weld pass. The presence of good quality weld results in two signals being detected by the system. One signal, referred to as the detection signal, indicates the quality of the weld. The second signal, referred to as the health signal, indicates the operational quality of the ultrasonic sensor system. In the presence of a defect condition, such as incomplete penetration or porosity, the sound path of the detection signal is disrupted, resulting in a decrease in signal amplitude or complete loss of the signal. A confidence level evaluation is made by monitoring the amplitude of the health signal in a time window that is not likely to be altered by unacceptable weld quality. The health signal provides a means of determining that loss of the detection signal is due to a defect condition rather than to an equipment problem.

In the detection approach used for the ultrasonic sensor, there are three preparatory steps before acquiring data during a weld pass. The system completes acknowledgment and calibration sequences. Data describing the next weld pass geometry are then down loaded from the off-line programmer. These data are used by the ray tracing program in the initialization sequence to calculate the position of the laser and EMAT needed to direct sound through the critical fusion zone. Ray tracing also provides the arrival time and tangential displacement values of the signals of interest for monitoring the weld pass. These times are used by the computer to set the time gates on the waveform analyzer. The displacement values are used to determine the expected wave amplitude of arriving signals when no defects are present in the weld.

The sensor system can store the voltage of the detection signal for system debugging. This information can be plotted against distance along the weld centerline. Distance information is approximated using the expected travel speed; therefore, distance values can vary by up to 12.7 mm (0.5 in.). Figure 2 shows such a plot for the fourth weld pass on a 31.8 mm (1.25 in.) V-groove weld sample. The area of interest for detecting defects is the sidewall between passes three and four.

Based on the results of the calibration and initialization sequences, the threshold for acceptable weld is placed at 1.2 V. Therefore, all voltage values above 1.2 indicate acceptable weld. The system threshold can be adjusted to increase or decrease sensitivity depending on the requirements of the welding application. Three consecutive signals above or below threshold are required for the sensor to call an area acceptable or unacceptable; this avoids defect calls resulting from minor surface variations or transient fluctuations in the laser power.

The sample was radiographed to confirm the location of incomplete sidewall penetration for sensor system validation. From the radiograph, areas of continuous incomplete penetration are located between 178 and

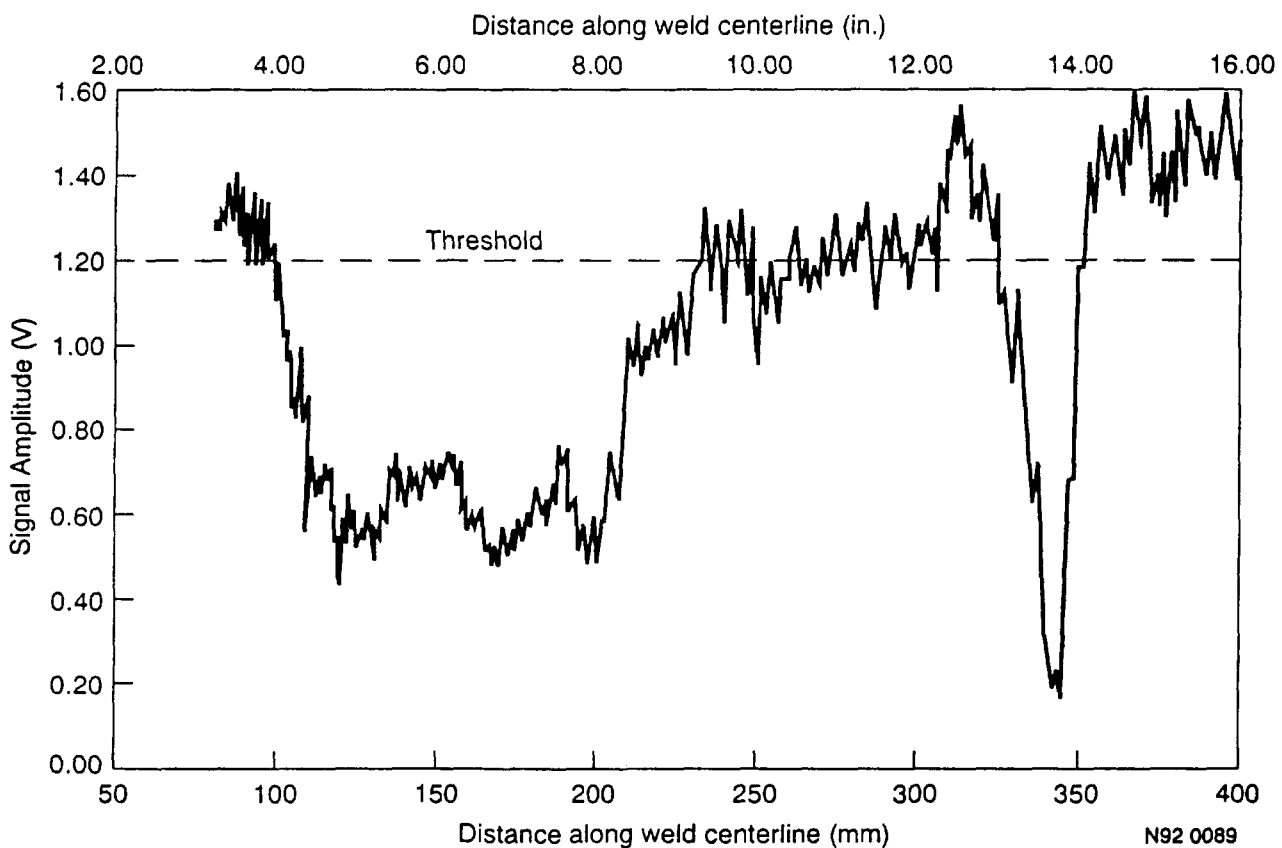


Figure 2. Distance vs. voltage for fourth weld pass.

279 mm (7.0-11.0 in.) and at 318 mm (12.5 in.). The ultrasonic system identified incomplete penetration in these areas as signal voltages are below the 1.2 V threshold (see Fig. 2). The sensor system detected other areas of intermittent incomplete penetration that were confirmed by the radiograph. Mild incomplete penetration is present in the first 381 mm (15 in.) of weld. The only area of good weld is from 381 mm (15 in.) to the end of the distance monitored. The sensor system's ability to detect incomplete penetration was validated for other selected passes using the procedures described above. Those tests confirmed the system's ability to detect incomplete penetration under GMAW conditions with travel speeds varying from 178 to 227 mm/min (7-9 in./min).

Ultrasonic Sensor Summary

An ultrasonic sensor system can be used to detect defects on a pass-by-pass basis when joining thick section plate using pulsed GMAW. The system is noncontacting and presents no weld contamination problems. The present system can detect defects in linear sections of weld on plate preheated to 93°C (200°F); a pulsed laser is used to generate ultrasound and an EMAT to receive the ultrasound. A PC-based computer system controls data acquisition and processing. When a defect condition is detected, the sensor computer alerts the controller that weld of unacceptable quality is being made. The sensor system provides the controller with defect information at 4 Hz for feed-back control of the GMAW process.

INTEGRATED OPTICAL SENSOR

An automated welding system must be capable of adapting to changing conditions encountered during the welding process. Many sensor systems have been developed to give automated welding systems the capability to adapt to variations in one parameter, e.g., laser striping for joint tracking [9], through-the-arc sensing [10], coaxial viewing of the weld pool [11], and infrared sensing [12]. The integrated optical sensor (IOS) is a multifunction, feedback control sensor that performs three distinct near-real-time measurements: weld pool position and width, standoff, and weld bead centerline cooling rate. The pool position and width are used to control the welding torch position relative to the weld pool, allowing the weld controller to compensate for such phenomena as arc blow. The welding system uses the sensor standoff distance in a feedback loop to control the contact-tip-to-work-piece distance. Cooling rate information is used to infer the final metallurgical state of the weld bead and heat-affected zone; therefore, postweld mechanical properties can be controlled.

The IOS consists of three major components: a remote head CCD camera with lens and filter pack, a continuous wave Ga-Ar diode laser, and a remotely located computer data acquisition and processing unit. The sensor head is mounted just behind the welding torch as pictured in Figure 3. The sensor's camera and laser are mounted in an industrially hardened case, allowing the sensor head to withstand harsh operating environments without any specialized cooling or power requirements. A cable attaches the sensor head to the computer data acquisition system. The computer processing system acquires images from the sensor's camera and analyzes them for weld pool width/position, standoff, and weld bead centerline cooling rate. Data are transmitted to the weld controller via an RS-422 serial interface at a rate up to 10 Hz.

Sensor Operation

The IOS is a stand-alone system that operates with minimal operator assistance. When the power is turned on the sensor computer is activated and boots the operating system, which then automatically starts the sensor software. The camera and laser power are activated and readied for operation. Once this has taken place, the sensor waits for an input command from the RS-422 serial communication port.

A calibration block centered underneath the IOS is used to calibrate the image intensity and distance measurements. The calibration procedure ensures that the level of illumination received by the camera is appropriate so that the temperature measurements made for the cooling rate calculation will be correct. The standoff is used to ensure that the correct distance values are reported. As long as the sensor-to-torch relationship is constant, the calibration need not be re-performed. When the calibration process ends, the sensor sends the calibration

complete command to the controller and is ready to acquire data.

During data acquisition, images are obtained with the frame grabber in the processing computer; the output data are determined and sent to the controller at a rate of up to 10 Hz. During sensor operation, the controller uses various commands to control the sensor. For example, the sensor may be paused and then continued. While the sensor is paused the laser shutter is closed and the sensor stops collecting data. The data output rate can be varied from 1 to 10 Hz by the controller. The temperature set point (the point at which the weld bead cooling rate is determined) may be changed, as well as the weld travel speed.

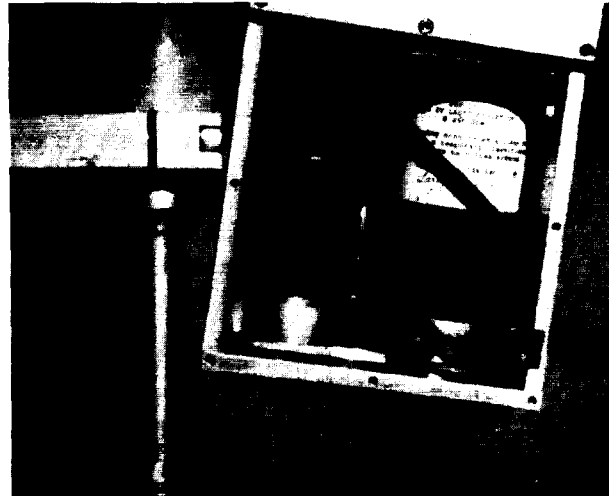


Figure 3. Sensor head with cover plate removed; remote CCD camera head is on left and diode laser on right.

Sensor Hardware

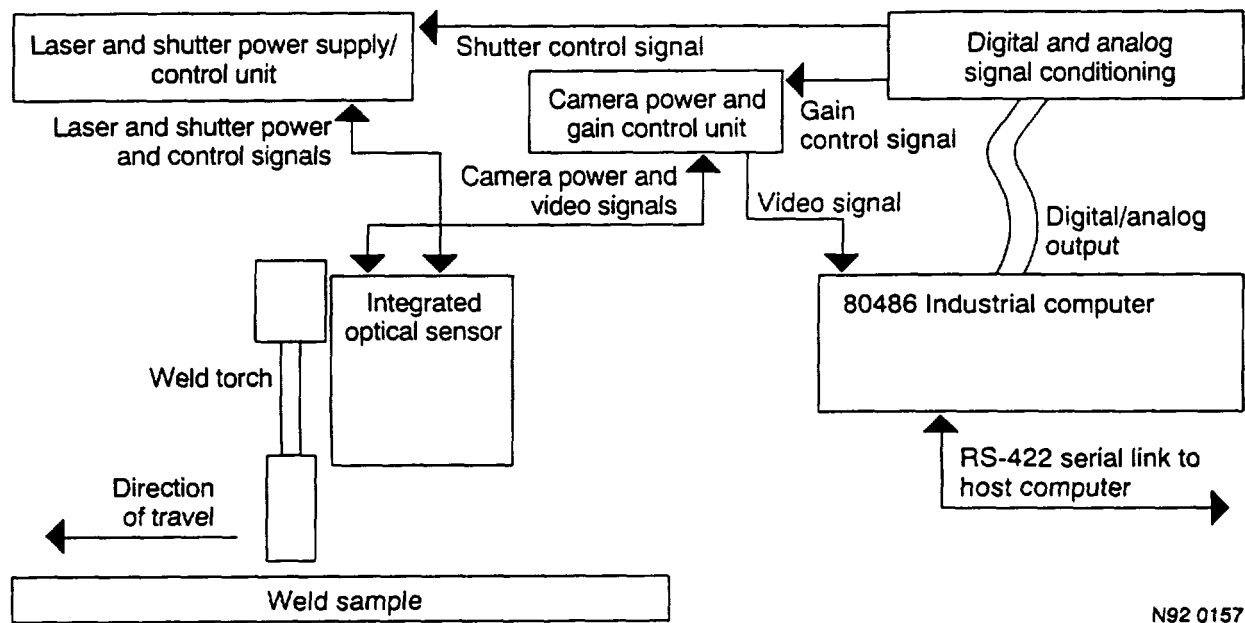
The sensor head, which is approximately 117 mm wide, 127 mm high, and 73 mm thick (4.6 x 5 x 2.9 in.) carries the camera and laser behind the welding torch. The sensor head is mounted on the welding torch at a slight angle so that the edge of the welding torch gas cup is visible in the image. This viewing angle ensures that the camera does not receive too much light from the welding arc. The camera view is approximately 63 x 45 mm (2.5 x 1.8 in.) at a standoff of 140 mm (5.5 in.). The diode laser supplies an infrared beam that is spread into a line using a cylindrical lens located in the lower portion of the laser housing. At the bottom of the laser housing is a shutter mechanism for controlling the laser beam. Underneath the laser are two mirrors that reflect the beam out of the IOS housing at the proper angle. All power, controls, and video signals are carried in a single umbilical cord from the sensor computer and laser control system. A diagram of the system is shown in Figure 4.

The IOS uses an industrial PC/AT compatible 80486 with 8 MB of memory, operating at 25 MHz, for data processing. The computer system is designed for stand-alone operation and does not require the use of a monitor or keyboard. The computer sends and receives data via an RS-422 serial communication port connected to the controller. A frame grabber is used to translate video images into arrays of pixel data. An analog and digital output board is used for interfacing with the laser shutter and camera gain controller. A watch-dog timer and a temperature monitor board are also installed in the computer. The watch-dog timer reboots the system if the computer "locks up" and is no longer processing data. The temperature monitor measures the internal temperature of the computer's case and can be used to send warning to the operator in the event of overheating. An electronic disk stores the software, thus avoiding the use of a more delicate hard disk. A floppy disk is required only for loading the software onto the electronic disk.

Sensor Software

The sensor software makes all the calculations for data output, as well as controlling the camera gain and laser shutter. To obtain the desired data output rate, the software was written using a 32 bit C compiler, which produces code that, with the help of a DOS extender, allows the software to take advantage of the protected mode of the 80486 CPU [13]. Protected mode allows the software to access all the memory installed in the machine and run approximately twice as fast as the same software would run in the typical real mode used by DOS [14].

To calculate output data, the computer obtains images of the weld pool from the camera and converts them into an array of numbers ranging from zero to 256 using a frame grabber residing on the I/O bus. The array of image data is available to the computer as part of the computer's protected memory. The array of pixels in



N92 0157

Figure 4. Diagram of IOS sensor system components.

memory is analyzed for intensities and object locations using common image processing techniques [15,16].

Data processing operations locate the edges of the molten weld pool, calculate the center of the weld pool, and scan the image at the center location. The laser line data and data from the calibration sequence are used to determine the standoff for each edge of the weld bead in millimeters. Cooling rate is determined using the scan of the image along the weld centerline. An exponential or linear equation is fit to the scanned data. The slope of the curve is then calculated, and with the travel speed data, converted into a cooling rate in Centigrade degrees per second. When all calculations are complete the data are sent to the controller. The complete processing time for all data operations is approximately one tenth of one second.

Sensor Calibration

The measurement of the step on the calibration block is used to develop a scale factor normal to the weld centerline; the scale factor along the weld centerline is derived using the known aspect ratio of the frame grabber. The known height of the step on the calibration block is used to determine a standoff scaling factor. With the known standoff sent from the controller, the sensor can determine the zero point for referencing laser line movement. The scale factors and the reference point are then used to calculate real-world measurements before they are sent to the controller.

The temperature measurement function of the sensor is used to determine cooling rate. The sensor uses the camera to detect the infrared radiant energy from the surface of the weld metal. The level of radiant energy indicates the temperature. For the measurements to be consistent, the camera gain setting is adjusted during the calibration procedure. The computer simply evaluates the level of brightness of the image received during the calibration procedure and adjusts it, using the camera gain control, to a predetermined level.

For the infrared energy received by the camera to reflect the real temperature of the material, the camera is evaluated using a black body source. ("A black body, or ideal radiator, is a body which emits and absorbs at any temperature the maximum possible amount of radiation at any given wavelength." [17]) The camera is aimed at the black body source and the pixel levels are recorded for temperatures set throughout the range of the source. The IOS reads temperatures in the range of 982 to 1425 C° (1800 to 2600 F°).

Integrated Optical Sensor Summary

The IOS is a multifunction feedback control sensor that makes three distinct measurements in near real time: weld pool position and width, standoff, and weld bead centerline cooling rate. Weld pool position and width are used by the weld controller to control the position of the weld pool in relation to the joint. The standoff is used to control contact-tip-to-work-piece distance based upon the distances measured from the sensor to each edge of the weld bead. Cooling rate information is used to infer the final metallurgical state of the weld bead and heat-affected zone.

Because of the sensor's small size, it mounts unobtrusively behind the welding torch; previous infrared measurement devices were too large to mount behind the welding torch. Since the IOS uses standard off-the-lab-shelf components, the cost of the sensor is relatively low, enabling the technology to be more readily utilized.

DYNAMICS OF DROPLET DETACHMENT

Growth and detachment of droplets in GMAW play an important role in predicting the heat and mass transfer to the weld pool. Previous work [18,19] shows that the droplets not only have momentum but also carry approximately 47% of the total heat transferred to the weld pool. Droplet size and detachment frequencies are important in controlling weld pool shape and solidified weld microstructure.

GMAW exhibits various modes of droplet transfer. With 98% argon/2% oxygen shielding gas, the common modes of transfer are globular, spray, streaming spray, and rotating spray transfers. Lesnewich [20] showed that the mode of metal transfer depends on process variables such as welding current, electrode extension, electrode diameter, and polarity. He showed that there is a sharp transition between the globular and spray modes of metal transfer that occurs at specific process variables. In the transition from the globular to spray transfer modes, the droplet detachment frequency dramatically increases while the droplet size correspondingly decreases. Recently, however, other researchers [19,21] have found that the globular to spray transition occurs over wider ranges of variables. Clark [19] suggested that during the transition from globular to spray, droplet size and detachment frequency bifurcate between larger droplet sizes and longer detachment times (globular) and smaller droplet sizes and shorter detachment times (spray) as electrode speed is increased.

Modeling and control of GMAW require both theoretical and experimental investigations into the physics of the process [20,22,23]. Several theories, such as force balance [24,25] and pinch instability [26,27], have been proposed to explain the droplet transfer. Limited success was obtained in predicting transfer mode. The models do not account for bifurcations in droplet detachment frequencies and size during the transition between globular and spray transfer modes. Measuring the dynamics of the metal transfer mode in GMAW is part of an ongoing effort. In the globular transfer region such measurements are mainly of academic interest and provide grist for the theoreticians and modelers. In the spray region these measurements may lead to new insights into the process, resulting in methods of controlling droplet transfer, and thus potentially controlling droplet momentum, which may have important implications for controlling the depth of penetration and other parameters of the weld pool.

Experimental Investigation

Data are acquired over a wide range of electrode speeds to analyze the transition of metal transfer from globular to spray. In previous work, [28,29] analysis of high-speed film data taken synchronously with the electrical data has been presented. Those preliminary results indicated a possible transition from a single frequency and droplet size to a bifurcation and then to a chaotic transfer. This section reports on measurements of the voltage and current over a range of electrode speeds encompassing the transition region in an attempt to confirm this transition to chaotic transfer [30].

Welding Parameters

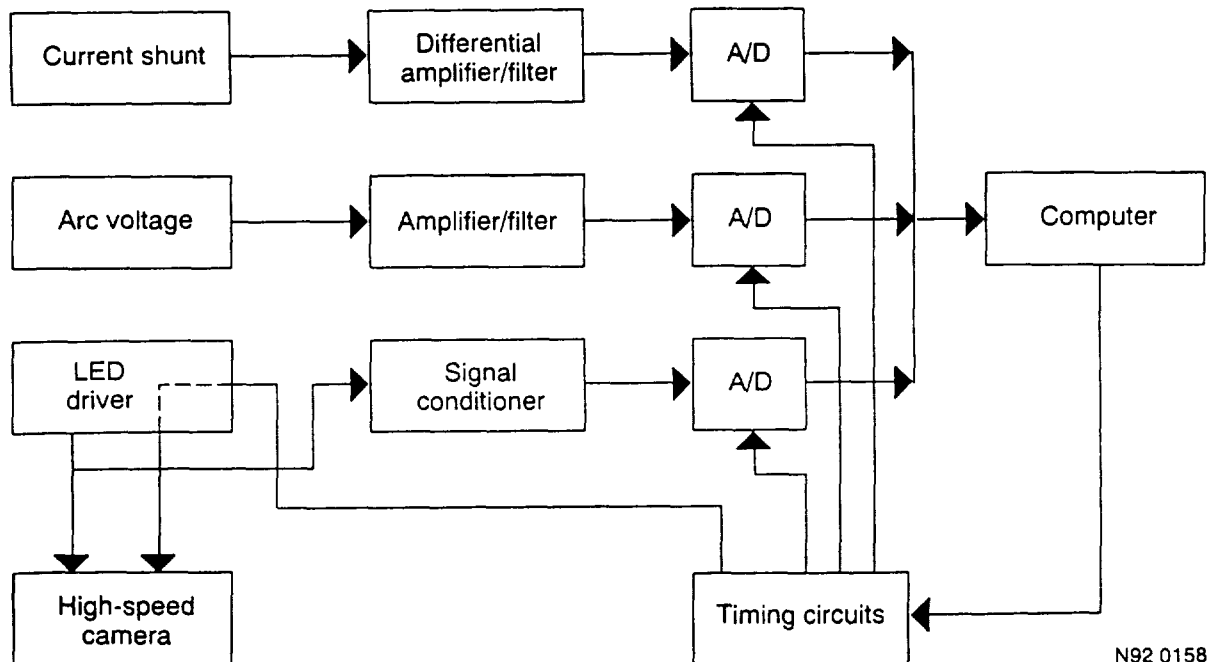
The electrode speed was changed to obtain the variation in transfer mode, with the contact-tip-to-workpiece distance, the open-circuit voltage, the materials and the travel speed kept constant for most of the measurements (see Table 1). At very low electrode speeds, the travel speed had to be decreased to obtain a stable arc.

Electronic Data Acquisition System

The system is similar to that described in [28]. The major change was to provide the capability to use significantly longer data acquisition periods. The sampling rate was decreased from 50 to 10 kHz and transient digitizers with 128k, instead of 8k, of memory were used. These changes made acquisition times of up to 13.1 s, in contrast to 0.164 s, possible. Thus a significantly larger number of droplet transfer events can now be observed. A schematic of the system is shown in Figure 5. Other changes included a more accurate calibration of the system and improved amplification and filtering. Both the current and voltage data had an analog 3 dB bandwidth between 0.3 and 3000 Hz. Some of the data were subsequently digitally filtered to a narrower bandwidth as required for different analyses. The system was calibrated by acquiring signals from a source with known sinusoidal voltage at several frequencies in the bandwidth.

Table 1. Welding Parameters

Electrode Speed	55 - 170 mm/s	Power-Supply Slope	0.004 V/A
Travel Speed	1.0 - 4.2 mm/s	Electrode Diameter	0.889 mm
Contact-Tip-to-Workpiece Distance	15.9 mm	Electrode Composition	AWS A5.18, ER70S-3
Open-Circuit Voltage	27.0 V	Shield-gas Flow	14.2 L/min
Shielding Gas	Ar - 2% O		



N92 0158

Figure 5. Diagram of droplet detachment sensor system components.

Detachment time intervals were measured for a number of electrode speeds using the variation in the acquired electrode-to-workpiece voltage. A typical voltage signal, after filtering to remove the low-frequency variations, showed a series of bipolar spikes. Each bipolar spike in the signal corresponded to a droplet detachment. A computer program was written to detect these detachments using the voltage signal and to calculate the average and range of detachment time intervals.

High-Speed Movies

High-speed movies were made using a laser back-lighting technique [23] to suppress the arc light and produce a silhouette of the electrode and droplets. A semiautomatic image analysis system was developed to obtain information about the droplets, including time between detachments, electrode position, droplet volume, and droplet kinematics. A frame of the film was projected on a film viewer and the image was transferred to a computer using a video camera and a frame grabber. The image was then enhanced to produce outlines of the electrode and the droplets. From these outlines the projected area and position of each droplet as a function of time were determined. The detachment time for each droplet could also be determined using timing marks placed in the region of the film between the sprocket marks. These timing marks were also recorded synchronously with the electrical data so that a one-to-one correspondence between that data and the film could be made. Figure 6 shows a typical frame, taken just after droplet detachment.

The volume of the droplets was calculated by measuring the area of the silhouette in square pixels for 10 to 20 frames after detachment. The average of these measurements was assumed to be the projected area of the equivalent sphere and the volume was calculated using this assumption. This averaging procedure also smoothes some of the quantum effects due to the finite pixel size. The droplet silhouettes are actually observed to oscillate from a distorted, elongated shape (see Fig. 6), to a circular shape, and then to a slightly flattened circular shape. Some larger droplets also showed flattened sides as they oscillated about the assumed equilibrium spherical shape.

Electrical Signals

The detachment time intervals are summarized in Table 2. The structure of the data can be seen better in Figure 7, where the percentage of droplets falling in a particular detachment time range is plotted as a function of the detachment time and the electrode speed.

The range of detachment times (0.1 ms to 1 s) is divided logarithmically into 50 bins. A gray scale ranging from white, corresponding to less than 1%, to black, corresponding to greater than 28%, is used to show detachments.

The data at the upper left of Figure 7 is from pure globular transfer with droplet diameters greater than the electrode diameter. As the electrode speed increases, a transition to shorter detachment times and smaller droplets is observed; at about 140 mm/s the system appears to transition to spray transfer. This can be seen from the second set of droplets with a much shorter detachment time that appears in the lower right-hand portion of Figure 7. This second set of droplets, however, then merges with the original set where most of the droplets are again larger than the electrode diameter, corresponding to globular transfer. Thus, these data indicate that no sharp transition between globular transfer and spray transfer exists. Rather, small droplets gradually become more prominent and the percentage of



Figure 6. Back-lighted image of a globular droplet just after detachment.

Table 2. Summary of Detachment Times

Electrode				Electrode			
Speed (mm/s)	DC Current (A)	Ave. Time (ms)	Range of Times (ms)	Speed (mm/s)	DC Current (A)	Ave. Time (ms)	Range of Times (ms)
55	90	379	114-689	115	163	52	9.9-142
60	94	311	59-543	120	167	48	13-140
65	97	251	37-435	125	176	36	6.8-62
70	106	218	37-560	130	184	28	2.3-59
75	112	196	62-418	135	180	21	1.9-126
80	124	160	20-265	140	184	18	0.8-77
85	135	136	26-285	145	187	12	0.2-48
90	139	106	15-208	150	195	8.1	0.1-27
95	142	89	32-196	155	195	10.3	1.7-21
100	148	77	26-214	160	197	5.0	0.2-30.5
105	150	65	9.9-140	165	190	8.2	2.2-15.1
110	154	57	2.3-160	170	190	6.8	0.5-13.8

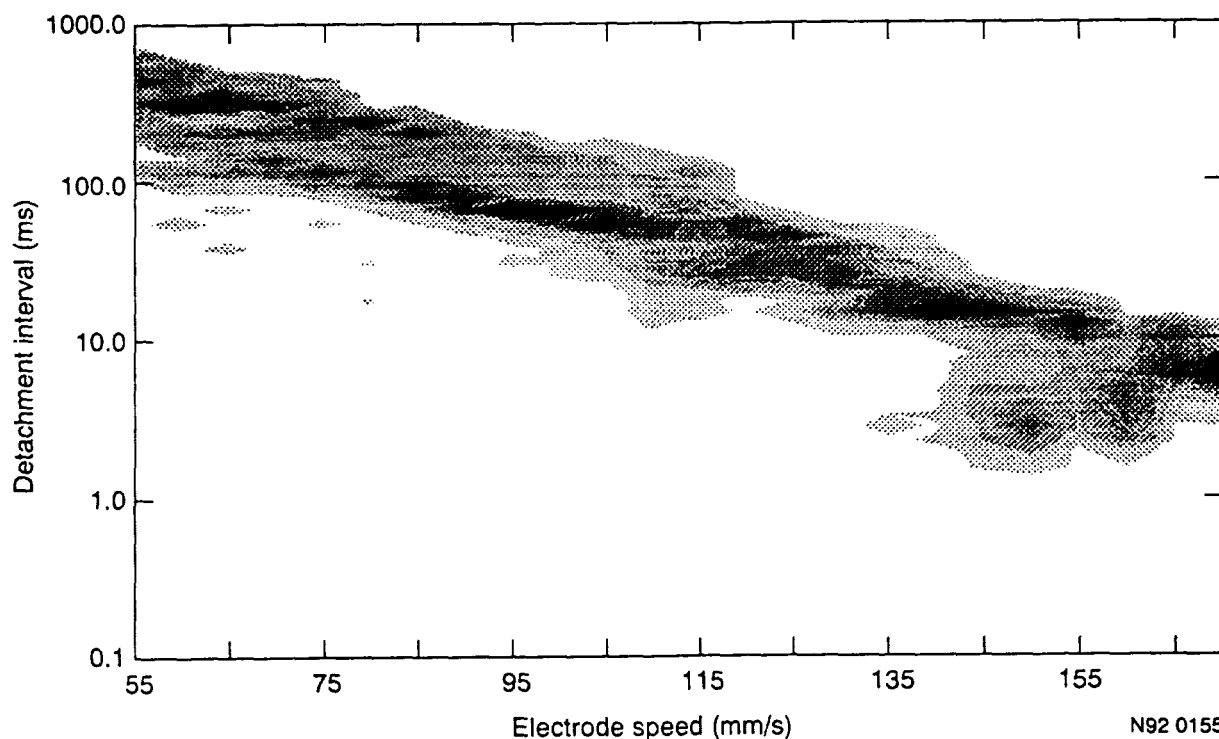


Figure 7. Distribution of droplet detachment interval as a function of electrode speed from experimental data.

larger droplets decreases as the electrode speed and current increase through the transition region. However, more data are required to characterize the transition fully. A model of this process, discussed briefly in the next section, shows a similar trend [30].

High-speed Film Analysis

If the electrode melted at a constant rate, independent of droplet size, the measured time interval between detachments versus the volume of the droplet would lie on a straight line, whose slope could be calculated from

the electrode speed and the electrode size. The data do not follow such lines. The smaller droplets are generally below the line, while a few larger droplets are above the line. This implies that the smaller droplets are detaching in less time than the average, that the electrode is getting shorter, and that the arc length is increasing as each small droplet detaches. The arc length, therefore, may have a very important role in determining melting rate and droplet size.

It was also observed that a particularly large droplet was often followed by a series of small droplets. During the detachment of the large droplet, the electrode extension increased, since these droplets melted slower than average. After a series of small droplet detachments, the electrode extension decreased, since these melted faster than average. This cycle sometimes repeated itself several times, with one or two large droplets followed by a series of small droplets, followed by another one or two large droplets, etc.

The kinematics of the falling droplets was also measured by determining the position of the center of the droplet as a function of time. These position data were then fit to a linear and to a quadratic function. For electrode speeds of 130 and 140 mm/s, the acceleration of the droplet determined in the quadratic fit was negligible and the data was fit just as well by a straight line. Thus the net force on the drop must be zero.

A plot of the reciprocal of the droplet velocity versus the area of the droplet was approximately a straight line, as would be expected from a Stoke's law friction force on the droplet. However, the data showed significant scatter, possibly corresponding to the fact that the droplet shape oscillates and is not spherical.

Discussion of Experimental Results

According to the standard definitions of globular and spray transfer, the distinguishing characteristic is the size of the droplet relative to the electrode size. However, in these experiments the experienced welding technician perceived that the process was in spray mode for electrode speeds above about 160 mm/s. This expert opinion was based on the sound of the process and the observation of a taper on the electrode [22]. Perhaps the standard definition is not exact enough for these purposes. The detachment time data for these experiments indicate that a large fraction of the droplets were larger than the electrode diameter. A more practical definition may be related to the fact that the penetration is greater in spray transfer. The penetration depends on the droplet momentum when it enters the pool [31], which depends not only on the droplet size, as shown here, but on the continued acceleration of the droplet after detachment. Very large accelerations (10 G) have been observed in spray transfer [19].

Further experiments are planned using both high-speed film and electrical sensing. Other parameters will be varied, including contact-tip-to-workpiece distance and open-circuit voltage. Observation of the spray region is limited since the bipolar voltage signal associated with the detachment decreases as the droplet size decreases and approaches the noise level. This makes it difficult to measure the detachment times at higher currents using electrical sensing.

Theoretical Investigation

The physics of droplet transfer in GMAW is analogous to water dripping or flowing from an orifice [26]. Shaw [32] showed that a dripping faucet is an example of a system of chaotic transitions, i.e., the system can change from a periodic and predictable to an aperiodic, quasi-random pattern of behavior as a single parameter (in this case, flow rate) is varied. The purpose of this work is to develop a dynamic droplet growth and detachment model that predicts droplet size and transfer frequencies in the globular and spray transfer modes, as well as in the transition region between the two modes, by extending the Shaw model.

Droplet Growth and Detachment Theories

A major theory on the growth and detachment of GMAW droplets is the static force balance theory. Kim and Eagar [33] showed that this theory gives good correlation between experimental and predicted values for droplet size in the globular transfer mode but deviates significantly in the spray transfer mode. The static force

balance theory predicts that droplet detachment occurs when the detaching forces exceed the retaining forces. Four forces have been identified as relevant: gravitational, electromagnetic, aerodynamic drag, and surface tension. Generally, when using an argon-rich shielding gas, the gravitational, electromagnetic, and aerodynamic forces are droplet detaching forces while the surface tension force is a retention force.

The physics of droplet transfer in GMAW is analogous to that of water dripping or flowing from the orifice of a faucet, except that the driving force for flow is primarily electromagnetic rather than gravitational. Shaw [32] showed that a dripping faucet is capable of a chaotic transition. Droplets flowing from a faucet detached at periodic intervals for low flow rates. However, as the flow rate increased, the droplet detachment intervals changed from periodic and predictable to aperiodic and quasi-random. Shaw constructed a model for water droplet growth and detachment where mass, representing the droplet, grows linearly in time, stretching a spring, which represents the force of surface tension on the drop. When the spring reaches a certain length, the mass is suddenly reduced, representing a detaching droplet, by an amount dependent on the speed of the droplet when the spring reaches the critical distance. The model represents a driven nonlinear oscillator, the nonlinearity arising from the sudden change in mass; position, velocity, and mass are the three variables required for the occurrence of chaotic behavior in a system in continuous time.

Model Derivation and Discussion

Growth and detachment of droplets can be simulated by a linear, constant coefficient, lightly damped, second order spring-mass system. A second order spring-mass system is a system in which energy is stored in the spring (potential energy) and in the displacement of mass (kinetic energy). The motion of a system containing two energy storage elements can be described by a second order differential equation (i.e. an equation in one variable and its first two derivatives.) The model development details are covered in [30]. The results indicate that the GMAW system can change from completely predictable and periodic to an aperiodic, quasi-random pattern of behavior as a single parameter is changed. Using electrode speed as the variable system parameter, the model predicts droplet displacement and detachment frequencies as a function of time.

Figure 8 shows the droplet detachment frequency, predicted by the model, as a function of electrode speed. Predictions indicate that the droplet transfer is quasi-periodic in the globular and spray transfer modes, while in the transition zone between these modes, droplet detachment bifurcates between the larger droplet sizes of globular transfer and the smaller droplet sizes of the spray transfer modes. The predictions are similar to the results shown in Figure 7. Clark [19] showed, from high speed movies, that the transition from globular to spray transfer modes was not an abrupt change, but occurred gradually over a range of weld currents. Droplet transfer in this transition zone was called mixed-mode transfer.

Theoretical Results

A dynamic model has been developed for droplet growth and detachment in GMAW. The derivation demonstrates that a second order spring-mass model can simulate GMAW droplet growth and detachment. The model predicts that the detachment of GMAW droplets is nonlinear. Model predictions are consistent with experimental data that show that the transition from globular to spray occurs gradually and not abruptly (Fig. 9).

ACKNOWLEDGMENTS

Appreciation is expressed to U. S. Wallace, J. E. Lee, J. G. Rodriguez, N. G. Boyce and L. D. Reynolds for their assistance. Appreciation is expressed to C. Null, Naval Sea Systems Command, and R. Morris and D. Rome, Carderock Division, Naval Surface Warfare Center, for their support. This work is supported by the U.S. Navy and by the U.S. Department of Energy, Office of Energy Research, Office of Basic Energy Sciences under DOE Idaho Field Office Contract DE-AC07-76ID01570.

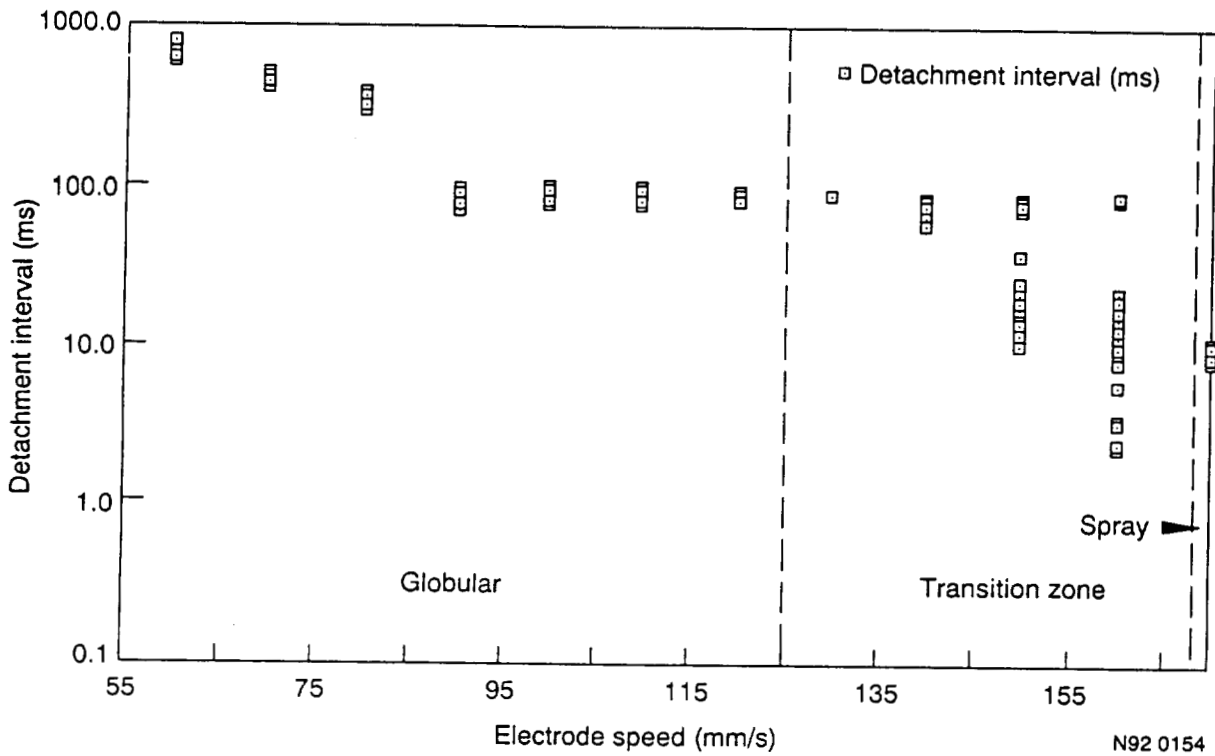


Figure 8. Distribution of droplet detachment interval as a function of electrode speed from theoretical model.

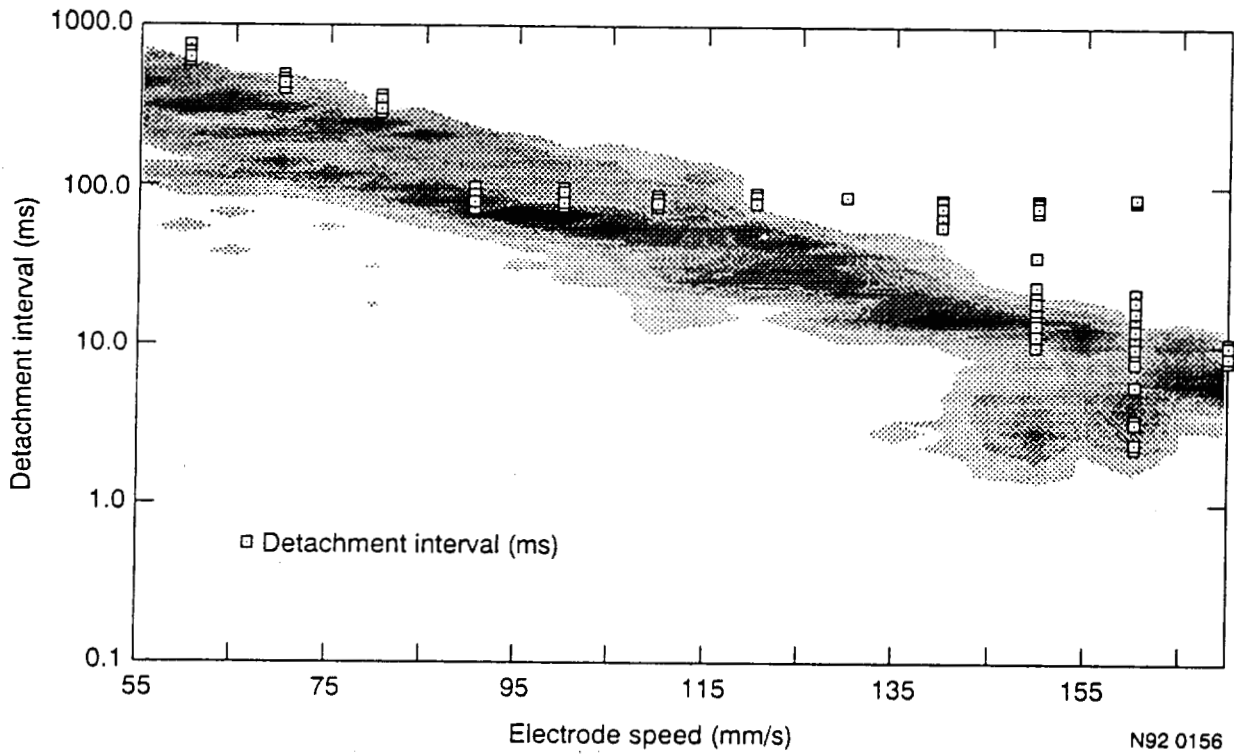


Figure 9. Overlay of experimental and theoretical results showing good agreement in all metal transfer regimes from globular to spray.

REFERENCES

1. Lott, L. A.; Johnson, J. A.; and Smartt, H. B. 1983. Proceedings, 1983 Symposium on Nondestructive Evaluation Applications and Materials Processing, 13-22.
2. Johnson, J. A.; and Carlson, N. M. 1986. NDT International, 19: 190-196.
3. Carlson, N. M.; and Johnson, J. A. 1986. Review of Progress in Quantitative Nondestructive Evaluation 5A: 773-780.
4. Carlson, N. M.; Johnson, J. A.; and Kunerth, D. C. 1990. Welding Journal 69: 256s-263s.
5. Johnson, J. A.; and Carlson, N. M. 1990. Review of Progress in Quantitative Nondestructive Evaluation 10: 2097-2104.
6. Johnson, J. A. 1988. Review of Progress in Quantitative Nondestructive Evaluation 7: 1485-1494.
7. Carlson, N. M.; and Johnson, J. A. 1988. Review of Progress in Quantitative Nondestructive Evaluation 7: 1485-1494.
8. Clark, A. V.; Fortunko, C. M.; Schaps, S. R.; and Capobianco, T. E. Proceedings, IEEE Symposium on Ultrasonics, Ferroelectronics, and Frequency Control, Orlando, FL, 1991, to be published.
9. Agapakis, J. E.; Katz, J. M.; Koifman, M.; Epstein, G. N.; Friedman, J.M.; Eyring, D. O.; and Rutishauser, H. J. 1986. Welding Journal 65(11): 33-41.
10. Hanright, J. 1986. Welding Journal 65(11): 19-24.
11. Richardson, R. W.; Gutow, D. A.; Anderson, R. A.; and Farson, D.F. 1984. Welding Journal 63(3): 43-50.
12. Lukens, W. E.; and Morris, R. A. 1982. Welding Journal 61(1): 27-33.
13. Duncan, R. 1990. Extending DOS: Reading, Massachusetts: Addison-Wesley Publishing Company.
14. Phar Lap Software. 1989. 386|DOS-Extender.
15. Pratt, W. K. 1978. Digital Image Processing: New York: Wiley.
16. Gonzalez, R. C.; and Wintz, P. 1977. Digital Image Processing: Reading, Massachusetts: Addison-Wesley.
17. Kreith, F.; and Bohn, M. S. 1986. Principles of Heat Transfer: p. 429, New York: Harper and Row Publishers.
18. Watkins, A. D. 1989. Heat transfer efficiency in gas metal arc welding. M.S. Thesis, University of Idaho.
19. Clark, D. E.; Buhrmaster, C. L.; Smartt, H. B. 1989. Drop transfer mechanism in GMAW. Proc. Trends in Welding Research, eds. by S. David and J. Vitak, Gatlinburg, TN.

20. Lesnewich, A. 1958. Control of melting rate and metal transfer in gas-shielded metal arc welding, part II - control of metal transfer. Welding Journal 37(9): 418s-425s.
21. Adam , G.; and Siewert, T. A. 1990 Sensing of GMAW droplet transfer modes using an ER100S-1 electrode. Welding Journal 69(3): 103s-108s.
22. Kim, Y.-S.; McEligot, D. M. and Eagar, T. W. , 1991. Welding Journal 70(1): 20s-31s.
23. Allemand, C. D.; Schoeder, R.; Ries, D. E.; Eagar, T. W. 1985. Welding Journal 64: 45-47.
24. Amson, J. C. 1962. An analysis of the gas-shielded consumable metal arc welding system," British Welding Journal 41(4): 232-249.
25. Waszink, J. H.; and Graat, L. H. J. 1983. Experimental investigation of the forces acting on a drop of weld metal. Welding Journal 62(4): 109s-116s.
26. Lancaster, J. F. 1984. The Physics of Welding: Oxford: Pergamon Press.
27. Allum, C. J. 1985. Metal transfer in arc welding as a varicose instability: I. varicose instability in a current-carrying liquid cylinder with surface charge. *and* II. development of a model for arc welding. Journal of Physics D: Applied Physics 18: 1431-1468.
28. Johnson, J. A.; Carlson, N. M.; Smartt, H. B.; and Clark, D. E. 1991. Welding Journal 70: 91s-99s.
29. Johnson, J. A.; Smartt, H. B.; Clark, D. E.; Carlson, N. M.; Watkins, A. D.; Lethcoe, B. J. 1990. Proc. Conf. on Modeling of Casting, Welding and Solidification Processes, Engineering Foundation, Davos, Switzerland.
30. Watkins, A. D.; Smartt, H. B.; Johnson, J. A. 1992. 3rd International Conference on Trends in Welding Research, Gatlinburg, Tennessee.
31. Essers W. G.; and Walter, R. 1981. Welding Journal 60: 37s-42s.
32. Shaw, R. 1984. The Dripping Faucet as a Model Chaotic System The Science Frontier Express, Aerial Press, Inc.
33. Eagar, T. W. 1992. Personal communication, Massachusetts Institute of Technology, Cambridge, MA.

25-1
244/

**A COMBINED ELECTRON BEAM/OPTICAL LITHOGRAPHY PROCESS STEP FOR
THE FABRICATION OF SUB-HALF-MICRON-GATE-LENGTH MMIC CHIPS**

p. 6

James S. Sewell
U.S. Air Force Wright Laboratory
Wright-Patterson Air Force Base, Ohio 45433-6543

Christopher A. Bozada
U.S. Air Force Wright Laboratory
Wright-Patterson Air Force Base, Ohio 45433-6543

ABSTRACT

Advanced radar and communication systems rely heavily on state-of-the-art microelectronics. Systems such as the phased-array radar require many transmit/receive (T/R) modules which are made up of many millimeter wave - microwave integrated circuits (MMICs). The heart of a MMIC chip is the Gallium Arsenide (GaAs) field-effect transistor (FET). The transistor gate length is the critical feature that determines the operating frequency of the radar system. A smaller gate length will typically result in a higher frequency. In order to make a phased array radar system economically feasible, manufacturers must be capable of producing very large quantities of small-gate-length MMIC chips at a relatively low cost per chip. This requires the processing of a large number of wafers with a large number of chips per wafer, minimum processing time, and a very high chip yield.

One of the bottlenecks in the fabrication of MIMIC chips is the transistor gate definition. The definition of sub-half-micron gates for GaAs-based field-effect transistors is generally performed by direct-write electron beam lithography (EBL). Because of the throughput limitations of EBL, the gate-layer fabrication is conventionally divided into two lithographic processes where EBL is used to generate the gate fingers and optical lithography is used to generate the large-area gate pads and interconnects. As a result, two complete sequences of resist application, exposure, development, metallization and lift-off are required for the entire gate structure. We have baselined a hybrid process, referred to as EBOL (electron beam/optical lithography), in which a single application of a multi-level resist is used for both exposures. The entire gate structure, (gate fingers, interconnects and pads), is then formed with a single metallization and lift-off process. The EBOL process thus retains the advantages of the high-resolution E-beam lithography and the high throughput of optical lithography while essentially eliminating an entire lithography/metallization/lift-off process sequence. This technique has been proven to be reliable for both trapezoidal and mushroom gates and has been successfully applied to metal-semiconductor and high-electron-mobility field-effect transistor (MESFET and HEMT) wafers containing devices with gate lengths down to 0.10 micron and 75 x 75 micron gate pads. The yields and throughput of these wafers have been very high with no loss in device performance. We will discuss the entire EBOL process technology including the multilayer resist structure, exposure conditions, process sensitivities, metal edge definition, device results, comparison to the standard gate-layer process, and its suitability for manufacturing.

INTRODUCTION

Fabrication of solid-state electronic devices and circuits is accomplished through a series of processing cycles. One of these consists of a lithography, a metal deposition, and a metal lift-off step. This particular cycle of steps may be repeated many times before fabrication is complete. Much work has been done in making this cycle faster and more reliable to decrease the semiconductor processing time.

Many variations of this cycle are used. The most common form of lithography is photolithography in which a wafer is coated with a thin film of a material that is sensitive to light (photoresist). The photoresist is then exposed by a pattern of light via a patterned quartz mask. After exposure the photoresist is developed and the exposed photoresist or unexposed photoresist (depending on the type of photoresist and developer used) is rinsed away. The next step of the cycle is to evaporate metal onto the wafer. Finally, a lift-off technique is used to remove the remaining unexposed photoresist and the metal on top of it. Thus,

only the desired pattern of metal remains. Photolithography is generally limited to geometries down to 0.6 microns with possible placement errors up to a micron.

For smaller geometries ($< 0.6 \mu\text{m}$) and/or geometries which require highly accurate placement, electron beam lithography (EBL) is commonly used. EBL is similar to photolithography except that an EBL resist (which is sensitive to an electron beam rather than UV light) is used in place of photoresist and the pattern is drawn onto the wafer with an electron beam rather than exposed through a mask. EBL can write both large geometries and small geometries (less than a tenth of a micron) with accurate placement.

Modern solid-state electronic devices or circuits require small-geometry structures (such as transistor gates) be connected to large-geometry structures (such as probe pads or interconnects) for continuity. To make these connections, the entire layer (small geometries and large geometries) could be fabricated by EBL/metal deposition/lift-off cycle. Although this technique produces good results, it is usually extremely time consuming. When an e-beam machine is set up to define smaller-geometry patterns, the beam spot size is small and larger geometries can take an extremely long time to write. When the machine is optimized for large-geometry writes, the beam spot size is large and ultra-fine features are very difficult to write. The write times in conjunction with lengthy switch-over times required to change the machine from "large-geometry mode" to "small-geometry mode" (i.e. change the accelerating voltage, switch the aperture selection, re-align the column, etc.) make this technique impractical for combination large geometry and fine geometry fabrication. More commonly, the large-and-small-geometry fabrication method is to use photolithography/metal deposition/lift-off cycle to form the large-geometry structures and EBL/metal deposition/lift-off cycle to overlap the small-geometry structures. Again, this method is time consuming because two cycles are required, and it also introduces a metal-to-metal coverage problem. If the overlapping metal is not thick enough, good electrical contact will not be made and a device failure mechanism is introduced. A third method is to use a deep ultraviolet (UV) light mask aligner to image the large-geometry patterns, EBL to image the small-geometry patterns, and a single metal deposition/lift-off for both geometry patterns¹. This method is excellent; however, it requires a deep UV mask aligner or stepper. Deep UV mask aligners are not found in every integrated circuit lab. We present an alternative fabrication process that combines optical photolithography and EBL into one process step with one metal deposition and one metal lift-off which can be used for high-throughput, fine-geometry device fabrication.

EBOL PROCESS

The EBOL process is as follows. The wafer is coated with standard e-beam resist scheme (1 to 3 layers), followed by a layer of optical photoresist. The wafer is then aligned and exposed to the gate pad mask using an optical mask aligner. The top photoresist is then developed. The resulting pattern is used as a mask for a deep UV exposure of the e-beam resists. The large patterns are now exposed. The top layer photoresist is then removed without damaging the underlying e-beam resists. Next, The gates are written by e-beam. Once the exposed resists are developed, metal is deposited. The resulting metal layer consists of very large gate pads and $0.25 \mu\text{m}$ gate fingers. The turn-around time is very fast compared to our standard 2 cycle process, and no step coverage problem exists of the gate fingers onto the gate pads.

The major obstacle in developing this process was to remove the top-layer photoresist after the deep UV exposure without affecting the underlying e-beam resists. It was first believed the optical photoresist could be developed out after the deep UV exposure if it was flood exposed by light. Poly-(methyl methacrylate) (PMMA)² was used for the initial process development. The optical photoresist used was 1400-27³. When 351 developer⁴ was used to remove the exposed 1400-27, a thin film formed between the PMMA and the 1400-27 resists which could not be removed by realistic methods (i.e. solvent clean, microposit remover 1165⁵, or oxygen plasma stripper). SAL 110-PLI⁶ (PMGI) was tried in place of PMMA and a similar film formed. After unsuccessful attempts to try to develop the photoresist away, dissolving it was tried. PMGI can be dissolved by 1165, PMMA by 1165 or by acetone, and 1400-27 by acetone. Fortunately, the dissolution rate of PMMA in acetone is much slower than 1400-27 in acetone. A short blast of acetone was shown to remove the 1400-27 without significantly affecting PMMA or PMGI resists. After the photoresist was removed the e-beam write, development, gate recess etch, gate deposition and liftoff were routine.

The following is an example of our EBOL process for a 0.25 μm mushroom gate⁷.

1. Solvent clean.

Spin e-beam resist - PMMA 496K 4% (60 seconds at 3000 rpm), P(MMA-MAA)⁸ Type I 9% (60 seconds at 3000 rpm), PMMA 496K 4%:chlorobenzene [2:1] (60 seconds at 3000 rpm).

Bake - 5 minutes on a 200 °C hot plate.

Spin optical photoresist - 1400-27 (30 seconds at 4000 rpm).

Bake - 5 minutes on a 100 °C hot plate.

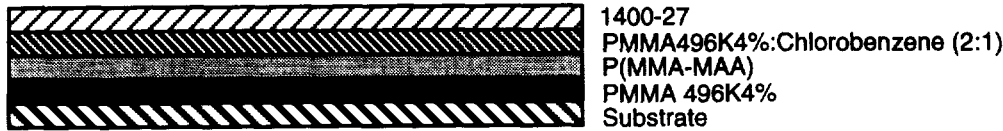


Figure 1. Schematic of resist scheme after coating

2. Align and expose optical resist using gate pad/interconnect mask - 12 mW/cm^2 for 42 seconds.

Develop 1400-27 photoresist - 351:de-ionized water [1:5] (30 seconds at 500 rpm), de-ionized water (30 seconds at 500 rpm).

Deep-UV exposure - 240 nm at 10 mW/cm^2 for 600 seconds.



Figure 2. Schematic of resist after deep UV exposure of large patterns.

3. 1400-27 removal - acetone spray (15 seconds at 500 rpm), isopropyl alcohol (15 seconds at 500 rpm).



Figure 3. Schematic of resist after the optical resist is stripped away.

4. E-beam direct write - JEOL JBX5DII(U), 5th lens, 50 kV, 50 pA, (A,10), center single-pass-lines (dose: 3.5 $\text{nC}/\mu\text{m}$), 0.1 μm offset wing areas (0.25 μm wide) (dose: 150 $\mu\text{C}/\mu\text{m}^2$).



Figure 4. Schematic of resist after e-beam write.

5. Develop e-beam resists - chlorobenzene 15 seconds at 500 rpm), isopropyl alcohol (30 seconds at 500 rpm), methyl-isobutyl-ketone (MIBK):isopropyl alcohol [1:1] (90 seconds at 500 rpm), isopropyl alcohol (30 seconds at 500 rpm).



Figure 5. Schematic of resist after e-beam resist development.

6. Oxygen plasma .
 Gate recess - standard.
 Pre-metal dip - standard
 Gate metal deposition - approximately 6000 Å (standard gate metal).

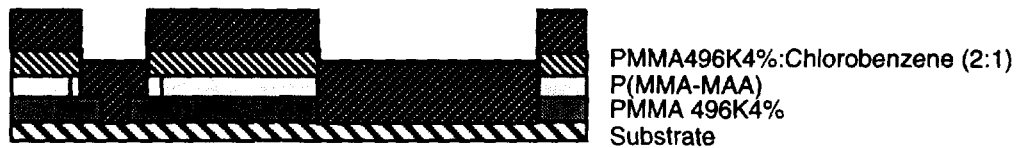


Figure 6. Schematic of sample after metal deposition.

7. Gate metal lift-off.
 Solvent clean.

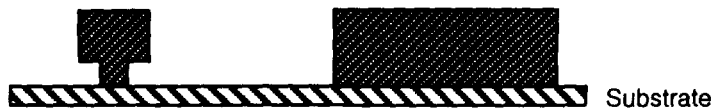


Figure 7. Schematic of sample after cycle is complete.

RESULTS

Figure 8 shows a conventional gate layer formation. This process fabricates the gate layer in two cycles. First the gate pads are formed by optical lithography/metal deposition/lift-off cycle and then the gate fingers are formed by a EBL/metal deposition/lift-off cycle. Aside from being time-consuming due to the two cycles, this process introduces a possible failure mechanism due to the gate finger metal overlap and adhesion to the gate pad metal. Figure 10 shows a typical EBOL device.

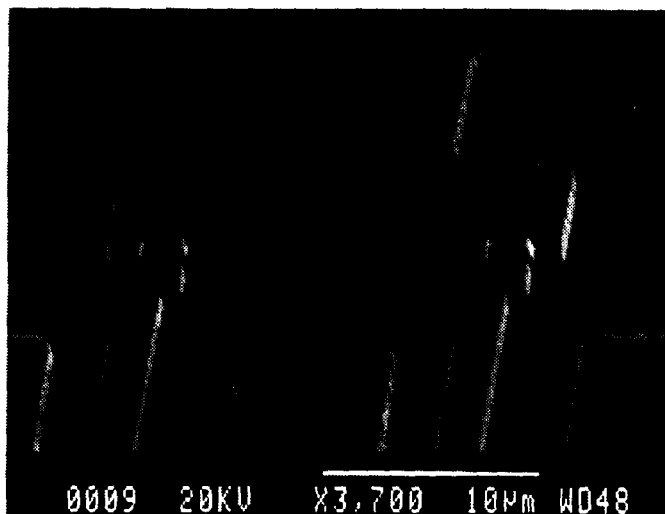


Figure 8. A conventional gate layer showing gate finger/pad step coverage

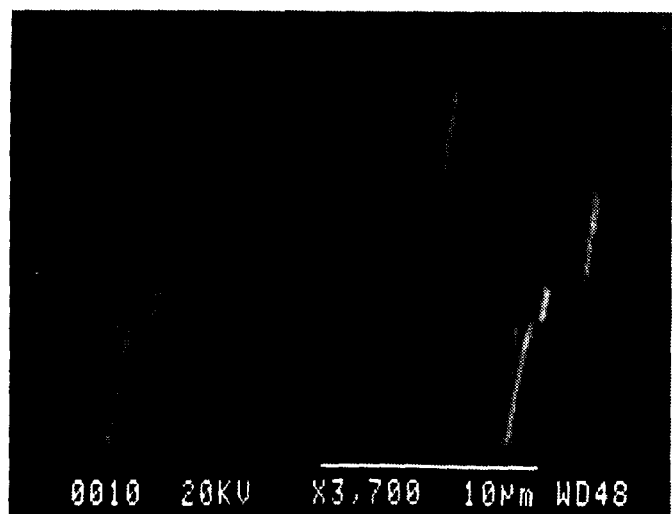


Figure 9. An EBOL gate layer showing the elimination of gate finger/pad step coverage.

This process has been used to fabricate various device types such as metal-semiconductor field effect transistors (MESFETs), high electron mobility transistors (HEMTs), and heterojunction bipolar transistors (HBTs). In addition, this process has been used to fabricate Low Noise Amplifier MMIC circuits. However, most of the device data has been taken from MESFET devices. The following are some of the results using the EBOL process for MESFET device fabrication. Figure 10 shows a wafermap and histogram of DC transconductance (gm) at zero gate voltage for 0.25 µm x 50 µm gate MESFETs on a 2-inch semi-insulating GaAs substrate with a 1µm undoped GaAs buffer followed by a 1000 Å layer of

7×10^{17} doped GaAs capped by a 500 Å layer of 2.5×10^{18} doped GaAs (MBE grown). The average value is 306 mS/mm with a standard deviation of 45 mS/mm. The median value is 323 mS/mm with a lower quartile value of 278 mS/mm and an upper quartile value of 333 mS/mm. The plots show that the device performance is extremely uniform across the wafer. Note that the majority of the poor devices are around the edge of the wafer.

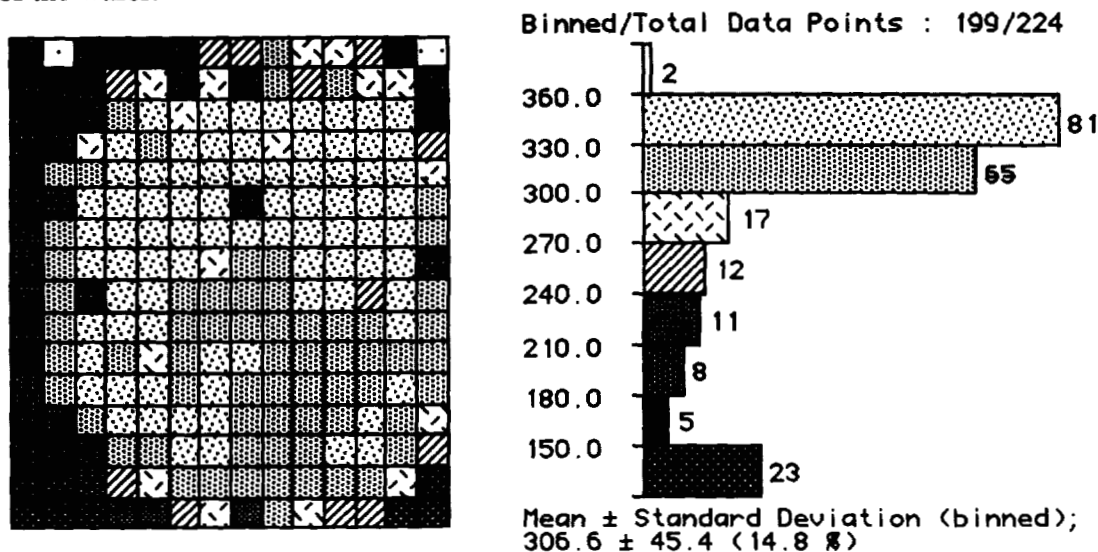


Figure 10. A wafermap and histogram of DC transconductance (gm) for MESFETs with an EBOL fabricated gate layer.

Figure 11 shows the RF transconductance wafermap and histogram from the same wafer as in figure 10. These devices have $2 \times 0.25 \mu\text{m} \times 75 \mu\text{m}$ gates. The average RF gm value is 374 mS/mm with a standard deviation of 90 mS/mm.

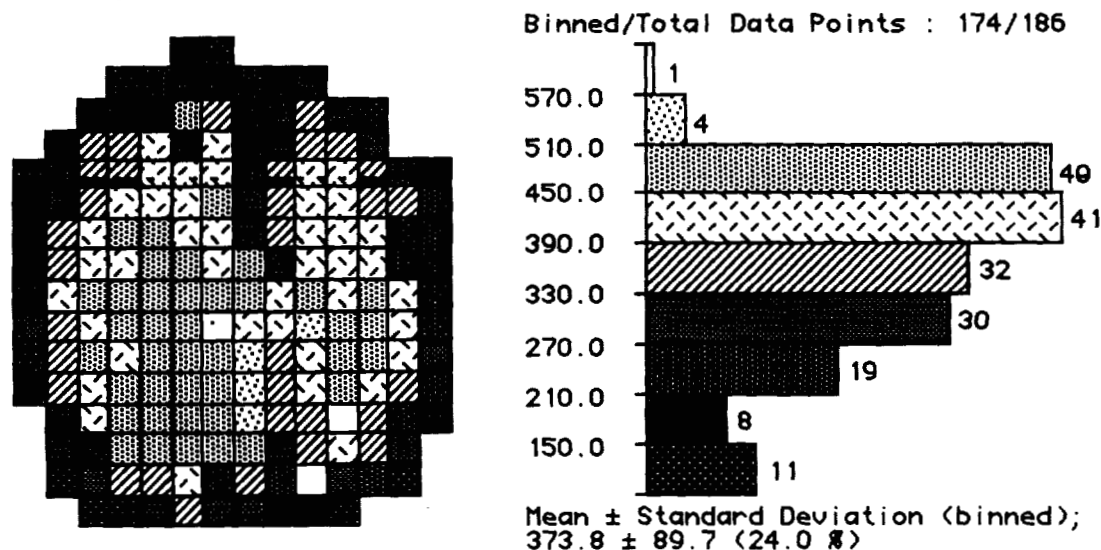


Figure 11. A wafermap and histogram of RF transconductance (gm) for MESFETs with an EBOL fabricated gate layer.

Figure 12 shows the cutoff frequency (F_t) wafermap and histograms for the same devices as in figure 11. The average F_t value is 42 GHz with a standard deviation of 4 GHz. The corresponding measured noise figure for a representative device was 0.3 dB at 12.6 mA at 10 GHz.

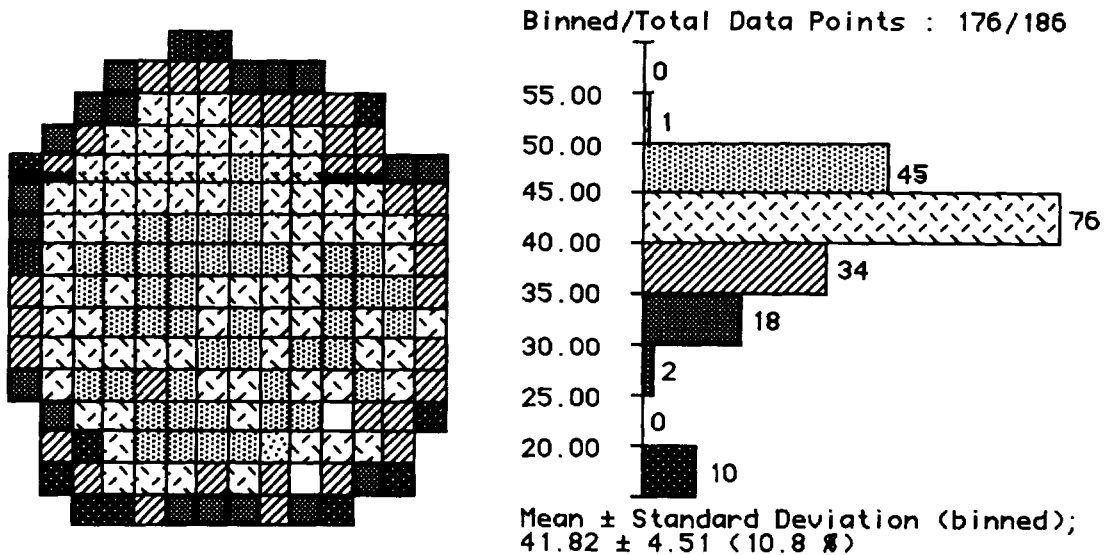


Figure 12. A wafermap and histogram of cut-off frequency (F_t) for MESFETs with an EBOL fabricated gate layer.

CONCLUSION

We have demonstrated that the EBOL process not only saves processing time due to a reduced number of metal and liftoff steps, but it is also capable of producing devices at least comparable to (if not better than) devices fabricated with a conventionally fabricated gate layer. The process has been proven successful and does not require any processing "tricks" to get acceptable results. Moreover, the yields have been exceptional most likely due to the elimination of step coverage problems. Finally, this process is quite flexible. Both a 2-layer (PMMA/P(MMA-MAA)) trapezoidal resist scheme and a 3-layer (PMMA/P(MMA-MAA)/PMGI) mushroom resist scheme have been used successfully. This process should be able to be combined with any existing e-beam process without any problems. These qualities make this process ideally suited for the manufacturing of sub-half-micron-gate-length microwave devices and circuits.

ACKNOWLEDGMENTS

The authors would like to acknowledge the following people for technical input and support: R. Dettmer, C. Eppers, K. Nakano, and D. Via.

REFERENCES

- 1) Y. Todokoro et al., "A Hybrid E-beam/Deep-UV Lithography for GaAs FET's", SPIE Electron-Beam, X-Ray and Ion-Beam Lithographies VI, Vol. 773, pp 54-60, 1987.
- 2) KTI Chemicals Incorporated, 1170 Sonora Ct., Sunnyvale CA 94086.
- 3) Shipley Company Incorporated, 2300 Washington St., Newton MA 02162.
- 4) Shipley Company Incorporated, 2300 Washington St., Newton MA 02162.
- 5) Shipley Company Incorporated, 2300 Washington St., Newton MA 02162.
- 6) Shipley Company Incorporated, 2300 Washington St., Newton MA 02162.
- 7) R.C. Tiberio et al., "Electron Beam Lithography and Resist Processing for the Fabrication of T-gate Structures", Proc. SPIE, 1089, 124, 1989.
- 8) KTI Chemicals Incorporated, 1170 Sonora Ct., Sunnyvale CA 94086.

56.26
2442
p. 4

METAFUSION A BREAKTHROUGH IN METALLURGY

Adrian A. Joseph, Ph.D.
The Metafuse Corporation
1875 Century Park East, #1790
Los Angeles, California 90067
(310) 557-0881

ABSTRACT

The Metafuse Process is a patented development in the field of thin film coatings utilizing cold fusion which results in a true inter-dispersion of dissimilar materials along a gradual transition gradient through a boundary of several hundred atomic layers. The process is performed at ambient temperatures and pressures requiring relatively little energy and creating little or no heat. The process permits a remarkable range of material combinations and joining of materials which are normally incompatible. Initial applications include titanium carbide into and onto the copper resistance welding electrodes and tungsten carbide onto the cutting edges of tool steel blades. The process is achieved through application of an R.F. signal of low power and is based on the theory of vacancy fusion.

MAJOR METALLURGICAL BREAKTHROUGH

After years of extensive research, the scientists of the Metafuse Corporation have achieved a major breakthrough in modifying or organizing matter at the surface of substrates. The process "fuses" materials to achieve new surface properties. With an absence of noticeable heat, the relatively simple process joins materials at the sub-atomic level. The process offers engineers a remarkable range of material combinations and alloys which can be formed to significantly alter the physical, electrical, optical, or thermal properties of a given substrate. There are no specific "clean room" requirements and results are achieved with almost no effluent waste.

The Metafuse Process is a patented development in the field of thin film coating by way of cold fusion. The process is achieved by the application of an R.F. signal of a low power to correspond with the matching resonance of the material applied and the substrate.

The process results in the fusion of several hundreds of atomic layers at the boundary, causing a true inter-dispersion of the materials and a gradual transition from one material to another.

Performed at ambient temperatures and pressures, the process requires relatively little energy and creates little or no heat.

The Metafuse Process produces results similar to those achieved by ion implantation. However, there are significant differences which clearly set it apart from both conventional high technology ion implantation processes and older more primitive processes such as

electroplating, welding and heat treating. The most significant differences are attributable to the relatively simple technique of application, the absence of heat and the remarkable range of material combinations and alloys which can be formed in-situ to significantly alter the properties of a given substrate. The company has demonstrated the uniqueness of its process by joining materials which are normally incompatible, such as tungsten, titanium or molybdenum on the surface of copper, gold on zirconium; aluminum on steel.

The fusion achieved using the Metafuse Process is an excellent non-peeling non-chipping bond. The ability to impart a desired new property such as reflectivity, corrosion resistance, color, or hardness depends on a high degree of peel resistance. The process achieves a bond that will not peel without damaging the substrate material itself. The system requires low energy consumption, is portable and can be operated by relatively unskilled labor. Being a cold process, it allows the use of a wide range of materials previously incompatible and permits changing surface characteristics of substrates that may otherwise be adversely affected by heat.

THEORY

The underlying theory for the Metafuse Process is based upon the theory of vacancy fusion as found in contemporary physics.

A more detailed analysis of the Metafuse Process enters the realm of atomic physics and dictates a brief review of our present knowledge of binding energies and entropies which exist between single vacancies and single substitutional solute atoms in metals. We define the Gibbs free energy of binding, G_{vs}^b , as the decrease in total free energy of the crystal G , which occurs when a vacancy and a solute atom are brought together from an essentially infinite separation to become nearest neighbors as in Figure 1.

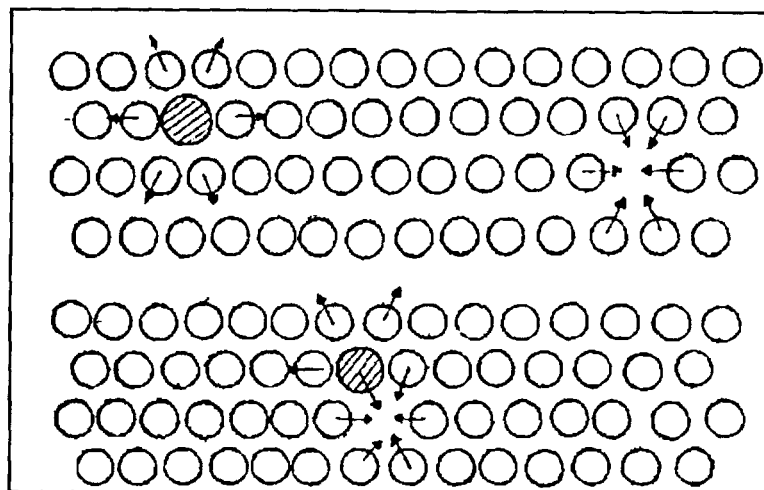


FIGURE 1: The association of a well-separated solute atom and vacancy (above) to form a nearest-neighbor vacancy-solute atom pair (below) in the plane of an fcc crystal. The arrows represent possible directions of the atomic relaxations near the defects.

With the following definition, and a positive binding energy, an attractive interaction occurs.

$$G_{vs}^b = G [\infty \text{ separation} - G (\text{nearest neighbors})]$$

The binding energy, E_{vs}^b , and entropy, S_{vs}^b , are defined in a similar manner, i.e.,

$$\begin{aligned} E_{vs}^b &= E (\infty \text{ separation}) - E (\text{nearest neighbors}) \\ S_{vs}^b &= E (\infty \text{ separation}) - S (\text{nearest neighbors}) \end{aligned}$$

so that

$$G_{vs}^b = E_{vs}^b = TS_{vs}^b$$

No attempt will be made to consider the binding of higher order vacancy-solute atom clusters. Even though such clusters are of great importance in many kinetic situations, essentially nothing is known at present about their properties. Even in the relatively simple case of the binding between single vacancies and single solute atoms, the accumulation of reliable information has turned out to be a slow and difficult process. Experimentally, it has been necessary to employ indirect techniques in order to gain information, and such experiments have often led to ambiguous or conflicting results. Theoretically, it has proven difficult to obtain exact solutions of the binding problem, and various approximate methods have therefore been employed. Nevertheless, a substantial body of knowledge has been accumulated, and progress has been made recently with the application of new experimental and theoretical techniques.

The cold diffusion process of Dr. Adrian Joseph is based on an electron movement created by an application of a pulsing current between the applied material i.e. solute atoms and the matrix movement of the electrons which are in a frequency equal to the atoms movements and the relaxation of the host matrix ions. The determination of the pulse current will of course vary depending on the lattice and grain boundary of the host metal.

The calculation of the formation entropy thus becomes a problem of determining the normal vibration (frequencies) of all the atoms in the defect lattice. The problem is complicated because a suitable interatomic potential between the defect and atoms has to be obtained. Secondly, the specific frequencies of the "jumping electrons" coupled to one another have to be determined. In addition, the frequencies have to be calculated for the defect crystal in which the atoms are in their relaxed positions. Therefore, the atomic relaxations around the defect have to be determined prior to the frequency calculation. In this case it will be equivalent to a capacity value. In order to simplify the calculations, the Einstein model, in which the atoms are treated as harmonic oscillators, is generally adopted.

Therefore, the F_0 will depend on the capacity of the total vacancies in the said circuit, and the resistivity of the host, multiplied by the resistivity of the material being applied, will determine the amount of solute electrons that will be delivered per time unit on a set host vacancy.

$$F_o = \frac{1}{2\pi\sqrt{L*c}}$$

Working with the above formula, assuming constant capacity, the Metafuse Process will occur.

Values of the binding entropies have not been calculated on a fundamental basis. However, methods for calculating the formation entropies of defects have been developed, and it is concluded that it should be feasible to apply these methods to the calculations of binding entropies.

SUMMARY

The frequency calculation of the Metafuse Process is related to the lattice structure and the atomic weight of the material. Although a precise calculation is possible, it would be accurate for only a 100% pure material, which is not found in practical applications. Therefore, approximations are incorporated into the calculations for ease of measurement and process, thus providing a frequency range of several percent. This has been proven effective in the testing of hundreds of different materials combinations.

To determine the proper frequency, a measurement of the resistance and capacitance of the materials is necessary. The remaining measurements of resistance are accomplished with standard meters. The figures are then inserted into the applicable formula and the frequency determined.

The Metafuse machine has been specifically developed to apply the precisely controlled R.F. electrical circuit to permit the process to occur. The ability of the machine to maintain both power and frequency when the electrode or solution is in contact with the substrate, is the key to the practical operation of this system.

The first commercial application of the Metafuse Process has occurred in the automotive industry for resistance spot welding. In this case, the industry standard copper welding tips have been surface treated with a fusion coating of titanium carbide. The titanium, being a reflector metal, lowers the energy requirement of the welding equipment to produce a weld and results in a tip life that is three times that of the unprocessed tip while reducing electrical consumption of the equipment by 15%. The product is now being introduced onto the production lines of the major automotive manufacturers, both in the United States and in Europe.

Other commercial applications are in the final stages of testing, including the deposition of tungsten carbide onto cutting blades for improved wear resistance and the replacement of traditional plating equipment owing to environmental concerns.

The company is available to assist manufacturers and developers of products that will benefit from material surface treatments. The patented process is available through licenses and joint ventures.

37-24
3443
2-10

**NEAR-NET-SHAPE MANUFACTURING:
SPRAY-FORMED METAL MATRIX COMPOSITES AND TOOLING**

**Kevin M. McHugh
Idaho National Engineering Laboratory
Idaho Falls, ID 83415-2050**

ABSTRACT

Spray forming is a materials processing technology in which a bulk liquid metal is converted to a spray of fine droplets and deposited onto a substrate or pattern to form a near-net-shape solid. The technology offers unique opportunities for simplifying materials processing without sacrificing, and oftentimes substantially improving, product quality. Spray forming can be performed with a wide range of metals and nonmetals, and offers property improvements resulting from rapid solidification (e.g. refined microstructures, extended solid solubilities and reduced segregation). Economic benefits result from process simplification and the elimination of unit operations. The Idaho National Engineering Laboratory is developing a unique spray-forming method, the Controlled Aspiration Process (CAP), to produce near-net-shape solids and coatings of metals, polymers, and composite materials. Results from two spray-forming programs are presented to illustrate the range of capabilities of the CAP approach as well as the accompanying technical and economic benefits. These programs involved spray forming aluminum strip reinforced with SiC particulate, and the production of tooling, such as injection molds and dies, using low-melting-point metals.

INTRODUCTION

In spray forming, liquid metal is converted to a spray of fine droplets and deposited onto a substrate or pattern to form a near-net-shape solid. Researchers at the Idaho National Engineering Laboratory are developing a unique spray-forming method, the Controlled Aspiration Process (CAP), to produce near-net-shape deposits of metals, polymers, metal matrix composites, and polymer matrix composites. CAP differs in design, operation, and performance from conventional spray forming. Conventional metal spray-forming nozzles atomize a stream of liquid metal issuing from the base of a crucible using a concentric array of gas jets. The resulting shower of droplets impinges upon a moving substrate to form a solid deposit. In contrast, CAP uses a close-coupled atomization technique in which a liquid is aspirated or pressure-fed into a de Laval (converging/diverging) nozzle. There it contacts a high velocity, high temperature inert gas that disintegrates the liquid into very fine droplets and entrains the droplets in a highly directed spray that can have any orientation.

Spray deposition with CAP nozzles typically involves transonic gas-particle flow through the nozzle and subsonic free jet flow from the nozzle to the substrate. After exiting the nozzle, metal droplets undergo rapid in-flight cooling, due to convection heat transfer to the surrounding inert gas, becoming partially solidified and undercooled. Upon impacting the substrate, the droplets weld together to form a coherent solid while releasing the remaining enthalpy by convection and conduction through the substrate. The unusually high cooling rates (normally $> 10^3$ K/s) result in a rapidly solidified product that can offer property improvements such as refined microstructures, extended solid solubilities, and reduced segregation compared to cast materials. The process provides economic advantages because the product is near-net-shape and fewer unit operations, such as machining, forging, or rolling, are required.

CAP is very versatile. Metals have been spray formed by feeding the melt through a slit orifice or a series of circular orifices that span the width of the nozzle. Polymers are dissolved in an appropriate solvent before spraying or, in some cases, a melt or plasticized melt is sprayed. Metal matrix composites, polymer matrix composites, and unique alloy systems are produced by codeposition of the phases.

Properties of the deposit are tailored by controlling the characteristics of the spray plume (droplet size distribution, velocity, heat content, flux, and flow pattern) and substrate (material properties, surface

finish, and temperature). Toward that end, an in-flight particle diagnostics system is used to simultaneously measure droplet size, velocity, and temperature in the atomized plume. This system measures particle diameters between 5 and 1,000 μm using an absolute magnitude of scattered light technique. Velocities of 10 to 100 m/s are measured with a dual beam laser Doppler velocimeter; particle temperature is measured with a high-speed two-color pyrometry technique. Modeling the multiphase flow, heat transfer, and solidification phenomena provides guidance for component design and process control.

While the nozzle design and operating parameters are customized for a particular application, the shape of the spray-formed object is largely dictated by the geometry of the substrate or pattern onto which the spray is deposited, allowing complex shapes to be readily produced. Applications include strip and sheet products, cylindrical and tubular products, tooling such as molds and dies, near-net-shape structural products, rapidly-solidified metal alloy products, superplastic alloy products, metal matrix composites, controlled porosity materials for membranes and electrodes, metal claddings, coatings for metals and nonmetals, and polymer products.

Results from two spray-forming programs are presented to illustrate the range of capabilities of CAP as well as the accompanying technical and economic benefits. These programs involved spray-forming aluminum strip reinforced with SiC particulate, and the production of tooling, such as injection molds and dies, using low-melting-point metals.

PARTICULATE-REINFORCED METAL MATRIX COMPOSITES

Metal matrix composites (MMCs) combine the properties of metals, such as high thermal and electrical conductivity, toughness, and thermal shock resistance, with ceramic properties, such as corrosion resistance, strength, high modulus, and wear resistance [1-10]. The composite's properties reflect a partitioning of the properties of the ceramic and metal based on the chemical nature and volume fraction of the components. However, improvements in certain properties usually come at some cost, such as a decrease in ductility and toughness relative to the matrix material [11]. Although the ability to tailor the properties of these "materials by design" makes them attractive candidates to the automotive, aerospace, and other industries for a variety of applications, lack of efficient processing technologies is a great impediment to large-scale commercial use of particulate-reinforced MMCs. Recent workshops devoted to evaluating priorities for future MMC research and development have concluded that processing is the most critical area for R&D, particularly near-net-shape production technologies for widely used shapes such as rods, tubes, and strip [12,13].

A variety of processing methods for particulate-reinforced MMCs have been devised over the last two decades. Casting techniques such as squeeze casting [14,15], melt oxidation processing [16,17], melt infiltration processing [18-20], and rheocasting [21] have received the greatest attention and have spawned several commercial products such as the Toyota diesel piston [10,22]. Susceptibility to interfacial reactions, segregation by gravity, particle agglomeration, segregation of the secondary phases in the metal matrix, and coarse matrix grain size have limited the scope of these techniques [10,23].

Powder metallurgical processing circumvents the problems associated with mixing and low cooling rate by cold mixing the components in powder form, followed by compressing, degassing, and final consolidation by extrusion, forging, rolling or other hot working below the liquidus of the matrix [10,24]. While this technique generates products with better properties, and is usually more reliable, than the casting routes, it is also more costly [25]. The rapidly-solidified matrix powders normally used are relatively expensive starting materials, and pressing equipment places limitations on component size. Furthermore, while interfacial reactions are reduced, poor particulate wetting by the matrix material has often led to the use of precoated particulate, another increased expense.

Spray forming is a unique processing method for particulate reinforced MMCs that combines rapid solidification processing and near-net-shape fabrication into a single step. By so doing, it simplifies processing, relative to powder metallurgy techniques, while bypassing difficulties found with most casting

methods--matrix/particulate interfacial reactions and nonuniform blending caused by density differences between the matrix and reinforcement phases [26-31]. The high rate of solidification inherent to the process improves the matrix properties and also enables the use of alloys prone to segregation. This extends the range of applications to include competitively-priced composites in which the matrix phase is in a metastable state.

Strip Preparation and Properties

CAP was used to produce composite strip of 6061 aluminum alloy reinforced with SiC particulate. The approach, illustrated schematically in Figure 1, involved codeposition of the phases onto a water-cooled, grit-blasted, mild steel drum. The ceramic phase was pressure-fed into the nozzle in the form of an aerosol upstream of the molten metal, which was also pressure-fed into the nozzle. Heat transfer from the atomizing gas was used to adjust the temperature of the ceramic particulate as it accelerated through the nozzle to the liquid metal atomization region. This approach provided independent control of the feed rates of the liquid metal and ceramic, good component mixing, and independent control of the temperatures of the metal and ceramic inside the nozzle.

Figure 2 shows the temperature response of the atomizing gas (argon) and particulate (1 μm SiC) as they travel through the nozzle from the inlet to the exit. The gas temperature is approximately constant until the gas accelerates as it approaches the nozzle's throat. The dramatic cooling effect is abruptly terminated at the location of the shock front, which, in this example, is located inside the nozzle. The particulate entered the nozzle at room temperature, but was quickly heated by the atomizing gas. The thermal profile of the particulate is similar to that of the gas except that it responds more sluggishly due to its greater thermal inertia. Figure 3 is a plot of the temperature of the SiC particulate at the location of molten 6061 Al injection into the nozzle. It further illustrates the degree of control of particulate temperature that is gained using CAP.

The spray-forming apparatus used for continuous strip production has been described previously [32]. The modular design consists of a gas manifold and associated electronics for controlling gas flow and temperature, a chamber housing the main spray forming components (induction gas heater, melt tundish, and nozzle), a chamber housing a water-cooled drum substrate, and data acquisition and process control electronics. Process control includes open- or closed-loop computer control of the spray process, laser-based feedback control of strip thickness and surface roughness, and remote video monitoring of the spray process. The in-flight particle diagnostics system is used to simultaneously measure single particle size, velocity, and temperature in the atomized plume.

A custom-designed, bench-scale linear converging/diverging spray nozzle was machined in-house from boron nitride with a throat width, transverse to the direction of flow, of about 17 mm (0.66 in.). The

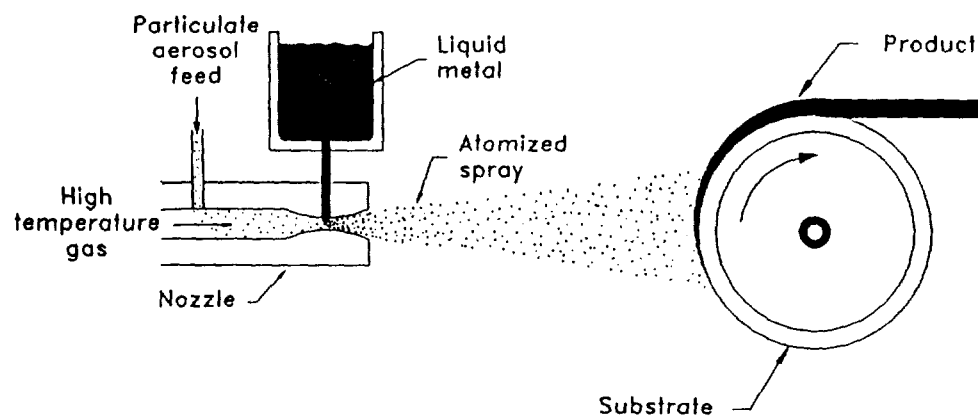


Fig. 1. Schematic of spray-forming composite strip.

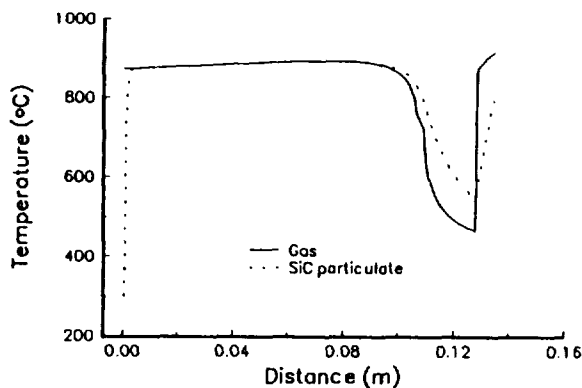


Fig. 2. Temperature profile of atomizing gas and particulate inside nozzle.

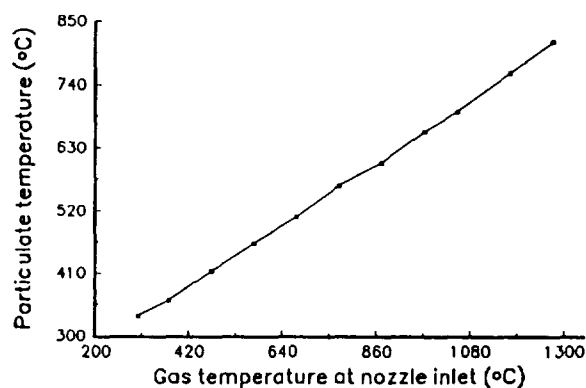


Fig. 3. Particulate temperature at liquid metal injection location as a function of gas temperature at nozzle inlet.

nozzle operates at a static pressure of 206 kPa (30 psia) absolute, measured at the inlet. Single-phase flow field measurements with pitot tubes indicated that this pressure gives rise to supersonic conditions inside the nozzle with the shock front located near the inlet of the liquid metal.

During a typical run, 0.5 kg of 6061 aluminum alloy was induction heated to about 150°C above the liquidus temperature and atomized with argon heated to about 750°C. A commercial fluidized bed powder feed device was used to introduce 13 μm diameter SiC particulate into the nozzle in aerosol form. After a transit time on the order of milliseconds, the multiphase flow impacted the substrate, positioned about 0.3 m from the nozzle, producing a strip of metal about 13 mm (0.5 in.) thick. A purged argon atmosphere within the spray apparatus minimized oxidation of the melt, surface oxidation of the strip, and in-flight oxidation of the atomized droplets.

Aluminum throughput was as high as 700 kg/h (0.8 ton/h), with a corresponding gas-to-metal mass flow ratio (G/M) of 0.1. G/M values as high as 7 were found to give acceptable results. The as-deposited density of the Al strip (without reinforcement), measured by water displacement using Archimedes' principle, was 90 to 95% of theoretical. Photomicrographs of polished strip samples taken at 10% increments in thickness reduction revealed that as little as 30% thickness reduction was needed for full densification (Figure 4).

As-deposited composite strip was sectioned, heated to 450°C in an argon-purged furnace, and hot rolled to 80% thickness reduction followed by quenching. Samples were then solution heat treated and precipitation hardened to yield a -T6 temper. Depending on spray conditions, particulate volume fraction ranged from 4 to 15%, as determined by acid dissolution of the matrix. Optical microscopy of polished samples indicated a uniform distribution of particulate in the matrix phase; an example is given in Figure 5.

Room temperature tensile properties were determined for spray-formed and hot-rolled matrix and 4 vol% composite samples; these results are summarized in Table 1. Both materials showed improvements (about 10%) in ultimate strength and yield strength over commercial 6061-T6 strip, but a reduction in elongation. The unreinforced spray-formed and hot-rolled material also had about 10% higher elastic modulus than commercial 6061-T6. The composite material exhibited a notable increase in modulus (about 33%).

These results are very encouraging but should be viewed as preliminary. Evaluation of a larger number of samples is necessary to optimize spray conditions and to establish statistical validity.

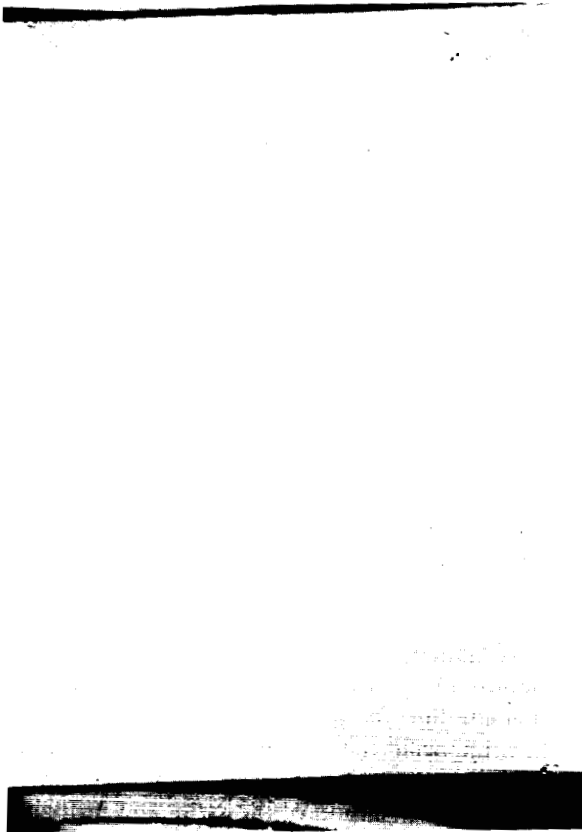


Fig. 4. Photomicrograph of polished matrix strip hot rolled to 30% reduction in thickness.



Fig. 5. Photomicrograph of hot rolled 15 vol% 6061/SiC_p composite strip. Polished, unetched.

Table 1. Tensile Properties of 6061 Al and 6061 Al/SiC_p Strip.

Sample	Yield Strength, 0.2% Offset, MPa (ksi)	Ultimate Strength, MPa (ksi)	Elongation in 50 mm, %	Elastic Modulus, GPa
Commercial 6061-T6	277.2 (40.2)	307.5 (44.6)	12.1	70
Spray Formed and Hot Rolled* 6061-T6	306.1 (44.4)	320.6 (46.5)	7.4	77
Spray Formed and Hot Rolled* 6061-T6/SiC _p (4 vol %)	307.5 (44.6)	336.5 (48.8)	5.4	93

*80% thickness reduction

SPRAY-FORMED TOOLING

Interest in rapid prototyping is growing because successful competition in global markets requires the ability to carry a design from its conception through the prototype stage to the production stage faster and at lower cost than ever before. The main long-term goal of rapid prototyping is quick, cost-effective production of prototype parts from the engineered materials that will actually see service.

Specialized tooling, such as injection molds and stamping dies, is used to produce prototype parts and, eventually, production parts. However, this tooling is both costly and time consuming to make. Most specialized tools, even for low-volume production runs, cost about \$20K to \$200K and can require months to fabricate. Large stamping dies can exceed \$1M. As a result, only the most conservative ideas ever reach the showroom or marketplace.

Researchers at INEL are developing spray-forming methods, based on CAP, to produce tooling by spray depositing rapidly quenched molten metal droplets onto patterns of plastic, wax, wood, clay, and other easy-to-form materials. The approach, which combines rapid solidification processing with near-net-shape fabrication, significantly simplifies the production of complex tooling, thereby reducing its cost and production time. Rapid solidification enables patterns made from plastic, wax, clay, etc. to be used for many applications despite their low softening temperatures, while near-net-shape fabrication allows objects with complex shapes to be made easily. The CAP method is compatible with most pattern making methods, including solid freeform fabrication techniques such as selective laser sintering, stereolithography, laminated object manufacturing, solid ground curing, and fused deposition modeling. These methods share the ability to build up 3-D models of prototype plastic or wax, directly from CAD drawings, in a sequential, step-like fashion [33-35].

Approach

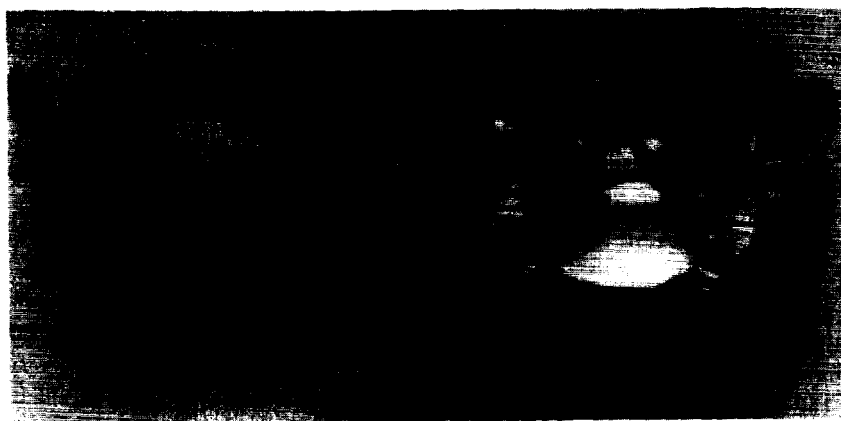
CAP was adapted to spray form molds and dies. Nozzle designs and operating conditions that favored the formation of finely atomized droplets having a narrow size distribution were used. These conditions offer the greatest flexibility for controlling droplet temperature and liquid fraction, the flow pattern and momentum of the spray, and, consequently, the microstructure of the deposit. A quasi one-dimensional computer model was used to estimate droplet temperature and solid fraction as a function of spray parameters. The model simulated the entire nozzle and free jet (plume) regions with full aerodynamic and energetic coupling between the metal droplets and the transport gas, and with coupled liquid injection into the gas stream.

All the spray system components were designed and constructed in-house. The main spray-forming components (spray nozzle, liquid metal reservoir, gas heater, and pattern) were enclosed in an inert-gas-purged glove box to limit the detrimental effects of oxide formation. Bench-scale nozzles having transverse throat widths of 17 mm (0.66 in.) were operated at gas-to-metal mass flow ratios as high as 10. Typically, the metal throughput was about 7 kg/h (15 lb/h) during the initial deposition stage as the pattern's surface features were replicated. Throughput was then increased to about 45 kg/h (100 lb/h) until the walls of the mold were the desired thickness. Much higher deposition rates are possible. A variety of commercial thermoplastics and advanced polymers have been used as pattern materials with good results, including low-density polyethylene (LDPE), polypropylene (PP), poly(methyl methacrylate) (PMMA), polycarbonate (PC), nylon 6/6, polystyrene (PS), polyetherimide (PEI), and polyimide (PI). Argon, nitrogen, and helium have been used as atomizing and purge gases with comparable results.

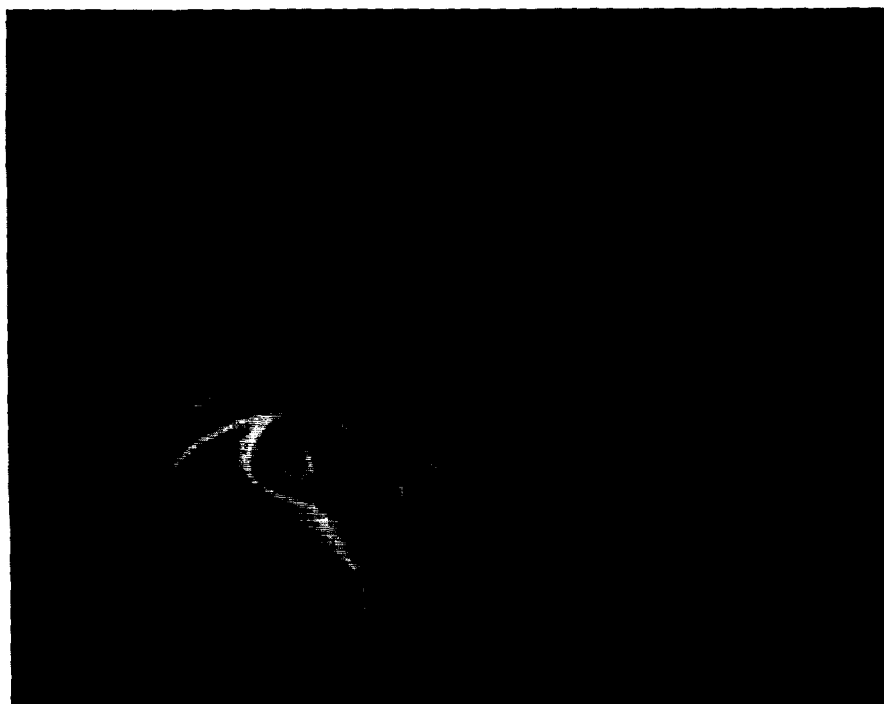
The metal to be sprayed was heated above its liquidus temperature and pressure-fed into a venturi-like nozzle transporting high velocity (mach number ~ 1.5) inert gas that also was heated to above the metal's liquidus temperature. Aerodynamic forces overcame the liquid metal's surface tension forces, resulting in a highly directed spray of finely atomized metal droplets. Outside the nozzle, the jet entrained relatively cold inert gas. This provided a heat sink for the spray, producing undercooled and semisolid droplets. The droplets were deposited onto a pattern that was manipulated in the jet to provide even coverage. The resultant metal shell was cooled to room temperature and separated from the pattern.

Results

Examples of spray-formed mold shells are given in Figure 6. Shells of tin (Figure 6a) and a zinc-base die-forming alloy (Kirksite, Figure 6b) were produced in about 5 min by spray depositing the metal onto LDPE patterns having the shape of sand toys. Replication of surface features, including fine scratches in the pattern, was excellent. Peak-to-valley surface roughness of the shell at the deposit/pattern interface was measured to be as low as $2\ \mu\text{in}$ using a profilometer. As-deposited density, measured by water displacement using Archimedes' principle, has been close to 100% of theoretical for tin. The porosity



(a) Tin mold (right) and polyethylene pattern (left).



(b) Kirksite molds (left and above) and polyethylene pattern (right).

Fig. 6. Spray-formed metal mold shells.

distribution in a thin-sectioned mold shell is shown by the photomicrograph in Figure 7a. There is very little porosity through the thickness of the material. The grain structure of the same material is shown in Figure 7b. The equiaxed grain structure, with an average grain size of $9\ \mu\text{m}$ (ASTM grain size number 10 1/2), is much more refined than that of the cast starting material (Figure 7c) due to rapid solidification.

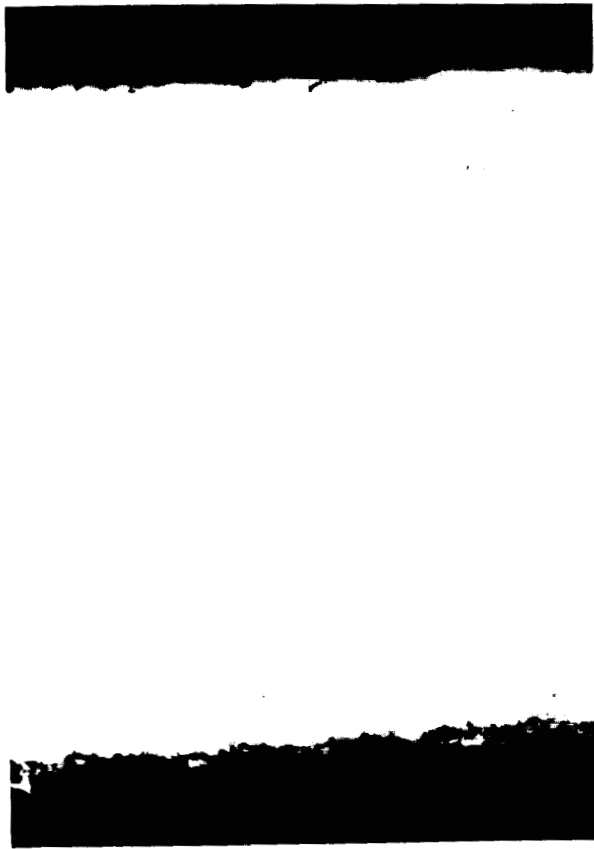
SEM analysis of overspray powder revealed that nearly all particles were spherical. Size analysis was performed using a laser aerosol spectrometer. Figure 8 gives the mass frequency of the tin and Kirksite alloy powders vs. size. The ordinate gives the mass frequency normalized for the channel size range, expressed as a percentage of the total mass. The mass median diameter was determined by interpolation of the cumulative weight vs. size data; it is the diameter corresponding to 50% cumulative weight (d_{50}). The Sauter (or area) mean diameter, d_{sm} , is sensitive to finer droplets, while the volume mean diameter, d_{vm} , is sensitive to coarser droplets. Together, they give a balanced view of the powder size. For tin, d_m , d_{sm} , d_{vm} , and the geometric standard deviation, $\sigma_v = (d_{84}/d_{16})^{1/2}$, were found to be $22\ \mu\text{m}$, $18\ \mu\text{m}$, $45\ \mu\text{m}$, and 2.4, respectively. For the Kirksite alloy these values were nearly identical: $22\ \mu\text{m}$, $18\ \mu\text{m}$, $44\ \mu\text{m}$ and 2.6, respectively. Increasing the mass loading by a factor of 5 to 100 lb/h while maintaining other spray parameters constant resulted in only a small increase in droplet size and size distribution. The type of atomizing gas (Ar, N₂, and He) did not have a significant effect on atomization behavior at these mass loadings but may play a more important role in droplet quench rate and degree of undercooling.

ACKNOWLEDGMENTS

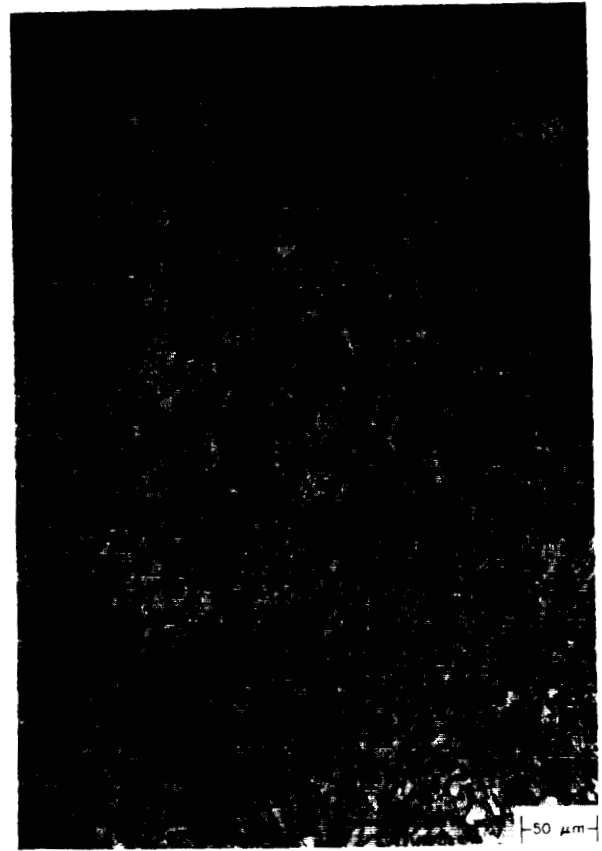
The author gratefully acknowledges significant contributions of Linda Wallace and Bruce Wickham in this research. This work was supported by the U.S. Department of Energy, Office of Conservation and Renewable Energy, Office of Industrial Technology, and by the EG&G Idaho Laboratory Directed Research & Development Program under DOE Idaho Field Office Contract DE-AC07-76ID01570.

REFERENCES

1. A. L. Geiger and J. Andrew Walker, *JOM*, August 1991, p. 8.
2. M. Paley and J. Aboudi, *Composites Science and Technology* **41**, 411 (1991).
3. A. P. Divecha, S. G. Fishman and S. D. Karmarker, *JOM*, Sept. 1981, p. 12.
4. A. P. Divecha and S. G. Fishman, *Proceedings of the 3rd International Conference on the Mechanical Behavior of Materials*, K. J. Miller and R. F. Smith, eds., Pergamon Press, New York, NY, 1980, p. 351.
5. V. C. Nordone, J. R. Strife and K. M. Prewo, *Metall. Trans.* **22A**, 171 (1991).
6. S. V. Nair, J. K. Tien and R. C. Bates, *Int. Metals Rev.* **30**, 275 (1985).
7. V. C. Nordone, *Scripta Metall.* **21**, 1313 (1987).
8. T. G. Nieh, *Metall. Trans.* **15A**, 139 (1984).
9. Y. Wu and E. J. Lavernia, *JOM*, August 1991, p. 16.
10. I. A. Ibrahim, F. A. Mohamed, and E. J. Lavernia, *J. Mat. Sci.* **26**, 1137 (1991).
11. F. A. Giroto, T. M. Quenisset and R. Naslan, *Composite Sci. Technol.* **30**, 155 (1987).
12. *Critical Research Directions in Metal-Matrix Composites*. ESNIB 91-03, p. 18.
13. *The Materials Revolution through the 90's - Powders, Metal Matrix Composites, and Magnetics*, ESNIB 89-10, p. 4.
14. Y. L. Klipfel, M.Y. He, R. M. McMeeking, A. G. Evans and R. Mehrabian, *Acta. Metall. Mater.* **38** (6), 1063 (1990).
15. P. Rohatgi, *Adv. Mater. Process*, February 1990, p. 39.
16. R. Mehrabian, *Mater. Res. Soc. Symp.* **120**, 3 (1988).
17. M. S. Newkirk, A. W. Urguhart, H. R. Zwickler and E. Breval, *J. Mater. Res.* **1**, 81 (1986).
18. A. Mortensen, J. A. Cornie and M. J. C. Flemings, *Metall. Trans.* **19A**, 709 (1988).
19. T. W. Clyne, M. G. Badger, G. R. Cappleman and P. A. Hubert, *J. Mater. Sci.* **20**, 85 (1985).
20. T. W. Clyne and J. F. Mason, *Metall. Trans.* **18A**, 1519 (1987).
21. R. Mehrabian, R. G. Rick and M. C. Flemings, *Metall. Trans.* **5**, 1988 (1974).



(a) Spray-formed mold, polished.

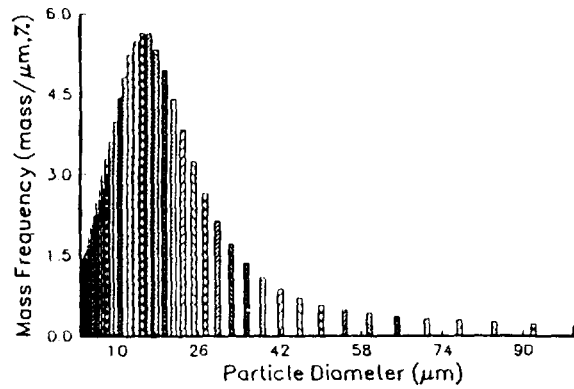


(b) Grain structure of spray-formed mold.

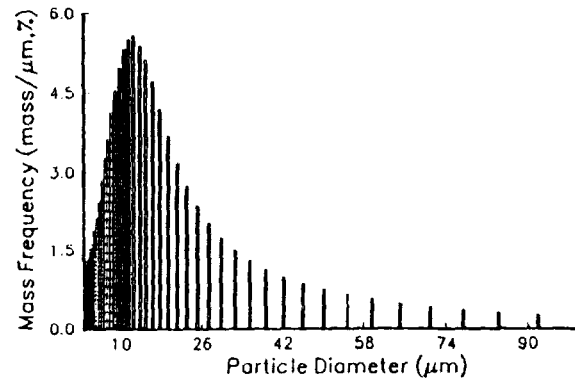


(c) Grain structure of cast metal.

Fig. 7. Photomicrographs of tin.



(a) Tin



(b) Kirksite alloy

Fig. 8. Mass frequency distribution of metal powders.

22. D. O. Kennedy, *Adv. Mater. Process.*, June, 1991, p. 42.
23. P. F. Chesney and R. Pratt, *Proceedings of the 1st International Conference on Spray Forming*, Sept. 1990, ICSF 90-20.1.
24. A. L. Geiger and M. Jackson, *Adv. Mater. Process.* 7, 23 (1989).
25. A. R. E. Singer and S. Ozbek, *Powder Metall.* 28(2), 72 (1985).
26. Pol Duwez and R. H. Willens, *Trans. Metall. Soc. AIME* 227, 362 (1963).
27. S. K. Das and L. A. Davis, *Mater. Sci. Eng.* 98, 1 (1988).
28. N. Zhang and Y. Wang, *Vacuum* 42 (15), 1017 (1991).
29. R. C. Pond, *Grain Boundary Structure and Kinetics*, ASM, Metals Park, Ohio, 1980, p. 13.
30. O. L. Krivanek, S. Isoda and K. Kobayashi, *Phil. Mag.* 36, 931 (1977).
31. W. Krakow and D. A. Smith, *J. Mater. Res.* 1, 47 (1986).
32. J. F. Key, R. A. Berry, D. E. Clark, J. R. Fincke, and K. M. McHugh, *Development of a Spray-Forming Process for Steel. Final Program Report*, Dec. 1991 (DOE Contract No. DE-AC07-76ID01570).
33. H. L. Marcus and D. L. Bourell, *Adv. Mater. Process.* 144 (3), 28 (1993).
34. C. R. Deckard, *Manufacturing Processes, Systems, and Machines: 14th Conference on Production Research and Technology*, S. K. Samanta (ed.), NSF, Ann Arbor, MI, 1987.
35. L. E. Weiss, E. L. Gursoz, F. B. Prinz, P. S. Fussell, S. Mahalingam, and E. P. Partick, *Manufacturing Review*, 3 (1), 40, (1990).

Composite Hot Drape Forming

**Thomas Ott
Boeing Defense & Space Group
Operations Technology
Helicopters Division
P38-50
215-591-3989**

INTRODUCTION/APPROACH

This program was initiated to replace labor-intensive ply-by-ply layup of composite I-beam posts and angle stiffeners used in the Space Station Freedom (SSF) rack structure.

Hot drape forming (HDF) has been successfully implemented by BCAG for 777 composite I-stringers and by Bell Helicopter/Textron for the V-22 I-stringers. The two companies utilize two vastly different approaches to the I-beam fabrication process. A drape down process is used by Bell Helicopter where the compacted ply charge is placed on top of a forming mandrel and heated. When the heated ply charge reached a set temperature, vacuum pressure is applied and the plies are formed over the mandrel. The BCAG 777 process utilizes an inverted forming process where the ply stack is placed on a forming table and the mandrel is inverted and placed upon the ply stack. A heating and vacuum bladder underneath the ply stack form the ply stack up onto the mandrels after reaching the temperature setpoint.

Both methods have their advantages, but the drape down process was selected for SSF because it was more versatile and could be fabricated from readily available components.

CONCLUSION

The HDF process replaces labor-intensive hand layup of SSF I-beam posts and angle stiffeners with an effective and simple process. Ply wrinkling and other forming problems are virtually eliminated providing that the prepreg material outtime is minimized. The material outtime is especially critical on the glass/epoxy prepreg layers where "old" material can adversely effect the part surface quality. Two plies of FEP film and one ply of TFP cloth placed between the ply stack and the forming bladder provide multiple slick surfaces which allow the plies to smoothly form without wrinkles.

The problem of indexing the compacted ply stack to the forming mandrels has been solved by using nylon tooling pins to position the ply stack prior to forming. With metal forming mandrels, it is important that the control thermocouple be placed within the laminate and not placed on top of the ply stack or between the forming mandrel and the ply stack.

The HDF process has been selected for production of SSF composite rack components in which the I-beam posts and horizontal angle stiffener can be produced using the normal one step (one tool) process. The lower rear horizontal member (W-stiffener) and the joggled skin stabilizers are candidates for continued development using a two step (two tool) forming process

HOT DRAPE FORMER SET-UP

The developmental hot drape former was constructed from unistrut tubing and aluminum sheets to form a box-shaped hot drape fixture 108 X 54 X 84 inches with a 104 X 60 inch opening for a forming table. A rolling aluminum table with a 48 X 96 X 1 inch thick aluminum tool plate surface was constructed to roll parts into the fixture for forming (See Figure 1). The table's toolplate surface was covered with Richmond Toolcoat 807S Pressure Sensitive TFE fiberglass sheet for part release and to provide a slick surface to minimize bridging of the silicone forming bladder.

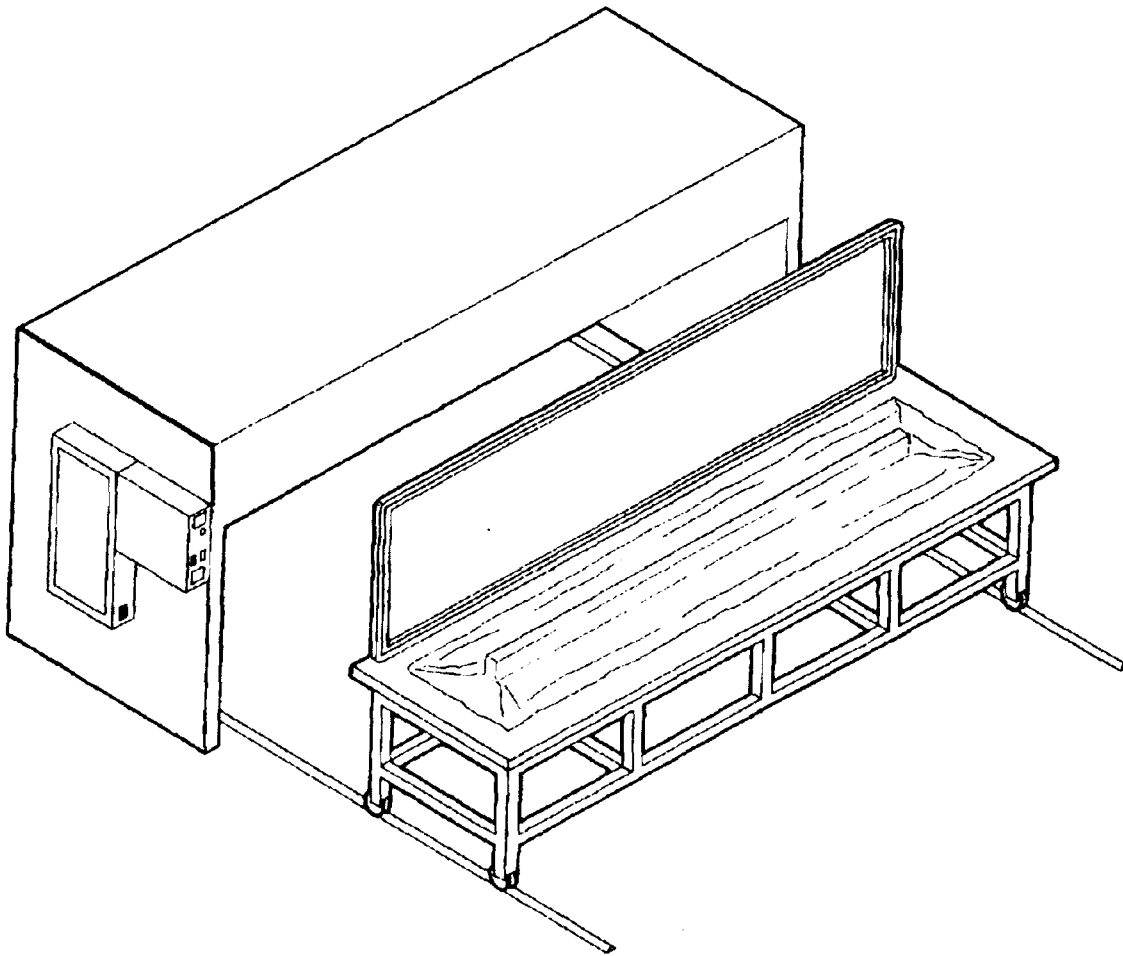


Figure 1 Hot Drape Forming Unit

Mosites Rubber Company fabricated the vacuum forming bladder using 2" aluminum box tubing, Mosites 1453-D silicone rubber sheet and a proprietary double bulb seal. The vacuum bladder utilized two vacuum ports with quick disconnect fittings to vacuum form the silicone rubber bladder, and one vacuum line to seal the frame and bulb seal to the tooling plate.

The heating was provided by using three banks of 480 volt, three phase infrared heaters controlled by a programmable digital controller. Feedback for the controller is provided using a J-type thermocouple placed in the composite ply stack excess trim area (at either end) during part forming (See Figure 2). To allow additional part temperature monitoring, capabilities a ten-channel switch and a digital temperature indicator was installed.

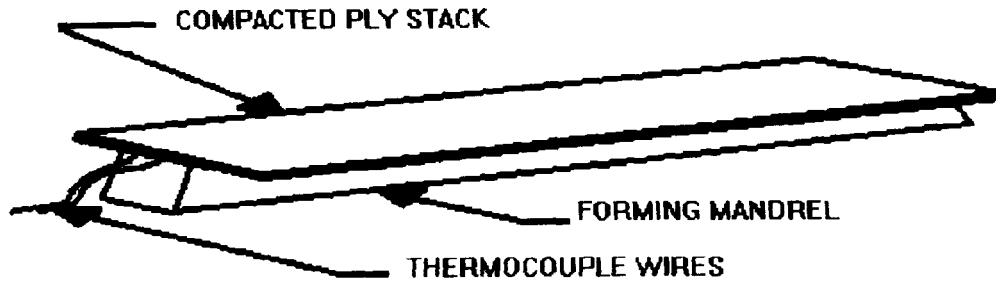


Figure 2 Thermocouple Wire Placement

PROCESS DEVELOPMENT

Process development consisted of forming 13 ply C-channels using developmental aluminum mandrels with a springback angle of 1.5 degrees to compensate for the original Developmental Rack I-beam post unsymmetric and unbalanced layup which were believed to cause excessive part springback.¹ The 13-ply forming charges were prepared by vacuum compacting (21" Hg minimum) ply stack then trimming out the 13-ply charge with a template and ultrasonic knife. The compacted ply stacks were indexed on the forming mandrels by cutting slots with an ultrasonic knife at each end of the ply stack, then pinning them to the mandrel using nylon tooling pins.

Vacuum tests showed that the vacuum bladder needed a slick surface to prevent bridging of the silicone rubber bladder and ensure that the plies form to the mandrels. A pad for the forming table was made from two plies of 10 ounce polyester breather cloth covered with a ply of TFP release cloth. To provide a slick surface over the part ply stack, two plies of non-perforated FEP film and one ply of 200 TFP-1 TFE coated glass fabric were placed over the compacted ply stack prior to forming (See Figure 3). The forming bladder was then lowered over the part, clamped into position, and the vacuum hoses connected. The table was rolled into the heating fixture, centered under the heaters, and the air draft curtain is closed.

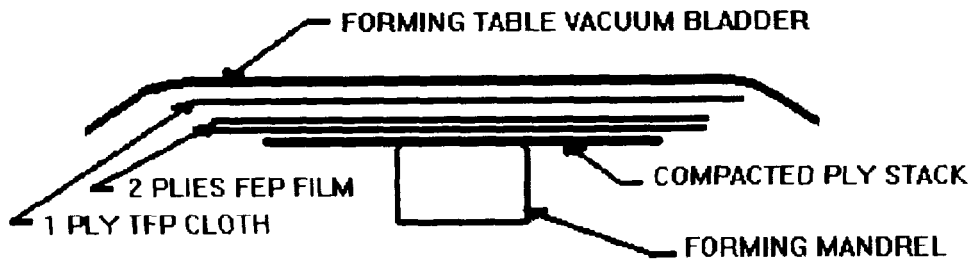


Figure 3 Part Preparation

The temperature control setpoint was set at 130° based on a process specification maximum of 150°F, and allowances for temperature overrun with the infrared heaters. The initial forming tests revealed a heat-up problem due to air drafts within the unit and the original location in a high bay fabrication area. To solve the draft problem, nylon vacuum bagging film was taped in place over the fixture openings, and welding curtains were placed around the unit. The draft problem was further solved by moving the hot drape fixture into a development clean room laboratory and installing a rubber seal strip to seal between the forming table and the heating unit. After removing

the draft problem, several developmental parts were formed including C-channels for I-beams or angle stiffeners, and multiple-flanged parts which would simulate a rectangular wing rib part or a five sided box.

Another process that was developed was two-step hot drape forming which involves forming an angle, removing it from the tool by inverting the angle and placing it on another tool to form opposite angles such as in a W-stiffener or Z-stiffener configuration (See Figure 4). The tool used in two step forming should be covered with a ply of FEP film to allow the part to be removed from the tool without damaging the part. The tool for the second step does not require FEP film unless the part requires transfer to a separate curing fixture. Alternatively a sheet of colored FEP or non-bondable Tedlar film can be incorporated into the ply stack and formed with the laminate providing good tool release later.

¹The flight rack design has changed to a symmetric and balanced layup which requires no springback allowance. Manufacturing Technology also recommends Invar steel mandrels for production to minimize the thermal coefficient of thermal expansion (CTE) differences between the part and tool, thus requiring only a minimum draft angle for part removal.

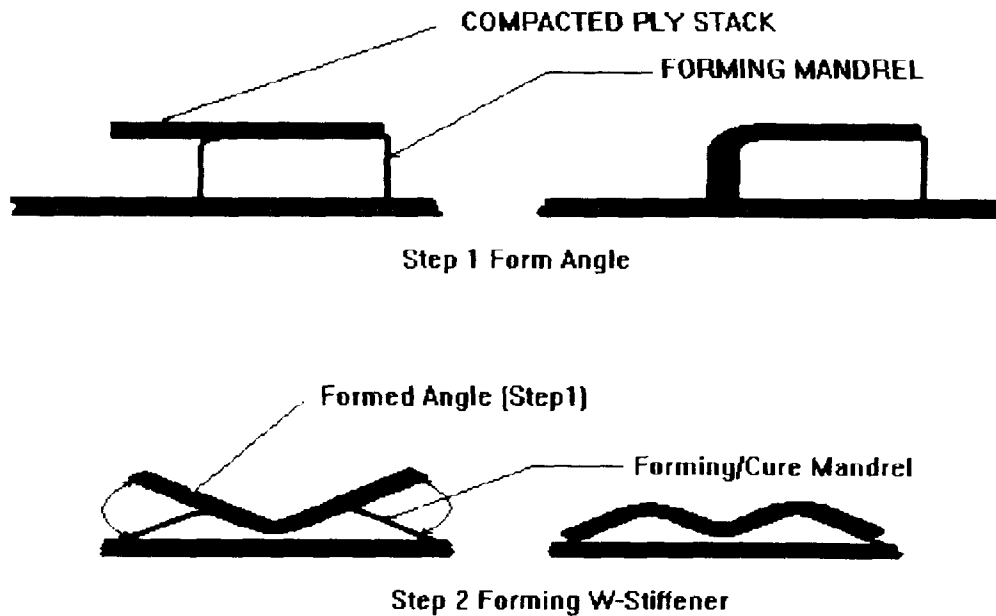


Figure 4 Two Step Hot Drape Forming

OPERATING PROCEDURES

A. Tool Part/Preparation

1. Lay-up and pre-compact laminate
2. Obtain the forming mandrel(s) and place on the forming table. Mandrel(s) shall be cleaned and treated with release agent.

3. Tape (Teflon or flash breaker tape) a J type thermocouple in the laminate at the mid-ply level. To allow additional monitoring, up to nine J type thermocouples may be placed in the laminate at the mid-ply level (preferred location) or taped to the tool surface. A minimum of one monitoring thermocouple per part shall be used (See Figure 2). All thermocouples used shall be placed in the part excess trim area.
4. Position the pre-compacted ply layup stack in position over the forming mandrel. Make sure the laminate is firmly located against the forming mandrel, and tape in place or secure using nylon tooling pins.
5. Cover the ply stack with two plies of non-perforated FEP film allowing 1-2 inches excess around the part periphery (See Figure 3).
6. Cover the FEP film layers with one ply of TFP cloth (Teflon coated fiberglass fabric). Trim the TFP cloth to 0.2 - 0.5 excess from the part periphery (See Figure 3).

B. Hot Drape Former Preparation

1. Turn on machine power, but do not turn on heaters.

Check controller temperature setpoint. Use a temperature setpoint between 120° and 140°F, with 130° ± 5° recommended by Manufacturing Technology.

2. Check the monitor or chart recorder to verify that each of the installed thermocouples is functioning properly.

C. Hot Drape Ply Forming

1. Position the forming table under the heaters.
2. Close the draft curtain or door on the front of the hot drape unit to expedite heating.
3. Turn on the heaters, and allow the ply stacks to warm up.
4. When the thermocouples indicate the ply stack temperature is 115-140°F, apply the vacuum to the tool assembly. Heat may be maintained if necessary for a maximum of five minutes, but do not exceed 150°F.
5. Turn off the heaters and move the tool to a cooling area. Allow the tool assembly to cool to 95°F or less. Maintain vacuum (15 inches/HG minimum) while the tool assembly is cooling.
6. Remove the vacuum source, vacuum bag, and release materials from the formed parts.
7. Inspect parts to make sure the plies are fully formed without any wrinkles. A properly formed part will tightly conform to the forming mandrel without wrinkles. Parts that do not appear to fully conform to the mandrel may be reformed.

CONCLUSION

The HDF process replaces labor-intensive hand layup of SSF I-beam posts and angle stiffeners with an effective and simple process. Ply wrinkling and other forming problems are virtually eliminated providing that the prepreg material out time is minimized. The material out time is especially critical on the glass/epoxy prepreg layers where "old" material can adversely affect the part surface quality. Two plies of FEP film and one ply of TFP cloth placed between the ply stack and the forming bladder provide multiple slick surfaces which allow the plies to smoothly form without wrinkles.

The problem of indexing the compacted ply stack to the forming mandrels has been solved by using nylon tooling pins to position the ply stack prior to forming. With metal forming mandrels, it is important that the control thermocouple be placed within the laminate and not placed on top of the ply stack or between the forming mandrel and the ply stack.

The HDF process has been selected for production of SSF composite rack components in which the I-beam posts and horizontal angle stiffener can be produced using the normal one step (one tool) process. The lower rear horizontal member (W-stiffener) and the joggled skin stabilizers are candidates for continued development using a two step (two tool) forming process.

HOT DRAPE FORMING CONCERNS

The primary concern with hot drape forming is ply wrinkling in the radius areas. The wrinkling problem was minimized by Engineering Design allowing fabric plies to be used in the $\pm 45^\circ$ ply orientations. The toolcoat covering on the mandrels, two plies of FEP film and one ply of TFP cloth collectively allow the compacted ply stack to smoothly form over the mandrels without wrinkles providing that the proper forming temperature is reached prior to the application of vacuum. The rate of vacuum application is also critical with some wrinkling problems noticed when vacuum was very slowly applied. To date, no problems have been encountered with a rapid application of vacuum.

Radius thin-out is another problem associated with HDF where the plies thin-out on the radius as a result of forming and/or curing. The C-channels formed for I-beams did not show any thin-out problems on cured I-beams, and the C-channels that were formed and cut into angle stiffeners showed a 0.001 - 0.003 inch thin-out on a 0.095 nominal part thickness. The all-fabric ply layup reduces the thin-out, and when problems occur, a rubber pressure pad is used to further minimize any radius thinning.

Non-destructive ultrasonic testing was conducted on formed C-channels, angles and I-beams. The only parts found to be unacceptable were made with materials that had excessive outtime.

PRODUCTION IMPLEMENTATION RECOMMENDATIONS

To prepare the developmental HDF for SSFP production several upgrades were required which included documentation, drawings and several fixture modifications. The modifications to the fixture include:

- 1) Design and fabrication of a new forming table with a hinged forming bladder. The table should also have drilled holes for thermocouple wire feed throughs and vacuum. To prevent vacuum leaks, the thermocouple wire holes should be potted with RTV silicone sealer.
- 2) Improved method to seal the table and the front opening of the heating unit (slide up door).
- 3) Temperature recording device for QA record of forming cycles.
- 4) Replace present miniature thermocouple jacks with the standard size jacks.
- 5) Convert present forming plate and bladder for use as a ply compaction table.
- 6) Wheel guides to positively locate table under the heaters. Metal angles bolted to the floor should serve as the necessary guide.
- 7) Provide grounding method which grounds forming table and unit to prevent static electricity shocks.

In addition to the fixture modifications, several other items are required for production implementation of the development hot drape former. These include calibration and certification of the controls (for temperature accuracy) and the heating system (for temperature uniformity).

Another suggestion for production would be to improve the ply stack indexing method by changing to Gerber cut slots or drilled holes rather than the present method of using a template and cutting slots with an ultrasonic knife.

3445
1-7

**PRECISION AND MANUFACTURING AT THE
LAWRENCE LIVERMORE NATIONAL LABORATORY**

**Theodore T. Saito, Richard J. Wasley, Irving F. Stowers,
Robert R. Donaldson and Daniel C. Thompson
Energy, Manufacturing & Transportation Technologies
Lawrence Livermore National Laboratory
P.O. Box 808, L-644
Livermore, CA 94551
Internet: SAITO1@LLNL.GOV**

ABSTRACT

Precision Engineering is one the Lawrence Livermore National Laboratory's core strengths. This paper discusses the past and present current technology transfer efforts of LLNL's Precision Engineering program and the Livermore Center for Advanced Manufacturing and Productivity (LCAMP). More than a year ago the Precision Machining Commercialization project embodied several successful methods of transferring high technology from the National Laboratories to industry. Currently LCAMP has already demonstrated successful technology transfer and is involved in a broad spectrum of current programs. In addition this paper discusses other technologies ripe for future transition including the Large Optics Diamond Turning Machine.

INTRODUCTION

The Lawrence Livermore National Laboratory (LLNL) is well known for the successful application of scientific principles to the solution of key technical problems and has addressed problems outside of the Department of Energy (DOE) for several decades. However, recent changes in legislation and national emphasis has opened up our doors to a broader spectrum of users.

LLNL's traditional mission of designing strategic weapons is changing, and economic competitiveness, particularly in advanced manufacturing, is becoming a new mission at Livermore. LLNL has unique capabilities in advanced manufacturing and supporting technologies that are strategically important to the competitiveness of key U.S. industries; e.g., automotive, machine tool, textile, consumer electronics, shipbuilding, computers, and aerospace. Expertise in technologies centrally important to advanced manufacturing include machine design, precision engineering, control systems, materials engineering, metrology, nondestructive evaluation, process modeling, and structural modeling. Furthermore LLNL has worked with many large and small businesses in executing its major projects, such as the NOVA, terawatt laser. As LLNL adjusts to new roles and missions it will build on its solid relations with industry and transfer its technology to help American industry be more competitive. Just as Livermore played a key role in the cold war, it looks forward to playing a key role in the economic battle of today and tomorrow.

This paper will describe just a portion of LLNL's contributions to NASA and the commercial community. Activities from both the Precision Engineering Program (PEP) and the Livermore Center for Advanced Manufacturing and Productivity (LCAMP) will be described. First a perspective on LLNL's technology transfer success will be given by a past effort. Then a recent program will be described, and finally other technologies ready for transfer will be outlined.

PAST TECHNOLOGY TRANSFER - PRECISION ENGINEERING PROGRAM

The Precision Engineering Program (PEP) mission is to develop and utilize precision engineering deterministic principles to solve problems of national interest. Precision engineering is one of LLNL's core strengths with many successful applications to Department of Energy (DOE) and Department of Defense (DOD) programs. In addition, PEP has worked closely with NASA and private industry to successfully solve their problems. PEP has been active in precision machine tool design, metrology, optics (design, diamond turning, polishing and coating), precision process development and technology transfer.

*This work was performed under the auspices of the U.S. Department of Energy by Lawrence Livermore National Laboratory under contract No. #W-7405--Eng-48.

Precision Machining Commercialization

LLNL has a long background of technology transfer and cooperation with industry. One such initiative, under the Precision Engineering Program, was the Precision Machining Commercialization (PMC) project funded by the USAF Manufacturing Technology (ManTech).¹ PMC successfully commercialized diamond turning technology developed within the Department of Energy, with an initial application to the Department of Defense.

Recognizing the order of magnitude cost savings as well as significant technical flexibility afforded by diamond turning, the USAF chartered LLNL in conjunction with DOE's Y-12 facility in Oak Ridge, Tennessee, to transfer the technology from the laboratory into commercial use. PMC had four major thrusts:

1. Documentation of the Diamond Turning Process
2. Seminars and Workshops Given to Private Industry
3. Technical Assistance to Private Industry
4. Hardware Demonstration

Documentation: Diamond turning is a highly technical but deterministic fabrication process. (A deterministic process is one in which much can be quantitatively defined through a cause-and-effect relationship.) Therefore, it was amenable to written scientific analysis. As is often the case with technologies and processes pushing the state-of-the-art, many of the lessons learned were not documented, but "understood" by the practitioners. PMC's goal was to describe in two volumes of documentation² the key elements of the processes and associated technologies important to the successful understanding of diamond turning.

Seminars and Workshops: PMC served the role of technology advocate, both explaining the intricacies of the technology as well as its advantages. In addition to technical meetings with professional societies, such as SPIE, the International Optical Engineering Society and Society of Manufacturing Engineers, PMC hosted workshops across the country. These workshops were sometimes held in cooperation with machine tool companies who were prospective providers of turn-key diamond turning systems. One of the most effective stimuli was from direct visits to prospective technology users either at the seminars and workshops or their own plants. Furthermore, endorsement of the Department of Commerce and the National Tool, Die and Precision Machining Association (NTDPMA) facilitated the acceptance of PMC's efforts.

Technical Assistance: Technical assistance took several forms. One was consultation with both machine tool companies and users. Key questions regarding the applicability and capabilities of diamond turning for users helped identify the high pay-off areas. Technical "how-to" questions were also answered for machine tool companies. In addition, technical support was provided to Air Force and Army ManTech partners pursuing diamond turning. Honeywell and Kollmorgen both had significant success in achieving in-house diamond turning capability and providing optics for Air Force and Army programs.

Hardware Demonstration: During the technical assistance phase it was often found that a key question arose regarding the possibility of diamond turning being able to achieve the required specifications. Therefore, PMC provided a demonstration component fabricated within the DOE community. In addition to delivering a part which demonstrated the required performance, PMC also identified what steps would be necessary to improve existing or planned commercial capabilities to satisfy the advanced requirements.

PMC had impressive successes. Just one small production run of several hundred infrared scanner mirrors saved \$500K. This savings was due to both reduced figuring and coating costs in the fabrication process. Infrared systems, such as those used in Desert Storm, have benefited from diamond turning. Furthermore applications have expanded to non-military uses such as hard disk drive platters, copier optics, contact lenses, and inter-ocular lenses.

During PMC's execution, it became apparent that diamond turning offered special fabrication capability which would enable a revolutionary resonator optic applicable to high power lasers. Shortly thereafter, the Precision Engineering Program was asked to build a special machine, the Large Optics Diamond Turning Machine (LODTM) (which will be described later), for this purpose.

RECENT TECHNOLOGY TRANSFER INITIATIVES: LIVERMORE CENTER FOR ADVANCED MANUFACTURING AND PRODUCTIVITY

LLNL is well positioned to support U.S. manufacturing competitiveness and accordingly has established the Livermore Center for Advanced Manufacturing and Productivity (LCAMP). The mission of LCAMP is to focus and leverage the Laboratory's resources, activities, and expertise in manufacturing technologies critical to U.S. industrial competitiveness. LCAMP provides a conduit to industry, through which industry needs and LLNL resources and core competencies are identified, communicated, and matched. These efforts have resulted in collaborations with industry, universities, colleges, and DOE in a set of broadly based technology transfer projects, including education and training programs in advanced manufacturing.

LCAMP has initiated over 20 projects with industry, coupling the various companies with Livermore's technologies for mutual benefit. The technologies not only include precision engineering thrusts, but also advanced material development and application; computer modeling of manufacturing processes; and testing, inspection, and nondestructive evaluation.

One recently completed example of a partnership was with a small California industrial tool company in which a new precision machining system was developed that can cut hard-to-machine materials such as ceramics, carbides, glasses, and plastics with an accuracy of 1 μm . Applications include cutting computer disk-drive recording heads made of alumina-titanium carbide and slicing large silicon wafers into chips in the semiconductor industry. This new machine is twice as accurate as the company's previous machine, and now is one of the most precise production units of its kind in the world and will enable the tool company to compete successfully against (primarily) foreign competition.

LLNL's precision engineering expertise had strong influence to the machine layout and overall design. This can be seen with the use of a "bridge" design for the X-axis indexing slide and with the use of an air bearing slide system for the Y-axis slide. The bridge design allows for increased dynamic and thermal stability over the company's original cantilever arrangement. The air bearing slide system, designed by LLNL, is a low friction slide that provides precise movement of the work piece, essential to providing the accuracy requirements of the machine.

LLNL engineers advised the tool company on how to systematically reduce as many sources of potential error as possible and economically reasonable. This was demonstrated to the company by applying deterministic manufacturing and precision engineering techniques to calculate stresses in structures, predict machine performance and thermal and vibration characteristics, and apply error-compensation methods to maximize system accuracy despite vibration and temperature fluctuations.

Along with the engineering design assistance, LLNL personnel provided hands-on assistance which included training and assembly of the Y-axis air bearing slide system, instruction of precision alignment techniques and procedures, and the application of proper precision metrology. The partnership between LLNL and the company produced the successful fabrication and testing of a prototype machine leading to sales of production units.

In addition to generating joint projects with industry, LCAMP is developing other support mechanisms to enhance U.S. manufacturing competitiveness. For example, LLNL is creating user facilities that will be formally recognized by DOE for industry and university interactions. These facilities are underutilized, unclassified, have state-of-the-art manufacturing equipment, and are accessible by industrial personnel, students, and faculty for project work, research, education and training classes, demonstration efforts, and outreach activities.

L-CAMP has also been centrally involved in establishing Regional Technical Assistance Programs, e.g., the National Machine Tool Partnership (NMTP) and the Small Business Technology Transfer Program (SBTTP). The NMTP is a partnership among the four Defense Program National Laboratories (LLNL, Los Alamos National Laboratory, Sandia National Laboratory, and the Oak Ridge National Laboratory) together with DOE, DOC (NIST) and DOD. Its purpose is to strengthen the U.S. machine tool industry to help the U.S. regain its worldwide lead by providing free quick turnaround solutions to real world problems being experienced by builders and users. The SBTTP supports smaller regional businesses (< 500 employees) by providing free technical assistance (up to \$5K) and partnership agreements (up to \$50K) to gain access to DOE facilities and equipment.

FUTURE TECHNOLOGY TRANSFER POSSIBILITIES

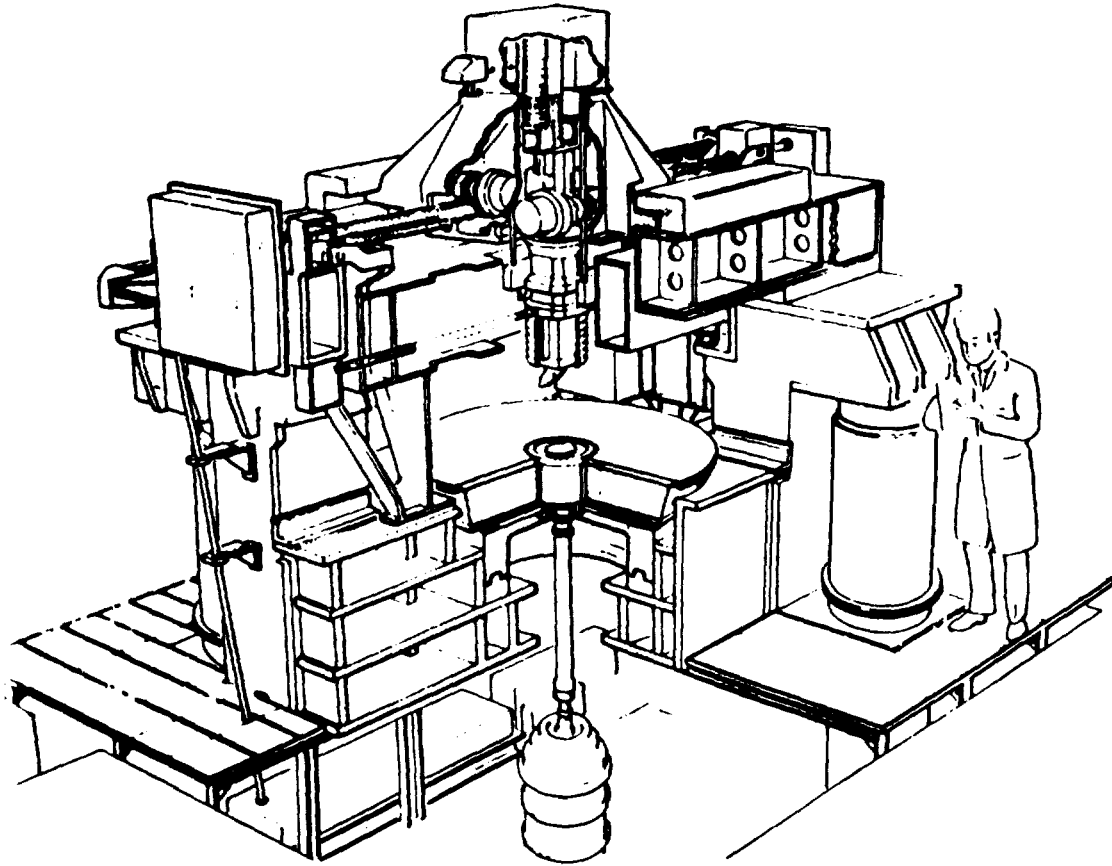


Figure 1.
The Large Optics Diamond Turning Machine

LODTM

As mentioned earlier, LLNL was asked in the late 1970's to design a state-of-the-art diamond turning machine for special DOD resonator optics for a space borne laser . This resulted in the Large Optics Diamond Turning Machine (LODTM) which is a precision vertical-axis lathe, shown in Fig. 1. The workpiece size limits are 162 cm in diameter, 50 cm in height, with a maximum weight of 1400 kg. Tool positioning on the LODTM is accomplished by a vertical tool bar (Z-axis) motion and a carriage which provides radial (X-axis) motion. LODTM's development included many technologies which have been or are ripe for technology transfer.

A fundamental problem in the design of a high accuracy feedback-controlled machine tool is measuring the relative position between the tool and the workpiece without intruding into the work volume, which is occupied by the workpiece. The measurement scheme that connects the tool tip to the workpiece is referred to as the 'metrology loop.' For the LODTM the active measurements are made by laser interferometers and capacitance gages, which are referenced to a passive metrology frame.

The metrology frame interconnects the interferometers and capacitance gages and surrounds the machine work zone, as shown in Fig. 1. To perform its intended function, the metrology frame must remain exactly constant in size and shape even though the mainframe may deform by up to 6 μm . Super Invar is used to provide a dimensionally stable structure with a low coefficient of thermal expansion.

All large-travel measurements are made by means of seven laser interferometers, each with a resolution of 1.2 nm and overall accuracy of 2.5 nm. Great care has been taken in developing a single frequency-stabilized laser and to minimize interferometer errors due to uncertainties in the index of refraction in the interferometer leg. The interferometric measurements are isolated from atmospheric effects by enclosing all but a tiny gap of the interferometer measurement pathway in vacuum.

Workpiece position, relative to the metrology frame, is determined by capacitance sensors mounted on metrology frame extensions, which measure drift of the outer edge of the spindle face plate. Two orthogonal capacitance gages at each edge of the face plate provide axial, radial, and tilt motion data with a resolution of 0.6 nm and a 0.1% linearity.

The design of moving parts for the LODTM relies heavily on the use of fluid film bearings for smooth, friction-free motion. To avoid pump vibrations, the oil systems are fed by pairs of blow-down tanks that are alternately pressurized by compressed air.

The primary actuators for both X and Z axis motion are capstan drives, each consisting of a 5 cm diameter smooth steel rollers driving against a flat steel bar approximately 2.5 cm wide. The roller is supported by externally pressurized oil bearings, and is driven directly by a DC motor, with a large DC tachometer for velocity feedback and a servo control system. The least increment for the computer control system driving the two axes is 2.5 nm.

Vibration and temperature are also carefully controlled. For vibration isolation, the LODTM mainframe rests on four air isolators, two of which have been connected together to provide a three-point kinematic support. The self-leveling pneumatic isolators have very low natural frequencies, well below LODTM's structural vibration modes. Since temperature control is crucial for achieving the required accuracy, the ambient temperature is maintained constant within 0.005 °C p-v and an air flow rate of 6 m³/s. Critical LODTM components are also temperature controlled directly by water flow whose temperature is held constant to 0.0005 °C p-v. The temperature stabilized water is gravity fed to avoid pump vibrations and temperature stabilizes the spindle thrust bearing stator, journal bearing stator and the metrology frame.

With the aid of the above (and other) technical features, the LODTM is capable of machining reflective metal optical surfaces to an rms figure accuracy of better than 1/25th of the wavelength of visible light (about 25 nm rms) with a surface roughness of about 5.0 nm rms. An interesting example of work done on the LODTM is a secondary mirror for the Keck Telescope, a major ground-based astronomical observatory located atop Mauna Kea in Hawaii. The secondary mirror is 50 cm in diameter, and collects light reflected from the 10 m Keck primary mirror. The mirror is a convex hyperboloid with a scalloped outline which follows the irregularities resulting from the primary mirror being made up of 36 hexagonal segments. Figure 2 shows the mirror being measured by the LODTM after diamond turning. The figure accuracy was found to be about $\lambda/40$ rms (He-Ne wavelength), and the mirror finish (evident by reflections in the surface) was adequate for the intended use in the near-infrared regime without any subsequent optical polishing. The figure accuracy extends clear to the mirror edge; it is an attractive feature of diamond turning that accuracy can be maintained in the presence of the interrupted cut caused by the scalloped edge.

In addition to the infrared secondary for the Keck telescope, LODTM has successfully diamond turned a wave front corrector, a non-rotationally symmetric optic³. A wave front corrector is a component of a telescope on which the primary can be imaged. Compensation of the errors in the primary can be achieved by fabricating the appropriate "anti-errors" into the wave front corrector, thus achieving correction over a modest field of view. This concept was demonstrated using the designs of Stacey, Meinel, and Meinel of NASA's Jet Propulsion Laboratory, and LODTM. The surface z of the optic can be described using Zernike polynomials:

$$(1) z = 1.73 \lambda r^2 \cos 2\theta + \lambda r^2 \sin 2\theta + 2 \lambda (3r^2 - 2) r \cos \theta$$

where z, r, and θ are cylindrical coordinates and $\lambda = 0.63 \mu\text{m}$. LODTM diamond turned this unusual figure to $\lambda/10$ rms.

FIGURE 2



Figure 2.
The infrared Keck secondary being measured on LODTM.

Ductile Grinding Research

Single-point diamond turning (SPDT) is now a mature technology capable of producing components with a contour accuracy approaching 20 nm rms and a surface finish approaching 5 nm. However, due to the fragile nature of the single-point diamond cutting tool and its chemical affinity with ferrous materials and glass the process has been strictly limited to non-ferrous soft metals such as copper, electroless nickel, aluminum, gold, silver and a handful of soft crystalline materials such as KDP^{4,5}. It is unfortunate that a similar process for economically and rapidly contouring ceramic materials such as silicon carbide, fused silica, ULE, Zerodur and ferrites^{6,7} does not exist. The soft non-ferrous metals are appropriate for the construction of near infrared high fluence cooled optics for imaging and laser resonator cavities, whereas the ceramic materials are highly desirable where low expansion and high precision components, such as Wolter grazing incidence telescopes, high temperature roller bearings, surveillance optics, and magnetic recording heads are needed.

The SPDT process can be highly cost effective for the fabrication of precision components of unusual shape compared with conventional grinding and polishing processes because it is a deterministic process. Determinism results in the ability to prescribe a contour in space with a single-point diamond tool (mounted to a computer controlled machine tool) and to have the resultant workpiece achieve this contour within the desired specification. Non-determinism as in conventional grinding results from the grinding process actually removing more than the depth of cut as a result of surface fracturing and spallation. Polishing is also a non-deterministic process that relies on the conformance of a lap, embedded with abrasive, to match the contour of the workpiece and to more rapidly remove those areas where the workpiece contour deviates from the lap contour. In addition, conventional grinding and polishing are less productive than SPDT because *in-situ* metrology has been difficult to integrate into the polishing process and must occur off-line.

During the past five years it has become more obvious that ultra-precision grinding (a.k.a. ductile grinding, shear mode grinding, or nanogrinding) could revolutionize the precision machining industry by allowing the rapid deterministic contouring of metals, brittle ceramic and glass materials. The often reported observation is that when very fine abrasives (1-2 μm) are employed in conjunction with precise control of the depth-of-cut a non-brittle material removal process (thus the name ductile grinding) ensues with low surface roughness and low subsurface damage. The observation of a brittle-to-ductile transition with a single-point indenter has been known for over 30 years; however, only recently has this knowledge been applied to the continuous grinding process^{8,9,10}. A complete understanding of how and under what circumstances this transition occurs will lead to a manufacturing process able to economically fabricate ceramic materials to nanometer contour accuracy^{11,12}.

LLNL has demonstrated a ground surface roughness on BK-7 and LG-750 of 0.4 nm rms^{13,14,15}. This process combines precision contour grinding and final polishing on a single grinding machine. As part of this same work these ultrasmooth surfaces have demonstrated a laser damage threshold at least as high as the best conventionally polished optics (17 J/cm² @ 1 ns)¹⁶.

The deterministic nature of the ductile grinding process (that it can be done with a precision contoured grinding wheel with high peripheral speed on a very rigid machine) coupled with the *in-situ* laser displacement metrology that is now common to all precision machine tools, leads to at least an order of magnitude higher overall productivity compared with conventional grinding and polishing and places it on a par with the productivity of diamond turning.

Potential commercial markets for ductile grinding are the economic fabrication of precision ceramic roller bearings, optical components for night-vision optics, and any optical component that would benefit from the replacement of up to four *spherical* optics with a single *aspheric* optic such as lightweight optics for spacecraft instrumentation or for portable optics for military troops.

Molecular Dynamics Modeling

Although single-point diamond turning is now becoming widely used in industry, little is understood of the tool-to-workpiece interaction, workpiece deformation, magnitude of residual stresses, and the nature of tool wear. Understanding tool wear and how to prevent or control it would substantially expand the variety of materials that could be successfully diamond turned. A detailed understanding of wear, however, would profit from the development of an atomistic description of material deformation and chemical interactions.

LLNL has applied the molecular dynamics (MD) modeling technique to understand the deformation of metals and ceramics subjected to sharp cutting tools as in high-speed single-point diamond turning. LLNL has developed several sophisticated molecular dynamics computer simulation codes and have begun to investigate the cutting of copper, silicon, and silica with diamond tools.

The precision machining of metal surfaces and the precision grinding of glass and ceramics are similar in that both can be viewed as being an orthogonal cutting process. For this reason and because fracture and plastic flow are inherently atomistic in nature rather than continuous as assumed by continuum mechanics, deformation is being modeled using realistic many-body atomistic interaction potentials and state-of-the-art computational techniques.

Recently, it has become possible to construct large-scale MD computer simulations of the orthogonal cutting of simple metals^{17,18,19,20,21,22}. LLNL has constructed such a simulation of the steady-state orthogonal cutting of single crystal copper. The model reveals considerable information on the evolution of chip morphology, chip stress, temperature distribution, and the effect of tool sharpness (edge radius) on cutting force and specific energy. The ability to model the cutting process with a depth of cut of 20 nm has allowed our cutting force and specific energy predictions to be directly compared with recently reported ultra-precision machining experiments utilizing single-point diamond tools.

Utilizing these computer models LLNL has found, for example, that the specific energy necessary to cut a surface increases exponentially with a decrease in the depth of cut. At very shallow depth of cut the energy input is equal to the energy necessary to evaporate the material off of the surface. LLNL has also found that during the machining of single crystal silicon the diamond cutting tool chemically reacted with the silicon to form a silicon

carbide compound. This is the first direct evidence of the chemical wear of diamond tool when machining carbide forming workpieces.

Fertile areas for future technology developments and transfer to industry also include the application of precision engineering principles to the design of conventional machine tools, precision motion control applied to the manufacture of flat panel displays, enhanced sensor technology applied to manufacturing quality assurance, and computer modeling of manufacturing processes, and the design of machine tools and associated equipment.

More specific examples of work currently under development include the fabrication of aspheric contoured optics for X-ray projection lithography where the use of short wavelength X-rays leads to a dimensional accuracy approaching 1 nm.

Further refinements to the molecular dynamics modeling code will be applied to the solution to tribological problem such as the head-to-disk interaction occurring in computer disk drives. A fundamental understanding of how to make the recording head fly closer to the recording surface will greatly increase data storage density. However, the closer flying head must be accomplished with greatly increased reliability to assure that data is not inadvertently lost during a head "crash".

CONCLUSION

Precision Engineering has evolved substantially over the past 30 years. It is being applied to ever more sophisticated problems and finding more and more commercial applications. An ultimate, is to be able to manipulate individual atoms and to place them wherever they are needed, either on or inside a structure. This will ultimately merge the current technologies of microfabrication, biotechnology, and precision engineering. The transfer of this technology has been very successful in the past and is currently being pursued with continued mutual benefit. With the changing world scene, an increasing availability of facilities, and an evolving mission, LLNL looks forward to future technology transfer possibilities with former and new partners.

¹ T.T. Saito and P.C. Wells, "Precision Machining of Optics and Other Elements" *Proceedings of the Manufacturing Technology Advisory Group Meeting*, Phoenix, Arizona, October 1979, ASTM.

² "Precision Machining Commercialization", UCID-17948, Vols. I & II, Prepared by Lawrence Livermore National Laboratory and United Carbide Corporation (Y-12), P.O. Box 808, Livermore, CA 94551 (1978)

³ A.B. Meinel, M.P. Meinel, J. E. Stacey, T.T. Saito, and S.R. Patterson, "Wave-front Correctors by Diamond Turning" *Appl. Opt.* 25: 824 (1986)

⁴ J. S. Taylor, "Precision Machining Studies at LLNL," (Nov. 20, 1987). (UCRL-97692).

⁵ C. K. Syn, T. T. Saito, J. S. Taylor, R. R. Donaldson, "Materials Properties Influence On Smoothness Of Diamond Turned Electroless Nickel," (UCRL-92260).

⁶ I. F. Stowers, R. Komanduri, E. D. Baird, "Review of Precision Surface Generating Processes and their Potential Application to the Fabrication of Large Optical Components," *32nd International Technical Symposium on Optical and Opto-Electronic Applied Sciences and Engineering*, San Diego, Ca, 14 Aug. 1988. (UCRL-99735).

⁷ C. K. Syn, "Diamond Turning of Silicon, Glass, and Beryllium," *Thrust Area Report FY88 - Engineering Research and Development*, (Jun. 1988). pp. 4-19-4-25. (UCRL-53868-88).

⁸ N. J. Brown, B. J. Fuchs, "Brittle to Shear Grinding Mode Transition for Loose Abrasive Grinding," *Optical Fabrication and Testing Workshop - Optical Society of America*, Santa Clara, CA, November 2-4, 1988. (UCRL-100043).

⁹ Norman J. Brown, Baruch A. Fuchs, "Shear Mode Grinding," *ASPE Spring Conference*, Tucson, AZ, April 25-27, 1989. (UCRL-100650).

¹⁰ N. J. Brown, "Some Speculations on the Mechanisms of Abrasive Grinding and Polishing," *4th International Precision Engineering Seminar*, Cranfield, UK, 11 May 1987. (UCRL-96159).

¹¹ J. S. Taylor, C. K. Syn, R. R. Donaldson, "Observations of Brittle to Ductile Cutting Mode Transition During Diamond Turning Tests," (Oct. 30, 1987). (UCRL-97607).

¹² J. Franse, K. L. Blaedel, "Mechanical Model for the Transition from Ductile to Brittle Material Removal in Precision Grinding," (Oct. 3, 1988). (UCRL-99489).

¹³ I. F. Stowers, N. J. Brown, K. L. Blaedel, "Recent Progress in Ductile and Shear Mode Grinding of Optical Surfaces," *RADC Large Optics Conference*, Rome, NY, Jul. 11, 1989. (MISC-4792).

-
- 14 K. L. Blaedel, R. W. Clouser, P. J. Davis, "Ductile Grinding of Glass," *Thrust Area Report FY87 – Engineering Research and Development*, (Apr. 1988). pp. 6-1–6-5. (UCRL-53868-87).
 - 15 K. L. Blaedel, P. J. Davis, J. Franse, "Ductile Grinding of Brittle Materials," *Thrust Area Report FY88 – Engineering Research and Development*, (Jun. 1988). pp. 4-26–4-28. (UCRL-53868-88).
 - 16 K. L. Blaedel, P. J. Davis, D. J. Nikkel, "Ductile Grinding of Brittle Materials," *Thrust Area Report FY89 – Engineering Research and Development*, in publication. (UCRL-53868-89).
 - 17 W.G. Hoover, C.G. Hoover, I.F. Stowers, W.J. Siekhaus, "Interface Tribology by Nonequilibrium Molecular Dynamics", *Mat. Res. Soc. Symp.*, Vol 140, Boston, MS, 1989. pp. 119-124.
 - 18 W.G. Hoover, C.G. Hoover, I.F. Stowers, A.J. De Groot, B. Moran, "Simulation of Mechanical Deformation via Nonequilibrium Molecular Dynamics", *CECAM Workshop on Microscopic Simulation of Macroscopic Flows*, Brussels, Belgium, Aug. 1989.
 - 19 W.G. Hoover, C.G. Hoover, A.J. De Groot, B.L. Holian, I.F. Stowers, T. Kawai, "Million-Atom Plain Strain Indentation Studies via Nonequilibrium Molecular Dynamics", *Third Workshop on Molecular Simulations*, Kyoto University, Japan, 1990. pp. 55-56.
 - 20 W.G. Hoover, A.J. De Groot, C.G. Hoover, I.F. Stowers, T. Kawai, B.L. Holian, T. Boku, S. Ihara, J. Belak, "Large-Scale Elastic-Plastic Indentation Simulations via Nonequilibrium Molecular Dynamics", *Physical Review A*, 10 (42), 1990, pp. 5844-5853.
 - 21 J.F. Belak, I.F. Stowers, "Molecular Dynamics Studies of Surface Indentation in Two Dimensions", *Atomic Scale Calculations of Structure in Materials*, Vol 193, San Francisco, CA, Apr. 16-21, 1990. pp. 259-264. Materials Research Society.
 - 22 J.F. Belak, I.F. Stowers, "A Molecular Dynamics Model of the Orthogonal Cutting Process", *ASPE Annual Conference*, Rochester, NY, Sept. 23-28, 1990. pp. 76-79. ASPE, PO Box 7918, Raleigh, NC 27695.

510-34
2446
p. 10

POTENTIAL CAPABILITIES OF REYNOLDS STRESS TURBULENCE
MODEL IN THE COMMIX-RSM CODE

F. C. Chang and M. Bottoni
Energy Technology Division
Argonne National Laboratory
9700 South Cass Avenue
Argonne, IL 60439, USA

ABSTRACT

A Reynolds stress turbulence model has been implemented in the COMMIX code, together with transport equations describing turbulent heat fluxes, variance of temperature fluctuations, and dissipation of turbulence kinetic energy. The model has been verified partially by simulating homogeneous turbulent shear flow, and stable and unstable stratified shear flows with strong buoyancy-suppressing or enhancing turbulence. This article outlines the model, explains the verifications performed thus far, and discusses potential applications of the COMMIX-RSM code in several domains, including, but not limited to, analysis of thermal striping in engineering systems, simulation of turbulence in combustors, and predictions of bubbly and particulate flows.

INTRODUCTION

The computer code COMMIX-1C [1] describes single-phase, three-dimensional transient thermo-fluid dynamic problems in engineering systems. This code has provided the framework for the extension of the standard k - ϵ turbulence model to a more sophisticated model based on 11 transport equations for the dependent variables describing turbulence: six transport equations for the components of the Reynolds stress tensor, three equations for scalar turbulent heat fluxes, one equation for variance of temperature fluctuations, and one equation for dissipation of turbulence kinetic energy. In isothermal calculations, the system reduces to seven transport equations. The complete Reynolds stress model (RSM) is presented in detail in the next section. A numerical verification of the reduced isothermal system has been made for homogeneous turbulence sustained by a uniform shear in the mean flow. In that case, the governing equations reduce to a system of ordinary differential equations that can be integrated directly, thus providing numerical verification of the code. Moreover, experimental data are available for comparison. The subsequent sections explain ongoing applications of the RSM to stratified flows, which also provide further code verification, and potential applications to several domains of interest for industrial applications where turbulence is highly anisotropic and the standard k - ϵ model therefore performs poorly. The envisaged domains of application include analysis of thermal striping, simulation of turbulence in combustors, and in multicomponent flows.

GOVERNING EQUATIONS FOR REYNOLDS STRESS MODEL

The transport equations for scalar heat fluxes are

$$\frac{\partial}{\partial t}(\overline{u_i \phi}) + U_j \frac{\partial}{\partial x_j}(\overline{u_i \phi}) = \frac{\partial}{\partial x_j} \left[\left(\nu_t + c_{s\phi} \frac{k^2}{\epsilon} \right) \frac{\partial(\overline{u_i \phi})}{\partial x_j} \right] + P_{i\phi} + G_{i\phi} + \pi_{i\phi}, \quad (1)$$

with

$$P_{i\phi} = - \left(\overline{u_i u_j} \frac{\partial \Gamma}{\partial x_j} + \overline{u_j \phi} \frac{\partial U_i}{\partial x_j} \right), \quad (2)$$

$$G_{i\phi} = - \beta g_i \overline{\phi^2}, \quad (3)$$

$$\pi_{i\phi} = - c_{1\phi} \frac{\epsilon}{k} \overline{u_i \phi} + c_{2\phi} \overline{u_j \phi} \frac{\partial U_i}{\partial x_j} + c_{3\phi} \beta g_i \overline{\phi^2} - c_{1\phi} \frac{\epsilon}{k} \overline{u_n \phi} \delta_{in} f \left(\frac{L}{x_n} \right). \quad (4)$$

The transport equation for variance of temperature fluctuations is

$$\frac{\partial g}{\partial t} + \frac{\partial (U_j g)}{\partial x_j} = \frac{\partial}{\partial x_j} \left[\left(c_\phi \frac{k^2}{\epsilon} + \frac{\lambda}{\rho c_p} \right) \frac{\partial g}{\partial x_j} \right] - \overline{u_j \phi} \frac{\partial \Gamma}{\partial x_j} - \frac{\epsilon}{k} \frac{g}{R}. \quad (5)$$

The transport equations for Reynolds stresses are

$$\begin{aligned} \frac{\partial (\overline{u_i u_j})}{\partial t} + U_\ell \frac{\partial (\overline{u_i u_j})}{\partial x_\ell} &= \frac{\partial}{\partial x_\ell} \left[c_k \frac{k^2}{\epsilon} \frac{\partial (\overline{u_i u_j})}{\partial x_\ell} + \nu_\ell \frac{\partial (\overline{u_i u_j})}{\partial x_\ell} \right] \\ &- (1 - c_2) \left(\overline{u_i u_\ell} \frac{\partial U_j}{\partial x_\ell} + \overline{u_j u_\ell} \frac{\partial U_i}{\partial x_\ell} \right) - \left[\frac{2}{3} \epsilon \delta_{ij} + c_1 \frac{\epsilon}{k} \left(\overline{u_i u_j} - \frac{2k}{3} \delta_{ij} \right) \right] \\ &- \frac{2}{3} c_2 \overline{u_n u_m} \frac{\partial U_n}{\partial x_m} \delta_{ij} - (1 - c_3) \beta (g_i \overline{u_j \phi} + g_j \overline{u_i \phi}) - \frac{2}{3} c_3 \beta g_\ell \overline{u_\ell \phi} \delta_{ij}. \end{aligned} \quad (6)$$

The turbulence kinetic energy is $k = \overline{u_i u_i} / 2$. The transport equation for the dissipation of turbulence kinetic energy ϵ is

$$\begin{aligned} \rho \frac{\partial \epsilon}{\partial t} + \rho U_j \frac{\partial \epsilon}{\partial x_j} &= c_{1\epsilon} \frac{\epsilon}{k} (P_k + G_k) (1 + c_{3\epsilon} R_f) \\ &- c_{2\epsilon} \frac{\rho \epsilon^2}{k} + \frac{\partial}{\partial x_j} \left(\mu_\ell \frac{\partial \epsilon}{\partial x_j} + c_\epsilon \frac{\rho k}{\epsilon} \overline{u_j u_k} \frac{\partial \epsilon}{\partial x_k} \right), \end{aligned} \quad (7)$$

with

$$P_k = \mu_t \left[\frac{\partial U_i}{\partial x_j} \left(\frac{\partial U_i}{\partial x_j} + \frac{\partial U_j}{\partial x_i} \right) \right] \quad (8)$$

$$G_k = -\rho \beta g_i \overline{u_i \phi} \quad (9)$$

The numerical values of the coefficients used in the above equations are as follows: $c_{2\phi} = 0.07$, $c_{1\phi} = 3.1$, $c_{2\phi} = 0.4$, $c_{3\phi} = 0.5$, $c_{1\phi} = 0.5$, $c_{\phi} = 0.13$, $R = 0.5$, $c_k = 0.09$, $c_1 = 2.8$, $c_2 = 0.47$, $c_3 = 0.4$, $c_{1\epsilon} = 1.44$, $c_{2\epsilon} = 1.92$, $c_{3\epsilon} = 0.8$, $c_{\epsilon} = 0.15$. Further details about the turbulence model and the boundary conditions used for all transport equations are given in Refs. [2] and [3].

VERIFICATION OF REYNOLDS STRESS MODEL

The RSM has been verified for isothermal homogeneous turbulence maintained by a uniform shear in the mean flow. Homogeneity requires an infinite spatial field that can be simulated numerically by a finite domain with slip-free boundary conditions. Experiments on nearly homogeneous turbulent shear flow have been made in a wind tunnel of height $h = 30.48$ cm and length $L = 10.5 h$ [4]. Turbulence generated by grids at the tunnel entrance becomes almost homogeneous in the center of the tunnel at some distance from the inlet. Measurements were taken in the region defined by $8.5 h \leq x_1 \leq 10.5 h$, x_1 being a coordinate along the horizontal wind tunnel axis. Let x_2 and x_3 be coordinates along a vertical and transverse axis of the tunnel, respectively. In homogeneous turbulence, the mean velocity components of the flow satisfy the conditions $U_1 = U_1(x_2)$; $U_2 = U_3 = 0$; $\partial U_1 / \partial x_2 = \text{constant}$ ($= 13$ in the test case we refer to); $U_2(h/2) = U_c = 12.4$ m/s (center velocity). Under these assumptions, the seven transport equations describing the isothermal flow (Eqs. 6 and 7), reduce to a system of ordinary differential equations that can be integrated directly with the Runge-Kutta algorithm. We made numerical calculations of homogeneous turbulence with the RSM in the COMMIX code and with the Runge-Kutta method in an independent program; we then compared the results with experimental values at $x_1/h = 10$ reported in Ref. [4]. A comparison of computed and experimental results is given in Table I. Under the assumptions made, $\overline{u_1 u_3}$ and $\overline{u_2 u_3}$ are negligibly small. The computed results are much closer to each other than to the experimental values, due to the difficulty of realizing in practice the theoretical conditions of homogeneous turbulence. Theoretically, it must be $\overline{u_2 u_2} = \overline{u_3 u_3}$, a condition satisfied by the results of the calculations but not strictly verified in the experiment. This comparison provides satisfactory verification of the RSM under the given conditions.

Table I. Comparison of experimental and computed turbulence values in homogeneous shear flow

Turbulence Value	Ref [4]	Runge-Kutta	COMMIX-RSM
\sqrt{k}/U_c	0.0185	0.0139	0.0147
$\sqrt{\overline{u_1 u_1}}/U_c$	0.0178	0.0140	0.0161
$\sqrt{\overline{u_2 u_2}}/U_c$	0.0132	0.0097	0.0093
$\sqrt{\overline{u_3 u_3}}/U_c$	0.0141	0.0097	0.0093
$\sqrt{ \overline{u_1 u_2} }/U_c$	0.0104	0.0101	0.0100
$P_k = -\overline{u_1 u_2} \frac{\partial U_1}{\partial x_2}$	0.218	0.202	0.201

APPLICATIONS OF REYNOLDS STRESS MODEL

In this section, we summarize ongoing and potential applications of the RSM in the COMMIX code. The applications involve, but are not limited to, the following fields:

- Stable and unstable stratifications of fluids in engineering systems.
- Thermal striping.
- Turbulence in combustors and in chemically reacting flows.
- Bubbly and particulate flows.

Stable and Unstable Stratifications of Fluids in Engineering Systems

In several engineering systems, including advanced nuclear reactors of the pool type, it is important to analyze the effect of fluid stratifications on turbulence and to predict under which operating conditions natural circulation flows can become established. Because turbulence in stratified flows is highly anisotropic, the standard $k-\epsilon$ model (which assumes isotropy) performs poorly and must be replaced by more sophisticated models, such as the RSM. This domain of applications is exemplified by the two following test cases, which provide further verification of the RSM.

Stratified Shear Flow

An experiment designed to study the effect of buoyancy on turbulent mixing is the case of a horizontal shear flow [5] as sketched in Fig. 1. This figure shows qualitatively the spreading of the region where two fluid streams mix upon entering the domain with different temperatures and velocities. The influence of buoyancy is measured by the reduced Froude number

$$Fr = \frac{|U_2 - U_1|}{\sqrt{g_z \beta h |T_2 - T_1|}}, \quad (10)$$

where the subscript z refers to the vertical component of the gravity acceleration. In stable stratification, when the hot fluid enters at the top, gravity forces oppose the diffusive character of turbulence, which tends to mix the fluids despite their density differences. The smaller the Froude number, the more stable the

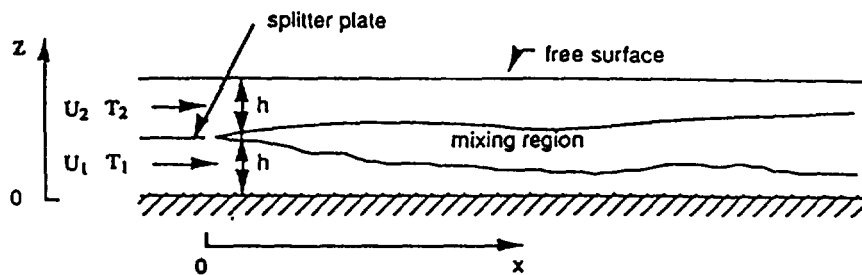


Fig. 1. Sketch of stratified shear flow

stratification. Below some threshold of the Froude number, turbulence is completely inhibited by the density gradients. In unstable stratification, when the hot fluid enters at the bottom, the effects of gravity and turbulence combine, forcing a region of highly effective mixing between the hot and cold fluids.

In this study, we used 100 meshes ($\Delta x = 0.03$ m) in the axial direction along the channel length and 30 meshes ($\Delta z = 0.006667$ m) in the transverse direction. The maximum length (x_{\max}) in the x direction is 3 m and the distance ($2h$) between the two plates is 0.2 m. Therefore, the length-to-height ratio (x_{\max}/h) is 30. We present results of a test case with unstable stratification and Froude number 0.9, in which hot water is injected at the lower half of the test section, with $U_1 = U_2/2 = 0.223$ m/s, $T_1 = 128.7^\circ\text{C}$, $T_2 = 20^\circ\text{C}$.

Figure 2 shows the temperature distributions at location $x/h = 20$. With strong mixing, the temperature distributions in hot and cold fluids reach almost the same values. Compared with the $k-\epsilon$ turbulence model, the RSM can produce results closer to the experimental results by accounting for anisotropy of natural circulation and turbulence transport.

Thermal Stratification in a Rectangular Cavity

Thermal stratification experiments have been made in a rectangular cavity filled with liquid sodium and simulating the hot plenum of a liquid-metal fast breeder reactor under steady-state and transient conditions [6]. The cavity communicates at the bottom with a rectangular channel (Fig. 3). A forced flow through the channel induces recirculation in the cavity. In steady-state experiments, temperature differences were induced by heating one wall of the cavity; in transient tests, by decreasing the temperature of the inlet flow.

We simulated one steady-state experiment (referred to as P1 in Ref. [6]). In this test, the inlet flow temperature was 300°C , while the right-hand wall of the cavity was kept at 316°C . Measured and computed vertical normalized temperature profiles in the cavity 200 mm from the left wall are given in Fig. 4. As in the previous test cases, the $k-\epsilon$ model performs poorly, while the RSM results agree fairly well with the experimental ones.

Thermal Striping

Thermal striping is characterized by random temperature fluctuations in regions where flows with different temperatures mix. The temperature fluctuations, with frequency components of 2 to 20 Hz, induce cycle fatigue in structural materials. The problem of analyzing thermal striping and minimizing its impact upon structures is of concern in both nuclear and conventional industries.

Combined buoyancy and striping phenomena have been investigated at ANL in piping, plena, heat exchangers, and steam generators. The distribution of temperature and velocity fields at the point where a horizontal pipe conveying water enters a plenum has been investigated as a function of the temperature difference between pipe inlet and bulk plenum temperature. In particular, the experimental program aimed at investigating (a) the length and height of the stratified recirculating flow carrying fluid from the plenum

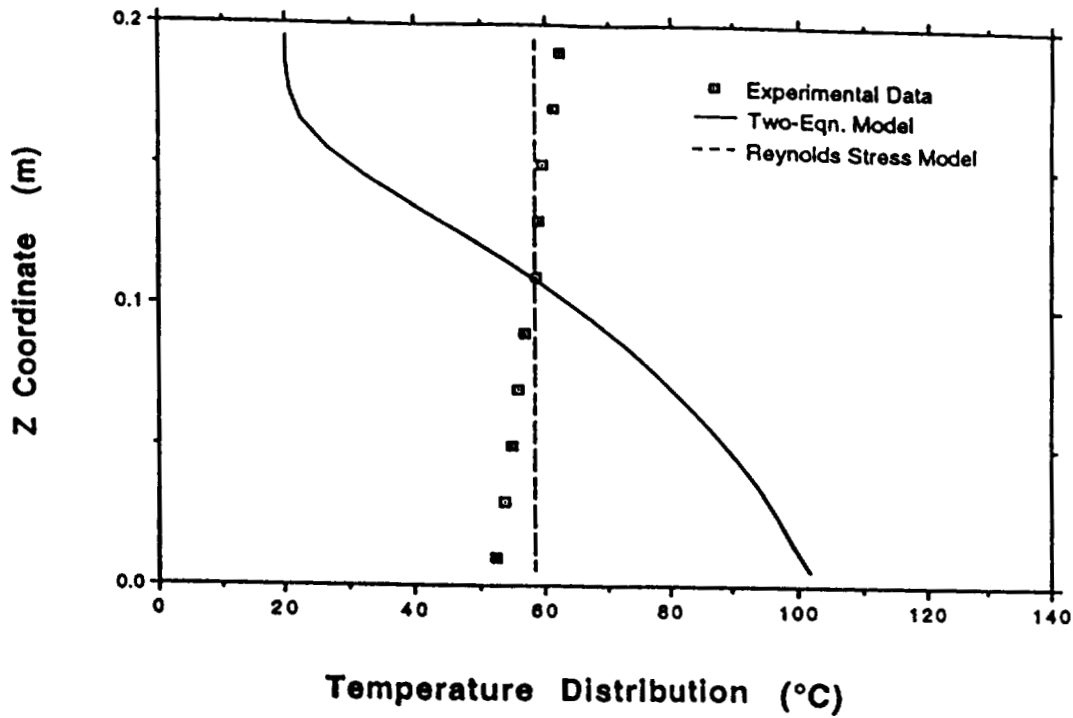


Fig. 2. Temperature distributions for unstable stratified shear flow at $x/h = 20$

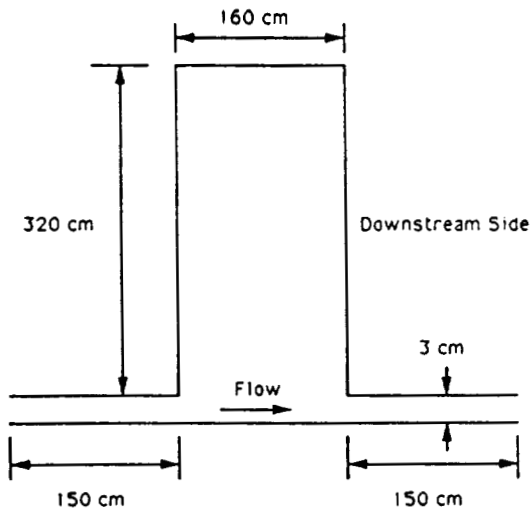


Fig. 3. Sketch of thermal cavity

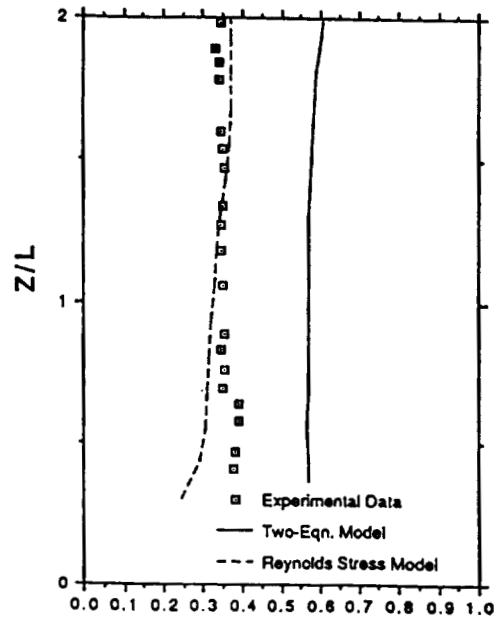


Fig. 4. Measured and computed normalized temperature distributions in the cavity, 200 mm from the left wall

into the pipe; (b) the temperature fluctuations at the pipe walls, hence the potential damage due to thermal striping; and (c) the interaction between the thermal plume and the fluid plenum, hence the buoyancy-generated large-scale eddies in the plenum and the time evolution of plenum temperatures.

Numerical simulations of the flow and temperature fields at the junction between a horizontal pipe conveying hot fluid and a plenum initially filled with cold fluid have been made with the k - ϵ turbulence model [7]. These computations failed to reproduce correctly the dynamics of the thermal plume in the plenum and the length of cold fluid penetration into the pipe. The latter was underestimated by a factor of 3. Thus, thermal striping analysis in the pipe could only be inferred. These discrepancies are due to the approximate representation of buoyancy forces and to the assumption of isotropy of turbulence inherent in the k - ϵ model. Both of these limitations are eliminated in the RSM, which is more appropriate for detailed analysis of this and related problems. Numerical simulation of this test case with the RSM is underway at ANL.

Turbulence in Combustors and in Chemically Reacting Flows

Advanced combustion technologies are being developed with the goal of achieving higher overall system efficiencies and reduced environmental loading of air and water with solid pollutants. Further developments tend toward systems combining a pressurized, high-intensity combustor (which produces higher entrainment of the ambient fluid and fast mixing) with gas or steam turbines to optimize cycle efficiency and minimize pollutant formation.

Computation of swirling turbulent flows in which turbulence is nonhomogeneous and anisotropic is a problem of major concern. It has been suggested that the assumptions leading to the formulation of the k - ϵ model are inadequate for the simulation of turbulence in highly swirling flows [8]. Traditionally, designers have relied on experiments to derive empirical correlations describing heat and mass transfer. The validity of these correlations is generally limited to the experimental conditions for which they have been obtained. This traditional approach can now be supplemented with computational turbulence modeling (e.g., COMMIX-RSM), which gives the designer the predictive capability to change parameters and choose the conditions that lead to improved combustors with higher efficiency and less pollution.

From the standpoint of numerical simulation of combustion involving several chemical components, the state-of-the-art code is KIVA-II [9]; this is the last of a series of programs developed for, but not limited to, applications to internal combustion engines. This code is applicable to a variety of multi-dimensional fluid-dynamic problems with or without chemical reactions. Turbulent flows are computed with either a standard version of the k - ϵ model or a subgrid scale (SGS) turbulence model in which large-scale eddies are resolved while small scale turbulence is modeled. These models, however, do not account for the presence of particles (e.g., coal particles in coal-fired diesel engines) in the carrying fluid and for the damping of the turbulence kinetic energy due to the presence of particles. Reynolds stress models can be applied to multifield turbulent transport by extending the procedure used for one-fluid turbulence to the several fields and taking into account their interactions [10]. The potential improvement of multiphase turbulence modeling provided by multifield RSM is worthy of consideration, at high computational costs, however.

Bubbly and Particulate Flows

Numerical simulations of bubbly and particulate flows in pipes are of interest for a variety of applications ranging from analysis of blood vessels to material transport by slurry flows. Numerical analysis aims at predicting pressure drops, relative velocity between continuous and particulate phases, and particle concentrations across flow stream lines. Turbulence predictions in the continuous phase have been

made [11] with a standard k - ϵ turbulence model and additional terms that account for the interfacial turbulent momentum transfer. Numerical analysis of turbulent bubbly flow and particulate flow is being carried out at ANL with the same approach as in Ref. [11]. Preliminary results for bubbly flows have been documented in Ref. [3]. The assumption of isotropic turbulence inherent in the k - ϵ turbulence model is however not satisfied in these cases. An extension of the RSM to two phases has been proposed in Ref. [12] and is being planned at ANL, in a way suitable for the numerical simulation of multicomponent flows.

CONCLUSIONS

In all cases where turbulence is anisotropic, and especially when enhancement or suppression of turbulence intensity due to buoyancy forces plays a dominant role, the RSM allows more realistic numerical predictions than the standard k - ϵ model, which is based on the inherent assumption of isotropic turbulence. The RSM can be applied to a variety of domains of interest for technological applications. Its extension to multicomponent flows is possible, at the expense, however, of high computational costs. To cope with these, more advanced solution algorithms for the transport equations and code parallelization are envisaged.

ACKNOWLEDGMENTS

The COMMIX-1C code, developed in the past years by colleagues Drs. H. M. Domanus, T. H. Chien, J. G. Sun, and W. T. Sha, has provided the framework for the incorporation of the Reynolds stress turbulence model. This work has been sponsored by the Laboratory Directed Research and Development Funds of the Argonne National Laboratory. Best thanks are due to Mrs. M. AnDavis for her accurate work in typing the manuscript.

NOMENCLATURE

c_p	Specific heat (J/kg-K)
F_r	Froude number
G_k	Production or suppression of turbulence kinetic energy due to buoyancy (J/s-m ³)
$G_{i\phi}$	Buoyancy production in scalar flux equations (m-K/s ²)
g	$\left(= \frac{1}{2} \overline{\phi^2} \right)$, one-half of variance of temperature fluctuations (K ²)
\vec{g}	Gravity acceleration (m/s ²)
k	Turbulence kinetic energy (m ² /s ²)
L	Length scale (m)
P_k	Mean shear production in k and ϵ equations (J/s-m ³)
$P_{i\phi}$	Mean field production in scalar flux equations (m-K/s ²)
R_f	$(= -G_k/P_k)$, Richardson number
T	Temperature (K)
t	Time (s)

U Mean flow velocity (m/s)

u Fluctuation of velocity (m/s)

$\overline{u_i \phi}$ Scalar heat flux (m-K/s)

$\overline{u_i u_j}$ Reynolds stress (m²/s²)

x_i Coordinate direction (m)

Greek

β $\left[-\frac{1}{\rho} \left(\frac{\partial \rho}{\partial T} \right)_p \right]$, volume expansion coefficient at constant pressure (K⁻¹)

δ_{ij} Kronecker delta

ϵ Dissipation of turbulence kinetic energy (W/kg)

λ Thermal conductivity (W/m-K)

μ Dynamic viscosity (kg/m-s)

ν Kinematic viscosity (m²/s)

$\pi_{i\phi}$ Pressure-scalar gradient correlation in scalar heat flux equations (m-K/s²)

ρ Density (kg/m³)

ϕ Temperature fluctuation (K)

$\overline{\phi^2}$ Variance of temperature fluctuations (K²)

Indices

l Laminar

n Normal to wall

t Turbulent

REFERENCES

1. Domanus, H. M. et al., COMMIX-1C: A Three-Dimensional Transient Single-Phase Computer Program for Thermal Hydraulic Analysis of Single and Multicomponent Systems, Volume I: Equations and Numerics; Volume II: User's Guide and Manual, NUREG/CR-5649, ANL-90/33, Argonne National Laboratory, Argonne, IL, 1990.
2. Bottoni, M. and Chang, F. C., Implementation of an Anisotropic Turbulence Model in the COMMIX-1C/ATM Computer Code, Proc. of the Pressure Vessel and Piping (PVP) Division of the ASME Conf., Denver, CO, July 25-29, 1993.
3. Bottoni, M., Chang, F. C., and Ding, J., First Assessment of Computations of Turbulent Bubbly Flow with the Program COMMIX-M, ANL internal report, in press (1993).
4. Champagne, F. H., Harris, V. G. and Corrsin, S., Experiments on Nearly Homogeneous Turbulent Shear Flow, J. Fluid Mech., Vol. 41 (1970), pp. 81-139.

5. Viollet, P. L., Turbulent Mixing in a Two Layer Stratified Shear Flow, Second Int. Symp. on Stratified Flows, Trondheim, Norway, (1980) pp. 315–325.
6. Vidil, R., Grand, D., and Leroux F., Interaction of Recirculation and Stable Stratification in a Rectangular Cavity Filled with Sodium, Nuclear Eng. and Design 125 (1988), pp. 321–332.
7. Bottoni, M. and Willerding, G., Advanced Solution Algorithms for Transient Multi-dimensional Thermohydraulics Flow Problems in Complex Geometries with the Programme COMMIX-2/KfK, Nuclear Eng. and Design 100 (1987), pp. 354–365.
8. Hwang, C. C., Zhu, G., Massoudi, M. and Ekmann, J. M., A Comparison of the Linear and Nonlinear $k-\epsilon$ Turbulence Models in Combustors, J. of Fluids Eng., Vol. 115 (1993), pp. 93–102.
9. Amsden, A. A., O'Rourke, P. J. and Butler T. D., KIWA-II: A Computer Program for Chemically Reactive Flows with Sprays, LA-11560-MS, Los Alamos National Laboratory, 1989.
10. Bernard, D. C. and Harlow, F. H., Turbulence in Multi-phase Flow, Int. J. Multiphase Flow, Vol. 14 (1988), pp. 679–699.
11. Simonin, O. and Viollet, P. L., Numerical Study on Phase Dispersion Mechanisms in Turbulent Bubbly Flows, Int. Conf. on Mechanics of Two-Phase Flows, National Taiwan University, Taipei, Taiwan, ROC, June 12–15, 1989.
12. Lopez de Bertodano, M., Lee, S-J., Lahey, R. T. and Drew, D. A., The Prediction of Two-Phase Turbulence and Phase Distribution Phenomena Using a Reynolds Stress Model, J. of Fluids Eng., Vol. 112 (1990), pp. 107–113.

AN IMPROVED PLATING PROCESS**John C. Askew****U.S. Army Armament, Munitions, and Chemical Command
Army Research, Development, and Engineering Center
Becht Laboratories, Watervliet, N.Y. 12189-4050****ABSTRACT**

An alternative to the immersion process for the electrodeposition of chromium from aqueous solutions on the inside diameter (ID) of long tubes is described. The Vessel Plating Process eliminates the need for deep processing tanks, large volumes of solutions, and associated safety and environmental concerns. Vessel Plating allows the process to be monitored and controlled by computer thus increasing reliability, flexibility and quality. Elimination of the trivalent chromium accumulation normally associated with ID plating is intrinsic to the Vessel Plating Process. The construction and operation of a prototype Vessel Plating Facility with emphasis on materials of construction, engineered and operational safety and a unique system for rinse water recovery are described.

HISTORY

Development of high performance ammunition for heavy artillery following the second world war presented new and challenging problems to the gun designer. Higher velocity, temperature and pressure caused gun tubes to erode at a much faster rate than had been previously experienced, resulting in reduced service life for the gun tube. Electrodeposition of chromium to the bore of small caliber tubes had resulted in enhanced bore life, consequently the decision was made to test chromium plate in large caliber tubes as an erosion barrier.¹

Electrodeposition of chromium had been accomplished in immersion processes requiring tanks large enough to completely immerse the part to be plated in the various cleaning, rinsing, pre-treatment and plating solutions. Lacking facilities to immerse a gun tube as long as twenty-five feet, researchers in Great Britain developed two alternative processes, one requiring only partial immersion and one requiring no immersion. The partial immersion process, and no immersion process to a lesser extent, were developed to apply conventional high contraction (HC) chromium to the bore of long gun tubes. A number of tubes were plated with favorable results.²

Early work in non-immersion plating demonstrated the advantages of chromium plating but was replaced with the more conventional immersion plating processes for a variety of reasons. The quest for higher performance artillery and tank cannon however has not been replaced but instead has brought us to the point where conventional HC chromium is only marginally acceptable as a bore coating. An alternative form of chromium has shown promise as a more protective bore coating, however the conditions required to deposit this coating preclude the use of immersion plating. A non-immersion or vessel plating process (VPP) was developed to evaluate this coating in full size large caliber gun tubes. This VPP draws heavily on previous work with significant enhancements in process control and pays particular attention to hazardous waste reduction.

Low contraction (LC) chromium, as opposed to conventional (HC) chromium, retains the body centered cubic crystal formation but exhibits a difference in grain growth pattern as well as a lack of the micro-crack network prevalent in HC chromium. Deposition of LC chromium is achieved at elevated solution temperatures and high current densities. These two requirements cause excessive solution loss, through evaporation, and gas generation when used in an immersion system. Tremendous amounts of energy are required to maintain immersion tanks of the required size at process temperature, thereby increasing the cost of the plating operation. Maintaining tank integrity for prolonged periods at operating temperature has also proven to be a problem. These difficulties could be overcome with proper system design and material selection, however the high current densities required and the large volume of gas generated at the anode and cathode present a problem which cannot be adequately addressed in the immersion process.

Hydrogen gas is generated at the cathode and oxygen gas at the anode during electrodeposition of chromium. Plating of internal diameters will only allow these gases to rise through the annulus. Since the

gases are generated along the entire length of both the anode and the cathode they accumulate as they rise, increasing the ratio of gas to liquid along the length of the tube. Resistance of the plating solution increases with the increase in gas to liquid ratio causing a reduction in the plating rate. The result is a tube with a heavy coating at the lower end and a thin coating at the upper end.³ In the extreme case no chromium is deposited at the upper end. This phenomenon occurs during deposition of HC chromium and is addressed through anode design, however at the current densities required to deposit LC chromium anode modification is not effective in reducing the tapering effect. Increasing the flow rate of plating solution through the annulus has been shown to reduce the tapering effect.³ This is accomplished quite easily in the VPP. Higher flow rates have the added benefit of higher plating rates and thermal stabilization of the system. A comparison of the two plating processes can be seen in Fig. #1.

DESIGN PARAMETERS

Development of the VPP was a step toward the larger objective of evaluating LC chromium in a variety of large caliber artillery and tank cannon, consequently the design parameters for a prototype facility were well defined. The vessel plating facility (VPF) is described here as two major systems, the control system and the plumbing system. The plumbing system is further divided into two subsystems: facility and process plumbing.

The process control system was designed to perform the following tasks:

- i monitor record and control valve and pump sequences
- ii monitor record and control rectifier function
- iii monitor record and control flow rates and pump pressure
- iv monitor record and control tank temperatures, fluid levels and chemical concentration
- v monitor and record chromium thickness⁴

These control functions, with the exception of item v were accomplished with off the shelf sensors and Allen-Bradley 2/30 PLC.

The facility plumbing subsystem consists of the steam and water supply for cooling and heating process solutions, rectifier cooling and pump seal water. The piping, valves and pumps which move process solutions through the gun tube and back to the proper tank constitute the process plumbing subsystem.

MATERIALS AND CONSTRUCTION

Material selection for facility plumbing was straightforward due to the standards for handling steam and water, however materials selected for the process plumbing subsystem required resistance to concentrated sodium hydroxide, concentrated acids as well as temperatures approaching 200 F at relatively high flow rates. Gaskets and seals required the same properties in addition to providing electrical isolation in some cases. Materials for the facility were selected considering these requirements and the anticipated operation schedule.

Figure 2 is an artist's representation of the Vessel Plating Facility. Although incomplete (all hardware not shown) it does provide a basic description of the pump-through concept.

Process tanks are 1200 and 600 gallons for chromium plating and pre-treating solutions respectively. All process tanks are lead lined steel. Heating and cooling capacity is provided with carbon filled teflon thin tube heat exchangers. Hypalon gaskets are used to seal CPVC pipe flanges connecting each tank to its respective pump. The pair of Kynar lined pumps on the chromium side are plumbed such that either pump can be fed from either tank. This increases reliability of the system and allows for the pumps to be run in tandem. Pumps servicing the caustic cleaner and electropolish tanks (not shown) are also plumbed for dual service although tandem pumping is not desirable. CPVC was selected for this application due to its excellent resistance to all chemicals involved even though the recommended temperature range was marginal. CPVC is also used between the caustic and electropolish pump outlets and the main vertical stack, the main vertical stack, and all return lines for caustic and electropolish solutions as well as parts of the chromium solution return line.

Pressures and temperatures between the chromium pump outlets and the main vertical stack are somewhat higher than the pre-treatment side. Safety and reliability precluded the use of CPVC for this application. A Kynar lined, fiberglass filled, phenolic resin pipe was specified. This pipe provides excellent

chemical resistance and the additional strength needed here for safety and reliability. Phenolic resin overlap reduced the concern of chemical attack from the pipe outside diameter (OD) which would have been a problem with Teflon lined steel pipe in a location where any of the solutions could drip on the pipe.

The main vertical stack terminates at the bottom builder (not shown) which is the steel structure that supports the weight of the gun tube and the anode. A combination of UHMW polyethylene, teflon and silicone seals are used here for reliable joining of the gun tube to the process plumbing and electrical isolation. These seals also serve to locate the gun tube and the anode on the same axis which is critical for concentric chromium deposition.

The "birdbath" is a four outlet manifold located on top of the gun tube. Here again a combination of seal materials are used for reliable joining and insulation. In addition to directing fluid flow this fixture locates the anode on the gun tube axis and provides two safety features. A rupture disk plumbed to a pressure relief valve is connected to one of the manifold outlets. This safety device is designed to release excess pressure generated by rapid expansion of hydrogen gas which can accumulated in the system. A second manifold outlet is fitted with a vacuum relief valve for relief of vacuum created by pumping large volumes of fluid through a closed system. At pump shutdown this vacuum can exceed 80 psi resulting in damage to process plumbing. As previously mentioned the plumbing from the birdbath back to the caustic and electropolish tanks is CPVC. Teflon lined steel pipe is used to return chromium plating solution to a level below the main deck. High flow rates and safety concerns preclude the use of CPVC for this pipe run. A leg off the chromium return line goes to a 300 gallon lead lined holding tank (not shown) which will be discussed later in this paper.

Electrically actuated CPVC ball valves are used in most 4" and all 2" applications. Teflon lined electrically actuated butterfly valves are used in the chromium pump supply plumbing as well as the main vertical stack for their compact size and better reliability over large temperature spans.

Process plumbing is the most critical subsystem in the Vessel Plating Facility, determining to a large extent the reliability and versatility of the Facility. This design has provided many hours of reliable operation with enough versatility to support development of production processes as well as investigations into many phenomenon unique to vessel plating.

PROCESS CONTROL

Electrodeposition of chromium in the Vessel Plating Facility consist of four steps, caustic cleaning, electropolishing, reverse etching and chromium plating. Each of these steps is followed by a water rinse. Valve and pump actuation, rectifier control, as well as process solution temperature and level control are accomplished by the process control subsystem.

An array of sensors and test instruments feed an Allen Bradley 2/30 Programmable Logic Controller (PLC) with information needed to affect chromium plating in a reliable, safe manner. Each process tank is equipped with temperature, level and conductivity sensors supplying analog outputs. Valves and pumps output discrete signals indicating on/off or open/closed. A pressure sensor in the main vertical stack and a temperature sensor in the drain sump provide early warning of spills or leaks. Flow is monitored with an ultrasonic instrument and controlled by a modulating butterfly valve in a return leg from the main vertical stack to the process tank. Safety interlocks between the process plumbing subsystem and the rectifier controls as well as a number of event sensing routines ensure that potentially dangerous situations are detected and corrected before damage or personal injury occur.

Operator interface with the control system is provided by an Advisor II process monitor. Identification of plating process parameters as well as a graphical representation of system operation is provided on a color CRT. System alarms are identified and cleared through this interface. The Advisor II is an old system and somewhat slow by today's standards but proven to be a reliable user interface.

Expansion of the rinse water recovery system, the addition of an on-line autotitrator for solution analysis, and an ultrasonic method for on-line measurement of chromium thickness has outstripped the capability of the existing control system. The Advisor II is being replaced with the Cimplicity control package from GE Fanuc running on a 486 PC imbedded in a VME rack. A GE Fanuc 90/70 PLC will be used in conjunction with the A/B 2/30 to provide extensive control and system monitoring capability.

HAZARDOUS WASTE MANAGEMENT

Reduction of hazardous wastes generated during chromium plating is a major advantage of vessel plating over immersion plating. Reduced air emissions due to the closed nature of the system are inherent, however the potential for rinse water reduction requires some engineering in order to fully exploit this potential. Water rinsing occurs between each process step and after the chromium plating process. Fresh water is fed into the main vertical stack under line pressure and flows through the tube, into the caustic/polish return line and to the floor drain which leads to an on-site waste treatment facility. Initial interest in rinse water reduction was focused exclusively on the chromium plating rinse waters. After the chromium plating cycle the rinse water is diverted to the chromium return line rather than the caustic/polish line. This does not return directly to the process tank but is instead diverted to the 300 gallon holding tank mentioned earlier. Diversion of the first 300 gallons of rinse water reduces the concentration of chromium in the rinse water which eventually goes to drain by approximately 80 percent. This captured rinse water is later used for solution make-up. Application of this method to the caustic cleaner and electropolish solutions is not practical due to the lack of sufficient water loss to the caustic tank and the incompatibility of water with the electropolish solution.

A rinse water recovery system applicable to all three solutions is shown in Fig. 3. The chromium rinse recovery loop only is shown here for clarity. Operation of this closed loop rinse is conceptually very simple. Rinse water is pumped from tank #1 through the tube and back to tank #1. A conductivity sensor in the rinse tank indicates when the rinse water has reached an equilibrium concentration. At this point valves 1 & 4 close and 2 & 5 open, pumping water from tank #2 through the tube and back to tank #2. Steady state conductivity in tank #2 moves the sequence to tank #3. Rinse tank #1 is now dumped to the process tank for make-up. Tank #2 is pumped to tank #1 and tank #3 is pumped to tank #2. Tank #3 is filled with fresh water and the tube rinsed a fourth time from tank #3. This system eliminates drag-out loss while providing adequate rinsing. Addition of evaporators and purification equipment make this system applicable to recovery of caustic and electropolish rinse waters.

OPERATIONS

Assembly of the tube, anode and sensors takes approximately one hour. Definition of desired plating parameters then allows the PLC to execute the plating process as previously described. Operator intervention is only required if a hardware malfunction occurs. Set-up time is roughly equivalent to the time required to fixture a tube for immersion plating, however in the immersion process the tube is moved ten times before it reaches the chromium plating operation. Vessel plating does not require the tube to move at all until the plating process is complete. During seven years of operation including over 60 plating runs, only two plating runs have been aborted due to equipment malfunction.

Several plating runs were executed to characterize the relationship between flow rate and current density to the mechanical properties of the chromium plate, the plating rate and the distribution of the plate (taper). These runs also served to verify previous laboratory testing. Variations in current density and to a lesser extent flow rate had an impact on the plating rate with plating rates as high as 0.005 in/hr being achieved. Variations in hardness values were observed with varying current density, as would be expected, however variations in flow rate also effected chromium hardness. Detailed correlations between these process parameters and plate qualities are considered sensitive manufacturing technology.

Subsequent to system characterization a number of tubes were plated with LC chromium and one with conventional HC chromium. These tubes are currently in firing tests.

COMMERCIAL APPLICATIONS

The vessel plating process can replace immersion plating wherever aqueous solutions are used for electrodeposition on long cylinders, either ID or OD. The work done here on chromium can be easily transferred to commercial items such as hydraulic cylinders, pipe used for handling abrasive slurries or aggressive chemicals, reaction vessels and mixing equipment. Conventional HC or LC chromium can be applied depending on the performance criteria for the particular application. Reduced plating times and

elimination of hexavalent chromium waste can have a positive impact on production costs.

There is evidence to suggest that lead electroplated on copper forms an anode superior to the current casting or burning process. Plating bath composition and solution velocities required to obtain these desirable properties makes vessel plating the only viable method of fabrication.

Recent developments in the area of sputtering depositions have developed a need for long sputtering targets with heavy, uniform deposits of chromium. Here again vessel plating is the only viable fabrication method.

CONCLUSIONS

Various metals and alloys have been deposited using Vessel Plating Technology including copper, nickel, zinc, and lead. Any material which can be electrodeposited from aqueous solution can exploit this technology. Cathode configuration is somewhat restricted to simple geometries due to the flow rates required however, innovative design has made such operations as electroforming electrical circuits from copper possible.³ In the current atmosphere of environmental regulation the potential for hazardous waste reduction could make Vessel Plating the predominant electroplating process of the future.

REFERENCES

1. National Bureau of Standards, Experimental Plating of Gun Bores to Prevent Erosion, 1955
2. R.A.F Hammond, The Chromium Plating of Gun Barrels, 1957
3. L.E. Vaaler, M.F. El-Shazly, E.W. Brown, High Speed Chromium Plating Using Enhanced Mass Transfer, Plating and Surface Finishing, Aug 1987
4. J. Frankel, M. Doxbeck, S.C. Schroeder and A. Abate, Proceeding of this Conference

WEAR AND EROSION TECHNOLOGY

BORE PLATING PROCESSES

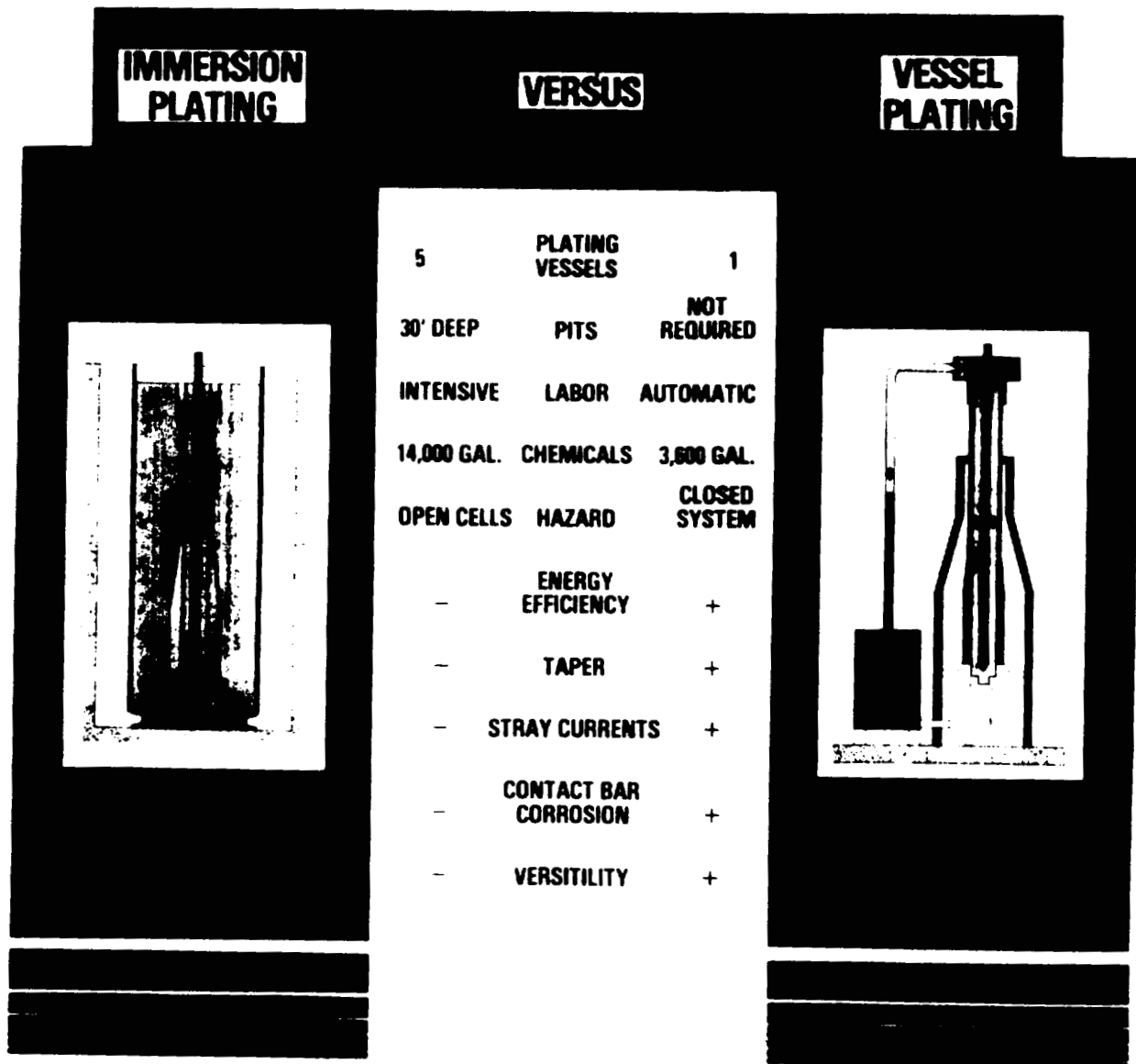
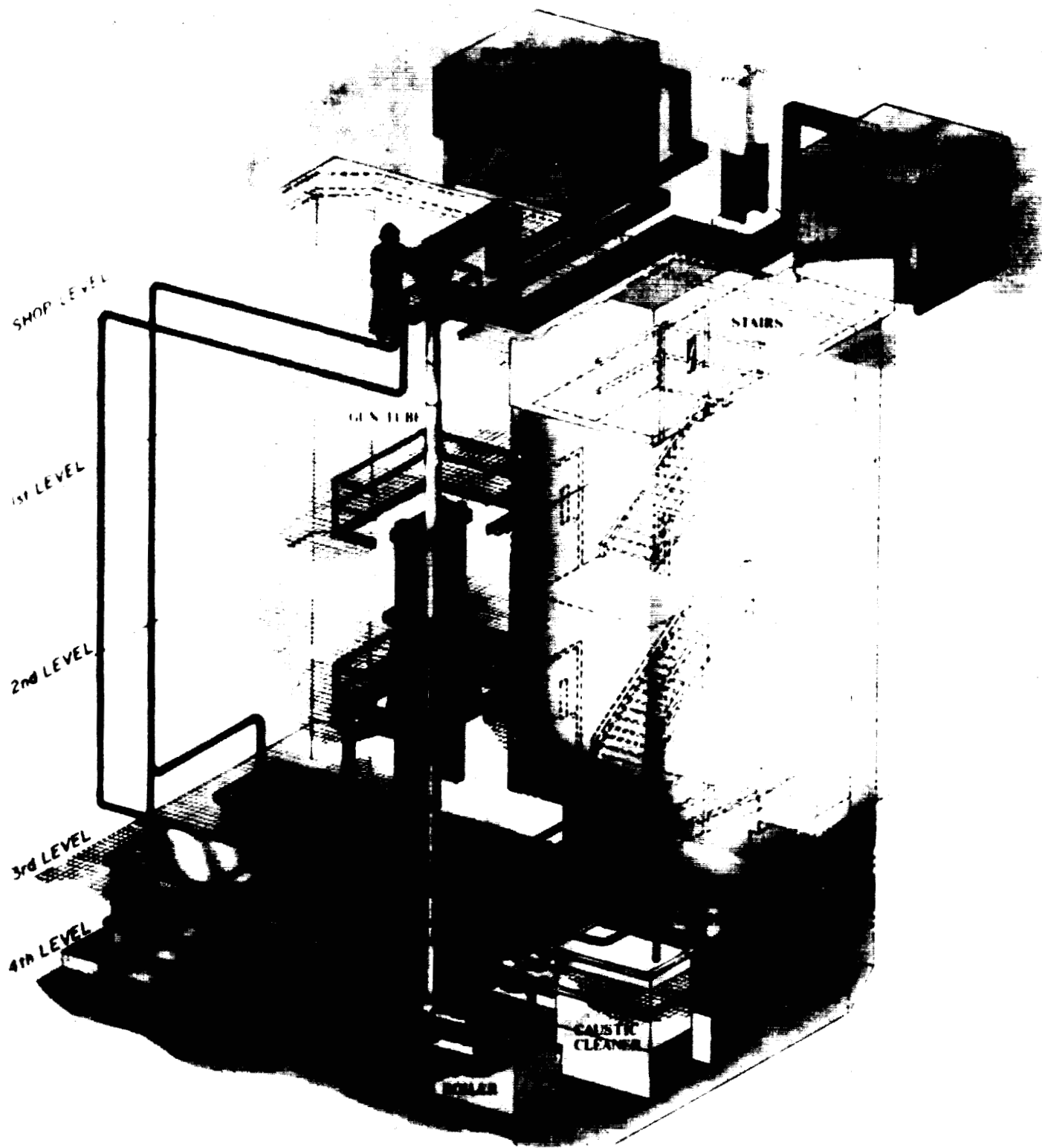


Figure 1



VESSEL PLATING FACILITY - BLDG 110

Figure 2

RINSE WATER RECOVERY SYSTEM

107

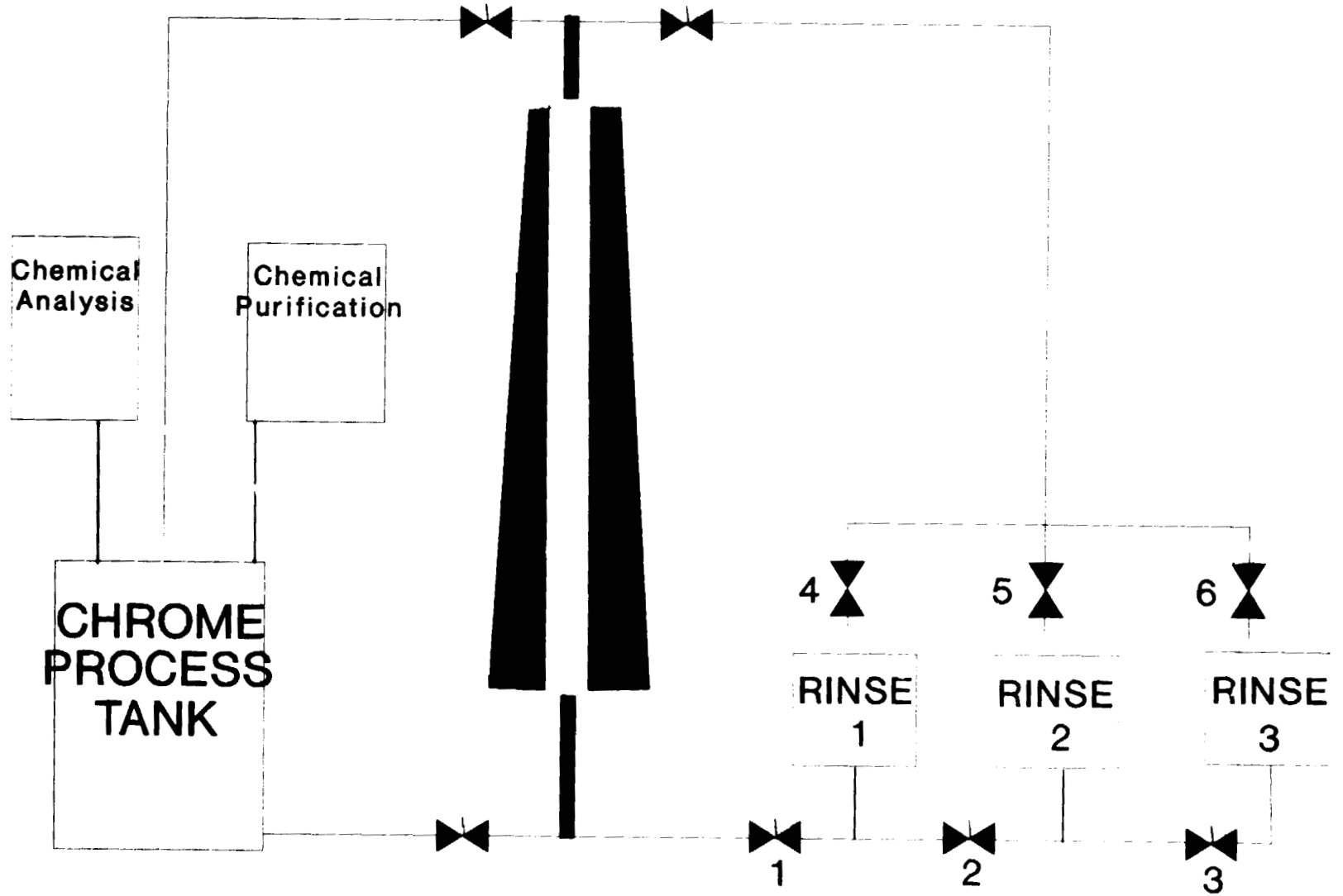


FIG. 3

512-24
2448
p. 6

THE UNIVERSAL APPLICATIONS OF MICROTUBES AND MICROTUBE COMPOSITES

Wesley P. Hoffman
Phillips Laboratory
OLAC PL/RKFE
Edwards AFB CA 93524-7680

Kamleshwar Upadhy
UDRI / Phillips Laboratory
Bldg. 8424
Edwards AFB CA 93524-7680

ABSTRACT

Microtubes, are a basic component for a myriad of potential products. They are very small tubes (hundreds can fit in a human hair) that can be made from practically any material. Tubes larger than 1 micron diameter can be made with any cross-sectional shape desired. The significance of microtubes and microtube composites is that they provide the opportunity to miniaturize (even to the nanoscale) numerous products and devices that are currently in existence as well as allowing the fabrication of products that have to date been impossible to produce.

INTRODUCTION

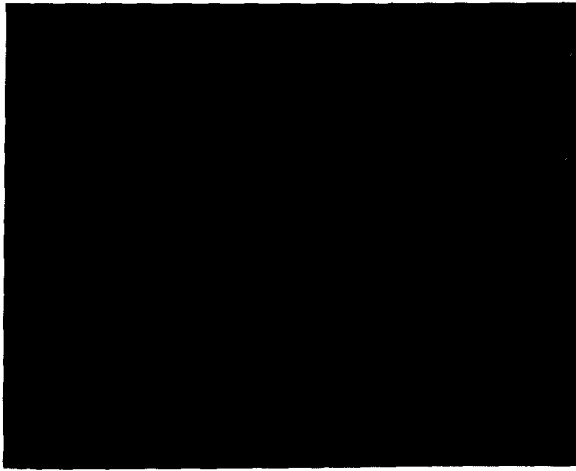
The world is becoming smaller each day. Not just in the field of transportation but more importantly in the field of miniaturization. This is probably most evident in the electronics field with each new generation of integrated circuits, i.e., from integrated circuits to... large scale integration to...very large scale integration to... ultra large scale integration to...? These advances have had a dramatic effect on almost every aspect of modern civilization. However, there are currently many other areas, such as: micromotors, sensors, detectors, microrefrigerators, and scanning tunneling microscopes (STM) where miniaturization is also playing a crucial role.

In many miniaturization applications, there is a need for micro tubing for uses such as: connecting parts, component cooling, sensors, and as probes, to name a few. If the proper micro tubing were available, numerous components and systems could be miniaturized and others could be made more efficient. In addition, many components and systems not currently in existence could become a reality.

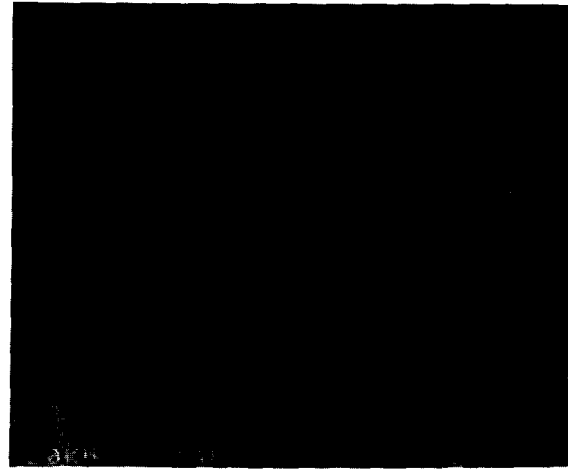
Commercially, tubing is extruded, drawn or pultruded, which limits the types of materials that can be used for ultra-small tubes as well as their ultimate internal diameters. As a result, ceramic tubes are currently available only as small as 1mm I.D., copper tubing is available as small as 0.05 mm I.D., polyimide polymer tubing is available as small as 80 microns I.D. and quartz tubing is drawn down as small as 2 microns I.D. This means that quartz is the only tubing available that is less than 10 microns in internal diameter. This quartz tubing is used principally for chromatographic applications. Thus, until the availability of microtubes, only quartz tubing has been available in micron dimensions and no tubing has existed with sub micron internal dimensions.

DESCRIPTION OF MICROTUBES

In contrast to tubing currently on the market, microtubes can be made from practically any material with precisely controlled composition down to internal diameters less than 5 microns. (There is no upper internal diameter limit.) In addition, for materials that can survive temperatures greater than 4000° C, tubes can theoretically be made as small as 5 nanometers. To date, tubes have been made from metals (copper, nickel, aluminum, gold, platinum, silver), ceramics (silicon carbide, carbon, silicon nitride, sapphire), glasses (silica), polymers (teflon), alloys (stainless steel) and layered combinations (carbon/ nickel, silver/sapphire) in sizes from 0.5 - 300 microns. (By comparison a human hair has a diameter of ~ 100 microns.) Some scanning electron microscope (SEM) micrographs of these tubes can be seen in Figure 1.



(a)



(b)



(c)



(d)

Figure 1. Examples of microtubes. (a) 10 micron silicon carbide tubes. (b) 10 micron nickel tubes. (c) 26 micron silicon nitride tube. (d) 0.6 micron quartz tube.

Since the process does not involve pultrusion, extrusion or drawing but rather a fugitive tube forming process, cross-sectional shapes as well as wall thickness can be very accurately controlled. A myriad of shapes have already been made as seen in Figure 2. These micrographs should be sufficient to demonstrate that practically any shape imagined can be fabricated. As seen in Figure 2, the wall thickness on the tubes can be held very uniform around the tube. It is also possible to control the wall thickness along the length of the individual tubes as well as among the tubes in a batch. To date, free-standing tubes with some mechanical strength have been made with wall thicknesses as small as 0.01 microns. (Figure 3) There is no upper limit to wall thickness as will be discussed below.

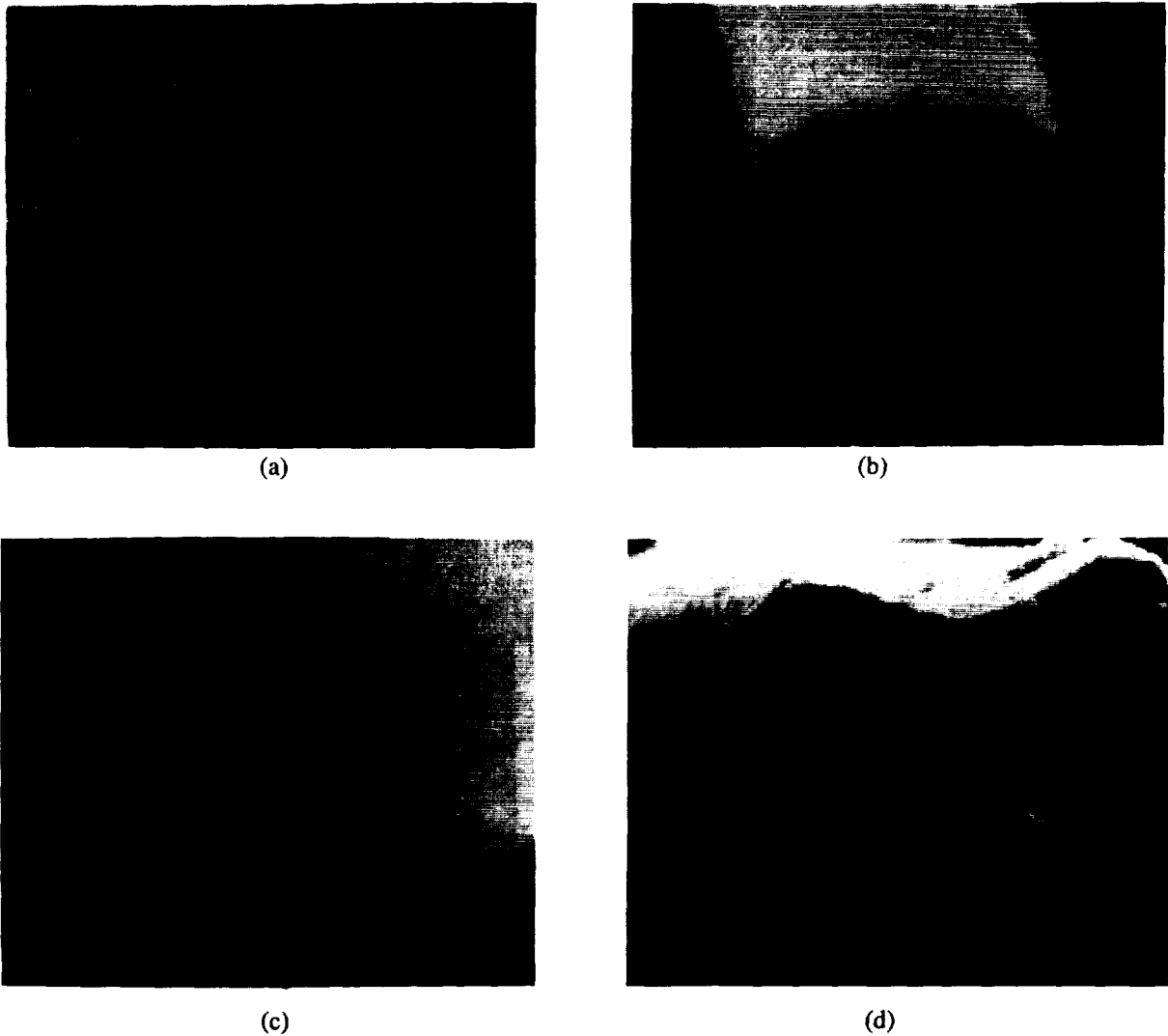


Figure 2. Above 1 micron inside diameter tubes can be made in any cross-sectional shape such as (a) 17 micron star, (b) 9 X 34 micron oval, (c) 59 micron smile, and a 45 micron trilobal shape.

The maximum length that these fibers can be made has yet to be determined because it depends on many variables, such as, type of tube material, composition of sacrificial tube forming material, degree of porosity in the wall, etc. It is possible that with a porous wall there is no limitation in length. For a non-porous wall the maximum length would probably be measured in feet with there being a direct relationship between the tube I.D. and the maximum possible length. However, for most applications conceived to date, the length need only be measured in inches. If one does a quick calculation it is apparent that even "short" tubes have a tremendous aspect ratio. For instance, a one inch long 10 micron I.D. Tube has an aspect ratio of 2500.

Currently, these tubes have been made by a batch process in the laboratory but the technique is equally suited to a continuous process which would not only be more efficient but in some cases easier. Obviously, a continuous process would reduce the cost which for most materials is already rather low because, unlike other processes, expensive tooling is not needed. For many materials such as quartz, aluminum, copper, etc. the cost is anticipated to be much less than \$0.01/ inch. For precious metals such as gold or platinum the cost would be significantly higher due to the cost of the raw materials.

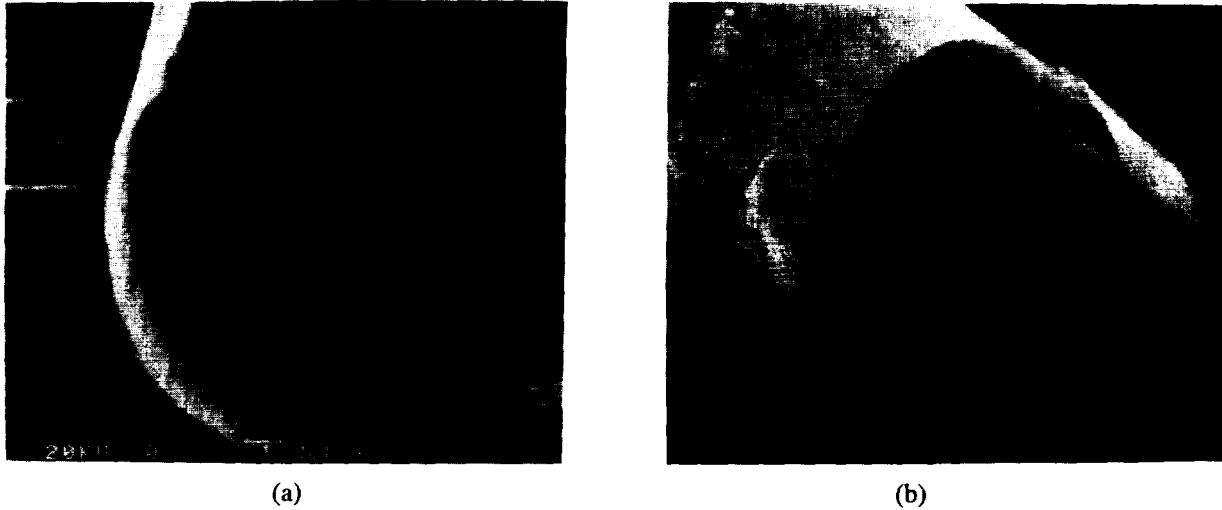


Figure 3. Tube can be structurally sound with very thin walls. (a) Unbroken tube. (b) Tube broken to expose interior.

MODIFICATIONS FOR VARIOUS APPLICATIONS

Microtubes can be made free-standing, with wall thickness as small as 0.01 microns, or the walls can be made so thick that the space between the tubes is filled producing a solid monolithic structure with micro channels (Figure 4). These micro channels can be randomly oriented or they can have a predetermined orientation. Any desired orientation or configuration of microtubes can be obtained by a fixturing process. Alternatively, composite materials can be made using a material different than the tube wall as a "matrix" that fills in the space between the tubes. The microtubes imbedded in these monolithic structures form oriented micro channels which like free-standing tubes can contain solids, liquids and gases, as well as to act as conduits for all types of electromagnetic energy. If the tubes are placed in a solid structure they can act as lightweight structural reinforcement similar to that found in bone or wood. The cross-sectional shape of these reinforcement tubes can be tailored to maximize mechanical or other properties.

The interior surface of these tubes can have practically any desired texture and degree of roughness which would be advantageous in many applications. In addition, the interior or exterior surface of these tubes can be coated with a layer or layers of another material (Figure 5) to form, for instance, a multiple path conductor or a tube for chemical reactions. When the tube is filled with another type of material, for example, it can become a sensor, detector, or an element in an electron multiplier.

Depending on the application, the walls of microtubes can range from non-porous to extremely porous as seen in Figure 6. In addition the tubes can be made straight, curved or coiled as seen in Figure 7. For many applications it is desirable to be able to interface microtubes with the macro world with a gradual decrease in the internal diameter. This is possible by a tapering process in which the diameter is gradually decreased to micron dimensions. Alternatively the tubes can be interfaced to the macro world through numerous types of manifold schemes.

APPLICATIONS AND USES

Microtubes appear to have almost universal application in areas as diverse as optics, electronics, medical technology, and microelectromechanical devices. As a result, their specific function depends on the product in which they are applied. Specific applications for microtubes are as diverse as chromatography, encapsulation, heat exchange, injectors, micro-pipettes, dies, composite reinforcement, detectors, micropore filters, insulation,



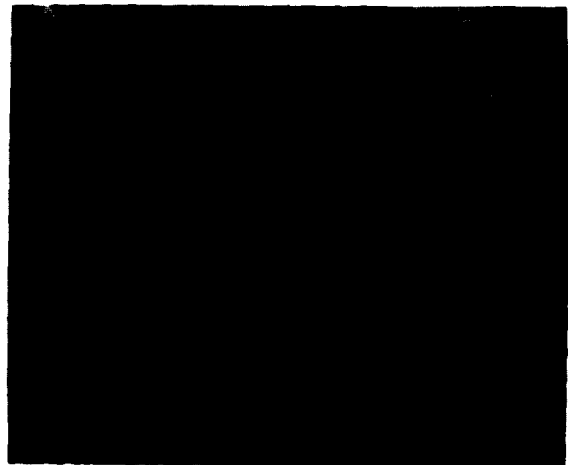
Figure 4. Solid carbon tube with microchannels.



Figure 5. Sapphire tube with silver liner.



(a)



(b)

Figure 6. Examples of porous tube walls. Pores mainly in the sides (a). Pores mainly longitudinal (b).

displays, sensors, optical wave guides, flow control, pinpoint lubrication, micro sponges, heat pipes, microprobes, plumbing for micromotors and refrigerators, arrays for printers and xerography drums, etc. The technology works equally well for high and low temperature materials and all applications that have been conceived to date appear possible at this time.



Figure 7. Example of a curved nickel tube.

SUMMARY

The significance of microtubes and microtube composites is that they can be fabricated inexpensively out of practically any material in a variety of cross-sectional shapes and in diameters orders of magnitude smaller than is now possible. These tubes will provide the opportunity to miniaturize (even to the nanoscale) numerous products and devices that are currently in existence as well as allowing the fabrication of products that have to date been impossible to produce. For example, as electronic circuits become smaller and more compact, there is a greatly increased need for micro-cooling. The solution to this problem currently does not exist. Microtubes can satisfy this need in the form of micro-heat pipes or heat exchangers.

From the above discussion, it has become evident that microtube composites have become "solutions in search of problems" and that future applications will be limited only by mankind's imagination.

Acknowledgment: The invaluable help of Hong Phan in fabricating most of the microtubes and of Jim King in taking the SEM micrographs is greatly appreciated. The financial support of the Chemistry and Materials Science Directorate of the Air Force Office of Scientific Research was responsible for the beginning phase of this work.

BIOTECHNOLOGY/MEDICAL
TECHNOLOGY

**"MICROENCAPSULATION OF ANTI-TUMOR, ANTIBIOTIC AND
THROMBOLYTIC DRUGS IN MICROGRAVITY"**

**Dennis R. Morrison, Ph.D.
NASA - Johnson Space Center / SD4
Houston, TX. 77058**

**Benjamin Mosier, Ph.D.
Institute for Research, Inc.
Houston, TX. 77063**

**John Cassanto
Instrumentation Technology Associates, Inc.
Exton, PA. 19341**

513-52

2449

p 10

ABSTRACT

Encapsulation of cytotoxic or labile drugs enables targeted delivery and sustained release kinetics that are not available with intravenous injection. A new liquid-liquid diffusion process has been developed for forming unique microcapsules that contain both aqueous and hydrocarbon soluble drugs. Microgravity experiments, on sounding rockets (1989-92) and Shuttle missions STS-52 (1992) and STS-56(1993) using an automated Materials Dispersion Apparatus, produced multi-lamellar microcapsules containing both Cis-platinum (anti-tumor drug) and iodinated poppy seed oil (a radiocontrast medium), surrounded by a polyglyceride skin. Microcapsules formed with amoxicillin (antibiotic) or urokinase (a clot dissolving enzyme), co-encapsulated with IPO, are still intact after two years. Microcapsules were formed with the drug so concentrated that crystals formed inside. Multi-layered microspheres, with both hydrophobic and hydrophilic drug compartments, can enable diffusion of complimentary drugs from the same microcapsule, e.g. antibiotics and immuno-stimulants to treat resistant infections or multiple fibrinolytic drugs to dissolve emboli. Co-encapsulation of enough radio-contrast medium enables oncologists to monitor the delivery of anti-tumor microcapsules to target tumors using computerized tomography and radiography that would track the distribution of microcapsules after release from the intra-arterial catheter. These microcapsules could have important applications in chemotherapy of certain liver, kidney, brain and other tumors.

BACKGROUND

Many cytotoxic or bioactive drugs and enzymes cannot be injected intravenously. Others can be injected, but are rapidly degraded before they reach the target tissue or they are cleared from the blood so quickly that their useful biological half-life is too short for good therapeutic value. Many drugs are insoluble in aqueous solutions and intravenous injection in hydrocarbon solvents is not well tolerated by patients. Encapsulation of drugs or biological therapeutics into liposomes or liquid microcapsules can enable delivery to target organs where the bioactive drug can be released directly to the target area by diffusion. Properly designed microcapsules can provide unique methods of direct delivery by parenteral injection, nasal inhalation and dermal administration for sustained release of important bioactive drugs [1]. The size and shape of the microcapsules is critical for the distribution and drug delivery in the tissues. Typically, microcapsules of 1-5 micron diameter are optimum for intravenous administration, whereas, 200-300 micron diameter microcapsules are used for intra-arterial delivery. Perfect microspheres are needed for maximum packing densities and maximum drug payload delivery to target organs or tumors. Anti-tumor liposomes containing doxorubicin [2] or muramyltripeptide [3] have already been studied extensively in clinical trials. The disadvantages of using conventional liposomes or microcapsules include manufacturing methods that require many batch process steps to: 1) form the liposomes, 2) remove unwanted organic solvents, detergents, and 3) to harvest the proper size micro-particles for optimum pharmacologic efficiency [4]. Also conventional liposomes often use natural lipids and lectins (from eggs, soybeans and other inexpensive sources) which attract certain phagocytic immune cells that rapidly remove the liposomes from the circulatory system before they arrive at the target tissue. This creates variable dose-responses which greatly complicates the pharmacokinetics and makes calculations of therapeutic doses very difficult [5]. New formulations of "stealth" liposomes have been made with lipids that are less detectable by immune cells in an attempt to avoid phagocytosis [6], however, new types of liposomes and microcapsules are needed to exploit the various unique applications of this type of drug delivery.

Conventional Methods

Current methods of forming liposomes are based on mechanisms that certain phospholipids exhibit by arranging themselves into bilayers when they are dispersed in an excess of water. Above the main transition temperature, which can vary from -20 to +90 °C (depending on the nature of the phospholipid), these bilayers spontaneously form microspheres that entrap an aqueous core. Drugs that are soluble in organic solvents are usually limited to those that bind inside the hydrophobic region of the liposome bilayer. However, most drugs are dissolved in the aqueous phase which is entrapped when the liposome forms and the drug is either incorporated into the aqueous core or electrostatically binds to the polar regions of the bilayer. Some drugs are insoluble and are not associated with the bilayer therefore these have very low encapsulation efficiencies. Table 1 summarizes the major classes of drugs that are used in liposome formulations. Major difficulties with commercial preparation of microcapsules often involves density-driven phase separation of the immiscible carrier fluids, esp. when forming water/oil emulsions or trying to encapsulate multiple drugs. This limits the yield and often results in microparticles that are not spherical nor uniform in size, thereby limiting the packing density (and drug payload delivered) when the microcapsules arrive at the target tissues.

Table 1. Classes of drugs used in liposome formulations.

<u>CLASS OF DRUG</u>	<u>LOCATION IN LIPOSOME</u>	<u>ENCAPSULATION EFFICIENCY</u>
Water-soluble, non-bi-layer interacting	Aqueous phase, usually inner core	High
Hydrophobic	Bound inside hydrophobic region of bi-layer	Low
Bi-layer associated - electrostatic interaction	Outer or inner polar regions of bi-layer	Low
Neither water-soluble, nor bi-layer associated	Suspended in aqueous or hydrocarbon phase	Very Low

Microcapsule formation by liquid-liquid dispersion of aqueous drugs and organic solvents typically produces water-in-oil (W/O) type liposomes, which then require the organic solvent to be removed (evaporated) to form reverse-phase evaporation vesicles (rev) or stable pluri-lamellar vesicles (splv). Multi-lamellar vesicles (mlv) are rarely formed by these methods, but usually require film casting with organic solvents, hydration and sizing using filtration through inert membrane filters [4]. Methods of forming multi-layered microencapsules often require emulsification of the aqueous phase into organic carrier solutions by shear, bubbling or sonication. Sophisticated, multi-step emulsion technology is required and yields of uniform type and size are often very low.

Liquid microemulsions also are being developed as drug delivery systems, especially for drugs that are poorly soluble in aqueous carriers. A microemulsion typically contains droplets in the range of 0.1 - 1 μ in diameter and is characterized by very fluid and dynamic micelles which are formed by sequential mixing one immiscible phase with another using surfactants and co-surfactants [7]. Typically, surfactants that produce water-in-oil (W/O) have a hydrophilic-lipophilic balance (HLB) rating of 3 to 6, while those that produce oil-in-water (O/W) microemulsions have an HLB of 8 to 18. The surfactants can be non-ionic, ionic, or amphoteric and often medium chain alcohols are added as the co-surfactant in the last step in achieving the final microemulsion.

NEW METHODS FOR MICROENCAPSULATION OF DRUGS

In the past few years, new methods have been developed for preparing microspheres specifically designed for intravascular delivery. The objective is to make the appropriate size microspheres and co-encapsulate both immiscible phases into microspheres that can withstand the shear forces of intravascular injection and flow through the blood vessels until they are entrapped at the target site. The outer lipid bilayer or microsphere matrix must also be designed for drug diffusion, at appropriate release rates, once the microcapsule has reached the target tissue. One of the authors (Mosier) had invented a new method of preparing microspheres by liquid encapsulation and solid-phase entrapment wherein the water-soluble drug is dispersed in a solid matrix material [8]. This method involves dissolving the aqueous drug and the matrix material in a organic solvent, in which they are mutually soluble, then dispersing this mixture in a second organic solvent to form an emulsion that is stable enough for intravascular injection.

Dispersion of finely divided solids in liquids or formation of microemulsions including dense materials can be achieved with similar techniques, however, successful formulations depend upon the interparticle behavior in the suspensions. For example, when finely divided Cis-platinum (anti-tumor drug), in saline solution, is dispersed in alcohol solution containing a lipid and surfactant, dense microspheres will form when the mixture is shaken in a reciprocating motion. These experiments illustrate a well known phenomenon wherein a second liquid phase (such as water) causes the solid to be preferentially wet therein causing sticky collisions of the solid owing to the interfacial tension between the two liquid phases, thereby causing dense microspheres to be readily formed. The sedimentation rate of the microspheres was found to be quite high compared with the original suspension. This phenomenon does not occur when Cis-platinum is dispersed in alcohol alone, which suggests that the hydrophilic nature of the diamino,dichloro, Cis-platinum complex in the hydrophobic polyglyceride solution causes spontaneous emulsification. These experiments are unique and offer interesting technical possibilities for separation of suspended solids, such as Cis-platinum from liquid carriers that have appropriate hydrophilic or hydrophobic characteristics.

Production of multi-layered microspheres with alternate hydrophobic and hydrophilic drug compartments opens up the possibility of developing multiple-therapy microcapsules which can allow sequential diffusion of two or more drugs out of the same microcapsules once they arrive at the target tissues. In some applications, the organic phase can include a tracer compound or radiocontrast medium to provide the additional advantage of real-time imaging of the microcapsules with computerized tomography (CT) scanning as they are released from the catheter and travel to the target tissue. Practical applications of immiscible, liquid-liquid microcapsule formation are limited, however, because of density-driven phase separation and stratification into horizontal layers resulting in the necessity to use multi-step batch processing with solvent evaporation phases and mechanical mixing, which often is not practical.

Gravity-dependent restrictions in our two step liquid-liquid spontaneous microencapsulation process led to the design of several microgravity experiments to explore the utility of this process when density-driven phenomena were eliminated. The microgravity flight experiments have led to the development of a new liquid-liquid microencapsulation process that involves use of surfactants and co-surfactants in the aqueous phase and co-surfactant alcohols in the organic phase, which also contains high molecular weight lipids that can form a tough outer "skin" on the final microcapsules. In microgravity a single step dispersion produced unique multi-lamellar microcapsules containing various aqueous drugs co-encapsulated with iodinated poppy seed oil (a radiocontrast medium with a sp. gravity =1.35). Subsequent ground control experiments also produced some of these unique microcapsules and illustrated that the 1-g process could be improved to yield useable microcapsules by using different formulations or electrostatic deposition to add the polymeric, outer coating.

MICROGRAVITY EXPERIMENTS

A collaborative research project was developed by the Institute for Research, Inc. and the Johnson Space Center starting in July 1987. The basic formulations and simplified liquid-liquid dispersion methods were developed in 1988 and 1989. Microencapsulation related experiments were attempted on eight space missions beginning in April 1989 with the Consort-1 sounding rocket using the Materials Dispersion Apparatus (MDA) mini-lab developed by Instrumentation Technology Associates, Inc. The sounding rocket flights produced only 6.5 minutes of microgravity conditions, but this was adequate to form the unique microcapsules in a single step. Experiments on the Space Shuttle permitted 10 minute dispersion times followed by curing of the outer polyglyceride skin for eight days under microgravity conditions. A summary of these experiments is shown in Table 2. New formulations were tested on Shuttle STS-52, using only aqueous-soluble drugs, polymers and surfactants, and on STS-56 using alcohols as co-surfactants.

Sounding rocket experiments

Initial experiments on Consort-1 and -3 were used to determine the effective mixing and diffusion kinetics in the MDAs. The first drug encapsulation experiments were attempted on the Joust-1 rocket, but the rocket was destroyed shortly after launch. The next attempt was on the Shuttle STS-43 mission, however, the experiment fluids were removed after a launch delay and concern about possible internal leakage of the alcohol solutions resulted in a decision to not reload the MDAs with the microencapsulation fluids. The first successful microencapsulation of drugs in microgravity was conducted on the Consort-4 mission in November 1991. The unique microcapsules were recovered and analysed by microscopic image analysis. Mono-dispersed fluorescent beads were included as internal size standards and fluorescent labels were used to determine the distribution of drug in the various fluid compartments. Additional experiments, conducted on Consort-5 in September 1992, confirmed the capabilities of the new method for forming multi-lamellar microcapsules with alternating layers of hydrophilic and hydrophobic drugs.

Table 2. MED Flight Experiments Summary:

<u>MISSION</u>	<u>DATE</u>	<u>EXPERIMENTS</u>	<u>MATERIALS</u>	<u>RESULTS</u>
Consort 1	April 1989	Protein Diffusion	Urokinase & antibodies	diffusion rates established
Consort 3	March 1990	Diffusion Kinetics	Urokinase & Myoglobin	kinetics verified
JOUST -1,	June 1991	Lipid Emulsions ^a	Urokinase & antibodies	None - Launch aborted
STS-43	July 1991	Lipid Emulsions ^a	Strept-avadin, Urokinase & Cis-Platinum	Expt. removed after 1st launch scrub
Consort -4	Nov.1991	Microencapsulation of Drugs ^{a b}	Cis-Platinum, Amoxicillin Urokinase & Strept-avadin	multi-lamellar vesicles w/ alternating hydrophilic & hydrophobic layers
Consort-5	Sept.1992	Microencapsulation of Drugs ^{a b}	Cis-Platinum, Amoxicillin & Urokinase	multi-lamellar vesicles w/ alternating hydrophilic & hydrophobic layers
STS-52	Oct. 1992	Microencapsulation of Drugs ^{a b} (aqueous polymers only)	Cis-Platinum, Amoxicillin & Urokinase	multi-lamellar vesicles crystals within microcaps
STS-56	April 1993	Microencapsulation of Drugs ^{a b} (alcohol co-surfactants)	Cis-Platinum, Amoxicillin & Urokinase	multi-lamellar vesicles crystals within microcaps

^a Fluorescent labels included

^b Fluorescent beads included

Microcapsules formed in 36 microgravity mini-experiments on sounding rockets used liquid-liquid dispersion of aqueous drug solutions, surfactant, and polyethylene glycol dispersed in alcoholic co-surfactant solutions containing soluble polyglycerides. Microcapsules of both oil/water and polymer/water/oil were recovered from the Consort flights. These experiments produced multi-lamellar liquid microspheres (concentric spheres within spheres) comprised of three or more, alternating immiscible layers. Image analysis of the microcapsules was made possible by co-encapsulation of standard size fluorescent beads. Microcapsules were formed in the ranges of 1-15 μ , 40-50 μ , 110-130 μ and 160-230 μ diameters. Digital analysis of phase contrast and fluorescent images taken with a fluorescent microscope also confirmed that the aqueous-soluble drugs were often encapsulated within the inner aqueous core and the outermost aqueous shell of the microcapsules. This typical distribution is illustrated in Figure 1, which is a composite of a transmitted light photomicrograph and a fluorescent photomicrograph (lower right) of the same multi-lamellar microcapsule. The polyglyceride skin is clearly shown in the normal-light photomicrograph (upper left).

Multilamellar microspheres were also formed which contained relatively large amounts of IPO in discrete lamella or vesicles. Figure 2 (left side) shows a microcapsule heavily loaded with IPO, which often comprised up to 38% of the total volume. Often small hemispheres of IPO were also found clinging to the outer surface of the large inner (aqueous) sphere or adhered to the outer polymer skin of the microcapsule as also shown in Figure 2 (upper center). Microcapsules formed by almost all of the formulations survived 15+g accelerations, severe vibrations and turbulent mixing, during the reentry of the experiment capsule, and have remained intact for two years after recovery from space. These multi-layered microcapsules are similar to liquid-filled, thin-skinned, micro-balloons which are flexible enough to be manipulated on a microscope slide without collapse. The microcapsules formed in just 6.5 minutes of micro-g retain their spherical shape and appear tough enough to survive the extensive physical manipulations required for sizing, final preparation and storage of parenteral suspensions, and the fluid shear encountered after intravascular injection. Augmented mixing, under microgravity condition, using finely dispersed iron particles drawn through the immiscible interface by a small magnetic field was also used to form microcapsules containing hydrophilic drugs, microbeads, and hydrophobic components.

Also we have formed very unusual structures (multiple small spheres of aqueous-soluble drug) distributed within multi-lamellar o/w/o microspheres, wherein the aqueous spheroids are arranged in an annular ring that appears fixed in a plane within the innermost sphere (not shown). These ring structures remain intact when the microcapsules are "rolled around" on the microscope slide.

Space Shuttle Experiments

Microencapsulation experiments on Consort 4 and Consort 5 used mixtures of aqueous-soluble drugs, IPO, C3-C8 alcohols and polyglycerides that are insoluble in aqueous solutions. Experiments on STS-52 co-encapsulated Cis-Platinum with IPO by forming liposomes from water-soluble polymers using special formulations of aqueous, non-alcoholic solvents. Polyvinyl pyrrolidone (PVP) and a commercial lecithin (Centrox-FTM)¹ were used to form the liposome-type multi-lamellar microcapsules at 20 °C. Fluorescent beads and fluorescent labeled were co-encapsulated with the drugs to permit drug-distribution measurements, within the various vesicles and lamellae, using fluorescence microscopy and digital image analysis at the Johnson Space Center. The final microcapsules were suspended and recovered in either aqueous solutions, IPO or mineral oil. The microcapsules formed by these formulations were similar to those made using alcohol-soluble polyglycerides, however, without the hydrocarbon-soluble polyglyceride skin these microcapsules were more fragile.

Another unique type of microcapsule was formed during these experiments that was characterized by drug crystals formed within the inner aqueous core of the multi-lamellar microspheres. Figure 3 shows an example of a microcapsule which is packed (approximately) 65% of the aqueous compartment) with crystals of Cis-platinum, anti-tumor drug. Figure 4 shows two microcapsules containing crystals of amoxicillin that were formed in the STS-52 experiments. These illustrate that aqueous-soluble drugs can be encapsulated at very high concentrations near the solubility limit of the drug. After the microcapsules are formed the drug can become further concentrated to form large crystals which can be more stable than the dissolved drug during prolonged storage.

In 1993 modifications to the MDA flight hardware enabled drug encapsulation experiments to be conducted on STS-56 at 20 °C. using alcohol solvents for the polyglycerides. Cis-platinum, amoxicillin and urokinase were each co-encapsulated with IPO, radio-contrast medium, using mixtures of aqueous-soluble polymers, dextran, C3-C6 alcohols (co-surfactants), and polyglycerides that are insoluble in aqueous solutions. These microcapsules were tougher than those formed on STS-52 using only water soluble polymers. The STS-56 experiments again produced multi-lamellar liquid microspheres (multiple concentric spheres within spheres) comprised of alternating immiscible layers. Using fluorescent 6.4 micron beads and image analysis, it was found that the most interesting microcapsules were formed in the range of 10-15 μ , 40-50 μ , 50-100 μ and 160-230 μ diameters. More microcapsules were formed containing crystals of cis-platinum or amoxicillin which were formed after encapsulation. Several microcapsules were formed that contained a single large cubic crystal of Cis-platinum which so completely filled the inner sphere that only about 15% of the inner volume remained as a liquid. One encapsulated, cubic Cis-platinum crystal was measured at 48 μ across within a 57 μ diameter microcapsule. (data not shown). After formation, some of the microspheres were dispersed in an external oil phase (either IPO or mineral oil) and allowed to cure for eight days before return to Earth.

Our space experiments have shown that formation of multilamellar, alternating-phase microspheres can be controlled by proper timed-sequence exposures of the immiscible phases using special solvent formulations and surfactants. Once formed these microcapsules remain spherical due to the predominant surface tension of the internal phases. High molecular weight polymers and polyglycerides can be included to form flexible, permeable "skins" around the liquid microcapsules as they are created by phase partitioning mechanisms. These experiments clearly demonstrated the capability to use liquid-liquid diffusion mixing to form unique microcapsules containing hydrophilic and hydrophobic drugs under microgravity conditions. The flexible microcapsules, formed under microgravity conditions, have more uniform size distributions than those formed in 1-g, largely due to the absence of thermal convection and instabilities that occur at the immiscible interfaces. The microgravity experiments illustrate the feasibility of co-encapsulating aqueous-soluble drugs, hydrocarbon-soluble drugs and oil-based contrast media within a lipid-soluble, polyglyceride, outer film which cures rapidly enough to be impervious to oil or hydrocarbon resolubilization. These methods allow the formation and harvesting of unique microcapsules which are durable enough to be removed from the external solvent without disruption or destruction of the internal phases. These new microcapsules have several advantages over conventional liposomes that are designed for intravascular injection.

¹ Centrox-FTM is a lecithin produced by U.S. Soya, Inc.

Other Microencapsulation Flight Experiments

Previously, aerosol dispersion of agarose-type gels, dissolved in aqueous vehicles, were used to encapsulate pancreatic cells during short periods of weightlessness (25 seconds) during parabolic flights of the NASA KC-135, Zero-g aircraft. These were commercial pilot studies conducted by the Canadian Aerospace Ltd. and NASA [9]. A joint microencapsulation program was planned to expand these experiments to use electrophoretic separations to harvest only those microcapsules containing the pancreatic cells so that animal trials could be conducted to treat diabetes by transplantation of the encapsulated cells that produce insulin.

Microencapsulation in Space (MIS) experiments were also conducted on Shuttle mission STS-53 in December 1993 under a joint program between the Department of the Army's Space Technology and Research Office and Dr. T. Tice, Southern Research Institute, Birmingham, AL., using a traditional approach to aerosol dispersion of ampicillin. The main objectives of the experiments were to compare formation and curing of the liposomes in an electrostatic field vs. no electrostatic field, without having the liposomes sediment to the floor of the test chamber. The results presented in testimony to the U.S. Congress in April 1993 indicate that more uniform liposomes were formed in microgravity as compared to the same process on Earth [10].

Flight Hardware Description

The microencapsulation experiments described in this paper were conducted using ITA's automated laboratory, the Materials Dispersion Apparatus (MDA). The MDA is a compact device capable of bringing into contact and mixing up to 100 separate samples of multiple fluids and/or solids at precisely timed intervals. The samples mix either by simple liquid-liquid diffusion or magnetic mixing techniques. The device also can be used to grow protein crystals by three different methods and to cast polymer membranes in the absence of thermal convection.

Experiments were conducted on the sounding rocket flights during approximately 6.5 minutes of microgravity and two Space Shuttle missions which lasted 8 days. The fluid volumes were 500 microliters per sample. Approximately 8-10 microencapsulation experiments were conducted on each flight. The MDA's consist of an upper and a lower block that contain chambers for each sample fluid. The blocks are misaligned at launch so that the chambers are not in contact with each other. Upon activation in microgravity, the blocks are moved to align the chambers so that the fluids can mix by liquid to liquid diffusion. For some experiments, a single-step, magnetic-mixing technique was utilized to accelerate the process. Some of the experiments were conducted with a single-step fluid mixing, and some were done with a two-step fluid mixing technique which allows diffusion of a third fluid or sample into the mixture of the first two fluids while still in the microgravity environment. Figure 5 shows four MDA Minilabs ready for experiments to be conducted on the Consort sounding rocket flights. Two of these MDA units were used in each sounding rocket and four of the MDA units were utilized in the space shuttle missions. Figure 6 shows the integrated package ready for a Shuttle flight. The MDAs are completely automated system with commands being given by an onboard process controller when used on the sounding rockets. When the MDA units are flown in the Space Shuttle, a controller activated by the crew provides commands to process the samples. In addition, the MDA minilabs contain a manual back-up mechanism for astronaut intervention if the controller fails. As a result of the space experiments conducted in the MDAs a new microencapsulation apparatus is now being developed by NASA-JSC, IRI and ITA to exploit this technology on Earth and for conducting new flight experiments dedicated to microencapsulation of drugs under microgravity conditions.

DISCUSSION

Commercially oriented space experiments have shown that microgravity can permit the encapsulation of drugs into unique microcapsules by liquid-liquid dispersion and spontaneous emulsification using alcohol/ water/ oil mixtures, appropriate surfactants, and co-surfactants [11-14]. Spontaneous formation of multi-lamellar, microcapsules containing alternating layers of aqueous and hydrophobic solvent compartments is strongly dependent on the interfacial tension and the amount of mixing between immiscible liquid phases. On Earth this process is limited by gravity-dependent, density-driven separation of the immiscible liquids into stratified horizontal layers. In microgravity, this process is largely dependent on the surface-free energies of the different liquids, but independent of density-driven convection or buoyant phase separation. Hydrocarbon soluble, high molecular weight polymers have been included in the formulations to form flexible, permeable "skins" around the liquid microcapsules as they are created by phase partitioning mechanisms. The microcapsules can be formed and cured without deformation by contact with container walls. This offers new possibilities for using electric fields to form the microspheres or deposit coatings.

Co-encapsulation of an aqueous-soluble, anti-tumor drug (Cis-platinum) and a radio-contrast medium (IPO), in microgravity, has produced a unique drug delivery system that can be visualized by radiologic or computerized tomography scanning to insure that the cytotoxic drug is delivered directly to the target tumor. Multi-layered microcapsules have been developed which can provide a new intravascular delivery system for targeted tissues and sequential, sustained release of multiple anti-tumor drugs. This method has formed perfect microspheres and more uniform sizes, which can provide maximum packing densities and maximum drug delivery to target organs or tumors.

The capability to obtain larger, more uniform size microcapsules opens up more possibilities to treat highly vascular tumors (liver and kidney) with chemoembolization. Therein, the microcapsules (100-200 μ) are injected via an arterial catheter to form artificial emboli which block the blood supply to the tumor. The reduced blood volume, that flows past the tumor, becomes loaded with the antitumor drug that diffuses out of the microcapsules, thus increasing the chemotherapeutic dose to the tumor cells. The use of multiple drugs within the same microcapsule can provide an opportunity to design microcapsules specifically for chemoembolization treatments. Multiple-drug microcapsules also could be used to deliver first a chemotherapeutic drug which would kill tumor cells, and then an immuno-adjuvant (tumor necrosis factor) or immunological stimulant (e.g. Interferon- γ) that would enhance the patient's immune response to the tumor.

Multiple-drug microcapsules can also be used to deliver combinations of chemotherapeutic drugs to tumors that are located in privileged sites, such as brain tumors. An example would be the simultaneous delivery of different types of drugs, e.g. Diaziquone and Cis-platinum, to brain tumors via the carotid artery [15]. Multi-layered microcapsules could also be used to treat deep infections that are resistant to systemic antibiotics. In these applications, one or more antibiotics could be sequentially delivered or an immuno-stimulating cytokine (Interleukin-1) could be delivered to the site of the infection. Multi-layered microcapsules can be designed to protect active forms of urokinase and other thrombolytic enzymes until they are delivered and entrapped at the local site of a blood clot, where therapeutic doses of the enzyme can diffuse out to dissolve the unwanted embolism. These immiscible-liquid diffusion methods also could be used for encapsulating certain labile drugs to make microcapsules for special purpose drug delivery systems, esp. those designed to deliver drugs via the nasal or buccal mucosa or via inhalation directly to the lungs. Examples include protected delivery of mucolytic DNase for sustained release treatment of cystic fibrosis [16] and α_1 -anti-trypsin for patients with deficiencies in the lung epithelium [17].

Our Earth-based research is now directed towards elimination of certain specific limitations of the liquid-liquid dispersion method of forming multi-lamellar microcapsules by modification of organic co-surfactants to improve the efficiency of initial microcapsule formation, characterization of those microparticles, then addition of an electrostatic coating step to create the final polymer skin in a more traditional fashion. These microcapsules will then be characterized and compared with those formed in microgravity. Another series of microgravity experiments is planned for the CMIX-3 payload now targeted to fly on Shuttle STS-67 mission in the fall of 1994. The data will be used to develop a new microencapsulation system that can be used for future commercial and microgravity encapsulation research. A joint Patent Disclosure has been prepared by NASA-JSC and the Institute for Research (IRI) to enable future commercial applications of this new microencapsulation technology.

SUMMARY

A new method of forming multi-lamellar microcapsules has been developed with the aid of microgravity experiments that eliminate the density-driven portions of phase separations that occur with immiscible liquids having different densities. Experiments on four different space missions produced unique microcapsules of Cis-platinum (antitumor drug), amoxicillin (antibiotic) and urokinase (fibrinolytic enzyme) that were co-encapsulated with iodinated poppy seed oil, which is a radio-contrast medium. Microcapsules also were formed with crystals of Cis-platinum or amoxicillin inside the aqueous liquid core. Two different solvent systems were used, based on either aqueous-soluble phospholipids and polymers or a system using aqueous-soluble drugs dispersed in alcohol solutions containing polyglycerides which form a tough outer skin around the liquid phases of the microcapsules. The formation of microcapsules with alternating hydrophilic and hydrophobic layers offers new advantages for drug delivery systems that are designed specifically for intravascular administration. Microcapsules can now be designed for chemoembolization and multiple-drug chemotherapy of vascularized tumors. Microcapsules containing the radiocontrast medium can be monitored by radiologists during intravascular administration. Other medical applications include multiple-drug therapy of resistant infections, blood clots and inhalation delivery of labile proteins to lung tissues.

REFERENCES

1. Rhoerdink, F. H. *et al.*, Therapeutic Utility of Liposomes, in J. G. Lloyd-Jones and P. Johnson, (Eds.) Drug Delivery Systems, Vol. 1. Ellis Horwood, Chichester, UK, pp. 66-80, 1987.
2. Gabizon, A., *et al.*, Liposome-Associated Doxorubicin: Preclinical Pharmacology and Exploratory Clinical Phase, in G. Lopez-Berestein and I.J. Fidler (Eds.) Therapy of Infectious Diseases and Cancer, Alan R. Liss, Inc., New York, pp. 189-203, 1929.
3. Urba, W. J. *et al.*, Phase I and Immunomodulatory Study of a Muramylpeptide, Muramyltripeptide Phosphatidylethanolamine, *Cancer Res.* 50: 2979-2986, 1990.
4. Talsma, H. and Crommelin, D. J. A., Liposomes as Drug Delivery Systems, Part I: Preparation. *Pharmaceutical Technology*, pp. 96-106, October 1992.
5. Allen, T. M., Interactions of Drug Carriers with the Mononuclear Phagocytic System, in G. Gregoriadis (Ed.) Liposomes as Drug Carriers, John Wiley & Sons Ltd., New York, pp.37-50, 1988.
6. Allen, T. M., Mehra, T., Hansen, C. and Chin, Y.C., Stealth Liposomes: An Improved Sustained Release System for 1- β -D-Arabinofuranosylcytosine, *Cancer Res.* 52:2431-39, 1992.
7. Bhargava, H. N., Narurkar, A., and Lieb, L. M., Using Microemulsions for Drug Delivery, *Pharmaceutical Technology*, pp. 46-54, March 1987.
8. Mosier, B., Method of Preparing Microspheres for Intravascular Delivery, U.S. Patent, 4,492,720, Jan. 8, 1985.
9. Personal communication, Richard Boudreaux, Canadian Aerospace Limited, Co. 1988.
10. Dr. Thomas Tice, Southern Research Institute, Birmingham, AL. Congressional Testimony, U. S. House of Representatives, Committee on Science, Space and Technology, Subcommittee on Space, April 9, 1993.
11. Morrison, D. R. and Mosier, B., Microencapsulation of Drugs, Microbeads and Radio-opaque Contrast Medium: Consort 4 Sounding Rocket Experiments in the Materials Dispersion Apparatus, December 1991, NASA-JSC Internal Report (unpublished).
12. Microencapsulation experiments on Consort 4 Sounding Rocket, Minilab I. Published in Earth Space Review, July - September, 1992.
13. Morrison, D.R. and Mosier, B., Preliminary Results of the STS-52 Experiments on Microgravity Encapsulation of Drugs, November 28, 1992, NASA-JSC Internal Report (unpublished).
14. Morrison, D.R. and Mosier, B., Microencapsulation of Drugs in Microgravity: STS-52 and STS-56 Results, May 6, 1993, NASA-JSC Internal Report (unpublished).
15. Kimler, B. F., *et al.*, Combination of Aziridinylbenzoquinone and Cis-platinum with Radiation Therapy in the 9L Rat Brain Tumor Model, *Int. J. Radiation Oncology Biol. Phys.*, 26: 445 - 450, 1993.
16. Aitken, M. L. *et al.*, Recombinant Human DNase Inhalation in Normal Subjects and Patients with Cystic Fibrosis. A Phase I Study, *JAMA* 267: 1947-1951, 1992.
17. Hubbard, R. C. *et al.*, Antineutrophil-Elastase Defenses of the Lower Respiratory Tract in α_1 -Anti-trypsin Deficiency Directly Augmented with an Aerosol of α_1 -Anti-trypsin, *Ann. Int. Med.* 111: 206-212, 1989.

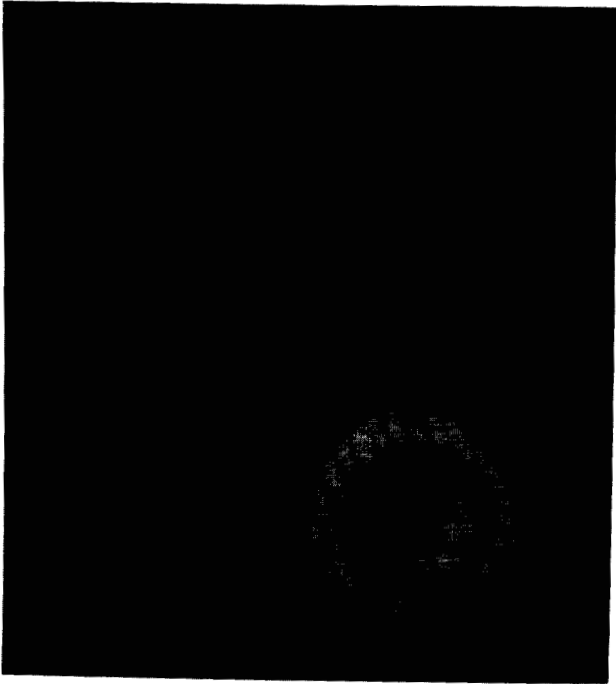


Figure 1. Multi-lamellar microcapsules

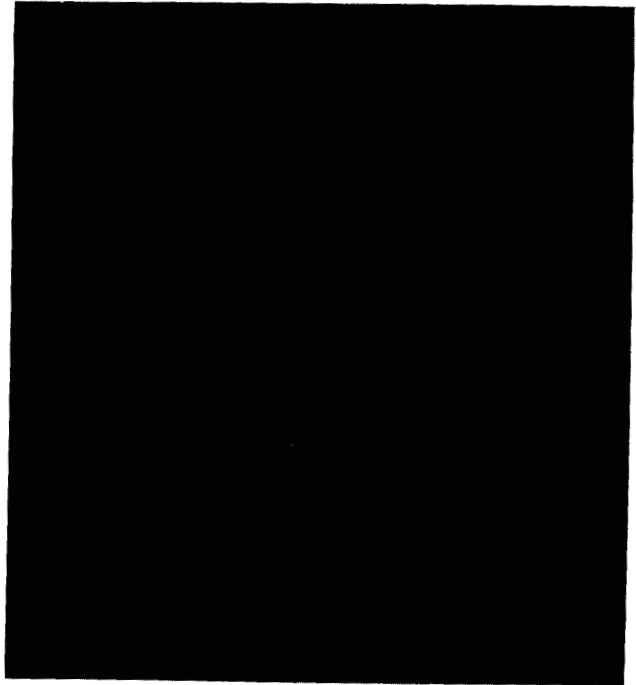


Figure 2. Microcapsules containing IPO.

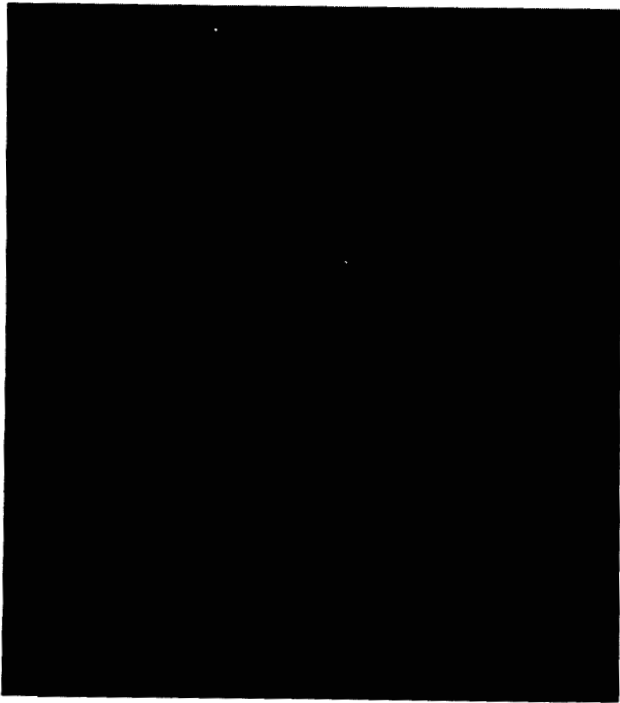


Figure 3. Cis-platinum crystals in microcapsules.

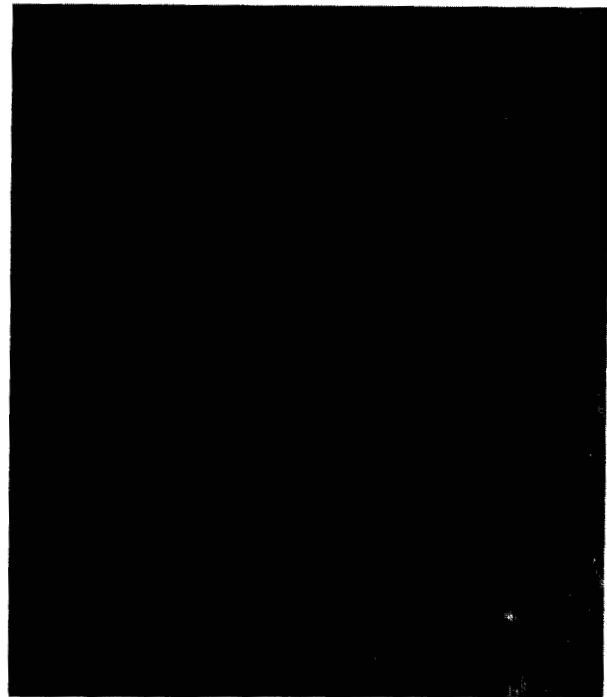


Figure 4. Amoxicillin crystals in microcapsules

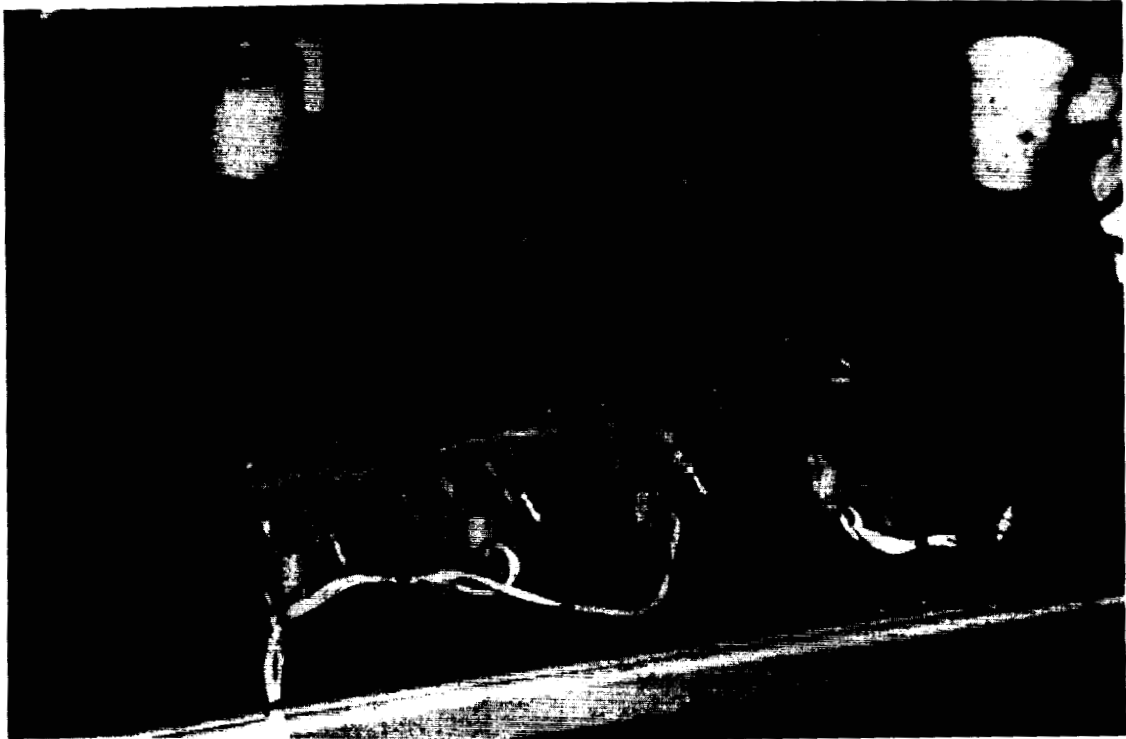


Figure 5. Four units of Materials Dispersion Apparatus (MDA) automated mini-lab configured for sounding rocket flights. Photo courtesy of ITA, Inc.

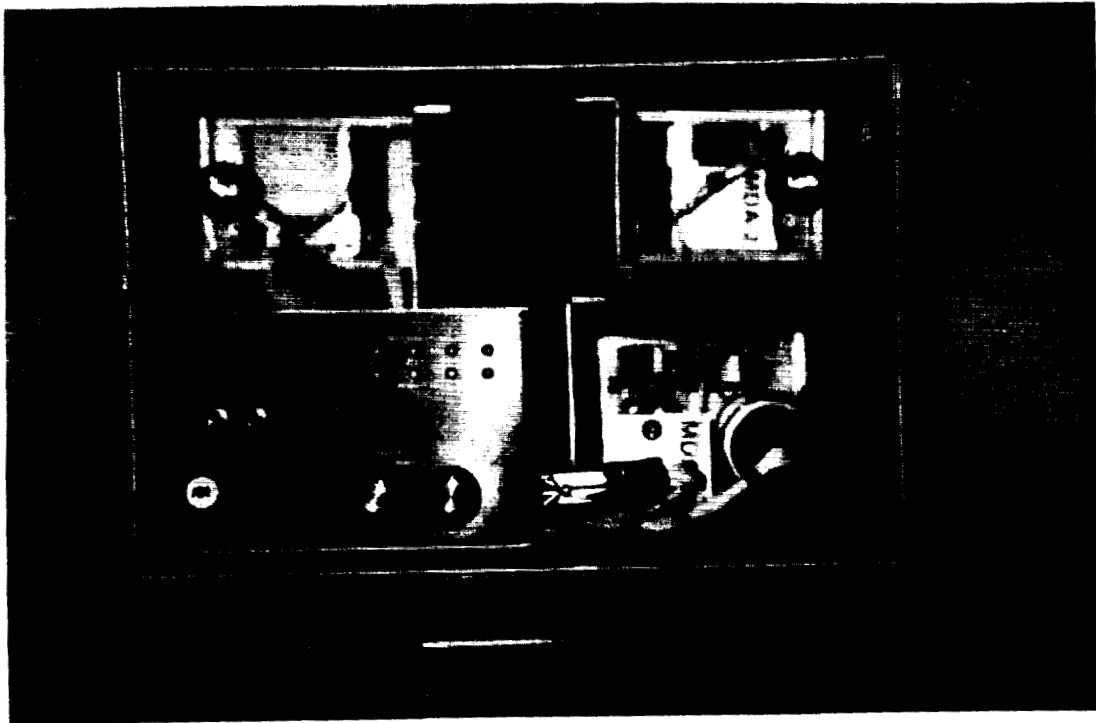


Figure 6. MDAs configured for the CMIX payload that flew in the Shuttle Middeck on STS-52 and STS-56 missions. Photo courtesy of ITA, Inc.

**CUBANES : SUPER EXPLOSIVES AND
POTENTIAL PHARMACEUTICAL INTERMEDIATES**2450
P 4**Dr. A. Bashir-Hashemi
GEO-CENTERS, INC.
762 Rt. 15 So.
Lake Hopatcong, NJ 07849****ABSTRACT**

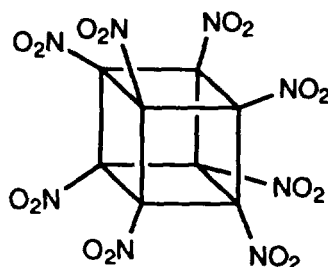
The cubane molecule, in which eight carbon atoms are locked in a cubic framework, shows great potential for both military and pharmaceutical applications. Octanitrocubane, with a predicted density of 2.1 g/cc and strain energy of more than 165 kcal/mol, is considered to be the "super-explosive", while cubane derivatives submitted to the National Institutes of Health for preliminary biological activity screening have displayed promising anti-cancer and anti-HIV activity.

DUAL-USE PROGRAM

With the end of the cold war and the subsequent scaling down of American munitions manufacture, a need arises for novel, effective and inexpensive civilian applications of explosives technology.

Should it be possible to convert final products or some of the intermediates to materials of commercial value, the payoff to the civilian economy could be substantial. At a time when the use of tax dollars for research is increasingly questioned, such a dual use of explosives technology would demonstrate the spillover benefits of defense research into entirely different areas of science.

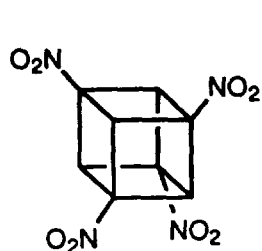
The cubane molecule shows great potential for both military and pharmaceutical applications. The cubane skeleton, in which eight carbon atoms are locked in a cubic framework, has a density almost 50% greater than its isomers, such as cyclooctatetraene. Octanitrocubane, with a predicted density of 2.1 g/cc and strain energy of more than 165 kcal/mole is considered to be the "super-explosive".

**Octanitrocubane**

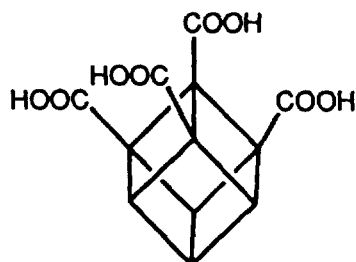
Despite intensive interest in cubanes as energetic materials, other applications of this fascinating molecule have not been explored thoroughly, mainly due to the unavailability of

simple methodologies for functionalizing the cubane skeleton. Recently, we have developed new methods for functionalizing the cubane skeleton photochemically, which have enabled us to synthesize a large class of cubane compounds with variety of functional groups.

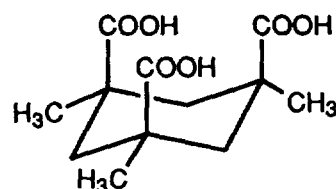
Cubane carboxylic acids are now readily available from commercially available starting materials. Cubane 1,3,5,7- tetraacid is a potential precursor to tetranitrocubane, a very powerful and stable energetic material. Meanwhile, cubane 1,2,3,5-tetraacid which has similar structural feature as Kemp's triacid, has been targeted for molecular recognition studies in the area of bioorganic chemistry.



Tetranitrocubane

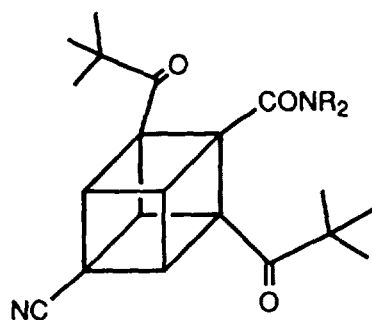


Cubane tetraacid

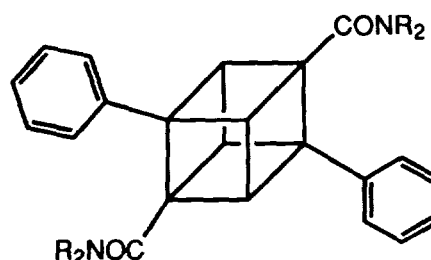


Kemp's Triacid

A number of functionalized cage compounds, notably adamantyl amides, amines and sugars have shown antiviral and antitumor activity. The value of the cage substituent seems to lie in its increasing the lipophilicity of the rest of the molecule, allowing easier transport across membranes. Encouraged by these observations, we submitted a number of cubane derivatives to the National Institutes of Health for preliminary biological-activity screening. Dipivalylcubane showed moderate anti-HIV activity without affecting healthy cells and one of the phenylcubanes displayed moderate anti-cancer activity.



Dipivalylcubane

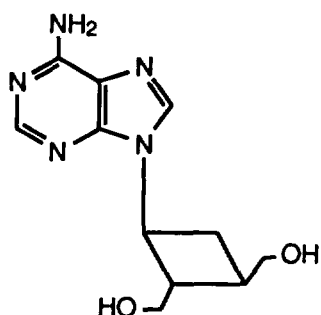


Diphenylcubane

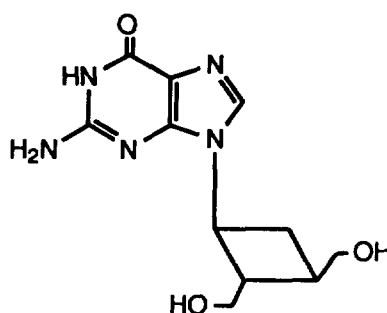
Perhaps most significantly, none of the submitted cubanes showed any toxicity. This suggests that the cubane moiety is, at worst, innocuous in pharmaceutical applications, while a number of adamantane derivatives exhibited toxicity. In military applications a cubane-based explosive should not constitute a pollution hazard in itself since, unlike TNT or RDX, it should be non-toxic.

Intensive efforts have been directed at finding potential anti-AIDS drugs under the National Cancer Institute's *In Vitro* Anti-AIDS Drug Discovery Program. Inhibition of the HIV virus in AIDS patients is most commonly achieved through the administration of azidothymidine (AZT). Although short-term treatment of AIDS patients with AZT leads to clinical, virological and immunological improvement, the long term use of AZT is associated with severe toxicity, in particular bone marrow suppression. Immunologic deterioration continues as well, despite continued administration of AZT. The other drugs which have been approved for AIDS treatment, ddC (2',3'-dideoxycytidine) and ddI (2',3'-dideoxyinosine) also have limitations imposed by side effects of peripheral neuropathy and pancreatitis, respectively.

Further search for effective inhibitors of HIV variants has led to the discovery of various carbocyclic nucleosides which hold promise for the treatment of retrovirus infections. Representative carbocyclic derivatives that are active against HIV are cyclobut-A and cyclobut-G. It is believed that the structural features of cyclobutyl rings attached to adenine or guanine play an important role in their activity.

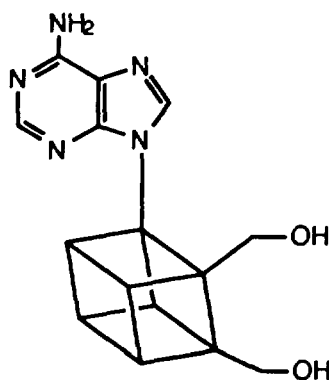


Cyclobut-A



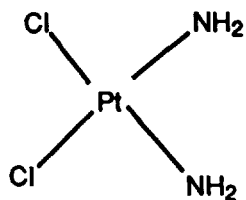
Cyclobut-G

The cubane nucleus consists of six cyclobutyl rings packed in a very stable frame. The recent availability of cubane derivatives, as well as their stability and non-toxicity, suggest that their therapeutic activities should be studied in greater depth. In the context of anti-AIDS drugs, one might readily envisage the synthesis of a cubyl analogue of Cyclobut-A, such as "Cubyl-A".

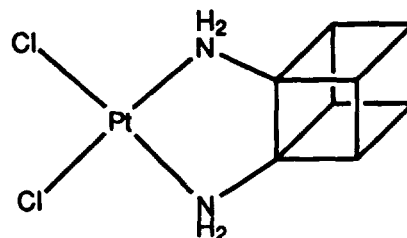


Cubyl-A

Molecular modeling studies predicted that special *cis* arrangements of the neighboring hydrogen atoms on the cubane frame, when replaced by amino groups, would lead to an intriguing analogue of *cis*-platin, an active anticancer drug.



Cis-Platin



Diaminocubane Complex

In our initial plan, a large number of cubane derivatives such as aminocubanes and di(hydroxymethyl)cubanes will be prepared. From these compounds, analogs of *cis*-platin and cyclobut-A and cyclobut-G will be synthesized and submitted for biological evaluation. Meanwhile, we will conduct modeling studies and seek the collaboration of experts in pharmaceutical research to help us identify potential targets.

Major accomplishments have already been achieved in cubane chemistry under the "More Powerful Explosives Program" funded by the U.S. Army. Under the current administration policy of dual technology, redirection of the cubane program toward civilian use will be most rewarding.

**DUAL USE OF IMAGE BASED TRACKING TECHNIQUES:
LASER EYE SURGERY AND LOW VISION PROSTHESIS**

515-52

2451

1 7

Richard D. Juday, Ph.D.
Manager, Hybrid Vision
Tracking and Communications Division
NASA Johnson Space Center
Houston TX 77058

ABSTRACT

With a concentration on Fourier optics pattern recognition, we have developed several methods of tracking objects in dynamic imagery to automate certain space applications such as orbital rendezvous and spacecraft capture, or planetary landing. We are developing two of these techniques for Earth applications in real-time medical image processing. The first is warping of a video image, developed to evoke shift invariance to scale and rotation in correlation pattern recognition. The technology is being applied to compensation for certain field defects in low vision humans. The second is using the optical joint Fourier transform to track the translation of unmodeled scenes. Developed as an image fixation tool to assist in calculating shape from motion, it is being applied to tracking motions of the eyeball quickly enough to keep a laser photocoagulation spot fixed on the retina, thus avoiding collateral damage.

INTRODUCTION

This is a difficult paper to write, with respect to striking an appropriate balance between being complete on the one hand, and too thinly spreading out information of use to the target audience on the other. I will try to leave much of the technical development to the reference material, presuming a technically competent reader who is not an expert in these disciplines.

NASA's Johnson Space Center (JSC) has been actively developing its image based tracking technology for two medical applications: noncontact retinal position stabilization for laser photocoagulation, and image warping as a prosthesis for certain field defect forms of human low vision. In the retina surgical application, JSC is working with Pinnacle Imaging, a small company dedicated to the development of surgical and robotic methods and equipment for the surgical market. In the image warping application, we are working with the University of Houston's College of Optometry (UHCO) and the University of Pennsylvania. As an Agency, NASA has formal connections with an industrial and medical group that has built a heads-up display system that can directly incorporate our results into prosthetic hardware.

Ophthalmic laser procedures

In the eye surgery application, our central problem is maintaining the aim point of a laser during retinal photocoagulation. Similar image processing hardware may allow tracking assemblyline parts in jumbled orientation, as on a conveyer belt, with no conditions on their placement or orientation. NASA is developing an applicable technology: image correlation based tracking. The eyeball (and the retina with it) undergo continual small-angle jitter, along with the larger jerky saccades that are typified by eye motion while reading. Both are detrimental to the photocoagulation procedure. Incorrect locations on the retina may be struck by the laser; in addition to causing collateral damage to the retina, this limits how close eye surgeons are comfortable working to the fovea (the highest resolution part of the retina -- the part we use when looking directly "at" an object).

JSC has patented¹ a technique that provides fixation; that is, regardless of exactly *what* is in the scene, the input sensor is given the information to allow it to stare at a single location in the scene even as the spacecraft moves or jerks. This is important to simplify analysis of the dynamic scene for information about the three dimensional nature of the unknown surface. "Optic flow" is the technical term for the intra-image motion that results from a shifting perspective of a three-dimensional surface, and computation of optic flow is far eased if fixation is maintained on some point in the image. Our method is based on what is technically described as the

optically derived joint Fourier transform correlation. Full details are presented in the patent and in other literature^{2,3,4,5}.

Field Defect Low Vision Prosthesis

NASA has an Agency presence in image processing technology for low vision sufferers. JSC's Tracking and Communications Division and an associated organization, the University of Houston's College of Optometry (UHCO), originally proposed image warping for field defect amelioration. We have developed hardware that either exists^{6,7} or is in advanced design^{8,9} that implements our specially designed mathematical image transformations^{10,11,12,13}, and we have also begun clinical studies whose initial results^{14,15} are favorable to the notion that video rate image warping may yield increased visual function for such disorders as central field blindness (maculopathy) or peripheral field loss (retinitis pigmentosa). If known portions of the retina are dysfunctional, an image may be warped so as to minimize the part of the world view that lands there, while retaining a balance between distorting the world view too much and losing part of that world view. We intend that the end result of this program will be visual prostheses (high tech "glasses"¹⁶) that are more capable, smaller, lighter weight, and less expensive compared with other methods. We intend that the current program will divine mathematical image warpings that maximally increase visual function as tested by reading speed, facial recognition, and so on, but implementing the warpings in inexpensive, lightweight hardware remains an unsolved problem. Among other practical items, we need to determine the range of visual function loss that can benefit from our technique, and then find a minimum set of transforms that span that range.

Fourier Optics

Fourier optics is an important discipline in which the diffractive properties of light become important in the way information is carried and processed. Journals such as Applied Optics, Journal of the Optical Society of America-A, and Optical Engineering carry current articles concentrating heavily in this discipline. Societies such as SPIE - The International Optical Engineering Society publish many Proceedings per year in the discipline. I will limit the discussion here to saying that we bring information to a Fourier optics correlator, usually in video image form, and that an element known as a spatial light modulator (SLM) has its light transmitting properties altered by that video image. Then as coherent light passes through the SLM, the information within the video signal is encoded onto the light beam. Diffraction can then be arranged so as to take the Fourier transform of the encoded image, and subsequent transmission (or reflection) of the light through other elements causes the information to be processed and then presented in simpler form (i.e. bright spots).

Optical Correlation Based Pattern Recognition

(Technically incorrectly, this section will mix some concepts from conjugating Fourier optics [the so-called VanderLugt, or 4-f, correlator] and joint transform correlation [JTC]. I am going to go ahead and do it, even if the expert would squawk; this is more of a tutorial heuristic device than a technical compendium. Just don't jump me for what looks like an error. There is not room to be rigorous. I am also using one-dimensional notation for a two-dimensional signal, pointing out that to do so has become common in Fourier filtersmithing.)

Suppose we have a function $f(x)$ and we wish to filter information from it with a linear system whose impulse response is $h(x)$. The convolution is $y(x) = f(x)*h(x)$:

$$y_{conv}(x) = \int_{-\infty}^{+\infty} f(x-\tau)h^*(\tau)d\tau \quad (1)$$

but we will not technically distinguish between a convolution, $f*h$, and a correlation, $f \star h$

$$y_{corr}(x) = f \star h = \int_{-\infty}^{+\infty} f(x+\tau)h^*(\tau) d\tau \quad (2)$$

since a time reversal of $h(\bullet)$ changes between the two, and $h(\bullet)$ has been arbitrary. As is well known in linear system theory, convolution can be expressed as the inverse Fourier transform of the product of transforms of the functions. That is, if $f(\bullet)$ and $F(\bullet)$ are a transform pair, as are y and Y , and h and H , then

$$\begin{aligned} y(x) &= \mathcal{F}^{-1}\{\mathcal{F}\{f(x)\} \times \mathcal{F}\{h(x)\}\} \\ &= \mathcal{F}^{-1}\{F \times H\} \end{aligned} \quad (3)$$

Also as is well known, there is a shift in $y(\bullet)$ corresponding to a shift in the input signal $f(\bullet)$, a property known as shift invariance. Correlation uses this property to locate a signal that has been identified by the presence of values of $y(\bullet)$ rising above an identification threshold. Optics offers the ability to do the transforms easily by the diffraction of light (once the signal is impressed on it) and to do the multiplication easily (by interacting the light with an SLM on which the function H has been created). There have been three difficult parts. One has been to manufacture SLMs on which desired functions for encoding the signal and the filter. The second is how to make appropriate use of the SLMs we do have; signal theory prescribes ideal values for the filter values, H , that are ordinarily not realizable. Recently¹⁷ we have achieved a breakthrough in optical filter theory that make some of the job easier, and we continue developing modulators and their characterization^{18,19} for other aspects of the problem. The third is how to accommodate the rotation of the retinal image that occurs as the eyeball rotates within the socket, as in response to signals from the vestibular function. Pattern recognition by image correlation is usually quite sensitive to rotation, so we continue our effort to achieve tailored amounts of rotation invariance, and the results will be fed into our activities under Memorandum of Understanding with our medical partner, Pinnacle Imaging. This effort is ongoing under university grant (see Formal Colleagues, below) following concepts laid down several years ago²⁰.

Somewhat simplistically, a Fourier optics image processor converts the video image of the object it has been trained to find into a bright spot of light, and then infers information from that spot. The difficult parts of the information extraction are done off-line and at leisure; the easy part is what happens on-line and in real time. As distinct from most digital image processing, this system determines the correlation between highly synthesized reference objects and the viewed object, and then extracts the information from those correlations. Synthesizing a reference object is a congruent process to obtaining the inverse transform of the optimal filter that can be realized within the limitations of the filtering spatial light modulator. The correlations run at a very high frame rate (tens of thousands per second), allowing comparisons of the input video object with all members of a library of views of that object. Careful crafting of the reference image set has the effect that the library element producing the highest correlation corresponds to the actual position and attitude of the viewed object.

In further distinction from most digital processing, optical pattern recognition operates on the whole input image, rather than individual features, and thus is robust against partial obscuration. The difficult technical challenges are principally in the physical devices — spatial light modulators — that encode the incoming video image and the correlation image.

VIDEO RATE IMAGE WARPING

Shift Invariance in Optical Pattern Recognition

As is well known in signal theory, the convolution (equivalently the correlation) of two signals is a linear and shift invariant operation. Also well known is that scale and rotation changes in a Cartesian geometry do not produce shift invariance. If we know $[x_0, y_0]$, the center about which scale and rotation changes occur, though, we can convert scale and rotation into translational shifts by performing a coordinate transformation. The log polar transformation is what we seek.

$$\begin{bmatrix} x-x_0 \\ y-y_0 \end{bmatrix} = \begin{bmatrix} r \cos\theta \\ r \sin\theta \end{bmatrix} \quad (4)$$

shows the conversion between the Cartesian $[x,y]$ and the polar $[r,\theta]$ as coordinate systems. Go one step further and define u as $\log r$. Then as the original image coordinates undergo a change expressed as

$$\begin{bmatrix} x' \\ y' \end{bmatrix} = k \begin{bmatrix} \cos\alpha & \sin\alpha \\ -\sin\alpha & \cos\alpha \end{bmatrix} \begin{bmatrix} x-x_0 \\ y-y_0 \end{bmatrix} + \begin{bmatrix} x_0 \\ y_0 \end{bmatrix} \quad (5)$$

we will find that the coordinate pair $[u,\theta]$ undergoes the change

$$\begin{bmatrix} u' \\ \theta' \end{bmatrix} = \begin{bmatrix} u + \log k \\ \theta + \alpha \end{bmatrix}, \quad (6)$$

so that the rotation through α and scaling by k become translations by α and $\log k$. For video rate pattern recognition that is to be shift invariant to scale change and rotation about $[x_0,y_0]$, and the difficult part is to create the log polar transformation at full video rate.

The Programmable Remapper

With the Programmable Remapper we have solved that problem, at least on a laboratory scale. Its generality allows us to create virtually unlimited geometric transformations at video rate. Conversion to practicality as a prosthesis remains an unsolved, but significant and potentially productive, interest. Read the References for technical details, but suffice it for the present purposes to say that the Remapper can wreak an arbitrary static geometric transformation (at video rate and incurring only a three frame delay) on an incoming video image. We conceived the Remapper as a tool for creating a log polar video image, but we rapidly understood its potential for manifesting other warpings. Human low vision field defects was the first such extracurricular application.

Field Defect Application for Low Vision Humans

As reported in a number of the papers in the References, we have investigated the applicability of image warping for various field defects. For examples of images, see in particular Ref[12]. One of the two principal ones is maculopathy, in which a lesion causes loss of function at the high resolution central portion of the normal field of view. The other principal application is RP (retinitis pigmentosa), also known as tunnel vision, where peripheral vision is progressively lost. Our intent is to move the active portions of a video image so that it falls onto portions of the retina that are still functional, thus having a more nearly complete mapping of the world into the visual cortex (albeit at the expense of local distortion in the normal world-to-cortex representation).

The fovea is the portion of the eye where the resolution is the highest; it is the part of the eye one naturally places into conjunction with the part of the world scene where visual detail is sought. It is the part of your field of view you use when looking "at" something. Loss of foveal function is particularly expensive to detailed functions like reading and facial recognition. Our method is to "rubber-sheet" a video image. Imagine that a television screen is made of rubber, that you poke a hole in the middle, and then stretch that hole out until it is just larger than the blind spot in the center of the field of view. There are many loose parameters in this description, but the core idea is there. In our initial tests, we used normally-sighted volunteers, and we simulated the central blind spot by forcing them to look at an obscuration on a television screen with text scrolling by. An eye tracker followed the gaze of the eye, controlling mirrors that directed the gaze onto the obscuration. The words scrolled by at various font sizes, angular rates, etc. There was significant (though highly variable from subject to subject) increase in reading rate

with image warping. Our next studies will use actual low vision volunteers, it will not force foveation, and we have some advanced mathematical transformations to try. These studies are beginning in Fall 1993.

To deal with the converse problem, we wish to squeeze the normal world field of view into a smaller solid angle. This is easily accomplished, of course, with a minifying telescope, and such is one weapon in the ordinary armamentarium of the RP patient. The problem is that the angular subtense of all elements in the field of view is reduced. Even though you see more of the things one needs to interact with in moving about (door frames, walls, stairs, etc.), the reduced size of objects may give difficulty in reading signs or otherwise resolving the world. Our approach is to give spatially varying magnification, so that localization of gross objects is possible, but full central magnification is maintained. Perhaps in Spring 1994 we will begin field tests with the Remapper in locations like grocery stores, to see if visual functionality is improved.

JOINT TRANSFORM TRACKING

When NASA was recently contemplating autonomous lunar and planetary landings, this project proposed two techniques for lander vision, and we set about demonstrating certain of the technical elements. The first technique was navigation as guided by image correlation, in which images of landmark features would provide reference to absolute geometric coordinates. The second was image fixation by joint Fourier transform correlation, in which unmodeled image structure correlates with itself and shows sequential error in pointing. It is the JTC, as applied to tracking retinal motions, where we have been vigorously spinning off to medical practice.

Dynamics of Eyeball Tracking

Tracking the human eyeball is very challenging. Consider the problem from the other side for a moment; think how quickly you can jerk your eyes over a really large angular distance and settle your viewpoint in on a small object that has caught your attention. Now consider keeping a laser beam fixated on an individual structure within the retina during that motion, to a precision at the same resolution of the smallest object you can resolve. The harmonic content of the eyeball motion extends to as high as 170 Hz, with speeds up to several hundred degrees per second. Those are really astounding figures. Nyquist sampling theory indicates immediately that to track the motion, about 400 independent measurements per second are necessary. If the eyeball motion is able to break lock (e.g. if the eye jerks during a blink), then it is important to know that track lock has broken and in which direction to move to reacquire, but the precision requirements on knowing the translation are reduced since the surgical laser will be inhibited immediately upon loss of track. The optical engineers in the project (the author cheerfully admits to this persuasion) think that the JTC is the preferable method because of the ease with which two qualities are achieved: spatially variable resolution, and a wide field of regard. If tracking is done by digital methods by time-domain correlation, the size of the field of regard is directly impacted by the serial nature of the digital correlation. In contrast, optical processing is inherently parallel, and the size of the field of regard is limited only by the number of pixels in the spatial light modulators. The project currently is headed for a showdown between digital and optical implementation, as the digital method (if practical) would be slightly less expensive to implement.

THE JOHNSON SPACE CENTER PROGRAM

The Hybrid Vision project at JSC has several civil servants (Richard Juday, Tim Fisher, Shane Barton, and Jennifer Yi), NRC post-doctoral fellow Colin Soutar, and in-house contractor personnel employed by Lockheed Engineering and Sciences Corporation (Stanley Monroe, Carlton Faller). Additionally we have either active or recently concluded contracts, fellowships, and grants at a number of universities and corporations (University of Missouri, Carnegie Mellon, Tennessee Technological University, University of Colorado at Boulder, University of Houston, Physical Optics Corporation, Boulder Nonlinear Systems, Physics Innovations) and working relationships with other Government laboratories (Army Missile Command, Air Force Rome Laboratory, ARPA, Air Force Wright Laboratory, Sandia), and others. The project bibliography for the past seven or eight years has over fifty entries including four issued patents (others in work). We are active in image warping, optimal filter theory, optical correlator architectures and applications, spatial light modulator development, with specific thrusts in robotic vision and human low vision. The author will provide copies of the bibliography upon request.

ACKNOWLEDGEMENTS

Financial, moral, and technical support from our military colleagues, mentioned just previously, is particularly appreciated.

REFERENCES

1. U. S. Patent 5,029,220; Richard D. Juday; Optical joint correlator for real-time image tracking and retinal surgery; Jul. 2, 1991.
2. Jerome Knopp and Richard D. Juday, "Optical joint transformation correlation on the DMD", Proc. SPIE 1053, 208-215 (1989).
3. Eddy C. Tam, Francis T. S. Yu, Don A. Gregory, and Richard D. Juday, "Autonomous real-time objects tracking with an adaptive joint transform correlator", Optical Engineering 29, 314-320 (April 1990).
4. Eddy C. Tam, Francis T. S. Yu, Aris Tanone, Don A. Gregory, and Richard D. Juday, "Data association multiple target tracking using a phase-mostly liquid crystal television", Optical Engineering 29, 1114-1121 (September 1990).
5. K. L. Schehrer, M. G. Roe, and R. A. Dobeon, "Rapid tracking of a human retina using a nonlinear joint transform correlator", SPIE Proceedings vol. 1959, April 1993 (Orlando).
6. U.S. Patent 5,067,019; Richard D. Juday and Jeffrey B. Sampsel; Programmable remapper for image processing; Nov. 19, 1991.
7. Timothy E. Fisher and Richard D. Juday, "A programmable video image remapper", Proc. SPIE 938, 122-128 (1988).
8. U.S. Patent 5,208,872; Timothy E. Fisher; Programmable Remapper with single flow architecture; May 4, 1993.
9. Timothy E. Fisher and Richard D. Juday, "An improved architecture for video rate image transformations", Proc. SPIE 1098, 224-231 (1989).
10. Richard D. Juday and David S. Loshin, "Some examples of image warping for low vision prosthesis", Proc. SPIE 938 163-168 (1988).
11. Richard D. Juday and David S. Loshin, "Quasiconformal remapping for compensation of human visual field defects: advances in image remapping for human field defects", Proc. SPIE 1053, 124-130 (1989).
12. David S. Loshin and Richard D. Juday, "The programmable remapper: Clinical applications for patients with field defects", Optometry and Vision Science 66, 389-395 (1989).
13. Richard D. Juday, Alan T. Smith, and David S. Loshin, "Human low vision image warping: channel matching considerations", Proc. SPIE 1705 (1992).
14. David S. Loshin, Janice Wensveen, Richard D. Juday, and R. Shane Barton, "Design of reading tests for low vision image warping", Proc. SPIE 1961, Orlando, April 1993.
15. Janice Marie Wensveen, "Reading Rate with Simulated Central Scotoma", Master's thesis, University of Houston College of Optometry, August 1993.

16. Anonymous, "High-Tech Help for Low Vision", NASA Tech Briefs vol. 17 no. 2, pp. 20-22 (April 1993).
17. Richard D. Juday, "Optimal realizable filters and the minimum Euclidean distance principle", Applied Optics 32, 5100-5111 (10 September 1993).
18. Colin Soutar, Stanley E. Monroe, Jr., and Jerome Knopp, "Complex characterization of the Epson liquid crystal television", Proc. SPIE 1959, Orlando, April 1993.
19. Colin Soutar, Stanley E. Monroe, Jr., and Jerome Knopp, "Measurement of the complex transmittance of the Epson liquid crystal television", Optical Engineering (accepted).
20. Richard D. Juday and Brian Bourgeois, "Convolution-controlled rotation and scale invariance in optical correlation", Proc. SPIE 938, 198-205 (1988).

516-52
2452
P. 8

**ANALYSIS AND AN IMAGE RECOVERY ALGORITHM
FOR ULTRASONIC TOMOGRAPHY SYSTEM**

**Michael Y. Jin
Jet Propulsion Laboratory
California Institute of Technology
Pasadena, California 91109**

ABSTRACT

The problem of an ultrasonic reflectivity tomography is similar to that of a spotlight-mode aircraft Synthetic Aperture Radar (SAR) system. The analysis for a circular path spotlight mode SAR in this paper leads to the insight of the system characteristics. It indicates that such a system when operated in a wide bandwidth is capable of achieving the ultimate resolution; one quarter of the wavelength of the carrier frequency. An efficient processing algorithm based on the exact two dimensional spectrum is presented. The results of simulation indicate that the impulse responses meet the predicted resolution performance. Compared to an algorithm previously developed for the ultrasonic reflectivity tomography, the throughput rate of this algorithm is about ten times higher.

INTRODUCTION

The geometry of a two dimensional reflectivity tomography can be depicted in Figure 1.a. It consists of a water tank of dimensions greater than that of the object to be imaged. A moving transducer and a receiver are scanning over the outer circle. Ultrasonic pulses are emitted from the transducer. Signals reflected from the object are sensed by the receiver and collected for further processing. For simplification, we shall consider that the transducer and receiver are collocated. Furthermore, the object shall be an idealized reflecting medium in which the velocity of the sound is constant, the medium is weakly reflecting, and absorption is uniform over the region of interest [1].

A spotlight mode SAR in circular path as shown in Figure 1.b is analogous to the reflectivity tomography system addressed here. In this SAR system, the altitude is assumed to be much smaller than the radius of the flight circle. The pulses transmitted periodically from the radar is a wide band electro-magnetic wave traveling at a constant speed in the atmosphere. The signal reflected from the ground spot within the radar footprint is received by the same radar used for emitting radar pulses. Echo signals are demodulated by the carrier frequency, converted into discrete digital format, and stored in an on-board recorder. The stored data will be processed by an on-board or ground based processor to reveal the ground image. The design of the radar pulse and echo timing for both systems must be coherent.

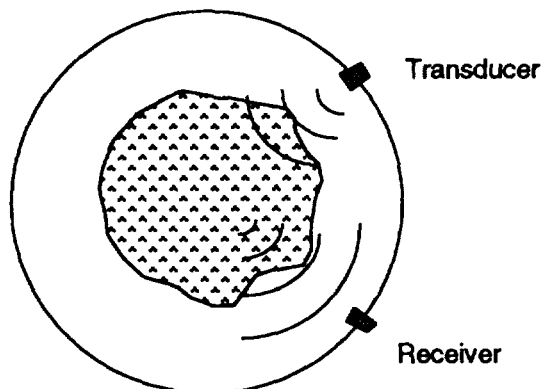


Figure 1.a The reflectivity tomography system

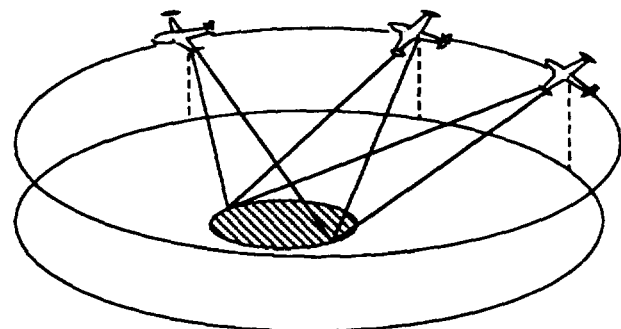


Figure 1.b A circular path spotlight mode SAR

Since the analysis and processing algorithm description for such systems were originated from the spotlight-mode SAR system, it will also be given in the following paragraph. However, it should be noted that both the analysis and processing algorithm are applicable to the ultrasonic reflectivity system as shown in Figure 1.a.

ANALYSIS

A wide azimuth beam SAR can offer higher resolution or wider azimuth viewing angle; two factors that help better characterize the backscattering property of targets for various scientific applications. One disadvantage of a wide beam SAR is that a much higher pulse repetition frequency (PRF) is usually required since PRF is proportional to the radar beam angle. This problem can be resolved using a spotlight-mode concept: steering a narrow beam SAR to a fixed spot on the ground. The drawback of a spotlight-mode SAR is its limited coverage.

A spotlight-mode SAR can be operated from a circular flight path as shown in Figure 1.b. This type of spotlight-mode SAR offers several advantages: (1) relatively easy to achieve the ultimate azimuth resolution, (2) it allows a full 360 degree of viewing angle, (3) there is no need to steer the radar, and (4) the required PRF can be scaled down according to the ratio between the radius of the radar spot to the radius of the flight path.

For an aircraft SAR in a circular path as shown in Figure 2, the slant range history of a point-target is given by

$$R(\theta_1) = \sqrt{A + B \cdot \cos \theta_1}$$

where

$$A = R_0^2 + 2R_b^2 - 2R_0R_b \cos \theta_e, \text{ and } B = 2R_b(R_0 \cos \theta_e - R_b).$$

In the above equations, θ_e is the radar elevation angle, R_0 is slant range between the radar and the target at the beam center, R_b is the radius of the flight path, and θ_1 is the angle between the radar at the minimum range to the target, the center of the flight circle, and the radar at time of interest. Since time is directly proportional to θ_1 , this function can also be expressed using time as the variable,

$$R(t) = \sqrt{A + B \cdot \cos\left(\frac{v}{R_b} t\right)}$$

where v is the speed of the aircraft. Let Z denotes the altitude of the aircraft. It is obvious that R_0 and Z are related by $Z = R_0 \sin \theta_e$. $Z=0$ is a special case that exactly follows the geometry of the ultrasonic reflectivity tomography as shown in Figure 1.a. Below, we shall denote the distance between the target and the center of the path projection on the ground as R_T , which is equal to $R_b - R_0 \cos \theta_e$.

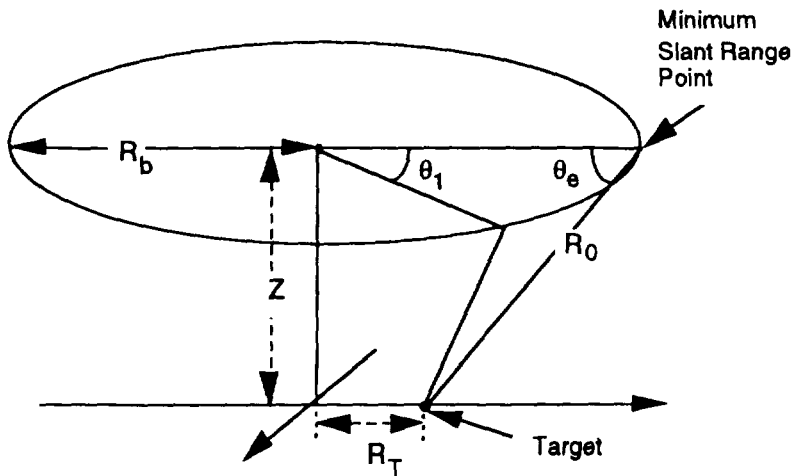


Figure 2. The spotlight SAR platform geometry

To provide better insight into the spot-light SAR characteristics, it is assumed that the radar beam width is unlimited such that any target within the path projection is illuminated all the time during mapping. To determine the azimuth resolution, it is necessary to determine the maximum Doppler bandwidth. This can be accomplished by evaluating the zero crossing time of the Doppler frequency rate. The Doppler history is the derivative of the slant range, i.e.

$$f_d(t) = \frac{-d(2R(t)/\lambda)}{dt} = \frac{k_0 B v}{2\pi R_b} \sin\left(\frac{vt}{R_b}\right) R^{-1}(t)$$

where k_0 is the wave number and is equal to $2\pi/\lambda$. λ is the wave length corresponding to the center frequency of the radar pulse. Plots of both the slant range history and Doppler history are given in Figure 3a and b. The history of the Doppler frequency begins with 0Hz at the minimum slant range point, decreases to the minimum Doppler (negative value), increases back to 0Hz at the maximum slant range point, keeps increasing up to the maximum Doppler, and then decreases back to 0Hz after a complete cycle. Based on this, one can divide a complete circle into two apertures with equivalent bandwidth. The aperture with a Doppler ranging from its minimum to its maximum and consisting of the minimum slant range point is referred to as the principle aperture. The other aperture spanning the rest of the flight path is referred to as the complement aperture.

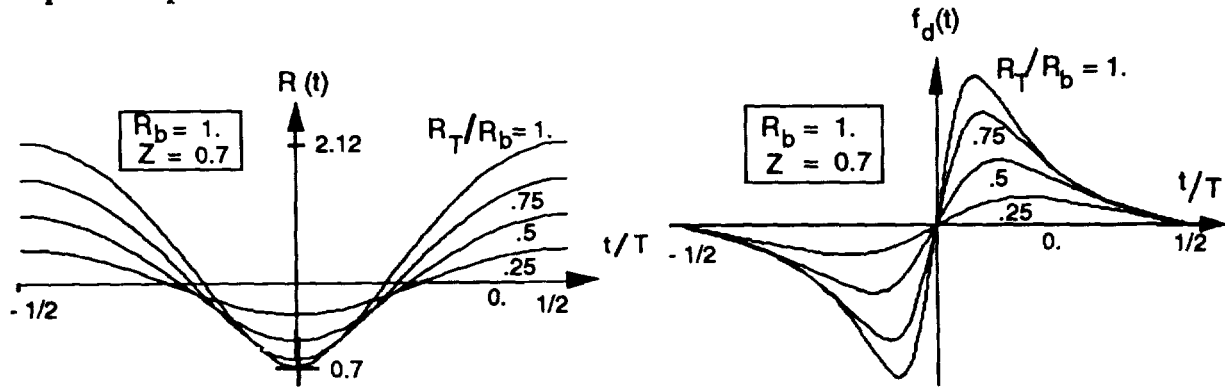


Figure 3.a Slant range history plots

Figure 3.b Doppler frequency history plots

The Doppler frequency rate variation is given by

$$f_r(t) = \frac{df_d}{dt} = \frac{k_0 B v}{2\pi R_b} \left(\frac{v}{R_b} \cos\left(\frac{vt}{R_b}\right) R^{-1}(t) + \frac{Bv}{2R_b} \sin^2\left(\frac{vt}{R_b}\right) R^{-3}(t) \right)$$

The solution of the time at which f_r equals zero is given by

$$t|_{f_r=0} = \frac{R_b}{v} \cos^{-1} \left(\frac{-A \pm (A^2 - B^2)^{1/2}}{B} \right)$$

Therefore, the Doppler bandwidth, denoted as F , is given by two times the absolute value of the Doppler at one of the solution given above. Since F varies as a function of both the aircraft altitude Z and target radius R_T , it is given by

$$F(Z, R_T) = \frac{2\sqrt{2}v}{\lambda R_b} (A^2 - B^2)^{-1/4} \sqrt{|A^2 - B^2 - A\sqrt{A^2 - B^2}|}$$

The azimuth resolution is thus given by the reciprocal of the bandwidth multiplied with the effective velocity $(R_T/R_b)v$, or

$$\Delta X(Z, R_T) = \left(\frac{R_T}{R_b} v \right) \frac{1}{F(Z, R_T)}$$

The variations of the resolution and the Doppler bandwidth as a function of the target location are plotted in Figure 4.a and Figure 4.b. It should be noted that these plots also include the targets located outside of the vertical cylinder containing the orbit because they can also be imaged as long as range ambiguity can be avoided. It is interesting to see that the ultimate resolution of $\lambda/4$ can be achieved for targets falling on the orbit plane and bounded by the circular orbit. The resolution width increases linearly as targets shift outside of the orbit in the radial dimension. The Doppler bandwidth decreases as the targets approach the center of the orbit. This implies that for targets located on the orbit plane and bounded by the orbit, the required PRF is proportional to the distance from target to orbit center.

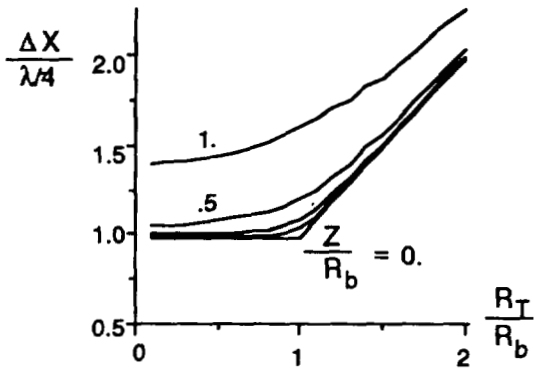


Figure 4.a Resolution vs target location

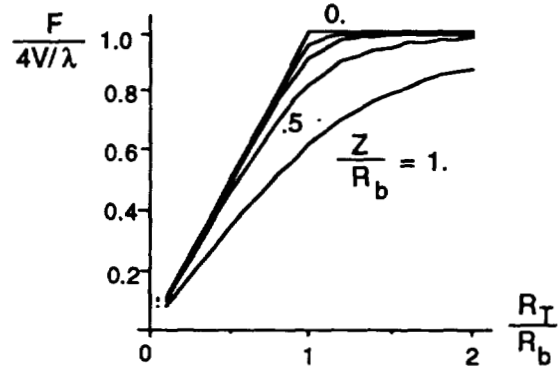


Figure 4.b Bandwidth vs target location

Consider a special case where $Z=0$ and R_T approaches R_b . According to the bandwidth equation given above, we may find that the required PRF is equal to $4v/\lambda$. This indicates that the required sampling spacing is exactly $\lambda/4$ which equals to the ultimate azimuth resolution. The time interval of the principle aperture is given by

$$T_p(Z, R_T) = \frac{2R_b}{v} \cos^{-1} \left(\frac{-A + (A^2 - B^2)^{1/2}}{B} \right)$$

It will be more convenient to express the aperture time interval as a value normalized by the period of a complete flight circle. The complexity of SAR processing is usually determined by the number of samples within the aperture or the value of the time-bandwidth product TBP given by $TBP(Z, R_T) = T(Z, R_T)F(Z, R_T)$. The time interval and time-bandwidth product of the principle aperture are shown in Figure 5.a and 5.b.

In summary, the analysis in this section leads to the determination of the PRF for operating the spotlight radar, the predicted resolution, the time interval of the aperture and the time-bandwidth product to be selected for signal processing.

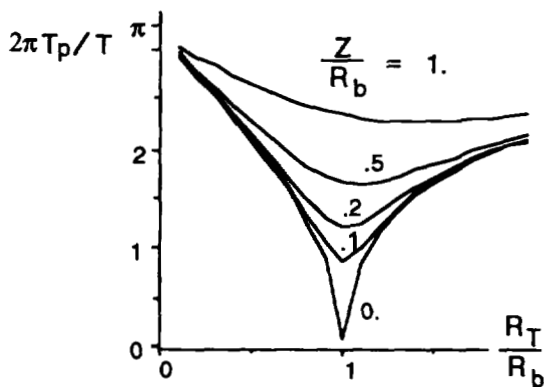


Figure 5.a Aperture Interval vs target location

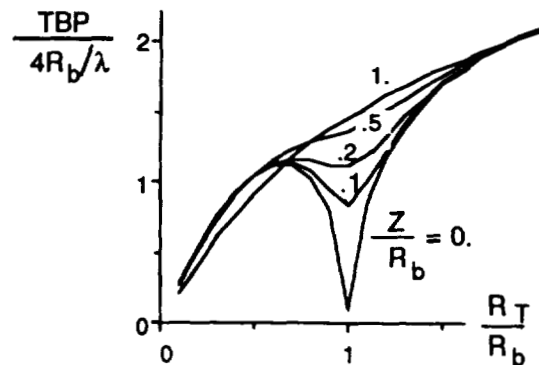


Figure 5.b Time-bandwidth product vs target location

PROCESSING ALGORITHM

Several algorithms were presented for processing spotlight-mode SAR data or the rotating object data. These algorithms include the well known range-Doppler algorithm applied to sub apertures, the backprojection processing method (Munson, et. al., [2]) commonly used in computer-aided tomography (CAT), and the polar format processing algorithm (Ausherman, et. al [3]). One essential assumption required for both the CAT and polar algorithms is that the dimension of the imaged area is much less than the radar to target distance. Other processing algorithms devised for imaging rotating object include a tomographic extension of Doppler processing algorithm (Mensa, et. al. [4]) and a range-Doppler processing algorithm (Walker, J. [5]). The first method is suitable only for imaging sparse arrays of objects due to its higher integrated sidelobe ratio (ISLR); and both algorithms also rely on the assumption of large radar to target distance. An exact solution for a circular aperture acoustic imaging system was presented by Norton [1]. This algorithm requires the implementation of a quasi fast Hankle transform which is not very efficient.

The difficulty in processing spotlight-mode SAR data collected from a circular path is that the Doppler history of a point target involves many higher order terms and that the depth of focus is very shallow. To overcome the first problem, the algorithm proposed here make use of an exact 2-D spectrum of a point target (Jin, 1992 [6]) in a range Doppler like processing approach. To overcome the second problem, this algorithm updates its reference function as frequently as required.

According to [6], the magnitude and the phase of a reference spectrum are given by

$$A(\omega_r, \omega) = \sqrt{2\pi} \left| \frac{d^2(-(\omega_r + \omega_0) \cdot 2R(t_s) / c)}{dt^2} \right|^{-1/2}$$

$$\psi(\omega_r, \omega) = \exp \left\{ j \left(\frac{\cos^{-1}(\alpha(\omega_r, \omega)) \omega}{v / R_b} - 2k_r \sqrt{A + B\alpha(\omega_r, \omega)} - \frac{\pi}{4} \right) \right\}$$

where ω is the azimuth angular frequency, ω_r is the range angular frequency, ω_0 is the angular frequency of the carrier, K_r is equal to ω_r/c , where c is the speed of light, and

$$\alpha(\omega_r, \omega) = \left(-\frac{\omega^2}{k_r^2} \pm \sqrt{\frac{\omega^4}{k_r^4} + 4 \frac{\omega^2 v^2}{k_r^2 R_b^2} (B - R_0^2) + 4 \frac{\omega^4}{k_r^4} B^2} \right) / 2 \frac{v^2}{R_b^2} B$$

The energy distribution of the 2-D spectrum of a point target is given in Figure 6. It can be seen that the amount of area with energy is proportional to the distance from the target to the center point.

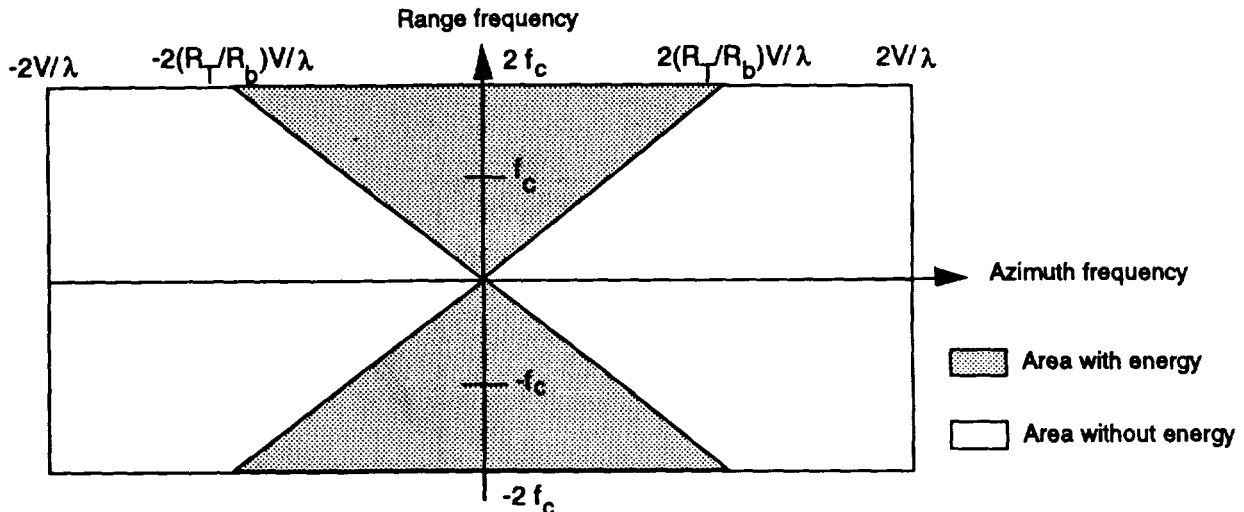


Figure 6. The 2-D spectrum of a point target

The basic correlation steps for the spotlight-mode processing are summarized below.

- (1) Perform subsampling for the echo pulses according to the radius of the spot area. This step is not required if the PRF of the sensor is tuned to that radius such that there is no redundant data. Transform the SAR data into its spectrum by a 2-D FFT process.
- (2) Perform a 2-D SAR correlation. For each azimuth line with a constant range position, a reference spectrum is generated according to equation (1). Correlation is performed by multiplying the data spectrum and the conjugated reference, averaging in range, and performing an inverse azimuth FFT. This is repeated for each azimuth line.
- (3) Perform geometric resampling to correct for the geometry and grid spacing. The mapping between image pixels generated from step (2) and points on the ground for a spotlight-mode SAR is given in Figure 7.

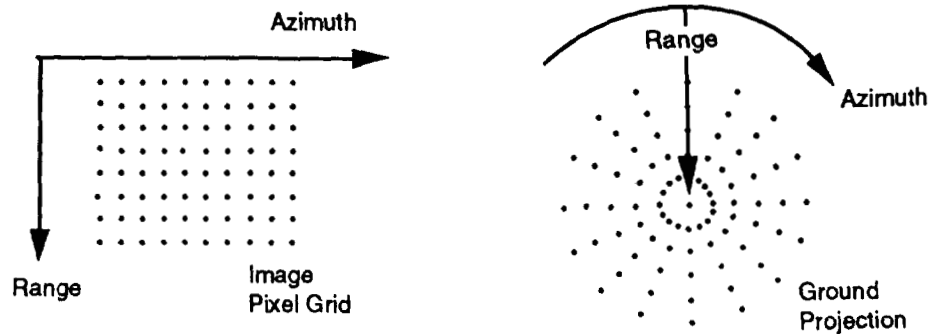


Figure 7. Image pixel to projection mapping in a spotlight mode SAR

COMPUTATION EFFICIENCY

The algorithm described above takes the advantage of computation efficiency of FFT operations. Therefore, it is a highly efficient algorithm as compared to a previous algorithm proposed by Norton [1]. To illustrate this, the Norton's algorithm is briefly reviewed first.

Let $f(r, \theta)$ denotes the reflectivity of the medium and $g(r, \theta)$ denotes the echo signals received in a polar coordinate with radial position r and angle θ . $f(r, \theta)$ can be recovered by the following three steps:

- (1) Perform spherical harmonic expansion for $g(r, \theta)$ for its coefficients,
$$g_n(r) = \frac{1}{2\pi} \int_0^{2\pi} g(r, \theta) e^{-in\theta} d\theta$$
- (2) Get the spherical harmonic expansion coefficients $f_n(r)$ of $f(r, \theta)$ by
$$f_n(r) = H_n \left\{ \frac{1}{J_n(Rz)} H_0 \left\{ \frac{g_n(\rho)}{2\pi\rho} \right\}_z \right\}_r$$
- (3) Reconstruct $f(r, \theta)$ from $f_n(r)$ by
$$f(r, \theta) = \sum_{n=-\infty}^{\infty} f_n(r) e^{in\theta}.$$

In the second step, Hankle's transform of the 0-th order and n-th order are implemented by a quasi fast Hankle transform. It is assumed that in both algorithms the reference functions are generated before processing and permanently stored in the computer memory. The computation efficiency will be examined only on the amount of complex multiplies performed to yield an image of a diameter of $2N$ pixels. These results are summarized in Table I and Table II.

Table I. Amount of complex multiply in spotlight mode algorithm

PROCESSING STEP	2-D FFT FOR ECHO DATA	REFERENCE MULTIPLY	1-D INVERSE FFT
NUMBER OF MULTIPLY	$\pi N^2 \text{Log}_2 \pi N$ $+\pi N^2 \text{Log}_2 N$	$\pi N^3 / 2$	$\pi N^2 \text{Log}_2 \pi N$

Table II. Amount of complex multiply in Norton's algorithm

PROCESSING STEP	HARMONIC EXPANSIONS	REFERENCE MULTIPLY	1-D HANKLE TRANSFORMS
NUMBER OF MULTIPLY	$2\pi N^2 \text{Log}_2 \pi N$	$\pi N N_h$ $N_h = K_1 N \text{Ln}(K_2 N)$	$2N_h \text{Log}_2 N_h$ $N_h = K_1 N \text{Ln}(K_2 N)$

The disadvantage of the quasi fast Hankle transform is that data samples must be oversampled from N to $N_h = K_1 N \text{Ln}(K_2 N)$, where K_1 and K_2 are constants. This oversampling increase the amount of data and the amount of multiplies. The computation bottleneck of the spotlight algorithm is in the reference multiply which is proportional to N^3 . For N being 128 to 512 points, the amount of multiplies in the spotlight algorithm is from 1/10 to 1/4 times of that in Norton's algorithm. Since a large portion of the point target spectrum has no energy as shown in Figure 6, the amount of multiply can further be reduced by a factor of two in reference multiply and inverse FFT processes.

SIMULATION

A simulation was performed to test the proposed algorithm and to verify the analysis on the azimuth resolution. Plotted in Figure 7.a and 7.b. are the impulse responses of two aircraft spotlight systems, both with zero altitude. The first one has a range bandwidth being twice the carrier frequency such that the range resolution is comparable to the azimuth resolution. The second system has a range bandwidth of .15 times the carrier frequency. The 3-dB resolutions in range and azimuth of the first system are very close to $\lambda/4$. The 3-dB resolutions of the second system are also close to $\lambda/4$. However, it has a much worse integrated sidelobe ratio.

Range Bandwidth = 2 x Radar Carrier Frequency

Range Bandwidth = 0.15 x Radar Carrier Frequency

Full Resolution Processing over the Principle Aperture

Full Resolution Processing over the Principle Aperture

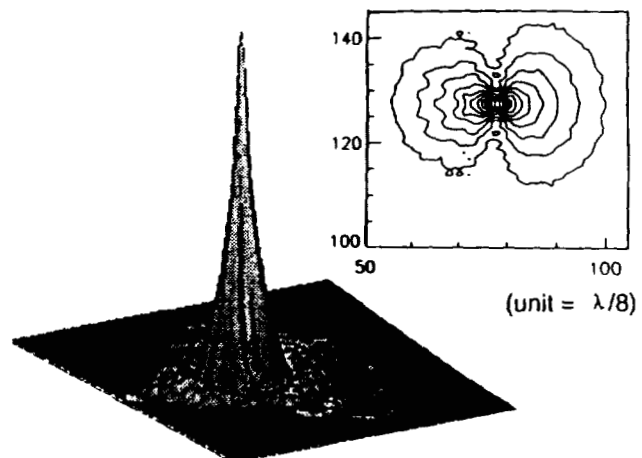
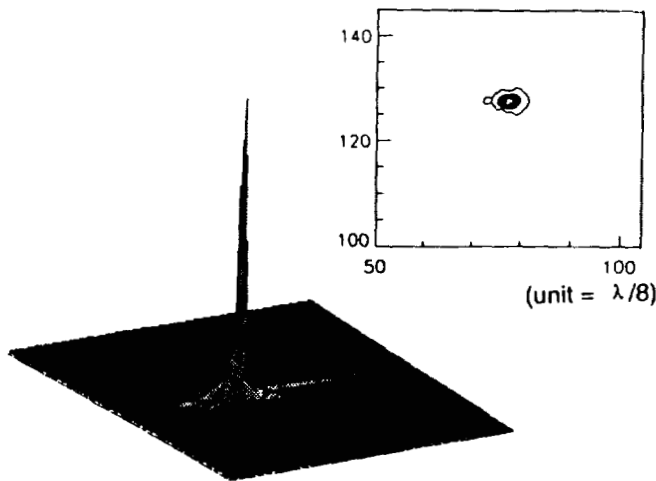


Figure 7.a Spotlight SAR impulse response

Figure 7.b Spotlight SAR impulse response

CONCLUSION

The spotlight-mode aircraft SAR in a circular flight path has been analyzed in terms of resolution, bandwidth, aperture arc, and the time-bandwidth product. An exact and efficient processing algorithm is proposed to recover spotlight-mode SAR images. The simulation result of the point-target response indicates that for full azimuth resolution processing both the azimuth and range 3-dB resolution can achieve the ultimate resolution of $\lambda/4$, regardless of the range bandwidth. This algorithm is directly applicable to ultrasonic reflectivity tomography system. With further optimization in computation efficiency, the processing throughput rate shall be about ten times faster than a previously proposed algorithm.

ACKNOWLEDGMENTS

The research described in this paper was carried out by the Jet Propulsion Laboratory, California Institute of Technology, under a Contract with the National Aeronautics and Space Administration.

Reference:

- [1] Norton, Stephen J., "Reconstruction of a Two-Dimensional Reflecting Medium over a Circular Domain: Exact Solution", *J. Acoust. Soc. Am.*, 67(4), 1980.
- [2] Munson, D. C., O'Brien J. D., and Jenkins, W. K., "A Tomographic Formulation of Spotlight-Mode Synthetic Aperture Radar", *Proceedings of the IEEE*, Vol. 71, No. 8, August, 1983.
- [3] Ausherman, Dale A., et. al., "Developments in Radar Imaging", *IEEE Trans. on Aerospace and Electronic Systems*, Vol. AES-20, No. 4, July, 1984.
- [4] Mensa, D., Heidbreder, G., and Wade, G., "Aperture Synthesis by Object Rotation in Coherent Imaging", *IEEE Trans. on Nuclear Science*, Vol. NS-27, No. 2, April 1980.
- [5] Walker, Jack L., "Range-Doppler Imaging of Rotating Objects", *IEEE Trans. on Aerospace and Electronic Systems*, Vol. AES-16, No. 1, January, 1980.
- [6] Jin, Michael Y., "An Exact Processing Algorithm for Wide Beam Spaceborne SAR Data", *ISY Conference, ERS-1/JERS-1 Workshop*, Tokyo, November, 1992.

517-52

2453

0 5
1-

N94-30457

COMPOSITE REDESIGN OF OBSTETRICAL FORCEPS

Seth W. Lawson
NASA Marshall Space Flight Center
MSFC, AL 35812

Stan S. Smeltzer III
NASA Marshall Space Flight Center
MSFC, AL 35812

ABSTRACT

Due to the increase in the number of children being born recently, medical technology has struggled to keep pace in certain areas. In these areas, particular needs have arisen to which the subject of this paper is directed. In the area of obstetrics, the forceps design and function has remained relatively unchanged for a number of years. In an effort to advance the technology, NASA Marshall Space Flight Center has been asked by the obstetrical community to help in a redesign of the obstetric forceps. Traditionally the forceps design has been of tubular stainless steel, constructed in two halves which interlock and hinge to provide the gripping force necessary to aid in the delivery of an infant. The stainless steel material was used to provide for ease of cleaning and sterilization. However, one of the drawbacks of the non-flexible steel design is that excessive force can be placed upon an infants head which could result in damage or injury to the infant. The redesign of this particular obstetric tool involves applying NASA's knowledge of advanced materials and state of the art instrumentation to create a tool which can be used freely throughout the obstetrics community without the fear of injury to an infant being delivered.

INTRODUCTION

The major function of the Technology Utilization office at NASA Marshall Space Flight Center(MSFC) is to aid individuals or industry representatives that require assistance in solving technical problems. Such a request was given to NASA's TU office by Dr. Jason Collins, a private practicing OBGYN from Slidell, Louisiana. The request was for assistance in redesigning the current stainless steel Simpson type forceps, so as to reduce the risk of injury to infants and mothers during a forceps type delivery, while at the same time keeping as much of the traditional appearance and functionality of the forceps as possible.

The forces induced onto the fetal head during a forceps delivery are primarily the traction or pull force (tensile) and the compressive force needed to overcome the friction or resistance of the maternal tissues. According to previous studies by Fleming, Pearse, Wylie and Ullery, the major factors which influence the performance of forceps are (1) the structure of the instrument; (2) the fetal head which the forceps must grasp; (3) the resistance of the maternal tissues; and (4) the force applied by the attendant. To further complicate this we must also consider parity, age of the mother, position of the infant, station and infant size. To address these problems, alternate delivery aids other than forceps have been constructed. One example is that of the Vacuum Extractor, however each has not been without its drawbacks. Though 40 percent less pull force is required with the Vacuum Extractor, suggesting an increase in safety in the area of cerebral compression, the possible advantage of the vacuum extractor may be offset by the potentially dangerous traumata which it may inflict on the fetal scalp¹.

Studies of the amount of pull force and compressive force applied to infants during delivery have been limited. Strain gages for measuring total force and calibrated instruments like the axis-tractionometer for measuring traction have been used with limited success to gain useful data with respect to measuring those forces imposed on the infant by the use of the forceps for delivery. Although no limits have been established, measurements from these field tests do give valuable data which can be used in this redesign effort^{2,3}.

APPROACH

Design

Composite materials have properties which can be tailored in the design to give even load distribution on an infants head for a given amount of input pressure applied to the handle by the delivering physicians hand. By using newly developed, state of the art instrumentation technology, fiber optic sensors can be embedded into the composite during manufacture which will be able to give the physician the ability to read the amount of compression load and tensile load he is applying to an infants head, and adjust as needed so that the delivery process will not result in injury to the infant. In addition, by utilizing the elasticity of the composite material and a tailored thickness along the length of the forceps, a fail-safe method can be achieved which will not allow the physician to place an unsafe amount of force upon an infants head under normal delivery conditions.

The major goal of this redesign effort was to provide a means by which instrumentation could be effectively incorporated into the existing obstetrical forceps configuration. A secondary desire was to provide a fail-safe method by which the compressive force applied to the fetuses head would be limited. The main goal will be accomplished by using a thermoplastic type material to mold a basic configuration which would allow state-of-the-art fiber optic instrumentation technology to be embedded within the forceps. By using a thermoplastic type material, structural fibers via a dry preform may also be added to increase the stiffness and strength of the hinge area as well as along the length of the forceps arms. Two fiber optic sensors will be embedded just below the surface of the forceps along each arm to provide both a reading for the compressive force at the tips and a tensile force as seen in Figure 1 below. The fiber optic strands will be located on the inner and outer surfaces of the arm to determine the bending moment at the point of maximum bending which in turn will provide the maximum compressive force exerted on the fetuses head. Design loads to be used in the detailed forceps design are five pounds (force) for the compressive loading and forty pounds (force) tensile force on the fetuses head which are well documented within the medical community². Using these loads an optimized design for the forceps will be produced centered around two criteria. The first criteria is that the curved section of the forceps that come into contact with the surface of the fetus head provide minor conformability yet are stiff enough that most of the bending due to compressive forces takes place in the forceps arms above the hinge. The second criteria is that when the handles come together (full compression) a maximum compressive force of five pounds be exerted at the forceps tips. The second criteria will be accomplished by using the elastic thermoplastic material and optimizing the cross-section of the forceps arms to produce the required bending deflection at the tip.

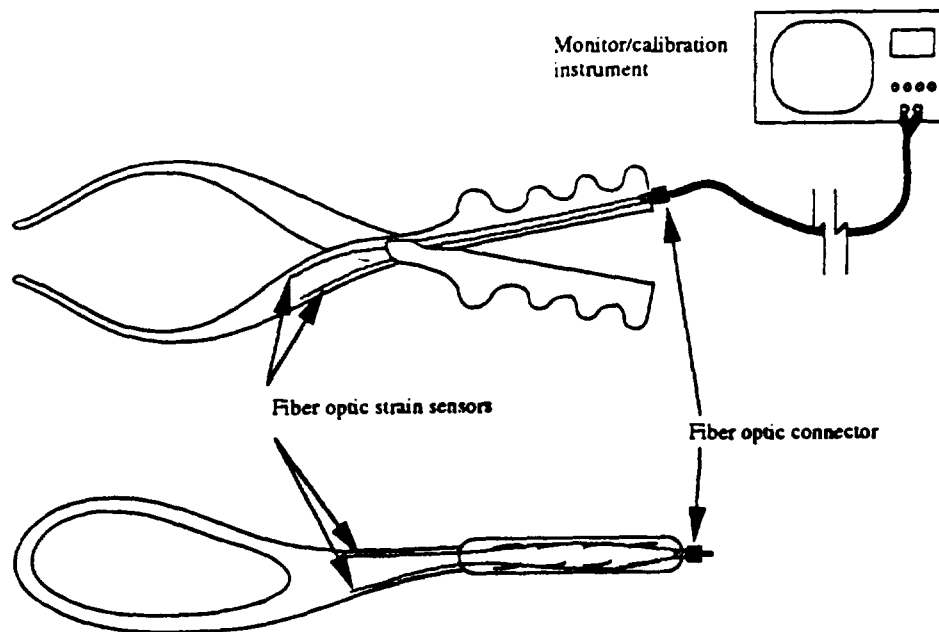


Figure 1. Typical Simpson type forceps with fiber optic strain sensors embedded into the composite.

The strain sensors selected to real time monitor the induced load will be embedded fiber optic grating reflectors. Dr. John Gilbert Ph.D. and Wei Su his associate, have developed a new technique using Bragg reflection gratings, with commercial fiber optics and modifying them to improve their ability to be used as strain sensors. Bragg reflection gratings and out-coupling taps for sensors are written holographically within the core of commercially available fibers. The process involves chemically germania doping the core of the optical fiber then writing in permanent holographic gratings. The gratings are made with a technique using interfacing beams of UV laser illumination on the side of the fiber. The formation of the grating forms a stop-band filter, as shown in Figure 2, by reflecting optical signals whose wavelength in the light guiding core is twice the grating spacing. This wavelength matching condition is known as the Bragg condition or Bragg Wavelength. When temperature and/or strain are applied to a section of fiber containing a grating, the grating spacing and index of refraction are modified and hence the Bragg wavelength changes. To separate the temperature and strain response, two grating elements may be required; one that is exposed only to the temperature and the other to both temperature and strain. The strain sensitivity of a fiber grating manifest itself through a change in grating spacing and the change in refractive index from the photoelastic effect. For a fiber grating placed under tension or compression, the change in Bragg wavelength per unit wavelength is typically 74% of the strain; i.e. $\delta\lambda/\lambda = 0.74\varepsilon$. To act as a generic sensor the fiber grating can be attached to or embedded in a material or on a diaphragm that changes shape under the action of the desired measureand. In an application as a strain sensor, for example, fiber gratings can be conveniently embedded in composite materials during fabrication for monitoring their cure, and later for monitoring their response in a completed structure⁴.

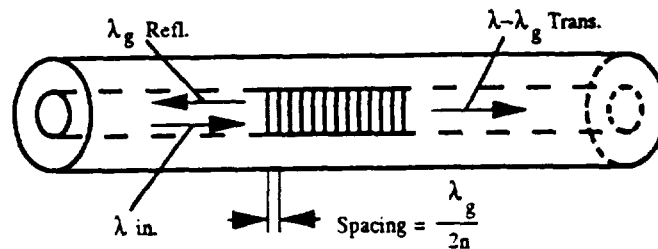


Figure 2. Illustration showing fiber grating reflector and the Bragg condition for reflection.

Material

The preliminary choice of material was between a thermoplastic composite which could be tailored to achieve a glass transition temperature (TG) high enough to facilitate sterilization in the current medical type autoclave, or which would be stable enough to allow sterilization by an alternate method like Beta radiation sterilization. The materials investigated which have a TG high enough to allow sterilization at autoclave temperatures were Polyetheretherketone (PEEK) and a Polyimide thermoplastic manufactured by Du Pont Polymers.

The other thermoplastic materials under consideration were three medical grade thermoplastics manufactured by NOVACOR Chemicals Inc. The materials being considered are ZYLAR[®] ST 94-560, ZYLAR[®] 93-546, AND NAS[®] 21. Each of these materials has been tested with Beta radiation sterilization and meet the USP XXI criteria for Class VI plastics for use in medical applications. The ZYLAR resins require little or no pre-drying when injection molded or extruded, which translates to savings in terms of machinery and energy costs. In addition, they can be blended with up to 15% regrind with no loss in color, clarity or physical properties, for a more complete utilization of the material without weakening the molded part. Plastics are playing an increasingly important role in medical applications, where a material's ability to withstand repeated radiation sterilization without yellowing or property loss is critical. Test data from the manufacturer indicate that ZYLAR resins exhibit less discoloration following Gamma and electron beam sterilization than other medical grade plastics, and will withstand the effects of alcohol exposure with no loss of key properties. These characteristics, as well as their good flow and molding

properties, helped to establish these materials as the materials of choice for use in the forceps redesign. These materials are all clear impact-grade thermoplastic resins and some of their typical properties are listed below in Table 1.

All data is for nominal 1/8 in. thick specimens.

Properties	NAS [®] 21	ZYLAR [®] 93-546	ZYLAR [®] ST 94-560
Tensile Strength, break.(psi)	8.8x10 ³	5.0x10 ³	3.9x10 ³
Tensile Modulus. (psi)	4.8x10 ⁵	3.3x10 ⁵	2.9x10 ⁵
Elongation. break, (%)	2.5	30	80
Flexural Strength, break.(psi)	13.7x10 ³	8.0x10 ³	8.3x10 ³
Flexural Modulus. (psi)	4.4x10 ⁵	3.2x10 ⁵	3.1x10 ⁵
Mold Shrinkage (in/in)	.002 - .006	.004	0.004
Water Absorption (24hr) (%)	0.11	0.1	0.1

Table 1. Properties of NOVACOR Thermoplastic material candidates.

Fabrication

The preferred method of manufacture for the forceps is by molding. The molding process can easily facilitate the use of the embedded fiber optic instrumentation as well as the use of any reinforcing fibers. Reinforcing fibers can be used to strengthen any portion of the forceps, i.e. the fulcrum or pivot point, by inserting the reinforcing fibers as a preform prior to molding, thereby achieving the proper stiffness and flexural properties. The fiber optics which are to be embedded can also be installed into the preform to hold it properly in place during molding.

RESULTS AND DISCUSSION

Testing

Once a prototype of the composite forceps has been built, complete with the embedded instrumentation, it must be tested in the laboratory, then ultimately in the clinical environment. The laboratory tests will be conducted in conjunction with Dr. John Gilbert Ph.D. and Wei Su of Optechnology, Inc., and will be performed at both the Optechnology, Inc. optics laboratory and NASA Marshall Space Flight Center. Once confidence is gained with the function of the prototype and its instrumentation, clinical field tests will be performed by Dr. Jason Collins at his clinic in Slidell, Louisiana.

Marketing

Following the successful testing of the prototype in the clinical environment, attention will be turned to the marketing of the product for use in the obstetrical community. As part of the design of the composite forceps the use of relatively inexpensive, high quality commercial materials and instrumentation allow the forceps to be relatively inexpensive as a unit. The high cost associated with this particular product would be the initial set up involving the purchase of the monitor/calibration device. The forceps themselves would arrive individually packaged as a sterile unit. When needed for use in a delivery, the package could be opened, the instrument quickly checked for calibration and then used and discarded into a container supplied by the manufacturer. The physician would then only be required to send the used forceps back to the manufacturer where they could be sterilized, the instrumentation checked and each unit checked for fatigue or microcracking, then repackaged for shipment back to the medical facility for reuse. Once the life cycle of the instrument is reached it could be destroyed and a new unit sent in its place. This alleviates the physician from the task of sterilization and handling of the used or contaminated instrument.

CONCLUDING REMARKS

Although this redesign attempts to make the use of the obstetrical forceps less complex and intends to reduce the amount of fetal injury during forceps deliveries, its use in the clinical environment must be combined with the knowledge and skill of the attending obstetrician. All of the elements which combine to contribute to the function of obstetrical forceps are interdependent and cannot be separated from one another. The obstetrician must be aware of the instrument, the resistance, and the force applied, and use this in conjunction with his knowledge of the delivery process. Comprehension of these factors and his ability to properly use these delivery tools are key ingredients in conducting a successful and safe forceps delivery.

REFERENCES

1. Mishell, Daniel Jr., M.D. and Kelly, John V. M.D. The Obstetrical Forceps and the Vacuum Extractor: An Assessment of their Compressive Force. *University of California Medical Center, Los Angeles 24, California.*
2. Ullery, John C. M.D., Teteris, Nicholas J. M.D., Botschner, Andrew W. M.D., and McDaniels, Betty. Traction and compression forces exerted by obstetric forceps and their effect on fetal heart rate. *Columbia, Ohio 1963*
3. Wylie, Burdett M. D. Forceps traction, an index of birth difficulty. *Lakewood City Hospital, Cleveland Clinic, Fairview Park, Metropolitan General, and University Hospital all of Cleveland. 1962*
4. Morey, W.W. Jr., Dunphy, and Meltz, G. Multiplexing fiber bragg grating sensors. *United Technologies Research Center East Hartford, CT. 1991*

2454
P-8

DEVELOPMENT OF THE NASA/BAYLOR VAD

G.S. Aber, J.W. Akkerman, R.J. Bozeman, Jr., D.R. Saucier
NASA Johnson Space Center
Houston, TX. 77058

J.W. Bacak, P.A. Svejksky
Lockheed Engineering and Sciences Company
Houston, TX. 77058

G.A. Damm, K. Mizuguchi, G.P. Noon, Y. Nose, M.E. DeBakey
Baylor College of Medicine
Houston, TX. 77030

ABSTRACT

A cooperative effort between the NASA/Johnson Space Center (JSC) and the Baylor College of Medicine (BCM) has been underway since 1988 to develop a long-term implantable Ventricular Assist Device (VAD). The VAD is intended to boost the cardiac output of patients with deteriorated cardiac function. For many of these patients, the best alternative is heart transplantation. Heart transplantation is a complex and expensive procedure and usually requires a long waiting period for a donor heart. The condition of the patient often deteriorates during this waiting period which complicates the pre and post-operative care. Because of these factors, the need for a long-term implantable VAD for use as a bridge-to-transplant device or as a permanent assist device has become the focus of much research. The need for a VAD has been estimated at 50,000 to 60,000 patients per year in the United States alone[1]. A device which satisfies all the system performance and reliability requirements has yet to be achieved. However, the development of the NASA/Baylor VAD has progressed to state in which commercial viability can begin to be considered. The device is small, simple, efficient and reliable which meets all requirements for a totally implantable VAD.

HISTORY OF VAD'S

The first widely successful device used to pump blood was invented over fifty years ago by Dr. Michael DeBakey. This pump was called the roller pump and utilized flexible tubing squeezed by rollers to propel the blood. This type of pump is still used today during open heart surgery; however, advances with other types of pumps is rendering the roller pump obsolete. During the 1960 - 1980 time period, much work was focused on the development of a Total Artificial Heart (TAH). This work was culminated by the implantation of the Jarvik-7 TAH in six patients[2] during the 1980's, but with limited success. Attention has recently shifted toward the development of a VAD rather than a TAH for several reasons. A VAD operates in parallel with the natural heart by drawing blood from the ventricle (usually the left) and discharging into the descending aorta as shown in Figure 1. Typically, VAD's are utilized in patients unable to be weaned from heart bypass systems after open heart surgery. Weaning is necessary after cardiac surgery when the natural heart is unable to sustain life. This application of a VAD is generally short term (up to one week); however, some cardiac patients could benefit from a permanently implanted device. For those patients who cannot be weaned from the temporary artificial assist system, a permanent implantable VAD can be used negating the need for a total transplant, artificial or biological. For these reasons several types of VAD's have recently been developed to fulfill a variety of medical needs.

Many of these second generation pumps are centrifugal designs which have been modified to meet the needs for providing circulatory assist. They are much smaller and more efficient than the original roller pump, but are restricted to extracorporeal pulmonary and systemic circulatory assist. The need for an implantable device led the NASA/Baylor team to pursue an axial flow design which has resulted in a VAD which is small enough to fit inside small children. The two main obstacles which had to be overcome were hemolysis and thrombosis. Hemolysis is the mechanical and chemical destruction of red blood cells resulting in the release of hemoglobin into the blood plasma. This causes two problems, the first being a reduction in the oxygen carrying capability of the blood and the second is toxicity due to excess levels of hemoglobin in the plasma. The kidneys and liver can remove small amounts of hemoglobin from the bloodstream through filtration and metabolic absorption, respectively. If the destruction of red blood cells exceeds a threshold, then hemolytic anemia and hemoglobin toxicity begin to occur. Thrombosis is the formation of blood clots within the pump which can cause pump seizure, increased hemolysis, or blockage of the circulatory system itself. Blood tends to clot when contact is made with any foreign substance

within the bloodstream. Other causes of thrombosis are stagnant areas in which blood is allowed to collect and coagulate and platelet damage which causes the release of platelet factors. These factors initiate the coagulation cascade which results in an aggregate of fibrin, platelets, erythrocytes, etc. These blood components can adhere to pump surfaces and cause the pump to seize. Coatings can to some extent reduce thrombosis, but the basic design of the pump must be antithrombogenic if the device is expected to last long periods of time within the circulatory system. Both the roller pump and second generation centrifugal pumps are limited to a pump life of less than two days for these and other reasons. Pulsatile VAD's using flexible diaphragms have demonstrated much longer pump life, but have yet to be reduced to a size which would allow implantation in a wide range of patients. In addition, pulsatile VAD's have proven to be very expensive and complex to produce prohibiting their use on a wide basis.

DESIGN REQUIREMENTS

The design requirements for the NASA/Baylor VAD were based on years of practical medical experience as well as the demanding environment inside the circulatory system. The basic requirements of low hemolysis and antithrombogenicity were of primary concern. However, careful attention to minimizing size and maximizing efficiency have resulted in a device which has the potential to satisfy wide ranging circulatory assist needs. As with any device which will be put to use in an environment with limited access, the importance of system and component reliability could not be overemphasized. This drove the design towards simplicity with a minimum number of components, both electrical and mechanical. Output was required to be 5.0 liters/minute against a pressure head of 100 mm-Hg. This was based on the required assist flow during previous clinical usage of temporary VAD systems. A power input of less than 10 watts was highly desirable to minimize the size of the battery pack and the frequency of recharging. After evaluation of these requirements, it was decided that a small, efficient, axial flow pump was most likely to fulfill all the criteria while maintaining a relatively low production cost.

PUMP DESIGN

The NASA/Baylor VAD is shown in Figure 2. The envelope dimensions of the device are 2.5 inches (7.0 cm) in length and 1.0 inch (2.5 cm) in diameter. The unit consists of a spinning inducer/impeller with a fixed flow straightener and diffuser which reside inside of a flow tube. The inducer/impeller is 0.46 inches (1.2 cm) in diameter and is designed to rotate between 10,000 to 15,000 RPM depending upon the required pump output. The inducer serves two roles, one is to pre-rotate the blood before entering the impeller section and the other is to provide a two-stage pumping effect. The impeller also serves a dual purpose by housing rare earth magnets in the blades to act as a rotor of a brushless DC motor as well as providing pumping action. Magnets implanted in the impeller blades allows for a small air gap which results in a high motor efficiency. The inducer and impeller perform together to provide an efficient pumping mechanism to propel the blood while maintaining low shear levels and minimizing strong vortices. As a result, hemolysis is kept at an acceptable level for permanent human use. The blood flow is axially directed by the flow straightener before entering the inducer to boost performance. The flow straightener also provides a support for the front bearing. The diffuser axially redirects the highly tangential flow leaving the impeller to build pressure for increased pump performance and also minimizes turbulence to reduce hemolysis levels. The diffuser also serves as a support for the rear bearing. The front bearing consists of a ceramic ball riding in a matching sapphire cup. This simple bearing design accommodates both radial and axial forces encountered during pump operation. The rear bearing, equally simple, consists of a ceramic shaft riding inside a sapphire sleeve. The clearance between the shaft and the sleeve is kept very small to ensure precise alignment and minimize blood leakage into the bearing. The small amount of blood which does initially enter the bearing area is cross-linked by localized heat and effectively fills all the bearing voids. This prevents a constant infusion of fresh blood which could cause the bearing to seize. A brushless DC motor winding is located outside the flow tube and placed over the impeller to provide a magnetic drive for the inducer/impeller. The pump components (inducer/impeller, flow straightener, and diffuser) are currently machined from polycarbonate, but other materials are being investigated in terms of both biocompatibility and mass production issues.

CONTROLLER AND POWER SYSTEM DESIGN

Minimizing the size of the controller was a major design goal since it also is intended for implantation. A brushless DC motor drive was chosen due to its simplicity, reliability and high efficiency. Commercially available controllers are relatively complex requiring multiple components and sensors, all of which are potential failure points. Among these are Hall effect sensors used to detect rotor position. These signals are used to commutate the motor. A control scheme was adopted for the NASA/Baylor VAD which is shown in Figure 3. This scheme eliminated Hall effect sensors and the related electronics by relying on the back-electromotive force (back EMF)

generated in the motor stator. The back-EMF signals can be used to detect the rotor position and enable optimum commutation of the motor. This control method not only reduced the number of electronic components to a minimum, but also was slightly more efficient than standard Hall effect sensor controllers. The power delivery system, borrowed from existing technology with little modification, is called the Transcutaneous Energy Transfer System (TETS). This system was developed for pulsatile VAD's and has proven to be safe, reliable, and efficient. It uses AC coupling to transfer power through the skin eliminating possible infection sites.

SYSTEM PERFORMANCE

Hydraulic and Electrical

Hydraulic performance of the device is shown in Figure 4. The RPM required for 5.0 liters/min against 100 mm-Hg is relatively low at 10,800 for a device of this size. These flow curves were obtained using a mixture of 37% glycerin and 63% water. This mixture produces a fluid viscosity and density similar to that of human blood. The pump is capable of producing much higher flows and pressures as can be seen in Figure 4. This capability allows the pump to supply sufficient flows for a wide variety of patients depending upon their cardiac output and mean arterial pressure. It also enables the pump to be used in applications which involve the use of an oxygenator for pulmonary assist such as Extracorporeal Membrane Oxygenation (ECMO). The hydraulic efficiency of the pump has been estimated at 33% using the glycerin/water mixture. This coupled with a high motor efficiency allows the pump to draw only 9 watts of power to produce the required flow and pressure. A new motor design which is currently under development is expected to reduce this power requirement to between 5 and 6 watts.

Hemolysis and Thrombosis

The hemolytic nature of a pump is characterized by the level of hemoglobin in the blood plasma. Evaluation of hemolysis *in vivo* is impractical due to the fact that the kidneys and liver remove or metabolically absorb hemoglobin to varying degrees depending upon organ function. If a pump is run with blood *in vitro*, the amount of liberated hemoglobin can be precisely determined by measuring plasma free hemoglobin levels at specific time intervals. In 1967, Koller [3] established an Index of Hemolysis (IH) to specify an acceptable level of hemolysis for human use and to facilitate comparison of different pumps under development. A normalized Index of Hemolysis (N.I.H.) [4,5] was established to compensate for different hematocrit levels found in different tests. It is defined as:

$$N.I.H = \Delta Hgb \times V \times (1 - Ht) \times 100 / (Q \times T) \quad (1)$$

where, ΔHgb = change in plasma free hemoglobin in grams per liter
 V = blood volume of fluid circuit in liters
 Ht = hematocrit of blood in decimal percent
 Q = blood flow rate in liters/minute
 T = time in minutes at specified flow rate

The N.I.H. is measured as grams per 100 liters and is defined as the grams of hemoglobin liberated by a pump which passes 100 liters of blood against a standard pressure of 100 mm Hg. An acceptable value of IH for permanent human use has been established at less than 0.06 g/100L. This value is characteristic of the performance of the original roller pump. The IH of the NASA/Baylor pump has been determined to be 0.018 g/100L using bovine blood. An increase of roughly three times is typical when transitioning from bovine to human blood due to an increase in the fragility. This would place the IH of the NASA/Baylor pump at 0.042 g/100L with human blood. Testing with human blood in the near future will likely confirm this extrapolation. *In vivo* experiments with calf models have shown that the pump produced no hemolysis problems. Further reductions in hemolysis are expected as the surface finish of the pump components is improved by a combination of mechanical and chemical polishing. Mass production parts are likely to be injection molded which will produce a superior surface finish.

Thrombosis can be evaluated *in vivo*. Blood clotting involves a complex cascade of chemical reactions which has not yet been duplicated *in vitro*. For this reason, initial animal studies have been conducted to evaluate thrombus formation with the NASA/Baylor VAD. Two calf implants have been conducted to date in which the pump was implanted paracorporeally. The first experiment was terminated after 36 hours due to excessive hemolysis caused by improper sealing of the magnets in the impeller blades resulting in rapid magnet corrosion. The magnet sealing problem was solved for the second implant. The second experiment lasted 4.5 days before termination. No hemolysis problems were observed and the pump provided more than sufficient flow while drawing 11 watts of power. The increased power required was due to the added resistance of the tubing used to implant the pump paracorporeally. This resulted in an increased RPM requirement which in turn required slightly

more power than expected. This increased power would not be required when the pump is implanted close to the heart. The animal tolerated the pump well with no adverse effects. The pump stopped after 4.5 days due to thrombus formation around the rear bearing. A redesigned rear bearing has been developed which will likely solve this problem. In addition some thrombus formation was noted on the leading edges of the inducer blades. Upon examination under a microscope, it was determined that this area possessed a very poor surface finish. It is expected that improvements in surface finish will not only reduce hemolysis, but also reduce if not eliminate thrombus formation on the leading edges of the inducer blades.

CONCLUSION

A small, implantable, and efficient VAD has been developed by the NASA/Baylor team. This system has a great potential for satisfying the requirements for a long-term VAD for use as a bridge-to-transplant or permanent assist device. The technology has been developed sufficiently to begin to consider commercial application. The potential market for an implantable VAD has been estimated to be substantial and will grow at a rapid pace once a safe, reliable, and cost-effective system is available. The potential benefit to mankind is equally great given the global shortage of donor hearts and the reality that a commercially viable TAH will probably not be achieved in the immediate future.

REFERENCES

1. Hogness J, VanAntwerp M, ed. *The Artificial Heart, Prototypes, Policies and Patients*. Washington, D.C.:National Academy Press, 1991.
2. Cecchin, A, Total Artificial Hearts, *Medical World News*, 1993,34:15-22.
3. Koller T, Hawrylenko A. Contribution to the in vitro testing of pumps for extracorporeal circulation. *J Thorac Cardiovasc Surg* 1967,54:22-9.
4. Damm G, Mizuguchi K, Orime Y, Bozeman R, Akkerman J, Aber G, Svejkovsky P, Takatani S, Nosé Y, Noon GP, DeBakey ME. In vitro performance of the Baylor/NASA axial flow pump. *Artif Organs* 1993,17:609-613.
5. Naito K, Mizuguchi K, Nosé Y. The need for Standardizing the index of hemolysis. *Artif Organs*. 1994,18:In press.

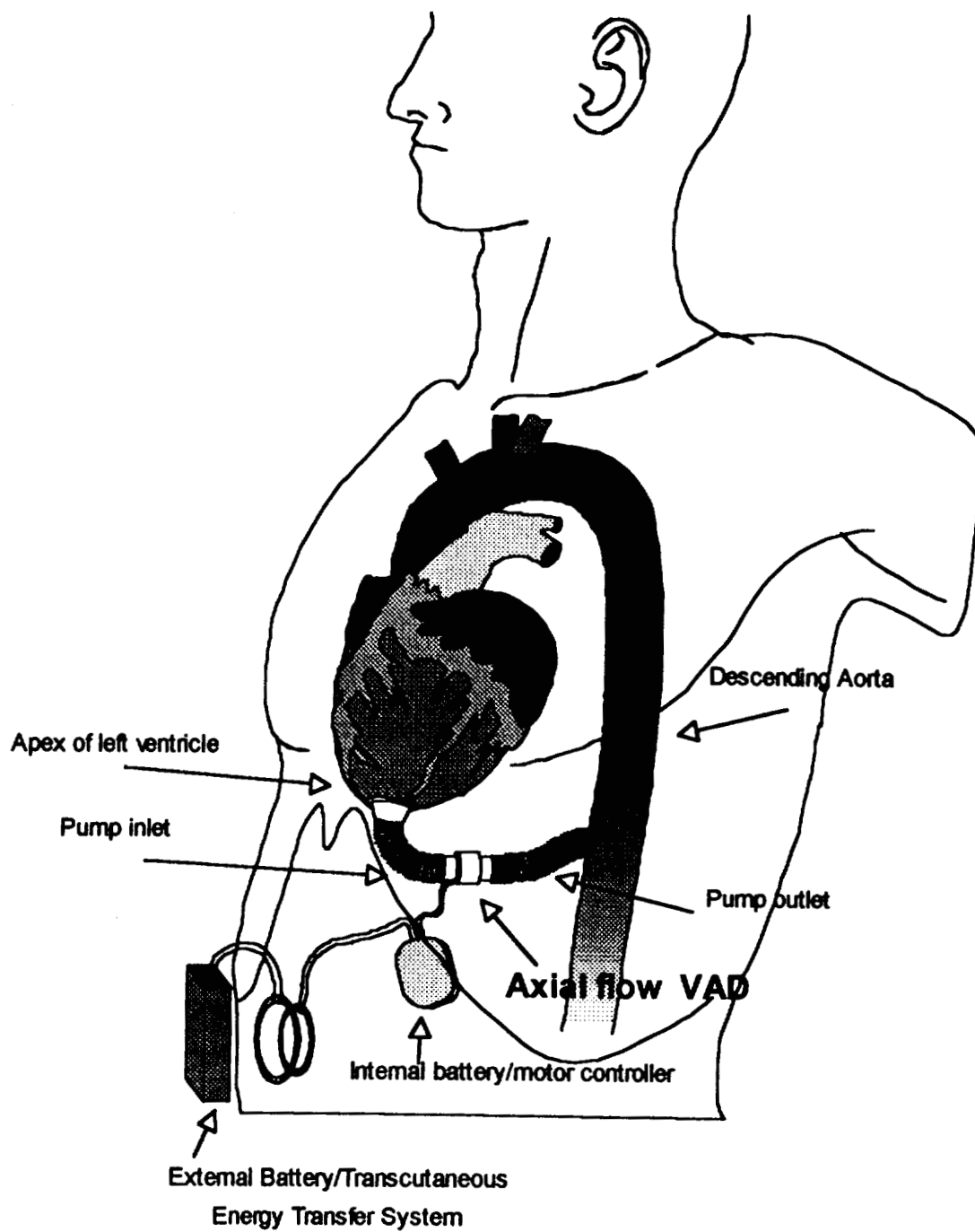


Figure 1. Placement and configuration of implanted NASA/Baylor axial flow VAD.

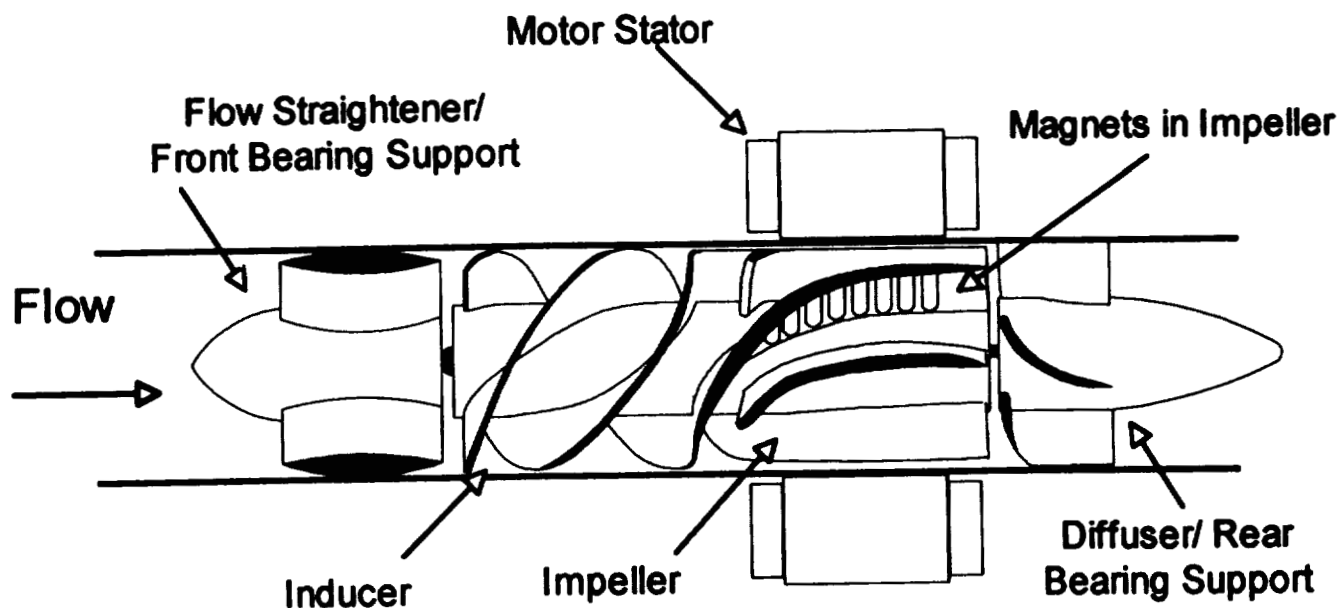


Figure 2. Schematic of NASA/Baylor axial flow VAD.

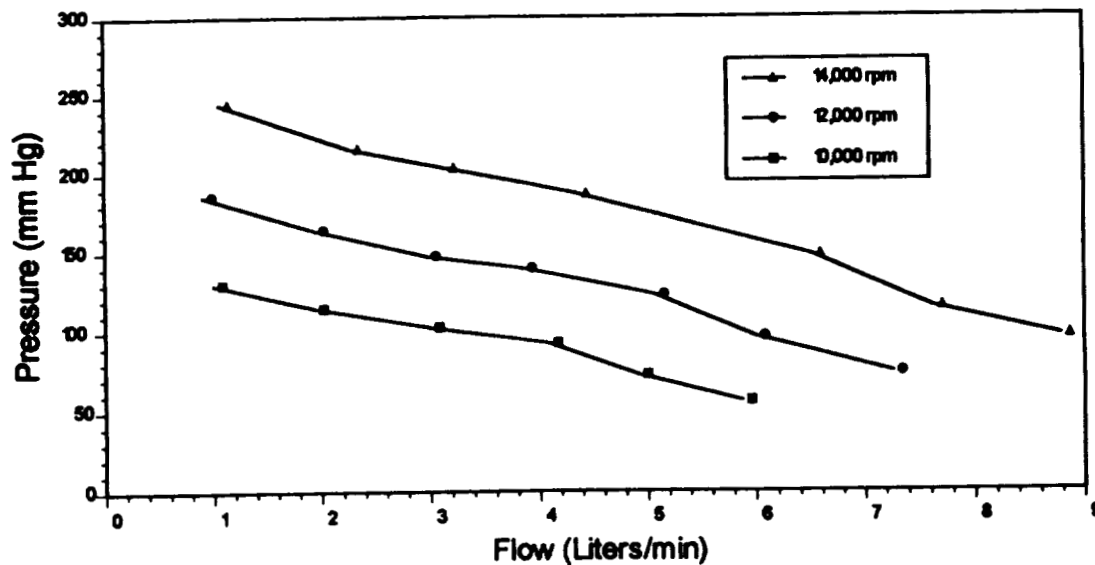


Figure 4. Flow-Pressure curves of the NASA/Baylor axial flow VAD.

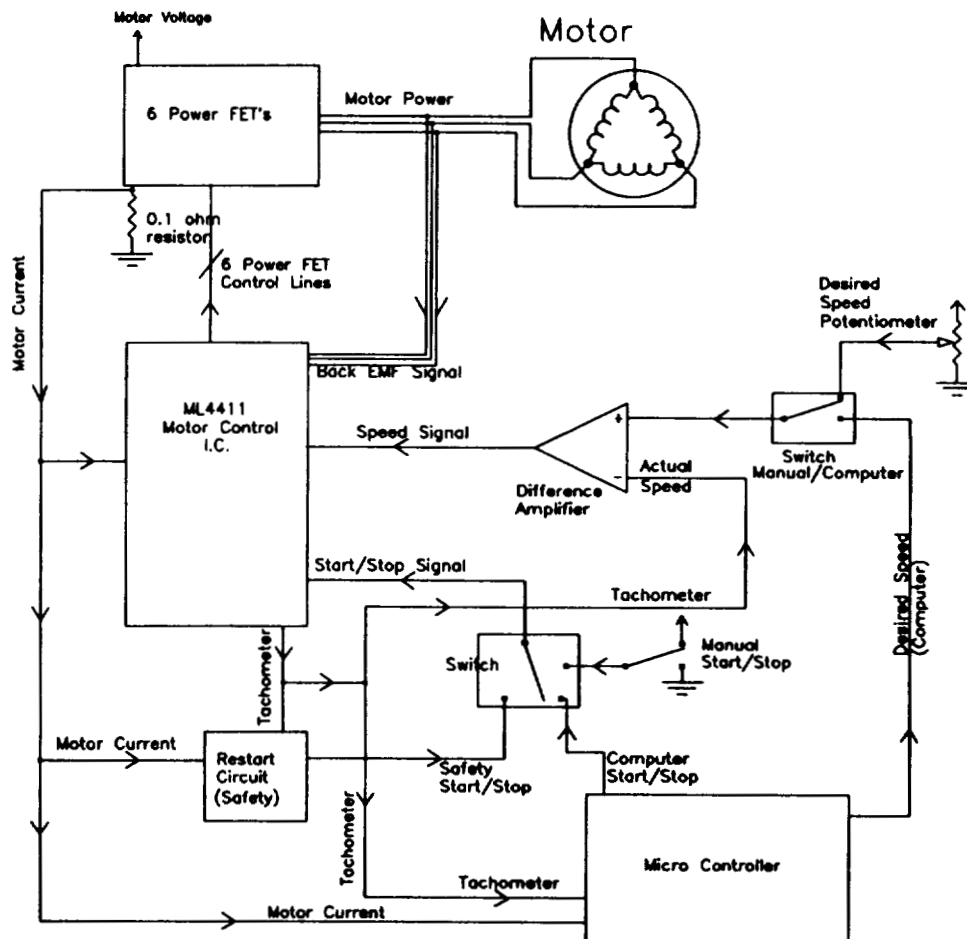


Figure 3. NASA/Baylor axial flow VAD controller.

219-52
2455
P-10

A FUZZY LOGIC CONTROLLER FOR HORMONE ADMINISTRATION USING AN IMPLANTABLE PUMP

L. Stephen Coles
Group Chief Technologist
Institutional Data Systems

George H. Wells, Jr.
Test and Measurement Laboratory
Jet Propulsion Laboratory
California Institute of Technology
Pasadena, CA 91109-8099

ABSTRACT

This paper describes the requirements for a Fuzzy Logic Controller for the physiologic administration of hormones by means of a FDA-approved surgically implantable infusion pump. Results of a LabVIEW computer simulation for the administration of insulin for diabetic adult patients as well as human growth hormone for pediatric patients are presented. A VHS video tape of the simulation in action has been prepared and is available for viewing.

INTRODUCTION

MiniMed Technologies, Inc. of Sylmar, California is currently conducting Phase II Clinical Trials for FDA approval on 335 patients of an open-loop implantable insulin pump for use by patients with insulin-dependent diabetes. This type of pump represents a significant advance over current practice, since it obviates the need for patients to self-administer insulin by Intra Muscular injections 2-3 times per day. On the other hand, this type of pump has the disadvantage that the patient must still anticipate their insulin requirements with each meal and dial in a specific dose level on a handheld calculator that in turn communicates with the implanted pump by means of a short-range digital radio-telemetry link. As a separate research and development activity, diabetes investigators are actively developing a variety of blood-glucose sensors. Anticipating the successful completion of such sensors at some future time, a physiologically-realistic algorithm for closed-loop control of blood-sugar levels would then provide the patient with the freedom to lead a relatively normal (more care-free) life, at least so far as eating is concerned. The final system, however, might fall short of the dream of a fully artificial pancreas, since the pump's reservoir must be periodically refilled with a concentrated form of insulin every few months, and this would be done by vacuum injection as an outpatient procedure.

A fuzzy control algorithm [1,2] was developed at JPL for the purpose of "closing the loop" based on the work of Prof. Richard Bergman at the USC Dept. of Physiology in the School of Medicine [3]. Refinements from Prof. Sam Bessman, M.D. of the Dept. of Pharmacology at the USC Medical School were added with respect to diabetic stress in a clinical setting [4]. Further refinements of complications secondary to pregnancy were added by Prof. Raul Artal, M.D. of USC Department of OB/GYN [5]. To verify the value of this sort of approach, a model for human growth hormone administration was developed based on the work of Prof. Johannes Veldhuis at the University of Virginia in Charlottesville [12-14]. Surprisingly, the time needed to construct the hGH administration model was just three hours.

Our models were implemented on an Apple Macintosh Quadra 950 using the LabVIEW software (v. 2.2.1) package, commercially available from National Instruments, Inc. of Austin, Texas. The CubiCalc Fuzzy Logic software development system from HyperLogic of Escondido, California will be considered in the next implementation on an IBM-PC. Later, the clinical importance and commercial potential of such implantable devices will be discussed.

RESULTS

Diabetes Model

Figure 1 shows the overall LabVIEW model of the pancreas, including the body's environment within which it operates, as developed by us at JPL over a four-day period. The high degree of model/developer interactivity, which is one of the major selling points of LabVIEW on a PC or MAC, is what permitted us to do the sort of "rapid prototyping" that allowed us to evolve of the model toward physiologically-correct behavior in such an accelerated time. In addition, the model included sub-models for patient-dependent parameters, food caloric values, stomach, liver, kidney, and body muscle/fat ratios. The patient model, shown in Figure 2, included age, gender, ethnic group, weight, family history of diabetes, and medication history. These were combined with temporal profiles for food consumption, physical exercise, and exposure to stress during the day, using rules of Fuzzy Logic to compute the relative sensitivity of the of body tissues to insulin for an individual patient.

Figure 3 illustrates a typical output of the model. The upper graph plots the change in blood glucose levels in mg/dl over a 24-hour period, while the lower graph plots the output of insulin from the artificial pump in micro liters over the same period. Breakfast at 7:00 AM, lunch at Noon, dinner at 6:00 PM, followed by a snack at 10:00 PM are conspicuous events. The "ringing" in blood sugar levels triggered by harp transitions in insulin levels at the onset of food consumption is likely to be an artifact of our computer implementation rather than representative of true physiological events in the body, since the tissues are likely to have a strong smoothing effect, and no effort was made to simulate this phenomenon in our model. Alarm conditions such as "excessive urination" or "headache," associated with hyper- and hypoglycemia respectively, are triggered in the model whenever certain blood glucose threshold values are exceeded or fall beyond normal limits, as specified by the investigator. This is manifested in the model by flashing error lights with alarm bells going off.

Pituitary Model

Figure 4 shows our proposed model of the hypothalamic/pituitary axis in the interface between the human brain and the endocrine system. The pulsatile diurnal output of human Growth Hormone (hGH) is subject to a "bang/bang" pair of antagonistic messenger molecules, Growth Hormone Inhibiting Hormone (GHIH) and Growth Hormone Releasing Hormone (GHRH), originating in the hypothalamus and connected to the pituitary by means of a specific portal vein network. GHRH secretion is essentially a series of pulses clocked at once a minute uniformly throughout the day, whereas GHIH secretion is the real "gate keeper" normally high and occasionally low, allowing pulses of hGH to flow out of the pituitary into the blood stream, where it has a constellation of effects in addition to growth in children.

Figure 5 shows the results of this model under conditions of significantly decreased GHIH at 2:30 AM and 5:30 AM (the top graph), normal uniform GHRH (middle graph), and resulting hGH output (bottom graph). This model accounts for the physiologically-observed major jagged-stairstep rises in hGH pulses several times during sleep with a few more randomly-distributed smaller pulses that occur during the waking hours. Figure 6 illustrates a different patient's parameters with greater bursts of hGH during the night. Figure 7 expands the resolution in the interval from Midnight to 6:00 AM for greater clarity of the cause-and-effect relationship between the two inputs (GHIH and GHRH) and the output (hGH).

DISCUSSION

The implications of such a control system running in LabVIEW for clinical and engineering applications is that, as pieces of the final hardware system are completed, they can be inserted into the model to replace their corresponding software component. In the case of the pituitary model, the existence of a physiologically-based secretion into the bloodstream of juvenile patients during the hours of sleep is much to be preferred over the bolus injections twice or three times a week, as they are administered now. Although the number of potentially affected children with shortness of height secondary to pituitary insufficiency (rather than receptor insensitivity) may be relatively small compared to the population as a whole, the potential to help the wider geriatric population with hGH supplementation in this manner could be enormous.

Block Diagram

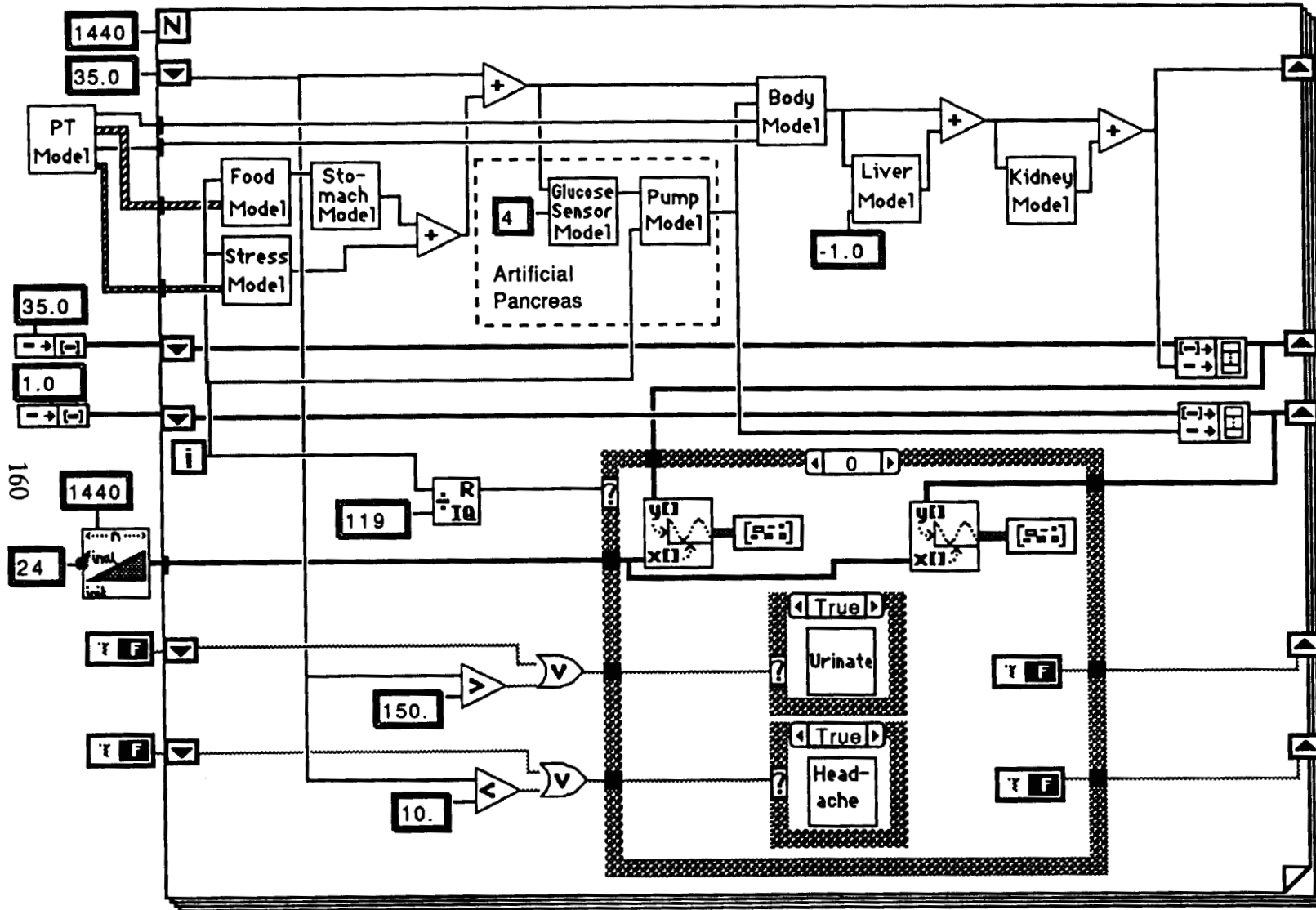


Figure 1: LabVIEW Block Diagram of the Artificial Pancreas System.

Front Panel

Patient name John Smith		Hospital ID# 1234567		IS 0.283	
Age (years) 31	Ethnic Group Cauc	Sex Male	Pregnancy negative	Weight (lbs) 190	Meds Prednisone
Family History none		Stress level 50.00		Exercise Level athletic	

Breakfast	Lunch	Dinner	Snack
Onset (hours) 7.00	Onset (hours) 12.00	Onset (hours) 18.00	Onset (hours) 22.00
Duration (minutes) 30	Duration (minutes) 30	Duration (minutes) 45	Duration (minutes) 10
Quality 1.00	Quality 0.90	Quality 0.80	Quality 1.50

Stress Onset (hours)	Stress factors
0 6.00 7.00 8.00 17.00 18.00 24.00	0 0.000 0.200 1.000 0.500 1.000 0.200
Age breakpoints	Age factors
0 12 50 65 120	0 0.280 1.000 0.900 0.240
Ethnic Group factors	Sex factors
0 1.000 0.420 0.400 1.000 1.000	0 0.561 0.758
Pregnancy factors	Weight breakpoints
0 1.000 1.000 0.320 0.180 0.463	0 100 200 300 500
Weight factors	Med factors
0 0.850 1.000 0.230 0.200	0 1.000 0.240 0.250
Family History factors	Exercise factors
0 1.000 0.300 0.300	0 0.800 1.000 1.200 1.400 1.500

Food	Stress
0	Stress breakpoints (minute) 1 420
Breakfast	Stress level 4 50.000
Onset (hours) 7.00	
Duration (minutes) 30	
Quality 1.00	
Lunch	
Onset (hours) 12.00	
Duration (minutes) 30	
Quality 0.90	
Dinner	
Onset (hours) 18.00	
Duration (minutes) 45	
Quality 0.80	
Snack	
Onset (hours) 22.00	
Duration (minutes) 10	
Quality 1.50	

Block Diagram

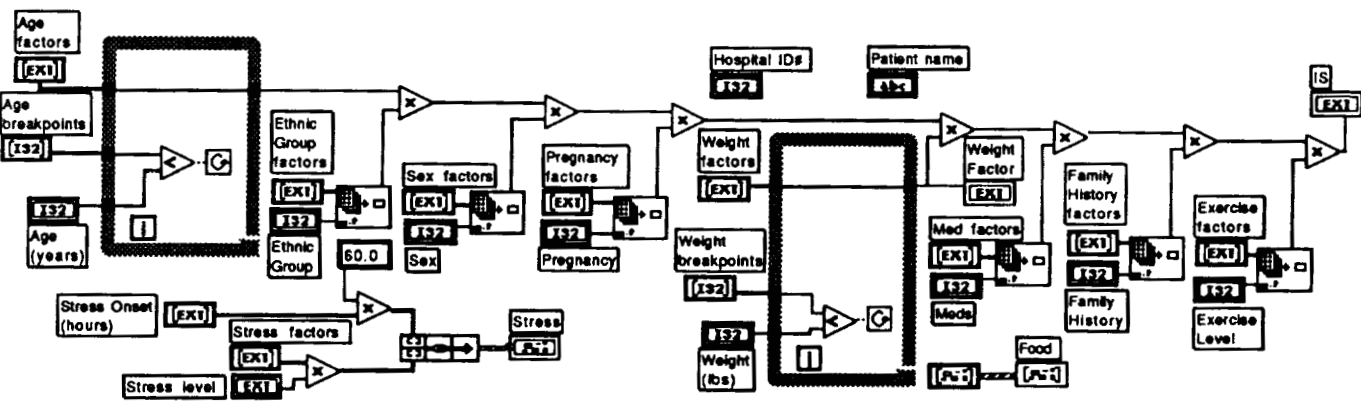
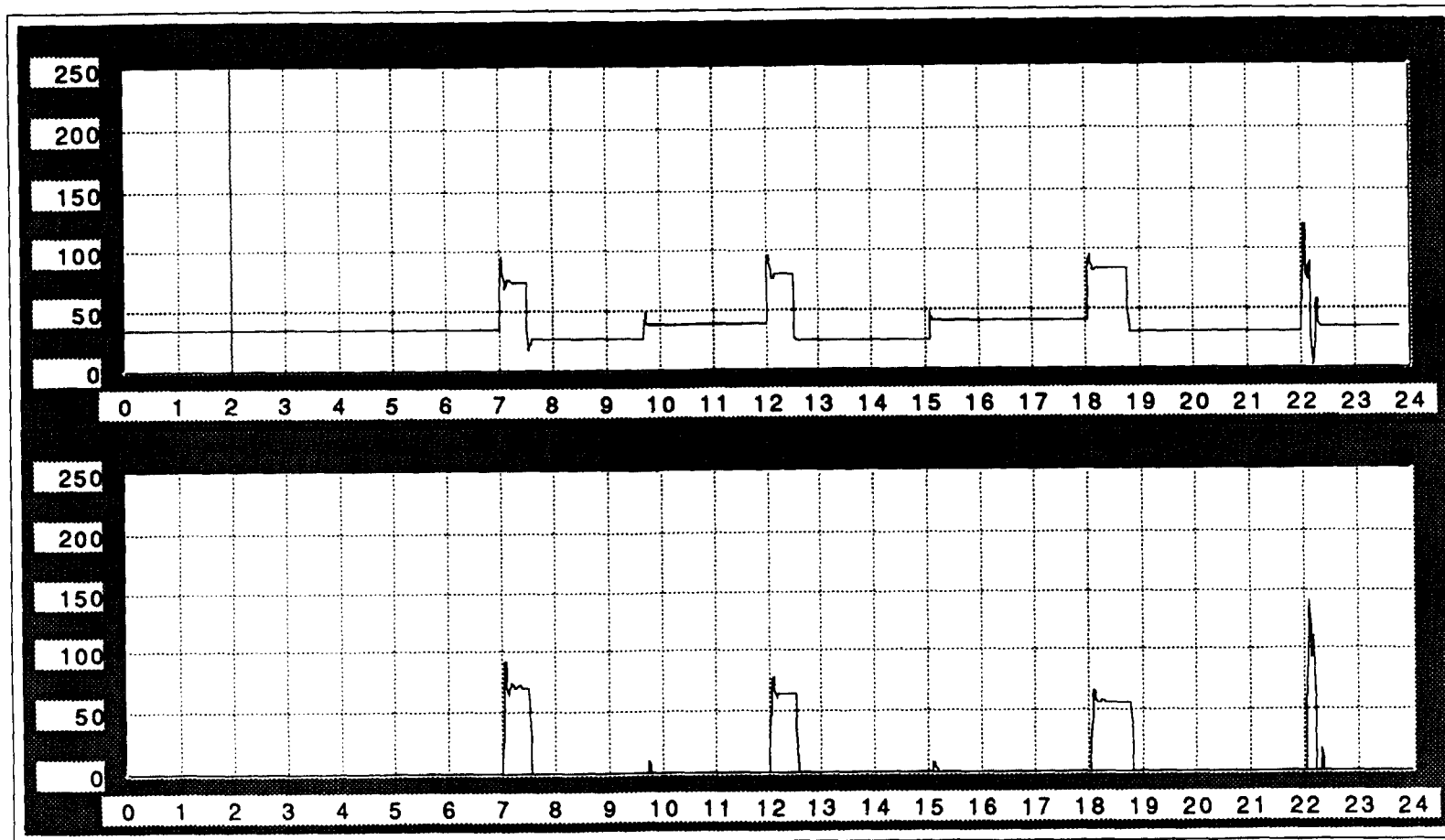


Figure 2: Front Panel for a Human Adult Patient with Diabetes Mellitus.

Front Panel



Block Diagram

Figure 3: Output from the Model

Upper Graph: Blood Glucose (mg/dl) vs. Time (hours)

Lower Graph: Blood Insulin (units secreted) vs. Time

Block Diagram

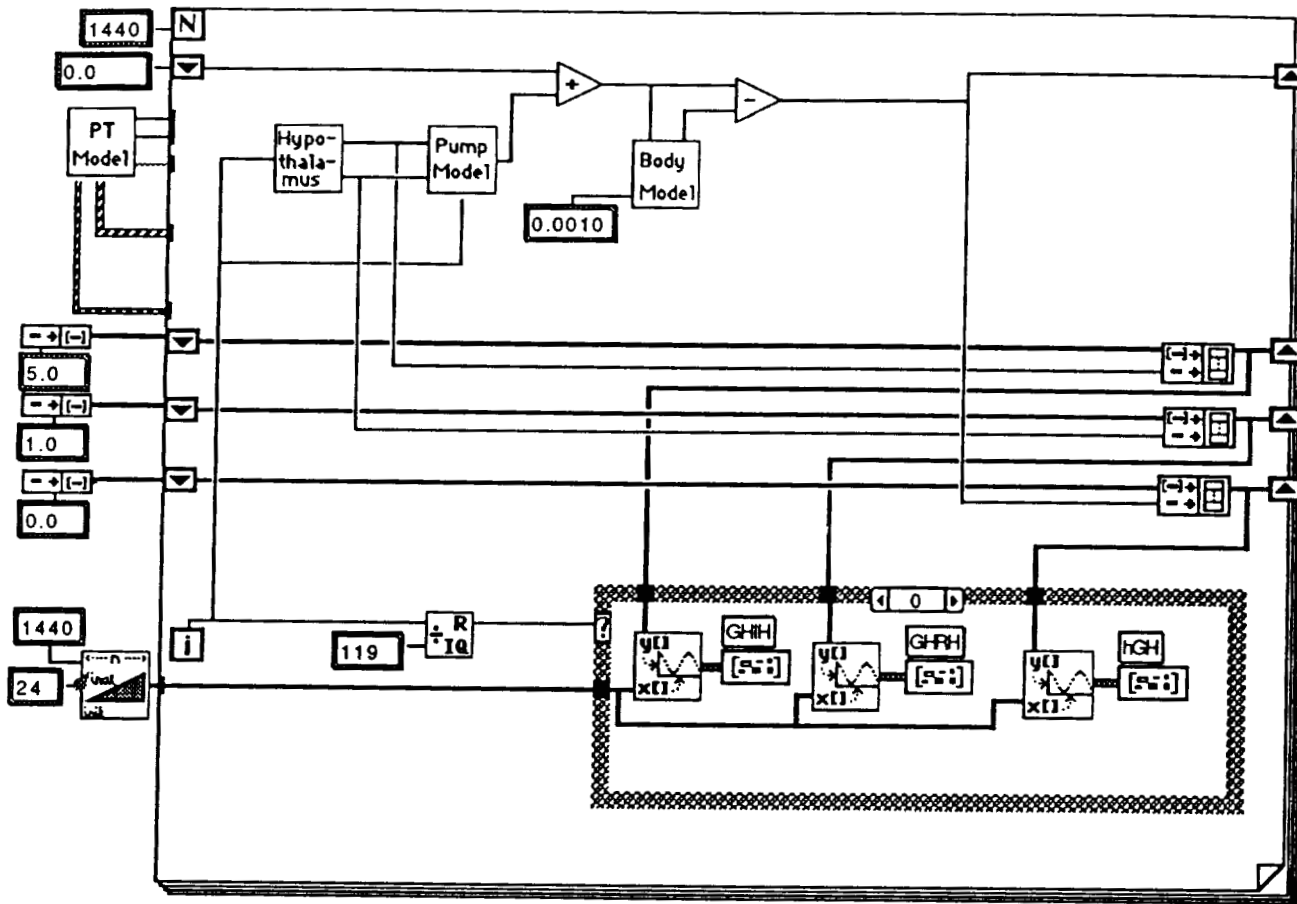
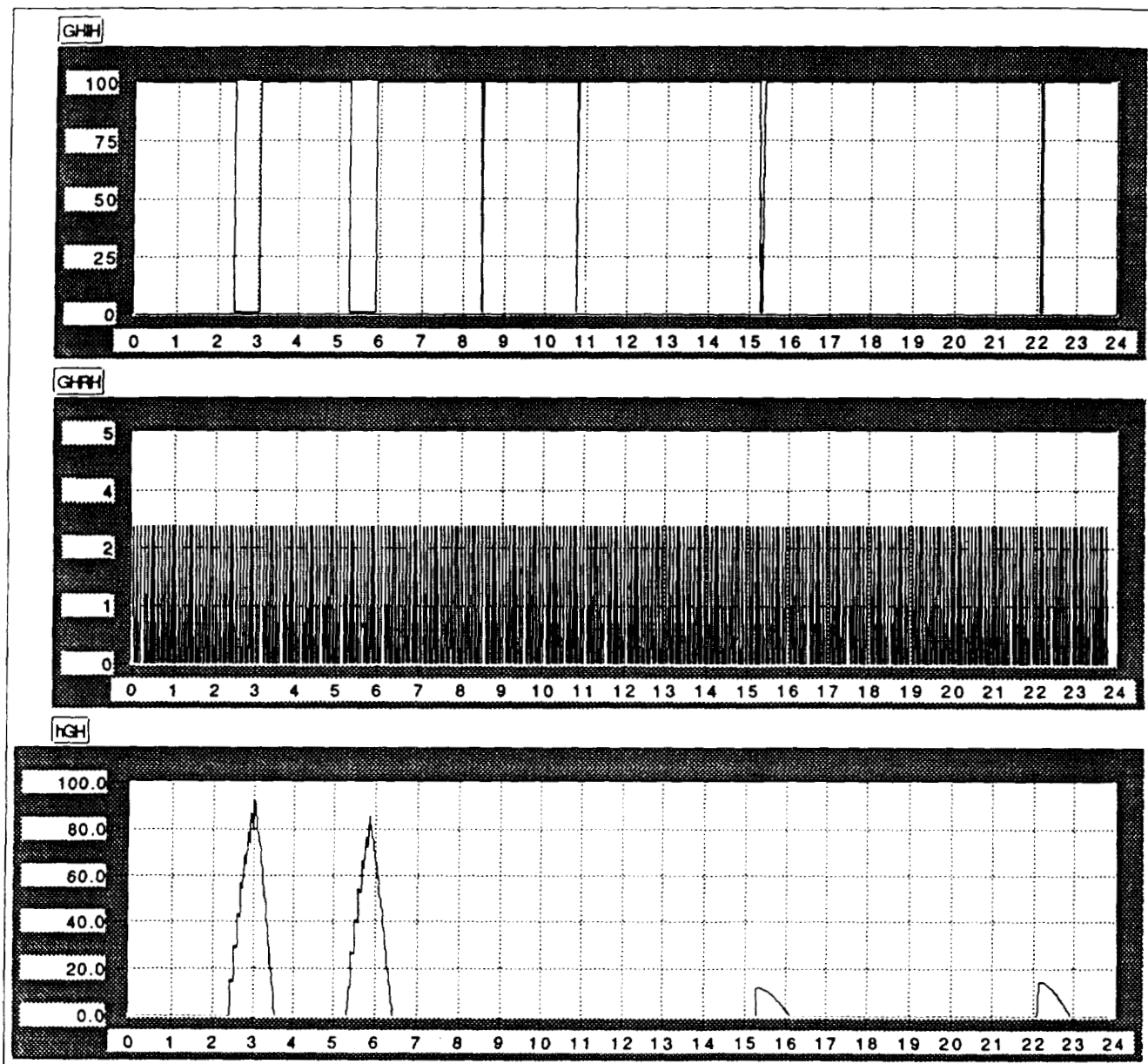


Figure 4: LabView Block Diagram of the Hypothalamic/Pituitary Model.

Front Panel



Block Diagram

Figure 5. Typical Diurnal Pulsatile Output from the Model

Upper Graph: Growth Hormone Inhibiting Hormone (GHIH)
Middle Graph: Growth Hormone Releasing Hormone (GHRH)
Lower Graph: Human Growth Hormone (hGH)

Front Panel

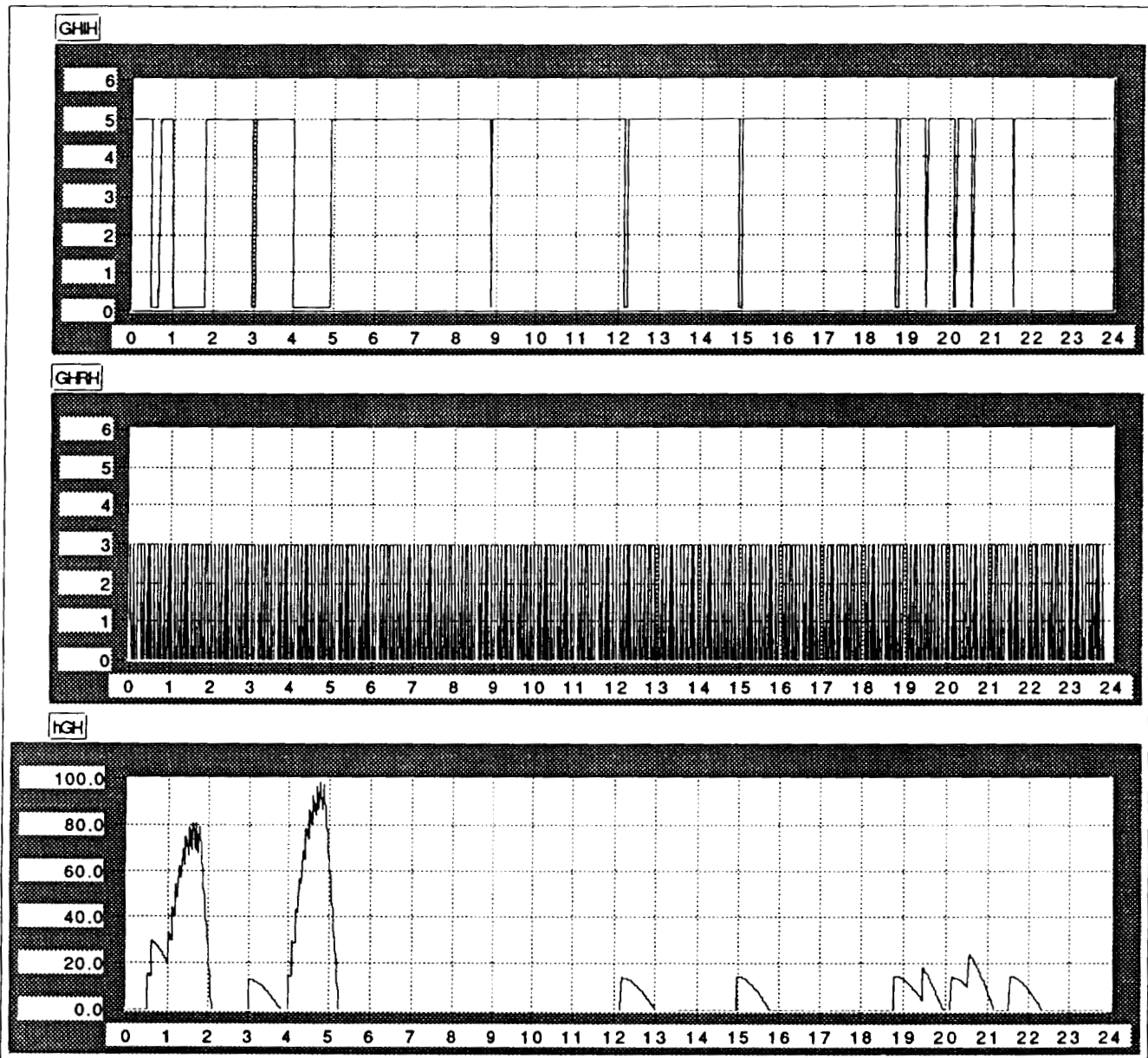


Figure 6: Another Model Output with Stronger hGH Secretion.

Front Panel

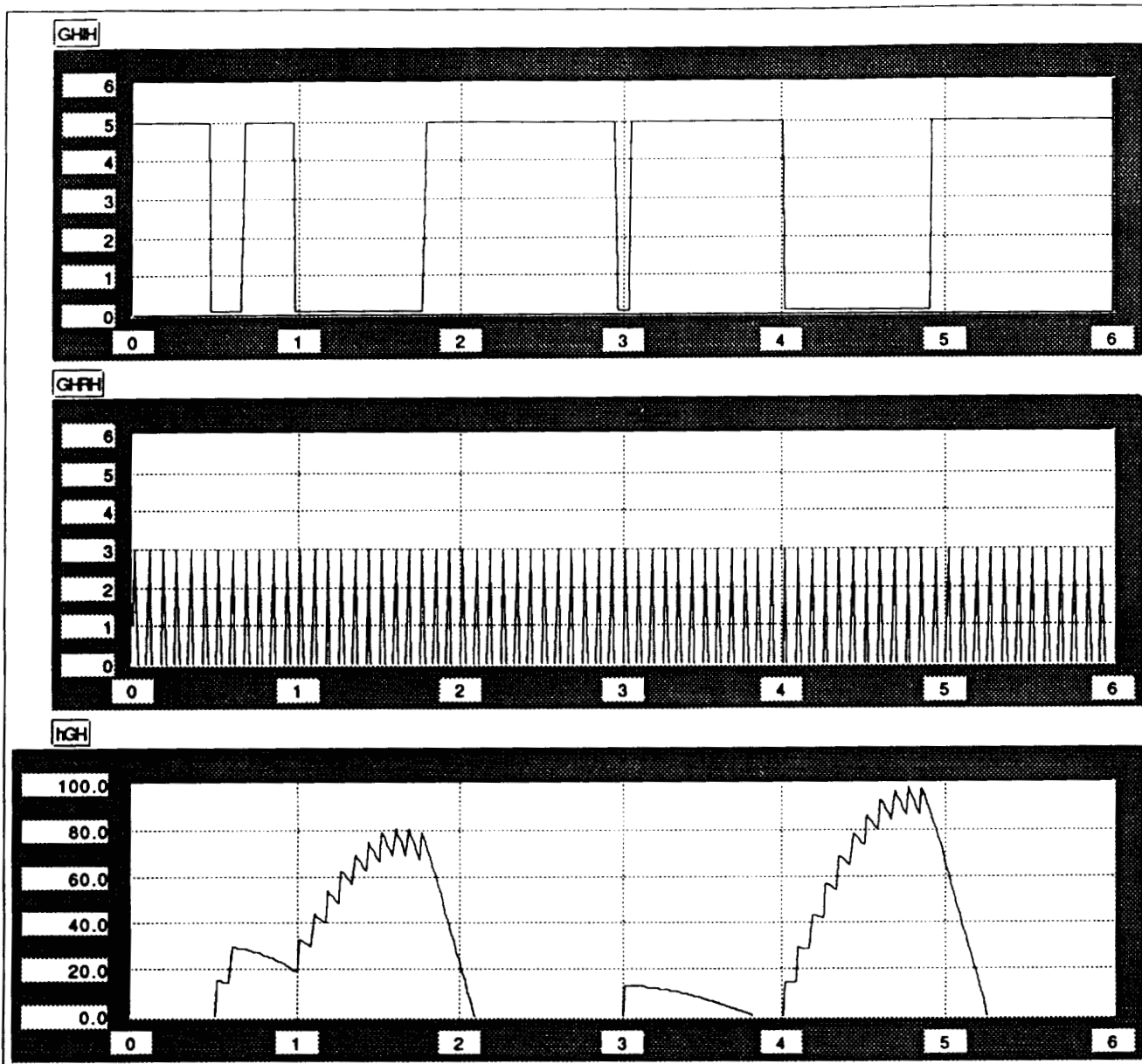


Figure 7: Higher Resolution from Midnight to 6:00 AM when hGH Secretion is most active.

ACKNOWLEDGMENTS

The work described in this paper was carried out by the Jet Propulsion Laboratory, California Institute of Technology under a contract with the National Aeronautics and Space Administration through the Office of the JPL Chief Scientist. Reference herein to any specific commercial product, process, or service by trade name, trademark, manufacturer, or otherwise, does not constitute or imply its endorsement by the United States Government or the Jet Propulsion Laboratory, California Institute of Technology.

REFERENCES

1. Bart Kosko, *Neural Networks and Fuzzy Systems: A Dynamical Systems Approach to Machine Intelligence* (Prentice Hall, New York, 1992), Signal and Image Processing Institute; Department of Electrical Engineering; University of Southern California; Los Angeles, California 90089.
2. Daniel McNeill and Paul Freiberger, *Fuzzy Logic: The Discovery of a Revolutionary Computer Technology-- and How it is Changing our World* (Simon and Schuster, New York, 1993).
3. Richard N. Bergman, "Toward Physiological Understanding of Glucose Tolerance: A Minimal-Model Approach," *Diabetes*, Vol. 38, No. 12 (December 1989), Department of Physiology; USC Medical School; Los Angeles, California 90023.
4. Samuel P. Bessman, "A Model of Diabetic Stress," Chairman Department of Pharmacology and Nutrition, USC Medical School, LA County Hospital, Los Angeles, California 90033.
5. Raul Artal, "Complications of Diabetes during Pregnancy," Department of Obstetrics and Gynecology; Women's Hospital; USC Medical School; Los Angeles, California 90033.
6. Vincent H. L. Lee, "Comparing Routes of Administration for Drugs," Gavin S. Herbert Professor and Chairman of the Pharmaceutics and Drug Delivery Department; John Stauffer Pharmaceutical Sciences Center, USC Medical School, Los Angeles, California 90033.
7. Joseph H. Schulman, "Implantable Pump Technology," Chief Scientist; MiniMed Technologies, Inc.; Sylmar, California 91342.
8. Jean-Louis Selam and M. Arthur Charles, "Devices for Insulin Administration," *Diabetes Care*, Vol. 13, No. 9, pp. 955-979 (September 1990).
9. Jean-Louis Selam, "Development of Implantable Insulin Pumps: Long is the Road," *Diabetic Medicine*, Vol. 5, pp. 724-733 (1988).
10. William C. Duckworth, Christopher D. Saudek, and Robert R. Henry, "Why Intraperitoneal Delivery of Insulin with Implantable Pumps in NIDDM?" *Diabetes*, Vol. 41, pp. 657-659 (June 1992).
11. Christopher D. Saudek, Jean-Louis Selam, Henry A. Pitt, Kenneth Waxman, Michelle Rubio, Nathalie Jeandidier, Dee Turner, Robert E. Fischell, and M. Arthur Charles, "A Preliminary Trial of the Programmable Implantable Medication System for Insulin Delivery," *New England Journal of Medicine*, Vol. 321, pp. 574-579 (August 31, 1989).
12. Mark L. Hartman, Amilton C. S. Faria, Mary Lee Vance, Michael L. Johnson, Michael O. Thorner, and Johannes D. Veldhuis, "Temporal Structure of in vivo Growth Hormone Secretory Events in Humans," *American Journal of Physiology*, pp. E101-E110 (January 1991), Division of Endocrinology and Metabolism, University of Virginia Health Sciences Center, Charlottesville, Virginia 22908.
13. Eve Van Cauter, Myriam Kerkhofs, Anne Caufriez, Anne van Onderbergen, Michael O. Thorner, and Georges Copinschi, "Quantitative Estimation of Growth Hormone Secretion in Normal Man: Reproducibility and Relation to Sleep and Time of Day," *Journal of Clinical Endocrinology and Metabolism*, Vol. 74, No. 6, pp. 1441-1450 (1992).
14. Michael J. Cronin, Director, Endocrine Research Department, Genentech, Inc.; South San Francisco, California 94080.

MONITOR FOR STATUS EPILEPTICUS SEIZURES

Mark Johnson and Thomas Simkins
SMCAR-CCB-RA
Benet Laboratories
Watervliet Arsenal, Watervliet, NY 12189-4050

ABSTRACT

This paper describes the sensor technology and associated electronics of a monitor designed to detect the onset of a seizure disorder called *status epilepticus*. It is a condition that affects approximately 3-5 percent of those individuals suffering from epilepsy. This form of epilepsy does not follow the typical cycle of start-peak-end. The convulsions continue until medically interrupted and are life threatening. The mortality rate is high without prompt medical treatment at a suitable facility. The paper describes the details of a monitor design that provides an inexpensive solution to the needs of those responsible for the care of individuals afflicted with this disorder. The monitor has been designed as a cooperative research and development effort involving the United States Army Armament Research, Development, and Engineering Center's Benet Laboratories (Benet) and the Cerebral Palsy Center for the Disabled (Center), in association with the Department of Neurology at Albany Medical College (AMC). Benet has delivered a working prototype of the device for field testing, in collaboration with Albany Medical College. The Center has identified several children in need of special monitoring and has agreed to pursue commercialization of the device.

EPILEPSY

Epilepsy is a disorder of the brain characterized by recurring seizures, in which there are uncontrolled electrical discharges of brain cells [1]. Epilepsy may arise from a very small area of damaged brain tissue, or from the entire brain. There may be no apparent brain damage, or damage limited to an area so small it cannot be detected. Therefore, in nearly one-half the cases, the cause of epilepsy is not known.

There are several types of seizures associated with epilepsy, the most common of which are generalized tonic-clonic (grand mal), absence, (petit mal), complex partial (psychomotor), and elementary partial (focal motor). Each seizure type can be characterized by various symptoms. However, the seizures are generally not life threatening, lasting at most up to three minutes. The exception is *status epilepticus*, also called continuous seizure state. This is the occurrence of repetitive or continuous seizures and affects approximately 3-5 percent of those individuals suffering from epilepsy. It can exist with all types of seizures and may result in irreversible brain damage or death without prompt medical treatment.

THE PROBLEM

We were requested to develop a device that could detect the onset of *status epilepticus* in a child during sleeping hours. The seizures begin as complex partial and progress to generalized tonic-clonic. The early stages of the seizures are characterized by a loss of consciousness during which there are minor, barely perceptible tremors. The monitor was to supplement the ineffectual periodic observation of the child by the parents.

A SOLUTION

A motion sensor has been designed with nearly omnidirectional response that can detect the 'hard shiver' activity characteristic of complex partial seizures. The sensor is small and inexpensive to produce since it detects without measuring. It is less responsive to casual and temporary body motion (rolling over, etc.) than to the activity of the tremors. Electronics provide further filtering to the sensor

signals to ensure consistent results at all orientations. Quasi-continuous activity for a finite period of time is used as an indication of seizure activity. Although the monitor is designed to ignore occasional movements not indicative of a seizure, false alarms will occur. Therefore, sensitivity adjustments have been included. If the alarm criterion is satisfied, a radio frequency signal is transmitted every 30 seconds to a compatible receiver that activates/deactivates any desired alarm mechanism.

The sensor, electronics, and commercially available, FCC compliant (HBW74A) transmitter are packaged in a small, lightweight, plastic housing that is easily attached to a child (figures 1a and 1b). An on/off switch is recessed in the side. A 120V, 60hz, alarm mechanism (light, radio, etc.) is plugged into a compatible receiver 'trained' to the transmitter signal. Although a number of devices may be used simultaneously, total power requirements should not exceed 600 Watts. The receiver is then plugged into a wall outlet within 20 feet of the monitor. The transmitter/receiver should be tested (manual button at the top of the monitor) to ensure the signal is properly received. The monitor is then attached to the child and powered on.

TECHNICAL DETAILS

The Sensor

The sensing element is an intermittent switch consisting of a small, electrically conductive sphere which is able to move within the confines of a small hollow cylinder with closed ends (figure 2). The sphere is stainless steel and has been chemically treated (Marble's Reagent) to enhance surface roughness. The wall of the cylinder is conductive as are the end plates each of which are separated from the cylinder wall by an insulator. The end plates are electrically connected and form one pole of the switch. The cylinder wall is the other pole. When the sphere is in contact with either of the end plates and the cylinder wall, the switch is mechanically closed. However, depending on the presence of oxides and/or surface roughness, the contact resistance may be quite high and the switch may or may not be electrically closed. The important feature is that even small motions of the switch cause the ball to roll. The mechanically closed position (sphere in contact with the cylindrical surface B and one of the end caps A) is the only stable position of the sphere, so most rolling occurs in this position. As the sphere rolls, electrical contact with the wall is intermittent due to the variations in contact resistance. The surfaces have been tapered to improve the probability of a weighted contact. Figure 3 shows typical sensor response characteristic of the complex partial seizures to be detected. No attempt has been made to optimize the taper or utilize curved surfaces since the design of figure 2 has proved to be satisfactory.

The Electronics

A schematic of the monitor electronics is given in figure 4. The electronics are based on an 8-bit RISC CMOS EPROM microcontroller [2]. The microcontroller is designed to operate between 3 and 6 volts from DC to 20Mhz. High speed is not required so the microcontroller operates at a low voltage (4 VDC) and low clock speed (75khz) to conserve power. Power is derived from the 12 volt power source of the transmitter. A Maxim MAX874 low-dropout, precision voltage reference is utilized to supply the 4 volts to our circuitry. This voltage reference was selected because of its low quiescent current (10 μ A) and dropout (200mV) voltage. The MAX874 sources or sinks up to 400 μ A at supply voltages ranging from 4.3 VDC to 20 VDC. Nominal current draw of the circuit (including 12 volt passive transmitter operation) is 25 μ A when the processor is in a quiescent mode and 85 μ A during oscillation. When activated, the transmitter draws 5 mA. Although there are many influencing factors, the useful battery life of an Eveready A23 12 volt alkaline battery or equivalent is estimated to be 2 months if the device is used every night for 9 hours.

With the exception of the 20 pF crystal tank capacitors, all capacitors (1000 pF) are for decoupling. The 262k feedback resistor in the oscillator circuit is required to prevent over driving the crystal. The 100k resistor eliminates spurious oscillations and reduces standby current drain. Battery voltage is dropped by a voltage divider network and periodically monitored by an on-chip A/D converter at pin 17. Pull-down resistors at terminals 9-12 define the default logic settings for the jumpers. The

jumpers may be used to disable the battery test (J1), increase the monitor sensitivity (J2), decrease the sensitivity (J3), and enable debug mode for diagnostics (J4). The diagnostic information is transmitted through a serial link at output port 2. Data is transmitted at 150 baud (6.7 msec pulses) with one start bit, 8 data bits, and 2 stop bits. A 1488 or similar protocol converter must be used to ensure RS232 compatibility (figure 5a). Information on jumper configurations, battery voltage, and pulse count are provided (figure 5b). A 9155 VMOS power FET driven by microcontroller output port 1 simultaneously switches the transmitter and alarm LED. The sensor is monitored at terminal 13.

450 lines of microcontroller code define the system operation. Upon power-up, interrupts are all disabled and the input/output port definitions established. The A/D converter characteristics are defined, but the converter is disabled to conserve power. The jumpers are monitored and the system initialized after which the processor goes into a power saving quiescent mode. Although a watchdog timer is available that is capable of resetting the system every 2.5 seconds, it was disabled to conserve power. Excessive current draw occurs while the processor forces the crystal tank circuit into oscillation at lower frequencies. Approximately 500 msec are required to achieve stable oscillation, with a 230 μ A peak current draw. In fact, contrary to the claims of the manufacturer, reliable start-up at 32 khz was unattainable, particularly with the SOIC (surface mount) package. While in the quiescent mode, the oscillator is disabled until it receives an interrupt indicating a signal change from the sensor. At this point a real time clock/counter (RTCC) is enabled and the interrupt vectors redefined to mask all interrupts except those from the internal clock/counter. Signal transitions are measured at 100 msec intervals to minimize sensitivity variations resulting from different sensor orientations. After approximately 35 seconds of multiple RTCC interrupts, the processor compares the acquired data with that of a threshold value defined by the jumper configurations and measures the battery voltage. If the activity or battery voltage do not warrant an alarm, the processor returns to the power saving mode. If either the battery voltage is too low (9 volts) or the activity exceeds the threshold, the processor toggles the receiver with a 500 msec pulse through the VMOS power transistor. For the transmitter/receiver control modules selected, pulse widths under 400 msec were unreliable and those in excess of 700 msec could cycle the receiver two times (i.e. no noticeable effect). The signal is retransmitted every 30 seconds until reset, which turn the alarm on and off periodically. This ensures the device attached to the receiver will be activated in the event an alarm condition occurs before the receiver is set. This also reduces the risk of an alarm signal being completely masked. The LED in series with the transmitter is used as a local alarm by transmitting 25 msec bursts (3 percent duty cycle) between the 500 msec. pulses. This is enough to flash the LED but not activate the receiver.

RESULTS

The monitor has only recently been turned over to the Center for the Disabled for preliminary testing. It is a replacement for an earlier design that provided much needed data. Many of the enhancements were made based on recommendations by the parents of the afflicted child. We believe the new design corrects all of deficiencies of the earlier model, but anticipate the need for refinements as the testing proceeds.

REFERENCES

1. EPILEPSY, Medical Aspects: Epilepsy Foundation of America # 022-1281-MSP
2. PIC16C71 8-bit CMOS EPROM Microcontroller with A/D converter, Microchip Corporation #DS30150B

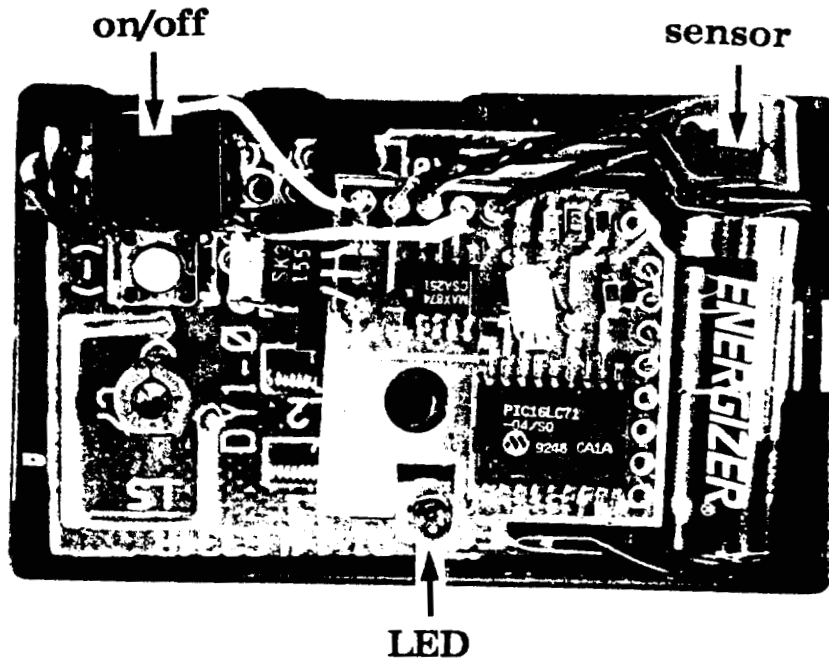


Figure 1a. Monitor Electronics and Sensor

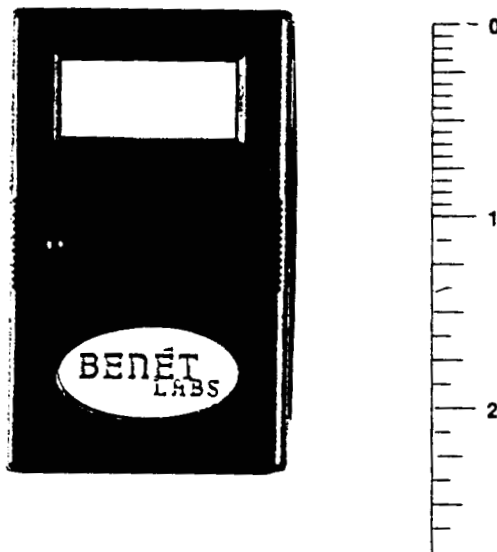


Figure 1b. Monitor (actual size)

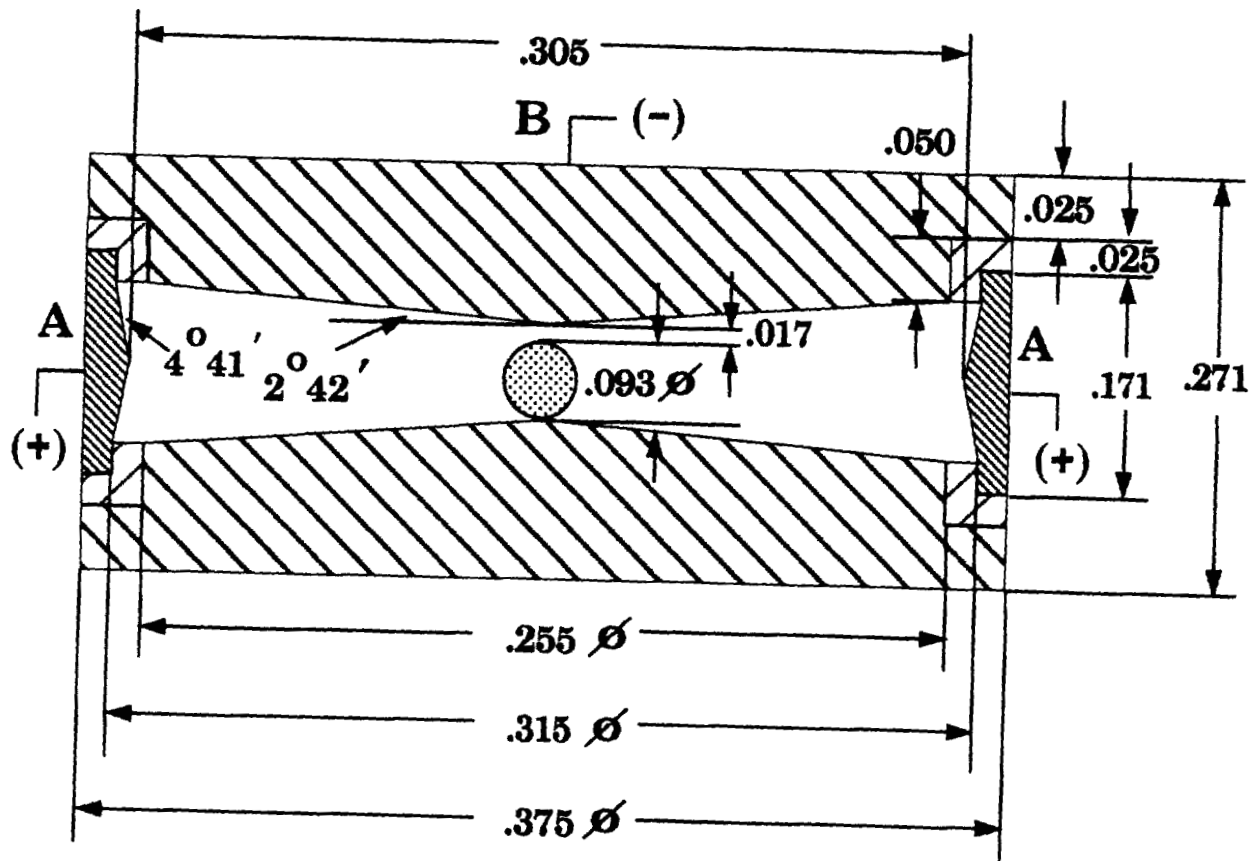


Figure 2. Motion Sensor

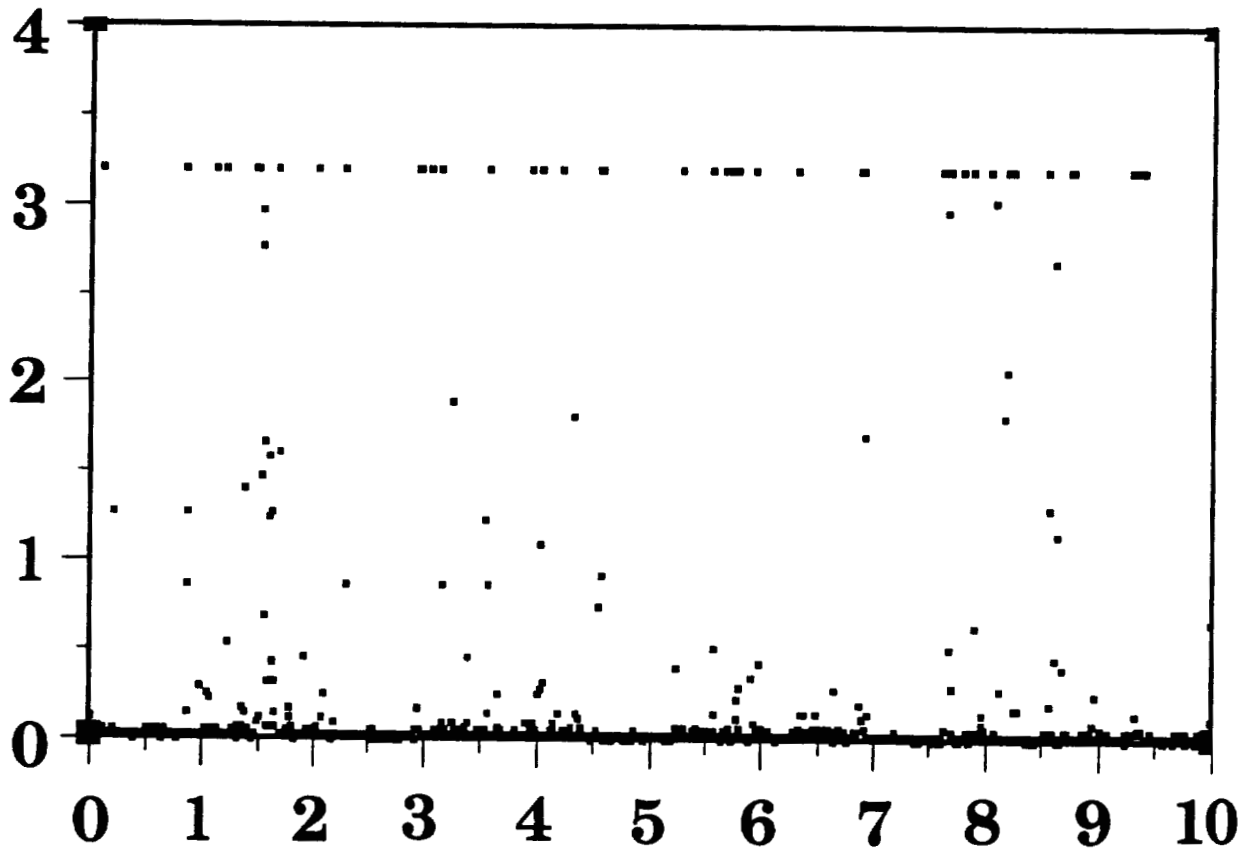


Figure 3. Sensor Response
(Volts vs. 100 msec)

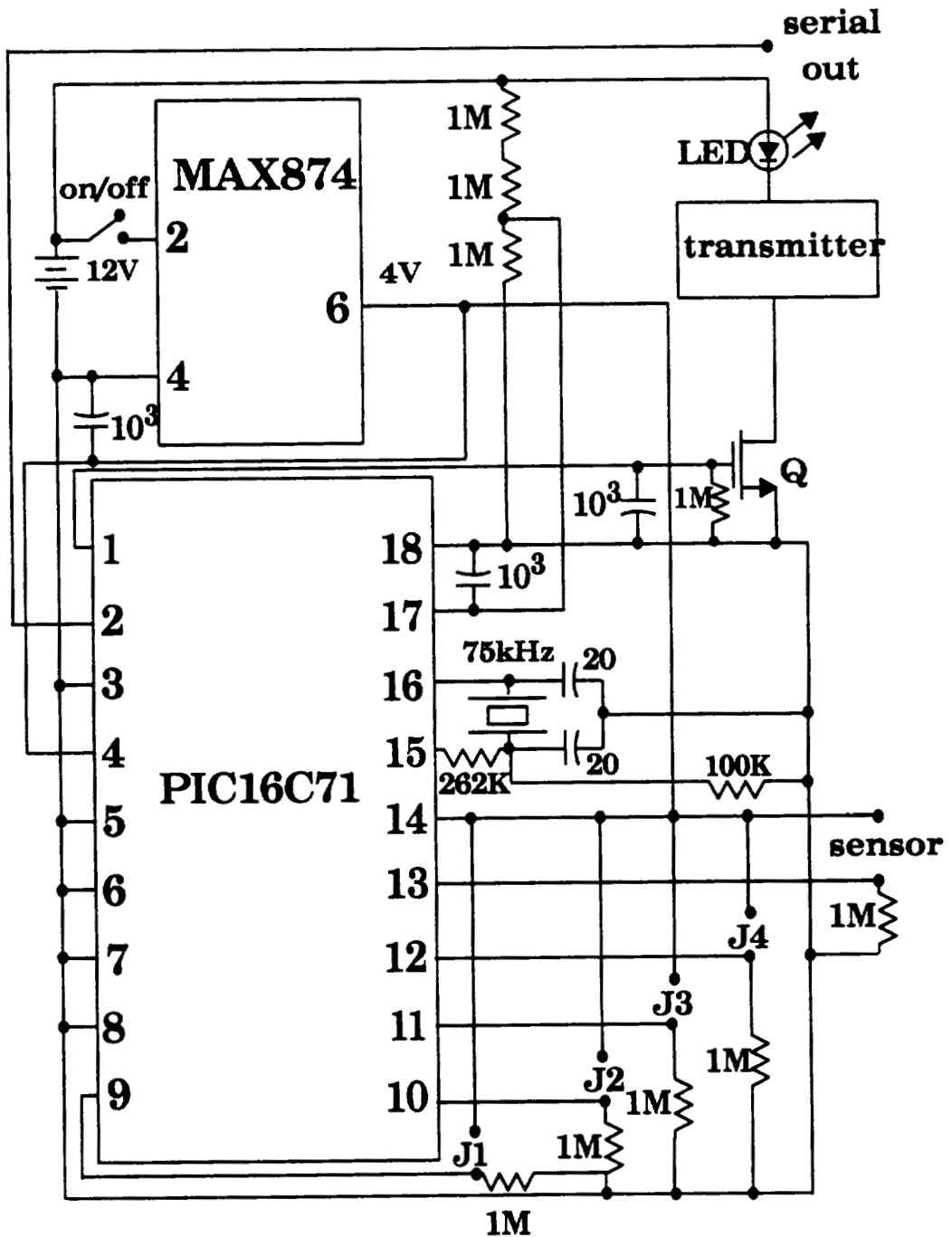


Figure 4. Monitor Schematics

all resistance values in ohms
 all capacitance values in pF
 unless otherwise specified
 Q1 = 9155 VMOS power FET

jumper settings
 J1 = battery test enable
 J2 = debug enable
 J3 = increase sensitivity
 J4 = decrease sensitivity

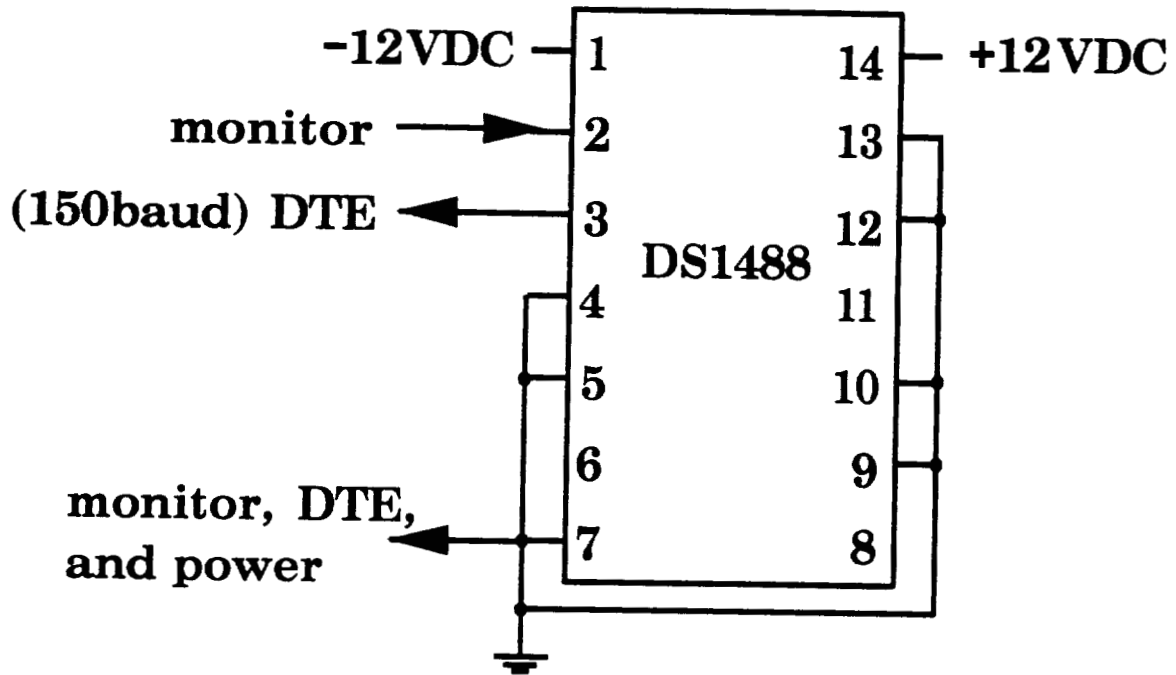


Figure 5a. Monitor-DTE Interface

done
 count = 00A8
 threshold = increased sensitivity (00C0)
 battery voltage = ED
 (alarm set)

Figure 5b. Sample Diagnostic Output

omit

ENVIRONMENTAL TECHNOLOGY

2457
P. 9

**SEED VIABILITY DETECTION USING COMPUTERIZED
FALSE-COLOR RADIOGRAPHIC IMAGE ENHANCEMENT**

J. A. Vozzo
Research Plant Physiologist
Forestry Sciences Laboratory,
USDA Forest Service
P. O. Box 906
Starkville, MS 39759

Michael Marko
Research Scientist
NY State Dept. of Health
Wadsworth Center
P. O. Box 509
Albany, NY 12201-0509

ABSTRACT

Seed radiographs are divided into density zones which are related to seed germination. The seeds which germinate have densities relating to false-color red. In turn, a seed sorter may be designed which rejects those seeds not having sufficient red to activate a gate along a moving belt containing the seed source. This results in separating only seeds with the preselected densities representing biological viability lending to germination. These selected seeds demand a higher market value. Actual false-coloring isn't required for a computer to distinguish the significant gray-zone range. This range can be predetermined and screened without the necessity of red imaging. Applying false-color enhancement is a means of emphasizing differences in densities of gray within any subject from photographic, radiographic or video imaging. Within the 0-255 range of gray levels, colors can be assigned to any single level or group of gray levels. Densitometric values then become easily recognized colors which relate to the image density. Choosing a color to identify any given density allows separation by morphology or composition (form or function). Additionally, relative areas of each color are readily available for determining distribution of that density by comparison with other densities within the image.

INTRODUCTION

Forestry is severely challenged by abusive cutting and global environmental change while its value increases as a revenue source for wood products. These social, environmental and economic strains are further reflected by biological ones. The seeds of economically important indigenous tree species are difficult, expensive and labor-intensive to collect, store and germinate. Considering that natural germination rates range from less than 50 percent to more than 90 percent, it then becomes significant to recognize good or viable seeds from poor or nonviable ones. An example shows that in 1991, 1.2 billion pine seedlings were planted in the southeastern United States. Assuming an average of 70 percent germination, at least 2 billion seed were required to meet the demand. If an average of 10,000 seeds per pound is assumed, then this required about 200,000 pounds of pine seeds. At an average of \$40 per pound, this is an \$8 million dollar investment per year in the southeastern U.S. only. Nurserymen are willing to pay an additional \$5 per pound for enhanced viability seeds.

Using the same figures as 1991, but with enhanced germination at 95% and increasing the average price per pound to \$45, would result in a savings of \$2,375,000 per year. If you consider the expenses of intensive labor to cull out the multiple seedlings planted to reach the goal of only 1.2 billion seedlings then there is an additional manpower savings in time and energy. The consistency of germination would

further allow planting to be timed with the 5-day weather forecast as to when to actually plant to account for local weather optimal for germination.

Radiographs of pine seeds clearly show empty and full seeds but will not distinguish which of the full seed will germinate. Densitometric values indicate variable but distinct density patterns within the seed seemingly unrelated to seed anatomy. Computerized imaging and densitometry assigns a color value to each of several density ranges, resulting in four of five different colored patterns which are more obvious than the original shades of gray density. Comparing the color distribution of seed which germinate to those that do not germinate leads to predicting individual seed viability. The significance of separation potential is within the gray level of densities physiologically active in the seeds. Actual false-coloring is not requisite to distinguishing densities so that a computer could detect predetermined gray ranges aside from false-coloring. For practical applications this would eliminate expense and software, as the computer would select by reading only the gray ranges of interest.

MATERIALS AND METHODS

We used a high-resolution TV digitizing system for scanning the images because it was important to be able to accurately compare different radiographs. The camera gain was adjusted so that the area of each film which had been covered by the lead letter label had a gray level of 250. This procedure reduces errors due to differing fog levels or developer activity for different individual films.

The radiographs each consisted of an array of several seeds, all of the same species, but with different germination potential, as confirmed by laboratory germination tests. A separate digital image of each seed in the array was created under identical illumination and recording conditions. The digitized image size in pixels was either 512 x 512, 256 x 256, or 512 x 64, depending on the size and shape of the species of seed. The contrast and brightness controls on the camera were adjusted for each array of seeds so that the full 0-255 range of gray levels was utilized. The density was not inverted, so the highest density values corresponded to the highest x-ray scattering (in our case, primarily due to water). We used a Dage model 81 high resolution video camera (Dage-MTI, Inc., Michigan City, IN) with an Androx ICS-400 image-processing board (Imaging Solutions Corp., Natick, MA) in a Sun 3/260 workstation (Sun Microsystems, Mountain View, CA). Our image-capture system is described in Hindus (1).

A montage of digital images of selected seeds (one image each of several categories of germination potential or x-ray appearance) was created for each species. This montage was then saved as a single image. A color lookup table was created for each montage by dividing the 0 to 255 density range into four or five sub-ranges colored in the sequence, green, yellow, blue, red, cyan, from lowest to highest density.

These limits were determined by moving a cursor around the image. At each point selected by the cursor, all of the pixels in the image with that gray-level blue flash on and off rapidly. In this way, both the optical density distribution and the morphology of the seeds could be taken into account in making decisions about color assignment. Colors were chosen to provide good contrast between areas of adjacent density ranges, while following a general plan of bright or warm colors for dense areas and dark or cool colors for light (empty) areas. The percent of the total pixel area of each seed represented by each color was found by counting the number of pixels of each color using a PIXAR II image computer.

The boundaries of the colors were fairly evenly-spaced, but adjusted to emphasize a difference in the seed which germinated. We chose to use the color red to indicate the density range which best correlated visually with germination potential. The background density was sufficiently low to be left uncolored, while all of the seed structure could be colored. The percentage of each color of each seed was obtained from pixel counts, and quantitatively related to germination potential. The image manipulation was done on a Raster Model One/80 graphics terminal (GS Computer Services, Inc., Nashua, NH), using the Sun 3/260 as a host. The software used was a portion of the Sterecon system described by Marko et al (2).

The pattern distribution is confirmed as lipid or free-water zones by magnetic resonance imaging after nuclear magnetic resonance analyses. Seed radiography is described with application examples by Vozzo et al (3, 4, 5, 6, 7, 8, 9, 10).

DISCUSSION

Water and air are natural radiopaque agents. That is, both are x-ray absorbent and therefore provide density on a radiograph. Even though each is requisite for seed germination, they are non-selective for viable and non-viable tissue. Additionally, seeds have numerous natural cavities which will accumulate both water and air. These are important factors because neither water nor air are then indicators of seed viability when imaged alone. Figures 1 and 2 show that significant amounts of water are imbibed by both viable and non-viable seeds. Fig. 1 is of Juglans nigra L. (Black Walnut) freshly collected and dry. Fig. 2 is of the same individuals radiographed after complete imbibition. Note that many walnuts appear full in Fig. 2 that do not in Fig. 1. The difference is water uptake. How then can good seeds be separated from nonviable seeds? An early false-coloring, density selective radiographic technique was xeroradiography. Using selenium activated aluminum, a positive or negative mode gave seeds another image perspective (Fig. 3). However, xeroradiography did not separate the nonviable seeds even though it did offer image advantages for morphology. False-color densities do separate seeds according to their viability. The walnuts in Fig. 4 represent an empty, a viable, and a nonviable image. Images A and D. are of the same individual. It is empty seed and will not germinate. However, images B and C appear full in black and white radiography and are expected to germinate. Actually, seed B germinated and seed C did not. There is a difference in their images after false-coloring (Figs. E and F respectively). Before false-coloring, the seeds can not be separated by radiography. Walnut is a practical specimen to illustrate image enhancement because it is relatively large and has an easily distinguished anatomy, *i.e.* embryo, cotyledon (stored food), and protective layerings.

Similar imaging for seven other tree seed species gave comparative results, *viz* false-coloring enhanced shades of gray density to separate seed which germinated from those which did not: Cornus florida L. (flowering dogwood), Fraxinus spp L. (ash), Liquidambar styraciflua L. (sweetgum), Liriodendron tulipifera L. (yellow-poplar), Magnolia grandiflora L. (southern magnolia), Pinus elliotii Engelm (slash pine), and Pinus taeda L. (loblolly pine). Each is seen as Figs. 5 - 11.

As represented in all species, the empty seeds have no red and are almost all green and yellow. The full seeds which germinated are predominantly red but may have also small areas of blue, green and yellow. Considering that even normal, healthy, viable seeds have tissue of low density, it is not unexpected to see the cool colors present. The absence of red in empty and poor seeds indicates a lack of heavier, denser tissue, requisite for initiating biochemical processes. Intermediate seeds are also evident as those individual within each Fig. 4 - 11 with an insignificant red present. These seeds may either germinate very slowly (as evidenced by germination rate), or not at all.

Germination trials showed that those individuals selected as being good seed were not only viable but vigorous, *i.e.* they had an extended primary root emerged from the seedcoat. Their germination rate was expressed simply by observing the number of seeds germinated every seventh day from their placement inside an incubating germination control box. The germination trial lasted 28 days.

The walnuts in Fig. 4, for example, show that images B and E represent viability while images C and F exhibit insufficient red to germinate. But what is the red representing?

Using magnetic resonance imaging (MRI) we can superimpose radiographs (conventional and false-colored) with MRI film and associate radiographic density and false-color red with proton presence in MRI. The proton presence is a combined imaging of free-water molecules and lipids. We think then, that the red false-color densities represent the distribution and percent of free-water and lipids necessary for germination. This is a valid biological assumption.

These findings have commercial application for separating substances by their inherent densities. Any matter with a radiopaque signature could be sorted by selecting an ejection device triggered by a color representing that signature. Theoretically, seeds or other matter could be introduced to a moving belt which passes under a radiographic beam. The beam projects sufficient energy to penetrate the subject and excite an image processor. A computer translates the subject's registered density from the radiographic receptor into spectral wavelengths of visible light. Pre-selected ranges of gray levels between 0 and 255 are assigned a visible light energy. Signals emitted from the color translators activate an ejection/selection gate along the moving belt which then channels each subject into its collector.

Commercial value is related to grading standards and quality control. A color-sorting system is currently available which can be mated to a radiographic survey unit. After determining the applicable density-color translations, this technique will sort and grade transparent, translucent, or opaque subjects unaffected by radiographic energies.

REFERENCES

1. Hindus, L.A. 1992. 2K images from a 1K camera: High resolution at lower cost. *Advanced Imaging* 7:52-53.
2. Marko, M., Leith, A., Parsons, D. 1988. Three-dimensional reconstruction of cells from serial sections and whole-cell mounts using multilevel contouring of stereo micrographs. *J. Elect. Microsc. Tech.* 9:395-411.
3. Vozzo, J. A., 1974. Special radiographic techniques. *Proceedings X-ray Symposium*, Nov. 7-8, Macon, GA. pp. 79-83.
4. Vozzo, J. A. and Sandra Linebaugh. 1974. Tomography in seed research. *Proceedings of the Association of Official Seed Analysts*, Vol. 64, pp. 94-96. Vozzo designed and wrote; Linebaugh collected data.
5. Vozzo, J. A., 1978. Radiographic terminology for biological research. *USDA For. Serv. Gen. Tech. Report. SO-18.* 45 p.
6. Vozzo, J. A. 1979. Radiopaque agents for seed research with *Juglans nigra*. *Proc. Flowering and Seed Development in Trees: A Symposium.* p. 272-280. *Int. Union For. Res. Org.*
7. Belcher, E. and J. A. Vozzo. 1979. Radiographic analysis of agricultural and forest tree seeds. *Assoc. Off. Seed Anal. Hanb. No. 31*, 29 p., 79 plates. (available only through A.O.S.A.) Vozzo shared equally in design, data collection, writing.
8. Vozzo, J. A. 1981. Xeroradiography for seed research. *In: Reunion Sobre Problemas em Semillas Forestales Tropicales.* pp. 299-302. San Felipe-Bacalar, Quintana roo, Mexico, Oct., 1980. *Instl. Nacional de Invest. Forestales Publ. Esp. No. 35.* 352 p.
9. Vozzo, J. A. 1988. Seed radiography. *Materials Evaluation* 46(11): 1450-1455.
10. Newberry, Sterling; Vozzo, J. A.; and Marko, Michael. 1992. Time-lapse x-ray microscope movie of the germinating garden pea seed. *In: Bailey, G. W., Bentley, J., Small, J. A., eds. Proceedings 50th Annual Meeting Electron Microscopy Society of America.* 1992. San Francisco, CA. San Francisco Press, Inc.: 836-837.



Figure 1. Conventional radiography of *Juglans nigra* seeds freshly collected. Note empty and full seeds.

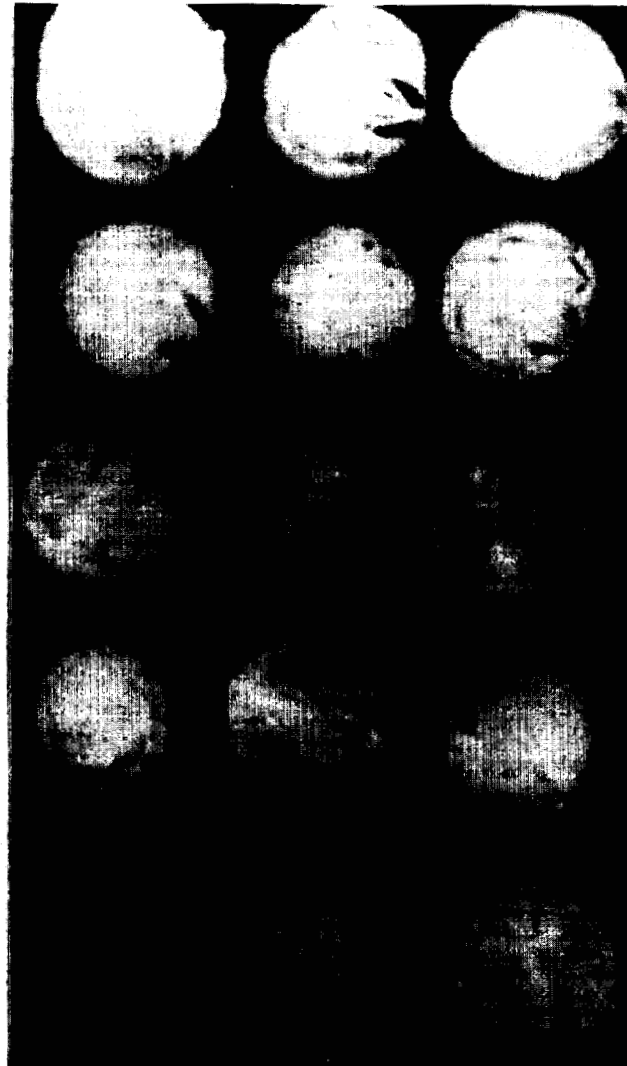


Figure 2. Same individuals as in Fig. 1, but after imbibition and water uptake. Note now that seeds appear full due to water density.

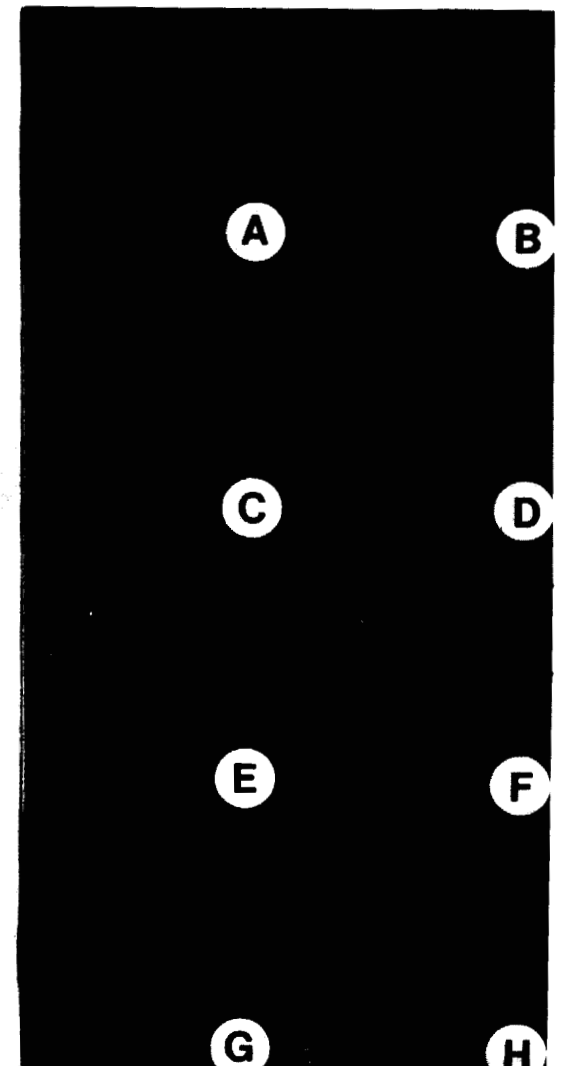


Figure 3. Xeroradiography of *Juglans nigra* seeds (C, D, E, F) as compared with conventional radiography (A, B, G, H). Note empty seeds in left column and full seeds in right column.

Figure 4. Juglans nigra seeds. Compare images A and D, B and E, and C and F of individual seeds. Only seed B, E germinated.

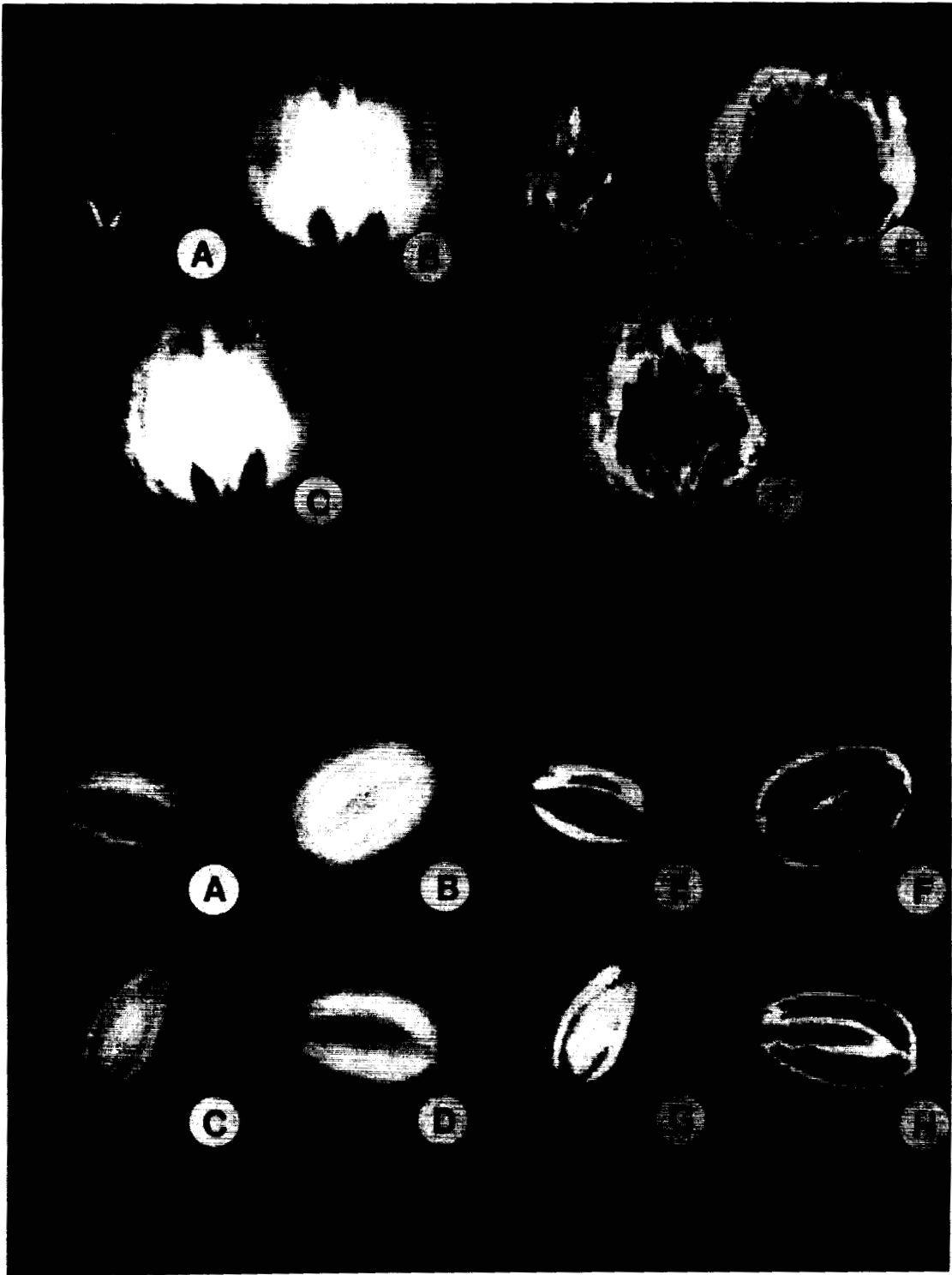


Figure 5. Cornus florida seeds. Individual B, F germinated.

Figure 6. Fraxinus spp seeds. Individuals C, I and E, K germinated.

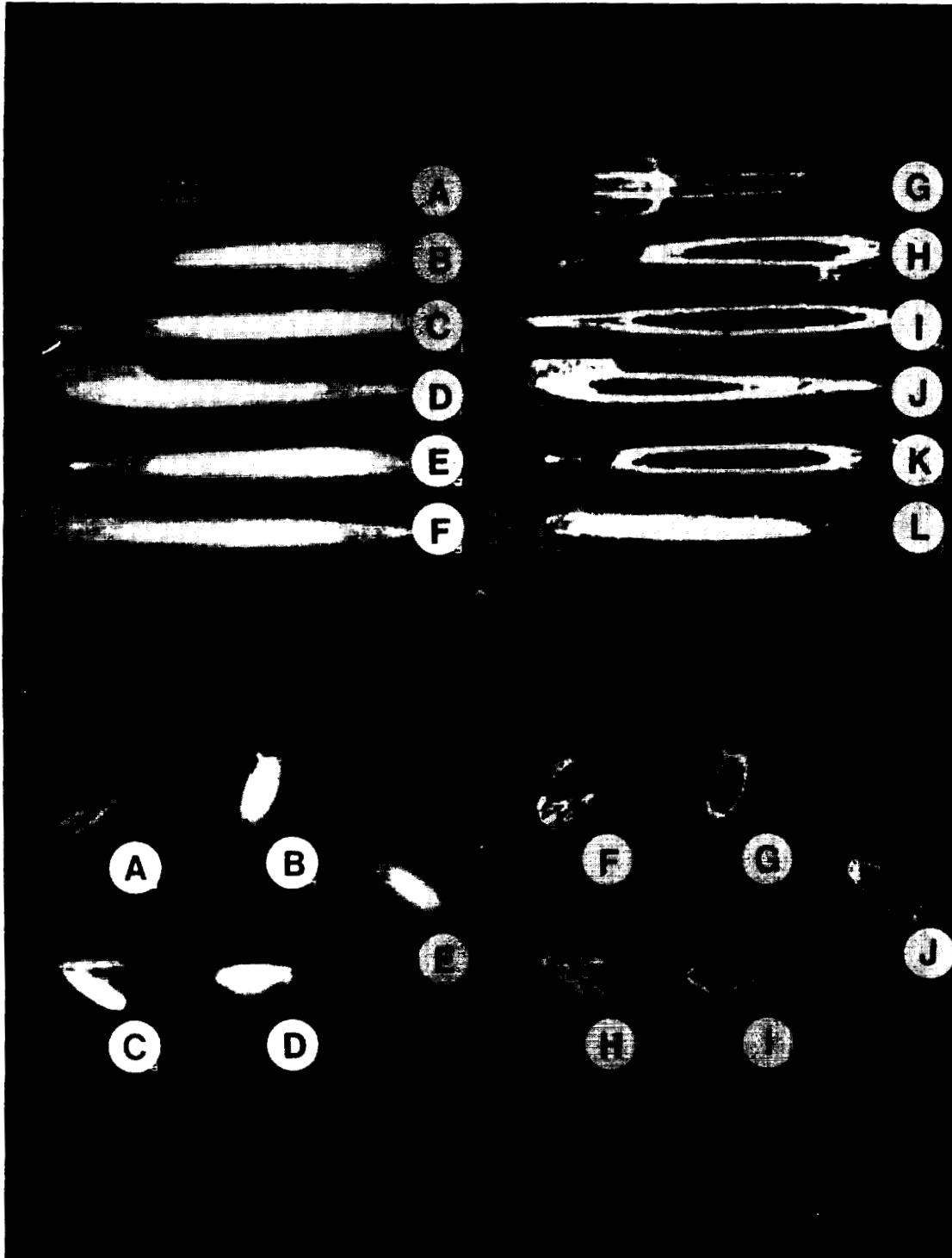


Figure 7. Liquidambar styraciflua seeds. Individuals D, I and E, J germinated.

Figure 8. Liriodendron tulipifera seeds. Individual D, H germinated.

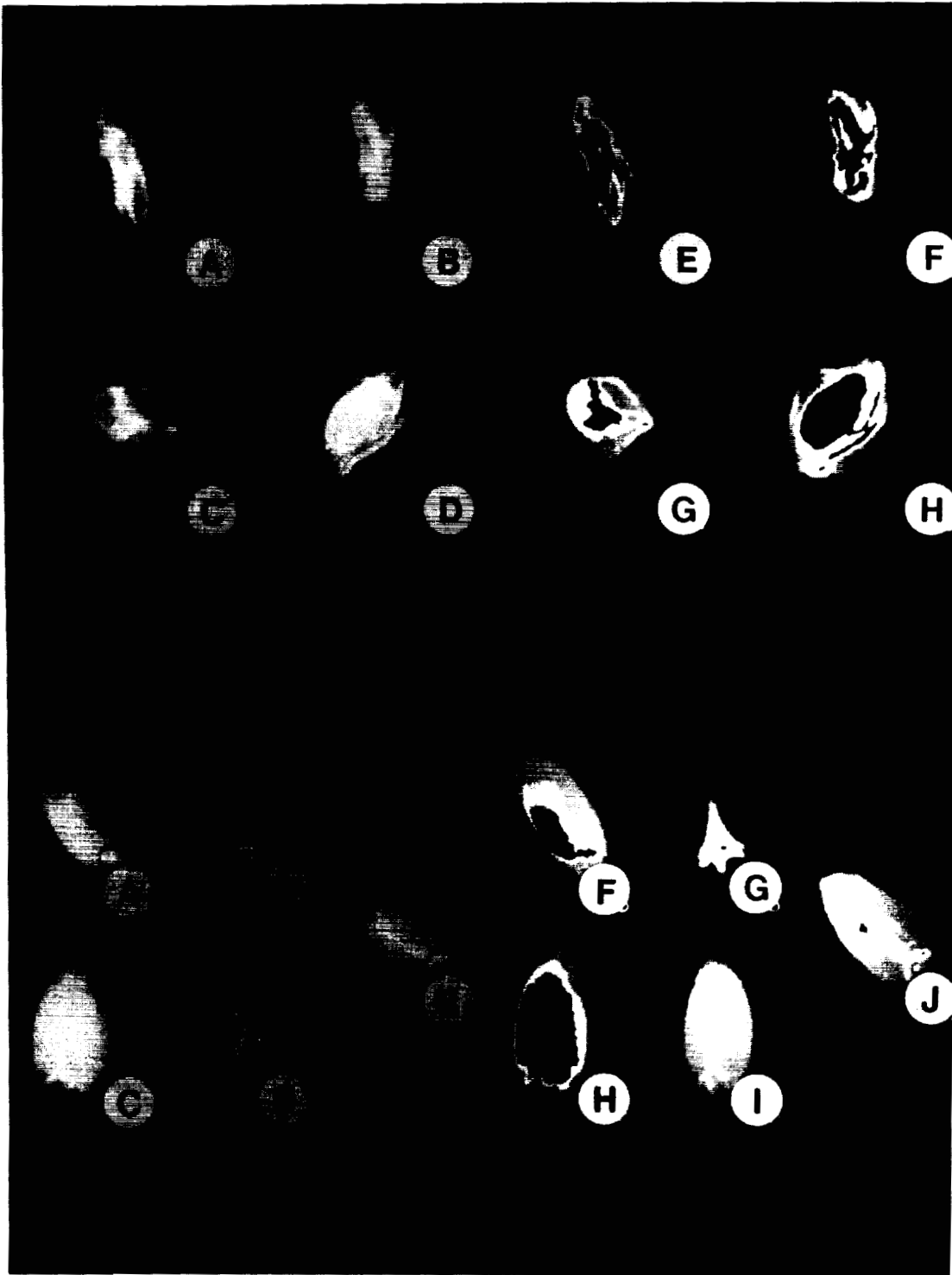


Figure 9. Magnolia gandiflora seeds. Individual C, H germinated.

Figure 10. Pinus elliotii seeds. Individual B, F germinated.

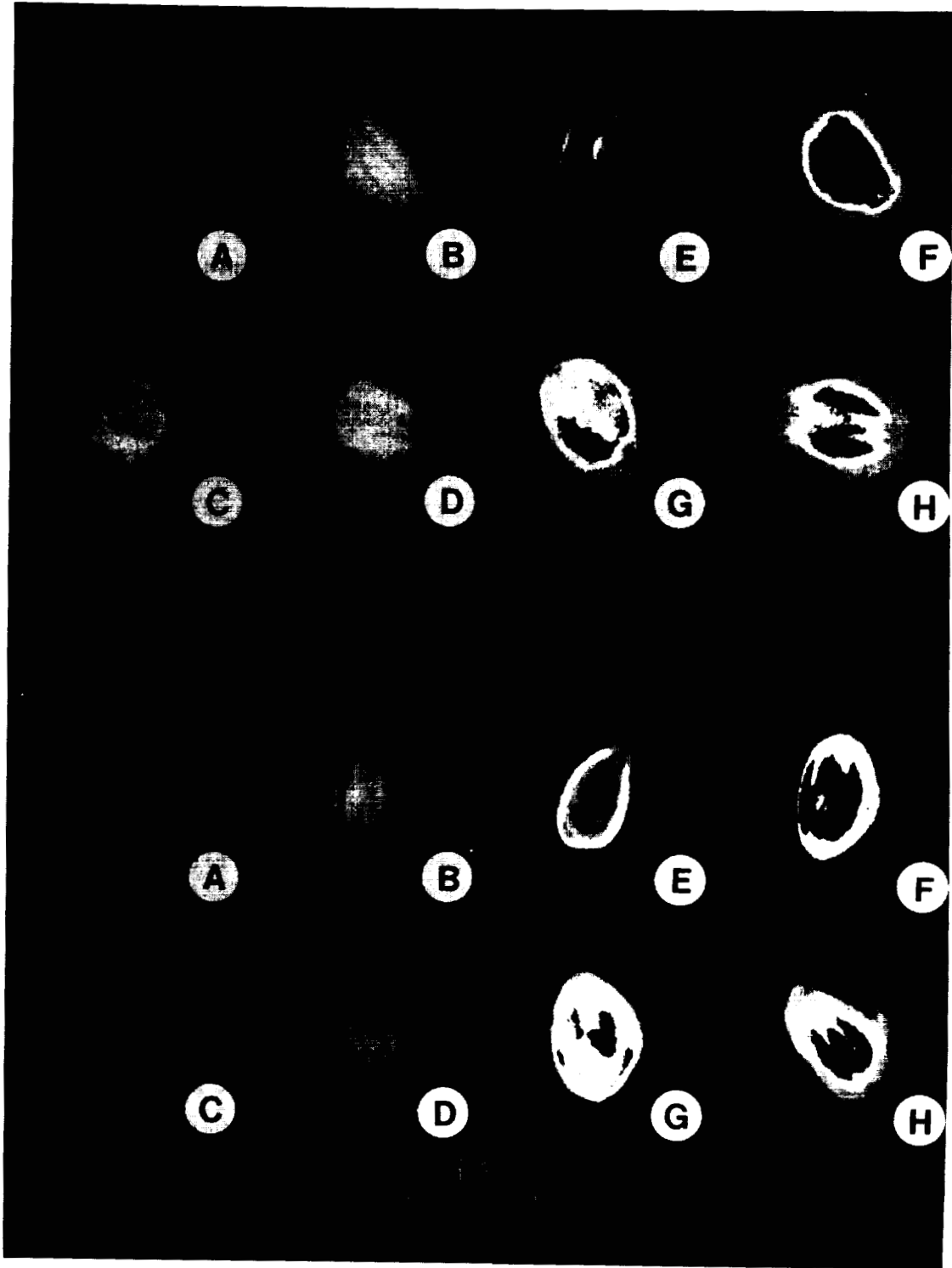


Figure 11. Pinus taeda seeds. Individual B, F germinated.

500-74
2458
17-8

A COMMERCIALIZED, CONTINUOUS FLOW FIBER OPTIC SENSOR FOR TRICHLOROETHYLENE AND HALOFORMS

James C. Wells and Mark D. Johnson
Purus, Inc.
2713 North First Street
San Jose, CA 95134-2010

ABSTRACT

Purus, Inc. has commercialized a fiber optic chemical sensor using technology developed by Lawrence Livermore National Laboratory and licensed from The University of California. The basis for the sensor is the development of color within a reagent when exposed to an analyte. The sensor consists of an optrode, reagent delivery and recovery system, fiber optic transmitter-receiver, controller, and display. Reagent is pumped through the optrode. Analyte diffuses across a gas permeable membrane and reacts with the reagent to form a colored product. The colored product is detected by measuring the absorbance of light from a 568 nm diode. Reagents are currently available for TCE and trihalomethanes. Initial reagent chemistry is based on the Fujiwara alkaline pyridine reaction. The optrode contacts only gas streams, but the volatility of the current analytes also allows measurements of aqueous streams, without being affected by aqueous interferences that are non-volatile. Sensitivity of the sensor has been demonstrated to 5 ppb aqueous solutions and 0.1 ppmv in flowing gas streams.

INTRODUCTION

There has been increasing concern regarding environmental contamination and the associated health hazards from the extensive use of chlorinated hydrocarbons. These concerns as well as increasing regulatory requirements have created extensive environmental remediation and monitoring efforts. Present assessment and monitoring methods are labor intensive and frequently suffer long delays between sample collection, analysis, and reporting. Fiber optic chemical sensors can provide a cost effective, real time, in-situ measurement technique to overcome these difficulties.

Purus, Inc. has introduced PurSense™, a fiber optic chemical sensor, under license from the University of California. This sensor technology was developed at Lawrence Livermore National Laboratory under the direction of Dr. F.J. Milanovich, and is an outgrowth of research first sponsored by the U.S Environmental Protection Agency and more recently by the Department of Energy.¹ The reagent is based on the Fujiwara² alkaline pyridine reaction with halogenated compounds.

PurSense™ technology has broad applicability limited primarily by product configuration and reagent availability. Some product configurations are shown in Figure 1 along with available reagents. Our initial design of PurSense™ allows it to be used as an industrial process monitoring device or as a laboratory screening instrument. This sensor configuration is currently undergoing field tests. Construction of a field transportable unit is underway with field testing planned to begin during April 1994. In this paper we discuss the packaging of the system into a commercial unit and review the sensor operation and response to both aqueous and gas mixtures of TCE.

MATERIALS AND METHODS

Sensor Description

A schematic diagram of the *PurSense*TM fiber optic chemical sensor probe (also called an optrode) is shown in Figure 2. The optrode is composed of a tubular reaction chamber, formed from a gas permeable membrane, and an outer stainless steel housing. Optical fibers to monitor the reaction and capillary tubing to deliver and recover reagent are mounted inside the outer housing and membrane.

A block diagram of the *PurSense*TM system is shown in Figure 3. Reagent is pumped through the reaction chamber using a stepper motor driven syringe with optically encoded position feedback. The pump operates from a single 24 volt power supply. Spent reagent is recovered in a waste reservoir.

APPLICATION	CONFIGURATIONS				
	Penetrometer Down hole	Lab Instrument	On Line Monitoring	Portable / Handheld	Reagents to Develop
Site Assessment	X TCE, CHCl ₃			X TCE	CCl ₄ , TCA, PCE, BTEX
Environmental Monitoring	X TCE, CHCl ₃		X TCE, CHCl ₃		CCl ₄ , TCA, PCE, BTEX
Field Screening	X TCE, CHCl ₃			X TCE	CCl ₄ , TCA, PCE, BTEX
Industrial Process Monitoring			X TCE, CHCl ₃	X TCE, THM	CCl ₄ , TCA, PCE, BTEX
Lab Sample Screening		X TCE			CCl ₄ , TCA, PCE, BTEX
Municipal Water		X THM	X THM		
Storage Tank				X	BTEX

Figure 1. Applications and Sensor Configurations.

The fiber optic transmitter receiver (FTR) produces a highly stable, chopped, green (568 nm) light from an LED. This light is coupled into an optical fiber using standard SMA connectors and transmitted to the optrode. Some of the light is absorbed as it travels through the reaction chamber. The remaining non-absorbed light returns to the FTR through a second optical fiber where it is focused and detected by a photo-diode. The electrical signal is conditioned for further

processing. The amplifier output is a DC voltage proportional to the light passing through the optrode. This analog signal is converted into a digital signal and passed to the microprocessor.

Control and analysis are accomplished using an Intel 8752 BH embedded controller. Concentration is displayed in ppb using a 4 digit LED display. Additional data are available through an RS-232 port. Calibration data are entered using solid state push button switches.

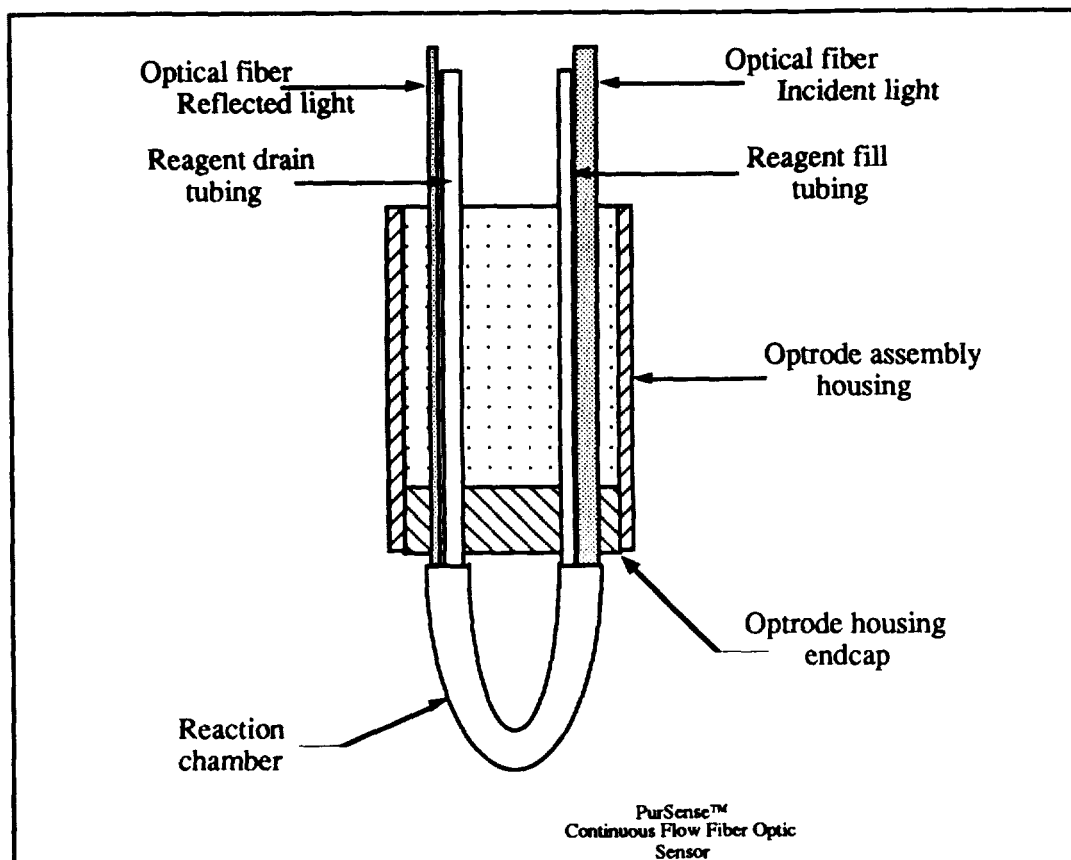


Figure 2. Construction of PurSense™ optrode.

Aqueous Measurement Procedures

Aqueous measurements were made in a 1 liter amber glass wide mouth bottle with a threaded glass top. The threaded top was modified to allow mounting of the optrode in the center of the top. Sample solutions for these measurements were prepared from methanolic stock solutions of TCE. The sample was transferred by slowly pouring about 850 ml from a volumetric flask into the sample chamber allowing a headspace volume of about 200 ml. The solution was at room temperature and slowly stirred during the measurements. Five measurements were made on each sample within 15 minutes.

Flowing Gas Mixture Measurement Procedure

Recently we have been investigating the sensor response to flowing gas containing TCE or chloroform. These experiments were performed using a permeation source flow system. The system consisted of a permeation tube holder/heat exchanger (VICI Metronics) immersed in a 30 °C

constant temperature water bath. The permeation source contained liquid organic analyte that diffuses through a permeable Teflon tube at a constant, calibrated rate. Nitrogen gas was used to dilute the analyte by varying the nitrogen flow rate. A needle valve and flow meter were used to control and measure the gas flow rate. The optrode was placed into a 1/4 inch stainless steel tee that was connected to the permeation tube holder by stainless steel tubing. Gas flow rates were calibrated with a soap film bubble flow meter.

All sensor measurements were performed using a 2.6 minute cycle. During the first minute the optrode was flushed with fresh reagent, and in the last 1.5 minutes, this aliquot of reagent was retained in the optrode and allowed to react with the TCE vapor. The chromophore that formed during this exposure attenuated the analyzing light, thus gradually decreasing the light transmission during the exposure time. A least square fit of absorbance versus time in the last 30 seconds of the cycle yielded the slope, or the rate of change in absorbance per unit time. This slope value was then correlated to concentration.

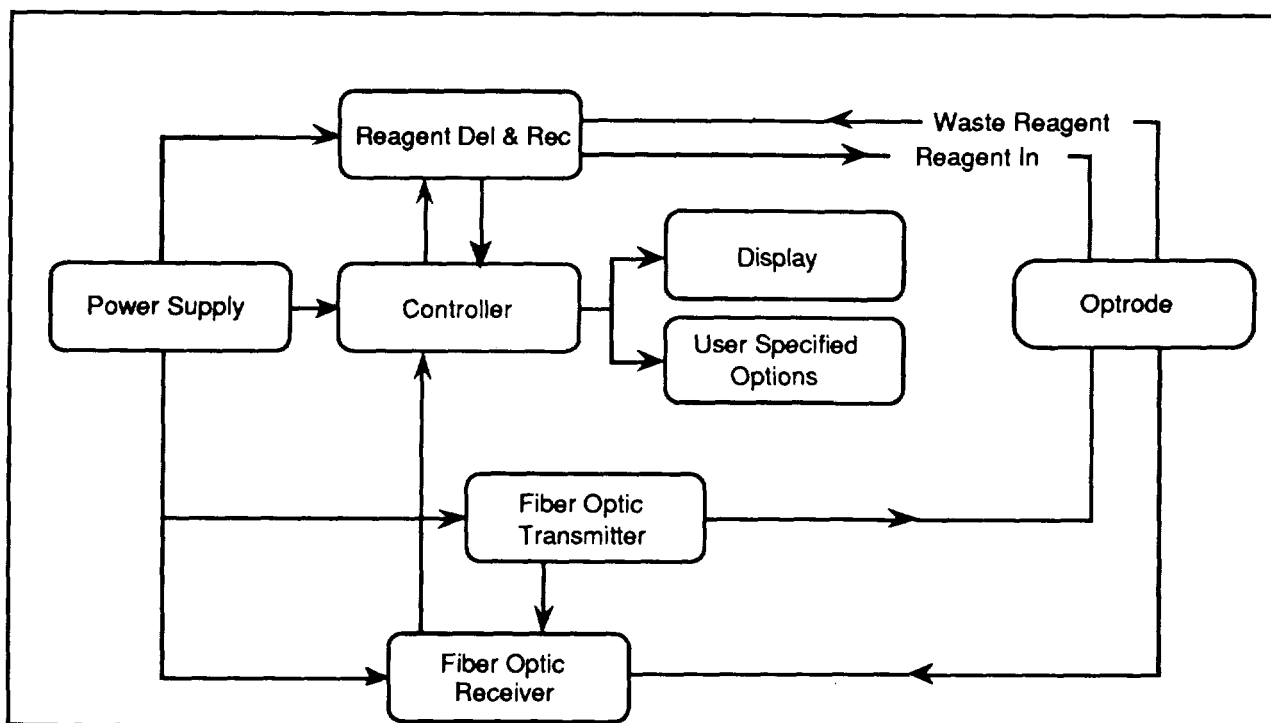


Figure 3. Block diagram of the *PurSense™ THM-1*.

RESULTS AND DISCUSSION

Absorbance spectra of our initial reagents for TCE and chloroform are shown in Figure 4. These spectra were taken after 150 seconds and show a slight shift in peak wavelength. This shift is probably due to slight differences in the colored product formed during the reaction. Several minutes to hours are required for the reaction to go to completion but by monitoring the rate of change in absorbance the headspace concentration may be determined without waiting for the reaction to go to completion.

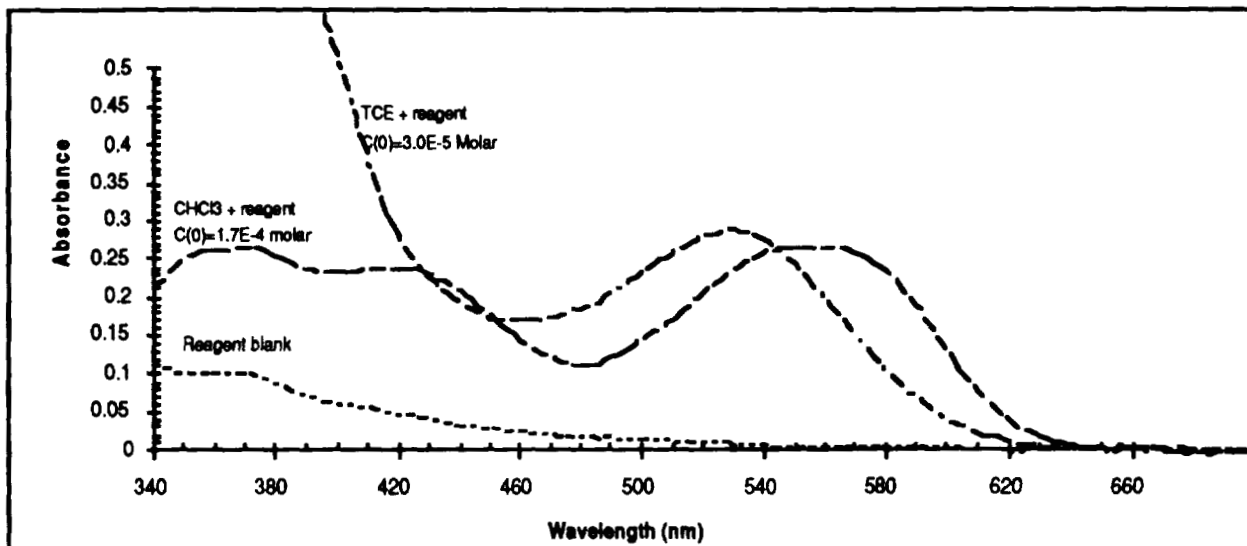


Figure 4. Absorption spectra of products from the reaction of reagents with TCE and Chloroform.

Typical sensor responses are shown in Figure 5 for various aqueous concentrations of TCE. The first measurement is systematically lower because the measurement cycle was started immediately after transferring the sample into the glass jar. When the sample is allowed to equilibrate for about 5 minutes before beginning the measurement cycle the first measurement is similar to the others.

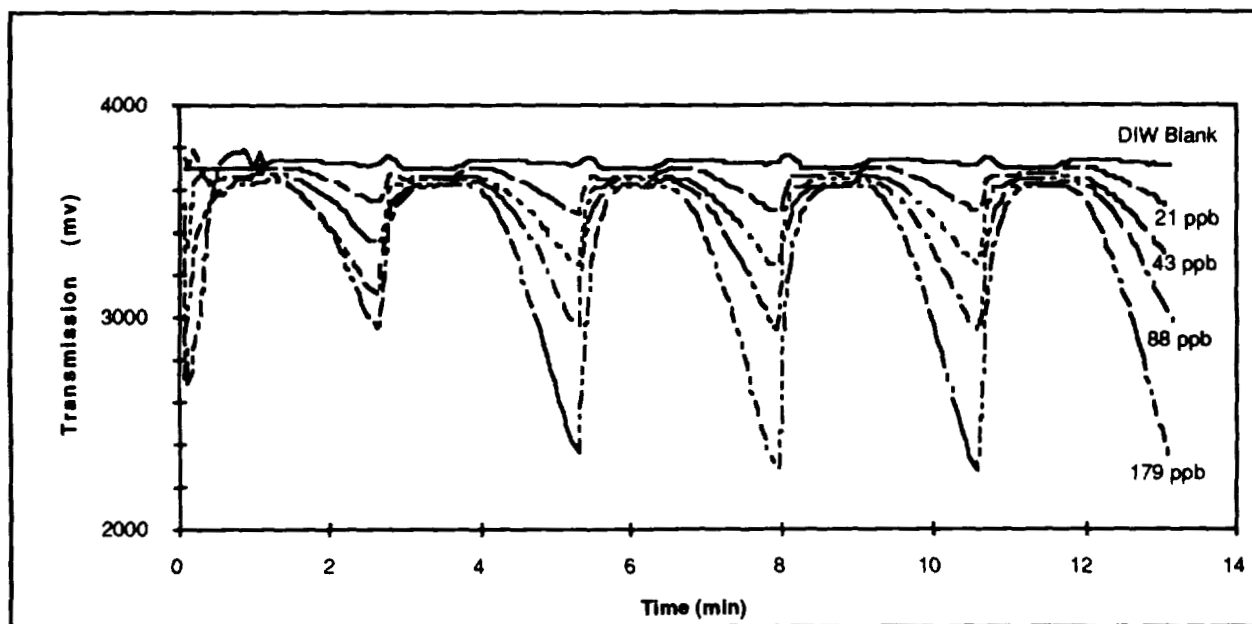


Figure 5. Typical sensor response to aqueous solutions of TCE.

A typical TCE calibration curve is shown in Figure 6. Sensor absorbance slope measurements are shown on the vertical axis while aqueous concentrations as determined by GC/ECD are shown along the horizontal axis. The linearity of sensor measurements is quite good below 500 ppb but begins to deviate significantly from linearity near 1 ppm.

Figure 7 illustrates the typical sensor response to mixtures of nitrogen and TCE. Sensor responses to gaseous mixtures are more reproducible and baseline shifts with time appear to be eliminated.

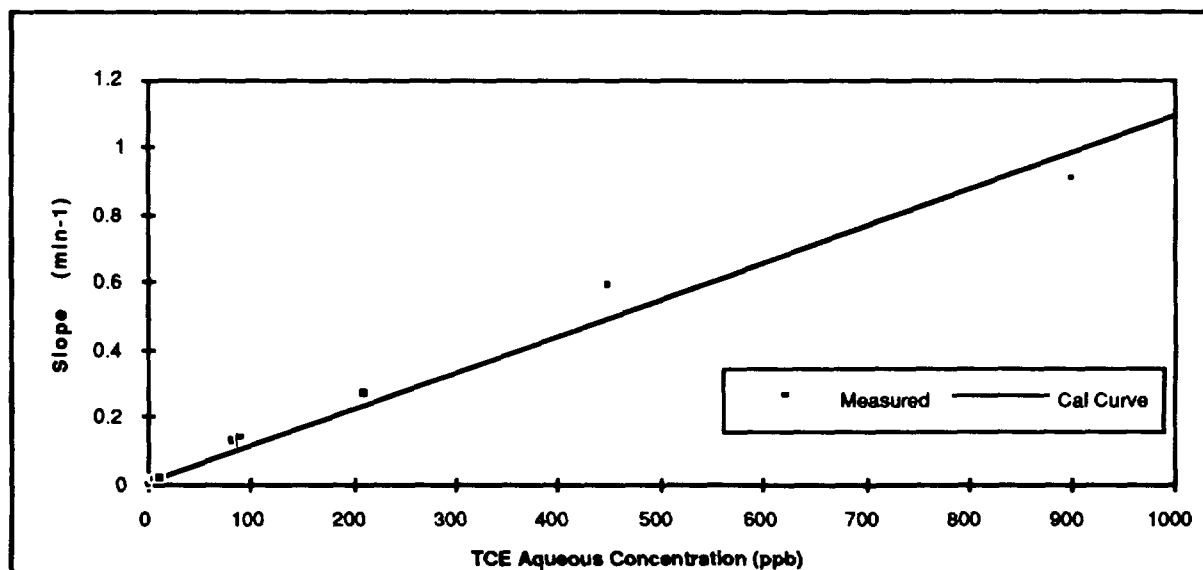


Figure 6. Sensor measurements plotted against calibration curve.

Reproducibility of the response for the TCE/nitrogen gas mixture is displayed in Figure 8. Over the span of ten replicate measurements, the worst set of measurements gives a relative 95 % confidence limit of $\pm 7.6\%$.

In Figure 9 we show the calibration curve that was determined from these measurements. Again we see some departure from linearity at the upper end of the concentration range but it isn't as pronounced as that seen with the aqueous measurements. The correlation coefficient over the entire range of measurements was .995.

CONCLUSIONS

We have demonstrated the viability of using a fiber optic sensor based on Fujiwara chemistry for on-line monitoring and testing of both aqueous and gaseous streams. The sensor is easy to operate and requires little training. The chemistry is highly selective and the methodology seems well suited for on-line monitoring applications but is limited by available reagents. Field testing is underway to assess the functionality and reliability of the system.

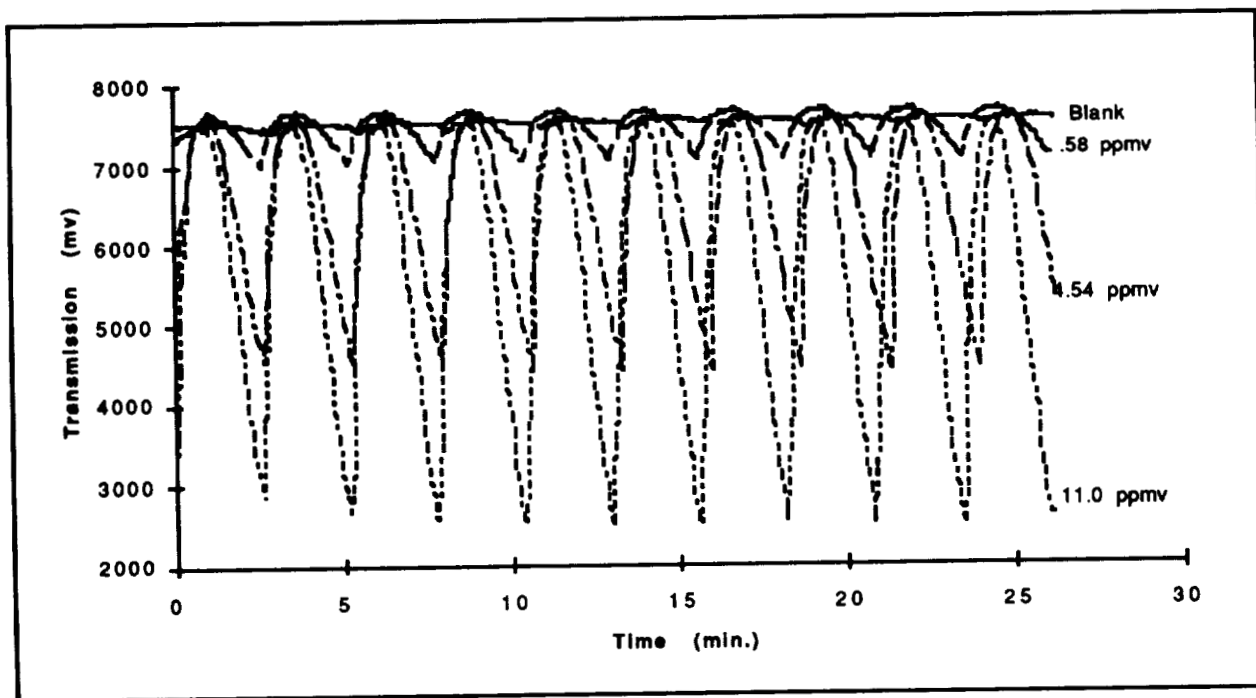


Figure 7. Typical sensor response to flowing mixture of nitrogen and TCE.

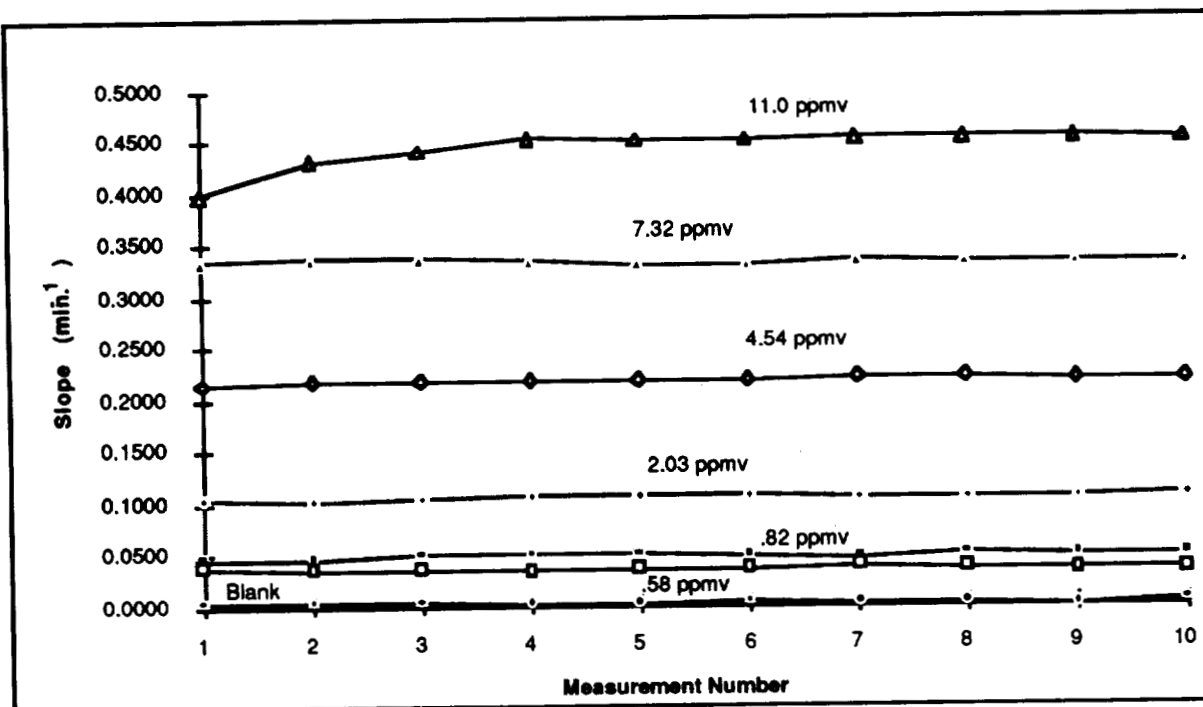


Figure 8. Sensor gas phase stability.

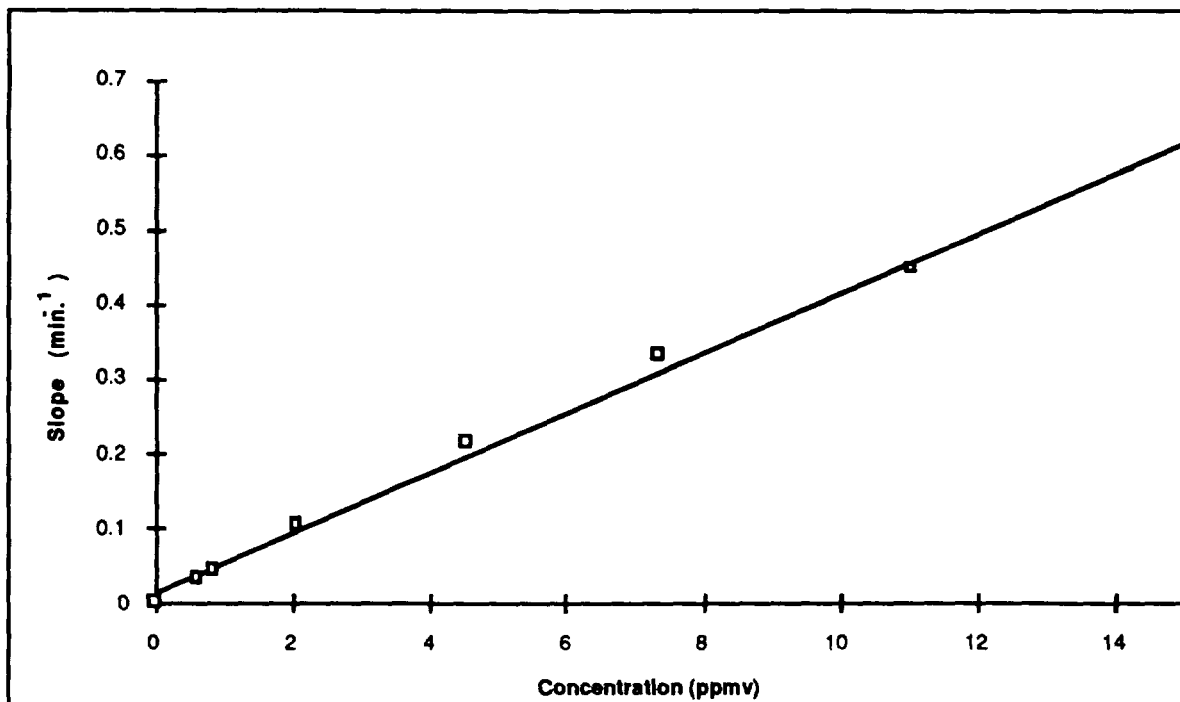


Figure 9. TCE/Nitrogen mixture calibration curve.

REFERENCES

1. F.J. Milanovich, P.F. Daley, K. Langry, et al., "A Fiber Optic Sensor for the Continuous Monitoring of Chlorinated Hydrocarbons," presented at the Air and Waste Management Association Annual Meeting, Feb. 12-14, 1991, Las Vegas, NV.
2. K. Fujiwara, "New Reaction for the Detection of Chloroform," *Chem. Abstracts*, 11:3201 (1917).

523-45
2459
p-13

COMPUTERIZED *IN VITRO* TEST FOR CHEMICAL TOXICITY
BASED ON *TETRAHYMENA* SWIMMING PATTERNS

DAVID A. NOEVER*, HELEN C. MATSOS, RAYMOND J. CRONISE,
LOREN L. LOOGER¹, RACHNA A. RELWANI
NASA Marshall Space Flight Center, ES-76, Huntsville, AL 35812 USA

JACQUELINE U. JOHNSON
Department of Animal and Food Science, Alabama A&M University, AL

Running title: Computerized chemical tests of Tetrahymena

Abstract

An apparatus and method for rapidly determining chemical toxicity has been evaluated. The toxicity monitor includes an automated scoring of how motile biological cells (*Tetrahymena pyriformis*) slow down or otherwise change their swimming patterns in a hostile chemical environment. The device, called the Motility Assay Apparatus (MAA) is tested for 30 second determination of chemical toxicity in 20 aqueous samples containing trace organics and salts. With equal or better detection limits, results compare favorably to *in vivo* animal tests of eye irritancy, in addition to agreeing for all chemicals with previous manual evaluations of single cell motility.

1. Introduction

For pollution monitoring, chemical testing and pharmaceutical approval, existing whole animal procedures are expensive, time consuming and increasingly restricted by federal law. Thus a combination of public pressure and high costs has stimulated the \$3 billion chemical testing market to look for alternatives to whole animal research.

In collaboration⁹ with Avon, Inc., Silverman⁸⁻⁹ demonstrated that hostile chemicals could change the swimming behavior of single biological cells (*Tetrahymena*) in a controlled and reliable way. For 21 chemicals and pharmaceuticals, he found equal or better results for the toxic response of single cells compared to alternative whole animal tests (e.g. FDA's Draize rabbit eye test). His method relied on two lab technicians performing a subjective evaluation of swimming behavior and scoring their opinions of regular vs. irregular swimming patterns'. Subsequent industrial interest has focused on finding more reliable and rapid ways to improve the toxicity evaluation.

Other experiments³⁻⁴ have demonstrated that for many (*Tetrahymena*) cells suspended in shallow culture dishes, the cells rapidly (20 seconds) aggregate to give a characteristic signature pattern (polygonal net). The honeycombed patterns change repeatedly when chemicals alter the culture media (water) and using image analysis of the aggregation patterns, chemical toxicity could be scored accordingly. This advance took away the capital investment in microscopes and technician time required by Silverman's test⁹, but nevertheless demanded an extended time for culturing cells to high enough densities (million cells/ml). The assay's aim was to make the advantages of the single cell method more widely accessible to smaller labs or for field tests where microscopic observation and individual cell counting might prove impractical.

*author inquiries, (205)544-7783; FAX (205) 544-1777

¹Stanford University, Stanford CA

While these innovative alternatives using single biological cells have shown promising results when compared to animal tests, they generally have suffered from a non-uniform procedure for scoring toxicity. Either microscopic observation of cell swimming patterns⁹ has required subjective and time consuming scoring by two lab technicians or alternatively, macroscopic observation of cell swimming patterns⁵ has required lengthy culture preparation. Industrial labs have therefore sought a more rapid and low cost device for implementing single cell monitoring on a wide scale.

Here we design and evaluate an automated method for computer aided scoring of single cell responses; 20 chemicals consisting of organics and salts are examined using *Tetrahymena* as the test organism. Changes in cell swimming velocity serve as the test's monitor, while computerized cell tracking provides the non-subjective evaluation. The method differs from previous approaches in its relative speed, reliability and operator ease. In several minutes, multiple chemicals can be either tested as they act alone or synergistically.

2. Materials and Methods

2.1. Organisms and culture conditions

The ciliate, *Tetrahymena pyriformis* (American Tissue Type Collection, Md., USA), were grown in (autoclaved) 2% proteose-peptone-yeast medium¹⁰. The organisms were cultivated axenically in a temperature-controlled (22° C) clean room (Class III). The protists were grown in 1 L glass containers without additional gassing or agitation.

T. pyriformis was pursued as a target organism because its chemical sensitivity has been well-characterized previously¹. Its short generation times and thoroughly investigated biology make it what one researcher⁷ called a "biochemical star." As a result, for more than 40 years, *T. pyriformis* has been the organism of choice¹ for assaying carcinogens, insecticides, fungicides, petroleum products and organics, mycotoxins, antimetabolites and heavy metals.

2.2 Laboratory preparations

Instructions for lab preparations of cell cultures include: 1) transfer freeze-dried *Tetrahymena* cells into rehydration fluid vial; 2) incubate 10 minutes at 35-37° C; 3) decant entire constituents into empty petri dish with either a dilution blank or previously measured concentration of chemicals.

2.3. Determination of pattern formation

For direct comparison with computerized scoring of single cell swimming, macroscopic aggregation patterns³⁻⁶ were also monitored at the same chemical dosages. Cell suspensions were prepared as dense, shallow cultures (3.2×10^5 cells mL⁻¹, culture depth, 4 mm). Assuming typical cell parameters (20-50% g carbon per g dry weight, 80% water content by weight, and cell specific gravity of 1.05 g cm⁻³), this cell population corresponds approximately to 1 g carbon per cubic meter.

Vertical migration and bioconvection patterns of the ciliate were determined in a rectangular polystyrene flask (33x77x15 mm inner dimensions). Since average pattern dimension was 1-2 mm, the effect of container dimensions on pattern formation was minimal. Different sized flasks did not affect either characteristic pattern size or overall morphology.

The flask was placed on a clear stage and illuminated (4000 lux, Edmund Scientific, USA, light meter) using two collimated incandescent beams angled at 45°. A continuously cooling fan maintained thermal control of the light source; each lamp was remotely placed on a gooseneck wand and focussed using 24 cm optical fibers. Thermal convection was not observed in either non-motile (dead) cells of *T. pyriformis* or with 0.1 mm aluminum flakes in water.

2.4 Image analysis

a. Single cells

Component parts of the signal detection system for single cells include: 1) compatible computer with printer; 2) 2 high-resolution black and white video monitors with black and white video camera; 3) compatible microscope with phase contrast or dark field optics and objectives; 4) 100 micron deep observation chamber. A live or videotaped image of 50 or more single cells of *Tetrahymena* is centered and delivered into the computer. The image is analyzed for cell identification and as applicable, *Tetrahymena* concentration, motile velocity and linearity data. A hard copy printout of test results can be made or optionally, stored as data in ASCII files. The assay device is able to recognize 50 micron swimming cells and to distinguish them from other biologicals based on their size, luminosity and motion.

b. Aggregation patterns

For comparison with single cell results, aggregation patterns were evaluated and reported for identical chemical conditions. The image of bioconvection patterns was recorded by a b/w camera (Nikon FM-2, lens, Medical Nikkor 120 mm) mounted above the observation flask. The photographic images were digitized by manually tracing their pattern boundaries (e.g. regions of high relative organism density), then scanned (Albaton 300S scanner, CA. USA) with a spatial resolution of 512 x 512 pixels. The digital images were further analyzed for geometric parameters of aggregation patterns using a main image analysis program (Image Analyst, CA. USA) written in the computer language C.

The outline and position of each pattern (polygon) was determined using a chain coding algorithm and analyzed spatially as a best-fitted centroid. For each polygon, the geometry was stored in the form of area, perimeter, and average radius (arbitrary pixel units) as well as the number of polygonal sides, then calibrated (normalized) to the average value for all polygons. As the pattern changed with chemical addition, the geometric measures of polygonal area and perimeter were plotted as a function of cell sides. The physical significance¹¹ of these results has been discussed elsewhere under the heading of statistical crystallography⁵.

3. Results

The potential importance of single cell swimming changes and chemical detection has been discussed previously^{3,7,8}. We therefore presently consider the computer-scored effects of chemical loading on single cell swimming and compare these results using geometric analysis on lab simulations which can include this aggregation mechanism for scoring chemical toxicity. Thus the comparative framework for chemical detection involves four different tests: 1) the present computerized scoring of single-cell swimming; 2) manual scoring of single cell swimming; 3) monitoring of many cells macroscopically through their chemically-hindered aggregation patterns (bioconvection)³⁻⁴; and 4) traditional whole animals, *in vivo* tests.

20 chemicals were tested for irritancy. Dosages are reported for organics (alcohols, ketones) as well as salts. To compare different assay results, we adopt the scoring formalism developed by Silverman⁹. Tolerated doses are found based on whether a particular applied chemical yields 10% (low dose) or 90% (high dose) of the cells immobile. In this way, a direct comparison is feasible between lab technician scoring of abnormal swimming vs. computerized cell tracking. Additionally, test results for the aggregation assay supplement this comparison, but instead of rendering a percentage of motile cells, the disappearance of macroscopic aggregation pattern signals the tolerated chemical dose. More toxic dosages disperse pattern formation by reducing cell mobility. All assays are effectively measuring cell swimming, whether the endpoint is direct single-cell trajectories or the overall indirect indicator of cell aggregation.

As a function of chemical concentration, a representative organic (methanol) and salt (DMSO) are tested using the computerized assay. The curve of concentration (g/kg) generally follows an increasing trend for both the percent of cells immobilized and the percent of swimming inhibition. Higher concentrations

generally react biologically to hinder cell movement. No saturation effect at high concentration (up to 100 g/kg) appears in the *Tetrahymena* system. A summary table for all the chemicals is shown in Table 1 for organics and salts and classified graphically by chemical family (Fig. 3) and rank order toxicity (Fig. 4)

To evaluate the assay results, Figs. 5-6 compare toxic thresholds for previously developed assays. Both the computerized and aggregation assays were carried out on identically grown cultures. Lab technician scoring was evaluated directly from previous results¹ and compared with standard *in vivo* results. A comprehensive report for 5 representative chemicals is shown in Fig. 7. The enlarged shaded region indicates that a lower average dose can be evaluated for toxic detection using the computerized assay compared to aggregation methods. The computer scoring method likewise signals positively at lower doses compared to scoring by the lab technician method.

The most illustrative comparison between different methods can be constructed using a simple three-outcome score. For dilution factors of 0-100 %, if a chemical reaction (toxic response) occurs only for high (0-30%) dilutions, then the chemical is scored as mild. Alternatively for medium dosages (30-60% dilutions), a reaction indicates moderate toxicity. Finally for low dosages (greater than 60% dilution) then the chemical toxicity scores as severe. To evaluate an average tolerated dose, reciprocal dilutions are summed for high and low values which deliver toxic reactions, with the high dose leaving 10% of cells mobile and the low dose leaving 90% of cells mobile. The computerized assay delivers these averages in an automated fashion and final results are shown in Fig. 8.

4. Discussion and conclusions

Using computerized scoring of cell motility, the present method differs from previous approaches in its speed (just 10 minutes from refrigeration to incubation to computerized evaluation of chemical toxicity), its ease-of-use (as easy as aqueous transfer) and laboratory stability (several month shelf life). Using computerized evaluation provides a documented report of toxicity in a labor-free (completely automated) and low cost (pennies per test) apparatus.

Advantages of the Motility Assay Apparatus (MAA) include: 1) instant results in a ready-to-use quality-controlled system of microorganisms; 2) quantitative reporting which delivers a specific range of swimming changes upon chemical addition; 3) ease-of-use which requires only push-button effort to give documented toxicity evaluation and reporting; 4) real economy, eliminating biological growth periods of several days. (No more trial-and-error dilution of suspensions to achieve desired cell counts, thus transforming lengthy technician scoring into a single objective result.); 5) safety which minimizes technician handling and exposure to potentially hazardous chemicals; 6) and finally reliability, including high enough speed evaluations to make many repetitions of results realistic to perform.

Alternative applications of the MAA include: 1) an alternative to Draize rabbit eye test for cosmetic testing; 2) research tool for pollution monitoring in organic and heavy metal detection; 3) chemical safety data for federal monitoring; 4) a standardized test for a) growth promotion; b) bacteriostatis; c) effectiveness testing of anti-microbial preservatives and disinfectants; d) microbial limit tests; e) media quality control in biotechnology, clean room testing, clinical, environmental, food and beverage, industrial, pharmaceuticals and cosmetic tests.

To summarize, the present results have surveyed 3 alternative embodiments for testing chemical toxicity on single cell swimming behavior. The alternatives gave similar results to existing *in vivo* results when adapted to a 3-tiered scoring scheme (mild, moderate and severe). In all chemicals tested (both organics and salts), the computerized assay gave equal or lower thresholds for detecting toxicity (reported as dosages which immobilize a percentage of cell activity). Given the potential time and money saving possibilities of an automated method, the computerized assay should receive further consideration as a scientifically competitive evaluator of chemical toxicity.

References

1. Hill D.L., 1972. *The Biochemistry and Physiology of Tetrahymena* New York: Academic Press.
2. Nillson, J.R., 1989, *Tetrahymena in Cytotoxicology*, *Europ. J. Protist.* 25, 2-21.
3. Noever, D.A. and Matsos H.C. 1991a, A Bioassay for Monitoring Cadmium Based on Bioconvective Patterns, *J. Environ. Sci. Health*, A26: 273.
4. Noever, D.A. 1991b. Fractal Dynamics of Bioconvective Patterns, *J. Physical Soc. Japan*, 60 3573-3581.
5. Noever, D.A. 1991c. Evolution of bioconvection patterns in variable gravity, *Phys. Rev. A* 44, 4491-4501.
6. Noever, D.A. 1991d. Fractal Patterns in Bioconvecting Cells of *Euglena gracilis*, *J. Physical Soc. Japan*, 59: 276-280.
7. Roberts R.O. and Berk S.G., 1990, Development of a Protozoan Chemoattraction Bioassay for Evaluating Toxicity of Aquatic Pollutants, *Toxicity Assessment*, 5: 279.
8. Silverman, J. 1983. Preliminary Findings on the Use of Protozoa (*Tetrahymena thermophila*) as Models for Ocular Irritation Testing in Rabbits, *Lab Animal Science*, 33:56-59
9. Silverman, J. Pennisi, S. 1987. Evaluation of *Tetrahymena thermophila* as an In Vitro Alternative to Ocular Irritation Studies in Rabbits, *J. Toxicol. Cut and Ocular toxicol.* 6: 33-42
10. Starr, R.C. and Zeikus, J.A., 1987, UTEX Culture Collection', *J. Phycology (suppl.)*, 23, 39.
11. Weaire, D. and Rivier, N.:1984 Soaps, cells and statistics, *Contemp. Phys.* 25, 73-91

Table I. Rank order toxicity from computerized assay. Toxicity scores shown as the tolerated dose (dilution factor) which immobilized a) dhigh, 90% of the swimming cells (high dose); b) dlow, 10% of the swimming cells (low dose); c) the average does as the reciprocal sum of the high and low dose ($1/d_{avg} = 1/d_{high} + 1/d_{low}$). Rank orders shown for 20 organics (alcohol, ketones, ethers, esters) and salts.

Table II. Comparison of irritancy rankings (mild, moderate, severe) between the four assay methods. Results refer to single cell swimming behavior of *Tetrahymena* scored with cell tracking (computerized assay), microscopic method using lab technicians (Silverman), aggregation patterns (bioconvection assay). Single cell results are compared to standard Draize tests (in vivo) as reported in Silverman.

Figure captions

Fig. 1 Schematic of assay procedure. A 5 ml sample of *Tetrahymena* cells (density 2.5×10^3 /ml) is diluted with 5 ml yeast media and test chemical at the desired concentration. 0.1 ml of the 10 ml preparation is placed on a 100 micron observation chamber, videotaped under microscopic observation and then analyzed for cell-tracking parameters (velocity and number of cells motile).

Fig. 2 Effect of chemical addition on *Tetrahymena* swimming patterns. Test results in aqueous media as a function of methanol concentration between 0-100 g/kg. a) Percent inhibition is the calculated reduction in swimming (forward) velocity, $P = 100(v - v_c/v_c)$, where v_c is the control velocity with no chemical addition, and v is the measured velocity with methanol. b) Percent immobilization is the calculated reduction in the number of cells swimming, $P = 100(n - n_c/n_c)$, where n_c is the control number of motile cells with no chemical addition and n is the measured number with methanol.

Fig. 3 Effect of chemical addition on *Tetrahymena* swimming patterns. Test results in aqueous media as a function of methanol concentration between 0-100 g/kg. a) Percent inhibition is the calculated reduction in swimming (forward) velocity, $P = 100(v - v_c/v_c)$, where v_c is the control velocity with no chemical addition, and v is the measured velocity with DMSO. b) Percent immobilization is the calculated reduction in the number of cells swimming, $P = 100(n - n_c/n_c)$, where n_c is the control number of motile cells with no chemical addition and n is the measured number with DMSO.

Fig. 4 Toxicity scores arranged by chemical families for computerized assay results. Dilution factors (x) of 1: x which immobilized 10% and 90% of the motile cells are reciprocally summed in agreement with Silverman. Chemicals which immobilize for dilutions less than 30 fold are mild, 30-60 fold are moderate, greater than 60 fold are severe. Arrows indicate severe toxicity which immobilized at trace composition for dilutions greater than 60-fold in yeast media.

Fig. 5. Toxicity scores for 20 organics and salts arranged by chemical family and rank order from computerized assay. Results shown as average tolerated doses with (lower) adjusted orders indicated in bottom graphs showing the finer details of chemical comparisons (e.g. thresholded higher toxicity like hexanol shown at arbitrary cutoff at 100 or 1000.)

Fig. 6. Graphical comparison of assay sensitivity for *Tetrahymena*. The circle perimeter correspond to an average tolerated dilution of 100% (no chemical), the central point to 0%. The shaded region (polygon) indicates that computerized results (larger polygon) has equal or better dose discrimination compared to models of either swimming aggregation (Noever) or lab technician (Silverman). The exception is a more sensitive aggregation test for acetone.

Fig. 7 Graphical comparison of assay sensitivity for *Tetrahymena* vs. in vivo rabbit irritancy. Three test outcomes (mild, moderate, and severe) are shown as a matrix. In vitro refers to the number of counts for the standard 20 chemicals which score in that test rating (eg. mild). Ideal correspondence between in vivo and in vitro results would fill the central diagonal with chemicals but leave the non-diagonal elements equal to zero.

Since the matrix results generally fill the higher columns and lower rows (a "bottom-heavy" matrix) then the in vivo tests can be understood to give a more sensitive assay.

Fig. 8. Summary comparison for assay methods from the 20 chemicals. Toxicity scored as mild, moderate, and severe. Score reported as average tolerated dose for computerized assay with *Tetrahymena*. Identical performance for all assays would correspond to similar rankings in a single row.

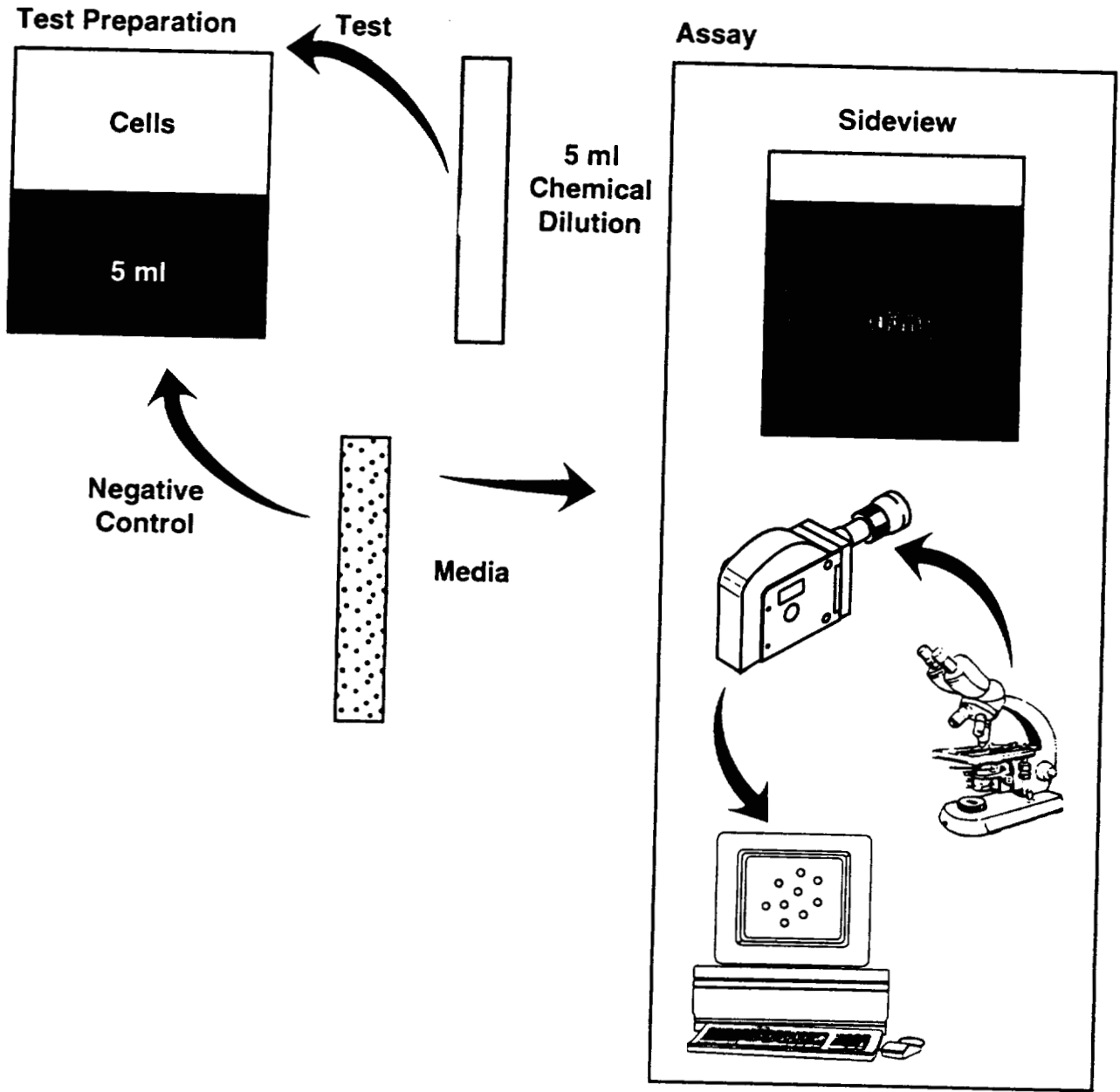
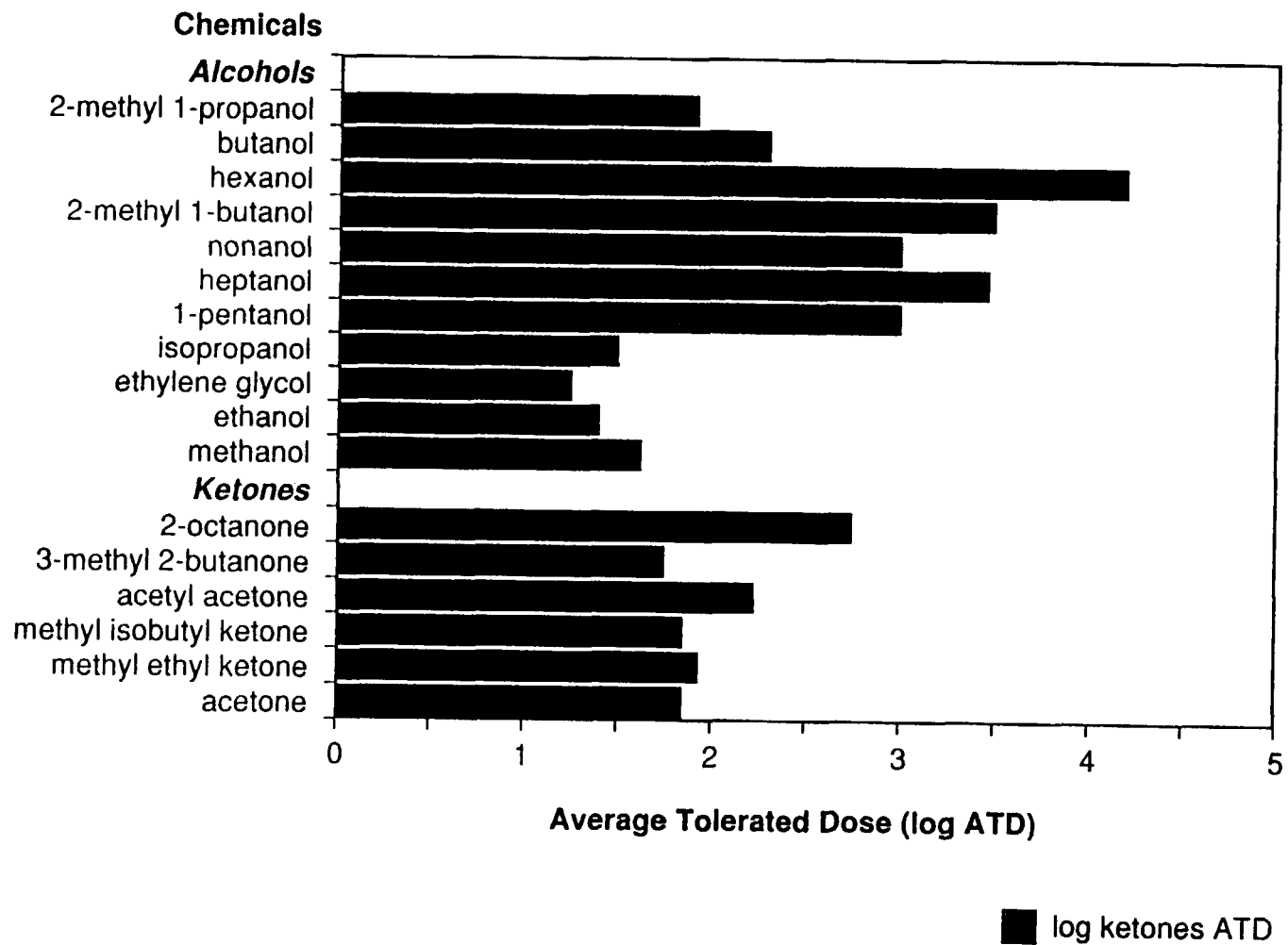


Figure 1. Schematic of Assay

In vivo In vitro	Mild	Moderate	Severe
Mild	1	0	0
Moderate	3	0	0
Severe	1	2	5



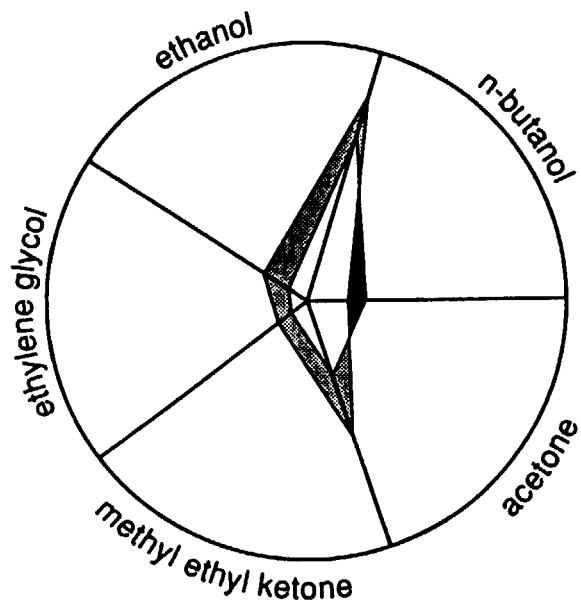


Figure a. Computerized results vs. swimming aggregation results.

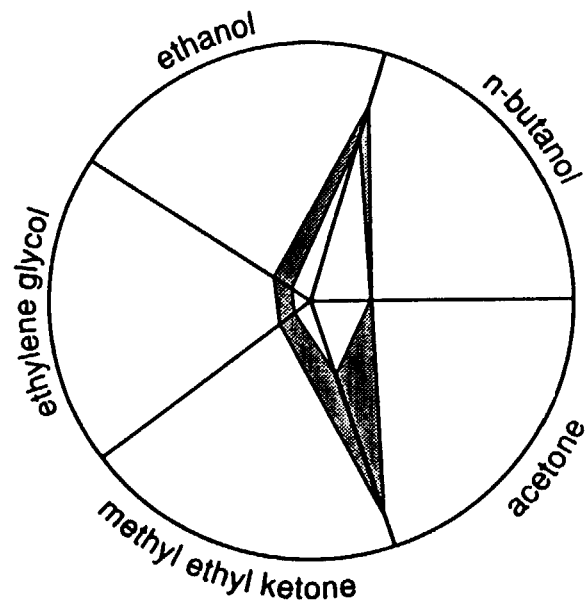


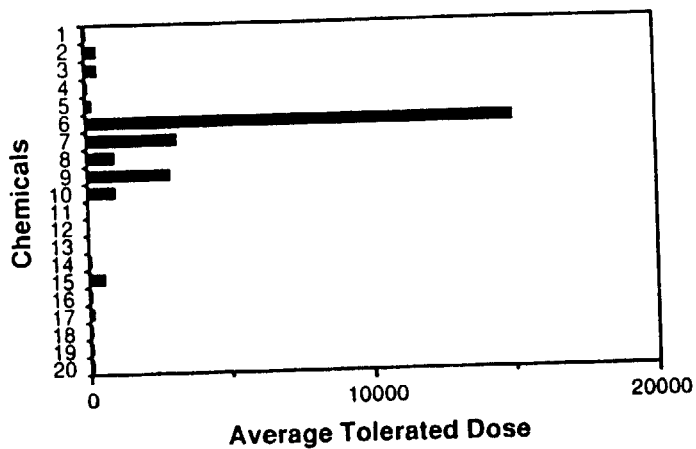
Figure b. Computerized results vs. Silverman results.

Irritancy

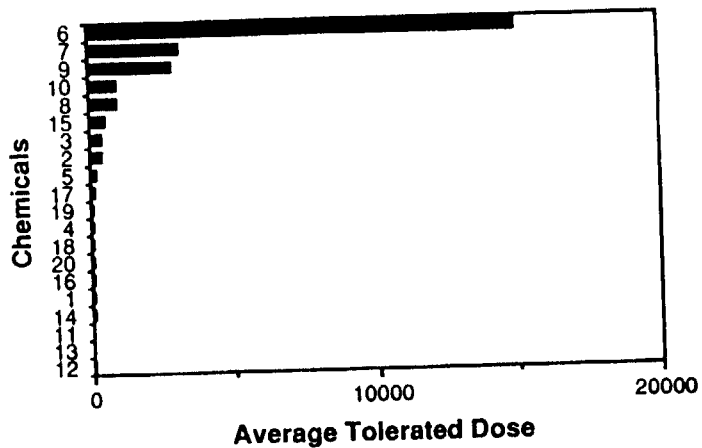
Chemical	Score	Computerized	Swimming	Silverman	In vivo
DMSO	47.500	○	○	○	○
bleach	391.000	●			
diethanolamine	404.000	●			
2-methyl 1-propanol	79.000	●	●	●	●
butanol	203.000	●	●	●	○
hexanol	15000.000	●	●	●	●
2-methyl 1-butanol	3238.000	●	●	●	●
nonanol	979.000	●	●	●	●
heptanol	2944.000	●	●	●	●
1-pentanol	1008.000	●			
isopropanol	30.300	○			
ethylene glycol	18.500	○			
ethanol	24.100	○	○	○	○
methanol	39.900	○	○	○	○
2-octanone	558.000	●	●	●	●
3-methyl 2-butanone	58.900	○	○	○	○
acetyl acetone	153.000	●			
isobutyl ketone	72.100	●			
methyl ethyl ketone	90.700	●	●	●	○
acetone	71.400	●	○	○	○

○ Mild ○ Moderate ● Severe

Chemical Family



Rank Order

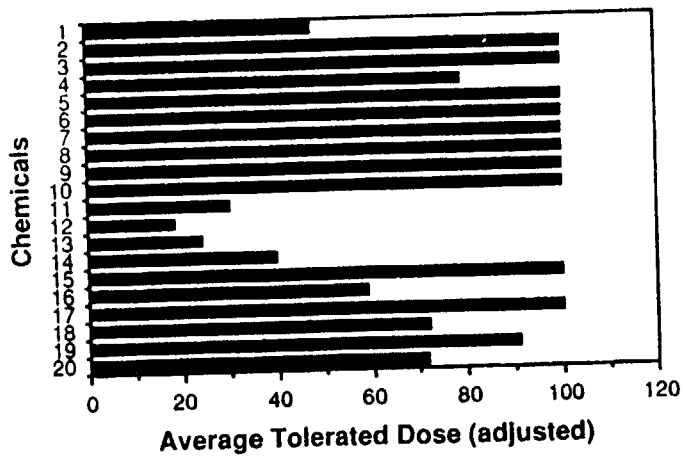


Legend

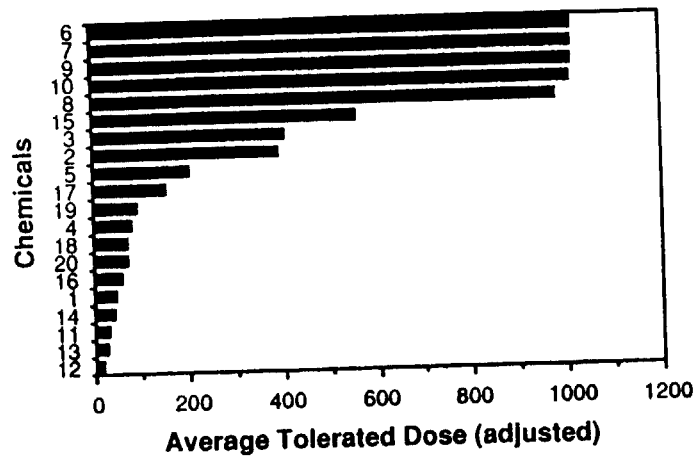
1	DMSO
2	bleach
3	diethylaniline
4	2-methyl 1-propanol
5	butanol
6	hexanol
7	2-methyl 1-butanol
8	nonanol
9	heptanol
10	1-pentanol
11	isopropanol
12	ethylene glycol
13	ethonal
14	methanol
15	2-octanone
16	3-methyl 2-butanone
17	acetyl acetone
18	methyl isobutyl ketone
19	methyl ethyl ketone
20	acetone

808

Chemical Family



Rank Order



**A MODULAR APPROACH FOR AUTOMATED SAMPLE PREPARATION
AND CHEMICAL ANALYSIS**2460
P. 10**Michael L. Clark, Terry D. Turner, Kerry M. Klingler, Randolph Pacetti
Idaho National Engineering Laboratory
Idaho Falls, Idaho 83415-3740****ABSTRACT**

Changes in international relations, especially within the past several years, have dramatically affected the programmatic thrusts of the U.S. Department of Energy (DOE). The DOE now is addressing the environmental cleanup required as a result of 50 years of nuclear arms research and production. One major obstacle in the remediation of these areas is the chemical determination of potentially contaminated material using currently acceptable practices. Process bottlenecks and exposure to hazardous conditions pose problems for the DOE. One proposed solution is the application of modular automated chemistry using Standard Laboratory Modules (SLM) to perform Standard Analysis Methods (SAM). The Contaminant Analysis Automation (CAA) Program has developed standards and prototype equipment that will accelerate the development of modular chemistry technology and is transferring this technology to private industry.

DEPARTMENT OF ENERGY ENVIRONMENTAL EFFORT

The environmental program has become one of the fastest growing segments of the DOE. The DOE and its predecessor agencies have been responsible for developing and maintaining the U.S. nuclear deterrence capability for more than 50 years. With the apparent need for deterrence reduced, the DOE is addressing issues involving the reduction of its nuclear stockpile. In addition to re-configuring the nuclear production complex, the DOE is addressing the environmental issues associated with nuclear power production and nuclear arms research and manufacture.

In 1993, DOE earmarked 25% of its budget for environmental work. The largest share of the environmental budget is allocated to remediation contractors at the various DOE sites. However, attention and dollars have been devoted to the development of new technologies to aid in the cleanup process. This effort is being organized within the Office of Technology Development (OTD). The OTD, through the Robotics Technology Development Program (RTDP), is developing robotic technologies currently unavailable. These technologies will make the remediation effort proceed more quickly, more safely, and more economically. The DOE and its contract laboratories make several million chemical, biological, and radiological determinations per year, and this number is expected to grow to approximately 10 million per year by 1995. Because of the unique characteristics of some DOE waste (e.g., the presence of radio-nuclides), offsite characterization is sometimes impractical. The sheer magnitude of the analysis load dictates an automated production approach to its solution.

CONTAMINANT ANALYSIS AUTOMATION PROGRAM

The Contaminant Analysis Automation (CAA) program was formed in 1990. The mission of the CAA program is to reduce the cost of the remediation effort by developing automation technologies that will reduce the need for human interaction. The program consists of a team of chemists and engineers from national labs, educational institutions and private industry. A by-product of reducing human interaction will be increased quality of the characterization by reducing operator caused variance in the analysis and reduced operator exposure. By developing machines that run continuously, more efficient use can be made of existing facilities, and improvements in the sample turn-around time will be realized.

Once the CAA team identified the priority analysis methods needing immediate attention to assist in the environmental remediation process, they set about to find solutions. Initial research revealed that standardized modular instrumentation and equipment, both hardware and control software, were necessary if automated systems were to be beneficial.

MODULAR CHEMISTRY

The concept of automated modular chemistry is very simple in theory. The idea is that the physical motions involved in the preparation and analysis of a sample can be reduced to discreet tasks, that these tasks can be emulated, and then replaced by interchangeable automated modules. A small number of these interchangeable modules can be configured to allow many different, complex processes to be automated.

Conceptually, all samples, whether they are analyzed in real time or using more traditional sampling methods, undergo three general categories of operations: first, preparation, second, analysis, and third, data interpretation. These steps combine to perform an analysis on an environmental sample. When a procedure is verified as yielding correct results, it is classified as a Standard Analysis Method or SAM. The steps of a SAM are depicted graphically in Figure 1.

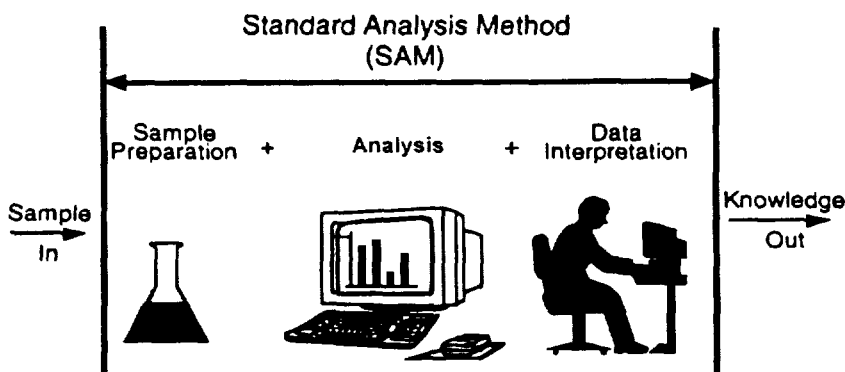


Figure 1. Standard analysis method.

In actual practice, a wide variety of sample preparation procedures, analysis equipment, and comparison data is used to determine whether a sample is contaminated. The condition of the sample, the chemicals of interest, and the regulatory requirements determine the combination of preparation, analysis, and interpretation tools used to make this determination. Each different configuration of modules constitutes a different SAM.

Embedded within the three general categories of process operations presented above are the sample-specific methods. These methods are procedures that govern sample processing and ensure uniform results. The approved protocol of the sample-specific method, such as the methods of EPA SW-846, are closely followed. One method, or combinations of several sample-specific methods, are used to perform a sample preparation, with the combination differing from sample to sample. These sample-specific methods are composed of the discreet tasks above and are generally performed by a technician or chemist. These tasks are arranged into the following classes of Laboratory Unit Operations (LUOs):

- Manipulation
- Measurement
- Data Management
- Separation
- Conditioning
- Documentation
- Transfer and Transport

Examples of LUOs include marking and recording a beaker, weighing a sample and recording the weight, moving a beaker, pouring a beaker, adding a solvent, or filtering a liquid sample. From an automation perspective, some LUOs will require a single module to perform, while other modules may combine multiple LUOs. A logical grouping of LUOs that together perform an operation of an analytical protocol is defined as a Standard Laboratory Module (SLM).

STANDARD LABORATORY MODULE

To illustrate an example of a sample preparation SLM, consider the task of "dissolve" in an analytical protocol. The process begins with the removal of the cap from the vessel containing the sample. This is a manipulation LUO. The next step is to add a dissolving agent (an acid or a solvent). This is a liquid handling operation. The cap is then replaced, resulting in another instance of a manipulation LUO. Waiting for the reaction to reach completion is a conditioning LUO. Finally, the first three LUOs are repeated as necessary to bring the resulting solution up to a target concentration. These steps may be combined into a single or multiple SLMs. A second example, that of an interpretation SLM, is the sequence of LUOs associated with taking the analytical instrument data and reducing them to an analytical result. This might require retrieving spectral data from a sample, and then comparing that data to standards and determining if the sample is contaminated, based on regulatory standards.

SLMs can be predominantly hardware, software, or both. For sample preparation functions, SLMs tend to be more hardware oriented, while in the data-handling and interpretation arena, they are more software intensive. The Standard Laboratory Module is the primary building block of the CAA program. The intent behind the SLM is to create an instrument with standardized interfaces, both mechanical and control.

SLM Boundaries

The boundaries of an SLM are by no means easy to identify in all cases; however, defining and standardizing these boundaries is a critical parameter of the standardization effort. Guidance for the logical grouping of LUOs into the inner boundaries of an SLM comes from an examination of analytical methods performed in the laboratory. Another grouping approach is to gather LUOs that are physically carried out in sequence into an SLM. Other potential SLM boundaries occur at branch points in the preparation and cleanup process. The EPA sample specific methods often can be encompassed in a single SLM. The SLM boundaries are also heavily influenced by commercially available equipment and the concerns to make an SLM that can be used outside of an automated system. A graphical representation of the boundary inputs, and outputs of a generic SLM is presented in Figure 2.

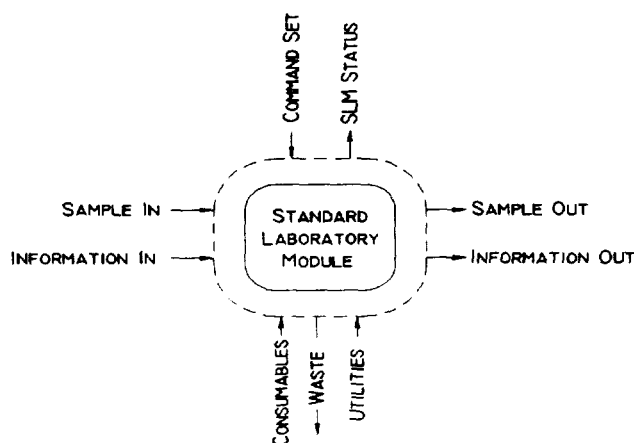


Figure 2. SLM and boundary interfaces.

Interface Standards

One solution to the interface problems is to redefine and reinvent the chemistry to improve the standardization effort; however, this would require years of research and development, and then additional years of validation work. In its initial charter, the CAA decided that, from the DOE standpoint, the most benefit would be realized from developing uniform automation protocol for existing chemistry rather than developing new chemistry protocols. This will result in a more immediate benefit as well as enhance the development of new analysis technology. The approach taken by the CAA team is to use a varied interface protocol. The SLMs will use input/output format conducive to the current manual method. This will slightly reduce the wide plug and play philosophy since not all SLMs will receive input from all other SLMs. However, a relatively short implementation time will expedite the use of existing commercial technology and equipment.

The interface connections to an SLM fall into four categories: First, Sample/Information In, Second, Sample/Information Out, Third, Utilities/Consumables/Waste, and Fourth, Communications. The major obstacle to defining an interface standard is determining the optimal size and format of sample input and output. This is due to the fact that when performing the methods manually, the technician is unaffected by the size of the container, or the amount of fluid in it. The technician can easily compensate for variances in the process. Automation is not quite so amiable. An example of one possible input is a 150 mL sample in a 300 mL beaker. The sample will also fit in a 500 mL beaker, but not in a 100 mL beaker. The input could be limited to 300 mL beakers, this is neither logical nor feasible as sample input size may vary between 0.5 mL and 500 mL. As illustrated, the interface standardization is limited by the current technology and methods. Several solutions are being investigated.

The current CAA approach defines a set of glassware standards that will be supported by the SLMs. This is not an unlimited configuration, but specifies a group of containers that will be used for ranges of sample volumes. However, when designing an SLM, the developer must carefully examine those modules that will receive and send samples. As new methods are developed, this disparity in sample format and size will be reduced.

One possible sample interface standardization solution is the use of direct sample transfer. In this method, the sample is transferred from SLM to SLM via connected tubing. This has distinct advantages and disadvantages. The use of tubing removes a large portion of the glassware from the system, and removes the associated problems. However, this adds the requirement for transfer stations to route the samples to the SLMs as required. The SLMs could be directly plumbed, but this might preclude the easy use of multiple SAMs on a single system. The SLMs being developed at the national laboratories have the provision to allow tube transfer. This feature will allow tube transfer concepts to be developed and evaluated.

Generally, sample preparation SLMs will require the same types of utilities, such as power, compressed air, vacuum, and solvents. These SLMs will also require waste disposal provisions such as off-gas, rinse, sample waste, and heat. An interface standard is under development that outlines what will be provided by the system, and what will be the flowrates, voltages, etc., for the utilities. It includes connector sizes and port connections. All SLMs will not have the same needs; thus they will not be required to provide connection provisions if the particular utility is not needed by that SLM.

The communications interface standards will be RS-232 and IEEE-488. A communications protocol is being defined. While the command requirements for different SLMs will not be the same, the command structure will be uniform to expedite development. This will include protocol for status reporting, information and data transfer, and remote control of the SLMs by the system controller.

To maintain a "plug and play" approach, a requirement was added that an SLM should not require a "knowledge" of or the existence of another SLM. Each SLM should be able to carry out its intended operation without relying upon another SLM. However, each SLM interacts with a controller through a standard interface as part of an automated system.

One major concern of a modular system is that a byproduct may be the creation of instruments that are not functional outside of the system. To reduce this problem, the ability to function independently, or in "stand-alone mode" is being developed. At this point, this is not a requirement, but function that has generated much interest. This feature also makes the technology and instrumentation developed by the DOE laboratories more desirable to commercial interests. The stand-alone feature is also very useful when the SLMs are brought into the laboratory for validation. Also, as SLMs are acquired, they can be used individually before assembling several into automated systems. This stand-alone capability also improves the desirability of the instrument by making it more adaptable.

AUTOMATED MODULAR PREPARATION AND ANALYSIS SYSTEM

One critical part of the definition of the SLM boundary standards is the determination of system conditions. This arrangement of SLMs is referred to as the Automated Modular Preparation and Analysis System (AMPAS). Inclusive in the AMPAS are both the software that coordinates the entire procedure and the hardware support that enables a SAM to function autonomously within the system.

The AMPAS will provide the means to perform LUOs that may or may not fit into a particular SLM. A specific example of such an LUO is the transportation of samples and consumables. This operation may cross the boundaries of many SLMs and therefore cannot be considered an SLM. In the current prototype system, this function is performed by a robot. These support devices are called Standard Support Modules (SSMs). While modularized, these devices do not fit the complete definition of the SLM. Individual SLMs have a knowledge of the SSMs when applicable. An example is the case where a robot is depositing a beaker into an SLM. The SLM must verify that the robot arm has been removed prior to beginning processing. Additionally, when the SSM is the supply source, the SLM must know if sufficient material is available to complete the process. SSMs are directed by the system controller and generally will not be used in a stand-alone fashion.

The consumables and service required by each SLM are coordinated and controlled by the AMPAS controller. The AMPAS will include supply resources for disposables, clean labware, disposal of labware, reagent reservoirs, and other system resources such as compressed air, potable water, vacuum, power, and heating, ventilation, and air conditioning (HVAC).

AMPAS CONTROL SYSTEM

With the AMPAS, a chemist will be able to acquire and link SLMs to follow the script of the method being performed. In other words, the chemist is operating at the chemical operation level in dealing with subtasks, such as "weigh sample," "dissolve," "extract," "separate," "measure," "interpret," etc., and not operating at the hardware or software level.

Before the AMPAS controller instructs an SLM to "dissolve," it must first be able to ascertain that enough acid is available to complete the task. It will check the acid-supply SSM, then either proceed or report that it cannot do so and state a cause. The real-time control system software runs VxWorks on a VME backplane with a VME card dedicated to each SLM. Commercial versions of the SLMs may have onboard processors rather than external VME cards for the real-time hardware control and external communication.

A UNIX-based platform was chosen for implementing the AMPAS control system software on the basis of its real-time capabilities and its multitasking features. The control software is written in the C++ language. A multi-tasking environment allows the system to process multiple samples. The system interfaces with the site facility through any existing laboratory information management system (LIMS). A methods manager provides translation from high level methods requested by the chemist into lower level scripts of SLM commands necessary to carry out the requested chemistry. The software architecture is shown in Figure 3.

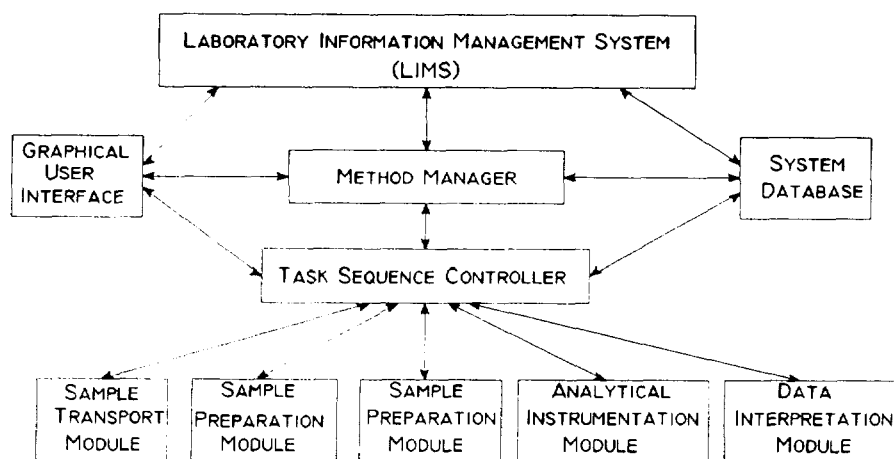


Figure 3. Automated modular preparation and analysis system.

The task-sequence controller performs script processing, scheduling, and supervisory control of the SLMs in the system by communicating with the dedicated SLM processors. The system database serves as information storage for the automated laboratory, providing a detailed audit trail for all phases of preparation and analysis. The user interface provides operator access to the LIMS, method manager, database, and task sequence controller.

TECHNOLOGY EVALUATION AND VALIDATION

The EPA procedures for extracting, cleaning, and identifying polychlorinated-biphenyls (PCBs) in soil samples were chosen as targets for the initial automation into SLMs. To evaluate the feasibility of the requirements, modules have been built to preliminary standards. A prototype AMPAS is being developed for use as a test bed that will allow insertion of

completed SLMs for performance and compatibility testing. Two sample preparation methods selected to provide the largest impact were U.S. Environmental Protection Agency (EPA) Methods 3540 (Soxhlet Extraction) and 3550 (Sonication Extraction). These methods were selected to use as test fixtures for the standardization and modularization technology.

SLMs that perform Soxhlet extraction, sonication extraction, sample drying and filtering, and gel permeation chromatography (GPC) cleanup (EPA Method 3640) were demonstrated in an integrated, hood-enclosed system in March 1992. Two rail robots were used to move samples between the SLMs. The test bed layout is shown in Figure 4.

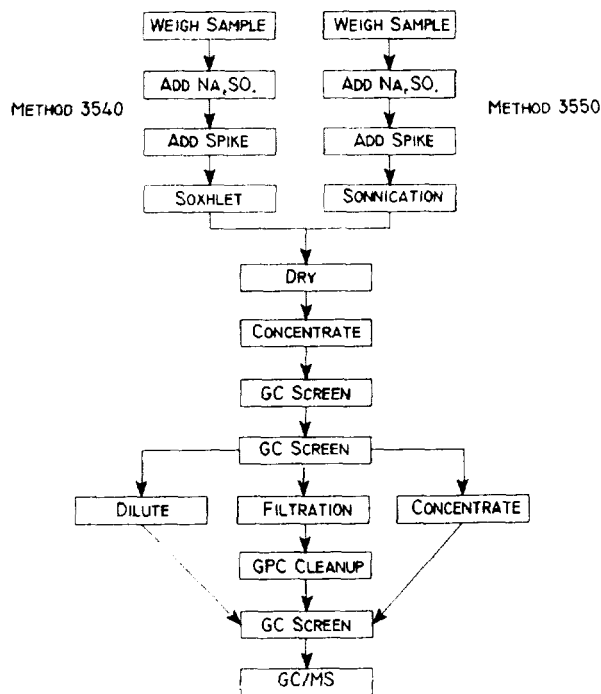


Figure 4. System test bed.

Currently, the remaining SLMs required to perform the steps in an automated PCB sample analysis are under development. A gas chromatography instrument is being incorporated into the SLM protocol, and the requirements for automated data analysis are being established. An integrated system carrying out a fully automated semivolatile organic SAM, that targets PCBs will be demonstrated in 1994. Other protocols will soon be addressed, including the acid digestion sample preparation methods and radiological methods not currently covered by EPA protocols.

In the initial attempts at automation, the manual steps were followed closely. While this approach did not result in the most efficient equipment, it did allow for automation that shows the chemistry can be automated and allows for easier validation to existing approved techniques. The completed SLMs are undergoing chemical validation tests in the DOE environmental laboratories. These tests will ensure the automated sample preparation meets the quality control criteria in the EPA methods. Validated SLMs will gain approval from the

DOE's Lab Managers Branch for their use in the DOE Methods Compendium. The Lab Managers Branch also will pursue EPA approval to use these devices to carry out EPA methods.

TECHNOLOGY TRANSFER AND COOPERATIVE RESEARCH

The automation of chemistry is not new, nor is it exclusive to the CAA program. The intent is not to redefine or reinvent the chemistry being used, but rather to define a standard for the equipment used to perform the chemistry. In terms of technology, the CAA found two needs, the lack of standardization, and the lack of a concerted effort and governing body for standardization.

The CAA team realized at the inception of the program that the DOE did not have the means or the resources to develop the modules needed to address the analysis problems. To accomplish the goals, required the use of existing technology by teaming with many organizations. The automated equipment needed to do most of the chemical analysis is widely available. However, the equipment does not work together, does not communicate, and is not conducive to automation.

Some modules developed to date used commercially-available equipment adapted to fit the SLM formalization. Several equipment manufacturing companies currently are working with the CAA program on a cost-sharing basis to develop SLMs or convert existing devices and instruments into SLMs. ABC Laboratories developed the GPC SLM from a pre-existing automated GPC device. The Soxhlet Extractor SLM was adapted from commercial manual equipment.

The CAA team also concluded that in order to develop sufficient quantities of automated systems for DOE's needs would require a system integrator. The role of the system integrator is to find potential customers, access their needs, and then configure and support the AMPAS operations. A second duty of the system integrator is to ensure that SLMs required for SAMs are readily available. To expedite the integration effort, the CAA program has partnered with U.S. Industry. The CAA program has selected Lockheed and Hewlett-Packard (Lockheed/HP) to act as the sole AMPAS Integrator to supply and support fully-automated laboratories to the DOE and commercial markets.

The DOE Headquarters-Office of Technology Development (DOE HQ) and Los Alamos National Laboratory (LANL) are in the process of completing a "Guidance Document" for the CAA program. This Document will detail the programmatic and technical interactions of all CAA participants. Additionally, the Document will describe the program management chain-of-command and recognize that DOE HQ will lead the effort utilizing LANL as a coordination focus. DOE HQ will not own any intellectual property rights.

Lockheed/HP has put into place a new organization to focus on commercial products to develop, manufacture and support CAA system and equipment. The CAA/Lockheed/HP team has initiated the technology transfer activities including, requirements definitions, lessons learned, system development and other value added activities. Fairness of Opportunity guidelines will be followed during the SLM partner selection process to select the most appropriate SLM manufacturer/s. The criteria/guidelines for the partner selection process will be determined by CAA/Lockheed/HP and the subject laboratory.

Participants

LANL is the lead laboratory in the CAA coordination area of the OTD. The other national laboratories, involved in the CAA effort include Pacific Northwest Laboratory (PNL), Idaho National Engineering Laboratory (INEL), Sandia National Laboratories (SNL), and Oak Ridge National Laboratory (ORNL). In addition to government agencies and private industry, numerous universities and educational institutions are involved in the CAA program. The DOE currently is also working with the National Institute of Standards and Technology as part of its Consortium on Automated Analytical Laboratory Systems (CAALS) to develop these standards. The CAA model is being tested by CAALS as a candidate standard.

CONTINUING DEVELOPMENT

Current efforts of the CAA program include the refinement of the test bed, development and review of interface requirements, development of the additional SLMs required to complete target SAMs, and transfer of the program technology to private industry. Research is underway to further identify chemical laboratory needs and wants. This will direct the development of new modules, systems, and technologies. Work is continuing with EPA and individual state certification agencies to expedite and refine the CAA technology to meet approval requirements.

The CAA/Lockheed/HP team has initiated joint discussions with the Department of Defense (DOD) to jointly configure a CAA system to assist in environmental compliance activities. The Air Force is working with the CAA team to provide sample analysis requirements, system requirements, support and cost/benefit evaluation. The DOD has initiated discussion of a multi-agency cooperation effort on the development of environmental technologies.

Once the standardization technology has been transferred to private industry, the CAA teams will concentrate on research and development of new technology to further improve the automation of sample preparation, analysis, data interpretation and information processing of environmental remediation activities.

PHOTOVOLTAIC POWER WITHOUT BATTERIES
FOR CONTINUOUS CATHODIC PROTECTION

W. W. Muehl, Sr.
Department of the Navy, Coastal Systems Station (COASTSYSTA)
Dahlgren Division, Panama City, FL 32407-7001

2461
P-4

ABSTRACT

The COASTSYSTA designed, installed, and started up on 20 January 1990, a state-of-the-art stand alone photovoltaic powered impressed current cathodic protection system (PVCPSYS) not requiring any auxiliary/battery backup power for steel and iron submerged structures. The PVCPSYS installed on 775' of steel sheet piling of a Navy bulkhead is continuing to provide complete, continuous corrosion protection. This has been well documented by COASTSYSTA and verified on-site by the U.S. Army Civil Engineering Research Laboratory, Champaign, Illinois and the Navy Energy Program Office-Photovoltaic Programs, China Lake, California. The Department of Defense (DoD) Photovoltaic Review Committee and Sandia National Laboratories consider this successful and cost effective system a major advance in the application of photovoltaic power. The PVCPSYS uses only renewable energy and is environmentally clean. A patent is pending on the new technology. Other possible PVCPSYS applications are mothballed ships, docks, dams, locks, bridges, marinas, offshore structures, and pipelines. The initial cost savings by installing a PVCPSYS vs a conventional CP system was in excess of \$46,000.00.

The objective of the initial project was to successfully demonstrate that renewable energy can efficiently and economically replace or be used instead of continuous non-renewable power sources. An opportunity to clearly show that photovoltaic power is practical and reliable was the result of a recommendation to provide cathodic protection to the Naval Diving and Salvage Training Center bulkhead.

The COASTSYSTA in Panama City, Florida, has broken new ground in the application of solar energy for cathodic protection. Photovoltaic arrays without battery backup have been connected to the 775 foot-long steel sheet piling of a dock bulkhead via a cathodic protection system, to prevent corrosion on that steel structure in a salt water environment.

Cathodic protection, as the name signifies, is the process by which, in the COASTSYSTA impressed current type application, the entire steel sheet piling is transformed into a cathode via a series of anodes mounted in PVC standoff racks, in the water, next to the piling. When direct current (DC) energy is applied to the anodes and sufficient electrical potential is attained by current flow from the anodes via an electrolyte (seawater) to the piling, the corrosion is transferred to the anodes, preventing piling corrosion.

Mr. Wally Muehl, Electrical/Mechanical Engineer at the Coastal Systems Station, was evaluating power sources to protect the Naval Diving and Salvage Training Center bulkhead when he focused on photovoltaics. Although there were 10 other impressed current cathodic protection systems installed on the docks, all were powered by a continuous power source with the current rectified to DC. Of these 10 systems, eight were down from 1 to 1 1/2 years due to

rectifier failures and/or the power source secured due to construction and as a result no corrosion protection was provided. PVCPSYS's would have continued to provide power and corrosion protection and would not have been affected by these type power outages.

The Naval Diving and Salvage Training Center is in a separate location from these docks, and it was determined that power was not readily available and would be expensive to provide rectifiers on the dock due to the dock configuration. Rectifiers would also pose a safety hazard on the dock that is regularly used for diver and salvage training. This bulkhead was 12-years old and other than the initial coating, received no corrosion protection.

Mr. Muehl developed a state-of-the-art solar powered impressed current cathodic protection system for submerged steel and iron type structures without requiring any battery backup power. Innovations in design and method of operation permits the photovoltaic arrays to easily provide and maintain complete continuous corrosion protection without the necessity of DC power backup such as batteries. Battery backup power is considered costly and an environmental problem. To date, all impressed current systems require a continuous DC power supply in order to provide cathodic protection.

The COASTSYSTA photovoltaic power system is a fixed-axis system which is suitable for the Panama City latitude of 30°10'N, 85°22'W. The tilt of the adjustable arrays were set at latitude instead of +15 degrees in January 1990, and have not been changed. This is a good indication that other areas with good distribution, but lower insolation levels, would be excellent prospects for a similar type of photovoltaic powered system. For higher latitudes, there are several other options to improve system performance without battery backup. These include one-axis East-West tracking, two-axis North-South, East-West tracking, or simply adding a module or two to meet the additional current requirements.

As engineer in charge, Mr. Muehl, who designed, prepared the specifications, and monitored the installation, also had two other problems that had to be considered and resolved in order to install a impressed current cathodic protection system. The first problem was ensuring that the steel piling had electrical continuity. Another problem was providing sufficient impression of current "carry over" to overcome a 155-foot section of piling that had to be bypassed, and provide cathodic protection, without anode placement in the area having a water depth of 27 feet, where diving takes place. Both problems were overcome in the design.

To facilitate the use of a photovoltaic powered cathodic protection systems without battery backup, the steel sheet pilings were provided an initial one-time only preconditioning polarization for a predetermined continuous time period to the extent that these pilings were initially polarized to a relatively high negative potential by a temporary DC power source. The photovoltaic power system was provided with blocking diodes to prevent any possibility of current reversal. It is to be noted that evolution of a protective hydrogen film is merely a by-product of the preconditioning polarization at the higher negative potentials. Additionally, depending upon the environment and if higher (more negative) polarized potentials could be maintained other than required to provide basic complete cathodic protection, formation of thicker calcareous deposits having protective value over a period of time could occur. The initial DC power for polarization can be provided by a DC power source such as a portable motor driven DC generator or a portable motor driven DC welder.

The COASTSYSTA photovoltaic powered cathodic protection system tests performed and other data obtained, provide a further explanation that the anode-seawater-cathode piling structure acts like a battery and when allowed to rest, the polarity level recovers and is electrochemical in nature. An electrochemical lead-acid battery, for example, can recover charge if allowed to rest after serving a load. The electrochemical reaction reverses slightly when the load is disconnected, however, a capacitor without an external current source cannot recover by

simply removing the load. It is believed that the one-time only initial preconditioning polarization (controlled conditions) of the structure embeds single hydrogen atoms in the steel sheet piling that can also migrate and diffuse in the structure. This system delays the decay of the negative potential and permits the photovoltaic arrays to supply sufficient power allowing the system to easily provide complete continuous cathodic corrosion protection including cloudy, overcast, rainy and nighttime conditions without the necessity for DC power backup such as batteries.

In summary, the foregoing novel method and system of a one-time-only preconditioning or prepolarizing the structure prior to energizing the PV solar array on-line with the system, provides a relatively higher negative potential that has a slow rate of decay. This permits the use of regulated PV solar energy with excess available power, and without any backup power, to easily provide complete continuous corrosion protection, including cloudy, overcast, rainy and nighttime conditions, with excellent polarization levels and improving with time. An analogy may be that the steel structure becomes very effectively polarized, and will remain so by the variable DC charge effect provided by the simple solar array system, much like a piece of steel or iron can become magnetized by the application of a DC electrical current.

The installation, start up, and continuing operation, including underwater inspections, are well documented to date by the Coastal Systems Station and verified on site, during the day and at nighttime by the U. S. Army Corps of Engineers, Construction Engineering Research Laboratory, Naval Energy Program Office and members of the Department of Defense (DoD) Photovoltaic Review Committee. The average amount of available sunshine for the three weeks prior to these organizations visit, per data provided by the National Weather Service, averaged 24%.

This system has been in operation almost 3 3/4 years without requiring any maintenance or adjustment. A patent is pending on the new technology. Other possible applications are mothballed ships, docks, dams, locks, bridges, marinas, offshore structures and pipelines.

The estimated cost in 1985 of a conventional Cathodic Protection (CP) system requiring continuous DC power was \$75,000.00 and the estimated cost in 1990 was \$108,000.00. The PVCPSYS cost at contract completion was \$61,816.00, complete and ready for use. The initial cost savings by installing a PVCPSYS was in excess of \$46,000.00.

The Department of Defense Photovoltaic Review Committee and Sandia National Laboratories consider this successful and cost effective system a major advance for the application of photovoltaics.

A photovoltaic power system without any backup power has been installed on another 800 foot bulkhead. The two previous 400 foot conventional rectifier powered impressed current cathodic protection systems were modified to allow this conversion. This PVCP system successfully started operation on 21 May 1993, without any backup power and is providing complete continuous corrosion protection. A state-of-the-art data collection systems is provided that among other capabilities, will monitor, report, analyze and record simultaneously the solar energy output DC Volts, DC Amps and the DC negative potential voltage of the steel sheet piling on a personal computer that is MS-DOS compatible located about 1/2 mile away from the site.

With reference to this manuscript, it is with pleasure that I acknowledge the "helpful cooperation and information" received from the following personnel:

- Dr. Michael G. Thomas and Mr. Terry Schuyler - Senior Members, Technical Staff, Photovoltaic Research Dept., Sandia National Laboratories, Albuquerque, NM
- Mr. James F. Jenkins, P.E., Corrosion & Metallurgical Engineer, Naval Civil Engineering Laboratory, Port Hueneme, CA
- * Mr. L. E. Humble, Photovoltaic Programs, Energy Program Office, Naval Weapons Center, China Lake, CA
- * Mr. Roch A. Ducey, Principal Investigator and Ms. Jearaldine I. Northrup, Research Engineer, U.S. Army Construction Engineering Research Laboratory, Champaign, IL
- Mr. Thomas F. Lewicki, P.E., Facilities Corrosion Program Manager, HQ Air Force Civil Engineering Support Agency, Tyndall Air Force Base, FL
- Dr. Thomas M. Cawthon, Hydrogen Program Manager and H. Dana Moran, Manager, Research and Technology Applications, National Renewable Energy Laboratory, Golden, CO
- Navy Divers & Dive Locker, Coastal Systems Station, Panama City, FL
- * Members of the DOD Photovoltaic Review Committee

NON-AQUEOUS CLEANING SOLVENT SUBSTITUTION

2462
P. 9

Gerald J. Meier, Senior Engineer
AlliedSignal Inc.
Kansas City Division*
P.O. Box 419159 D/343 MY40
Kansas City, Missouri 64141-6195

ABSTRACT

A variety of environmental, safety, and health concerns exist over use of chlorinated and fluorinated cleaning solvents. Sandia National Laboratories, Lawrence Livermore National Laboratories, and the Kansas City Division of AlliedSignal have combined efforts to focus on finding alternative cleaning solvents and processes which are effective, environmentally safe, and compliant with local, state, and federal regulations. An alternative solvent has been identified, qualified, and implemented into production of complex electronic assemblies, where aqueous and semi-aqueous cleaning processes are not allowed. Extensive compatibility studies were performed with components, piece-parts, and materials. Electrical testing and accelerated aging were used to screen for detrimental, long-term effects. A terpene, *d*-limonene, has been selected as the solvent of choice, and has been found to be compatible with the components and materials tested. A brief history of the overall project will be presented, along with representative cleaning efficiency results, compatibility results, and residual solvent data. The electronics industry is constantly searching for proven methods and environmentally-safe materials to use in manufacturing processes. The information in this presentation will provide another option to consider on future projects for applications requiring high levels of quality, reliability, and cleanliness from non-aqueous cleaning processes.

INTRODUCTION

For many years, complex electronic assemblies have been successfully cleaned with trichloroethylene (TCE), rinsed with isopropyl alcohol (IPA), and dried with trichlorotrifluoroethane (FREON). Spray cleaning by hand and vacuum baking have been used in production at the Kansas City Division for over twenty years, and are the preferred methods for cleaning and drying electronic assemblies. This cleaning process has been extremely effective in removing the intentional surface contaminants (solder fluxes and mold releases) and any unintentional contaminants (silicones, greases, lotions, and oils) from electronic assemblies prior to encapsulation.

* Operated for the U.S. Department of Energy under contract number DE-ACO4-76-DP00613.

© Copyright 1993, AlliedSignal Inc.

However, a variety of environmental, safety, and health concerns exist over use of these chlorinated and fluorinated solvents. Sandia National Laboratories, Lawrence Livermore National Laboratories, and the Kansas City Division of AlliedSignal combined efforts to find alternative cleaning solvents and processes which are effective, environmentally safe, and compliant with local, state, and federal regulations. Work was performed to identify, qualify, and implement the alternatives to the chlorinated and fluorinated cleaning solvents. Several aqueous, semi-aqueous, and non-aqueous cleaning solvents and processes were evaluated. *d*-Limonene, a terpene, has been selected as the solvent of choice to replace TCE and FREON in electronic assembly cleaning.

STATEMENT OF THE PROBLEM

In January 1989, the future availability of halogenated cleaning solvents was in jeopardy. There was growing concern over the environmental impacts of FREON usage and an increased awareness of TCE toxicity. New development programs were reluctant to select baseline cleaning processes because of the uncertainty of halogenated solvents.

Non-Aqueous Requirements

Systems Engineers are concerned with the material compatibility problems caused over time by water (i.e. corrosion). As a result, system requirements prohibited the use of water in processes where organic materials are present, to limit the amount of water absorbed by the organic materials and control the overall water content of a final assembly. Since most of the mechanical parts and assemblies that require solvent cleaning are inorganic, aqueous and semi-aqueous cleaning solvents and processes could be used as replacements for TCE and FREON. However, most electrical parts and assemblies contain organic materials that absorb water (which sometimes can not be easily removed), and new non-aqueous cleaning solvents and processes had to be found. The majority of the work performed on this project went into identifying and evaluating suitable non-aqueous cleaning processes for use on the electrical parts and assemblies.

Eliminating CFC and CHC Usage

The search for alternative cleaning solvents and processes began at the Kansas City Division, and was primarily driven by draft requirements to reduce and eliminate use of chlorofluorocarbons (CFC's) and chlorinated hydrocarbons (CHC's) in traditional cleaning processes. Since then, increasing numbers of regulations have been issued by federal, state, and local regulatory agencies to ban, or to place more stringent controls on the production, use, and disposal of these halogenated solvents. In addition, company policy also dictated that usage of CFC and CHC materials at the Kansas City Division be eliminated.

CLEANING EVALUATIONS

A new development project, consisting of a final unit with twelve subassemblies, was selected as the pilot project to evaluate new cleaning solvents and processes. The subassemblies were primarily printed wiring boards containing resistors, capacitors, diodes, transformers, and hybrid micro-circuits; special design components bonded together with epoxy adhesives and electrically connected with wires or flat cables; and multi-pin connectors in wiring harnesses. These modules were assembled in a stainless steel housing to become the final unit.

Solvents and Processes Evaluated

Seven different cleaning solvents and processes (two aqueous, three terpenes, a hydrocarbon, and an alcohol) were evaluated. They are listed below:

- 1) An aqueous mixture of ethanol amines (5% solution in deionized water), rinsed with deionized water and then isopropyl alcohol.
- 2) An aqueous solvent based on n,n-dimethylacetamide, rinsed with deionized water and then isopropyl alcohol.
- 3) A terpene (*d*-limonene) with emulsifiers, rinsed with deionized water and then isopropyl alcohol.
- 4) A terpene (*d*-limonene) with phase separation agents, rinsed with isopropyl alcohol only.
- 5) *d*-Limonene (Food Grade--97% pure), rinsed with isopropyl alcohol only.
- 6) A hydrocarbon solvent based on octadecyl acetate, rinsed with isopropyl alcohol only.
- 7) Isopropyl alcohol (solvent and rinse).

Musts and Wants

Four "must" requirements were defined for the solvents:

- not compromise quality or reliability,
- not require a design change,
- be acceptable to the Environmental, Safety, and Health Departments, and
- have cleaning comparable to TCE.

Only after meeting these four must requirements would the new solvents be judged against other requirements, including:

- compatibility,
- corrosion-resistance,
- cleaning effectiveness,
- environmental, safety, and health conformance,
- manufacturing efficiency, and
- low implementation and operating costs.

Solvent Screening

A solvent evaluation matrix was defined to screen each solvent. The matrix contained four general categories:

- 1) Cleaning Evaluations, consisting of solvent cleaning, ionic contamination testing, organic contamination testing, AES/XPS surface analysis, and process development;
- 2) Solvent Analysis, consisting of composition, removal, and residuals;
- 3) Material Compatibility, consisting of screening tests, individual evaluations, and physical properties; and
- 4) Hardware Evaluations, consisting of accelerated aging and electrical performance testing.

There were three categories of contaminants that each replacement solvent had to remove from various substrates. The categories were: solder flux, mold release, and general contaminants consisting of resins, curing agents, cover coats, waxes, greases, oils, lubricants, plasticizers, and other contaminants found in a typical manufacturing environment. Other solvent evaluation methods used to screen the candidate cleaners were adhesion strength testing, high voltage testing, corrosion testing, and thermal characteristics testing.

Cleaning Results

For solder flux and mold release removal, the hydrocarbon solvent and the three terpenes were comparable to TCE. For removing the general contaminants, only the hydrocarbon solvent and the terpene containing emulsifiers were comparable to TCE for all of the general contaminants. *d*-Limonene and the terpene containing phase separation agents were able to remove most of the general contaminants, but more time and solvent were necessary. Generally speaking, *d*-limonene was not quite as effective as the terpene containing phase separation agents, which was not quite as effective as the terpene containing emulsifiers. Table 1 highlights the cleaning results for the general contaminants that were the most difficult to remove.

Test results from adhesion strength testing, high voltage testing, and corrosion testing agreed with the solvent cleaning results mentioned above: the hydrocarbon solvent and the terpene containing emulsifiers are comparable to TCE; *d*-limonene was not as effective as the terpene containing phase separation agent, which was not as effective as the terpene containing emulsifiers. However, *d*-limonene had the best thermal characteristics of the three terpenes.

FREON was used primarily as the drying agent in the TCE cleaning process, and was not used for removing contaminants from the assemblies. Adequate drying was being obtained from the existing nitrogen drying and vacuum baking processes, and the FREON drying process was simply halted.

<u>Solvent and Rank</u>	<u>Epoxy Resin</u>	<u>Curing Agent</u>	<u>Acrylic Cover Coat</u>	<u>Mold Release</u>
1) Baseline (TCE)	Clean 15 sec	Clean 30 sec	Clean 15 sec	Clean 60 sec
2) Terpene With Emulsifiers	Clean 15 sec	Clean 90 sec	Clean 4 min	Clean 2 min
3) Hydrocarbon Solvent	Clean 15 sec	Clean 3 min	Clean 2.5 min	Clean 4 min
4) Terpene With Separation Agent	Clean 45 sec	Clean 4 min	*Gross 4 min	Clean 4 min
5) <i>d</i> -Limonene (97% Pure)	Dirty 1 min	Dirty 4 min	*Gross 4 min	Dirty 4 min

* Note: Although the coupons were still grossly contaminated, there was no concern. This acrylic material was used as a cover coat for ink marking, and there was no desire to remove it. In actual practice, it was discovered that both solvents easily remove normal amounts of the acrylic cover coat.

Table 1: General Contaminant Removal From Aluminum Coupons (grossly contaminated and allowed to air cure for 3 days).

CLEANING SOLVENT SELECTION

The hydrocarbon solvent and the terpene containing emulsifiers were chosen for further evaluation. However, the terpene containing emulsifiers was used with only an isopropyl alcohol rinse, to make its cleaning process similar to the hydrocarbon solvent's, and to avoid anticipated compatibility problems from cleaning with water. Both solvents were eventually eliminated, though, because solvent residue from either solvent could not be removed from the actual assemblies with the isopropyl alcohol rinse. Next the terpene containing phase separation agents was evaluated. It did not require any deionized water rinse, which eliminated the compatibility concerns from using water. However, the terpene containing phase separation agents was eliminated. Once again, the isopropyl alcohol rinse could not remove the residual solvent.

Selection of *d*-Limonene

During the cleaning evaluation of the terpene containing phase separation agents, two extreme formulations were detected. While most of the formulations contained 90% *d*-limonene, one formulation contained nearly 100% *d*-limonene. The key discovery was not finding the two extreme formulations but in the observed cleaning results. There were no differences in the cleaning efficiencies of the two extreme formulations. The presence of the additives (which remained on the assemblies after the cleaning process) did not affect the cleaning ability of the *d*-limonene. When this fact was determined, the terpene containing phase separation agents was replaced with food grade *d*-limonene (97% pure). The existing cleaning processes had little difficulty removing the residual *d*-limonene, and since the additives were no longer present, the amount of residual solvent remaining in each assembly was substantially decreased.

COMPATIBILITY EVALUATIONS

Compatibility studies involving accelerated aging, functional testing, solvent absorption, and residual solvent removal were performed on all of the components, piece-parts, and materials in the assemblies. The materials were divided into two categories: organic and inorganic. The inorganic materials compatibility testing consisted of corrosion studies on copper and solder dipped copper. The organic materials were further divided into adhesives, encapsulation foams, and a general category consisting of polyurethanes, acrylics, polycarbonates, silicones, polyolefins, epoxies, solder masks, cables, inks, and others.

Material Compatibility

No adverse affects were observed in the inorganic material corrosion studies or in the organic material encapsulation foam studies. As for the remaining organic materials, only one known material was determined to be completely incompatible with *d*-limonene: polystyrene. Other organic materials that are known to absorb *d*-limonene are: polyurethane elastomers, polyolefin sleeveings, some nylon tie wraps, acrylics, silicones, and rubbers (EPDM). Note that these conclusions were based upon worst-case *d*-limonene exposure testing--soaking and/or saturated vapor. Vacuum baking processes are effective in minimizing actual amounts of absorbed solvent in these materials. All other organic materials, and all of the components and piece-parts tested were judged to be compatible with *d*-limonene. Table 2 contains selected information on material compatibility with TCE and with terpenes containing at least 90% *d*-limonene.

	<u>90+ % Terpene</u>	<u>TCE</u>
<u>POLYURETHANES</u>		
Polyurethane EN-7	15 %	33 %
Polyurethane EN-8	15 %	30 %
L-100/Cyanocure	5 %	16 %
Polyurethane Sleevling	30 %	N/A
<u>ACRYLICS</u>		
Lacquer Covercoat	5 %	22 %
<u>POLYCARBONATES</u>		
Polycarbonate	< 1 %	4 %
<u>SILICONES</u>		
Sylgard 184/GMB	5 %	7 %
Cellular Silicone	200 %	126 %
Red Silicone	40 %	40 %
747U (white)	20 %	22 %
Floro- (blue)	3 %	7 %
<u>POLYOLEFINS</u>		
Sleevling (as received)	25 %	14 %
Sleevling (shrunk)	20 %	16 %
Sleevling (white)	15 %	3 %
Sleevling (black)	15 %	6 %
<u>POLYSTYRENE</u>		
Not Compatible With Either Solvent		

Note: This information is primarily comprised of weight gain data taken immediately following soak testing in solvent at 50°C (122°F, TCE soaked at ambient) for 15 minutes, rinsing with IPA, and blow drying with dry nitrogen. Data not presented in percentages (%'s) was considered functional, or "pass/fail" compatibility data only.

	<u>90+ % Terpene</u>	<u>TCE</u>
<u>OTHERS</u>		
Scotchcast 8	< 1 %	3 %
Syntactic Polysulfide	< 1 %	6 %
Diallyl phthalate (DAP)	< .1 %	< .1 %
Polytherimide	< 1 %	< 1 %
Polyethyleneterephthalate	< 1 %	N/A
Polyetheretherketone	< 1 %	< 1 %
Polyphenylene sulfide	< 1 %	< 1 %
Phenolic (cotton)	< 1 %	< .1 %
Teflon rod	< .1 %	< .1 %
Nylon rod	1 %	< .1 %
Polymethylpentene	< 1 %	1 %
Polyvinylidene fluoride	< .1 %	< .1 %
Mylar (PET)	.2 %	< .5 %
Kapton/Pyrallux/Kapton (14 mil)	↓ data per in ² ↓	
	< 1mg	40mg
Kapton/Pyrallux/Kapton (6 mil)	< 1mg	0.3mg
Polyimide/glass	< 1mg	< 1mg
Parylene	.1mg	1.5mg
<u>CABLES</u>		
ETFE wire (black)	.4 mg	2 mg
ETFE wire (white)	5 mg	8 mg
ETFE wire (white)	2 mg	3 mg
Coax cable (white)	25 mg	33 mg
Coax cable (white)	10 mg	15 mg

	<u>90+ % Terpene</u>	<u>TCE</u>
<u>EPOXIES</u>		
Epon 828/Versamid 140	2 %	5 %
FM123 (epoxy/glass)	1 %	8 %
Epon 826/U	< .1 %	< .1 %
Green Hysol	< .1 %	< .1 %
Red Epoxy/Z/Mica	< .1 %	< .1 %
Epoxy Glass Cloth	< .1 %	< .1 %
A2 (white)	< .1 %	< .1 %
Brown Epoxy Molding	< .1 %	< .1 %
Brown Epoxy/Z/Mica	< .1 %	< .1 %
GMB/CTBN/DEA	< .1 %	< .1 %
GMB/CTBN/U	< .1 %	< .1 %
<u>INKS</u>		
Stamp pad	OK	OK
Epoxy (blue)	OK	OK
Epoxy paints	OK	OK
Hysol DK17 conformal coating on components	OK	OK
<u>SOLDER MASK</u>		
Dark Green (non-aqueous)	OK	OK
Apple Green (aqueous)	OK	OK
<u>COMPONENTS</u>		
(Component Material Before & After Soaking)		
Epoxy Capacitors	OK	OK
Epoxy Resistors	OK	OK
Epoxy R&P Connectors	OK	OK
DAP Triax Connector	OK	OK

Table 2: Solvent Weight Gain in Samples of Selected Materials.

Hardware Compatibility

Ten complete sets of modules and five complete final units were built for the accelerated aging testing. The units were separated into three groups of five. Within each group, one set was cleaned with TCE and aged in a nitrogen environment, while four sets were cleaned with *d*-limonene and aged in a saturated *d*-limonene environment. Each unit completed 99 thermal cycles from -54 to 71°C (-65 to 160°F) and six months of isothermal aging at 71°C (160°F). After the accelerated aging testing was complete, all ten module sets and all five final units were judged to be compatible with *d*-limonene (no visual or electrical failures caused by *d*-limonene).

RESIDUAL SOLVENT ANALYSIS

A gas analysis technique was developed and optimized to quantitatively determine the amount of *d*-limonene remaining in a final unit. The *d*-limonene concentrations were measured as a function of time. Aging canisters containing units cleaned with *d*-limonene were evacuated through a liquid nitrogen cold trap. The trap was washed with methylene chloride, and the wash solution was analyzed using gas chromatography (flame ionization detection). Known quantities of *d*-limonene were used to characterize and optimize the process. After six generations of improvement, recovery efficiencies from 92% (for a 50 mg sample) to 99.5% (for a 2000 mg sample) were achieved. Earlier in the project, it was estimated that 1000 to 2000 mg would remain in the final unit after the subassemblies and the final unit were cleaned with *d*-limonene.

Results

Three *d*-limonene units were tested three repetitive times using this gas analysis process (one unencapsulated unit, one encapsulated unit, and one alternate encapsulated unit). Test results concluded that negligible amounts of *d*-limonene were detected in these assemblies. The results are tabulated in Table 3.

	<u>Sample 1</u>	<u>Sample 2</u>	<u>Sample 3</u>
Unencapsulated Unit:	1.26 mg	1.70 mg	1.08 mg
Encapsulated Unit:	2.75 mg	0.31 mg	< .01 mg
Alternate Encapsulated Unit:	< .01 mg	< .01 mg	< .01 mg

Table 3: Residual Solvent Remaining in a Final Unit

Given this actual data and the uncertainty at these detection levels, it was decided (with at least 92% confidence!) that less than 50 mg of solvent remained in the final units cleaned with *d*-limonene. These measured values were acceptable and quite pleasing, especially when 1000 to 2000 mg was expected!

CONCLUSIONS

Halogenated cleaning solvents used to clean complex electronic assemblies have been replaced with *d*-limonene, an environmentally safe, terpene cleaning solvent. This enhances the hazard elimination efforts at the Kansas City Division by following company policy to eliminate CFC and CHC usage, and complies with environmental regulations by eliminating the emission of CFC's (known ozone depleters) and the exposure to CHC's (suspect carcinogens).

All materials tested in this evaluation were judged to be compatible with *d*-limonene under routine, everyday operating conditions. Through accelerated aging testing, the long-term compatibility of the modules and final assemblies *d*-limonene was verified. Functional testing of complex electronic assemblies was completed. No electrical failures were caused by the use of *d*-limonene. New analytical techniques were developed and used to measure and quantify residual solvent levels in the assemblies. Only trace amounts were detected in each of three consecutive tests.

527-31

N94-30467

2463

P. 9

SUPERSONIC GAS-LIQUID CLEANING SYSTEM

Raoul E. B. Caimi
NASA, DM-MED-11
Kennedy Space Center, FL 32899

Eric A. Thaxton
NASA, DM-MED-11
Kennedy Space Center, FL 32899

ABSTRACT

A system to perform cleaning and cleanliness verification is being developed to replace solvent flush methods using CFC 113 for fluid system components. The system is designed for two purposes, internal and external cleaning and verification. External cleaning is performed with the nozzle mounted at the end of a wand similar to a conventional pressure washer. Internal cleaning is performed with a variety of fixtures designed for specific applications. Internal cleaning includes tubes, pipes, flex hoses, and active fluid components such as valves and regulators. The system uses gas-liquid supersonic nozzles to generate high impingement velocities at the surface of the object to be cleaned. Compressed air or any inert gas may be used to provide the conveying medium for the liquid. The converging-diverging nozzles accelerate the gas-liquid mixture to supersonic velocities. The liquid being accelerated may be any solvent including water. This system may be used commercially to replace CFC and other solvent cleaning methods widely used to remove dust, dirt, flux, and lubricants. In addition, cleanliness verification can be performed without the solvents which are typically involved. This paper will present the technical details of the system, the results achieved during testing at Kennedy Space Center, and future applications for this system.

BACKGROUND

Cleaning and cleanliness verification are essential in the initial installation and maintenance of all fluid systems at Kennedy Space Center. The strict cleanliness requirements are derived from liquid oxygen (LOx) system compatibility. Hydrocarbon greases and oils can easily ignite in the presence of LOx. Any system connected to a LOx system must be as clean as the LOx system itself. Cleaning involves removing both particulate and non-volatile residue contaminants from LOx components. Cleanliness verification is essentially identical to cleaning except that a sample of the remaining contaminants, both volatile and non-volatile, must be collected and their levels measured. Freon 113 (CFC 113) has been used almost exclusively at Kennedy Space Center for cleanliness verification in LOx systems and in most other fluid systems where high levels of cleanliness are important. It is also used for some cleaning applications. CFC 113 is being phased out of production due to its detrimental effects on the Earth's ozone layer. This fact has prompted an effort within NASA to replace CFC 113 cleaning and cleanliness verification methods.

The current method for cleaning fluid systems at Kennedy Space Center is to flow large quantities of detergent and water at elevated temperatures through or across the components. The method for verifying cleanliness is to flush the component with CFC 113 which is then collected and evaluated. Evaluation of the collected CFC 113 consists of two parts, particulate and non-volatile residue (NVR). Particle counting is done by pouring the CFC 113 through filter paper and examining the paper under a microscope. NVR is measured by heating the sample until all volatile compounds evaporate then weighing the remaining material. Other cleaning and verification methods include solvent flushing and high-pressure water jets.

The new cleaning and cleanliness verification method uses impingement instead of a controlled solvent like CFC 113. This system uses supersonic two-phase flow nozzles to create high velocities at the surface of the component to be cleaned. The nozzle has a converging-diverging (de Laval) geometry. The compressibility of the gas accelerates the liquid droplets to velocities high enough to remove contaminants from impinged surfaces. The

liquid can be collected for verification purposes. Currently, air or nitrogen is being used for the gas, and water is the liquid. The use of water has eliminated the environmental problems associated with CFC 113. The water is the cleaning and cleanliness verification agent. It can be collected so the particulate and the total organic carbon (TOC) content can be measured for cleanliness verification purposes.

This system has several advantages over high pressure water jets and solvent flushing methods. The pressures required to generate high velocities in a gas are considerably lower than in a liquid. The consumption of solvent in a gas-liquid spray is at least an order of magnitude lower than in a liquid only spray. The consumption advantage over solvent flush methods is even more dramatic. Also solvent flushing may leave behind insoluble particulate which impingement methods remove.

DESIGN APPROACH

The initial requirements which led to the development of this system were: (A) it must remove at least 80% of contaminants; (B) the 80% removal efficiency must be achieved using less than 100 ml of water per square foot of area to be cleaned; (C) it must be able to provide a stable water blank; and (D) water samples must be collectible for total organic carbon (TOC) analysis. The first requirement was based on the fact that a replacement system had to be able to clean at least as well as the CFC 113 cleaning method it replaced. Supersonic gas-liquid cleaning, water impingement, and alternate solvent flushing all could meet this requirement. The second requirement presented the greatest challenge, and ruled out systems using only water impingement or solvent flushing. This led to the idea of using high velocity gas-liquid flow to generate high impact velocities while simultaneously using less than 100 ml of water per square foot of cleaning area. A supersonic gas-liquid flow was the solution to the above constraints and considerations.

Theoretical Development

The design of the supersonic gas-liquid flow nozzles was based on equations for the one-dimensional, irrotational, frictionless expansion of a gas containing a dispersion of small liquid droplets. The flow was assumed to be homogeneous and adiabatic with uniform velocity. In addition, thermal equilibrium was assumed to exist between the gas and the liquid.

Denoting the air temperature by T, and using subscript a for all air properties. The usual equation of state is

$$P_a v_a = R_a T \quad (1)$$

If the liquid droplet density is very large compared to the air density and if the mixture contains mass, m_1 of liquid droplets and mass m_a of air. The mass ratio $m = m_1/m_a$. The apparent density (or specific volume) will be related to the air density (or specific volume) by

$$\frac{\rho}{\rho_a} = \frac{v_a}{v} = 1 + m \quad (2)$$

where

$$m \ll 1$$

From equation (2),

$$v_a = v(1 + m) \quad (3)$$

also,

$$P_a = P \quad (4)$$

Substituting equations (2), (3), and (4) into equation (1) gives

$$Pv = \frac{R_a}{1 + m} T$$

This is the equation of state for the mixture.

If the gas and liquid droplets are in thermal equilibrium, the total entropy of both together remains constant. Thus, if the droplets have a specific heat of c , their entropy increase accompanying a heat transfer dQ to the air is

$$ds_d = \frac{dQ}{T} = cm \frac{dT}{T}$$

The entropy increase for the air is

$$ds_a = \frac{dQ}{T} = c_{pa} \frac{dT}{T} - R_a \frac{dP}{P}$$

Since

$$ds_d + ds_a = 0$$

then

$$\frac{dT}{T} (c_{pa} + mc) - R_a \frac{dP}{P} = 0$$

or

$$\frac{dT}{T} = \frac{R_a}{c_{pa} + mc} \frac{dP}{P}$$

or

$$\ln T = \frac{R_a}{c_{pa} + mc} \ln P + \ln C_1$$

where

$$C_1 = \text{constant}$$

Therefore,

$$TP^{-\Psi} = \text{constant}$$

where

$$\Psi = \frac{R_a}{c_{pa} + mc}$$

or

$$\frac{P^{(\gamma-1)/\gamma}}{T} = \text{constant} \quad (5)$$

where

$$\frac{\gamma-1}{\gamma} = \frac{R_a}{c_{pa} + mc} \quad (6)$$

Equation (5) is the expansion law of the gas-liquid mix, hereinafter called the pseudo gas. Since

$$R_a = c_{pa} - c_{va}$$

Equation (6) gives

$$\gamma = \frac{c_{pa} + mc}{c_{va} + mc} \quad (7)$$

The effect of mutual heat transfer (thermal equilibrium) is therefore to modify the isentropic exponent to the value given by equation (7).

Therefore, the pseudo gas behaves as if it possessed a specific gas constant given by

$$R = \frac{R_a}{1+m}$$

and a value of the specific heat ratio, γ , given by equation (7), but in other ways obeys all of the well-known one dimensional flow relations of gas dynamics that can be taken from a standard text.

Technical Development

The supersonic nozzle design parameters were chosen based on the 100 ml per square foot of cleaning area requirement, and the need to achieve high velocity at impact. The first requirement led to the choice of a flowrate of 30 ml/min based on a cleaning rate of one square foot in three minutes. The gas flowrate of 30 scfm (standard cubic feet per minute) was chosen based on existing gas supply capacity. This set an m value of ~ 0.03 with a corresponding pseudo gas γ of 1.34. These values were used to generate an isentropic flow table for the pseudo gas.

The Mach number versus area ratio (exit area/throat area) values from the isentropic flow table were plotted in order to decide which area ratio to use (refer to Figure 1). The area ratio was chosen at a point where the rate of change in Mach number with area ratio began to decrease significantly. The rationale was that before this point a small change in area ratio produced a large change in Mach number, and after that point the converse was true. Thus high exit velocities could be achieved without making an inordinately large exit cone.

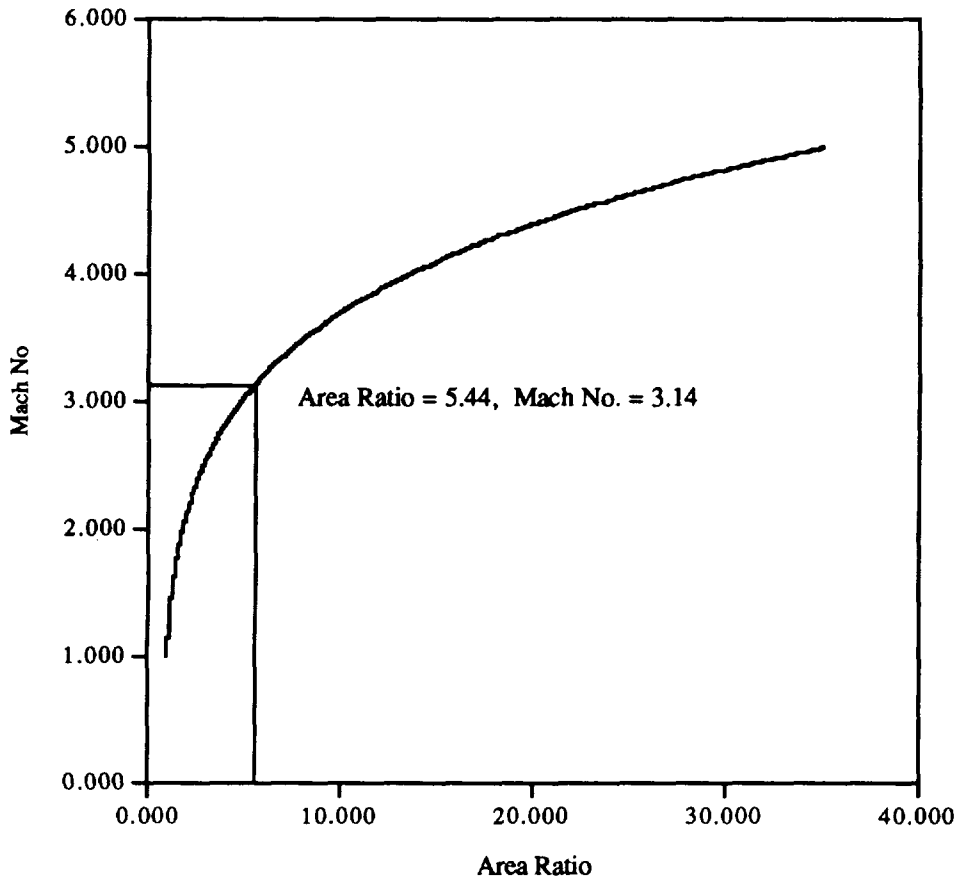


Figure 1. Mach Number Versus Area Ratio Plot

The liquid injection and mixing was the next problem which had to be tackled to make the 5.44 area ratio nozzle (hereinafter referred to as the nozzle) work as intended. The liquid which was to be used was distilled water, and the chosen gas was initially nitrogen and later breathing air. The water needed to be injected so that it would atomize and mix with the gas flow. Several ideas were considered; these included pre-mixing, injection in the center of the gas flow both towards and against the flow, and side injection into the gas tube through a small orifice. The last idea was implemented for the sake of design simplicity and ease of manufacturability and maintenance. The injection location was initially chosen just upstream of the nozzle. It was deemed that this location would not give the water sufficient time to form large droplets and subsequent stratified flow. A hand-held prototype system with this configuration was successfully tested.

The prototype system used three nozzles with axes arranged at the vertices of an equilateral triangle. The water was injected at the center of one of the sides of the triangle. This configuration provided excellent mixing and water distribution to all three nozzles. The water injection location also made the system insensitive to nozzle/injector orientation, so the nozzles could be pointed in any direction allowing access to all sides of a part being cleaned. Figure 2 is a diagram of the prototype system.

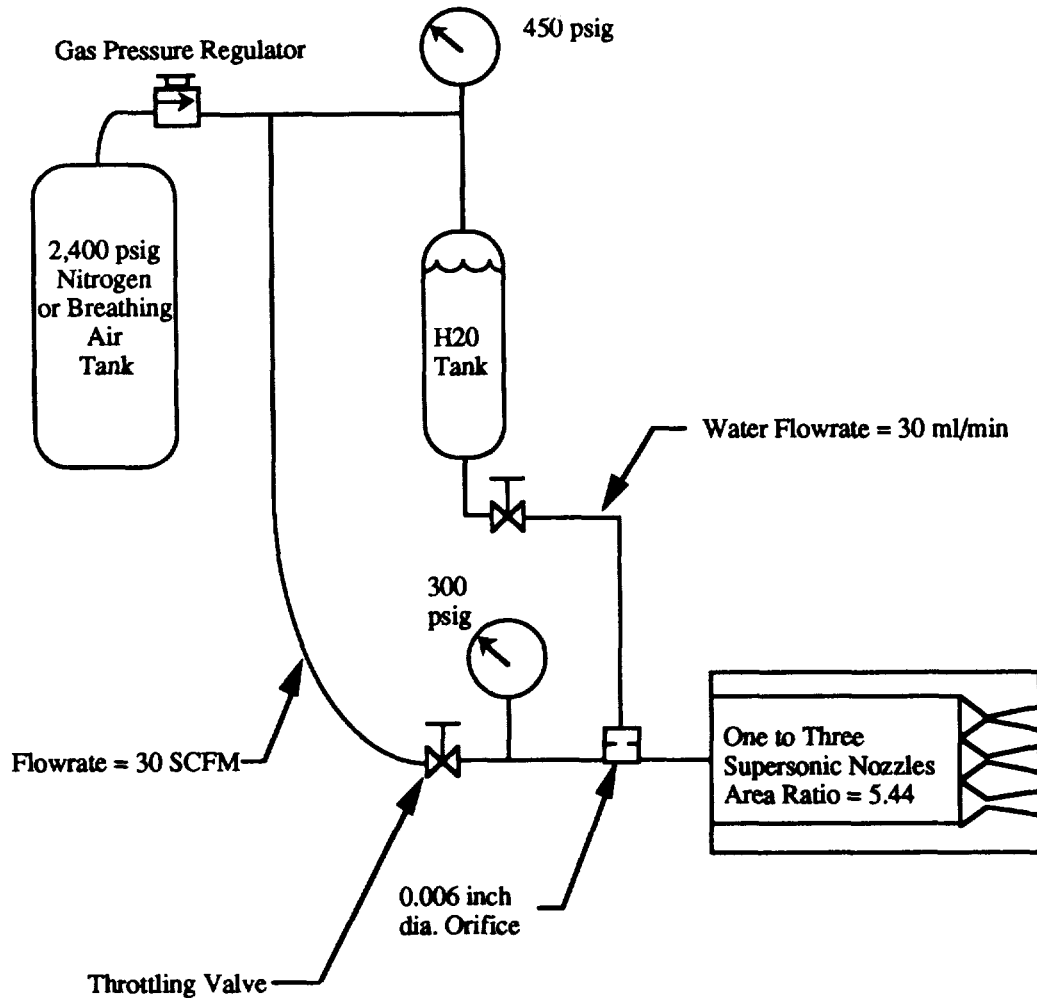


Figure 2. Gas-Liquid Supersonic Cleaning System Schematic

The system, as developed, required two hoses to extend to the nozzles, one for water and the other for air. Suggestions by the prototype system operators indicated that a single hose configuration would improve the ease of use of the spray nozzle. This prompted a modification of the injector location.

The injector was moved to the exit of the gas supply port prior to the twenty foot flexible hose to which the nozzles were attached. In order to keep the water and air mixed, the flow was made to go through a contraction upon exiting the flexible hose. This contraction served to increase the turbulence in the flow (Reynolds number > 5,000) which was sufficient to maintain mixing. This system configuration was also subjected to validation testing which is the subject of the next section.

SYSTEM VALIDATION

The existing specification for cleaning and cleanliness verification at Kennedy Space Center is based on using CFC 113. Before a new system can be accepted, it must be validated against the existing CFC 113 method. In the past, cleanliness was measured by weighing the non-volatile residue (NVR) and comparing it to the area of the surface in question. The rinse CFC 113 was collected, heated until the solvent and volatile residue evaporated, and weighed. The new verification method measures the total organic carbon (TOC) in the collected water sample. There needs to be a correlation between the NVR remaining on the surface and the TOC reading of the water sample.

The first set of tests were performed on one square foot witness plates made of type 304 stainless steel. The majority of fluid components used at KSC are from the 300 series (austenitic) stainless steels so the data should be representative. The plates were contaminated with a known quantity of one of the following substances:

- Hydrocarbon Grease
- Hydraulic Fluid
- Silicone and Fluorosilicone Greases
- Fluorinated Grease

Fluorinated greases, such as Krytox 240AC or Tribolube 16, are used for assembling all fluid systems at KSC except hydraulic systems which are lubricated with hydraulic fluid. The other substances are common lubricants. The plates were contaminated with two to ten milligrams each with one of the contaminants then impinged for between two and eight minutes each. The results showed that two minutes is sufficient to sample one square foot of surface area. The data correlating the TOC to the removed and remaining NVR is shown in Figures 3 and 4. The supersonic nozzle tends to emulsify hydrocarbon contaminants, so the concentration is much higher than the contaminant solubility limit in water. To test the emulsification, the water samples were subjected to an ultrasonic agitation after collection, and then the resulting TOC readings were compared. The data from that test is shown in Figures 5 and 6. This test indicated that the nozzle emulsifies well enough such that another step was not necessary.

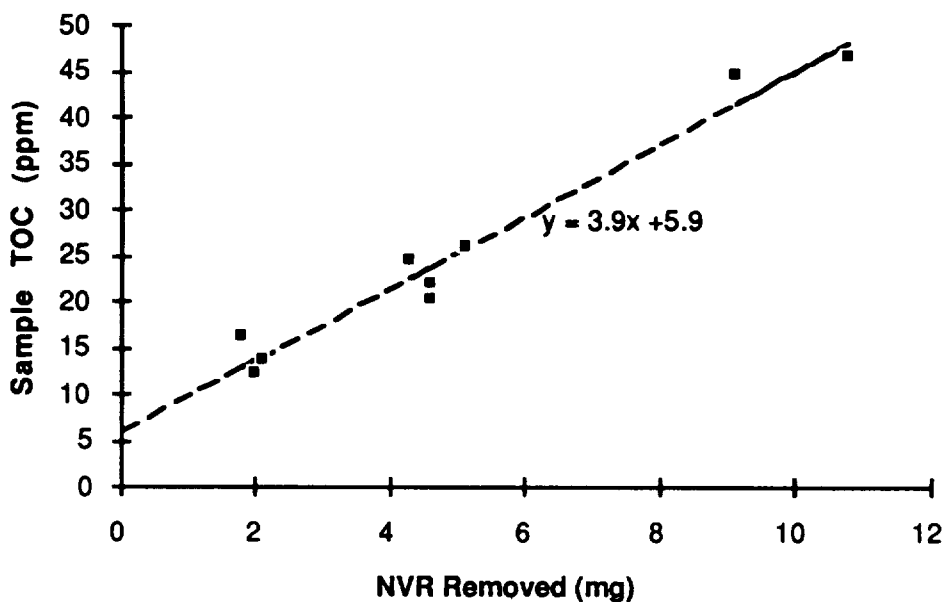


Figure 3. Correlation Between TOC Reading and NVR Removed

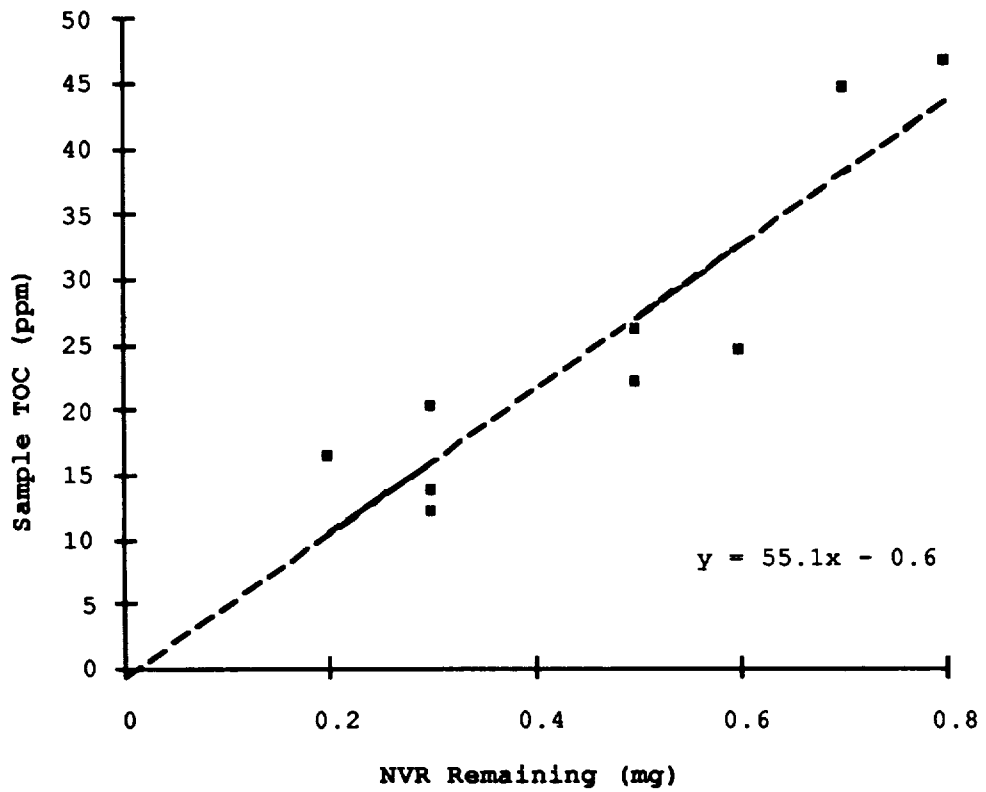


Figure 4. Correlation Between TOC and NVR Remaining After Cleaning

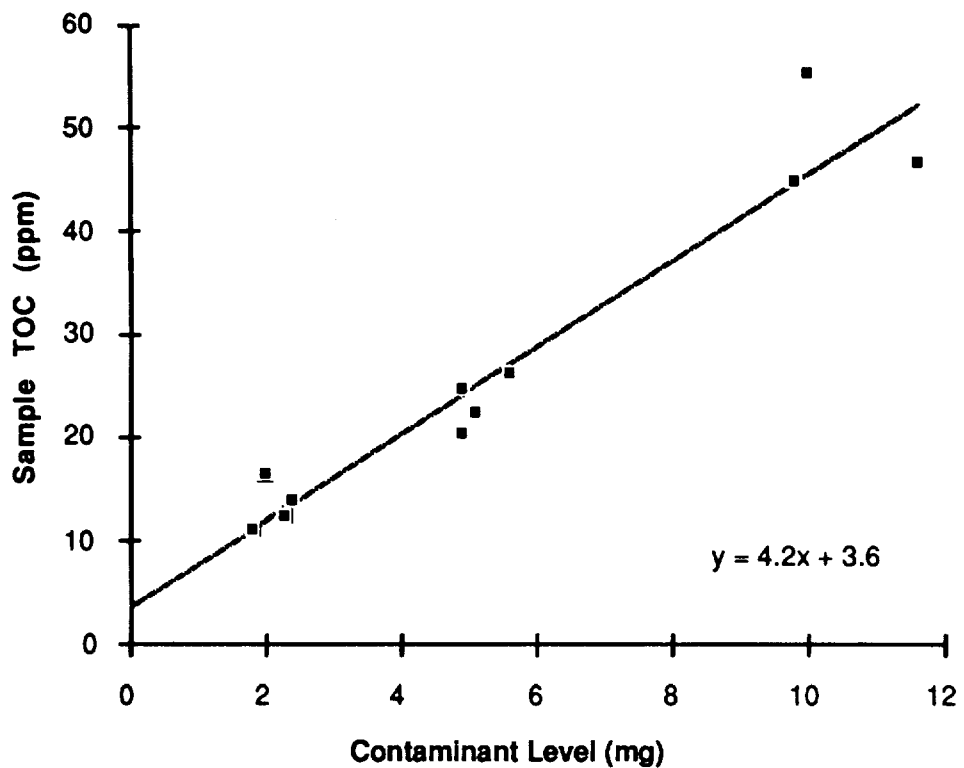


Figure 5. TOC vs. Initial Contaminant Level

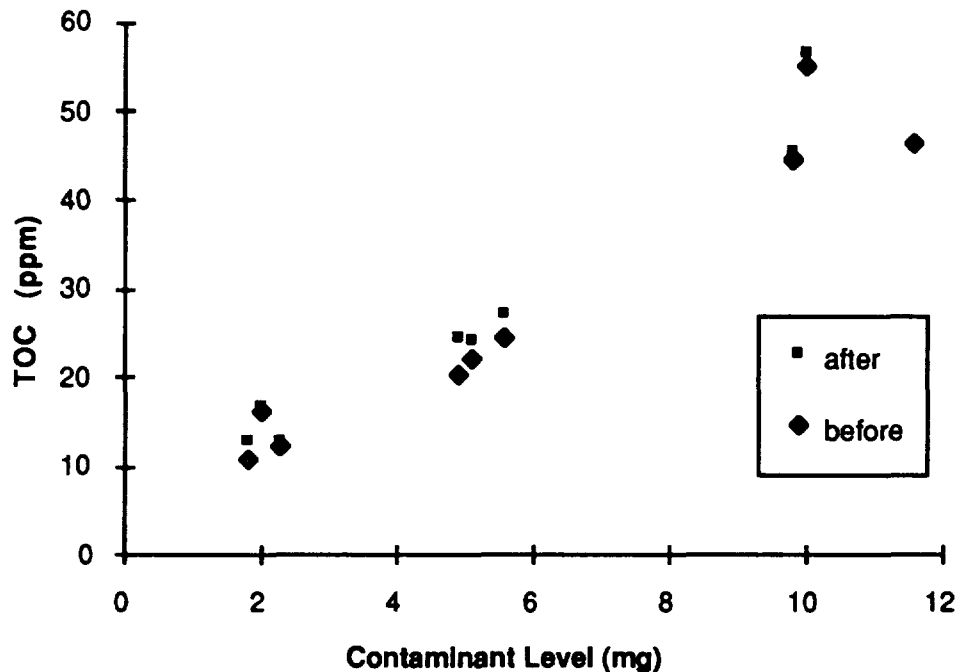


Figure 6 TOC Levels Before and After Ultrasonics

CURRENT AND FUTURE DEVELOPMENTS

The system was developed to clean and verify fluid components for the Space Shuttle program, but there are several other direct applications. Compressed gas bottles are required to be cleaned to the same levels as the LOx system components. These bottles are difficult to clean without an effective solvent due to the limited access to the inner surface. The widely used 2400 psig compressed gas bottles (k-bottles) are approximately eight inches in inside diameter. The only opening in a k-bottle is the single one-half inch pipe thread fill and drain connection. The current method for cleanliness verification is to flush the k-bottle with CFC 113. The gas-liquid nozzle would be a good candidate for verification except that the nozzles as designed would not fit through the opening. Several designs to use the existing nozzle on a rotating spray head were studied and abandoned. Finally a new nozzle was designed which has no converging section. With only a diverging section the nozzle is much smaller than a full converging-diverging nozzle. In theory a nozzle with no converging section is a diffuser which can achieve sonic velocity at the throat and lower velocity at the exit. This design controls the geometry of the approach to the throat of the diverging-only nozzle. This diverging-only nozzle design is supersonic with approximately a 20% loss in fluid momentum compared with a converging-diverging nozzle of the same dimensions and area ratio. The k-bottle spray head contains three diverging-only nozzles, one aimed straight down the bottle, one at 30° from the bottle axis, and one at 210°. The two angled nozzles are collinear so there is no side load on the spray head. The only net load on the spray head is the axial force created by the thrust of the straight through nozzle. The 210° nozzle covers the entrance region of the bottle and contributes to cleaning the side wall. The straight through and 30° nozzles combine to clean the flat bottom while the 30° nozzle also helps clean the side walls. This spray head design may be used to clean short, straight pipes and other small diameter pressure vessels.

Another application of the nozzle is the cleaning of large diameter pipes and pressure vessels. This design uses a rotating spray head like the k-bottle cleaner. In large pipes there is room for the full converging-diverging nozzle so the cleaning is more efficient. The nozzles in the large pipe spray heads are offset to produce a torque around its axis to cause rotation. The k-bottle cleaner requires an external force to spin the spray head. There will be a different spray head for different size ranges of pipe. Current development work is being done on cleaning large pipelines with this device. A pipe crawler is used to carry the rotating nozzle through the pipe while pulling a gas-liquid supply hose. Verification of cleanliness can be accomplished by collecting the liquid either at the crawler or at the entrance to the pipe and examining it by any of a number of methods.

SUMMARY

The system was developed to eliminate CFC 113 for cleanliness verification of large fluid system components at Kennedy Space Center. The supersonic nozzle arrangement was tested extensively against the CFC standard. Once the system was verified, work began on development of this technology for other applications. These include: the compressed gas cylinder spray head using the diverging only supersonic nozzles; and a nozzle configuration with the rotating spray head for large pipes and pressure vessels. Other potential applications include flux removal from printed circuit boards, degreasing operations, and cleaning operations which require minimization of the quantity of solvent used.

**REGENERATING USED AQUEOUS CLEANERS
WITH OZONE AND ELECTROLYSIS**

Michael P. McGinness
Custom Process Systems & Service Co.
2710 South Shaver Unit 'D'
Pasadena, Texas 77502
(713)-941-0907

2464
P 7

ABSTRACT

A new process converts organic oil and grease contaminants in used water based cleaners into synthetic surfactants. This permits the continued use of a cleaning solution long after it would have been dumped using previously known methods. Since the organic soils are converted from contaminants to cleaning compounds the need for frequent bath dumps is totally eliminated.

When cleaning solutions used in aqueous cleaning systems are exhausted and ready for disposal, they will always contain the contaminants removed from the cleaned parts and drag-in from prior cleaning steps. Even when the cleaner is biodegradable these contaminants will frequently cause the waste cleaning solution to be a hazardous waste. Chlorinated solvents are rapidly being replaced by aqueous cleaners to avoid the new ozone-depletion product-labeling law (1). Many industry standard halocarbon based solvents are being completely phased out of production and their prices have nearly tripled. Waste disposal costs and cradle-to-grave liability are also major concerns for industry today.

This new process reduces the amount of water and chemicals needed to maintain the cleaning process. The cost of waste disposal is eliminated because the water and cleaning compounds are reused. Energy savings result by eliminating the need for energy currently used to produce and deliver fresh water and chemicals as well as the energy used to treat and destroy the waste from the existing cleaning processes. This process also allows the cleaning bath to be maintained at the peak performance of a new bath resulting in decreased cycle times and decreased energy consumption needed to clean the parts. This results in a more efficient and cost effective cleaning process.

INTRODUCTION

Industrial cleaning processes are currently being re-evaluated and redesigned in order to minimize the amount of waste produced and the resulting cost of waste disposal. Waste disposal costs have soared in recent years. There is increasing pressure from congress, and the public to reduce the amount and the toxicity of all industrial waste streams.

Aqueous cleaning formulations used in spray washers are frequently quoted as being environmentally safe and biodegradable. However, when they are exhausted and ready for disposal they will always contain the contaminants that were removed from the dirty parts. Automotive contaminants include motor oil, transmission fluid, benzene, lead, cadmium and drag in from other cleaning processes which frequently contain phenols, cresols, xylenes and various chlorinated solvents.

In the past, disposing of weak contaminated cleaners and replacing them with fresh cleaners has been the most cost-effective option. Replacing a cleaning bath requires shutting down the cleaning process, draining out the old cleaner, and filling the tank with the new cleaner. Then the old cleaner must be tested and disposed of properly. Testing and disposal costs have soared in recent years.

Most cleaning system users are looking for ways to extend the life of their cleaning solutions. Mechanical filters, oil skimmers and special oil releasing cleaning formulas are becoming quite common. None of these

methods has eliminated the need for continued frequent disposal of used cleaning solutions. Solvent based cleaners can be distilled and reused. However, they tend to be flammable, sources of air pollution, odorous, or depleters of the ozone layer. There is a major shift underway from hazardous solvent based cleaners to aqueous based cleaning products(2).

Products are available to separate oils and greases from the cleaning solutions to help increase the life of the cleaning bath. However, these products do not eliminate the eventual need for disposal of the contaminated oil or the spent cleaner. Some facilities have switched to burn off ovens to burn off the oils and greases, followed by dry shot blasting. This option is extremely energy intensive and costly(\$30,000.00/oven), and is not usable on plastic or aluminum.

Waste generators must determine if their used cleaning wastes are hazardous before disposing of them. A complete lab analysis of just one waste stream can cost from \$2,000 to \$3,000 and disposal costs for hazardous waste vary from \$300.00 to \$1,200.00 per barrel. Even when the waste has been properly disposed of the generator remains forever liable for any future problems caused by the waste.

The U.S.Environmental Protection Agency (EPA) now requires hazardous waste generators to certify on their hazardous waste manifests that the amount of hazardous waste produced has been minimized prior to shipping the waste.One current method is to boil the water off and ship the solids. This is one of the most energy intensive and costly methods available. Systems that boil 50 gallons/day can cost over \$10,00.00 to purchase. They tend to scale easily reducing their energy efficiency and they do not solve the problem of solids disposal.

Another disposal option is to set up and man a small scale waste water treatment and neutralization system. This option requires trained operators, more chemicals, the energy required to pump and filter the solution prior to discharge, and a permit to discharge the treated waste water. These systems also produce large volumes of wet sludge requiring further treatment prior to disposal.

Chlorinated solvents are rapidly being phased out and replaced by aqueous cleaners in order to avoid the new ozone-depletion product-labeling law (1). This new law requires manufactures to label products which have been cleaned with ozone depleting chemicals as having been manufactured with an ozone depleting chemical. These solvents are being heavily taxed and considering waste disposal costs and cradle to grave liability issues they are no longer cost effective. These market forces are driving industry to replace solvent cleaners with aqueous cleaners.

Past experience has already demonstrated that the advanced oxidation process will oxidize the organic compounds that are frequently dragged in on parts from other processes such as carburetor cleaner (9). These compounds include phenol, benzene, creosols, xylenes, chlorinated hydrocarbons and various paint solvents. Most of these compounds are now on the EPA's new "TCLP" hazardous waste list. Waste cleaners frequently leach more than the limit of these organic compounds and are therefore considered to be hazardous wastes. Since the advanced oxidation process destroys these compounds as they are introduced, (3,7,9,11) they will not accumulate in the cleaner.

Waste water treatment using ozone is well known and documented in the literature(7). Recent work has been published on advanced oxidation techniques using combinations of oxidizers including hydrogen peroxide, ultraviolet light, and ozone(10). Only one article has been found to date dealing with the use of ozone and electrolysis at the same time (10). This article suggests that any compound that can first be oxidized by either process into formaldehyde or glycolic acid can be further oxidized to carbon dioxide by simultaneous exposure to both ozone and electrolysis.Neither ozone nor electrolysis accomplish this alone. Ultraviolet light is highly dependent on the clarity of the fluid being treated and therefor is not a candidate for this type of process since the cleaning solutions are highly opaque.

Recent work in Florida (4,8,12) has demonstrated the feasibility of cleaning laundry with ozonated water on a large scale. The process has eliminated the use of chemical cleaning compounds and heat in a major

laundry facility. The process Patent Number 5,097,556 was issued on March 24,1992. The laundry systems success is due to a chemical reaction between ozone and the unsaturated hydrocarbons (soil in the fabric) which form soluble surfactants that emulsify and clean the laundry while the ozone disinfects it. The waste water is then ozonated, filtered and reused again.

Industry manufactures surfactants and detergents by oxidizing various oils (hydrocarbons) into polar (oxygenated hydrocarbons) water soluble compounds(6). They are manufactured on a very large scale in chemical plants around the world. By converting the oils and greases into detergents as they are dragged into the cleaning solution and the detergents into carbon dioxide and water we will be able to keep the cleaner operating indefinitely.

CONCEPT DESCRIPTION

Custom Process Systems has developed an advanced oxidation process which uses ozone and electrolysis to oxidize the oils and greases which are dragged into used cleaning solutions into polar water-soluble surfactants that can be used in the same cleaning process. The process shown in Figure 1.1 consists of an external tank and plumbing which accommodates the circulation of an aqueous cleaning solution from the parts washer to the tank and back to the washer. The solution in the tank is treated with an advanced oxidation process utilizing ozone and electrolysis.

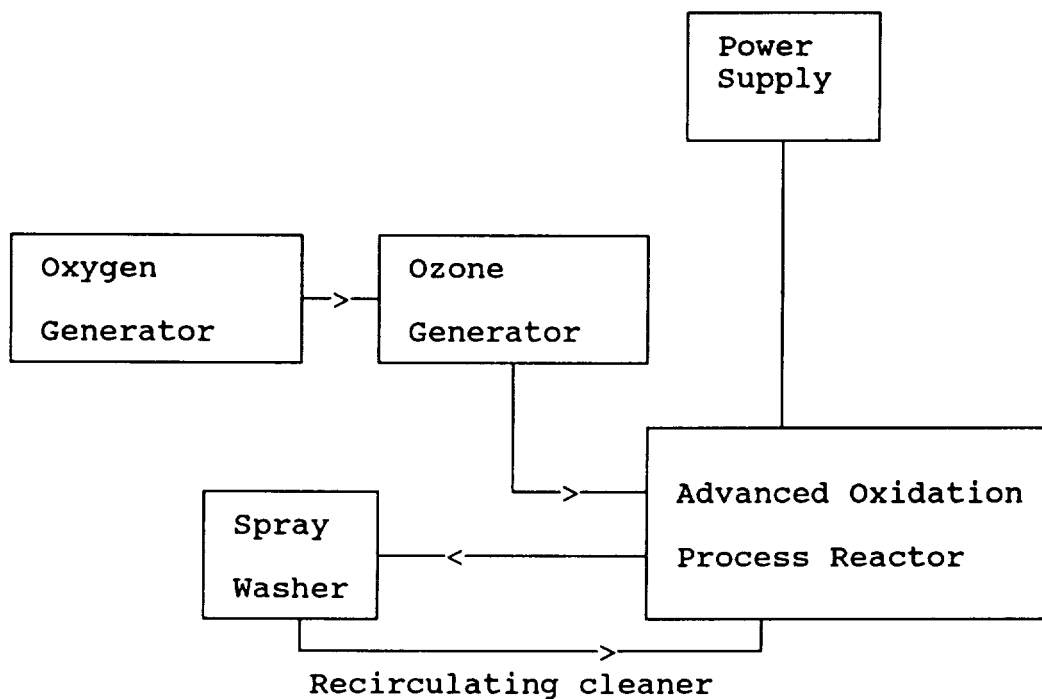


Figure 1. Process flow chart.

The oxidation process converts insoluble organic fatty acids, greases and oils into a variety of soluble surfactants and wetting agents (6). At the same time existing surfactants and organic contaminants are oxidized into carbon dioxide and water (9,11).The process is designed to generate its own cleaning surfactants directly from the oils and greases cleaned off of the prior batch of soiled parts. The only waste produced by the process would be a very small amount of precipitated inorganic solids. These solids can easily be rendered non-hazardous or even be recycled should they contain heavy metals such as lead.

The process includes a pressure swing adsorption oxygen generator which feeds dry high purity oxygen to a corona discharge ozone generator. The oxygen and ozone are generated and used as needed. Alternating D.C. current is feed to permanent electrodes immersed in the tank.

The basic concept of the entire process is never to let anything except the cleaned parts themselves leave the cleaning process. This eliminates the cost of testing the waste to determine if it is hazardous waste and the cost of disposal. The second step is to re-design the cleaning process to operate in such a way that if any waste does leave the system it will be non-hazardous, minimal in volume and can be sold as a by-product. These two concepts taken together constitute the ultimate waste minimization process.

Once we eliminate the concern about disposal of the cleaner itself we are able to consider cleaning formulations that others avoid due to various environmental considerations. The next step is to determine why these cleaners stop cleaning and find ways to reverse the process. In cleaning processes where the same cleaning bath is reused repeatedly we find two main problems. One is the loss of cleaning solution to drag out by the parts and the subsequent loss of the cleaning chemicals to the rinse water. The other is bath contamination.

The bath contamination has several sources. One is the make up water used to replace water lost to evaporation and drag out. The other is soil cleaned off of the parts themselves. The water used for make up can be filtered and deionized prior to use. If the cleaning process is heated the rinse water can be deionized and filtered prior to use and after use as rinse water it can be reused as make up water for the cleaning bath to replace the water lost to evaporation. This also allows us to recover the cleaning chemicals that were previously lost to the rinse water. Even if the cleaning process is not heated a triple dead deionized rinse system can be used and the majority of the cleaning salts recovered and returned to the cleaning bath using various concentration and recovery methods such as reverse osmosis.

The current industry practice is to dispose of the cleaning bath once it is contaminated with oil and grease or to skim the oil and grease off in an attempt to extend the life of the bath before eventually disposing of both. Replacing a cleaning bath requires shutting down the cleaning process, draining the old cleaner out and filling the tank up with the new cleaner. The old cleaner must be tested to determine if it is hazardous then stored in storage containers and finally disposed of. Even if the material is not a hazardous waste disposal can still be a very costly and time consuming task.

KEY EXPERIMENTAL RESULTS

A full scale prototype has been tested on an automotive spray washer that is used to clean engine blocks and heads prior to their being remanufactured. In a recent test a one year old, completely exhausted cleaning bath was restored to 80 % of the performance of the original cleaning bath in less than 8 hours of processing. In a second test, 4-gal. of motor oil were introduced into the same 60-gal cleaning bath. The cleaning solution and oil mixture was then processed for 16 additional hours. Careful evaluation revealed that oxidation of the motor oil had generated enough oxygenated water soluble synthetic surfactants to increase the cleaning performance far beyond the capability of the original cleaner. The cleaning bath was now performing 100% better than the new original formulation. We succeeded in making a better cleaning solution out of a dead-unusable cleaning bath that was loaded with grease and oil.

The cleaner was heated and operated at 140°F and 200°F. The cleaning solution was feed through the nozzles at 60 pounds of pressure by a 5 HP pump. Since the cleaner was heated a great deal of water was lost to evaporation. The rinse water was reused as make up water to replace the water lost to evaporation.

ECONOMICS AND MARKET POTENTIAL

The economics of the process are based on the following cleaning system cost reductions:

- (1) Water is reused.
- (2) Cleaner is reused. The need to purchase replacement cleaning chemicals is eliminated.
- (3) Waste disposal costs are eliminated.
- (4) Since the cleaning performance is constant and does not decline with use, and considering the improved cleaning performance when compared to standard purchased formulas, the cost of power and fuel to operate the cleaning process can be reduced by 50 to 90 %.

The advanced oxidation process varies in cost from \$5,000 to \$10,000 for the smallest basic system. More complex automated systems or heavy loadings of oil and grease would increase the cost. This is a fraction of the cost of waste water treatment systems. Most water evaporators start at \$10,000. Offsite disposal can run anywhere from \$.50/gal for waste water to \$20/gal for exotic sludges. Replacement cleaning compound can cost several hundred to several thousand of dollars per year.

A typical rebuilding facility could be expected to reduce the amount of (hazardous) waste it generates by 20,000 to 30,000 lbs. per year. Facilities in the more heavily regulated areas like California, where used oil is a listed hazardous waste, should experience a payback in 6 months to one year based just on reduced disposal costs alone.

Eliminating the expense of purchasing new cleaning compounds can save several thousands of dollars per year. This alone could generate a two to three year payback in many cases. The increased efficiency of the cleaning process will result in reduced cycle times, heating costs and a substantial increase in productivity. The reduced heating costs alone can produce a six month payback. The increased productivity can result in an expansion of cleaning capacity without incurring the capital expense of purchasing additional cleaning equipment.

Considering all of these benefits at the same time indicates that most aqueous cleaning systems could be retrofitted with this process and expect a six month to one year payback. A recent marketing study by D'Ruiz(2) indicates that the aqueous cleaning systems market is in a major growth stage. 147,000 aqueous cleaning systems are projected to be sold in the next ten years just to replace chlorinated solvent cleaning systems. According to another survey(5) there are over 300,000 separate shops of various types that do some level of automotive engine repair work. 60,000 of them are engine remanufacturers. There are over 19,000 automobile transmission rebuilders as well.

Other potential markets also exist such as cleanup of hazardous waste or superfund sites, cleanup of process waste water in a number of industries, detoxification of waste water prior to biological waste water treatment, treatment in combination with processes such as reverse osmosis prior to water reuse, treatment of cooling water in cooling towers, and cleanup or disinfection of medical waste just to name a few. Another possible application would be nuclear decontamination. A mixed radioactive organic waste cleaning solution could be decontaminated and continuously reused to clean hazmat uniforms, respirators or other radiation contaminated equipment thereby reducing the volume of radioactive waste needing disposal.

Although it is not the subject of this paper, it has not escaped our attention that by carefully manipulating various process parameters such as PH, temperature, voltage, electrode type, and electrode surface area, in combination with various membrane separation techniques, it will be possible to modify the hydrophilic and lipophilic nature of various compounds. This means that it will be possible to carefully neutralize the hazardous or dangerous properties of numerous wastes and convert them into useful compounds and

materials. Some of these materials may turn out to have new properties that could lead to useful technological spin offs that could be useful in the fields of energy production, industrial manufacturing, electronics, pharmaceuticals and agriculture.

SUMMARY

This new technology eliminates the need for frequent bath dumps required by many cleaning processes. Many cleaning processes require frequent bath replacement due to build-ups of oily contaminants which reduce the performance of the cleaning bath to unacceptable levels. By converting these contaminants into cleaners the problem is eliminated. The need for waste treatment and disposal is eliminated thereby eliminating the original environmental impact of the cleaning process (waste cleaner disposal). By increasing the efficiency of the cleaning process by nearly 100% we reduce the need for fuel to heat and operate the process and the pollution that results from that fuel consumption is prevented.

FUTURE DEVELOPMENT NEEDS

This process is ready for limited introduction into the market place. A large variety of cleaning formulas, cleaning processes, soils, contaminants and part compositions are in use today. Because of this variety of process conditions that exist we are currently looking for a select group of clients who wish to try this process out on their cleaning lines as part of their waste minimization and/or pollution prevention plans and strategies for compliance with federally mandated requirements to prevent and minimize waste. We are also looking for clients who need or wish to go to closed loop systems otherwise known as zero discharge. This process can make zero discharge a reality. We are also looking for cleaning systems manufactures who wish to license this technology for sale as an integral part of their cleaning processes.

REFERENCES

- 1) Bergeson,Lynn L., "Labeling of Ozone-Depleting Chemicals Approaches", Pollution Engineering,Jan.15,p49-52,1993.
- 2) D'Ruiz,Carl D., "Aqueous Cleaning as an Alternative to CFC Chlorinated Solvent-Based Cleaning", Noyes Publications,1991.
- 3) Huang,C.P.,and Chu, Chieh-sheng, "Electrochemical Oxidation of Phenolic Compounds from Dilute Aqueous Solutions", Proceedings of the First International Symposium, Chemical Oxidation: Technology for the Nineties, Technomic Publishing Co., Lancaster Penn.,p.239-253, 1991.
- 4) "Jail Laundry Saves Money ,Time ", Anonymous, Product Spotlight.
- 5) "Jobber and Warehouse Executive Fact Book " , James J. Halloran Ed., Hunter Publishing Co., 1986.
- 6) "Kirk-Othomer Concise Encyclopedia of Chemical Technology ", Martin Grayson Ed., John Wiley and Sons, N.Y., 1985.
- 7) "Ozone in Water Treatment, Application and Engineering " , B.Langlais Ed., Lewis Publishers, 1991.
- 8) "Revolutionary Laundry System Promises Spectacular Results", The Shariff's Star, Feb.,1991,p.10.

- 9) Rice, Rip G. and Browning, Myron E., " Ozone for Industrial Water and Waste Water Treatment, a Literature Survey ", EPA-600/2-80-060, 1980.
- 10) Serota,L., " Science for Electroplaters 33, Cyanide Waste Treatment --Ozone and Electrolysis ", Metal Finishing, Feb.,p.71-74, 1958.
- 11) Takahashi,N. and Katshuki, O., " Decomposition of Ethylene Glycol by the Combined Use of Ozone Oxidation and Electrolytic Methods ", Ozone Science and Engineering, Vol.12, Num.2, 1990, p.115-131.
- 12) "The Tri-O-Clean Laundry System ", O3-Tech product bulletin, Fortpierce, Florida.

GAS STREAM PURIFIER

Steven J. Adam
Lead Engineer/Scientist
McDonnell Douglas Aerospace - West
5301 Bolsa Ave. Huntington Beach, CA 92647

ABSTRACT

A gas stream purifier has been developed that is capable of removing corrosive acid, base, solvent, organic, inorganic, and water vapors as well as particulates from an inert mixed gas stream using only solid scrubbing agents. This small, lightweight purifier has demonstrated the ability to remove contaminants from an inert gas stream with a >99% removal efficiency. The Gas Stream Purifier has outstanding market and sales potential in manufacturing, laboratory and science industries, medical, automotive, or any commercial industry where pollution, contamination, or gas stream purification is a concern. The purifier was developed under NASA contract NAS 9-18200 Schedule A for use in the international Space Station. A patent application for the Gas Stream Purifier is currently on file with the United States Patent and Trademark Office.

INTRODUCTION

Due to the high cost of using the Space Shuttle as a refueling vehicle for the international Space Station, a supplemental reboost system (SRS) was designed to augment the primary hydrazine propulsion system. The SRS collects waste gases generated from the Space Station laboratories, compresses and stores them at high pressures (1000 psi), and vents them through heated resistojets to provide extra reboost capability for the Space Station. Implementation of the SRS provides a savings of 3500 pounds of propellant per year and reduces the number of refueling shuttle launches by 1/3. The mixed waste gas produced by the Space Station laboratory modules is composed primarily of nitrogen, air, inert gases, oxygen and carbon dioxide. The mixed waste gas will also contain a wide variety of trace contaminant vapors and particulates generated from experiments performed in the laboratory modules (Table 1). The high pressure storage of mixed waste gases containing an uncertain mixture of chemical contaminants has caused grave concerns in regard to material reliability, corrosion, and stress corrosion cracking of hardware in the high pressure areas of the system. One method of alleviating these concerns was to remove the chemical contaminants from the mixed waste gas stream prior to entering the system. A gas stream purification unit was developed to remove corrosive acid, base, solvent, organic, inorganic, and water vapors as well as particulates from the mixed gas stream in one step using only the gas flow across the purifier. Because of Space Station weight, space, pressure drop, and dew point requirements and the zero gravity environment, commercial aqueous scrubbers could not be used. The Gas Stream Purifier (GSP) was designed to be small, lightweight, utilize solid scrubbing agents, and maintain a less than 2 psi pressure drop across the unit at flow rates up to 24L/min.

Table 1
Possible Waste Gas Contaminants

Acetic Acid	Carbon	Formaldehyde	Indium	Methanol	Silver Nitrate
Acetone	Tetrachloride	Freon	Iodine	Methyl Ethyl	Sodium Acetate
Acetylene	Chlorine	Gallium	Isopropyl	Ketone	Sodium Chloride
Aluminum	Chromic Acid	Arsenide	Alcohol	Nitric Acid	Sodium
Aluminum	Cobalt	Germanium	Lactic Acid	Oxalic Acid	Hydroxide
Oxide	Copper	Glycerol	Lead	Perchloric Acid	Sodium Nitrate
Ammonia	Copper Nitrate	Hydrochloric	Lithium	Phenol	Sulfuric Acid
Ammonium	Dimethyl	Acid	Magnesium	Potassium	Toluene
Hydroxide	Sulfide	Hydrogen	Chloride	Dichromate	Trichloroethylene
Ammonium	Ethanol	Iodide	Mercuric	Potassium	Trichloroethane
Chloride	Ferric Chloride	Hydrogen	Chloride	Permanganate	Xylene
Benzene	Fluorine	Peroxide	Methane	Silicon	Zinc Chloride

CONCEPT DESCRIPTION

The Gas Stream Purifier (GSP) prototype unit measures 15 inches in length by 2 inches in diameter (Figure 1). The Gas Stream Purifier from its gas stream input end serially through its output end consists of a stepwise arrangement of medium-coarse grade solid scrubbing agents designed to remove a wide variety of chemical contaminants. Particulates in the gas stream are removed by a particulate trap at the entrance of the purifier and a particulate filter at the exit end of the unit. Gas purification is performed by a series of purification stages inside the unit. Stage 1 of the purifier removes water vapor and large organic molecules. Stage 2 of the purifier removes water vapor and other small chemical contaminant molecules. Trapped water vapor also facilitates the removal of additional chemical contaminant vapors. Stage 3 of the purifier removes organic solvents and many other chemical compounds. Stage 4 removes inorganic and organic acid and base vapors by reaction, generating CO₂ and water, and transforming the stage 4 compound into salts. Stage 5 removes inorganic and organic acid and base vapors, ammonia, sulfur dioxide, and other chemical contaminant vapors by reaction, generating CO₂ and water, and transforming the stage 5 compound into salts. As an option, a 6th stage can be added to the purifier to remove a specified contaminant from a known process. Each purification stage is separated from the next by a layer of glass wool. Following stage 5 (or 6) the gas stream passes through another series of stage 3, stage 1, and stage 2 at the exit end of the purifier (Figure 1). The final three stages ensure complete removal of solvent contaminant vapors, and any water vapor generated by the central stages of the purifier. The pure dry gas exits the purifier through a particulate filter. The purification stages of the Gas Stream Purifier can be modified in quantity or substance to meet different contaminant removal applications. The Gas Stream Purifier will remove chemical contaminant vapors and particulates from any inert gas stream, or any mixed gas stream consisting of air, nitrogen, inert gases, carbon dioxide, hydrogen, or oxygen. The Gas Stream Purifier will remove corrosive acid, base, solvent, organic, inorganic, and water vapors as well as particulates from an inert or mixed gas stream in one step using only the gas flow across the purifier. The purifier is not consumed by carbon dioxide or oxygen. The 15" by 2" diameter prototype purifier weighs 4.2 pounds, and has a less than 2 psi pressure drop across the unit at flow rates up to 24 L/min. The purifier is effective in removing chemical contaminants at levels from <1 to 10,000 ppm

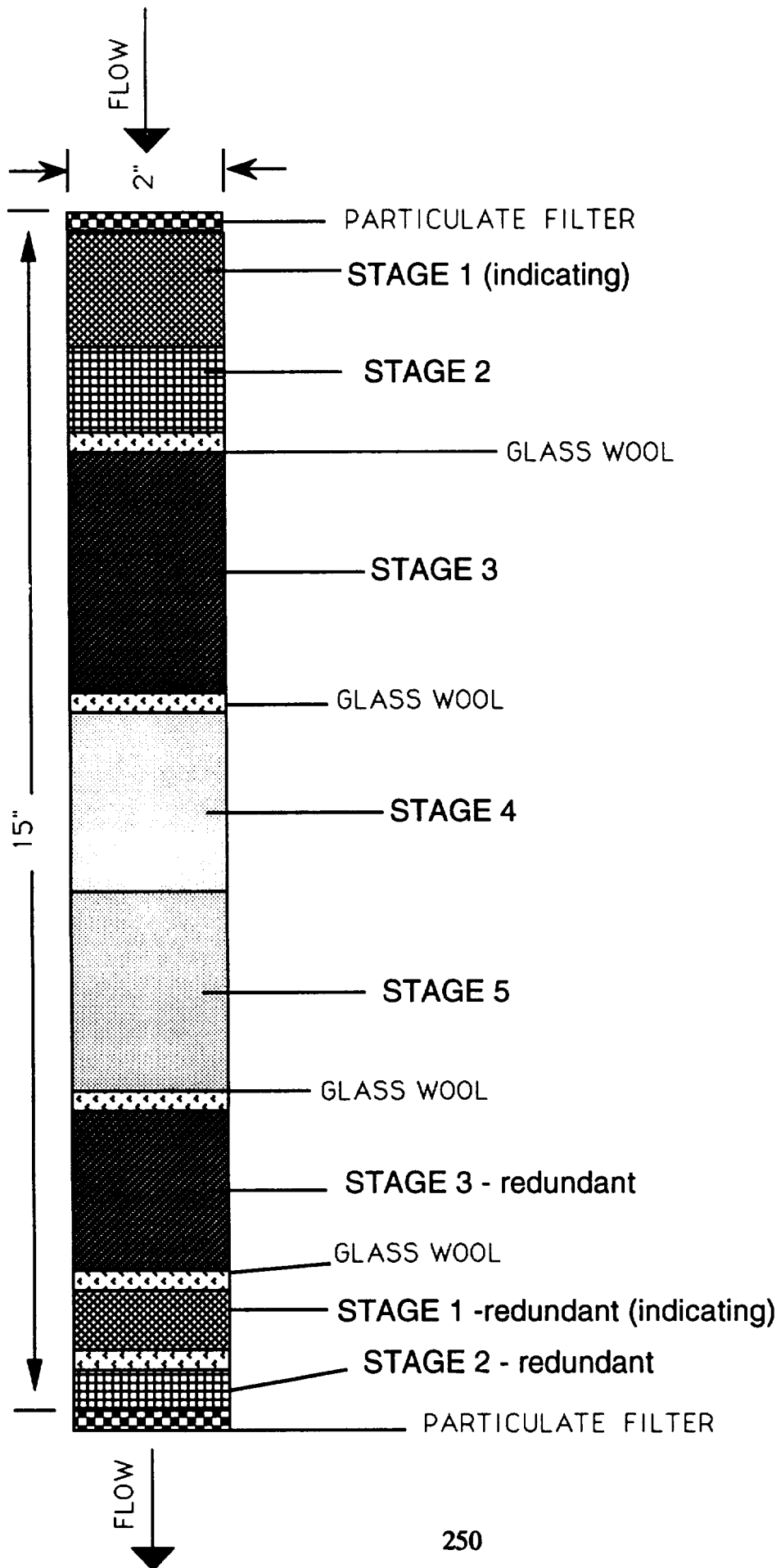


FIGURE 1 - GAS STREAM PURIFIER

with a >99% removal efficiency, and is designed to last for periods of 2-4 months or longer depending on the levels of contamination seen. After the purifier has been exhausted, the contents can be disposed of or regenerated. The cannister can be repacked with new purification stages and used again. The Gas Stream Purifier can be configured in different sizes and scaled up to meet higher contaminant removal and flow rate requirements.

TESTING

Pressure Drop Testing

Pressure drop testing was performed on the Gas Stream Purifier using the apparatus shown in Figure 2. The flow rate of a nitrogen gas stream circumventing the purifier was set and the corresponding back pressure was recorded with a calibrated Seeger Precision Pressure Transfer Standard pressure gauge. A valve leading to the gauge was closed and a valve at the exit end of the purifier was opened. The flow rate through the purifier was reset and the corresponding pressure drop across the purifier was recorded. Pressure drop measurements were taken for a tightly packed and loosely packed purifier at flow rates of 7 and 24 L/min. As the flow rate across the purifier increased the pressure drop also increased. The Gas Stream Purifier pressure drop tests yielded a pressure drop of 0.3 psi at a flow rate of 7 L/min for a loosely packed purifier constructed with medium-coarse grade materials. A pressure drop of 1.8 psi was observed for this same purifier at a higher flow rate of 24 L/min. A tightly packed purifier of the same configuration had a pressure drop 0.7 psi at a flow rate of 7 L/min and a pressure drop of 4.0 psi at a flow rate of 24 L/min. A tightly packed purifier containing fine mesh materials will have a much greater pressure drop than a loosely packed purifier with coarse mesh materials. The trade off is that finer mesh materials provide more surface area and thus more reactivity and will contribute to a longer lasting unit. Although coarse materials have less surface area than fine materials, they do not restrict flow as much and are less prone to channeling effects. By using medium-coarse grade materials of the same mesh size for each of the purification stages, where possible, and packing the purifier using only gravitational forces, the pressure drop vs surface area trade off can be optimized. Increasing the inlet and outlet line sizes and diameter of the purifier will also decrease the pressure drop and allow for a higher flow rate across the unit.

Efficiency Testing

Efficiency testing was performed on the Gas Stream Purifier using the apparatus shown in Figure 3. A solution containing the contaminant to be measured was placed in an impinger. Nitrogen gas was bubbled through the solution and the vapor generated was run through a line circumventing the purifier at a flow rate of 24 L/min. This gas/vapor mixture was tapped off into another line where a Drager Tube specific to the contaminant being measured was placed in line with a wet test meter. The wet test meter measured the quantity of gas being passed through the Drager Tube. A reading corresponding to the part per million (ppm) level of contaminant being generated was taken and recorded. The valve leading into the purifier was opened, and the valve on the line circumventing the purifier was closed, forcing the contaminated gas stream through the purifier. The flow rate was reset to 24 L/min and after a few minutes of flow another reading was taken with a new Drager Tube. This reading corresponded to the amount of contaminant not being consumed by the purifier, or the contaminant ppm level after purification. A

percent purification efficiency for the Gas Stream Purifier for each contaminant tested was calculated by taking the ppm level after purification, and dividing by the ppm contaminant level prior to purification, subtracting this number from 1, and multiplying by 100. The Gas Stream Purifier was tested for purification efficiency with hydrochloric acid, ammonium hydroxide, methyl ethyl ketone (MEK), xylene, isopropyl alcohol (IPA), ethanol, acetone, and trichloroethylene. The same purifier was used for all of the efficiency tests without replacing any of the purification stages.

The results of the Gas Stream Purifier efficiency tests are listed in Table 2. The purifier demonstrated a removal efficiency of 99% or more for each of the chemical contaminants tested. Although contaminant levels in the Space Station mixed waste gas are anticipated to be in the 10-50 ppm range, the ability of the purifier to remove large slugs of contaminants in the case of accidental spillage was also demonstrated during the efficiency tests. Most of the testing was performed at a flow rate of 24 L/min, a worst case flow for the Space Station SRS. After this testing was performed a purifier was constructed that can handle flow rates up to 3 CFM (85 L/min). At lower flow rates removal efficiency will be slightly improved over experimental values due to increased contact time of the gas stream with the purification stages. During the efficiency testing no chemical reactivity of the purification stages with the reagents tested was observed, with the exception of the stage 4 and 5 reactions with the acid and base vapors which were part of the design. These reactions transform the stage 4 and 5 compounds into salts, and generate CO₂ and water along with a small amount of heat. Contaminant breakthrough of the purifier was tested by flowing nitrogen through the purifier for two hours after the efficiency tests were completed, and checking for breakthrough with new Drager Tubes. No breakthrough of contaminants was observed following the efficiency tests.

Duration Testing

Duration testing was performed using the apparatus shown in Figure 3. Hydrochloric acid was chosen as the contaminant due to its highly corrosive nature. A HCl solution was prepared and placed in the impinger. The solution generated 350 ppm of HCl vapor by volume when measured with a Drager Tube and a wet test meter at a flow rate of 24 L/min. A new Drager Tube was placed in the apparatus and the 350 ppm HCl vapor nitrogen stream was run through the Gas Stream Purifier for 16 hours at a flow rate of 24 L/min until a reading was finally observed on the Drager Tube. Purifier duration times were calculated based upon 5 and 20 ppm levels which are more representative of the contaminant levels that the purifier will see in actual usage. Theoretical values were calculated for the consumption of HCl by the stage 4 and stage 5 compounds based on stoichiometric calculations. At a 350 ppm HCl contaminant level, the purifier lasted 16 hours, which was 12.12% of the calculated theoretical value. There are two reasons why the actual consumption was only a fraction of the theoretical consumption. The first reason is the high flow rate at which the duration test was run. A lower flow rate will increase the amount of contact time of the contaminant with the purification stages, thus consuming more of the contaminant, which will increase the amount of time before breakthrough occurs. The second reason is surface area. Theoretical calculations were based on a total weight of purification stages 4 and 5, when in reality, the HCl vapor was only reacting with the outside surfaces of the particles in these stages. Thus, particle size and surface area are the limiting factors in determining solid purifier duration. Duration values for HCl were calculated for anticipated ppm contaminant levels based on a flow rate of 24 L/min. At 20 ppm the purifier should last for 281 hours of constant usage or 35 days based upon 8 hours of laboratory work with HCl per day. At 5 ppm the purifier should last for 1124 hours or 140 days. If the contaminant to be removed from the gas

stream is known, the appropriate purification stage of the Gas Stream Purifier can be increased in quantity to promote a longer lasting purifier.

COMMERCIAL APPLICATIONS

The Gas Stream Purifier has outstanding market and sales potential in manufacturing, laboratory and science industries, medical, automotive, or any commercial industry where pollution, contamination, or gas stream purification is a concern. The Gas Stream Purifier can be implemented in a variety of commercial applications by simply resizing or reconfiguring the basic prototype unit to fit a particular application. The Gas Stream Purifier can be used to purify compressed gases, or it can be used to remove contaminants generated in an industrial manufacturing process. The Gas Stream Purifier is effective as a process tool in waste stream reduction and can also be configured as an air purification or smog removal system for homes, offices, and buildings. The advantages of the Gas Stream Purifier over presently known devices are numerous. Most gas scrubbers are large, heavy industrial units which use water as the scrubbing agent. Other known devices are capable of removing only one type of contaminant. Small lithium based gas purifiers used for instrumentation also react with oxygen and CO₂ and thus cannot be exposed to air. In applications that require a dry gas or low dew point, small size, and/or low weight, commercial aqueous scrubbing units are not feasible. The Gas Stream Purifier is able to remove many types of chemical contaminants (acid, base, solvent, inorganic, organic) without using aqueous scrubbing agents. Contaminants are effectively removed by using the gas flow through the purifier. The Gas Stream Purifier is small in size, lightweight, moveable, and can be plumbed into any existing system. The purifier maintains a low pressure drop, is not consumed by CO₂, oxygen, or air, and will effectively remove contaminants for a period of 3-4 months. By manifolding 2 or 3 purifiers together, change out can be accomplished by simply turning a valve. The purifier removes chemical contaminants at high and low contaminant levels with a >99% removal efficiency, and is an excellent safeguard against large contaminant mishaps in systems. The purification stages of the Gas Stream Purifier are composed of low cost solid materials, so that the purifier can be produced at a low cost and sold at a competitive price. The Gas Stream Purifier can be configured in different shapes and sizes to suit different applications, and the purification stages can also be scaled up or down to meet the individual customers' specific needs.

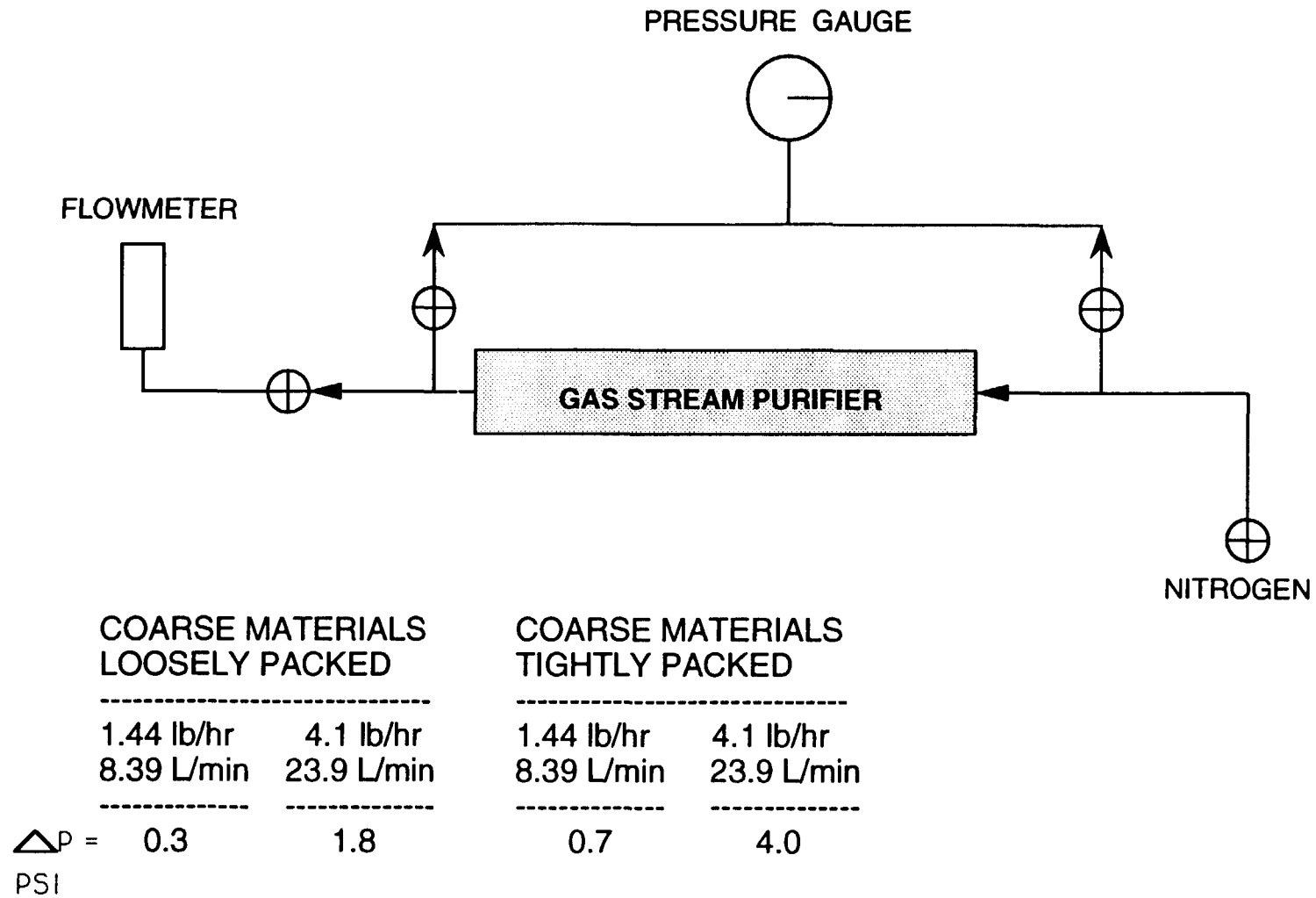


FIGURE 2 - GAS STREAM PURIFIER - PRESSURE DROP TESTING

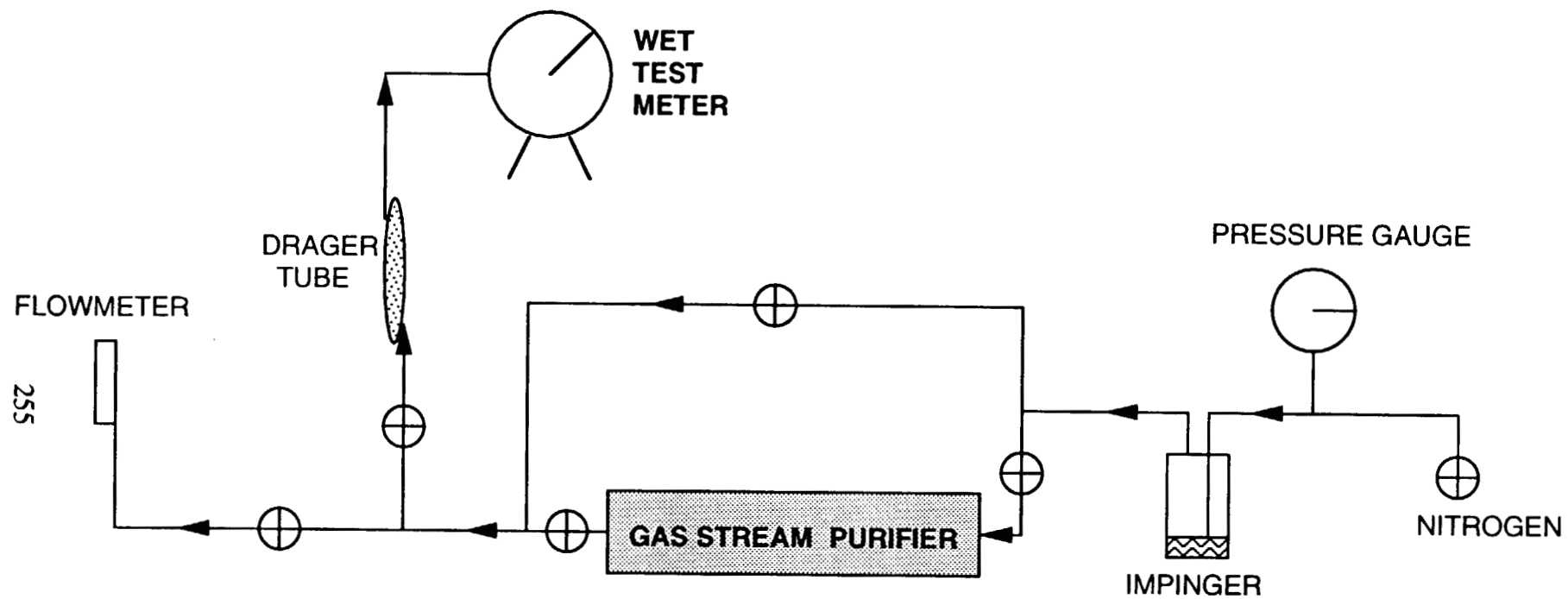
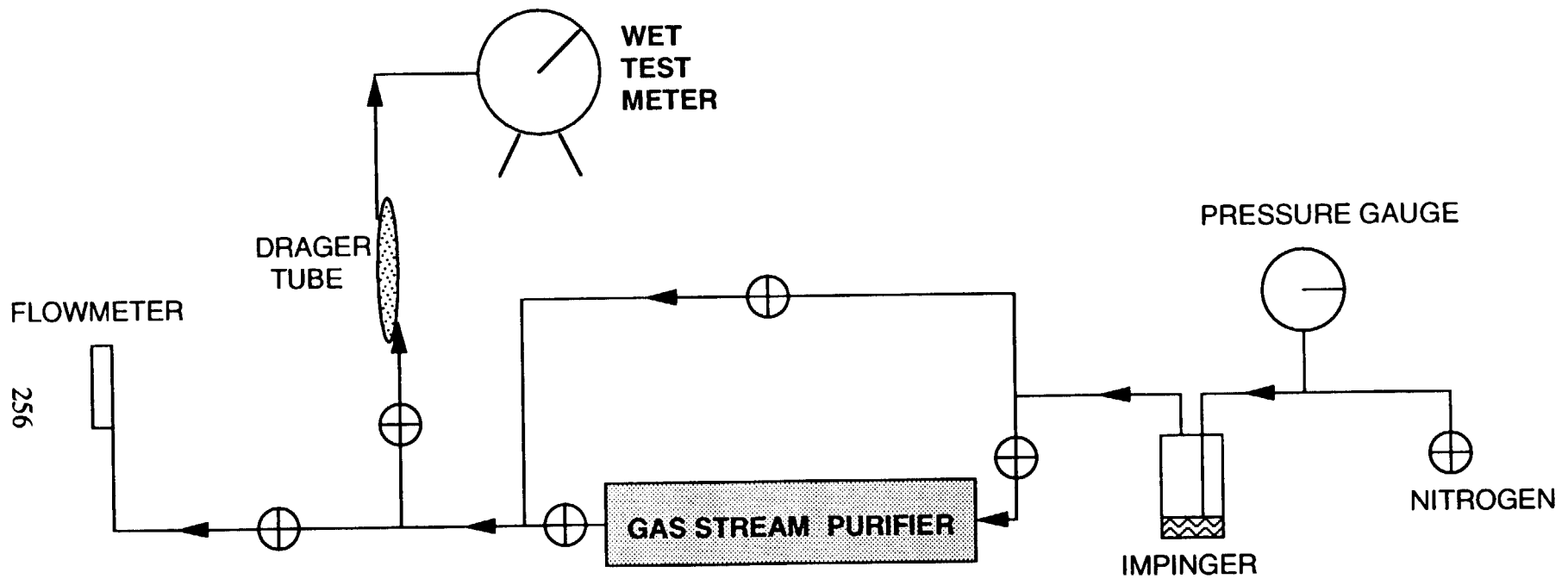


FIGURE 3 - GAS STREAM PURIFIER EFFICIENCY TESTING



256

FIGURE 3 - GAS STREAM PURIFIER EFFICIENCY TESTING

TABLE 2

GAS STREAM PURIFIER CONTAMINANT REMOVAL EFFICIENCY

CONTAMINANT	Flow Rate LBm/Hr	PPM Level Contaminant	PPM Level After Purification	% Efficiency
HCl	1.4	1.9	0.0	100%
HCl	4.1	3.0	0.0	100%
HCl	1.4	20	0.0	100%
HCl	4.1	20	0.0	100%
HCl	4.1	350	0.5	99.76%
NH ₄ OH	4.1	500	1.0	99.80%
NH ₄ OH	4.1	2000	10	99.50%
MEK	4.1	15,000	50	99.67%
XYLENE	4.1	11,155	50	99.55%
IPA	4.1	10,000	100	99.00%
ETHANOL	4.1	15,000	100	99.33%
ACETONE	4.1	40,000	100	99.75%
TCE	4.1	10,000	50	99.50%

530-45

2460

P-4

USING SPACECRAFT TRACE CONTAMINANT CONTROL SYSTEMS TO CURE SICK BUILDING SYNDROME

John C. Graf
Crew and Thermal Systems Division
Mail Code EC 3
NASA Johnson Space Center
Houston, TX 77058

ABSTRACT

Many residential and commercial buildings with centralized, recirculating, heating ventilation and air conditioning systems suffer from "Sick Building Syndrome." Ventilation rates are reduced to save energy costs, synthetic building materials off-gas contaminants, and unsafe levels of volatile organic compounds (VOCs) accumulate. These unsafe levels of contaminants can cause irritation of eyes and throat, fatigue and dizziness to building occupants. Increased ventilation, the primary method of treating Sick Building Syndrome is expensive (due to increased energy costs) and recently, the effectiveness of increased ventilation has been questioned. On spacecraft venting is not allowed, so the primary methods of air quality control are; source control, active filtering, and destruction of VOCs. Four non-venting contaminant removal technologies; strict material selection to provide source control, ambient temperature catalytic oxidation, photocatalytic oxidation, and uptake by higher plants, may have potential application for indoor air quality control.

INTRODUCTION

The similarities between providing spacecraft trace contaminant control and treating the indoor air pollution problems in "tight" buildings have been recognized for several years (Limero et. al. 1990). Both spacecraft and "tight" buildings support continuous human occupancy for extended periods of time; both recirculate air through a closed volume with limited venting, both have contaminants introduced through off-gassing of materials and human metabolic activity, both must remove a wide range contaminants found at very low concentrations, and both must use removal techniques that are simple, regenerable, robust, operate at ambient temperatures and pressures, and have low energy requirements.

The increased cost of energy has forced the designers of commercial and residential buildings to seal windows, further limit the exchange of outside air, and recirculate indoor air longer before venting. Commercial and residential buildings are becoming more and more like spacecraft (Litten, 1993). Because the needs of air quality control are similar for spacecraft and commercial and residential buildings, air quality control techniques considered for spacecraft may have potential application in commercial buildings.

Indoor Air Quality is a complex field involving ventilation, temperature control, atmospheric monitoring, smoke and thermodegradation events, microbial and viral control, and particulate removal. This paper will focus on the control and removal of Volatile Organic Contaminants (VOCs) from spacecraft and "tight" residential and commercial buildings.

SICK BUILDING SYNDROME

An epidemic of illness confined to a group of people residing or working in a building with no secondary spread of illness to persons encountered outside of the building has been ascribed to Sick Building Syndrome (SBS). Symptoms of building occupants often include irritation of eyes and throat, headache, dizziness, and fatigue. The National Institute for Occupational Safety and Health (NIOSH) has noted a marked increase in the number of complaints related to office buildings since 1970 (Walsh, 1984). 71% of the buildings investigated by the NIOSH were hermetically sealed and had central air conditioning which recirculated a portion of filtered air. The increase in incidence of Sick Building Syndrome has been largely attributed to two factors; the use of new synthetic building materials that continuously off-gas volatile contaminants, and the use of recirculating centralized Heating Ventilation and Air Conditioning (HVAC) systems operating at reduced ventilation rates in order to decrease energy costs (Brooks, 1992).

Building materials, especially carpet, caulking, adhesives, paint, and particle boards have been found to emit VOCs. Table 1 summarizes emissions from some materials tested in chamber studies. New buildings have been found to have the highest concentration of VOCs (Baechler, 1991). Two new buildings were found to have levels of total organics up to 400 times greater than outside air. After six months, concentrations dropped to 30 times outdoor levels. Molhave (1985) suggests that SBS may result from the additive or synergistic effect of the complex mixture found in buildings, rather than any single component. Molhave's work suggests that a major component of SBS may be common indoor organic vapors at levels far below occupational health standards.

Sample	Emission Rate $\mu\text{g}/\text{m}^2/\text{h}$			Total Organics
	Aliphatic Hydrocarbons	Aromatic Hydrocarbons	Halogenated Hydrocarbons	
Cove Adhesive	sat*	sat*	sat*	>5000
Latex caulk	252	380	5.2	637
Latex paint A	111	52	86	249
Carpet adhesive	136	98	nd	234
Rubber molding	24	78	0.88	103
Telephone cable	33	26	1.4	60
Vinyl cove molding	31	14	0.62	46
Linoleum tile	6	35	4	45
Carpet	27	9.4	nd	36
Particle board	27	1.1	0.14	28

* detectors were saturated during this analysis. Total organic value is a minimum number. It is estimated that cove adhesive is one of the highest emitters of VOCs.

Table 1. Summary of Emission Rates from Building Materials (from Baechler, 1991)

Recommended ventilation rates have decreased in an effort to make buildings more energy efficient. In 1975, the American Society of Heating, Refrigerating, and Air-Conditioning Engineers (ASHRAE) dropped their recommended rates from 10 cubic feet per minute (cfm) per occupant to 5 cfm/occupant. Since 1981, this minimum is considered appropriate only where smoking is not permitted; 20 cfm/occupant is recommended where smoking is permitted (Turiet, 1982).

Remediation of a building with indoor air quality problems almost always involves increased ventilation. This technique can be effective (Sterling 1981) but expensive, with increased energy costs and the cost of modifying an existing ventilation system. The Du Page County IL courthouse was closed for six months and redesign and retrofitting cost \$2.8 million (Sjostrom, 1993). New buildings sometimes go through a process called a bake-out, where indoor air temperatures and ventilation rates are increased for a short time when the building is not occupied. The effectiveness of bake-outs are being questioned (Raloff, 1989). The effectiveness of increased ventilation rates is also being challenged. A series of European research studies found that workers in naturally ventilated buildings had fewer building related symptoms than those in mechanically ventilated buildings, and recirculating HVAC systems may promote sick building syndrome even with increased ventilation rates (Kreiss, 1993). Another study examined the effect of changing the outdoor air supply on the symptoms of sick building syndrome experienced by 1546 office workers in four buildings over three two-week periods. Changes in the outdoor air supply did not significantly affect the frequency of the symptoms or the office worker's perceptions of the office environment (Menzie, 1993). Except for the extremely limited use of activated charcoal, airborne trace contaminants are not actively removed from indoor air in residential or office buildings.

SPACECRAFT TRACE CONTAMINANT CONTROL

While venting is the primary mechanism of removing trace contaminants from commercial and residential buildings, venting is not allowed on spacecraft. Spacecraft designers are concerned that vented gases will condense on the outside surfaces of spacecraft, damage optical surfaces, and degrade with radiation exposure into caustic substances. Because of these concerns, the baseline venting allowances for the Space Station are presently limited to 100 liters per vent with the maximum concentration of most organic gases limited to 500 ppm (Martin, 1992).

The primary methods of spacecraft air quality control are; (1) source control, (2) active filtering and removal of VOCs from the cabin atmosphere, and (3) destruction of VOCs where the organics are chemically or biologically

converted into carbon dioxide and water. The sophistication of air quality control systems increases as mission duration increases.

The Mercury, Gemini, Apollo Command Module, and Apollo Lunar Module all removed particles and VOCs from the cabin air with a series of filters, canisters of activated charcoal, and canisters of LiOH. Skylab also used filters, activated charcoal, and LiOH, but the Skylab was also vented between missions to help avoid long term contaminant buildup. The Russian space stations Salyut and Mir fly filters and activated charcoal canisters, and they also have ambient temperature catalytic chemical absorbents. These catalysts are expendable (Diamant, 1990).

The Shuttle Orbiter, Spacelab, and proposed Space Station trace contaminant control systems use traditional "scrubbers" (filters, LiOH, and activated charcoal canisters), but they also have systems that convert contaminants into less harmful substances. The Space Station has plans to fly a high temperature catalytic oxidizer that will mineralize a wide range of volatile organic contaminants. The Shuttle Orbiter and Spacelab fly an ambient temperature catalytic oxidizer (ATCO) which converts CO to CO₂ (Diamant, 1990).

Residential and commercial buildings with high levels of combustion products (often from cooking stoves or cigarette smoking) often have excessively high levels of CO. In many cases, increasing the ventilation rate can reduce the concentration of many of the smoke constituents, but effective removal of CO would require unrealistic ventilation rates (DHEW, 1979). Although the use of an ambient temperature catalytic oxidizer to destroy CO in a residential setting is not reported anywhere in the literature, there may be some potential uses for an ATCO to reduce the level of CO in a residential setting.

MITIGATION TECHNIQUES: SOURCE CONTROL

The most effective method of spacecraft air quality control has been a rigorous program of source control. All materials must be approved by a Payload Safety Review Board before they can be flown on the Shuttle Orbiter. Minimizing the off gassing products and flammability potential is a primary concern in the materials approval process. Materials must undergo two separate tests before acceptance for use in flight hardware. The material is first subjected to flammability and off gassing testing. After all of the materials used in the flight hardware are approved separately, the assembled piece of flight hardware is subjected to a second test. This second off gassing test of the finished flight item is performed to ensure that any VOCs are released at safe levels (Limero, 1990).

Compound	Concentration Level (ppm)	
	7-day SMAC	ACGIH TLV
Isobutyl alcohol	40	50
Ethylene glycol	50	50
Phenol	2.0	5.0
Acetaldehyde	30	100
Formaldehyde	0.1	1.0
Methyl styrene	30	50
Ethylene chloride	10	10
Trichloroethylene	0.1	50
Freon 21	5.0	10
Freon 112	100	500
Isopropyl ether	50	250
Cyclohexane	60	300
Acetone	300	750
Ammonia	25	25
Carbon monoxide	25	50
Sulfur dioxide	1.0	2.0

7-day SMAC is the maximum concentration of individual contaminants allowed in spacecraft atmospheres. Threshold Limit Value (TLV) is the recommended maximum 8-hour per day weighted average concentration of a toxic contaminant that may be present in the industrial workplace atmosphere.

Table 2. Maximum Allowable Concentrations for Spacecraft and the Work Environment
(from Coleman, 1990 and ACGIH, 1993)

The acceptable levels of the individual chemical contaminants are defined as Spacecraft Maximum Allowable Concentrations (SMACs). A list of representative 7-day SMAC limits are listed in Table 2, along with a list of Threshold Limit Values (TLVs) which are the recommended maximum concentrations for workplace environments. SMAC and TLV guidelines can provide a standard for indoor air quality, assist in material selection and off gassing standards, and also drive the design of air quality control systems and building designs.

Builders and engineers concerned with air quality control for commercial and residential buildings do not focus on materials selection nearly as much as spacecraft designers. Some states have legislation limiting the amount of Urea Foam Formaldehyde Insulation (UFFI) used in mobile homes. Some Wisconsin homes with excessively high levels of formaldehyde had pressed-wood and UFFI removed after the buildings were found to have unsafe levels of formaldehyde. This source removal proved to be an effective (if expensive) solution to the indoor air problem (Dally, 1981).

Careful selection of building materials, especially insulations, adhesives, caulks, and particle boards could improve indoor air quality by limiting much of the contaminant source. Building designers should remember the increased ventilation needs, energy cost, and indoor air quality problems associated with cigarette smoking when establishing smoking areas in buildings.

MITIGATION TECHNIQUES: PHOTOCATALYTIC OXIDATION

Advanced Trace Contaminant Control Systems are needed to support missions of longer durations. VOC removal systems based on non-regenerable "scrubbers" such as activated charcoal or LiOH become excessively large as mission length increases. Advanced TCCS concepts must operate at ambient pressure and temperature, treat a wide range of organic contaminants found at low concentrations, use no expendables, and have low energy requirements. An advanced system that could capture organic contaminants and convert them to useful product gasses would reduce the need for make-up gasses. Two concepts; photocatalytic oxidation and uptake by higher plants, appear to have many of the attributes needed for an advanced TCCS. They are presently being studied for future use in spacecraft TCCS and will be described in the next two sections.

Photocatalytic oxidation is an ambient temperature process in which the surface of an illuminated semiconductor (often TiO_2) acts as a reaction catalyst by using bandgap light as a source of solid excitation. The source of light can be UV lamps or solar light. When illuminated by photons with sufficient energy, the valence band electrons in the semiconductor are photo-excited into the conduction band, creating highly reactive electron-hole pairs. If the electron-hole pair encounters a water molecule, a highly reactive OH radical is formed. If the electron-hole pair encounters an O_2 molecule, O_2^- is often formed. If volatile organics are introduced into a photocatalytic reactor in the presence of oxygen or water, they will eventually be converted to CO_2 , simple acids, and water (Peral, 1992). The rates of photocatalytic reactions, effect of contaminant concentrations, effect of humidity, and photocatalytic reactor design are the subject of ongoing research.

Many researchers have reported using photocatalysis to successfully purify contaminated water (Ahmed, 1984) and the treatment of trichloroethylene and perchloroethylene in water has been the first commercially successful photocatalytic process. Solar energy has been used as a light source to keep energy costs down (Nimlos, 1992). Studies involving gas phase heterogeneous photocatalysis are far fewer, but the modest existing literature has demonstrated that near-UV illumination in concert with a TiO_2 photocatalyst and molecular oxygen can carry out the complete oxidation of methane, benzene, ethane, toluene, trichloroethylene, acetaldehyde, isobutyric acid, isoprene, ammonia, methyl mercaptan, hydrogen sulfide, formaldehyde, and carbon monoxide (Peral, 1992 Raupp, 1992 Suzuki, 1993 and Nimlos 1992).

Raupp has studied the reaction kinetics of a range of halogenated and aromatic organics. He has found that the reaction kinetics are sufficiently fast so that complete hydrocarbon oxidation can be achieved with no formation of partial oxidation products. Raupp and Peral have reported reaction rate dependencies on O_2 , H_2O , and contaminant concentration. Organic contaminant and O_2 exhibit Langmuir type rate dependencies, the effect of water vapor is more complex. With no water, rapid oxidation rates cannot be sustained and the catalyst eventually becomes deactivated, at high water concentrations the reaction rate decreases, and at low water concentrations reaction rates are the most favorable. Nimlos has demonstrated photocatalysis of organics in an airstream with a solar trough reactor.

Photocatalytic oxidation is being investigated as a way to treat the air in passenger areas of automobiles (Suzuki, 93). Contaminants in the air of automobile cabins come from the off-gassing of interior materials and adhesives, and from cigarette smoke, pet odors and passenger metabolic products. Acetaldehyde, toluene, isobutyric

acid, isoprene, ammonia, methyl mercaptan, and hydrogen sulfide were all tested in a stirred box reactor using a TiO_2 coated honeycomb support. The rate constant of photocatalytic reaction of these contaminants was found to be pseudo first order (see figure 1). Suzuki's study is well suited for considering spacecraft trace contaminant control and indoor air quality. Contaminant concentrations used in this study are realistically low, and the oxygen concentration and humidity is nominal for indoor air. Three aspects of this study make photocatalysis an appealing technique for treating airborne trace contaminants; (1) destruction is pseudo 1st order, and contaminants found in low concentrations can be removed, (2) degraded catalysts could be refreshed by exposing the bed to UV light and clean air, (3) acetaldehyde was found to be completely oxidized to CO_2 with no intermediate reaction products. Complete oxidation is especially important to spacecraft contaminant control. Air purification using O_3 can lead to partially oxidized substances that remain as noxious contaminants.

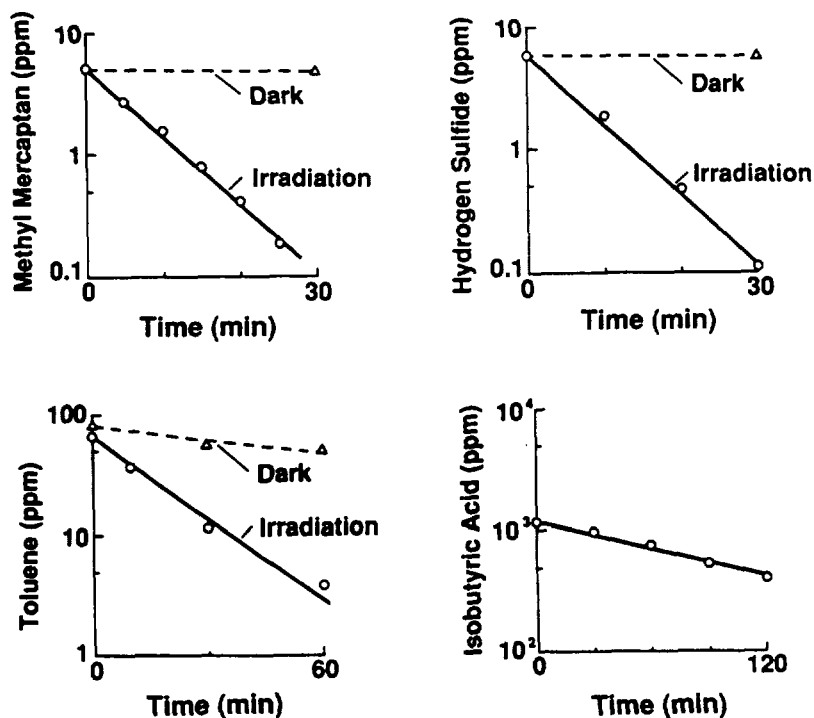


Figure 1: Reactions of contaminants in air at room temperature in the presence of TiO_2 photocatalyst. The reactor uses a 500 watt UV lamp, a 20 L reaction chamber, a photocatalyst 30mm in diameter and 50 mm in length, and a 5L/min recirculating pump (from Suzuki, 1993).

Taken all together, the findings of Suzuki, Peral and Ollis, Raupp, and Nimlos indicate a favorable technical potential for photocatalyzed treatment of air in order to degrade and remove all major classes of oxidizable contaminants. The catalyst sometimes degrades and deactivates, but can be refreshed by exposing to the catalyst to light and fresh air. A wide variety of organics can be treated at low concentrations, contaminants can be completely oxidized, and the operating costs of treating large amounts of air can be greatly reduced if solar energy is used. A solar trough reactor may have great potential for commercial and residential applications.

MITIGATION TECHNIQUES: UPTAKE BY HIGHER PLANTS

Chamber studies have demonstrated that when plants were exposed to contaminant gasses (ozone by Rich 1970, sulfur dioxide by Spedding 1969), the contaminants were taken up by the plants, rapidly when the lights were on and slowly when the lights were off. Further studies have shown that the uptake of ozone and sulfur dioxide are controlled by the same resistors as the loss of water, so the cleansing of air can be realistically simulated. One simulation involving representative greenhouse conditions and 140 ppb ozone concentrations calculated that if scrubbing goes on for one hour, foliage will remove about an eighth of the ozone in the air mass above it (Waggoner 1971). Another chamber study has demonstrated that higher plants biologically uptake a wide range of organics including; ethyl alcohol, acetone, methyl alcohol, ammonia, formaldehyde, and xylene (Wolverton, 1992).

Plants remove VOCs from the surrounding air by two mechanisms; diffusion based mass transfer through the leaves, and degradation by microorganisms associated with the roots. The mechanisms of VOC removal have been confirmed with chamber studies which compared the removal rates of plants with exposed soil, plants with soil covered with a sterilized material, exposed soil with no plant, and soil covered with a sterilized material (Wolverton, 1993). The uptake by leaves is a function of the concentration of the pollutant (greater concentration drives faster uptake) and the properties of the plant. Rate of pollutant uptake is influenced by the effective plant surface area and the density of its active sites, by total diffusion resistance, and by metabolic activities (Rogers, 1977). The rate of degradation by microorganisms associated with the roots is often limited by mass transfer of VOCs into the soil.

Plants remove a wide range of VOCs from the surrounding air, but they also emit organics into the air. Plants emit a wide range of species, but isoprene and methane are the compounds most frequently reported (Sharkey, 1991). The effects of trace gas emissions by plants into indoor air must be more thoroughly understood before plants can be used in a closed spacecraft atmosphere. In a partially vented residential setting, low level emissions of trace gases from plants may be less critical.

The challenge of using plants to remove VOCs from indoor air is to make a few plants treat a large amount of air. Rogers reports that in a well mixed, well lit chamber with initial NO₂ concentrations of .5ppm, six soybean plants removed 459 µg NO₂/hr. Wolverton reports that two Boston ferns would be capable of removing formaldehyde from a 9.3 m² office area with a 2.4 m ceiling height. Wolverton's projection may prove to be overly optimistic, because it is based on chamber studies where the initial formaldehyde concentration is more than 10 times the TLV. In an office area where formaldehyde concentrations are lower and gas mixing less vigorous, formaldehyde uptake will likely be less efficient than chamber studies.

Common interior house plants that thrive in low-light conditions (including Boston fern, dieffenbachia, ficus, chrysanthemum and Janet Craigs) have demonstrated the ability to remove significant quantities of VOCs from sealed chambers. Some plants are more effective in removing organic chemicals than others. Studies to identify especially effective plants, along with studies to understand the removal efficiencies of VOCs in low concentrations for long durations are the subject of active research. Interior house plants such as ferns and mums may be a cost effective way of improving the indoor air quality in "tight" buildings. The only limit to the number of house plants used relates to indoor humidity. House plants transpire water, and too many plants make indoor air excessively humid.

There is another biological method for removing VOCs from air. Although Biological Air Filters (BAFs) may not be especially well suited to indoor air systems that recirculate air, they have a great potential for many industrial and environmental applications and should be briefly mentioned. Biological air filters have been used to treat VOC and air toxics emitted from industrial facilities such as foundries and print shops (Leson, 1991). Biological air filters are especially well suited to off-gas streams that contain low concentrations of volatile organics. Product gasses are vented through a biologically active solid material (often moist composted soil) and the organics are aerobically digested in the filter. These systems have low energy requirements and reduce contaminants completely to CO₂, water, and microbial biomass. More than 500 BAFs have been built in the last decade in Germany and the Netherlands, many in response to strict environmental legislation. It has been proposed to use Biological Air Filters for Air Quality Control on spacecraft (Binot, 1989). Presently the fundamental technical issue of BAFs for spacecraft and indoor air is humidity. Air coming into a biological air filter must be saturated with water or the filter will dry out and the microbes in the filter will die. Air exiting a BAF is too moist to be recirculated directly into a building or spacecraft. Until a "dry" biological air filter is demonstrated, the use of BAFs will be restricted to industrial applications where moist product gas can be vented directly.

CONCLUSIONS

There are many similarities between the indoor air quality requirements for spacecraft and "tight" commercial and residential buildings. Both indoor air quality control systems must operate at ambient pressure and temperature, treat a wide range of organic contaminants found at low concentrations, produce no toxic by-products, use no expendables, and have low energy requirements. NASA is presently using two technologies; rigorous material selection for source control, and ambient temperature catalytic oxidation, that may have application in commercial and residential buildings. NASA is also studying two advanced technologies; photocatalytic oxidation and uptake by higher plants, that may prove to be useful methods of indoor air quality control. Building designers and environmental engineers should learn more about these four systems, and consider applying them to commercial systems where they are most appropriate.

REFERENCES

- ACGIH 1993-1994 Threshold Limit Values and Biological Exposure Indices. ACGIH, Cincinnati OH. 1993.
- Ahmed, S. Ollis, D.F. Solar-Driven Photocatalyzed Decomposition of Trichloromethane in Water. *Solar Energy*. Vol 32, pp 1-8. 1984
- Baechler, M.C. Hadley, D.L. Marseille, T.J. and Stenner, R.D. et. al. *Sick Building Syndrome: Sources, Health Effects, Mitigation*. Noyes Data Corporation, Park Ridge NJ. 1991.
- Binot, R.A. and Paul, P.G. BAF - an Advanced Ecological Concept for Air Quality Control. SAE technical paper #891535. SAE international, Warrendale PA. 1989.
- Brooks, B.O. and Davis, W.F. *Understanding Indoor Air Quality*. CRC Press, Boca Raton. 1992.
- Coleman, M.E. James, J.T. *Spacecraft Maximum Allowable Concentrations for Airborne Contaminants*. NASA-JSC Document #20584. 1990.
- DHEW *Involuntary Smoking, in Smoking and Health: A Report of the Surgeon General*. DHEW Publication No. PHS79-50066. 1979.
- Dally, K.A. Eckman, A.D. Hanrahan, L.P. *A Followup Study of Indoor Air Quality in Wisconsin Homes*. International Symposium on Indoor Air Pollution, Health and Energy Conservation. Amherst MA. 1981.
- Freeman, H.M. *Standard Handbook of Hazardous Waste Treatment and Disposal*. McGraw Hill Book Company, New York NY. 1989.
- Godish, T. *Air Quality*. Lewis Publishers, Chelsea MI. 1985.
- Kreiss, K. *The Sick Building Syndrome in Office Buildings - a Breath of Fresh Air*. *The New England Journal of Medicine*. Vol 328, pp 877-878, March 25, 1993.
- Leson, G. and Winer, A.M. *Biofiltration: An Innovative Air Pollution Control Technology for VOC Emissions*. *Journal of Air & Waste Management Association*, vol 41, no 8. pp 1045-1054. August, 1991.
- Limero, T.F. Taylor, R.D. Pierson, D.L. and James, J.T. *Space Station Freedom Viewed as a "Tight Building"* SAE technical paper #901382. SAE international, Warrendale PA. 1990.
- Litton, C.E. Crump, W.J. *Basic Issues in the Closure of Space Life Support Systems: Lessons Learned from the Sick Building Syndrome Phenomenon*. SAE Technical Paper #932287. SAE Warrendale, PA. 1993.
- Martin, G. *Venting of Payload Waste Gases*. Space Station Internal Document CRN BB003421. August 18, 1992.
- Menzies, R. Tamblin, R. Farant, J. Hanley, J. Nunes, F. Tamblin, R. *The Effect of Varying Levels of Outdoor-Air Supply of the Symptoms of Sick Building Syndrome*. *The New England Journal of Medicine*. Vol 328. pp 821-827. March 25, 1993.
- Nimlos, M.R. Jacoby, W.A. Blake, D.M. Bohn, M.S. Noble, R.M. Milne, T.A. *Laboratory and Outdoor Testing of Photocatalytic Destruction of Organics in Air Streams*. *The First International Conference on TiO₂ Photocatalytic Purification and Treatment of Water and Air*. London, Ontario. 1992.
- Peral, J. and Ollis, D.F. *Heterogeneous Photocatalytic Oxidation of Gas-Phase Organics for Air Purification: Acetone, 1-Butanol, Buraldehyde, Formaldehyde, and m-Xylene Oxidation*. *Journal of Catalysis*, Vol 136, pp 554-563. 1992.
- Raloff, J. *Bake-offs May Not Cure "Sick Buildings"*. *Science News*, pp 206-207. September 1993.

- Raupp, G.P. Photocatalytic Oxidation of Dilute Organics in Air Streams over UV-Excited Titania. Proceedings of the First International Conference on Photocatalytic Purification of Water and Air. London, Ontario, Canada. NSERC of Canada. November 8-13, 1992.
- Rich, S. Waggoner, P.E. Tomlinson, H. Ozone Uptake by Leaves. *Science*. Vol 169, pp 79-80. 1970.
- Rogers, H.H. Jeffries, H.E. Stahel, E.P. Heck, W.W. Ripperton, L.A. and Witherspoon, A.M. Measuring Air Pollutant Uptake by Plants: A Direct Kinetic Technique. *Journal of the Air Pollution Control Association*. Vol 27 no 12. pp 1192-1196. 1977.
- Sharkey, T.D. Holland, E.A. Mooney, H.A. Trace Gas Emissions by Plants. Academic Press, Inc. 1991.
- Sjostrom, J. Becker R. Courthouse is Given a Clean Bill of Health. *The Chicago Tribune*. Sec 2D, p 1. April 1, 1993.
- Spedding, D.J. Uptake of Sulphur Dioxide by Barley Leaves at Low Sulphur Dioxide Concentrations. *Nature*. Vol 224, pp 1229-1321. 1969.
- Sterling, E. Sterling T. The Impact of Different Ventilation and Lighting Levels of Building Illness. International Symposium of Indoor Air Pollution, Health, and Energy Conservation. Amherst Mass. 1981.
- Suzuki, K. Photocatalytic Air Purification on TiO₂ Coated Honeycomb Support. Photocatalytic Purification and Treatment of Water and Air. pp 421-434. Elsevier Science Publishers, 1993.
- Turiel, I Rudy, J.V. Occupant Generated CO₂ as an Indicator of Ventilation Rate. *ASHRAE Transactions* 88 (1) Number 2674. 1982.
- Waggoner, P.E. Plants and Polluted Air. *Bioscience*. Vol 21, pp 455-459. 1971.
- Walsh, P.J. Dudney, C.S. Copenhaver, E.D. Indoor Air Quality. CRC Press, Boca Raton FL. 1984.
- Wolverton, B.C. and Wolverton J.D. Bioregenerative Life Support Systems for Energy Efficient Buildings. Proceedings of the International Conference on Life Support and Biospherics. Huntsville AL. 1992.
- Wolverton, B.C. and Wolverton, J.D. Plants and Soil Microorganisms: Removal of Formaldehyde, Xylene, and Ammonia from the Indoor Environment. *Journal of the Mississippi Academy of Sciences*. Vol 38, no 2. pp 11-15. 1993.

A NEW MATERIAL FOR REMOVING HEAVY METALS FROM WATER

Warren H. Philipp, Jr.
National Aeronautics and Space Administration
Lewis Research Center
Cleveland, OH 44135

Kenneth W. Street, Jr.
National Aeronautics and Space Administration
Lewis Research Center
Cleveland, OH 44135

ABSTRACT

The NASA Lewis Research Center developed and is patenting a new high capacity ion exchange material (IEM) that removes toxic metals from contaminated water in laboratory tests. The IEM can be made into many forms, such as thin films, coatings, pellets, and fibers. As a result, it can be adapted to many applications to purify contaminated water wherever it is found, be it in waste water treatment systems, lakes, ponds, industrial plants, or in homes. Laboratory tests have been conducted on aqueous solutions containing only one of the following metal cations: lead, copper, mercury, cadmium, silver, chromium (III), nickel, zinc, and yttrium. Tests were also conducted with: (1) calcium present to determine its effects on the uptake of cadmium and copper, and (2) uranium and lanthanides which are stand-ins for other radioactive elements, (3) drinking water for the removal of copper and lead, and (3) others compositions. The Results revealed that the IEM removes all these cations, even in the presence of the calcium. Of particular interest are the results of the tests with the drinking water: the lead concentration was reduced from 142 ppb down to 2.8 ppb (well below the accepted EPA standard).

BACKGROUND

Many industries, such as the electroplating and mining companies, produce large amounts of waste water that contains hazardous amounts of mercury, lead, cadmium, silver, copper, and zinc ions. They are required by law to reduce the concentrations of these toxic metals in their waste water before it is discharged into sewers, lakes and streams. A number of companies we have contacted have told us that existing technology appears to be too expensive or inadequate for meeting the new lower limits. Also pressure is developing for eliminating the disposal of the wastes in land fills. For these reasons, industries and some government agencies are looking for new technology with which to clean the water.

The IEM is a spinoff from research done on space batteries. During the research, it was discovered, quite by accident, that it had an affinity for heavy metal ions, **even when calcium ions are present**. This is an important feature because many commercial ion exchange materials cannot remove heavy metals when the calcium is present. The calcium saturates the resins, thereby blocking the adsorption of heavy metal ions. This is not the case for this new IEM. Those commercially available ion exchange resins that do pick up the metal cations when calcium is present are very expensive. As a result, it was realized that this new IEM may have direct application to cost effective purification of contaminated water.

Once this potential became apparent, the NASA Lewis Research Center started a program in fall of 1991 to determine if the IEM was indeed an advance over existing technologies and if the IEM could be spun off as a new commercially viable product. The Cleveland Area Manufacturing Program (CAMP) helped by pointing out that the local electroplating industry was seeking new technology with which to remove heavy metal cations from their waste rinse water. The Northeastern Ohio Regional Sewer District also helped by explaining the nature and magnitude of the heavy metal disposal and cleanup problems facing the electroplaters and other

industries. Opinions were sought from waste water treatment experts, in particular an expert at the Cleveland State University. He called the IEM "an exciting new material". With this information, it was decided to proceed with a modest program to first characterize the key heavy metal adsorption rates, quantity adsorbed per unit weight, and other important physical properties such as the mechanical strength, tear resistance, resistance to degradation by chemical attack from a variety of aqueous solutions, etc. Simultaneously, the Lewis Technology Transfer Office began to search for the potential applications for the IEM and to determine the status of the existing technology being used to remove the heavy metals from waste and potable water.

THE ION EXCHANGE MATERIAL - IEM FILM PREPARATION

The IEM is composed of a crosslinked copolymer of polyvinyl alcohol and polyacrylic acid (Patent Pending). The IEM is made, in sheet form, by casting an aqueous solution of the two polymers on a flat surface to the desired thickness and allowing the water to evaporate. The water soluble sheet is crosslinked at elevated temperature in an aqueous solution containing a salting-out agent, the crosslinking agent and an acid catalyst. The resulting water insoluble film, in the acid form, is then converted to the desired salt form which is usually the calcium form.

LABORATORY TESTS AND EXPERIMENTS

The following adsorption characterization tests have been completed on:

- (1) Single ion aqueous solutions contaminated with one of the following ions: lead, copper, mercury, cadmium, silver, chromium(III), nickel, zinc, yttrium, and mercury.
- (2) Hard water solutions containing cadmium or copper to determine the effects of the hard water on the adsorption.
- (3) An electroplater's rinse water containing primarily zinc, some other heavy metal ions, and some unknown contaminants, e.g. brighteners and chelating agents.
- (4) Solutions of uranium and lanthanides, which are stand-ins for other radioactive elements.
- (5) Drinking water containing copper and lead at levels exceeding those recommended in the new drinking water standards. These tests were conducted in a flow system. The lead laden water was passed through an annulus whose inner surface was coated with the IEM. The calcium content of the water was approximately 40 ppm.
- (6) Copper and lanthanides to determine if superior spectroscopic chemical analysis methods could be developed.

TEST RESULTS

This report contains some of the significant results from the tests conducted to date. They are described below and supported by tabular and graphical illustrations. A study of those results show that the adsorption rates and the mass adsorbed per gram of the IEM vary with the pH of the solutions and on the initial concentrations. The most noteworthy findings are:

- (1) The adsorption of an ion is not affected by the presence of other ions (including calcium) in the mixture so long as there is sufficient ion exchange material in the solution to absorb all ions. For example, it is seen in Figure 1 that the rate and amount of copper adsorbed is the same whether it is in a mixture containing other ions (listed in Table 2) or it is the only ion in a solution.

- (2) The amount of an element adsorbed varies with the pH of the solution. This is shown in Figure 2 for cadmium, mercury, copper and zinc. For most metals the lower pH limit for effective uptake of metal is governed by the acid exchange constant for the film, and the upper pH limit is governed by the affinity of the particular metal to form insoluble or anionic hydroxy species. Using the zinc curve, for example, the lower limit is at approximately pH=5, and the upper limit is approximately pH=7.
- (3) Acid and base titrations of the IEM indicate the capacity for metal uptake to be in the range of 3.5 to 5.0 milliequivalents/gram, depending on the form of the IEM film. These uptakes are comparable to commercial high capacity ion exchangers. In Table 1 are the calculated maximum uptakes of various metals based on the titration capacity. For comparison, the experimentally determined IEM saturation for zinc occurred at 170 grams zinc per kilogram IEM in a system containing a limited amount of IEM and excessive amounts of zinc ions.
- (4) Table 2 gives the IEM recoveries from an actual electroplaters waste solution which contained all of the ions listed in the table plus others not measured.
- (5) The final concentration of most of the elements tested are below the EPA discharge limits for those ions.
- (6) Table 3 indicates the ability of the IEM to recover uranium and other elements used to model the behavior of various radioactive elements.
- (7) The results presented in Table 4 indicate that the IEM, when used in a flowing system, removes copper and lead in drinking water from an order of magnitude above the recommended concentration levels down to levels an order of magnitude below the recommended value.
- (8) A simple colorimetric test was developed for use in the field or in homes to determine the concentration of copper in water. This test is done by simple eye comparison similar to a color chart. More sophisticated methods of spectroscopic analysis have also been developed based on the superior optical properties of the IEM film.

Other tests have shown that the ion exchange polymer is:

- * Easy to use and inexpensive to make.
- * Strong, flexible, and cannot be easily torn.
- * Chemically stable in storage, in aqueous solutions, and in acidic or basic solution.
- * Although no toxicity tests have been performed, it is anticipated that this IEM is safe and non-toxic to handle.

DISPOSAL

Another important feature of the material is that the adsorbed metals can be easily reclaimed by either a destructive or a non-destructive process. With the destructive process, the spent IEM is burned, thereby producing carbon dioxide, water vapor, and oxides of the adsorbed metals which can be recycled. With the non-destructive process, the heavy metals are removed from the IEM and reclaimed by an acid stripping process. The IEM is then reusable and the metal concentrate can be recycled.

The acid stripping procedure uses nominal concentrations of simple mineral acids to strip the IEM of metals within 5 to 10 minutes. Tests with zinc and other heavy metals indicate that the recovery of metal is in the range of 95-100% (see footnote Table 3). The film is then reconverted to the appropriate salt form for reuse as discussed above in the Film Preparation discussion.

PROJECT STATUS

- (1) Some of the characterization tests, which were conducted on the thin film form of the IEM, are complete.
- (2) The patent covering this IEM has been filed.
- (3) A test has been started at a local electroplating firm to determine the effectiveness of the IEM in a zinc plating process. The test will determine how well the waste zinc ion is removed from the first wash bath which also contains brighteners, carriers, etc. associated with the plating process.
- (4) Work has started to develop the methods for making the IEM into fine pellets for use in packed columns and to measure their adsorption properties.

CONCLUDING REMARKS

It is the mission of the NASA Lewis Research Center's Technology Utilization Office (TUO) to spin-off technology developed inside NASA to U.S. industry. When a new NASA technology is developed, usually for an aerospace application, the TUO tries to determine where in the U.S. market the new technology might be used and whether there is a market potential for it. We learned through many contacts with industries and government agencies who are addressing the problems of heavy metal removal from waste water, that there is a need for new technology because the existing technology is either too expensive or not suitable. Based on the responses we received from these contacts, we concluded that the IEM appears to be a promising technology that could contribute to improving the environment. Our contacts told us that the IEM appears to have some unique characteristics that are not available in ion exchange resins on the market today and that it should be developed to the point where it can be made available commercially.

The IEM is still in the development stage. Much work remains to be done to fully characterize the adsorption characteristics of the film and pellet forms. At present, only the film form has been well characterized in the laboratory. Tests of the film in an industrial setting has started. A number of such tests are planned in selected applications. The method for making pellets is under development. Once pellets are available laboratory characterization tests and industrial tests will also be performed. However, if any companies are interested in licensing the IEM technology at this stage, they are invited to do so.

Table 1 - CALCULATED ION EXCHANGE UPTAKE OF INDIVIDUAL METALS.

METAL ION	gms metal/kg IEM
Zinc	168
Cadmium	289
Lead	533
Chromium(III)	89
Copper	163
Mercury	516
Nickel	151

Table 2 - ADSORPTION PROPERTIES OF THE IEM IN AN ELECTROPLATERS WASTE MIXTURE¹

METAL	pH = 5		pH = 7	
	INITIAL CONCENTRATION (ppm)	PERCENT RECOVERY	INITIAL CONCENTRATION (ppm)	PERCENT RECOVERY
Zinc	8.38	97.6	8.38	96.4
Cadmium	0.88	> 97.7 ²	0.88	> 97.7 ²
Nickel	1.11	82.0	1.11	82.0
Copper ³	0.11	> 90.9 ²	0.07	85.7
Manganese	0.22	95.4	0.22	> 99.6 ²

¹ The mixture contained ions of all of the metals listed in this table. The following elements are initial concentrations measured at pH 7 which were not followed during the course of this experiment: Silver, 0.01 ppm; Sodium, 1415 ppm; Cobalt, 0.01 ppm; Magnesium, 0.9 ppm; Lead, <0.03 ppm; Chromium (III), 0.03 ppm, Iron, 0.02 ppm.

² Final concentration at or below limit of instrument detection.

³ Northeast Ohio Regional Sewer District determination.

Table 3. Uranyl and lanthanide ion uptake by the IEM from water.

METAL	INITIAL CONCENTRATION (ppm)	PERCENT REMOVED	pH
U (VI)*	15.2	68	6.3
	15.2	78	6.6
	1.0**	80	6.6
Ce (III)	14.2	99.6	7.0
Eu (III)	15.6	96.4	6.9
Gd (III)	13.4	99.9	7.0
Tb (III)	16.6	86.7	7.0

* UO_2^{2+} + dimers, etc.

** 96% U(VI) recovered by acid stripping of film.

Table 4. Removal of lead and copper from spiked tap water.

<p>Batch Testing Technique for Lead</p> <p>Test Conditions: Sample Size: 1 liter with 0.4 grams of IEM film Sample continuously stirred Initial Lead Concentration: 56 ppb Equilibration time: 2.5 hrs.</p> <p>Results: Final lead concentration: 1.5 ppb</p>
<p>Dynamic Testing Process for Lead and Copper</p> <p>Test Conditions: Flow inside an annulus (length 3 ft.) IEM film wrapped around inner surface of annulus Residence time: 3 hrs.</p> <p>a) Lead tests Initial Lead Concentration: 142 ppb</p> <p>Results: Final lead concentration: 2.8 ppb</p> <p>b) Copper tests Initial copper concentration: 15 ppm</p> <p>Results: Final copper concentration: 0.004 ppm</p>

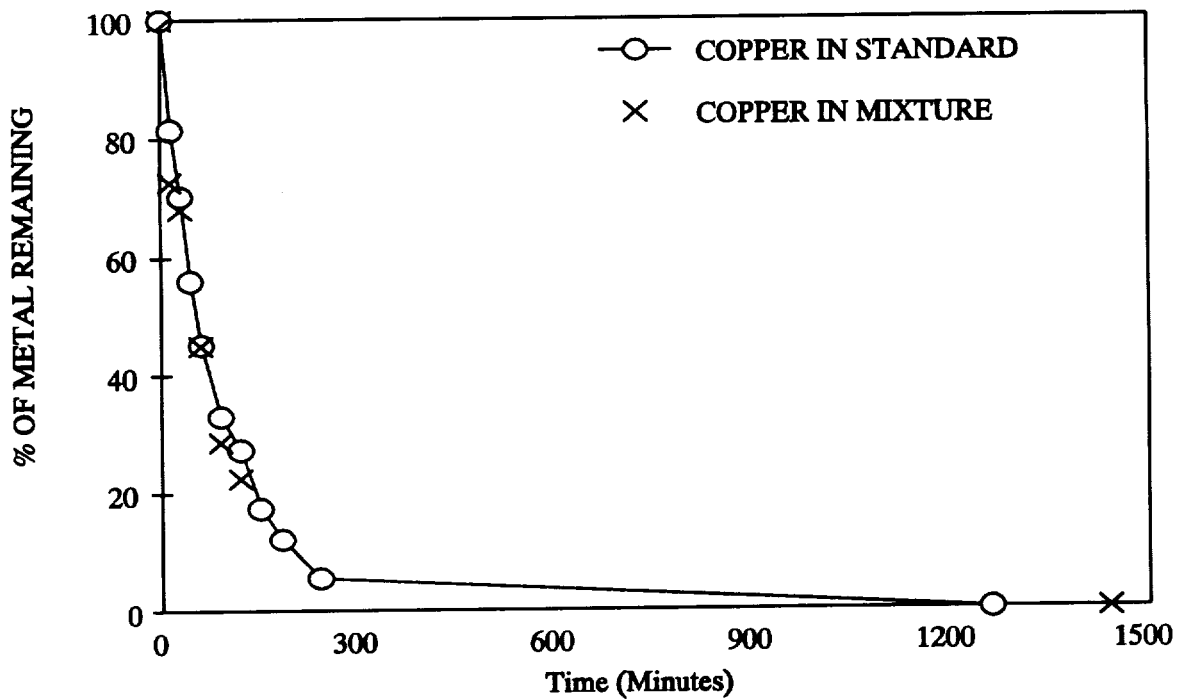


Figure 1. The adsorption rate characteristics of the New Ion Exchange Material for copper alone in a standard solution and in a solution of the rinse water from a copper electroplating process.

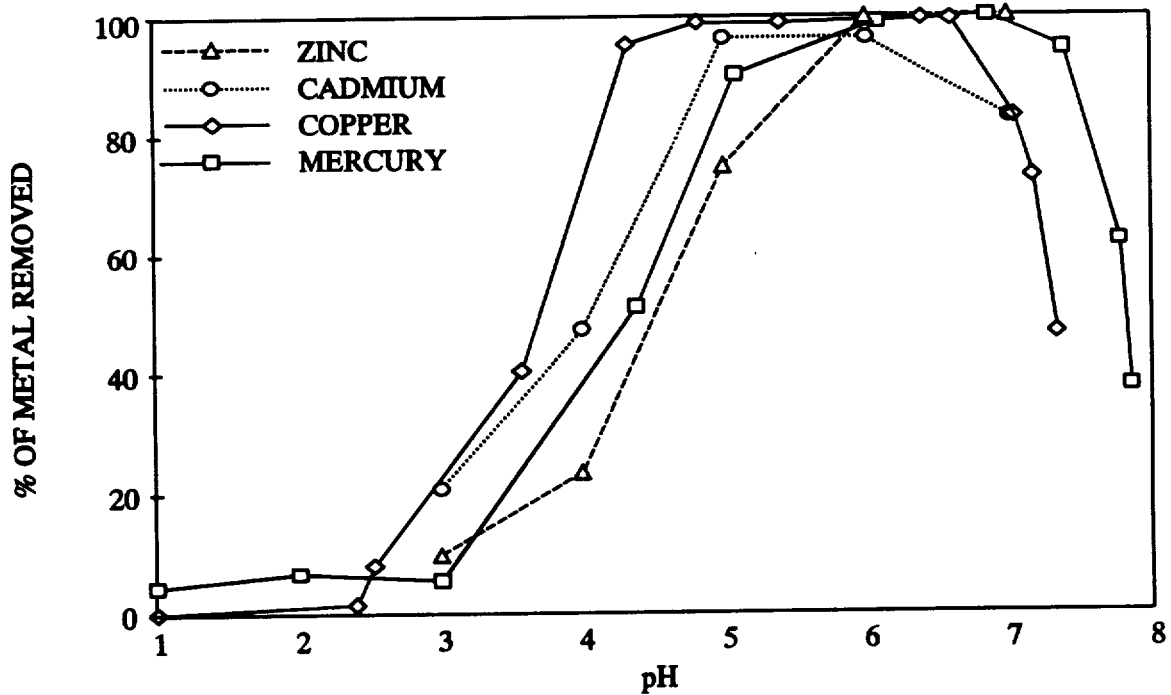


Figure 2. Metal Adsorption by the New Ion Exchange Material as a function of the solution pH.

DEWATERING OF CONTAMINATED RIVER SEDIMENTS

Ronald H. Church
U.S. Bureau of Mines
Tuscaloosa Research Center
P.O. Box L, Univ. of Alabama Campus
Tuscaloosa, AL 35486-9777

Carl W. Smith
U.S. Bureau of Mines
Tuscaloosa Research Center
P.O. Box L, Univ. of Alabama Campus
Tuscaloosa, AL 35486-9777

Bernard J. Scheiner
U.S. Bureau of Mines
Tuscaloosa Research Center
P.O. Box L, Univ. of Alabama Campus
Tuscaloosa, AL 35486-9777

ABSTRACT

Dewatering of slurries has been successfully accomplished by the proper use of polymers in flocculating the fine particulate matter suspended in mineral processing streams. The U.S. Bureau of Mines (USBM) entered into a cooperative research effort with the U.S. Army Corps of Engineers (Corps) for the purpose of testing and demonstrating the applicability of mining flocculation technology to dredging activities associated with the removal of sediments from navigable waterways. The Corps has the responsibility for maintaining the navigable waterways in the United States. Current technology relies primarily on dredging operations which excavate the material from the bottom of waterways. The Corps is testing new dredging technology which may reduce resuspension of sediments by the dredging operation. Pilot plant dredging equipment was tested by the Corps which generated larger quantities of water when compared to conventional equipment, such as the clam shell. The transportation of this "excess" water adds to the cost of sediment removal.

The process developed by the USBM consists of feed material from the barge being pumped through a 4-in line by a centrifugal pump and exiting through a 4-in PVC delivery system. A 1,000-gal fiberglass tank was used to mix the polymer concentrate. The polymer was pumped through a 1-in line using a variable speed progressive cavity pump and introduced to the 4-in feed line prior to passing through a 6-in by 2-ft static mixer. The polymer/feed slurry travels to the clarifying tank where the flocculated material settled to the bottom and allowed "clean" water to exit the overflow.

A pilot scale flocculation unit was operated on-site at the Corps' "Confined Disposal Facility" in Buffalo, NY. A loaded barge containing sediments dredged from the Buffalo River was delivered to the disposal facility for the flocculation studies. Contaminated sediments were pumped from the barge to the flocculation unit. Tests were conducted using polymer concentrations of 0.01, 0.02, 0.03 pct, pumped at variable flow rates. Feed slurry from the barge consisting of approximately 1.5 pct solids was pumped through the unit at approximately 230 gal/min. The Nephelometric Turbidity Units (NTU) values (which measures the turbidity of the water by measuring the light scattered at 90° or 270° through the incident beam) of the discharge water ranged from 12 to 17 with the underflow discharge containing approximately 31 pct solids. This would require only one barge (at 31 pct solids) instead of 20 (at 1.5 pct solids) to deliver the same quantity of contaminated river sediments.

Costs associated with the polymer requirements were calculated from the original costs of the polymer when purchased in bulk (\$0.50 per lb). Treatment of 1,000 gal of 1.5 pct contaminated river sediments requires less than \$0.01 of polymer (less than \$10.00 per 5,000 cubic yard barge).

BACKGROUND

The 1987 amendments to the Clean Water Act authorized U.S. Environmental Protection Agency's (EPA) Great Lakes National Program Office (GLNPO) to coordinate and conduct a 5-year study and demonstration project on the treatment of toxic pollutants in bottom sediments. Five priority areas were selected for demonstration projects: Saginaw Bay, MI; Sheboygan Harbor, WI; Grand Calumet River, IN; Ashtabula River, OH; and Buffalo River, NY.

In response, GLNPO launched the Assessment and Remediation of Contaminated Sediments (ARCS) program. (In November 1990, the Great Lakes Critical Programs Act was passed, extending ARCS by one year, until December 1993.) ARCS is an integrated program for developing and testing assessment and cleanup alternatives for contaminated sediments. Information from the ARCS program will be used to guide the development of Lakewide Management Plans and remedial action (cleanup) plans for the 43 Great Lakes "Areas of Concern" identified by the U.S. and Canadian governments.

GLNPO is responsible for administering the ARCS program, but it is a joint effort. Other participants in ARCS are EPA headquarters and EPA Regions 2, 3, and 5; U.S. Fish and Wildlife Service; National Oceanic and Atmospheric Administration; Bureau of Mines; Great Lakes State agencies; and many universities and public-interest groups (1).

As part of this program, the Bureau of Mines entered into a cooperative research effort with the U.S. Army Corps of Engineers for the purpose of testing the applicability of mining technology in clean-up activities associated with contaminated river sediments. Over many years, pollution of the rivers has resulted in concentrated toxins being deposited in the river bottom sediments. Current technology relies primarily on dredging operations which "digs" the material from the bottom; which in turn, can reintroduce the toxins into the waterways.

As part of the ARCS program, the Corps of Engineers is testing new technology which may help eliminate the reintroduction of toxins. Pilot plant dredging equipment was tested which generated larger quantities of water than the current technology employed. The transportation of this "excess" water adds to the cost of sediment removal.

The USBM's contribution in this effort has been the development of low cost methods to flocculate the particulates which would allow the "clean" water to be directly returned to its source, i.e., the river, reducing costs by eliminating the transportation, handling, and disposal of excess water in the CDF (confined disposal facility). Also, techniques such as flocculation result in higher percent solids of dredged material in the CDF and could therefore increase the capacity of the CDF. The technology tested was pioneered by USBM in the dewatering research activities associated with mineral recovery, waste minimization, and waste utilization at mining operations (2).

TECHNOLOGY EMPLOYED

Dewatering of slurries has been successfully accomplished by the proper use of polymers in flocculating the fine particulate matter suspended in mineral processing streams. The adsorption of polymers on particulates is dependent upon the type, molecular weight, and concentration of functional groups associated with the polymer, as well as the surface charge, porosity, purity, and solution properties associated with the suspended particulates.

Three series of polymers (anionic, zero charge, and cationic) were lab tested on a sample of Buffalo River sediment obtained from the Corps. From these studies, a slightly anionic polymer (Photafloc 1110¹ manufactured by Neutron Products, Inc.) was selected for the field demonstration. This polymer sells for \$0.50 to \$0.75/lb depending upon the volume purchased. A 3.2-pct solution of this polymer was obtained from the manufacturer for the testing program described in this report.

POLYMER CHARACTERISTICS

Photafloc 1110 is an anionic copolymer of acrylamide and sodium acrylate with a molecular weight in excess of 10 million. It is a slightly basic, nonhazardous aqueous solution. The polymer solution contains a small amount (less than 0.02 pct) of unreacted acrylamide monomer, CAS 79-06-1, which has an OSHA-PEL (permissible exposure limit) of 0.03 mg/m³.

The American Council of Governmental Hygienists recommends a TLV-TWA (threshold value limit; 8 hour time weighted average) of 0.03 mg/m³ for skin exposure. This acrylamide monomer level will not normally be reached when handling the solution. Also present is a small amount of sodium acrylate. The polymer is not listed as a carcinogen by the NTP, nor is it regulated by OSHA. Also, it is not listed in Federal hazardous waste regulations (40 CFR 261.33, Paragraphs (e) and (f)), and does not exhibit any of the hazardous characteristics listed in 40 CFR 261, Subpart C.

SYSTEM DESIGN

Figure 1 is a drawing of the field test flow sheet used for the Buffalo River demonstration project. For this test, the feed material from the barge was pumped through approximately 200 ft of 4-in line to a 6-in diesel centrifugal pump necked down to a 4-in PVC delivery system. A 1,000-gal fiberglass tank was used to mix the polymer concentrate.

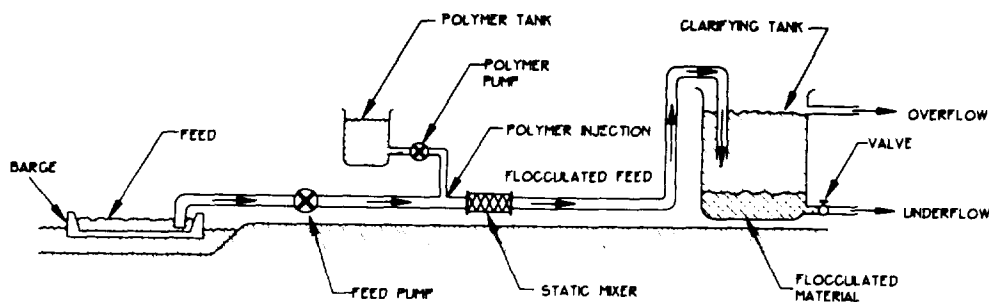


Figure 1. Flowsheet for the flocculation tests conducted at the Buffalo River.

The polymer was pumped through a 1-in line using a variable speed moyno type pump and introduced to the 4-in feed line prior to passing through a 6-in by 2-ft static mixer. The polymer/feed slurry traveled approximately 270 ft to the clarifying tank (approximately 1,700 gal at the overflow) where the flocculated material settled to the bottom, and allowed "clean" water to exit the overflow.

¹Reference to specific products does not imply endorsement by the U.S. Bureau of Mines.

RESULTS OF TESTING PROGRAM

A loaded barge from the hydraulic dredge demonstration site on the Buffalo River was delivered to the disposal site on August 6, 1992, with the flocculation studies beginning the following morning (Figure 2). In order to simulate an "on barge" system of treatment, the suction pump head at the unloading dock was lowered into the barge to "sweep" the settled sediments from the barge bottom. This was done to resuspend the settled material to represent the percent solids normally associated with the water in the barge during loading.

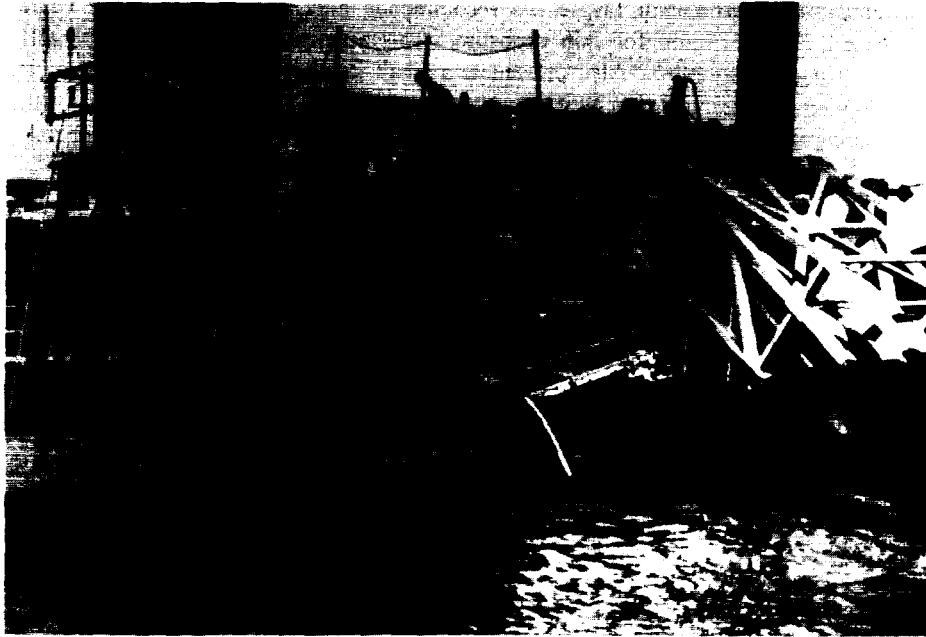


Figure 2. Suction feed line (4-in flexible) adjacent to the suction pump head of the loaded barge.

A series of three polymer concentrations was prepared during the study (0.02 pct, 0.03 pct, and 0.01 pct). This was accomplished by the addition of 5.04, 7.56, and 2.52 gal of 3.2 pct polymer to the polymer concentration tank. The tank was then filled to the 807-gal level with lake water to yield the desired polymer concentrations. The flow rates of the feed material from the barge and the flow rates of the discharge from the polymer concentration tank were determined by timing the movement of the fluids in the tanks and calculating the volume used. Figure 3 shows the polymer concentrate tank and pump.

Tables 1 through 3 indicate the polymer flow rate, feed rate, and percent solids of the feed for each series of tests. Cost of treating 1,000 gal of feed is based upon a polymer cost of \$0.50/lb. For each series, the polymer concentration was held constant and the dosage was changed at 10 min intervals by varying the flow rate of the polymer. Samples of the overflow were also collected for determination of the NTU values. Over 200 gpm of feed being pumped into the clarifying tank created turbulent conditions which allowed some of the flocculated material to overflow with the clean water (Figure 4). For this reason, the overflow samples were allowed to settle for 8 min prior to making the NTU measurements.



Figure 3. Small polymer pump on right beside concentrate tank, large diesel powered pump on left, and 2,000 gal clarifying tank in foreground with CDF beyond.

Table 1.--Test results for series 1 using the following conditions:
polymer concentration of 0.02 pct, feed rate of 241 gpm at 1.6 pct solids

Test number	Polymer dosage, gpm	Overflow, NTU	Cents per 1,000 gal of feed
1	19.87	17	8.23
2	16.90	15	7.01
3	11.51	13	4.78
4	7.06	17	2.93
5	3.96	13	1.64

Table 2.--Test results for series 2 using the following conditions:
polymer concentration of 0.03 pct, feed rate of 228 gpm at 1.5 pct solids

Test number	Polymer dosage, gpm	Overflow, NTU	Cents per 1,000 gal of feed
1	20.15	14	13.24
2	17.38	14	11.42
3	12.22	12	8.03
4	4.16	13	2.73
5	2.37	16	1.56

Table 3.--Test results for series 3 using the following conditions:
 polymer concentration of 0.01 pct, feed rate of 219 gpm at 1.3 pct solids

Test number	Polymer dosage, gpm	Overflow, NTU	Cents per 1,000 gal of feed
1	20.43	12	4.66
2	17.91	12	4.08
3	12.11	13	2.76
4	6.96	15	1.59
5	2.27	27	0.52



Figure 4. Clarifying tank (2,000 gal) with 8-in to 6-in
 overflow (top left) and 4-in underflow line (bottom right).

The NTU values remained relatively constant for all 3 series of polymer concentrations except for Series 3, Test 5, where a significant increase in the NTU values occur. It is at this point where insufficient polymer is added to feed material to flocculate all of the suspended solids.

A sample of the flocculated material from the underflow was collected to determine the percent solids. The underflow solids were approximately 31 pct by weight for test 5 of the series shown in Table 3. Figure 5 shows the clean water overflow from the clarifier along with the flocculated material being drained off with the underflow.

BIOASSAYS

One of the major concerns for utilizing a polymer treatment system and discharging the "clean" water back into the Buffalo River, is the effect the polymer would have on organisms living in the river. From the data shown in Table 3, Test 5, approximately 2.27 gpm of 0.01 pct polymer was added to the 219 gpm feed material entering the tank clarifier. This is equivalent to approximately 1 ppm of polymer being added to the feed material from the barge.

Bioassays were conducted by the Corps, Waterways Experiment Station, Environmental Laboratory, Vicksburg, MS. A sample of the feed (untreated water), along with 2 samples of the clean water overflow (polymer treated) from the tank clarifier were collected for the purpose of conducting biological studies to determine if the polymer had any toxic response on living organisms (*Daphnia magna*). The *Daphnia magna* were tested in glass beakers containing 250 mL of each sample and survival rates were determined over time. The data from the different tests are shown in Tables 4 through 6.

Table 4.--Survival of *Daphnia magna* (48 h exposure)

Treatment sample	Percent survival			
	Test 1	Test 2	Test 3	Test 4
Feed	90	80	90	70
Overflow - 1	100	100	90	100
Overflow - 2	90	80	90	100

Table 5.--Survival of *Daphnia magna* (96 h exposure)

Treatment sample	Percent survival			
	Test 1	Test 2	Test 3	Test 4
Feed	20	10	10	0
Overflow - 1	60	50	40	50
Overflow - 2	50	60	50	40



Figure 5. "Clean" water overflow (top) beside flocculated underflow material (bottom).

Table 6.--Duplicate test of survival of *Daphnia magna* (96 h exposure)

Treatment sample	Percent survival			
	Test 1	Test 2	Test 3	Test 4
Feed	50	90	100	80
Overflow - 1	50	80	70	80
Overflow - 2	20	60	70	30

From Table 4, at the end of 48 h, the *Daphnia magna* survival rate was higher in the treated water than the feed material. Table 5 data (96 h survival rate) shows similar results, with the survival rate in the feed diminishing to between 0 and 20 pct. Because of the higher indicated toxicity of the feed than the treated feed, another 96 h survival rate test was conducted with the results shown in Table 6. This second test seems to indicate higher survival rates in the feed and diminishing survival rates in the overflow samples.

The *Daphnia* did not thrive in any of these samples. However, because there are no clear cases where the data shows greater toxicity of the treated water than that of the feed, these test are inconclusive.

CONCLUDING REMARKS

Costs associated with the polymer requirements were calculated using \$0.50/lb as the cost of the polymer. The NTU values remained relatively constant for all series of tests except the last test of Series III (Test No 5) with the NTU values increasing to 27. This most likely represents the transition point for complete flocculation of the particulate matter, with this NTU value still likely to be lower than the required regulatory level. This represents a cost of approximately \$0.0052 per 1,000 gal of feed or \$5.20 for 1,000,000 gal. Figure 6 shows a conceptual drawing of how this technique could be used as the dredge is operating.

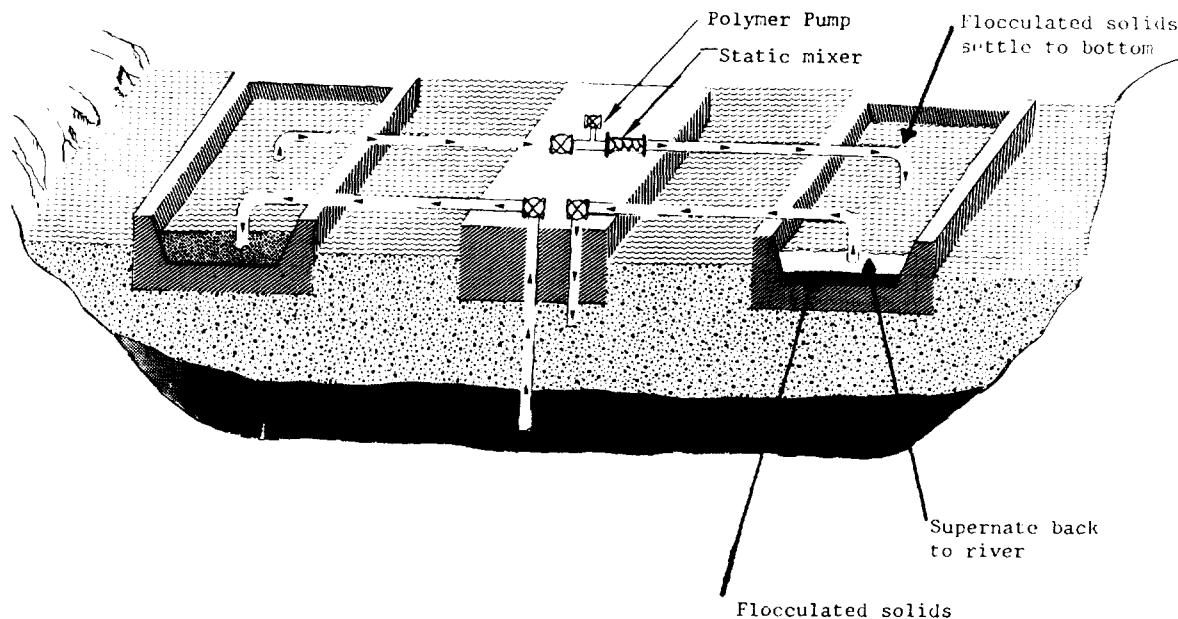


Figure 6. Flowsheet for continuous operation of flocculation system.

- (1) River sludge to holding barge;
- (2) suspended solids treated with polymer to holding barge;
- and (3) flocculated solids settle to bottom and supernate pumped into the river.

REFERENCES

1. Environmental Protection Agency, Assessment and Remediation of Contaminated Sediments (ARCS) Program - An Overview, Environmental Fact Sheet, United States Environmental Protection Agency, Great Lakes National Program Office, 77 West Jackson Blvd. Chicago, IL 60604, July 1992.
2. Sharma, Sandeep K., and B. J. Scheiner, Effect of Physico-Chemical Parameters on Dewatering: A Case Study, Fluid/Particle Separation Journal, v. 4, No. 3, September 1991, pp. 162-165.

0 11

MATERIALS SCIENCE

BENCH-SCALE SYNTHESIS OF NANOSCALE MATERIALS

M. F. Buehler
Pacific Northwest Laboratory
Richland, Washington 99352

J. G. Darab
Pacific Northwest Laboratory
Richland, Washington 99352

D. W. Matson
Pacific Northwest Laboratory
Richland, Washington 99352

J. C. Linehan
Pacific Northwest Laboratory
Richland, Washington 99352

533-31
2469
1

ABSTRACT

A novel flow-through hydrothermal method used to synthesize nanoscale powders is introduced by Pacific Northwest Laboratory. The process, Rapid Thermal Decomposition of precursors in Solution (RTDS), uniquely combines high-pressure and high-temperature conditions to rapidly form nanoscale particles. The RTDS process was initially demonstrated on a laboratory scale and was subsequently scaled up to accommodate production rates attractive to industry. The process is able to produce a wide variety of metal oxides and oxyhydroxides. The powders are characterized by scanning and transmission electron microscopic methods, surface-area measurements, and X-ray diffraction. Typical crystallite sizes are less than 20 nanometers, with BET surface areas ranging from 100 to 400 m²/g. A description of the RTDS process is presented along with powder characterization results. In addition, data on the sintering of nanoscale ZrO₂ produced by RTDS are included.

INTRODUCTION

Industrial demand for advanced materials has motivated the development of new methods to produce ultrafine powders. Ultrafine powders, also known as nanocrystalline or nanoscale powders, are defined here as those having crystallite sizes of the order of 1 to 100 nanometers. These powders can be used as feedstocks to fabricate materials such as cost-effective catalysts, high-performance components for aerospace and power generation applications, and lightweight/high-strength automotive materials. Ultrafine powders offer distinct advantages over more common microcrystalline powders because they provide high grain boundary area and/or high specific surface area. Unfortunately, common synthesis methods to produce nanoscale powders do not provide production rates sufficient to accommodate industrial needs. In this paper, we describe a hydrothermal process developed at Pacific Northwest Laboratory (PNL) that economically produces nanocrystalline oxide and oxyhydroxide powders at high rates suitable for industrial applications. The process is called Rapid Thermal Decomposition of precursors in Solution (RTDS).

Powders produced by the RTDS process are making an impact in many industries, an important example is in the field of heterogeneous catalysis. Often, the cost of bulk catalyst material may be high, but for ultrafine material having a high specific surface area, the cost per active surface site is very low. This reduces both capital and operating costs. As will be shown in this paper, the

flexibility of the RTDS process allows the powder to be used as catalyst material and as precursors for the fabrication of advanced materials. In the latter application, RTDS powders offer the ability to control the microstructure of a consolidated advanced material which enhances certain mechanical properties.

POWDER SYNTHESIS

Several existing synthesis methods can produce nanoscale powders. Some of the more common nanocrystalline powder synthesis methods are gas-phase condensation, sol-gel processing, and combustion synthesis (1). However, all of these processes have limitations for industrial applications, in particular, low production rate of the powder product. These methods are briefly summarized below.

Gas-phase condensation was first suggested by Gleiter (2) and uses an ultrahigh vacuum system fitted with a heating assembly and a liquid-nitrogen-filled cold finger. Unfortunately, the gas phase condensation process is inherently a batch operation and the production rates are low for industrial standards. Although this process is not yet generally useful in industrial applications, it has enabled researchers to demonstrate the improved room-temperature mechanical properties of nanoscale materials relative to their coarse-grained counterparts (3-5).

Sol-gel technology is a chemical method used to produce oxide material, including ultrafine powders, at room temperature. However, relatively pure precursors for industrially important materials such as nickel, iron, chromium, and zinc oxide are either very expensive or must be synthesized in-house prior to sol-gel processing. In addition, many of the precursors are moisture sensitive, making them difficult to store and handle.

Combustion synthesis combines soluble metal salts and a complexant/fuel such as carboxylate azides, urea, or glycine (6-10). The mixture is heated, and an autoignition reaction occurs which produces the desired powder. This technique is useful for the production of ceramic powders with specific stoichiometry and also for multicomponent systems. However, the technique does not easily yield hydroxides, and the distribution of grain-sizes is large. Also, the powders produced by this method are highly aggregated into hard clusters or agglomerates.

RTDS is a new, flow-through hydrothermal process with the capability to continuously produce nanocrystalline powders at rates of pounds per day using a bench-scale apparatus (11). The RTDS process was recently recognized for its innovative contribution to powder synthesis by receiving the prestigious R&D 100 award for 1993 (12). The process offers a flexibility to control the crystallite size and uniformity while producing powders at high rates.

RAPID THERMAL DECOMPOSITION OF PRECURSORS IN SOLUTION

Process Description

The synthesis of RTDS nanoscale powders begins with a feedstock solution of a metal salt or mixture of metal salts dissolved in water. The bench-scale system primarily consists of a high-pressure pump, a heated region, and a pressure reduction nozzle. The liquid feedstock is pressurized by a reciprocating piston pump and heated to reaction temperature by a standard-tube furnace. Within the heated region, hydrothermal (forced hydrolysis) reactions occur that produce solid oxide and oxyhydroxide particulates. Typical RTDS operating conditions include pressures ranging from 5000 to 8000 psi and temperatures from 200°C to 400°C. After the particles are formed in the heated region, the resulting suspension passes through a pressure reduction orifice. The solid/liquid aqueous suspension is then either used in slurry-based processes or the particulates are separated and dried by standard industrial methods (sedimentation, centrifugation, spray drying, etc.). The RTDS process is shown schematically in Figure 1. Although the present

RTDS system is a bench-scale apparatus, the technology uses standard unit operations which can readily be incorporated into existing industrial facilities.

A key feature of the RTDS process is that the nuclei are formed quickly and are allowed very little time to grow in the hydrothermal region. Typical residence time of the solutions in the heated region ranges from 2 to 30 seconds. This variable can be controlled by either changing the length of tubing within the heated region or varying the flow rate. As a result of the short residence time, crystallite sizes produced by this method are limited to the nanometer range. The particles produced are typically aggregates of nanometer-sized crystallites and are of the order of 100 nanometers. Some control over crystallite size can be exercised by adjusting the residence time of solution in the heated zone.

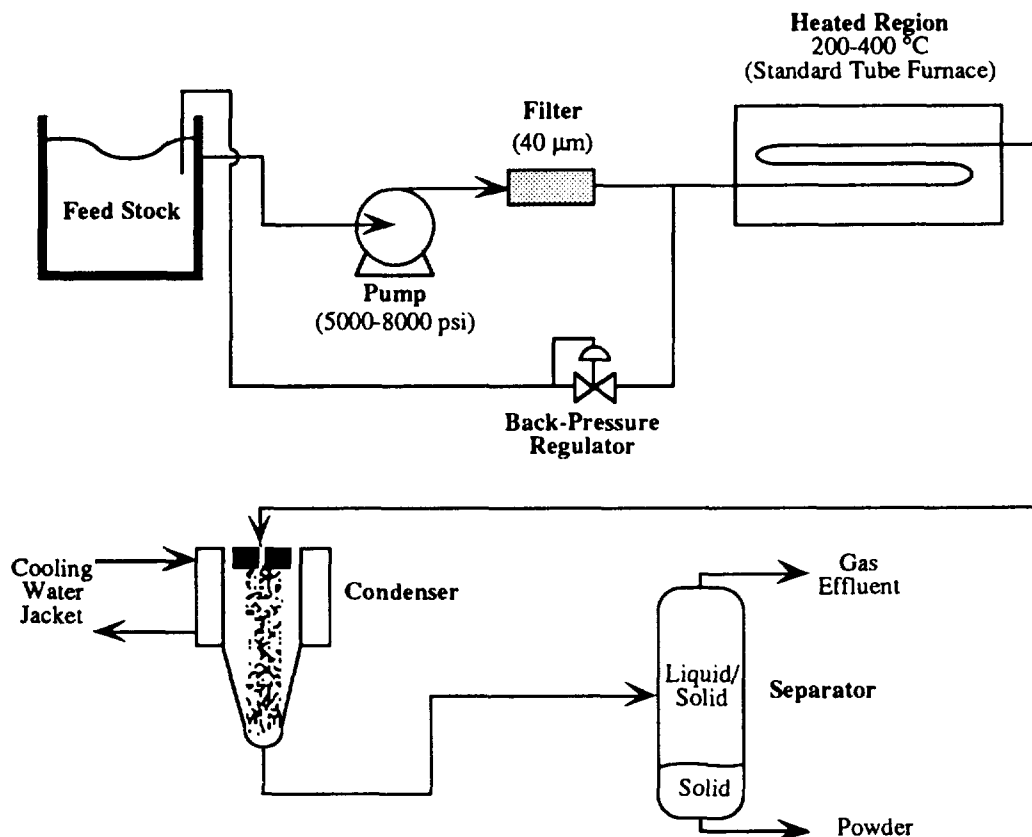


Figure 1. Schematic diagram of the RTDS process.

Powder Characterization

The RTDS powders have been characterized by several techniques, including X-ray diffraction (XRD), scanning electron microscopy (SEM), transmission electron microscopy (TEM), and Brunauer-Emmett-Teller (BET) nitrogen adsorption analysis. The XRD measurements, which allow phase identification and provide crystallite size information, were obtained using a Philips 3000 series X-ray diffractometer with a copper source operated at 40 kV and 45 mA. SEM was performed on an ElectroScan MEM-20 multi-environmental electron microscope. Both bright-field and dark-field TEM micrographs were obtained using a Philips EM400T electron microscope with a 120 keV electron beam. The BET surface area measurements were performed on a Micromeritics ASAP 2000 using multipoint analysis. Some of the powders produced using the RTDS method

and the corresponding crystallite sizes (determined by XRD line broadening analysis) are shown in Table 1.

Table 1. Typical powders produced by the RTDS process.

Material	Chemical Formula	Crystallite size (nm)
Ferrihydrite	5Fe ₂ O ₃ ·9H ₂ O	<10
Hematite	α-Fe ₂ O ₃	23
Magnetite	Fe ₃ O ₄	12
Tenorite	CuO	20
Trevorite	NiFe ₂ O ₃	<10
Bunsenite	NiO	12
Zirconia	ZrO ₂	<10
Zincite	ZnO	34
Anatase	TiO ₂	<10

Figure 2 shows a composite bright-field TEM micrograph of iron oxyhydroxide/oxide powders produced at three different RTDS processing temperatures from an iron nitrate solution. This figure clearly illustrates that RTDS operating conditions affect the characteristics of the resulting powders. In this example, both crystallite size and phase were affected by changes in the RTDS processing temperature. These observations are confirmed by analysis of the XRD patterns for these three materials (Figure 3). The XRD patterns show peak width broadening with decreasing temperature, which indicates a reduction in crystallite size. The XRD measurements were also used to identify the phases present. The predominant phase at the lower RTDS processing temperature (200°C) was 6-line ferrihydrite, while at high temperatures (greater than 350°C) the predominant phase was hematite. A mixture of these two phases was produced at intermediate temperatures.

The BET surface-area measurements of RTDS powders typically range from 100 to 400 m²/g. For example, the 6-line ferrihydrite shown in Figure 2 has a specific surface area of 280 m²/g. Other high surface area RTDS powders of industrial importance include: zirconia = 428 m²/g, anatase = 136 m²/g, and hematite = 153 m²/g.

Suspensions of nanocrystalline materials produced by RTDS provide unique feedstocks for spray drying. Using this method, micrometer-scale spherical aggregates of nanocrystallites are readily produced. Figure 4 shows a SEM micrograph of a ZrO₂ powder produced by spray drying a RTDS-generated suspension of ZrO₂. The drying process yielded solid-core spherical aggregates in the 0.5-μm to 5-μm size range. The morphology of the spray-dried powder is ideally suited for subsequent consolidation processes, such as powder injection molding, isostatic compaction, or hot pressing.

POTENTIAL COMMERCIAL APPLICATIONS FOR RTDS POWDERS

Catalysts

The RTDS powders are an attractive option for heterogeneous catalysts because of their high degree of crystallinity and high specific surface areas. RTDS powders typically do not need to undergo pretreatment steps (such as increasing the number of acidic sites) before becoming

RTDS Powders Produced from 0.1M Fe(NO₃)₃ Solutions

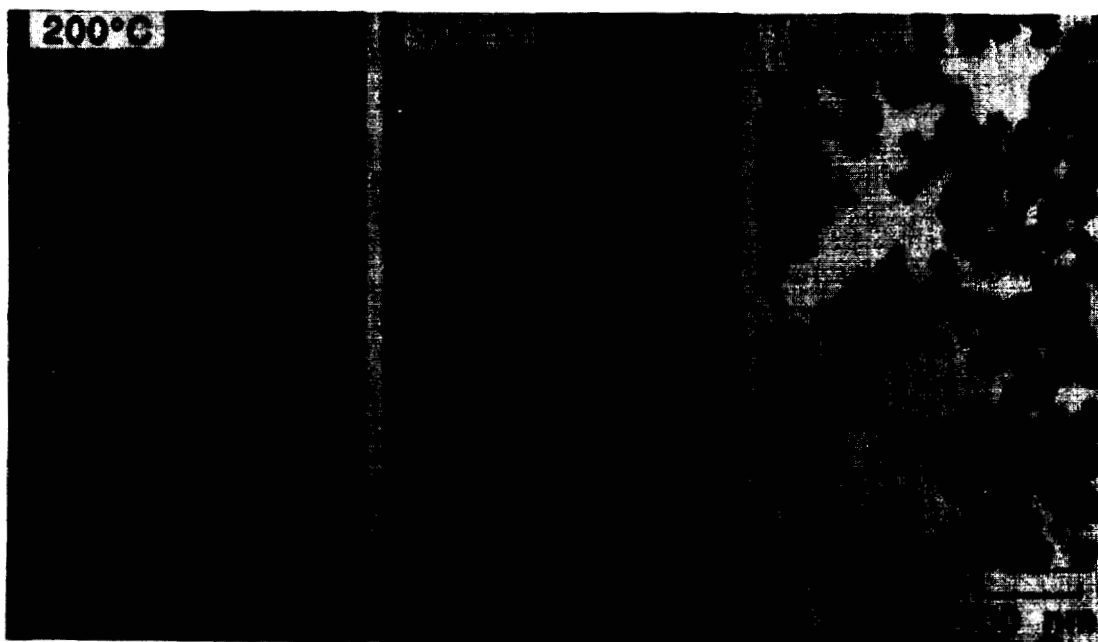


Figure 2. TEM micrographs of RTDS powders produced from iron nitrate solutions at 200°C, 300°C, and 350°C.

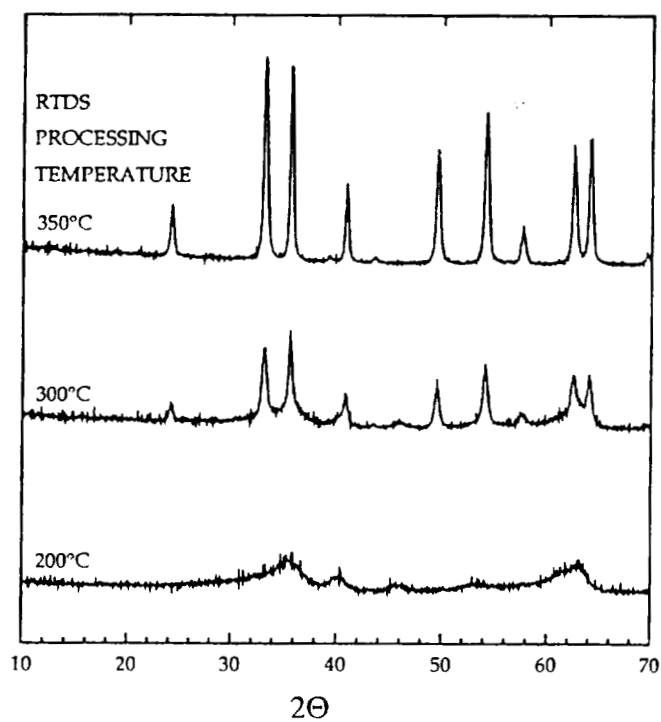


Figure 3. The corresponding XRD patterns for the RTDS powders shown in Figure 2.

"activated" catalysts. For many applications, the RTDS production conditions can be tailored to simultaneously synthesize and pretreat the catalyst powder so that the powder is "preactivated" when collected. RTDS powders can also be consolidated and sintered into porous, high surface area supports for catalysts, or catalyst and support material precursors can be co-processed in the RTDS apparatus to yield a pre-formed supported catalyst.

RTDS powders and supports were tested by workers at PNL and by their industrial clients. Nanoscale RTDS ferrihydrite powder, similar to that shown in Figure 2, was used as a coal liquefaction catalyst, and the activity of the RTDS produced powders was compared with other commercially available catalysts. The RTDS material yielded more liquefied products than any of the other iron-based catalyst tested.

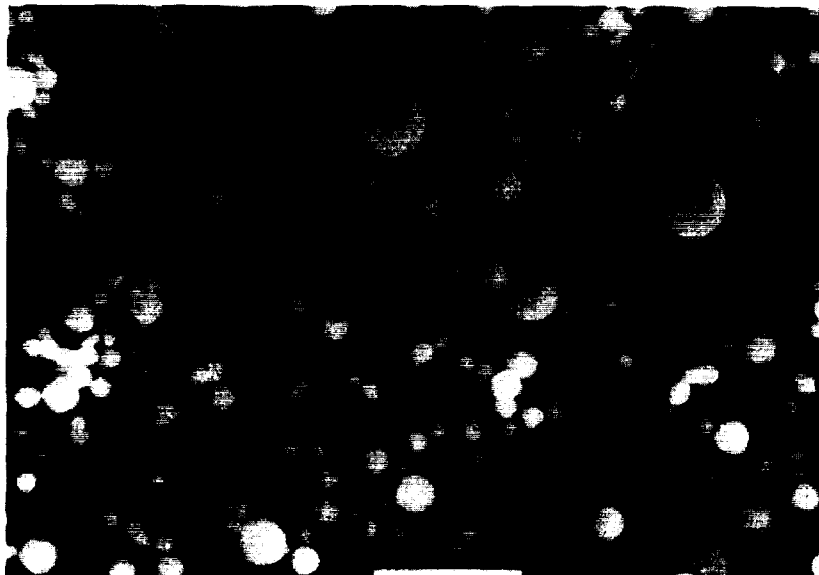


Figure 4. SEM of a spray-dried ZrO_2 powder produced using a ZrO_2 suspension generated by RTDS processing of a zirconyl nitrate solution at $300^\circ C$.

Powder Manufacturing of Components

The properties of nanoscale powders are dominated by their small crystallite size and high interfacial area (i.e., high grain boundary area and/or high surface per unit mass). Therefore, the interfacial mechanism of mass transport under certain processing conditions will control the microstructure of a component produced from a powder precursor. The ability to control the microstructure of the bulk product is advantageous because the physical properties of the material are dependent on the grain size and microstructure of the bulk material. Consequently, nanocrystalline powders provide a unique opportunity to control the microstructure of a fabricated component.

Interfacial phenomena are important when powders are fabricated into bulk materials by consolidation and sintering (13). In conventional powder processing, powders are consolidated into a desired component geometry under high pressure. Subsequently, the component is heated at high temperature (sintered) to produce a part with little porosity. The sintering kinetics for a nanocrystalline powder compact are dominated by grain boundary diffusion because of the extremely high grain boundary areas. In contrast, for microcrystalline powder compacts, volume diffusion typically dominates the sintering kinetics. The activation energy for grain boundary diffusion is lower than that of volume diffusion for nanoscale compacts. Therefore, the lower

activation energy provides nanocrystalline powder compacts with lower sintering temperatures as compared with conventional microcrystalline powder compacts. This fundamental difference in the sintering mechanism also provides an alternative pathway to control the microstructure of the bulk monolith.

The importance of microstructural control in materials is demonstrated by examining the relationship between the mechanical properties of a material and its microstructure. The yield strength and the fracture strength of a polycrystalline material are related to grain diameters in the bulk material by similar expressions:

$$\text{Strength} = K_1 + \frac{K_2}{d^{1/2}} \quad [1]$$

where K_1 is a materials-related constant, K_2 is a collection of appropriate constants, and d is the grain diameter (14). Clearly, smaller grain size improves the strength of such materials.

Creep deformation, or time-dependent strain under an applied stress, is also related to grain size in the bulk material by the relation:

$$\text{Creep Rate} \propto \frac{1}{T d^3} \quad [2]$$

where T is the temperature (15). From Equation 2, the smaller the grain diameter of the material, the lower temperature is required to provide a given creep rate. This is important for nanocrystalline material because creep deformation occurs at lower temperatures, and, therefore, grain boundary rearrangement occurs without grain growth. Also, superplastic forming of nanocrystalline bulk materials becomes more feasible as grain size is decreased (15).

RTDS nanoscale powders can be consolidated and sintered into useful components, often with unique properties. Researchers at PNL and their clients are currently investigating the agglomeration, consolidation, and sintering behaviors of a variety of single and multi-phase RTDS powders. Figure 5 is a plot of relative sintered density as a function of normalized temperature showing two regions: one for nanocrystalline zirconia and the other for microcrystalline zirconia (16). Region I defines an area where 10 nanometer crystallite microstructure will sinter under typical conditions. Region II describes a similar area for 200 nanometer crystallites, which is typical of many conventional microcrystalline oxide systems. Figure 5 also shows sintering characteristics of zirconia produced by the RTDS process.

The RTDS zirconia sintering data fall well within Region I and densifies at lower normalized temperature than the microcrystalline counterpart. The reduction in sintering temperature for the RTDS powder is due to the difference in mass-transport mechanisms and activation barriers associated with each microstructure grain size. Darab *et al.* (13) have shown that the mechanism of sintering for nanocrystalline RTDS zirconia is grain boundary diffusion with an activation barrier of 250 kJ/mol, whereas that of microcrystalline powders is volume diffusion with an activation barrier of 430 kJ/mol. The lower sintering temperatures associated with nanoscale powders can provide significant energy savings when used as a feedstock for powder manufacturing processes.

SUMMARY

The RTDS process enables the production of nanoscale, crystalline oxide/oxyhydroxide powders at industrial-scale rates. The flexibility of the process allows control over the crystalline size and phase. Other synthesis methods are limited by low production rates, and RTDS fills an existing gap in industrial powder production. The powders produced by RTDS have been shown to be

effective catalysts for coal liquefaction and provide lower sintering temperature for zirconia compacts. The bench-scale apparatus is easily scaled to pilot-scale level because the process uses standard industrial unit operations. It is anticipated that the RTDS process will produce unique advanced materials for numerous applications, such as: 1) powders for pigments, magnetic media, and abrasives; 2) additives for advanced composites; and 3) starting materials for the preparation of separation media such as nanoporous filters.

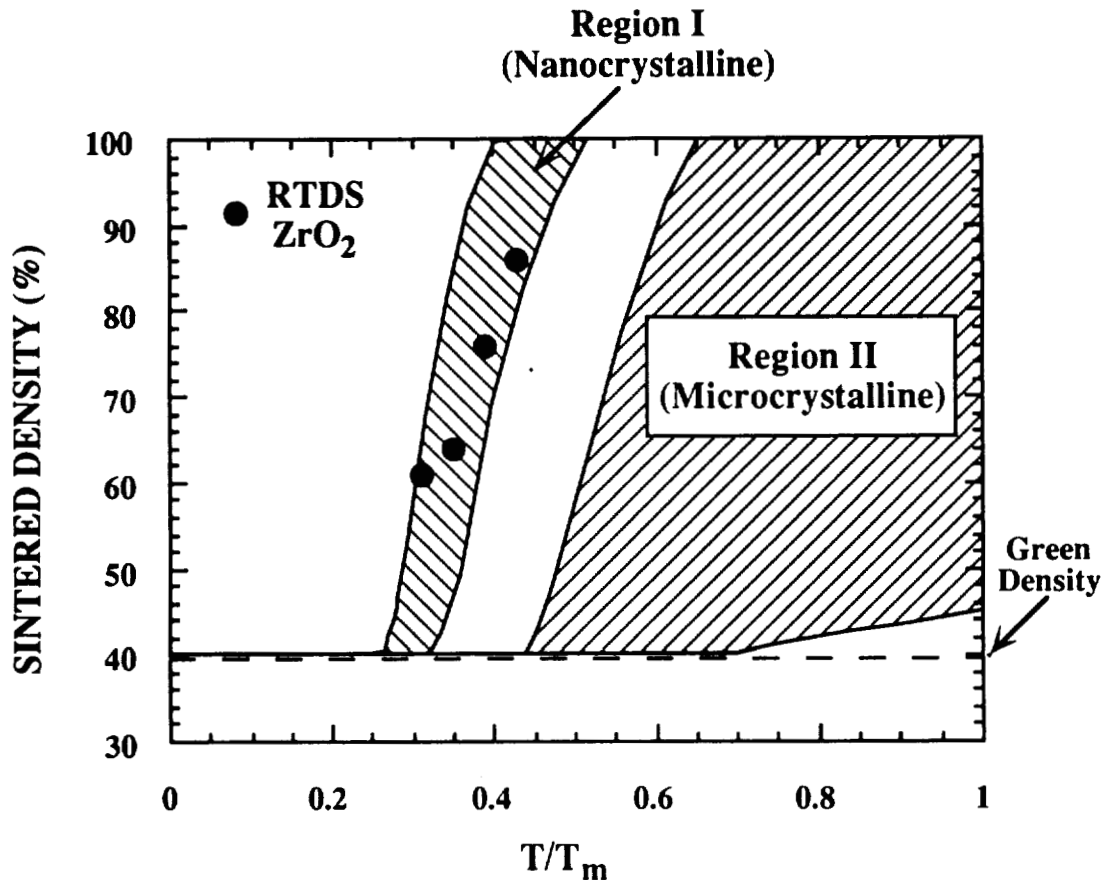


Figure 5. Relative sintered density as a function of normalized temperature ($T_m = 2570^\circ\text{C}$) for nanocrystalline RTDS ZrO_2 and theoretical behavior.

ACKNOWLEDGMENTS

The work described in this paper was supported by the U.S. Department of Energy (DOE). Pacific Northwest Laboratory is operated for DOE by Battelle Memorial Institute under Contract DE-AC06-76RLO 1830. The authors gratefully acknowledge the assistance of the following PNL staff: James Coleman (SEM), Dave McCready (XRD), Larry Thomas (TEM), Tim Armstrong (spray drying), and Ron Stevens (powder processing and sintering).

REFERENCES

- 1.) Williams, J. C., and Kear, B. H., "Research Opportunities for Materials with Ultrafine Microstructures," National Materials Advisory Board, National Academy Press, NMAB-454, 1989.
- 2.) Gleiter, H., "Deformation of Polycrystals: Mechanisms and Microstructures," Eds. N. Hansen *et al.*, Riso National Laboratory, Roskilde, p.15, 1981.
- 3.) Averback, R. S., Hofler, H. J., Hahn, H., and Logas, J. C., *NanoStructured Mat.*, **1**, 173 (1992).
- 4.) Nieman, G. W., Weertman, J. R., and Siegel, R. W., *J. Mat. Res.*, **6**, 1012 (1991).
- 5.) Siegel, R. W., Ramasamy, S., Hahn, H., Zongquan, L., Ting, L., and Gronsby, R., *J. Mat. Res.*, **3**, 1367 (1988).
- 6.) Ravindranathan, P., and Patil, K. C., *J. Mat. Sci. Letters*, **5**, 221 (1986).
- 7.) Ravindranathan, P., and Patil, K. C., *Am. Cer. Soc. Bull.*, **66**, 668 (1987).
- 8.) Ravindranathan, P., Mahesh, G. V., and Patil, K. C., *J. Solid State Chem.*, **66**, 20 (1987).
- 9.) Kingsley, J. J., and Patil, K. C., *Materials Letters*, **6**, 427 (1988).
- 10.) Chick, L. A., Pederson, L. R., Maupin, G. D., Bates, J. L., Thomas, L. E., and Exarhos, G. J., *Materials Letters*, **10**, 6 (1990).
- 11.) Matson, D.W., Linehan, J. C., and Bean, R. M., *Materials Letters*, **14**, 222 (1992).
- 12.) Buehler, M. F., Matson, D. W., Linehan, L. C., Phelps, M. R., Neuenschwander, G. G., Fulton, J. L., and Bean, R. M., *R & D Magazine*, **35**, 57 (1993).
- 13.) Darab, J. G., Buehler, M. F., Linehan, J. C., and Matson, D. W., submitted to *Part. Sci. and Tech*, 1993.
- 14.) Dieter, G. E., Mechanical Metallurgy, 3rd Ed., McGraw-Hill, New York, Chapters 6 and 7, 1986.
- 15.) Kingery, W. D., Bowen, H. K., and Uhlmann, D. R., Introduction to Ceramics, John Wiley and Sons, New York, p. 704, 1976.
- 16.) Ashby, M. F., HIP-Maps, Version 6.0, Personal Computer Program, University of Cambridge CB2 1PZ, England, 1990.

334-27
2470
P-13

**SYNTHESIS AND CHARACTERIZATION OF ADVANCED
MATERIALS FOR NAVY APPLICATIONS**

J. Covino

**Naval Air Warfare Center Weapons Division
China Lake, CA. 93555-6001**

I. Lee

**Naval Air Warfare Center Weapons Division
China Lake, CA. 93555-6001**

ABSTRACT

The synthesis of ceramics and ceramic coatings through the sol-gel process has extensive application within the United States Navy and a broad range of potential commercial applications as well. This paper surveys seven specific applications for which the Navy is investigating these advanced materials. For each area, the synthetic process is described and the characteristics of the materials are discussed.

INTRODUCTION

The sol-gel process has been in use since 1950 [1]. However, it wasn't until the mid-1970s that increased interest by many researchers in this process became visible and the quantities of published papers, ranging from basic mechanistic understanding to applied component design, escalated. The sol-gel and modified sol-gel processes can be used to synthesize many advanced materials both for military and commercial applications. For example, the sol-gel process can be used for the manufacture of multicomponent glasses [2-5], coatings [6,7], fibers [8,9], monoliths [10,11], thermal insulation materials [12-14], controlled particle size powders [15,16], as well as special types of ceramics such as electronic ceramics [17,18], superionic conductors [19], and high-temperature super conductors [20,21].

This paper gives an overview of the synthesis, via the sol-gel process, of ceramics and ceramic coatings for use in specific Navy applications. Among the applications are coatings for electrochromic devices [22,23], laser gyro bodies [24-26], hermetic coatings for optical fibers for use in ocean environments [23,27], coating development for advanced lightweight structural applications [28-30], ceramic foams for catalysis and thermal insulation [31], and incorporation of organic and inorganic dyes in silica-based ceramics for lasers and ceramics for radomes [32-34]. The paper also addresses the characterization of these systems as well as advanced structural materials with respect to durability, chemical stability, optical properties, and other properties that are more specific to their applications and end use.

The sol-gel process is one in which the final product is obtained from reactive precursor materials (such as metal organics or metal alkoxides) by chemical or thermal means. This process involves the formation of a solution or colloidal suspension (sol) followed by a gelling stage (gel) prior to conversion to the final product. There are numerous advantages of sol-gel synthesis over the conventional melting techniques. Some advantages are (1) better homogeneity, (2) better purity, (3) speed and affordability, (4) lower temperature of preparation, (5) bypassing phase separations, (6) bypassing crystallization, (7) preparation of new noncrystalline solids outside the range of normal glass formation, (8) preparation of new crystalline phases from new crystalline solids, (9) better control of the fiber properties because it is easier to control gel properties than those of a melt, (10) better fiber products from special properties of the gel, (11) ability to be scaled-up for large production, (12) and tailorable microstructure and coating composition. When compared to the many advantages, the disadvantages are few: crack free non-porous coatings are difficult to manufacture, parts of the methodology are more of an art form than a well understood science, and purity can be difficult to control (i.e., carbon impurities are often measured).

The sol-gel process and the new materials that can be obtained by its use have tremendous commercial potential. Among these applications are the manufacture of high-quality oxide-based electronic substrates, coatings for use in the automotive industry, optical quality materials for a myriad of applications, high-temperature resistive coatings for use in industrial and consumer products, and controlled molecular sieves for use as catalysts and catalyst support in the petroleum and recycling industries.

EXPERIMENTAL

Synthesis

All oxides systems addressed in this paper were synthesized using the sol-gel process. The precursors used were high purity alkoxides, metal organics, or water-soluble salts. The specific syntheses and annealing processes used for each product can be found in the journal articles cited in each section.

Characterization

Characterization tools used to evaluate the chemical and physical properties of these materials included X-ray diffraction, thermal gravimetric analyses, thermal diffusivity, infrared spectroscopy, hydrogen permeation, electrochemical evaluation, scanning electron microscopy, dielectric properties measurements, and mechanical properties measurements. Not all techniques were used for all materials studied. For specific characterization and properties measured, refer to the references cited in each section.

RESULTS AND DISCUSSION

This section summarizes some of the pertinent material properties for each material studied. It does not give all the physical and chemical properties measured for each system. For more information on each class of compounds, refer to the proper references.

Coatings For Electrochromic Devices [22-23]

Electrochromism is the property of a material or system to change color reversibly in response to an applied potential. The use of ceramics in electronic applications is widespread and expanding rapidly (e.g., ECD displays and "smart windows"). For many of these increasingly demanding applications, improved materials and methods of fabrication are becoming necessary. The sol-gel process was used to synthesize a WO_3/Ni electrochromic device. This device was evaluated electrochemically in 0.3M LiClO_4 and $\text{NaClO}_4/\text{DMF}$ electrolyte solutions. Figure 1 shows the electrochemical results for the WO_3/Ni device in a 0.3m $\text{NaClO}_4/\text{DMF}$ electrolyte solution.

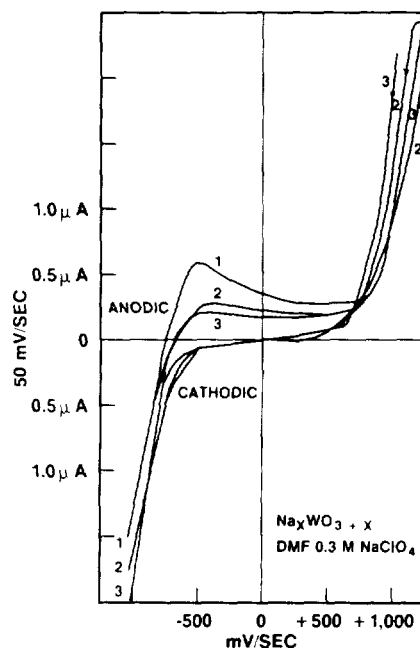


Figure 1. Electrochemical Cycling of the WO_3/Ni Device in a 0.3M $\text{NaClO}_4/\text{DMF}$ Solution With a Standard Calomel Electrode. A scan rate of 50 mV/sec was used.

Our major objective in this study was to demonstrate that the fine particulate nature of the sol-gel-deposited WO_3 could be stabilized in nonaqueous solvents, thus taking full advantage of the fast device response time engendered by small grain size and minimizing difficulties due to WO_3 dissolution. Layers of WO_3 coating formed on the nickel substrates were relatively thick (about 0.1 μm) and quite fragile. The particles produced by the sol-gel process were very small, and the WO_3 coating was nearly stoichiometric. Some dissolution of the WO_3 in DMF was noted. This was exacerbated in CH_3CN and DMSO; hence, only results obtained in DMF will be discussed here.

The electrochemical formation of the lithium bronze, Li_xWO_3 , in nonaqueous media is a kinetically facile process at about -500mV (SCE). Formation of the Na_xWO_3 bronze occurs at significantly higher overpotentials (about -250 mV). The lithium bronze is stable, and reproducible cycling behavior is readily obtained. The sodium bronze appears to be less stable and less reproducible during cycling.

In both cases, the shift from the blue (bronze) to yellow (WO_3) state is readily achieved simply by stepping from -1,000 mV to +1,000mV. Unfortunately, response times are highly variable, depending not only on film thickness but also on the history of the electrode, the nature of the supporting electrolyte/intercalation cation, the cell geometry, and the solvent. The bronzes Na_xWO_3 , for example, have colors ranging from golden yellow ($x = 0.9$) through red ($x = 0.6$) to deep violet ($x = 0.3$). These color changes are attributed to the oxidation state of tungsten, which is varying from VI to V, as well as to the molar ratio of the two concentrations.

Evidence of H^+ inclusion in WO_3 overlays prepared by the sol-gel process has been observed using nonaqueous electrochemical studies. The H_xWO_3 phase is apparently readily converted (after a few cycles) to the Li_xWO_3 or Na_xWO_3 form. The irreversible formation of a more deeply blue-brown phase at high overpotentials was observed. The electrochromic devices presented in this study have been cycled reversibly for thousands of cycles.

Laser Gyro Bodies [24-26]

Lithium aluminum silicate (LAS) glass-ceramics have long been used in applications requiring ultra-low thermal expansion and in ultra-precision measurement experiments such as low helium gas permeability. However, for decades these glass ceramics have been made by conventional high temperature (above 1500°C) glass melting techniques. In order to demonstrate significant cost savings and improved material properties, the sol-gel process was explored in the synthesis of two glass ceramics. Table I summarizes these compositions.

Table I. Compositions of Nominal LAS Glass-Ceramic as Compared to Synthetic Sol-Gel-Derived NZ and NZP.

Constituents	Nominal LAS	NZ	NZP
Silicon dioxide (SiO_2)	55.50	61.35	56.10
Aluminum oxide (Al_2O_3)	25.30	27.97	25.60
Lithium oxide (Li_2O)	3.70	4.08	3.70
Titanium dioxide (TiO_2)	2.30	2.30	2.30
Magnesium oxide (MgO)	1.00	1.00	1.00
Zirconium dioxide (ZrO_2)	1.90	1.90	1.90
Zinc oxide (ZnO)	1.40	1.40	1.40
Phosphorous pentoxide (P_2O_5)	7.90	--	8.00
Miscellaneous oxides (arsenic, iron, potassium, calcium, and sodium)	1.01	--	--

Preliminary casting experiments were performed on NZ and NZP powders. Results showed that both NZ and NZP can be casted quite readily to produce a β -quartz lithium aluminum-silicate glass ceramic. Results of casting experiments (Figure 2) show that the most promising candidate was NZ-AH (produced by heating NZ at 2.93°C/min. to 735°C, holding for 6 hr.; heating at 2.17°C/min. to 800°C, holding for 96 hr.; cooling at 8°C/min.). This glass ceramic material exhibited an 82% crystallinity with crystallite size averaging 400Å. Both the virgilite and β -eucryptite structures are disordered quartz structures with varying degree of disorder. The NZ-AH material had a predominantly virgilite structure (or β -eucryptite structure, since the two X-ray powder patterns are very similar) and a 3-5% alpha-spodumene impurity. These results are in agreement with the currently most popular, commercially-available β -quartz LAS glass-ceramic material. By using the sol-gel process to make the LAS glass ceramics

significant reductions in annealing temperatures have been achieved, 800°C maximum with gellation and 1500 to 1700°C with conventional glass melting techniques.

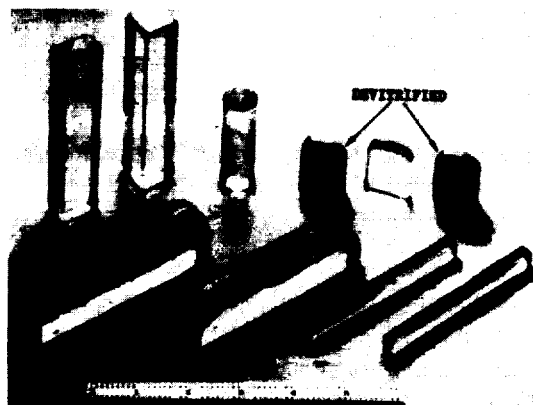


Figure 2. A Variety of Cast and Devitrified NZ Glass Samples.

Hermetic Coatings For Optical Fibers [23-27]

This section addresses a feasibility study to determine whether the sol-gel method could be employed for SiO₂ optical fiber coatings. Many fiber optical communication applications can be made possible with hermetically sealed coatings for SiO₂ fibers that are durable and nonpermeable to moisture, do not degrade the optical quality of the original fiber, and are cost effective and available. Materials of choice for the SiO₂ fiber coatings are LAS glass ceramics having stuffed β-quartz structure. These materials have crystalline phases from 60% to 100% and show low helium permeability. They have a low thermal expansion coefficient, with a varying from $\pm 10^{-8}$ to 10^{-6} in the 0 to 600-K temperature range. They are very chemically and thermally stable, do not allow water to permeate, and have a composition of approximately 50% silica for material matching with SiO₂ fibers. It is because of these basic material properties that the LAS glass ceramic compositions are the materials of choice to attempt to make sol-gel coatings for SiO₂ fibers.

Two approaches were considered in the synthesis of these coatings. In Method I, a "LAS-like" composition chosen to be close to the nominal composition of a commercially available lithium aluminum silicate (CALAS) glass ceramic was prepared by the sol-gel method and was used as the coating material. In Method II, a finely ground CALAS composition was suspended into a tetra-ethoxysilane [TEOS, (C₂H₅O)₄Si] solution which was then used as the fiber coating. Table II shows the composition of the CALAS, with the weight percent of the representative oxides in it.

Table II. CALAS Composition Represented as Weight Percent of Oxide Present.

Constituents	LAS (wt %)
Silicon dioxide (SiO ₂)	55.50
Aluminum oxide (Al ₂ O ₃)	25.30
Lithium oxide (Li ₂ O)	3.70
Titanium dioxide (TiO ₂)	2.30
Magnesium oxide (MgO)	1.00
Zirconium oxide (ZrO ₂)	1.90
Zinc oxide (ZrO)	1.40
Phosphorous pentoxide (P ₂ O ₅)	7.90
Miscellaneous oxides ^a	0.95
Trace elements ^b	0.01

^a Oxides of arsenic, iron, potassium, calcium, and sodium.

^b Trace elements such as barium, tin, manganese, lead, gallium, copper, silver, and strontium.

Two different sol-gel processes were used to make SiO₂ fiber optic coatings having the "LAS-like" compositions. X-ray diffraction data on dried powder made from the sol-gel Method I indicate that it is noncrystalline up to 800°C. Above 800°C, the powder appears to crystallize with a vergilite-like structure. It should also be noted that the currently most popular CALAS glass ceramic, which has the lowest helium permeability and thermal expansion coefficient, has an identical X-ray powder diffraction pattern. Thermal gravimetric analysis (TGA) data show that the majority of the solvent (water and alcohol) in the gel is removed by 80°C and thus makes such a treatment temperature adequate for heat treatment of the coated fibers.

From the optical microscope and scanning electron microscopy data, it was concluded that Method I produced better coatings. These coatings were better adhered to the SiO₂ fibers, and they were of a more uniform nature. Acid treatment of the SiO₂ fibers did make a pronounced difference in coating quality, with 49% HF showing the best results (see Figure 3).

In summary, the preliminary results illustrate that the coating adhesion and/or quality depends on (1) type and viscosity of the gel (Method I vs. Method II), (2) pretreatment of the SiO₂ fibers (no acid treatment vs. various types of acid treatment), (3) drying/annealing profile of the coated fibers (slower heating rates showed better coating adhesion), and (4) coating thickness. The sol-gel process offers the means to coat fibers by simple dipping techniques during production as well as to "fine tune" the chemical bonding of the coating to the fiber for strength and durability. It also offers a cost-effective and mass-production-suitable method to coat fibers during the drawing stages.

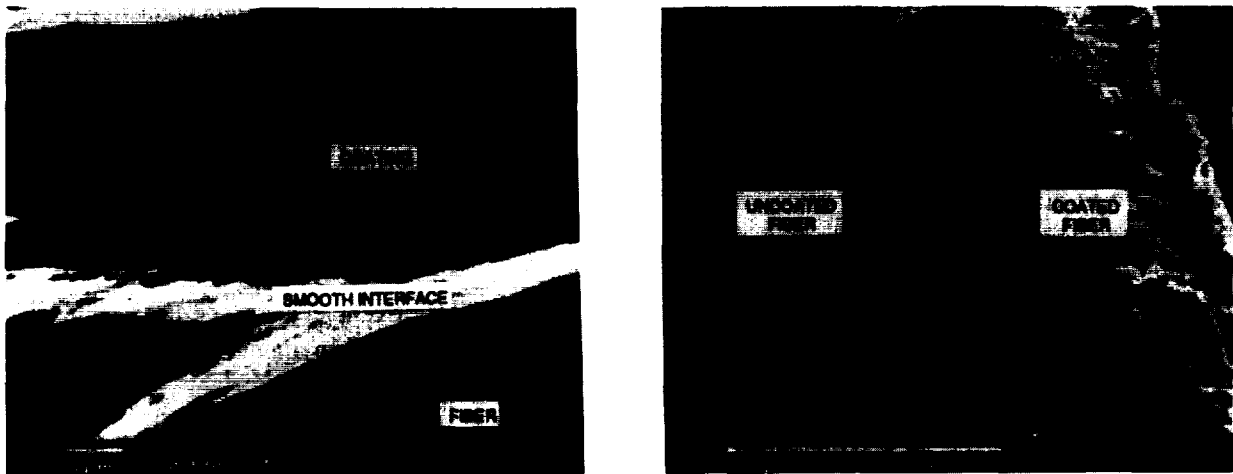


Figure 3. Scanning Electron Micrographs of Fibers Dipped in 49% HF Solution and Coated With Gel Synthesized Using Method I. Drying of the coatings was conducted at a rate of 0.5°C/min. to 80°C and held at 80°C for 6 hr.

Coatings for Light Weight Structural Applications [28-30]

Today there are many novel applications that require temperature resistant, lightweight, and durable coatings with properties far above presently available materials. Thus, much effort is going into the development and characterization of coatings. Coatings of choice are expected to be lightweight, have good mechanical properties, and show protection against oxygen and hydrogen both at cryogenic conditions and at high temperatures and pressures.

Protective coatings for both titanium-aluminum (Ti-Al) alloys and for carbon-carbon (C-C) composites have been synthesized and characterized with respect to protection against oxygen and hydrogen under both mild environments of low flows and low temperatures and severe environments of high flows and high temperatures. Mixed oxide glass ceramics were chosen as coating candidates because they are stable to temperatures of 1500°C, are nonreactive to oxygen, and are minimally reactive to hot hydrogen.

In the structural coatings effort three different synthetic methods have been addressed. These are: (1) the sol-gel process, the lacquer-slurry process, and the Chemical vapor deposition (CVD) method.

The sol-gel process for coatings is affordable and scalable. Coating composition can be tailored by the solution composition. Coating thickness and uniformity are controllable by solution viscosity, method and rate of coatings for application, and sintering conditions. In this work, the sol-gel method was used to develop coatings for Ti-Al alloys. The Ti-Al alloys used were the α -2 Ti-Al and a variety of γ Ti-Al alloys. The coatings applied using the sol-gel method are Al₂O₃, Si-Al-oxide, and Si-Al-Ti-oxide.

The lacquer-slurry process involves the dispersion of powders into an organic lacquer, application of this slurry on the substrate, and sintering of the coated substrate to achieve densification. Coating composition can be controlled by both materials and lacquer selection.

The last type of coating application method investigated was the CVD method. SiC, Si₃N₄, ZrC, and Ni coatings were applied to C-C using the CVD method, and characterization of these coatings was performed. Table III summarizes the measured coating thickness for many of the coatings characterized in this study.

Table III. Measured Coating Thickness for a Variety of Coatings.

Coating material/substrate	Method of application	Coating thickness
Al ₂ O ₃ / α -2 Ti-Al	Sol-gel	1.5 μ m
Si-Al-oxide/ α -2 and γ TiAl	Sol-gel	1.5-6.0 μ m
C-C coatings	Lacquer slurry	0.5 mm
SiC / C-C	CVD	0.3 mm
Si ₃ N ₄ / C-C	CVD	0.3 (0.17-0.59) mm
Ni / C-C	CVD	0.3 mm
ZrC / C-C	CVD	0.14 mm

To evaluate Al₂O₃ and Si-Al-oxide coatings stability on both α -2 and γ Ti-Al alloy, Thermal gravimetric analyses were performed in oxygen and in hydrogen/inert gas (either Argon or Nitrogen). All TGA data were taken from room temperature to 1000°C at a rate of 2°C/min. Very little weight gain was observed for the Al₂O₃ coated α -2 Ti-Al alloy either in oxygen (1% weight gain) or in 10% H₂/90% N₂ (0.6% weight gain). However, the data show a significant increase in the rate of weight gain from 600 to 1000°C. Furthermore, when the coated α -2 Ti-Al alloy was removed from the TGA, coating flake-off was apparent. The TGAs show no signs of separation of the Al₂O₃ coating from the γ Ti-Al system and showed the coating to be more stable in both oxygen (0.6% weight gain) and 10%/H₂/90%N₂ (4% weight gain) than the coated α -2 Ti-Al alloy. The TGA residue for the Al₂O₃ showed no signs of separation from the γ Ti-Al alloy, this result is consistent with the γ Ti-Al being more oxygen resistant than α -2 Ti-Al.

The TGA data in Figure 4 clearly show that the coated α -2 Ti-Al alloy behaves better than the uncoated alloy in both pure oxygen and in 50% H₂/50% Ar (argon). In oxygen, the coated α -2 Ti-Al alloy gains less than 0.1 wt % as compared to a 6 to 10 wt % for the uncoated material. These data also show that the oxide coating significantly improves the reactivity of the α -2 Ti-Al alloy in 50% H₂/50% Ar. In hydrogen, the uncoated α -2 Ti-Al alloy gains 10 wt % and turns black, while the coated α -2 Ti-Al alloy gains only 0.6 wt % and has no apparent color change. It should be noted that both in oxygen and in 50% H₂/50% Ar, the coated material gains the majority of its weight by 300°C. After 500°C, the weight gain levels off. This study confirms that the Si-Al oxide coating is more thermally stable than the Al₂O₃ coating. For example, in the case of Si-Al-oxide coated α -2 in oxygen, a total weight gain of 0.1% was observed, while for the Al₂O₃ coated α -2 weight gain of 1% was seen.

Hydrogen permeation experiments were performed as a function of temperature (from 25°C to 300°C) using the "membrane permeation" technique. Data obtained for coated and uncoated C-C composites and for Si-Al-oxide coated and uncoated Ti-Al alloys are illustrated in Figures 5 and 6. These data were calculated by subtraction of the measured background level. When the sample achieved a desired temperature, it was saturated with deuterium for a 24-hr. period to assure equilibrium. To verify equilibrium, three flow rate measurements were made over an 8-hr. period. If the flow rate was equivalent all three times, the value was reported.

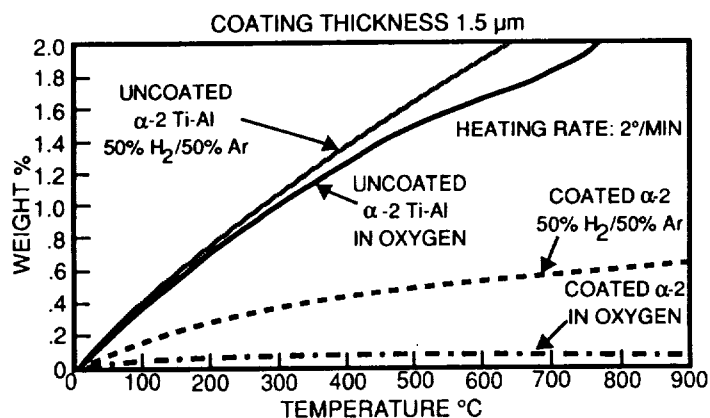


Figure 4. Thermal Gravimetric Analysis of Uncoated and Si-Al-Oxide Coated α -2 Ti-Al Alloy.

Figure 5. shows the permeability vs. temperature data for SiC, Si₃N₄, ZrC coated C-C composite, and uncoated C-C. The Figure key notes whether the C-C composite was coated on a single side or on both sides. The data show no temperature dependence, which is usually an indication that the samples have high porosity. The SiC (two sides) is the least hydrogen permeable coating for the C-C composites measured to date. The permeation data for ZrC-coated C-C composite illustrate that of the coatings evaluated, the ZrC coated by the CVD method tends to degrade the C-C substrate. The permeation data for ZrC coated C-C are higher than even the uncoated C-C composite. Further characterization of the ZrC C-C coating system is continuing in order to better identify changes that are taking place that can cause an increase the permeation with respect to uncoated C-C.

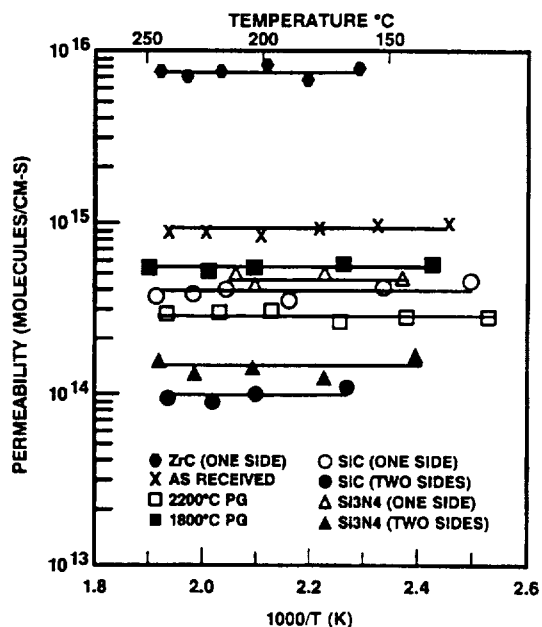


Figure 5. H₂ Permeability Vs. Temperature for Coated and Uncoated C-C Composites.

At low temperatures, the permeation of the Ni-coated C-C is 5×10^{10} molecules/cm-s, at approximately 200°C the permeation is 5×10^{10} molecules/cm-s; and at approximately 200°C the permeation is 2×10^{13} molecules/cm-s. The drastic increase in permeation at approximately 200°C was caused by spalling of the Ni coating. This conclusion was verified by post-test visual inspection.

Two Ti-Al alloys having nominal compositions of Ti-33Al-5Nb-1Ta (γ alloy) and Ti-14Al-20Nb-3.2V-2.0Mo (α -2 alloy) were coated with a Si-Al-oxide by the sol-gel process. The coated samples were annealed to 850°C before

any measurements were made. Hydrogen permeation measurements were performed on the coated and uncoated Ti-Al alloys, and the data are shown in Figure 6. The data show that the hydrogen permeability of the γ Ti-Al alloy is not very much affected by the 1.5 μm coating, while the permeability is drastically reduced for the coated α -2 Ti-Al alloy.

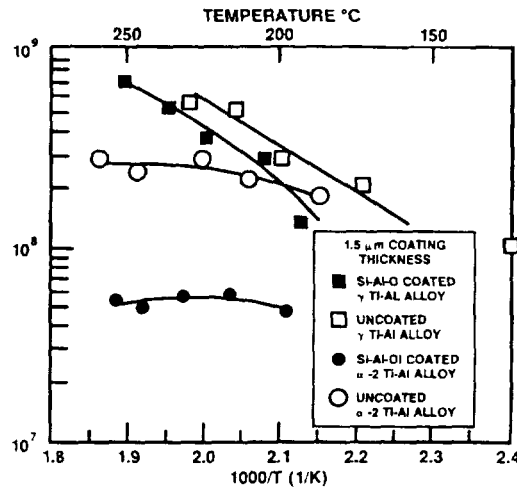


Figure 6. H₂ Permeability Vs. Temperature for Si-Al-Oxide Coated α -2 and γ Ti-Al alloys.

Ceramic Foams [31]

Today lightweight ceramics are finding many and varied applications due to their unique properties. These properties include high specific stiffness, high damping capacity, excellent dimensional stability, high thermal shock resistance, high surface area, low thermal conductivity, and low dielectric permittivity. This mix of properties makes the materials useful in either structural or functional applications such as high-temperature insulation, catalyst supports, chemical and moisture sensors, and as possible candidates for high-speed computer device packaging. Additionally, these porous materials offer a potential alternative for fabrication of composites by their infiltration with polymers, metals, fibers, or ceramics. Because of the ease of processing and their varied properties, these highly porous materials may lead to a new generation of lightweight ceramics and composites. Processing methods for cellular inorganic materials include foaming of molten glasses and cements, sintering of hollow glass spheres, and replication of polymer foams. Unfortunately, these processing methods are not reproducible, and materials with small, uniform cell size and with a tailored cell structure are very difficult to make.

Recently Fujii et al. [35] reported the use of a modified sol-gel process for making porous inorganic materials with tailored cell structure. The method applied the polymer foaming concept to sol-gel systems. Polymer foaming is performed by decomposition or evaporation of a foaming (Freon) agent followed by a rapid polymerization reaction to stabilize the foam structure. For this paper, the synthetic process of Fujii et al. [35] was used to synthesize SiO₂ ceramics having tailored cell structures for use as lightweight insulation materials. Characterization of these materials included: microstructure as a function of foaming process, density measurements, viscosity measurements as a function of time at different temperatures and varying pH, X-ray crystallography, dielectric constant measurements, and thermal diffusivity measurements.

A variety of cellular SiO₂ materials have been synthesized using a foaming sol-gel process and their properties have been characterized. The process uses the rapid viscosity change during gelation to stabilize the structure of a foamed silica sol. It was found that the properties of these porous oxides depend on the method of agitation and addition of Freon during the foaming process. However, in all samples, as the Freon concentration increased the percent porosity also increased and the density decreased. From 0 to 0.01 cc/g of Freon, the density ranged from 0.5 to 0.9 g/cc and the porosity ranged from 40 to 70%.

Dielectric constant measurements were also made on both sintered foams and incubated foams and are summarized in Table IV. The data show that the less dense samples have a lower dielectric constant when compared to the more dense samples.

Compression strength measurements on sintered cellular SiO₂ produced by the laboratory stirring process are shown in Table V. In all cases, except for the 0.005 cc/g of Freon samples, 10 to 20 samples were measured. The more dense samples are stronger (have a larger ultimate compressive strength). In the case of the 0.005 cc/g of Freon samples only two measurements were made, and the data is not accurate.

Table IV. Dielectric Constant for Cellular SiO₂ Taken at 10⁵ Hz.

Type of SiO ₂ foams	Freon conc. (cc/g)	ε
Sintered foams	0	1.72
	0.005	1.69
	0.01	1.52
Incubated foams	0	1.75
	0.005	1.63
	0.01	1.58

Table V. Ultimate Compressive Strength for Cellular SiO₂.

Freon conc. (cc/g)	Ultimate compressive strength (psi)
0	487 ± 192
0.005	133 (two samples)
0.01	251 ± 91

Thermal diffusivity data for sintered cellular SiO₂ are plotted in Figure 7. The scatter can be attributed to the irregular porosity of the samples. The data show a decrease in diffusivity with decreasing density.

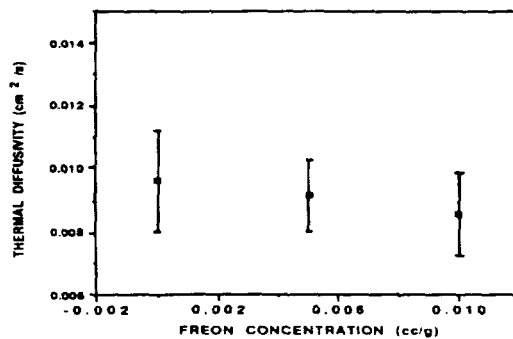


Figure 7. Thermal Diffusivity as a Function of Freon Concentration. Data taken at 25°C.

Incorporation Of Dyes In Silica Based Ceramics For Laser Applications [32-33]

In the past two decades, organic laser dyes have found wide use in different fields of science and technology including spectroscopy, optics, and lasers. The lasing media based on organic dyes may be in the form of solids, liquids, or gas. These lasing media cause spectral shifts of both absorption and emission and affect photochemical stability. They also alter the distribution between processes that the excited states may undergo. Although polymers are the earliest and the most common solid-state host for organic laser dyes, they have limited photostability and low thermal stability. Recently, sol-gel methods, with their low processing temperature, have made it possible to incorporate a dye into a transparent inorganic matrix. Embedding organic dyes into silica glass has significant advantages over the other types of matrixes. The silica glass is photochemically inert and can enhance the thermal stability of most organic dyes.

The sol-gel process was used to incorporate organic dyes including Rhodamine 6G (Rh6G), 2-(4-pyridyl)-5-(4-phenyl) oxazole (4PyPO) and the n-methyl tosylate salt of 2-(4-pyridyl)-5-(4-methoxy phenyl)oxazole (4PyMPO-MePTS) in silica gel. TGA and differential scanning calorimeter (DSC) analysis of the dye doped gels showed that the gel structure loses the adsorbed water molecules from room temperature to 150°C and decomposition of the dye molecules followed at the higher temperature. Absorption and emission of the dyes in the sol-gel glass matrix were also studied and compared with the results of the dyes in alcohol solution. The environments of the dye in silica were different than in alcohol solution.

TGA showed that all three of the dye-silica samples lost weight when heated to 600°C (Figure 8). This corresponds to a 20 to 25% weight loss. The approximately 5% weight loss below 150°C was due to the removal of physically adsorbed solvent molecules including surface water. The 15 to 20% weight loss up to ~600°C was due to the decomposition of residual organics and silanols. Above 600°C the weight loss was negligible. Figure 9 shows the DSC curves for the silica xerogels with and without the presence of dyes (the insertion is the DSC curve for 4PyMPO-MePTS itself). The curves indicate that the xerogels with dyes have a much broader exothermic peak between 250 and 350°C than silica itself, indicating that organic molecules are being oxidized. The figure also shows that silica gel has a much narrower endothermic peak at 150°C. In contrast, the silica samples that have the incorporated organic dye have much broader endothermic peaks. This result can be attributed to a combination of dye decomposition and silica dehydration.

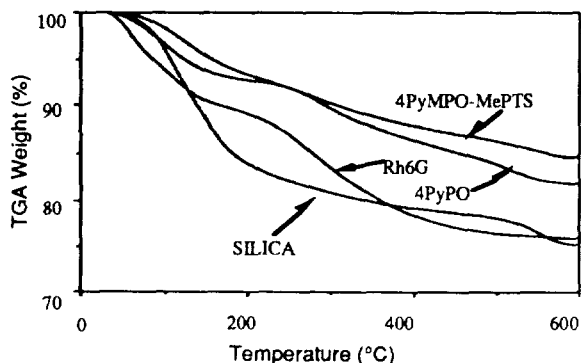


Figure 8. TGA Data for SiO₂ and SiO₂ With Incorporated Dyes.

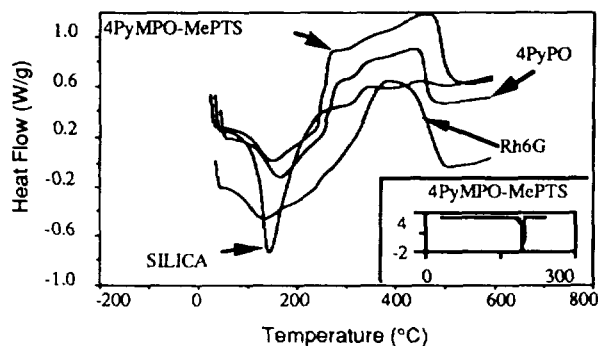


Figure 9. DSC Curves for Pure SiO₂ Gel and SiO₂ Gel With Incorporated Dyes.

Table VI summarizes the absorption and emission spectra of dyes in silica gel and solution. The experiments performed with Rh6G incorporated in silica gels have demonstrated that the silica matrix does not significantly alter the absorption maximum of the dye molecules when it is compared with the value in methanol. However, a slight blue shift (7 nm) in fluorescence spectra with respect to the methanol solution suggests that the silica gel is more polar, probably due to the remaining Me(OH)/H₂O solvent in the gel. Red shifts are observed for both absorption (6 nm) and emission (11 nm) spectra of 4PyMPO-MePTS in silica gel as compared with Et(OH)/H₂O solution. Since similar shifts are often observed in polar organic solvents [36], this may indicate that, in silica gel, the local environment around the dye is slightly less polar than an Et(OH)/H₂O solution.

Table VI. Emission and Excitation Characteristics of Rh6G, 4PyPO and 4PyMPO-MePTS in Silica Gel.

Dye	In sol-gel silica matrix			In solution	
	Fluorescence maximum	Absorption maximum	Fluorescence lifetime (rs)	Fluorescence maximum	Absorption maximum
Rh6G	552	522	12.5	559 in Me(OH)	523 in Me(OH)
4PyPO	493	-	12.5	-	325 in Et(OH)
4PyMPO-MePTS	568	408	10	562 in Et(OH)/H ₂ O	397 in Et(OH)/H ₂ O

For the 4PyPO dye, Ott et al. [37-38] reported that a significant spectral shift of absorption maxima in Et(OH)/HCl with respect to that in Et(OH) is due to the high reactivity of the nonbridging electrons on the pyridyl nitrogen atom for pyridine derivatives. Therefore, significant spectral shifts observed in silica gel compared to the solution spectra are due to the modification of dye chemistry in the initial sol and, subsequently into oxide gel.

Thermal analyzers (TGA and DSC) were used to study the thermal reaction of the gels with and without dyes. The TGA data indicated that the samples lost weight continuously until 600°C. The DSC data of the dye doped silica gel showed a broader endothermic peak than the silica gel itself, indicating the combination of silica dehydration and dye decomposition. Spectral shifts of the absorption and emission maxima to longer or shorter wavelengths were observed as compared to the dye solution spectra. This is attributed to a modification of the chemistry of the dyes with respect to their local environment during the incorporation of dye molecules into a liquid sol and, subsequently, into an oxide gel.

Ceramics for Radome Applications [34]

Ceramics based on monoclinic celsian ($\text{BaO} \cdot \text{Al}_2\text{O}_3 \cdot \text{SiO}_2$) can be useful in applications requiring high melting point, low thermal expansion, high thermal shock resistance, low dielectric constant and low $\tan \delta$, high frequency working capabilities, low and thermally stable dielectric constant, and low loss tangent. For example, celsian is a promising ceramic for use as a thermally stable dielectric and refractory material. Celsian has two polymorphs: the monoclinic and the hexagonal. The high-temperature polymorph, hexacelsian, undergoes a rapid and reversible transformation at 300°C from the hexagonal structure to an orthorhombic structure accompanying a significant volume change of approximately 3 to 4%. Therefore, this phase transformation in hexacelsian is detrimental in applications where the material is subjected to thermal cycling. Monoclinic celsian, on the other hand, does not undergo such a phase change. Unfortunately, hexacelsian readily forms during conventional solid-state processes at temperatures below 1590°C, and once this hexagonal structure is formed it is extremely difficult to transform to the desirable monoclinic phase. It would be desirable to provide a method for making pure monoclinic celsian at lower temperatures and shorter heating times without the use of contaminating additives.

Barium aluminosilicate (BAS) powders have been synthesized by the sol-gel process. X-ray analysis and thermal analysis including differential thermal analysis (DTA), DSC, and TGA, have been performed to characterize the powders. Also the effects of catalysts have been examined through an appropriate drying and sintering schedule for the formation of monoclinic celsian. It has been shown that the type of acid used as a catalyst controls the formation of polymorphs (hexagonal vs. monoclinic) of BAS ceramic. Because synthesis of monoclinic celsian by the sol-gel process requires relatively low temperatures and no seed crystals, it is less expensive, more manufacturable, and easier to scale up than other synthesis processes.

The scanning electron micrographs of the gels prepared from the sol-gel process using HCl, HF, and acetic acid catalysts of the hydrolysis process show significant morphological differences. The gels catalyzed with HCl and acetic acid appeared to be heterogeneous with rod-shaped barium salt that had crystallized during drying, while HF-catalyzed gel showed relatively good homogeneity with larger surface area.

Figure 10 shows composite curves of TGA and DTA data for the three samples. Although the total weight loss was dependent upon the method of synthesis, the average weight loss for all samples ranges from 20 to 30 wt % over the temperature range of 25 to 1000°C. It is interesting to notice that the gel catalyzed with HF undergoes BAS formation via a different mechanism than the gels catalyzed with HCl or acetic acid. The change in slope of the DTA baseline at 815°C in Figure 10(c) is indicative of a change in specific heat capacity, which corresponds to the gel-to-glass transition temperature. Around 1200°C, there is no significant weight change. Therefore, the broad exotherm shown in Figure 10(c) near this temperature was attributed to crystallization, and the endothermic peak at 1220°C is due to sample melting.

The X-ray pattern of BAS powder catalyzed with HCl and acetic acid show hexagonal phase formation even after extensive heat treatment. While the X-ray diffraction pattern for the gels catalyzed with HF showed the hexacelsian predominantly at low temperatures, the monoclinic phase dominated the X-ray powder pattern after annealing at 1200°C for many hours.

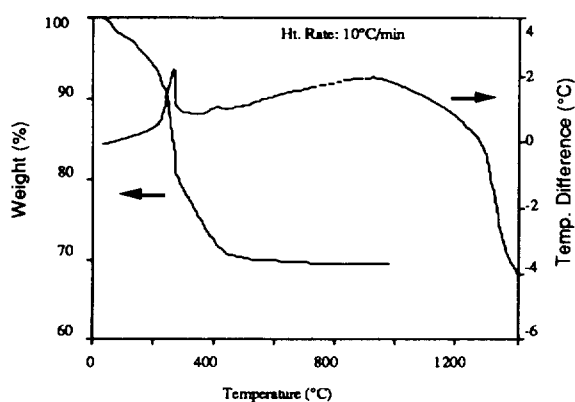


Figure 10(a). TGA and DTA Curves for the Gel Catalyzed With HCl.

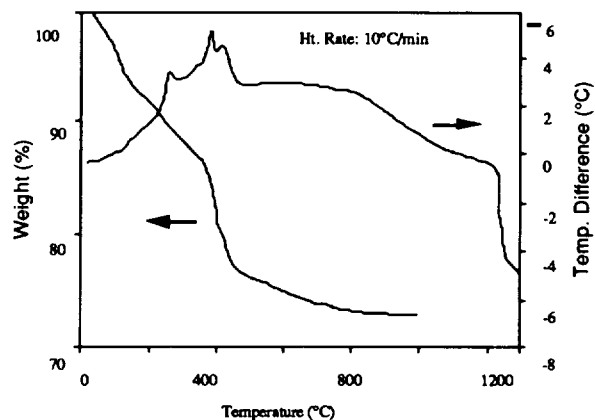


Figure 10(b). TGA and DTA Curves for the Gel Catalyzed With Acetic Acid.

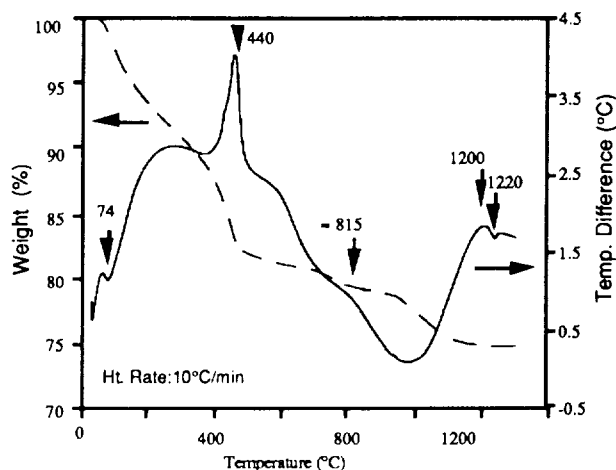


Figure 10(c). TGA and DTA Curves for the Gel Catalyzed With HF.

CONCLUSION

The sol-gel process offers great advantages for making films coatings, bulk ceramics, foams, and monoliths. This synthetic process offers control of microstructure and material properties during the entire process and can be commercialized quite readily due to the ease in scale up, versatility of materials, selectivity of properties, and low cost. The sol-gel process and the new materials that can be obtained by its use have tremendous commercial potential. Among potential commercial markets are electronics, automobiles, home insulation, toys, cosmetics, glass products, and consumer ceramics. This paper has presented only some examples of the materials that can be produced by the sol-gel process. The real commercialization of sol-gel derived materials can only be achieved if material scientists, chemists, and production engineers address the overall process and work together to remove possible obstacles .

REFERENCES

1. D. M. Ray and R. Royu, *Am. Mineralogist* 40, 1147 (1955).
2. M. Decottignies, J. Phalippou, and J. Zarzycki, *J. Mater. Sci.* 13, 2605 (1978).
3. S. J. Teichner, G. A. Nicolaon, M. A. Vicarini, and G. E. E Gardes, *Inorganic Oxide Aerogels, Advances in Coll. and Interface. Sci.* 5, 245 (1976).

4. I. M. Thomas, & J.J. Tillman, Ger. Offen. DE 3,247,1173, August 4, 1983; assigned to Owens-Illinois, Inc.
5. B. E. Yoldas, and T. W. O'Keeffe, *Appl. Opt.* 18, 3133 (1979).
6. C. J. Brinker, D. E. Clark, and D. R. Ulrich, Eds., *Mat. Res. Society Symposia Proceedings*, Vol. 32, NY: Elsevier Science Publishing Co. In., (1984).
7. L. C. Klein, Ed, *Sol-Gel Technology for Thin Films, Fibers, Preforms, Electronics and Speciality Shapes, Materials Sciences and Process Technology Series*, Noyes Publications, NJ, 1988, Part II. pp 50-136
8. W. C. La Course, *Better Ceramics Through Chemistry. Mat Res. Soc. Symp. Proc.* Vol. 32 (C. J. Brinker, D. E. Clark and D. R. Ulrich, Eds.), pp 53-58, North Holland, NY (1984).
9. W. Mahler, and M. F. Bechtold, *Nature* 285: 27-28 (1980).
10. L. C. Klein, Ed. *Sol-Gel Technology for Thin Films, Fibers, Preforms, Electronics and Speciality Shapes, Materials Sciences and Process Technology Series*, Noyes Publications, NJ, 1988, Part IV. 10, pp 200-222.
11. J. D. Mackenzie, in: *Ultrastructure Process of Ceramics, Glasses and Composites* (L. L. Hench and D. R. Ulrich, Ed), John Wiley and Sons, NY, 1984, pp 15-26
12. G. Dardel, S. Henning, and L. Svensson, European Patent Specification 0018 955 B 1, Date of Filing 17.4.1980, Date of Publication 1.12.1982.
13. P. H. Tewari, A. J. Hunt, and K. D. Lofftus, *Advances in Production of Transparent Silica Aerogels*, in: *Aerogels, Springer Proceedings in Physics 6*, J. Fricke (Ed.), Springer Verlag, Heidelberg, Berlin, New York, Tokyo (1986).
14. F. J. Broecker, W. Heckmann, F. Fischer, M. Mielke, J. Schroeder, and A. Stange, *Structural Analysis of Granular Silica Aerogels*, in: *Aerogels, Springer Proceedings in Physics 6*. J. Fricke (Ed.), Springer Verlag, Heidelberg, Berlin, New York, Tokyo (1986).
15. E. M. Rabinovich, *J. Non-Cryst. Solids*, 71, 1985, pp 187-193.
16. D. W. Johnson, Jr., *J. Amer. Ceram. Soc.*, 66, 1983, pp 683-688.
17. R. G. Dosch, *Mater. Res. Soc. Symp. Proceed.*, 32, 1984, pp 199-204.
18. K. Oda, and T. Yoshio, *J. Mater. Sci. Lett.*, 5, 1986, pp 545-548.
19. L. C. Klein, Ed., *Sol-Gel Technology for Thin Films, Fibers, Preforms, Electronics and Speciality Shapes, Materials Sciences and Process Technology Series*, Noyes Publications, NJ, Part V, Section 15, pp 303-329.
20. F. Uchikawa, H. Zheng, K. C. Chen, and J. D. Mackenzie, *Materials Research Society*, 1988, pp 89-92.
21. S. Kramer, G. Kordas, *High-Temperature Superconductors II* (Ed. D. W. Capone II, W. H. Butler (B. Batlogg, C. W. Chic) *Materials Research Society*, 1988, pp 67-68.
22. J. Covino and G. E. McMannis, *Material Research Society Symp. Proc.*, *Better Ceram. Chem.* 3, Vol. 121, pp. 553-556, 1988.
23. J. Covino and A.C. Finlinson, *5th Ultrastructure Processing of Ceramics, Glasses, Composites, Ordered Polymers and Advanced Optical Materials*, February 1991.
24. J. Covino, F. DeLaat, and R. Welsbie, *3rd International Workshop, "Glass and Glass Ceramics from Gels,"* Montpellier, France, 12-14 September 1985.
25. J. Covino, F. DeLaat, and R.A. Welsbie, *Mater. Res. Soc. Symp. Proc.*, Vol. 73, No. 2, *Better Ceram. Chem.*, pp. 135-142, 1986.
26. J. Covino, F. DeLaat, and R. Welsbie, *J. of Non-Cryst. Solids*, Vol. 82, No. 1-3, pp. 329-42, June 1986.
27. J. Covino and C. Wilson, *Third International Conference on Ultrastructure Processing of Ceramics, Glasses and Composites, Ultrastructure Processing of Advanced Ceramics*, pp. 981-993, John Wiley & Sons, Inc., 1988.
28. J. Covino and A. Finlinson, *1st international Symposium on Environmental Effects on Advanced Materials*, ADVMAT/91 June 1991.
29. J. Covino, J. Dykema and A. Finlinson, *Minerals, Metals and Materials - High Performance Composites for the 1990's*, pp. 171-182, June 1990.
30. J. Covino, K. Klemm, and J. Dykema, *Mat. Res. Soc. Symp. Proc.* Vol. 175, pp 187-192.
31. J. Covino and A.P. Gehris Jr., *Material Research Society Symposium, Mech. Prop. Porous Cell. Mater.*, Vol. 207, pp. 129-134, 1991.
32. B. Abramoff, J. Covino, M.E. Hills and R. Chaundhuri, *Chemical Processing of Advanced Materials*, John Wiley & Sons, Inc., pp 973-979, 1992.
33. I. Lee, J. Covino, and M. Seltzer, *Better Ceramics through Chemistry V, Material Research Society Proc.* Vol 271, pp 657-661 (1992).
34. I. Lee and J. Covino, *Sol-Gel Synthesis of Barium Aluminosilicate Ceramics*, accepted for publication in the *Material Research Bulletin*, Sept. 1993.
35. T. Fujiu, G.L. Messing and W. Huebner, *J. Am. Ceram. Soc.* 73 (1), pg. 85 (1990).
36. D. Avnir, V.R. Kaufman and R. Reisfeld, *J. Non-Cryst. Solids*, 74, 395 (1985).
37. D.G. Ott, F.N. Hayes and V.N. Kerr, *J. Am. Chem. Soc.*, 78, 1941 (1956).
38. D.G. Ott, F. N. Haye, E. Hansbury and V.N. Kerr, *J. Am. Chem. Soc.*, 79, 5448 (1957).

DEPOSITION OF TANTALUM CARBIDE COATINGS
ON GRAPHITE BY LASER INTERACTIONS

2471
P. 5

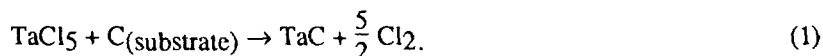
Dr. James Veligdan,
D. Branch, P.E. Vanier and R.E. Barletta
Engineering Research and Applications Division
Department of Nuclear Energy
Brookhaven National Laboratory
Upton, NY 11973

ABSTRACT

Graphite surfaces can be hardened and protected from erosion by hydrogen at high temperatures by refractory metal carbide coatings, which are usually prepared by chemical vapor deposition (CVD) or chemical vapor reaction (CVR) methods. These techniques rely on heating the substrate to a temperature where a volatile metal halide decomposes and reacts with either a hydrocarbon gas or with carbon from the substrate. For CVR techniques, deposition temperatures must be in excess of 2000° C in order to achieve favorable deposition kinetics. In an effort to lower the bulk substrate deposition temperature, the use of laser interactions with both the substrate and the metal halide deposition gas has been employed. Initial testing involved the use of a CO₂ laser to heat the surface of a graphite substrate and a KrF excimer laser to accomplish a photodecomposition of TaCl₅ gas near the substrate. The results of preliminary experiments using these techniques are described.

INTRODUCTION

The use of refractory carbide coatings for protecting materials from corrosive gases at high temperatures or to provide surface toughness is well established. Recently, we have become involved with the use of these materials for the protection of graphites and carbon-carbon composites from attack by hot hydrogen at high temperatures [1]. Typically, these coatings have been applied to the carbon substrate using either conventional chemical vapor deposition (CVD) or chemical vapor reaction (CVR) techniques. The latter process has proven quite effective in producing dense, adherent and protective coatings. In this process a metal halide vapor reacts with carbon in the substrate to produce the carbide. For a refractory carbide such as tantalum, the reaction is



This reaction typically occurs at temperatures in the range of 1700 to 2600 K, depending on the carbide with coating thicknesses on the order of 10 to 100 micrometers [2]. Since these coatings are produced at high temperatures, the grain size is quite large.

In an effort to reduce the overall substrate temperature as well as to provide a means to perform "spot repairs" for coatings, work has been initiated to develop an alternative coating method which could achieve the same grain morphology and coating stoichiometry as the CVR process. Thermochemical data [3,4] indicate that high surface temperatures are necessary for the carbide formation to proceed. Since the region of carbon diffusion is small, however, bulk heating of the substrate is not required. Thus, the use of surface heating of the carbon with an infrared laser was chosen. Further, experiments on the photo-assisted formation of TaO from TaCl₅ indicate the efficacy of UV photons in the photo-decomposition of the starting metal halide [5,6]. Given these considerations, a coating process in which the metal halide is decomposed by ultraviolet radiation while the surface is heated using an infrared laser could result in coatings which are effectively the same as high temperature CVR coatings while being made at lower overall substrate coating temperatures. In order to test this hypothesis, initial coating studies have been performed using the TaC/graphite system.

EXPERIMENTAL

The basic experimental setup consisted of a gas handling system for the TaCl₅ vapor and a deposition cell (see Figure 1). The TaCl₅ vapor was produced by heating solid TaCl₅ in a reservoir. The vapor pressure in the reservoir was calculated using the following relationship between 363 and 490 K [7]

$$\text{Log}\{P(\text{Torr})\} = 12.323 - \frac{4729}{T} . \quad (2)$$

The gas from the reservoir was throttled through a heated needle valve and ducted to the deposition cell where it was directed onto the graphite sample through a nozzle. The graphite sample was attached to a heated stage whose temperature could be varied between room temperature and 700 K. Light from a carbon dioxide laser was focused on the graphite sample through a KBr window. Light from an excimer laser was admitted through a quartz window at 90° to the CO₂ beam. The excimer laser used was a KrF laser operating at 248 nm. This line was chosen since it is coincident with the absorption maximum of the TaCl₅ [6]. The graphite was locally heated with a 3.5 W, cw-CO₂ laser focused to ~ 1 mm in diameter.

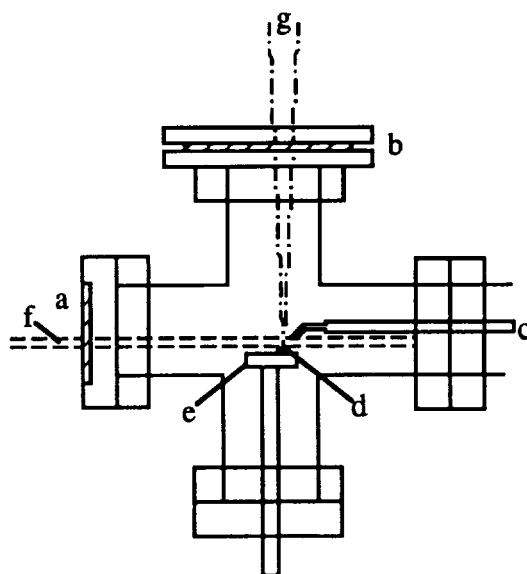


Figure 1. Schematic of deposition cell. a. Silica window; b. KBr window; c. TaCl₅ inlet nozzle; d. Graphite substrate; e. Heated sample pedestal; f. Excimer laser beam; g. CO₂ laser beam.

Experiments were performed by heating the deposition tube to a temperature some 10 to 20 K higher than the reservoir temperature. The sample in these tests consisted of a small piece of graphite (0.16 cm) embedded in a refractory disk and attached to the pedestal. The substrate pedestal was also heated at this time to the test temperature. Gas flow was then initiated by opening the reservoir needle valve and irradiation (infrared alone or infrared plus UV) was begun. Throughout the course of the experiment, system pressure, reservoir and substrate temperatures and excimer laser power were monitored. Upon completion of the test the gas flow was stopped and the apparatus was cooled to room temperature. The graphite sample was then examined using scanning electron microscopy (SEM) and energy dispersive x-ray analysis (EDX).

An initial experiment was also performed with a graphite disk in place of the heated platform. In this test, only infrared radiation was used. Since the graphite remained at room temperature, TaCl₅ condensation on the disk in areas not heated by the laser was expected. In other respects, the experimental procedure was identical to that described above.

RESULTS AND DISCUSSION

Infrared Irradiation

The initial experiment on the graphite disk resulted in a limited thermal decomposition of the pentachloride in the region heated by the laser. During the course of CO₂ irradiation (about 5 minutes), the temperature of the area heated by the laser appeared to decrease dramatically. This was evidenced by a change in color of the graphite at the laser focus from bright white to dull orange to dark during the test. These changes indicate that the temperature went from a point where decomposition and carbide formation is thermochemically favorable to a temperature where only condensation of the chloride is expected. EDX examination revealed that the region irradiated by the CO₂ laser was in fact Ta rich and Cl deficient with respect to other areas on the disk. The presence of TaC could not be confirmed in this test.

Irradiation of graphite on the heated platform proved much more successful. With the platform at 573 K only minimal chloride was deposited. This was presumably due to thermal decomposition of the pentachloride at the surface resulting in traces of a lower vapor pressure chloride condensing during the course of the experiment. Direct heating of the pentachloride molecule itself by the 10.6 μm radiation can be eliminated from a consideration of the vibrational spectroscopy of the molecule [8]. EDX analysis was used to subtract the contribution of this chloride and the graphite background and, when this was done, only an x-ray spectrum of Ta remained (Figure 2). Thus, with CO₂ radiation alone, we observed complete thermal decomposition of the pentachloride can be accomplished leaving only Ta on the surface. The substrate surface temperature in this case was insufficient to cause a reaction of the Ta with the graphite substrate.

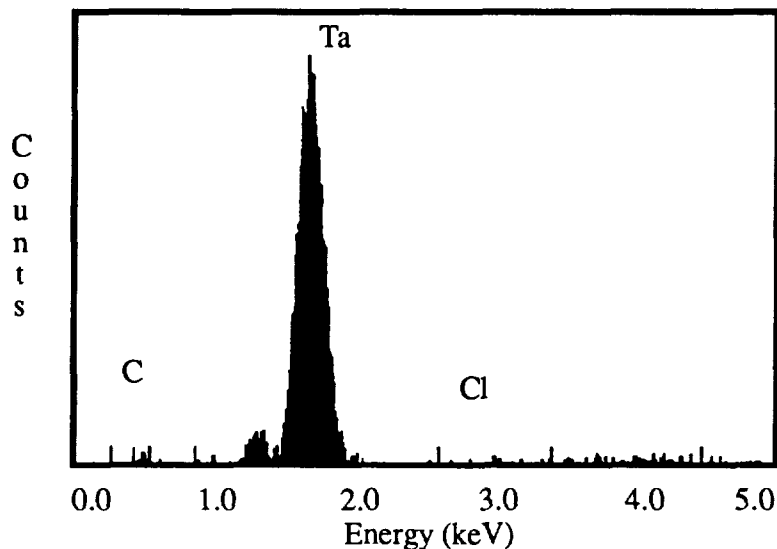


Figure 2. EDX spectrum of deposit on graphite disk after irradiation with infrared photons alone. The background contributions to this spectrum have been subtracted using the spectrum of an unirradiated graphite specimen under identical conditions. The deposition time in this experiment was 30 s.

Infrared plus Excimer Irradiation

Under experimental conditions identical to that of the infrared irradiation of a heated graphite substrate described above, the coincident irradiation of the gas phase pentachloride stream with excimer light at 248 nm resulted in the production of a coating which contained both Ta and C. Figure 3 shows an EDX spectrum of this coating after background subtraction. In this experiment, the UV flux density was on the order of 2 W/cm² as a result of irradiation with an unfocused excimer light. The pulse energy was ~ 145 mJ pulse and the pulse duration was on the order of 20 ns. The results of this experiment when compared with those of infrared irradiation alone indicate that UV absorption by the TaCl₅ vapor is instrumental in allowing the carbide formation to proceed. The TaC film formed by this process is quite fine grained (on the order of a few micrometers). Figure 4 shows an SEM photograph of the film after 10 minutes of deposition. Although film coverage appeared to be uniform across the graphite surface, holes in the coating are evident at high magnification. Detailed characterization and testing of this coating has not been performed at this time. It should be noted that the grain size of these initial coatings is much smaller than that seen in the TaC films produced by the process described in Reference 2.

The photon flux density in these experiments was approximately three orders of magnitude higher than that used in the photo-CVD production of TaO [6]. Indeed, the laser power used is more consistent with multiphoton dissociation processes [9]. In those experiments, photodissociation of a variety of metal halides and carbonyls as well as other organometallic compounds was found to proceed in a step-wise fashion, ultimately producing electronically excited metal atoms. For photons at 248 nm, it can be readily calculated from thermochemical data [3] that a minimum of 2 photons would be necessary to completely dissociate TaCl₅. Such a process is expected to result in photon emission from the Ta(I). We are currently in the process of investigating the photophysics of this system.

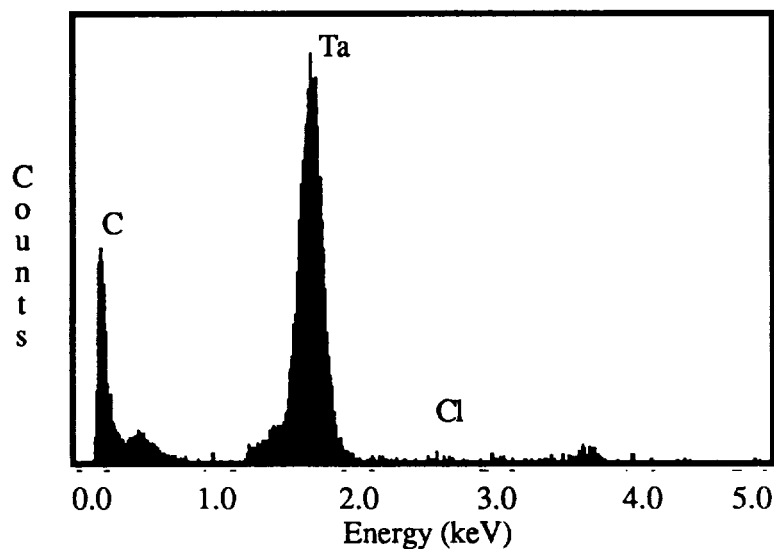


Figure 3. EDX spectrum of deposit on graphite disk after irradiation with both infrared and UV photons. The background contributions to this spectrum have been subtracted using the spectrum of an unirradiated graphite specimen under identical conditions. The deposition time in this experiment was 30 s.

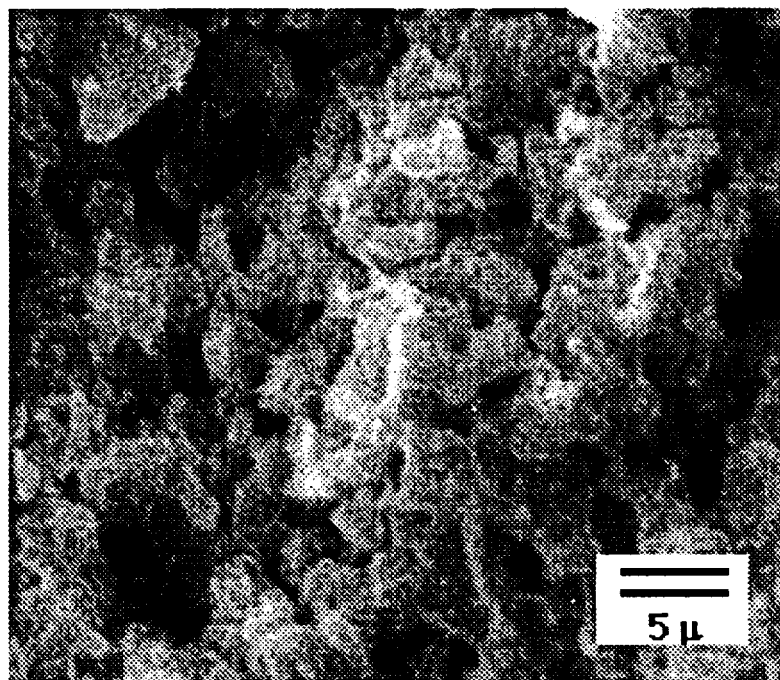


Figure 4. SEM photograph of TaC coating on graphite after 10 minute deposition (2000 X).

CONCLUSIONS

The results of these initial experiments indicate that it is possible to produce refractory metal carbides at very low substrate temperatures (< 700 K) using a two laser process. The photochemical process produces carbides via a CVR-like reaction in which the carbon source is the substrate itself. This carbide formation reaction has only been observed thermally at temperatures almost 2000 K higher. The UV photons in this carbide reaction give rise to dissociation of the halide reactant while infrared photons cause heating of the immediate substrate surface. We are currently in the process of investigating the details of the process (photochemistry, photophysics, deposition rate, coating characteristics and hydrogen permeability, etc.) and expect to extend our investigations of this multiple laser coating process to other coating systems.

ACKNOWLEDGEMENTS

The authors would like to thank R. E. Davis for his helpful discussions of the thermochemistry of the system as well as J. Adams for his assistance with the SEM and EDX work. This work was carried out under the auspices of the U. S. Department of Energy under Contract No. DE-AC02-76CH00016.

REFERENCES

1. R. Barletta, P. Vanier, J. Adams and J. Svandrlik, Carbon Corrosion in Hydrogen - the "Midband" Problem Revisited, edited by M. S. El-Genk and M. D. Hoover, 10th Symposium on Space Nuclear Power and Propulsion, 1993.
2. Union Carbide Advanced Ceramics Technical Information Bulletin, Metal Carbide Coatings on Graphite : NbC, TaC, TiC and ZrC, no date.
3. O. Kubashewski and C. B. Alcock, Metallurgical Thermochemistry, 5th ed., (Pergamon Press, Oxford, England, 1983).
4. H. Schafer and F. Kahlenberg, *Z. Anorg. Allgem. Chemie*, **305**, 178-89 (1960).
5. S. Tanimoto, M. Matsui, M. Aoyagi, K. Kamisako, K. Kuroiwa and Y. Tarui, *Jap. J. Appl. Phys.*, **30** (3A) L330-33 (1991).
6. M. Matsui, S. Oka, K. Yamagishi, K. Kuroiwa and Y. Tarui, *Jap. J. Appl. Phys.*, **27** (4) 506-11 (1988).
7. Gmelin Institute, Gmelin Handbook of Inorganic Chemistry, System Number 50, Ta [B1], (Weinheim, Verlag Chemie, 1970) p. 117.
8. I. R. Beattie and G. A. Ozin, *J. Chem. Soc. (A)*, **1969**, 1691-3; R. A. Walton and B. J. Brisdon, *Spectrochim. Acta*, **23A**, 2489-92 (1967).
9. Y. Nagano, Y. Achiba and K. Kimura, *J. Phys. Chem.*, **90**, 1288-93; D. P. Gerrity, L. J. Rothberg and V. Valda, *J. Phys. Chem.* **87**, 2222-5 (1983); Z. Karny, R. Naaman and R. N. Zare, *Chem. Phys. Lett.*, **59**, 33-7 (1979).

536-27
2472
P. 6

Development of a Unique Polyurethane Primer/Topcoat

Howard L. Novak
USBI Company
P.O. Box 21212
Kennedy Space Center, Florida 32815

James M. Klotz
Coatings For Industry
319 Township Line Road
Souderton, Pennsylvania 18964

ABSTRACT

USBI Company, a Division of Pratt & Whitney Government Engines and Space Propulsion, is involved in corrosion and environmental research and development activities both at their headquarters in Huntsville, Alabama and their Florida Operations at Kennedy Space Center, Florida. The programs involve the development of environmentally compatible materials that improve the corrosion protection of expensive Solid Rocket Boosters (SRB) that are part of the Space Shuttle systems developed and managed by Marshall Space Flight Center in Huntsville, Alabama. Coatings For Industry, a paint manufacturer in Souderton, PA helped formulate and produce the first lot of BOOSTERCOAT paint. High strength aluminum aerospace flight hardware exposed to harsh seacoast environments and seawater immersion presently uses high volatile organic compound (VOC) chromated and lead bearing primers and epoxy topcoats for corrosion protection. Epoxy paint tends to be brittle and has relatively low Ultraviolet (UV) exposure resistance. A unique, environmentally compatible, non-lead/non-chromated, low VOC polyurethane single coat (primer/topcoat) trade named BOOSTERCOAT® has been developed for excellent corrosion protection, flexibility, adhesion, chemical and solvent resistance properties. This report will discuss the development of BOOSTERCOAT® and the potential opportunities for commercial use in the energy, transportation, chemical, maritime, structural fields.

INTRODUCTION

USBI Company is responsible for the assembly and refurbishment of the non-motor components of the Solid Rocket Booster (SRB) as part of the Space Shuttle system shown in Figure 1, and which is developed and managed by Marshall Space Flight Center in Huntsville, Alabama. Programs are underway to develop and evaluate environmentally compliant coatings for use on aluminum alloy and high strength steel alloy aerospace flight hardware in order to mitigate corrosion and ultimately extend the useful service life of these unique and expensive structures. The initial study focused on the replacement of high VOC, chromated / lead bearing epoxy primers with that of an environmentally compatible polyurethane single coat primer/topcoat. Coatings For Industry (CFI) located in Souderton, Pennsylvania helped formulate and manufacture the unique polyurethane single coat primer/topcoat. A significant joint effort was required between USBI and CFI in order to establish a production test article in a relatively short time frame. The new coating had to be compatible with the application of special thermal protective system (TPS) materials that coat the majority of SRB non-motor components. Operations such as robotic sanding Figure 2, vapor blast and vacuum cleaning and finally the spraying of TPS materials that contain aggressive solvents were all severe tests that the new paint system would have to endure. Launch vehicles located by the ocean are also subject to harsh seacoast environments before launch (sitting on the launch pad for months at a time, in close proximity to the ocean) and immersion after splashdown at sea and tow back to the refurbishment facility. Thus the coating, trade named BOOSTERCOAT®, was developed for excellent corrosion protection, flexibility, adhesion, abrasion resistance, chemical and solvent resistance and productivity enhancing electrostatic spray and plural component/air assisted airless spray capabilities. These same environmentally compatible and operationally desirable properties are needed for coating structures of fossil and nuclear power plants, also chemical processing plants and transportation equipment such as railcars, tractor trailers and earth moving equipment. The same paint resin system has also been tested as graffiti resistant for architectural structures and will sustain the use of methylene chloride solvent for removing the graffiti without removing the basecoat.

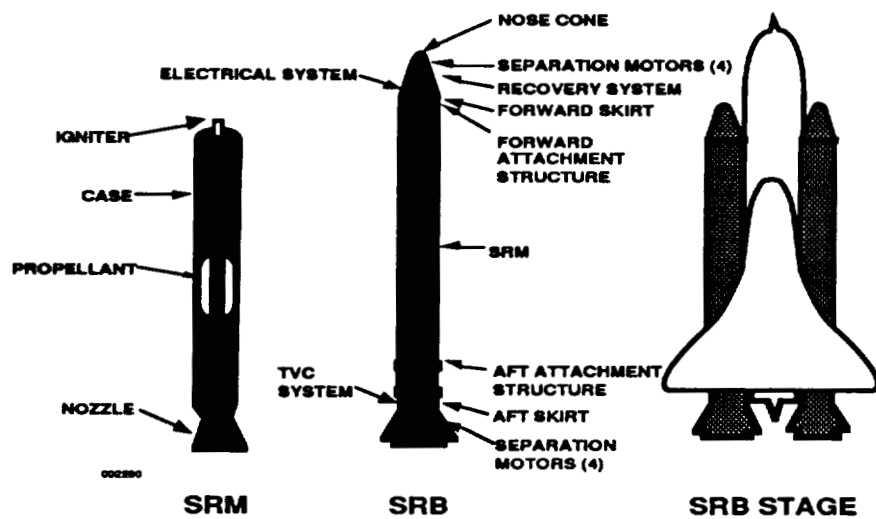


Figure 1 Space Shuttle's SRB

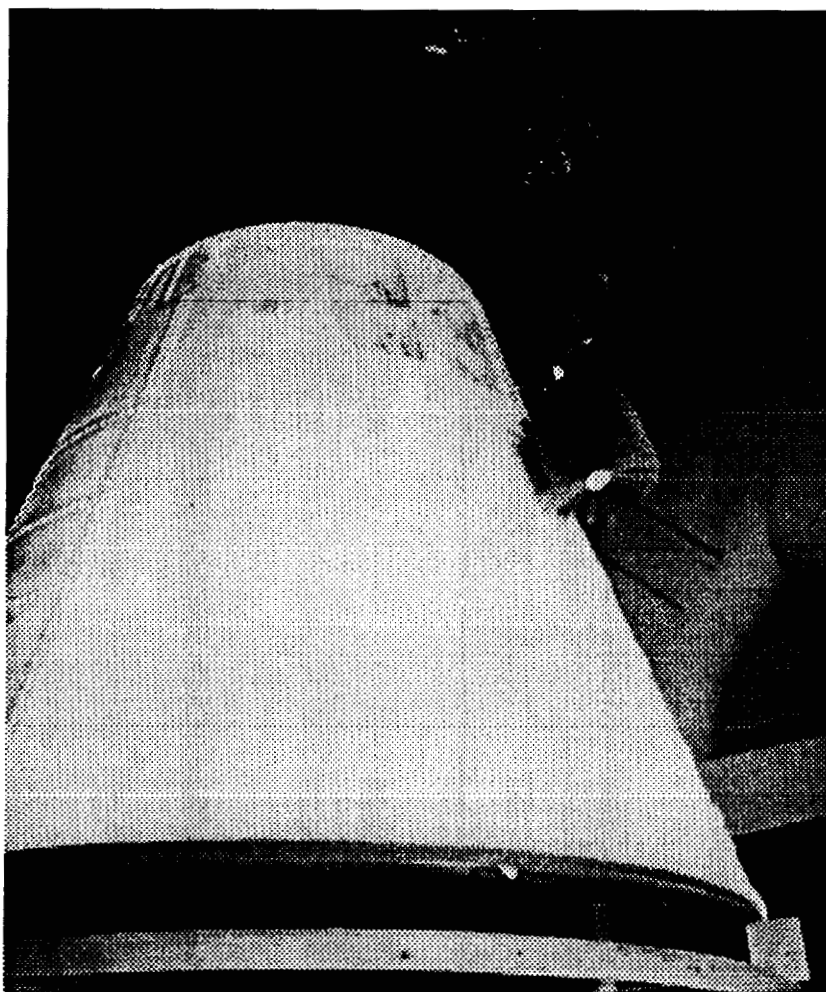


Figure 2 Robotic Sanding

DISCUSSION

Neat Resin Evaluation

The first phase of this program involved the selection and screening of eight resin systems consisting of saturated polyester and polyester polyols that were applied to deoxidized and chromate conversion coated 2219-T87 test panels and also to coated 4130 and 4340 high strength low alloy steel materials.. Specimens were allowed to cure for seven days at room temperature and were then checked for adhesion using ASTM D-3359⁽¹⁾(Adhesion by Tape Test) procedures. Results of adhesion tests were 5B or 4B rating for all resin systems, where 5B corresponds to no removal of the coating and 4B corresponding to small flakes of the coating that are detached at intersections with less than 5% of the area is affected, after the tape is pulled from the coating. The eight resin systems were also applied to 2024-T0 test panels and bent 180 degrees over a mandrel for flexibility testing. Chemical and solvent resistance testing consisted of the following: immersion of the test panels in 15% hydrochloric acid and 31% sodium hydroxide for 96 hours. Methyl ethyl ketone (MEK) and methylene chloride were also rubbed 100 times (200 passes) using a saturated cotton rag with firm finger pressure. From these initial screening tests, two resin systems were then selected for further evaluation.

Pigmented Resin Evaluation

Various environmentally compatible corrosion inhibiting pigments were then mixed with the two candidate resins and applied 0.003”(0.08mm) dry film thickness to deoxidized and chromate conversion coated 2219-T87 test panels and allowed to cure for seven days at room temperature. Initial critical pigment volume concentration (CPVC) was determined by establishing high and low limits through manufacturer’s pigment volume concentration (PVC) recommendations and other relevant literature⁽²⁾, then exposing those panels to salt spray testing. Panels were scribed with an “X” through the coating to substrate, and then placed in a 5% neutral salt spray solution in accordance with ASTM B-117. Additional scribed panels were placed on beach exposure racks located at NASA - Kennedy Space Center facilities as shown in Figure 3. Photos of the salt spray panels were taken weekly and Figure 4 shows coating #1 after 2000 hours of exposure.

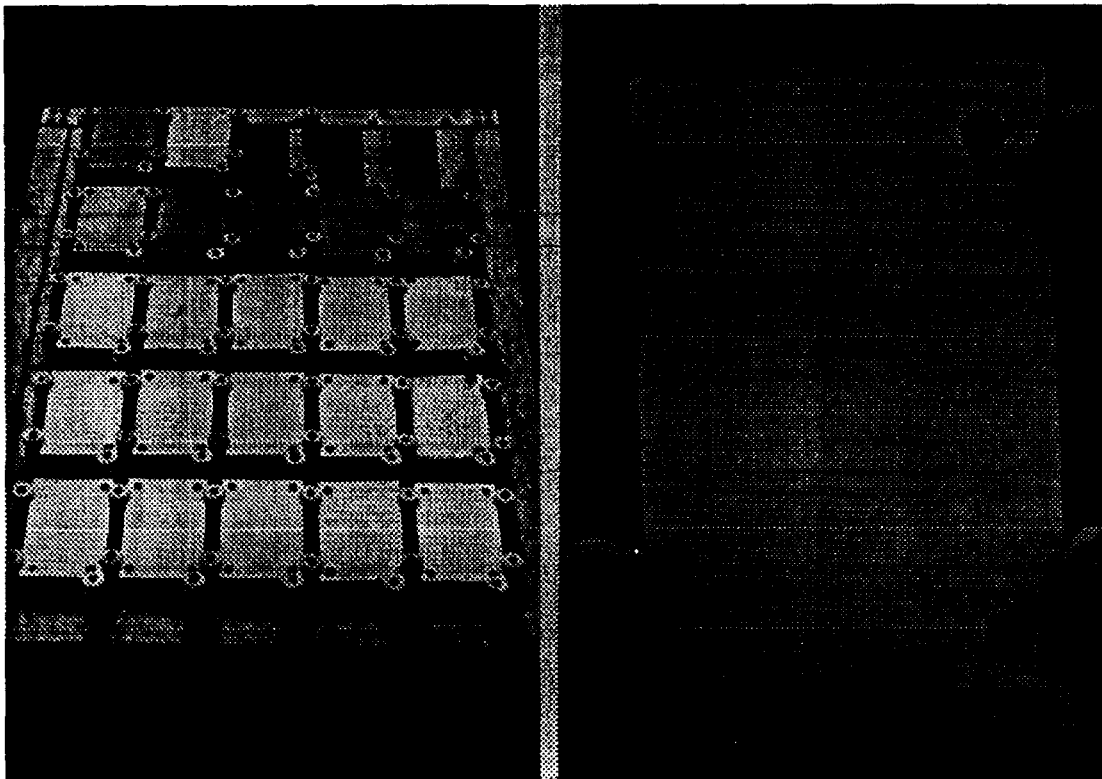


Figure 3 Beach Exposure Racks and Panel

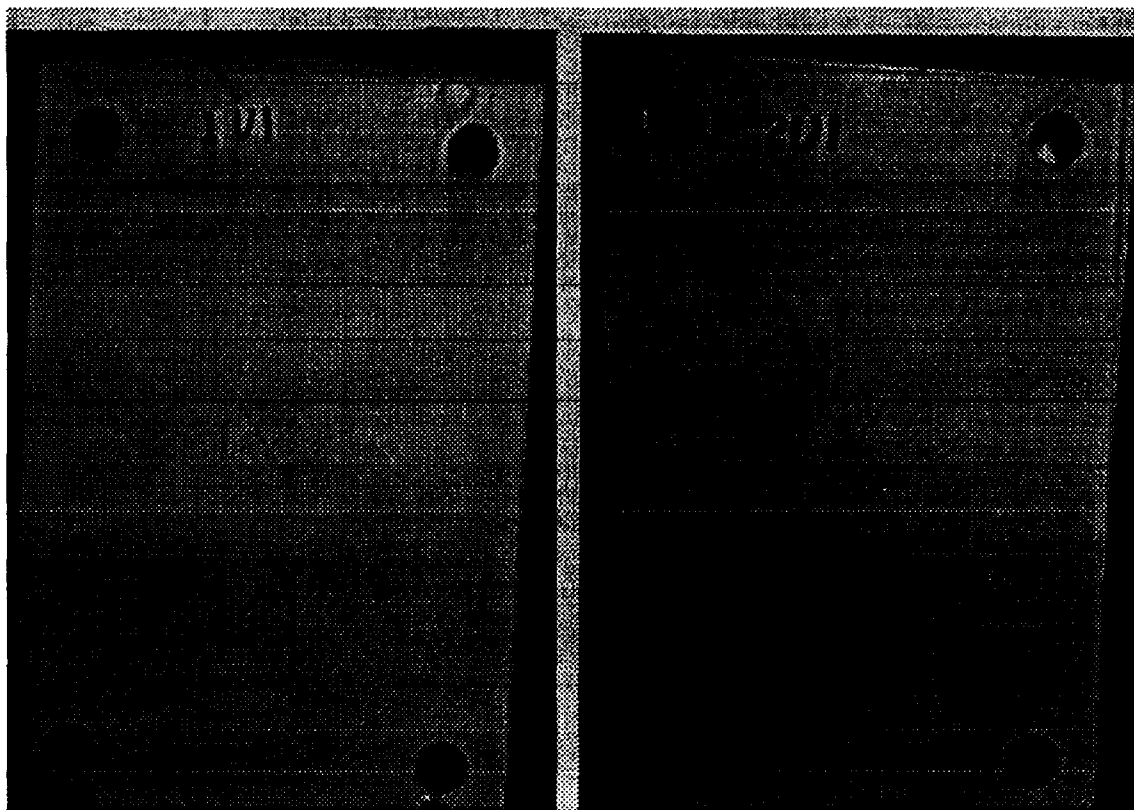


Figure 4 Booster Coat After 2000 Hours Salt Spray

Results of salt spray tests showed that resin #1 outperformed resin #2 using visual standards outlined in ASTM D-714 (Standard Test Method for Evaluating Degree of Blistering of Paints). This test method provides a standard procedure for describing the size assessed on a 0-10 scale, with "No.10"-no blistering, No.8 representing the smallest size blister easily seen by the unaided eye. Blister standards Nos.6, 4, and 2 represent progressively larger sizes. Blister density of an area is described as : few, medium, medium dense and dense, using photographic reference standards as the guide. Beach exposure testing confirmed the results obtained by ASTM B-117, although taking many more months for results. A study was initiated to evaluate the optimized coatings using electrochemical impedance spectroscopy (EIS) as a method for short term testing to predict long term performance. EIS measurements were made using an EG&G PARC 273A potentiostat interfaced to a EG&G Model 5210 lock-in amplifier; the system was computer interfaced for scanning and data manipulation (Figure 5). A three electrode cell configuration developed by EG&G and denoted as the Flat Cell and consisted of a Pyrex glass cylinder body with polypropylene end caps and working electrode clamping system. The reference electrode was silver and the reference electrode solution was silver chloride / saturated potassium chloride. The counter electrode was platinum plated rhodium. The working electrode sealing gasket was knife edged teflon with an exposed area of 1 cm^2 . Impedance scans were made between 100 kHz and 10 mHz, with occasional excursions to 1 mHz. An applied voltage amplitudes of 10-20 mV were utilized for the tests. As can be seen in Bode plots (Figures 6 and 7) very little change in impedance as related to ionic pore resistance occurred in a year and further substantiates the results found in salt fog chamber and during beach exposure tests. Panels were manufactured in the production environment using shop personnel and equipment. Paint was flatwise tensile tested for adhesion and all BOOSTERCOAT tests surpassed the present coatings being used. Additional tests were performed on the adhesion of TPS materials to the prepared substrate and the adhesion values were equal to or greater than the present system.

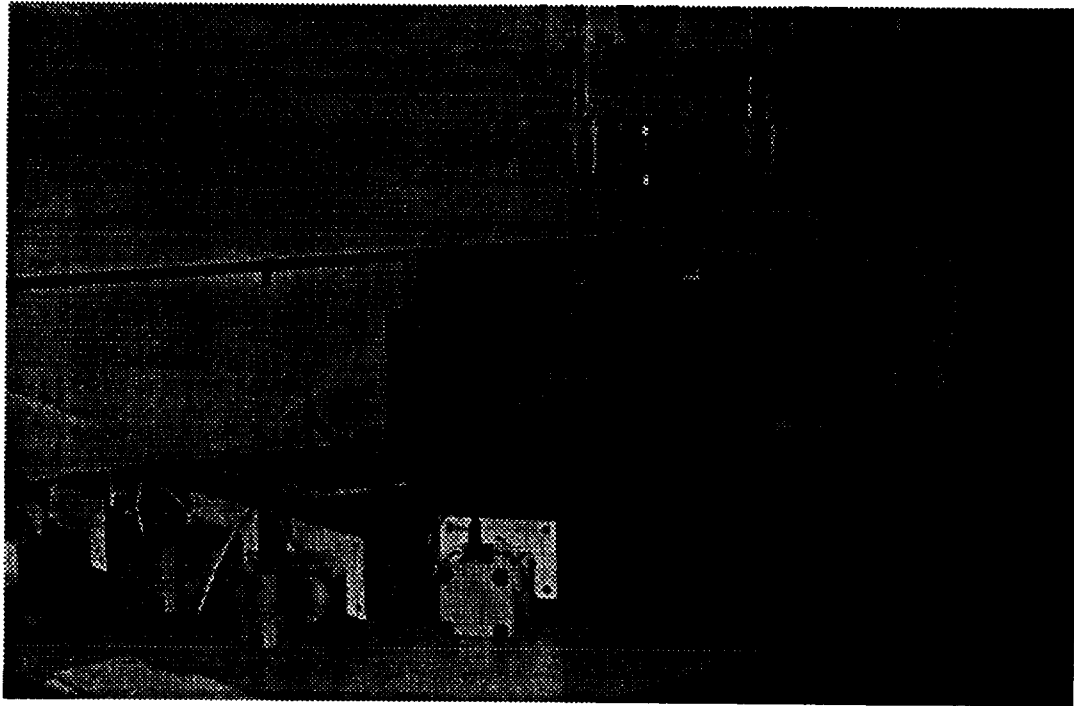


Figure 5 EIS Equipment With Flat Cell

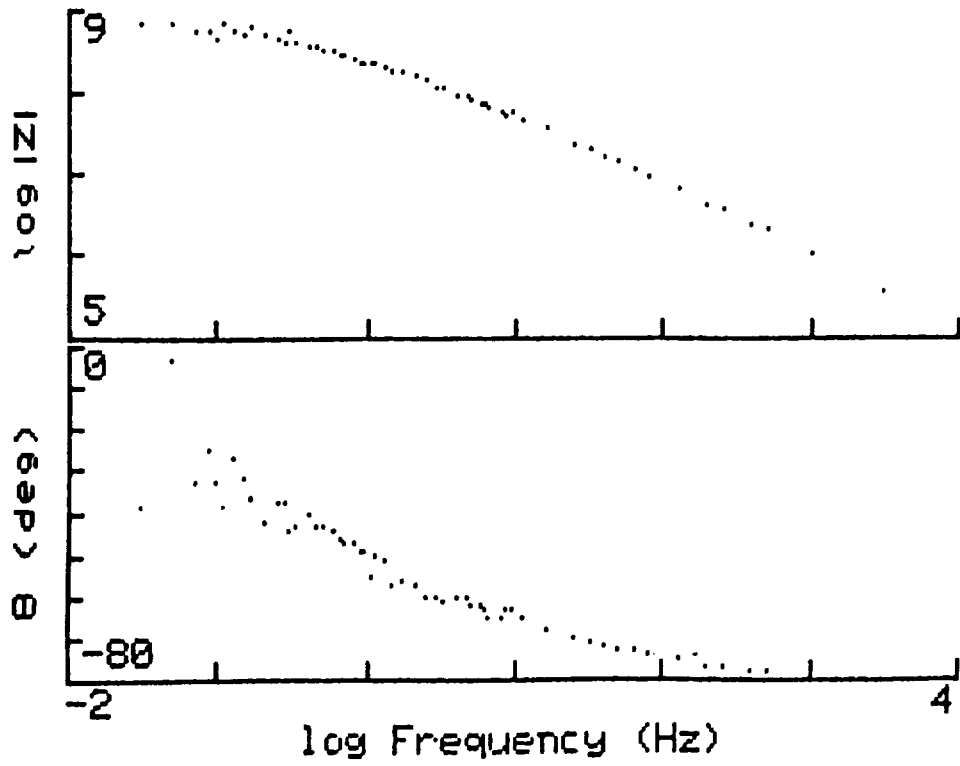


Figure 6 Bode Plots - 4 Mil Coating

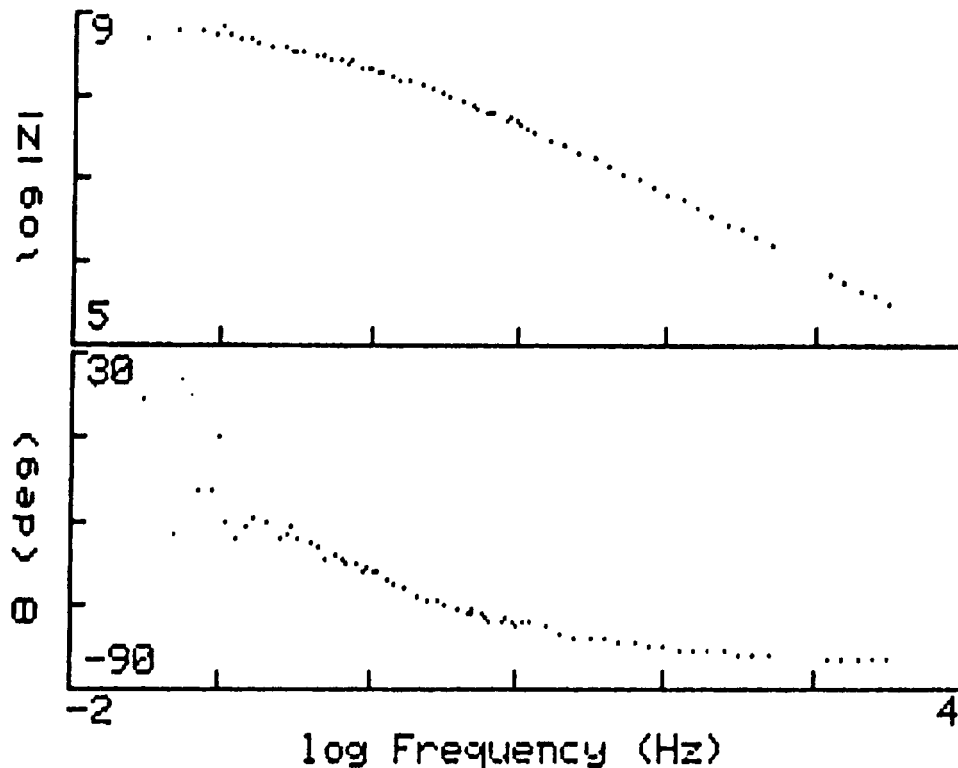


Figure 7 Bode Plots - 3 Mil Coating

CONCLUSION

The environmental testing of a non-chromated, non-leaded polyurethane single coat primer/topcoat allowed for optimization of the resin and corrosion inhibiting pigmentation system. Additional testing under production environments such as robotic sanding, vapor-blast cleaning and application of TPS materials with aggressive solvents helped prove its compatibility with the SRB environments. The new paint was accepted by technicians preparing and applying it to various substrates, and found it easier to work with than the present two coat system. The polyurethane paint does not require induction time prior to use, and with only one type of paint required greatly simplifies the logistics of shelf life and certification requirements. Applications for many other fields than aerospace exist. Energy and power generation, chemicals, transportation, architectural and many others await its application.

ACKNOWLEDGMENTS

The authors would like to thank the various USBI departments both in Huntsville, Alabama and Kennedy Space Center, Florida for supporting and assisting in program management, production operations, logistics and testing. Many thanks to NASA Marshall Space Flight Center Materials and Processes Laboratory and SRB Program Office who were supportive of this program and to the NASA Kennedy Space Center Corrosion Branch who offered the use of their beach exposure and salt spray test facilities.

REFERENCES

- (1). Annual Book of ASTM Standards, Vol 6.01, "Paint-Tests for Formulated Products and Applied Coatings," ASTM, Philadelphia, PA 1992.
- (2). Symposium on CPVC - Critical Pigment Volume Content, Proceedings of the ACS Division of Polymeric Material; Science and Engineering Vol 63 (1990).

537-27
2473
p. 19
HIGH ELONGATION ELASTOMERS¹

V. L. Brady, R. Reed, L. Merwin, and R. Nissan
Naval Air Warfare Center Weapons Division
China Lake, CA 93555-6001

ABSTRACT

A new class of liquid curable elastomers with unusual strength and elasticity has been developed at the Naval Air Warfare Center Weapons Division, China Lake. Over the years, studies have been conducted on polymer structure and its influence on the mechanical properties of the ensuing composites. Different tools, including nuclear magnetic resonance, have been used.

This paper presents a summary of the factors controlling the mechanical behavior of composites produced with the new liquid curable elastomers, including the effects of plasticizers. It also provides an overview of the nuclear magnetic resonance study on polymer structure, the composition and properties of some live and inert formulations produced at China Lake, and some possible peace-time applications for these new elastomeric materials.

INTRODUCTION

In the recent past, composites having unusual toughness were developed for use as explosives, propellants, and inert simulants. This advance comes after several years of investigating the effect of polymer structure on mechanical properties. A new class of liquid curable elastomers has emerged from this work. These elastomers display unusual strength and elasticity and are attained by converting solutions of polyether polyols high in functionality (F4) and in molecular weight (18,000 to 27,000 daltons) in plasticizers to lightly cross-linked polyurethanes. Typically, fillers are added to enhance both energy and mechanical properties. This work was stimulated by the need to attain more insensitive munitions. As the toughness of energetic materials is increased, their sensitivity to stimuli such as impact and cookoff is reduced.

Toughness, indicated by the area under the stress-strain curve of composites, is related to the energy that can be absorbed before fracture occurs. Several major factors influencing toughness have been identified in composite propellants and explosives [1,2]. The most important factor is the backbone structure of the polymeric binder. It must be such that the chains can freely bend and rotate. Another critical aspect is the formation of a regular and fully cross-linked network. The new class of binders developed at the Naval Air Warfare Center Weapons Division (NAWCWPNS), China Lake is superior to conventional polyethers in that the length of the polymer chain between cross-links is increased, while the regularity and degree of cross-linking is enhanced. Other backbones such as polyesters can also be used at comparable functionality and molecular weight.

These polyols are waxes and must be dissolved in non-volatile liquids (plasticizers) that separate the crystalline chains to allow bending and rotation to occur. Plasticizers also provide the liquid necessary to attain a castable composite. Since plasticizers enhance polymer chain mobility, they also retard crystallization at reduced temperatures. Other factors such as the functionality of the curative and its ratio to hydroxyl, the relationship of cross-link density to chain length, level and type of plasticizer, as well as the binder filler interaction, also influence mechanical properties.

¹ Approved for public release; distribution is unlimited.

The progress in attaining tough composite energetic materials by adjusting the factors cited above is discussed. Variations in mechanical properties caused by altering the polymer structure, plasticizer-to-polymer ratios (PI/Po), and other factors are presented.

FACTORS CONTROLLING THE MECHANICAL BEHAVIOR OF COMPOSITES

The major factors that control the mechanical behavior of the new composites are shown in Table 1. These factors, which are not significantly different in the case of inert composites, have been reported for propellants [1,2,3] and explosives [4].

TABLE 1. Factors Controlling Mechanical Behavior.

Polyol	Fillers	Isocyanate Curative
Flexibility and structure of backbone	Binder-Filler Interaction	Functionality
Equivalent Weight	Particle Size	NCO Reactivity
Functionality	Loading	
Hydroxyl Reactivity		
Internal Carbon Cross Links		

Backbone Structure and Flexibility

Of the major controlling factors in Table 1, the most critical is the backbone structure of the polyol. Polyethers are generally preferred for making elastomers because of their ability to bend and rotate. Of the various polyether polyols, polyethylene glycols are the most useful since they are

- 1) able to retain inert and energetic plasticizers,
- 2) terminated in primary hydroxyl,
- 3) attainable in a variety of molecular weights and functionalities,
- 4) high in the fraction of weight made up by load-bearing carbon and oxygen atoms,
- 5) chemically compatible with typical fillers.

Other polyethers, some of which are liquids such as polypropylene glycol (PPG), polytetramethylene glycol (PTMG), and butylene glycol (BG), are incompatible with inert and energetic plasticizers. PPG and BG have secondary hydroxyl groups which react more slowly and less completely than primary hydroxyls. It is more difficult to attain toughness with these glycols than with polyalkylene oxide (PAO) and polyethylene glycol (PEG).

Polyol Equivalent Weight

Equivalent weight determines the length of the flexible segments existing between cross-links or urethanes. In the relaxed state, the flexible segments may form coils. Upon extension, the flexible segment uncoils and then ruptures. The length of the coiled segments limits the extension that can be achieved prior to rupture.

Polyol Functionality

Polyol functionality has a dominant effect on the area under the stress-strain curve (Figure 1). Difunctional PEG compositions display a slowly rising area as chain length, measured by skeletal or backbone atoms, increases. In the case of PEG, there are two carbons and one oxygen, or three skeletal atoms per mer unit. As these are increased, elongation at rupture increases modestly while stress decreases because of the continuing decrease in cross-link density. Compositions containing F3 and F4 polyols are much tougher and exhibit a greater dependence on skeletal atoms. At these functionalities, a given chain length is more effective because the quaternary and tertiary carbon cross-links in F3 and F4 polyols are more efficient than those containing urethanes. Urethane linkages may be relatively fragile, since they are polar and rigid in nature, as compared to the resilient carbon cross-links in the polyol moiety. The polypropylene glycol units near the polyol central carbon atoms should enhance resilience.

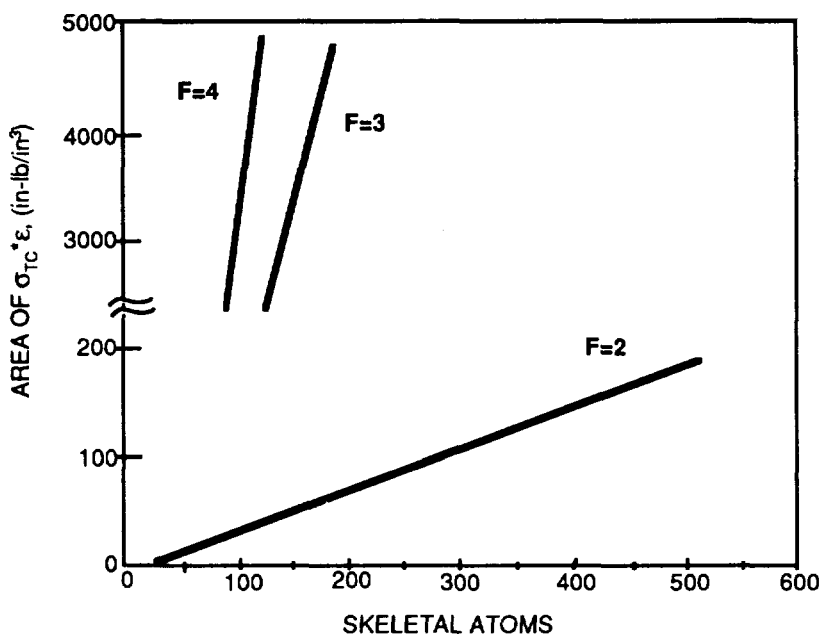


FIGURE 1. Toughness (in-lb/in³) of Gumstocks vs. Skeletal Atoms for Di-, Tri-, and Tetrafunctional Polyols.

Hydroxyl Reactivity

The relative reactivity of hydroxyl groups is instrumental in determining the polymer network structure. All hydroxyl groups should have equal reactivity so that a regular network can be formed. Furthermore, the hydroxyls should be unhindered and primary. Secondary hydroxyl groups react more slowly than primary and, perhaps, less completely, factors which may limit the molecular weight of the network.

Carbon Cross-Links

Carbon cross-links, as mentioned above, are critical in attaining a regular and fully cross-linked polymer network. Some plasticizers such as nitrate esters tend to inhibit cross-linking and, as a result, degrade molecular weight and toughness [5]. Plasticizer retention is also degraded.

Binder-Filler Interaction

The interaction of the solid fillers with the binders has a large effect on modulus, as well as on stress and strain at failure. Polyether binders have an affinity for polar solids. Solids that have a strong affinity for binders are generally not desirable because they reduce elongation, probably by preventing the formation of coiled flexible segments. A weak affinity of the hard urethane linkages for the solid may be desirable to reduce the tendency of the binder to pull away from the solids (dewetting) when the composite undergoes tensile stress. Binders with no affinity for the solids undergo early irreversible dewetting and tend to exhibit poor strain values.

Particle Size and Solids Loading

The particle diameter of the fillers has a dramatic effect on the mechanical properties. As the particle diameter is increased beyond 5-10 μm , the stress values decrease rapidly as the average distance between particles is increased. Elongation is degraded, but to a lesser extent.

As the content of solids increases, the modulus and stress typically increase while strain decreases. Higher levels of solids require that a distribution of particle sizes be used to enhance the packing fraction. The presence of coarser particles tends to degrade mechanical properties. In modern tough propellants the use of energetic plasticizers allows the solids to be reduced so that all fillers can be $\geq 10 \mu\text{m}$.

Isocyanate Functionality and Reactivity

The isocyanate curative greatly influences the cross-link density and molecular weight of the polymer network. Energetic compositions containing nitrate esters are known to inhibit the formation of cross-links and thus reduce cross-linking density. As a result, comparatively higher functionality isocyanates (F3 and F4) are required to attain an adequate cross-link density equivalent to that of inert or non-nitrate-ester-containing compositions. Since the carbon cross-links existing in the F3 and F4 polyols are very likely more robust and flexible, it is advantageous to maximize carbon cross-links relative to isocyanate cross-links so that both stress and elongation can be enhanced. Therefore, difunctional isocyanates such as hexamethylene diisocyanate (HDI) are preferred in inert compositions containing a tetrafunctional binder. This allows the isocyanate to act as a chain extender, while all the cross-links are a result of the PAO quaternary carbon.

Equal reactivity of the NCO groups contributes to the formation of regular, high molecular weight polymer networks, enhancing toughness.

PLASTICIZERS, THEIR EFFECTS, AND INTERACTIONS WITH POLYOLS

In addition to polymer structure, another factor that affects toughness in urethane compositions is the plasticizer type and content.

Liquids that are nonvolatile and soluble in polymeric binders have been widely used to plasticize binders in castable energetic materials. Some of the effects of plasticizers on the properties of propellant binders have been discussed by Oberth [1]. Plasticizers generally enhance the following properties:

- processibility,
- low temperature mechanical properties,

- energy,
- toughness,
- insensitivity.

Plasticizers increase the mobility of the polymer backbone in the polyol (in the case of polyurethane binders) and, therefore, decrease viscosity and generally enhance processibility of propellants and explosives. Carboxylated polybutadienes tend to be viscous because of the association of the carboxyl groups, a problem that is overcome with plasticizers. Plasticizers also increase the mobility of the backbone between cross-links in cured propellants so that the tendency to form crystallites or glassy regions at low temperatures is reduced. For example hydrocarbon esters are added to propellants containing polybutadiene binders to improve elongation at -65°F. An ester such as isodecyl pelargonate tends to dissolve the glassy polybutadiene polymers at low temperatures, thus lowering their melting range and allowing them to retain a rubbery matrix. While polybutadiene binders use modest levels of plasticizers (PI/Po of ≤ 0.2), modern binders such as PEG and PAO are waxes and have to be dissolved in plasticizers to attain a processible propellant slurry. High molecular weight binders tend to be higher in viscosity and may require additional plasticizer (i.e., PI/Po ≥ 3).

Plasticizers are often used to increase energy, particularly in propellants having a PEG binder. Energetic nitrate ester plasticizers increase binder energy, as the inert polymer is being replaced. Conventional PEG polyols (F2) limit the PI/Po to about 3 due to exudation at reduced temperatures. In addition, the tensile stress at failure is decreased to unacceptable stresses, as plasticizer is increased beyond a PI/Po of 3.5. Energetic plasticizers are especially advantageous in modern high energy propellants because they increase binder energy and allow the solids levels to be reduced. As solids are reduced, it is possible to reduce their average particle size, while maintaining processibility. In the absence of coarse particles, toughness can be achieved if tri- and tetrafunctional polyols having a chain length of 4500 daltons or more are used to form the polyurethane binder.

Tri- and tetrafunctional binders that are comparatively high in molecular weight ($\geq 18,000$ daltons) have been found to retain high levels of plasticizer (PI/Po ≥ 10) while maintaining toughness [6]. At a PI/Po of 5 or 6, they have exhibited elongations of 900% when pulled to failure. Compositions containing energetic plasticizer and fine solids such as cyclotetramethylenetetranitramine (HMX) exhibit high tensile stress at failure and high elongation. Past work has shown that F3 and F4 polyols such as polyethers, PAO, and polycaprolactones (PCP) form tough compositions retaining high levels of plasticizer [7] (Table 2). Polyols having large pendant groups such as the oxetanes exhibit somewhat less toughness, an effect that may be due to the internal plasticization contributed by the pendant group. In addition, the pendant group effectively reduces the load-bearing atoms between cross-links. Toughness appears to decrease as the length of the segments between cross-links is reduced [2,7].

TABLE 2. Polyol Properties.

Binder (Polyols)	Molecular Weight	Functionality	Load-Bearing Atoms**	Source
PAO 24-17*	21,000	3	474	BASF
PCP-1	21,000	3	427	UCC
PAO 24-13	18,000	4	315	BASF
PCP-2	25,000	4	381	UCC
PEG E-4500***	4,500	2	306	DOW

* A polypropylene glycol, polyethylene glycol copolymer.

** Load-bearing carbon and oxygen atoms (skeletal) between cross-links.

*** PEG E-4500 is a conventional binder widely used in modern propellants.

More recently, the tetrafunctional polyol PAO 24-13 (Table 2) has been found to be superior to its trifunctional analog in plasticizer retention and toughness [2,8,9]. The formation and structure of PAO 24-13 is given in Figure 2. PAO 24-13 has been used for most of the work at China Lake because of such factors as cost, availability, and superior toughness as compared to multifunctional PCP and BAMO/NMMO polyols.

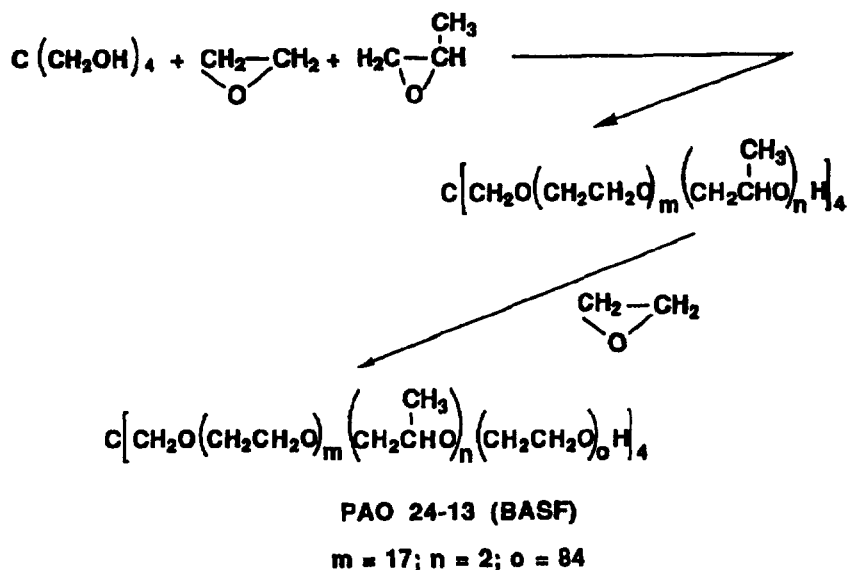


FIGURE 2. Formation of PAO.

The mechanical properties of energetic compositions containing the PAO 24-13 polyol are markedly superior to those of corresponding formulations containing the conventional PEG 4500, a polyol that is widely used in high energy, Class 1.1, high elongation propellants. The superiority of PAO 24-13 may be due to several factors including: 1) increased functionality (F4), 2) a favorable relationship of cross-link density to chain length, 3) enhancement of cross-link density by the tertiary carbon at the center of the PAO, 4) the relatively long chain lengths between cross-links, and 5) the ability of the plasticized chains to freely bend and rotate due to the ether linkages.

Plasticized compositions containing the difunctional PEG 4500 (4500 daltons) tend to have values of tensile stress at failure and elongations that are one-half or less than those of corresponding PAO compositions. Such properties are the result of incomplete cross-linking and a partially formed polymer network. Chi and Hartman have reported that cross-link density of PEG/NG gumstocks decrease markedly as a PI/Po of ≥ 3 is reached [5]. This lack of regularity in the polymer network tends to degrade mechanical properties.

This problem is in large part overcome by the use of tetrafunctional PAO polyols having quaternary carbon atoms which act as cross-links. Another factor in determining toughness is the length of the polyether segments between cross-links. In the relaxed state, segments between cross-links tend to form coils. As the elastomer is extended, the polyether is uncoiled easily so that stress increases slowly as strain increases. Continued elongation brings the chains closer together so that interaction between urethane cross-links or chains can occur, and, as a result, the stress rises increasingly with additional strain (Figure 3).

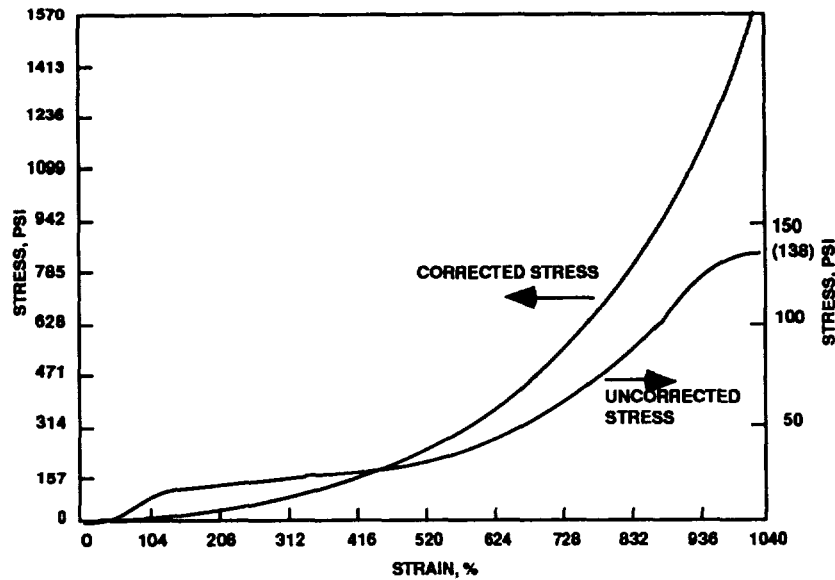


FIGURE 3. Typical Stress-Strain Curve for PAO 24-17 (F3) / BTTN (PI/Po = 3) HMX Composition.

The mechanical properties of PAO compositions are different from those of many inert and energetic composites. When dog bones are pulled, PAO compositions show a typical rubber expansion in that the stress is increasing as extension increases. Volume expansion on dilatation (Figure 4) is relatively small and appears reversible. Typical compositions containing PEG 4500 show a decreasing stress as extension increases and exhibit much greater volume expansion. The dilatation is not reversible upon relaxation. Thus indicating that chemical bonds in the binder are being broken even early in the extension. PAO composites tend to be more fully cross-linked to form a higher molecular weight network able to take up energy without bond breaking.

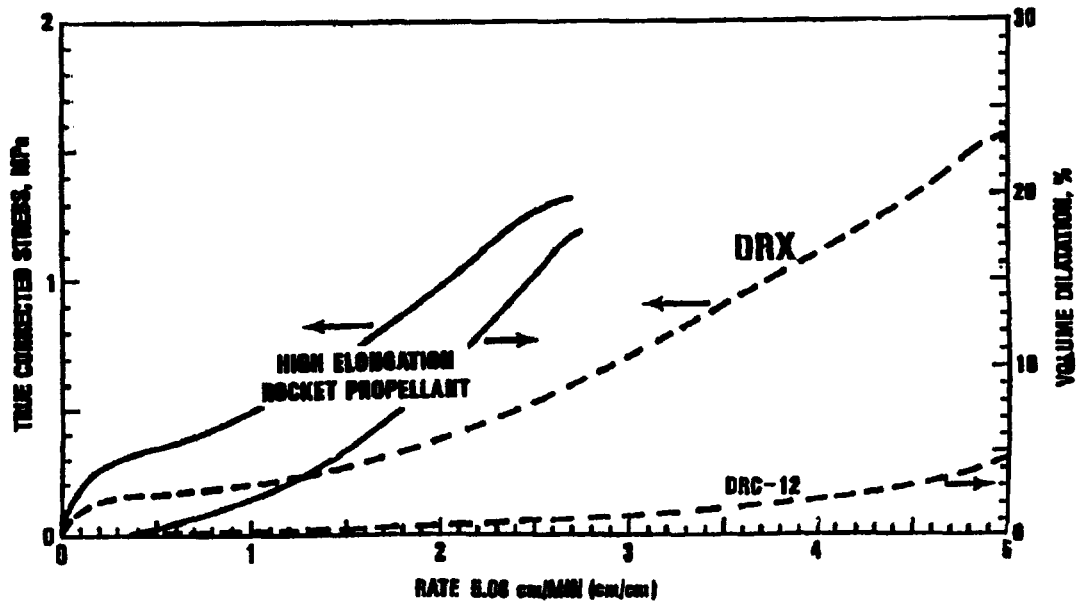


FIGURE 4. Mechanical Damage Behavior.

The properties of plasticizer retention are superior in propellants containing PAO 24-13 because of the tetrafunctionality and the formation of a more complete cross-linked network as compared to corresponding formulations having PEG 4500 binder. Plasticizer-to-polymer ratios of 5 to 6 can be achieved in compositions having excellent toughness; ratios from 6 to 10 do not exude, but toughness decreases because of a decrease in tensile stress at failure.

Generally propellants having PEG 4500 are limited to a PI/Po of about 3 because of exudation.

Sensitivity is directly related to solids loading, particle size, and toughness. The addition of energy to the binder by adding energetic plasticizers while reducing solids is, in effect, transferring energy from the crystalline phase to that of the rubbery binder matrix. By reducing the solids level and particle size, the tendency to form hot spots as a result of crystal fracture is minimized, and sensitivity is reduced. Additionally, binder toughness plays a large role in protecting crystalline solids from damage by absorbing energy of physical stimuli. As a result, higher plasticizer levels and tougher binder systems should, in theory, minimize sensitivity.

EXPERIMENTAL STUDY USING NMR

In recent years, solid-state nuclear magnetic resonance (NMR) spectroscopy has become increasingly important in the study of polymer phase structure, molecular dynamics, and blend miscibility [10-14]. Two sets of experiments were conducted to investigate the effects of PI/Po variations.

A series of cured gumstock compositions were made in which the ratio of polymer (PAO 24-13) to plasticizer (1,2,4-butanetriol trinitrate (BTTN)) was varied from 0.5 to 6.0. N-100, the biuret trimer of hexamethylene diisocyanate, was used as the curing agent.

¹³C Magic-Angle Spinning (MAS) nuclear magnetic resonance (NMR) spectra were obtained for the compositions. Representative spectra are shown in Figure 5, and chemical shift values for the series are given in Table 3. It is clear from comparing the two spectra that the resonance at ~70 ppm may be assigned to the PAO. The four remaining resonances arise from the BTTN. The changes in chemical shift, as one goes down any column of the table, are comparatively small from the standpoint of solid-state NMR which supports the view of the plasticizer (BTTN) as an extender that does not react with the PAO.

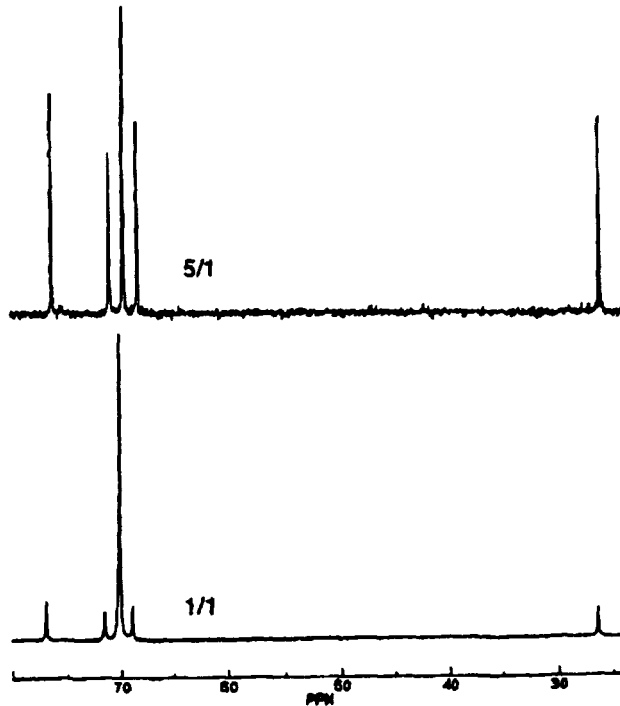


FIGURE 5. ^{13}C MAS NMR for 5/1 and 1/1 BTTN/PAO Composition Cured Gumstocks. For both spectra, the largest resonance line represents the PAO and the four remaining lines arise from the BTTN.

TABLE 3. Solid-State ^{13}C NMR Chemical Shifts.

Sample	^{13}C Chemical Shift ^a				
PAO			70.0		
GS-0.5	76.8	71.4	69.9	68.9	26.1
GS-1	76.9	71.4	70.1	68.9	26.3
GS-2	76.7	71.3	70.0	68.7	26.3
GS-3	76.5	71.1	69.9	68.6	26.2
GS-4	76.4	71.0	69.8	68.4	26.2
GS-5	76.3	70.9	69.7	68.4	26.1
GS-6	76.3	70.9	69.7	68.3	26.1

^a Referenced to TMS, ± 0.1 ppm.

Due to the high levels of plasticizer being evaluated, there was a question on whether some of the relatively volatile BTTN would be driven off during processing. This question was resolved by quantitative evaluation of the MAS NMR spectra. In Figure 5, the BTTN resonances are proportionately larger in the 5/1 sample than the 1/1 sample. Figure 6 shows the plasticizer content as determined by MAS NMR plotted against the calculated plasticizer content for the compositions. This figure indicates that there is no loss in plasticizer during processing or cure.

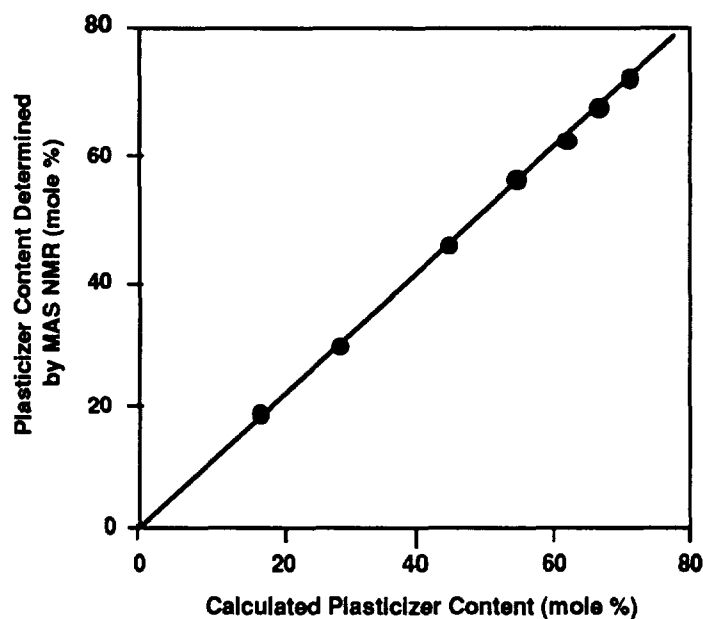


FIGURE 6. Verification of the Plasticizer Content of the Cured Gumstocks by Solid-State MAS NMR. The linear relationship indicates that no plasticizer is lost during gumstock processing.

The solid-state ^{13}C NMR spin-lattice relaxation times (T_1) were also determined for the cured gumstock compositions. For ^{13}C , the T_1 value is generally site-specific within a molecule, and may be seen to reflect the degree of megahertz frequency motions at that particular site. The spin-lattice relaxation results are given in Table 4. The 69.7 ppm column represents the relaxation of the PAO line, while the remaining columns contain data for the four BTTN resonances.

Two main conclusions may be drawn from the relaxation study. First of all, in comparison with the pure PAO relaxation time of 184 ms, the T_1 value of 147 ms for the PAO resonance of the GS-0.5 composition is significantly reduced, with no subsequent systematic change. The initial drop in T_1 may be seen to result from the plasticizer "breaking up" or extending the PAO. From that point onward, the unchanging T_1 suggests that the PAO portion of the polymer does not undergo any significant change in its internal mobility or motion. This would further imply that subsequent macroscopic flexibility arises solely from the increased BTTN content. The picture is one of relatively rigid subunits (PAO) dispersed in a soft/rubbery matrix. Increasing the amount of matrix only increases the distance between subunits and does not affect the internal motion or mobility of the subunits.

Secondly, the ^{13}C T_1 values for the BTTN resonances all increase monotonically with increasing BTTN content (Figure 7). The fact of increasing T_1 correlated with an increasing macroscopic mobility (a softer and more rubbery overall consistency) suggests that these materials have already reached what in NMR is called the fast exchange regime, an increasing degree of microscopic mobility with correlation times faster than 1×10^{-9} s. The results indicate that the BTTN component of these systems is highly mobile and that this mobility increases proportionally with BTTN content.

TABLE 4. ^{13}C Spin Lattice Relaxation Times.

Sample	^{13}C T_1 /ms					
	δ /ppm	76.3	71.0	69.7	68.3	26.1
PAO				184		
GS-0.5	137	91	147	115	99	
GS-0.5	143	87	147	117	96	
GS-1	166	109	151	138	118	
GS-2	203	129	155	156	140	
GS-2	187	119	144	156	129	
GS-2	209	140	159	168	137	
GS-3	216	127	142	176	144	
GS-3	216	136	156	182	145	
GS-4	218	138	142	184	145	
GS-4	228	137	146	182	147	
GS-5	241	155	154	198	154	
GS-6	251	152	154	202	164	
GS-6	257	156	155	108	178	
Slope	-2.2	-1.2		-1.8	-1.3	
Intercept	271	166		220.8	178.4	
Correlation	0.97	0.95		0.98	0.96	

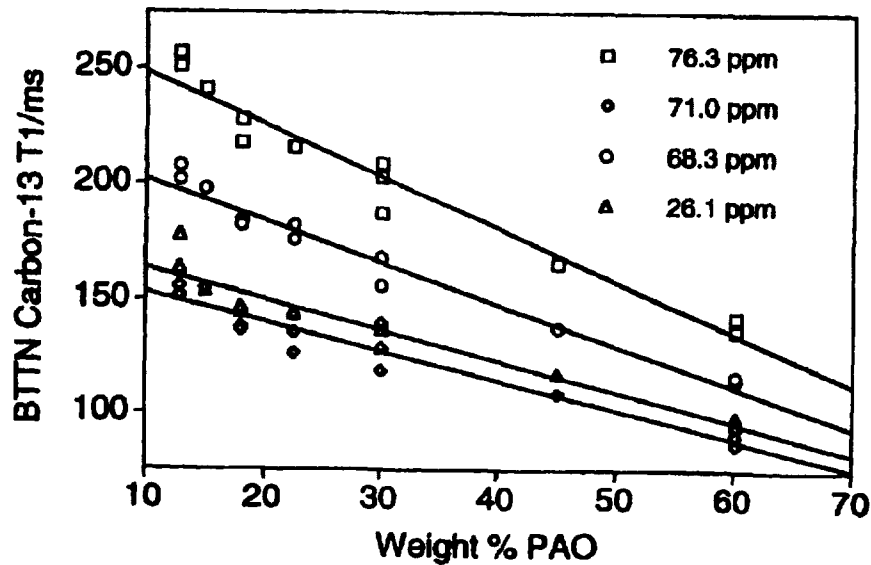


FIGURE 7. Plot of the ^{13}C Spin Lattice Relaxation Time (T_1) for BTTN as a Function of PAO Content in the Gumstock.

In the second experiment, several compositions consisting of 40% binder (analogous to the gumstock compositions in the first experiment) and 60% HMX (~10 μm) and were also examined. Plasticizer-to-polymer ratios were varied from 0.5 to 6.0 as in the first experiment.

As noted, the T_1 results discussed above reflect molecular mobility on the MHz time scale. However, motions on a slower time scale can be a particularly sensitive indicator of the phase structure of polymers. One method to access such information is through the solid-state NMR experiment referred to as cross-polarization (CP). The magnetization transfer process responsible for CP is sensitive to, among other factors, distance, and the presence of motion in the solid system. The CP transfer process is most efficient for rigid systems in close proximity.

Figure 8 shows the cross-polarization spectra for two of the filled compositions with PI/Po of 3/1 and 5/1. As is clearly evident, the spectrum of the 3/1 material exhibits the PAO and BTTN resonances expected, as well as a broad resonance arising from the HMX. In the spectrum of the 5/1 material, however, the BTTN resonances have disappeared and the intensity of the PAO resonance has been significantly reduced in comparison to the 3/1 spectrum and to the intensity of the HMX resonance. Remembering that these are CP spectra, it is evident that, in the 3/1 spectrum, the magnetization transfer process responsible for CP is active. Even though the T_1 results indicate that the PAO is extended, this result shows that, to the point of the 3/1 BTTN/PAO ratio, there is still some degree of ordering in the polymer network. This ordering may be envisioned as folding or overlapping of the cross-linked PAO lattice. At 5/1, however, any residual order has been completely lost. The BTTN is now completely mobile on the kHz time scale and cross-polarization to it is no longer possible. The fact that the intensity of the PAO resonance has been significantly reduced also reflects significantly decreased order and increased mobility for the PAO. This threshold or break-point at the 5/1 BTTN/PAO ratio is believed to represent the optimum plasticizer level for this system in terms of producing an elastomeric binder. At 5/1, the system has been fully plasticized, as is shown by the complete loss of the BTTN resonances. Plasticization beyond this point should have little further effect on the ordering of the polymer network.

It is known that other factors influence plasticizer retention levels such as the type and ratio of curative in the composition, functionality of the polymer, chain length between cross-links, surface area of solids (affected by particle size and solids loading), and type of solids. Therefore, it is likely that threshold PI/Po levels would be altered by varying the compositions. The CP method of determining threshold plasticizer levels of composites would be a valuable formulation tool. Studies should be made to demonstrate the effect of formulation variations on threshold plasticizer levels and correlate these to optimum mechanical properties.

COMPOSITIONS AND PROPERTIES OF HIGHLY PLASTICIZED FORMULATIONS

Recently, tough compositions have been prepared with high plasticizer-to-polymer ratios. A PI/Po of 5.0 was selected to enhance the energy as well as the mechanical properties of a composition containing PAO binder, BTTN plasticizer, HMX, and Al. A series of compositions were developed ranging in solids from 65% to 75% (Table 5). HMX of variable particle sizes was selected as the energetic filler for its high energy density, processibility, and good mechanical properties. Some compositions contained 10% aluminum (H-5).

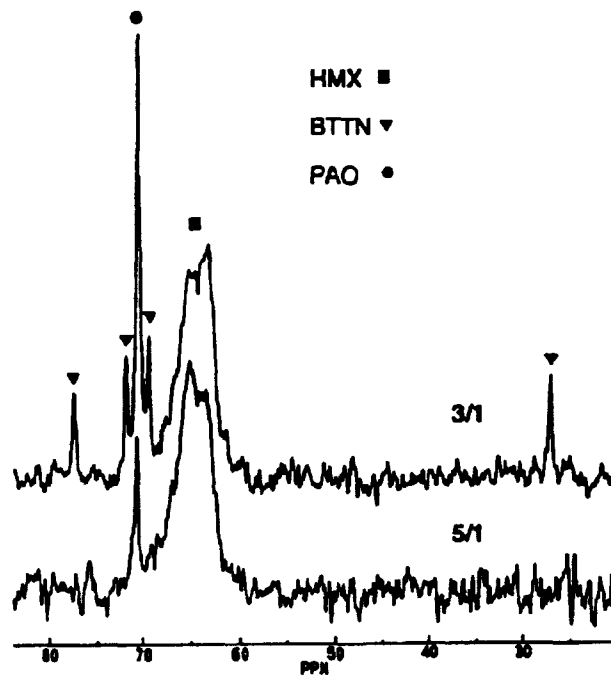


FIGURE 8. ^{13}C Cross-Polarization MAS NMR Spectra of Formulations Containing 60 weight % HMX and 40 weight % BTTN/PAO Binder for BTTN/PAO Ratios of 3/1 and 5/1. The resonances arising from HMX, BTTN, and PAO are marked. Note the disappearance of the BTTN resonances at the higher BTTN/PAO ratio.

TABLE 5. Formulations.

Ingredient	Formulation				
	PBX 1	PBX 2	PBX 3	PBX 4	PBX 5
Binder/curative	5.543	5.543	3.957	3.166	3.957
BTTN	29.167	29.167	20.833	16.667	20.833
MNA	0.291	0.291	0.210	0.167	0.210
HMX (6, 12, 57 μm)	65.000	55.000	65.000	70.000	75.000
Aluminum (H-5)	--	10.000	10.000	10.000	--
PI/Po	5	5	5	5	5

The mechanical properties of these compositions exhibited high tensile stresses between 150 and 180 psi at failure, and elongations from 400 to >1000% (Table 6). PBX 2 filled with all fine solids (< 10 μm) exhibited the highest degree of toughness with a stress of 180 psi and elongation of 970%. As both particle size and solids level increased, the mechanical properties worsened. While strain values were still respectably high, stress values degraded, reducing toughness. These compositions are extremely flexible with a bend radius of < 1/4 inch (in a 0.3-inch cylindrical rope-like configuration).

TABLE 6. Mechanical Properties.

Property	Formulation				
	PBX 1	PBX 2	PBX 3	PBX 4	PBX 5
Packing fraction	0.639	0.640	0.769	0.768	0.750
EOMV, kP ² /F	5.0/120	9.5/116	2-4/123	13.5/124	7.5/121
Modulus, psi	58*	9*	74	118	134
Stress, psi	107	180	46	26	39
Strain, %	1019	970	695	541	740

* Result is uncorrected.

Mechanical properties over a range of operating temperatures were evaluated for three of the compositions (Table 7). Strain values, optimum at ambient temperatures, were still remarkably high at 25°F and even 120°F. As expected, stress values were higher at 25°F and decreased as temperature increased. Even at elevated temperatures, PBX 2 retained its toughness.

TABLE 7. Mechanical Properties of Three Selected Formulations Over a Range of Operating Temperatures.

Property	Formulation		
	PBX 2	PBX 3	PBX 5
Modulus, psi			
25°F	165	319	211
77°F	151	161	243
120°F	161	241	248
Stress, psi			
25°F	235	87	85
77°F	180	46	39
120°F	99	33	25
Strain, %			
25°F	644	455	593
77°F	970	695	740
120°F	614	282	339

In addition, high rate mechanical properties were evaluated (Table 8). Typically, low rate mechanical properties are evaluated at an extension rate of 2 in/min; high rate mechanical properties are evaluated at rates from 10,000 in/min up to and exceeding 60,000 in/min. Generally, mechanical properties at high rates are half or less than those obtained at low rate for the same composition. However, PBX compositions, evaluated at an extension rate of 16,524 in/min, demonstrated strain values greater than half their low rate values, and stress values were virtually unchanged.

TABLE 8. High Rate Mechanical Properties.

Property	Formulation		
	PBX 2	PBX 3	PBX 5
E ₀ , psi	619	463	538
σ _m , psi	171	31	51
ε _b , %	506	344	420
Work/toughness, in-lb/in ³	419	73	127

Using a high-molecular-weight, high-functionality polymer (PAO 24-13) and a PI/Po of 5, it is possible to attain unique compositions. With a bend radius of < 1/4 inch, these compositions are flexible, tough (both over a wide range of temperature and extension rates), and exhibit superior performance (~ 15-20% over the developmental baseline).

An inert simulant for the PBX formulation was also developed. In earlier work, an inert simulant matching the mechanical properties of a Class 1.1 high-elongation propellant was prepared and characterized [15]. The objective was to simulate the mechanical properties as well as the density of the PBX formulation. The challenge was to maintain the density of each of the formulation ingredients and the overall density of the composition, as well as the volume % of binder. (In order to simulate mechanical properties it is important to maintain the same volume % of binder in the simulant formulation as in the live one.) Initial inert simulant formulations targeted the PBX 2 composition. Dimethyl phthalate (DMP) (density 1.1 g/cm³) and a dense (1.9 g/cm³) mixture of brominated diphenyl ether and aryl phosphate esters (DE 60F and DE 62) were blended to achieve the density of BTTN (1.52 g/cm³) and used with PAO 24-13 as the binder. Dechlorane Plus, a chlorinated tricyclic hydrocarbon flame retardant (1.82 g/cm³) was used as the inert filler to replace HMX (1.9 g/cm³). Aluminum levels were increased slightly to adjust for the lower density of Dechlorane Plus.

A series of compositions were evaluated varying plasticizers (DE 60F vs. DE 62) and curatives (N-100 vs. HDI) (Table 9). The compositions using HDI (IPBX 3 and 4) as a curative exhibited superior mechanical properties (Table 10) compared to those made with N-100 (IPBX 1 and 2). Nitrate esters used in live formulations require high levels of isocyanate (F3 to F4) to achieve an optimal cross-link density. Inert plasticizers do not exhibit this cure-inhibiting effect and, as a result, do not require high functionality isocyanates at increased levels to achieve optimal cures. Since the properties of IPBX 3 and IPBX 4 were virtually equivalent, IPBX 3 was selected for further development because of the enhanced aging characteristics expected with DE 62 (a cleaner version of DE 60F with respect to acid content). Table 11 compares the mechanical properties of PBX 2 to those of IPBX 3 at both low and high extension rates. The strain values at high loading rates are high, but, otherwise, the properties of the inert simulant closely reflect those of the live PBX 2. Some inert simulant compositions have exhibited high rate strain values in excess of 2000% and low rate strains in excess of 1000%. These results have been observed after varying cure catalyst and temperature profiles.

TABLE 9. Inert Simulant Formulations.

Ingredient	Formulation			
	IPBX 1	IPBX 2	IPBX 3	IPBX 4
PAO 24-13	5.482	5.482	5.663	5.663
N-100	0.326	0.326	--	--
HDI	--	--	0.145	0.145
DMP	15.838	15.838	15.838	15.838
DE 62	13.329	--	13.329	--
DE 60F	--	13.329	--	13.329
Aluminum H-5	15.000	15.000	15.000	15.000
Dechlorane 515	50.000	50.000	50.000	50.000
TPB	0.015	0.015	0.015	0.015
DNSA	0.010	0.010	0.010	0.010

TABLE 10. Properties of Inert Formulations.

Property	Formulation			
	IPBX 1	IPBX 2	IPBX 3	IPBX 4
EOMV, kP/°F	5.0/121	3.5/123	4.4/122	4.2/123
E _o , psi	168	127	115	134
σ _m , psi	48	47	126	138
ε _m , %	260	377	876	884
ε _b , %	273	377	884	885

TABLE 11. Comparison of Mechanical Properties.

Property	Formulation			
	PBX 2	IPBX 3	PBX 2 (HR)	IPBX 3 (HR)
E _o , psi	151	115	619	324
σ, psi	180	126	171	132
ε, %	970	884	506	940

DISCUSSION

Liquids that can be cured to form elastomers have an inherent ability to bond to fillers and to substrates since they are composed of relatively small molecules that are able to penetrate into the surface microstructure of solids to a degree not possible for the macromolecules contained in many latices. In situ polymerization of polyols occurring in the microsurface tends to enhance the polymer-filler adhesion. The polar nature of the urethane groups tends to enhance bonding to many substrates. The urethane group is similar to the amide linkage in proteins, one which is well known to bond tenaciously to polar substrates. Unfortunately, proteins tend to have amide units that are not separated by long flexible segments. Hence, they have little elasticity. Further, even synthetic amides are not conveniently formed by the curing of liquids at ambient temperature.

The rate of curing to form polyurethane rubbers can be varied widely (minutes to days) by the choice and amount of cure catalyst, as well as the cure temperature. Triphenylbismuth and acidic activators can be used to achieve pot lives of 1-3 days. Ferric acetyl acetate can affect curing in a few minutes. Small amounts of dibutyltin dilaurate may take 4 to 8 hours to gel, where larger concentrations can cause curing within 10 minutes. Curing can be accomplished at temperatures from ambient to 70°C.

Filled urethanes made from the tri- and tetrafunctional PAO polyols tend to show relatively little increase in volume when extended. The volume dilatation appears reversible and largely disappears when extended samples are relaxed. Generally filled polyurethanes using the conventional binder PEG 4500 show much greater dilatation upon extension, much of which is not reversible, and is, therefore, evidence of the rupture of the polymer chains. It is likely that the more robust nature of the PAO is due to the formation of a more completely cross-linked network higher in molecular weight. The quaternary carbon cross-links in the PAO may be more resilient than the more rigid and polar urethane. There are about 3% of propylene glycol polyether groups near the center of the PAO, which should enhance the flexibility of this region of the polymer.

These characteristics allow the composites to repeatedly stretch without causing much damage to the polymer. The existence of a relatively large high-molecular network allows the stress to be dissipated over a large volume to minimize rupture of the polymer. Samples that are cut 25% of the distance through a dog bone also show comparatively little loss in elongation and tensile stress at failure. Thus, these samples display unusual toughness.

Urethanes can be made by simple processing techniques which do not require high pressures or elevated temperatures. Curing times can be varied widely and are easily reproduced. Mechanical properties can be tailored for a variety of applications making urethanes uniquely advantageous as liquid curable elastomers and resins.

APPLICATIONS OF LIQUID CURED ELASTOMERS

Liquid mixtures capable of being cured to yield tough elastomers are potentially useful in a variety of applications including coatings, caulking compounds, potting liquids, adhesives, and cast parts with intricate shapes.

Adherent coatings with hydroxyl terminated polyethers and polyesters can be formed without the presence of volatile solvents. Volatile solvents are not desirable since voids or microporosity can be introduced when the solvents evaporate. Nonvolatile isocyanates such as polyols capped with isocyanates, which are relatively non toxic, can be used.

In addition, these liquid curable elastomers have some potential application in the fabrication of bladders, gloves, and condoms. When these products are made from rubber latices, small holes tend to form occasionally where the coagulation of the rubber particles is interrupted by solid impurities. The liquid curable plasticized urethanes are single-phase and contain no volatile substances, therefore no voids or holes would be created. As polymerization occurs there is essentially no shrinkage or exotherm because of the relatively high molecular weight of the polyol (~18,000 daltons).

Since the polyols are dissolved in a plasticizer to form these compositions, a variety of solid ingredients such as medicinals or antiseptics can be added by dissolving them in the liquid binder solution.

NOMENCLATURE

BAMO/NMMO	copolymer of poly-3,3-bis(azidomethyl)oxetane and 3-nitro-3-methyl methyloxetane
BG	butylene glycol
BTTN	butanetriol trinitrate
CP	cross-polarization
DE 60F	brominated diphenyl ether
DE 62	aryl phosphate ester
DMP	dimethyl phthalate
DNSA	3,5-dinitrosalicylic acid
EOMV	end-of-mix viscosity
F	functionality
HDI	hexamethylene diisocyanate
HMX	cyclotetramethylenetetranitramine
HR	high rate
kP	kilopoise
MAS	Magic-Angle Spinning
MNA	n-methyl-p-nitroaniline
N-100	Desmodur multiisocyanate curative (Mobay Chemical Company)
NCO/OH	ratio of isocyanate and hydroxyl
NG	nitroglycerine

NMR	nuclear magnetic resonance
PAO	polyalkylene oxide
PCP	polycaprolactone polymer
PEG	polyethylene glycol
PI/Po	plasticizer-to-polymer ratio
PPG	polypropylene glycol
ppm	parts per million
PTMG	polytetramethylene glycol
T ₁	spin-lattice relaxation times
TMS	tetramethylsilane, an NMR standard
TPB	triphenyl bismuth
UCC	Union Carbide Corp.

REFERENCES

1. A. E. Obert. "Principles of Solid Propellant Development," CPIA Publication 469, September 1987, pp. 4-19. Paper UNCLASSIFIED.
2. R. Reed, Jr., and V. L. Brady. "Factors Influencing the Mechanical Properties of Propellants," Proceedings of the Joint International Symposium on Compatibility of Plastics and Other Materials with Explosives, Propellants, Pyrotechnics, and Processing Explosives, Propellants and Ingredients, 22-24 April 1991, p. 492. Paper UNCLASSIFIED.
3. R. Reed, J. M. Hitner, H. P. Richter, L. R. Boyer, T. J. Jacks, and V. L. Brady. "Damage Resistant Propellants," AIAA Propulsion Conference, Orlando, FL, 1990. (AIAA Paper 90-2330, publication UNCLASSIFIED.)
4. R. Reed, and B. Y. S. Lee. "Tough PBX's," Proceedings of the Joint International Symposium on Compatibility of Plastics and Other Materials with Explosives, Propellants, Pyrotechnics, and Processing Explosives, Propellants and Ingredients, Virginia Beach, VA, 23-25 October 1989, p. 226. Paper UNCLASSIFIED.
5. M. S. Chi and K. O. Hartman. "Relationship of Polymer Structure to Mechanical Properties in Cross-Linked Double Base Binders," presented at the 15th Joint AIAA/SAE/ASME Propulsion Conference, Las Vegas, NV, June 1979. (AIAA Paper 79-1244, publication UNCLASSIFIED.)
6. R. Reed, J. W. Fisher, B. Y. S. Lee, and B. A. Zentner. "High Molecular Weight Trifunctional Binders: The Key to Damage Resistant Propellants," Proceedings of the 1989 JANNAF Propulsion Meeting, Cleveland, Ohio, CPIA Publication 515, Vol. II, P. 215, May 1989. Paper UNCLASSIFIED.
7. R. Reed, Jr. et al. "The Characterization of Polyoxetanes and the Influence of Structure Upon Polyurethane Formation and Upon Mechanical Properties," Proceedings of the 1986 JANNAF Propulsion Meeting, 26-28 August 1986, New Orleans, LA, CPIA Publication 455, Vol. III, August 1986, pp. 721-736.
8. R. Reed. *Multifunctional Polyalkylene Oxide Binders*, US Patent 4,799,980.
9. R. Reed, J. M. Hitner, T. J. Jacks, and V. L. Brady. "Tough Propellants Formed From Tetrafunctional Binders," Proceedings of the 1990 JANNAF Propulsion Meeting, Anaheim, CA, 1990, CPIA Publication 550, p. 315.
10. Richard M. Komoroski. *High Resolution NMR Spectroscopy of Synthetic Polymers in Bulk*. Deerfield Beach, FL, VCH Publishers, 1986, pp. 379.

11. F. Heatley. "Synthetic Macromolecules," in *Nuclear Magnetic Resonance*, Vol. 18, 1989, pp. 259-288.
12. Alan E. Tonelli. *NMR Spectroscopy and Polymer Microstructure*. New York, VCH Publishers, 1989, pp. 252.
13. Jack L. Koenig. *Spectroscopy of Polymers*. Washington, D.C., American Chemical Society, 1992, pp. 328.
14. Jean-François Masson and R. St. John Manley. "Solid-State NMR of Some Cellulose/Synthetic Polymer Blends," *Macromolecules*, Vol. 25, No. 2 (1992) pp. 589-592.
15. R. Reed and V. Brady. "An Inert Simulant for a High Elongation Class 1.1 Propellant," Proceedings of the JANNAF Propulsion Systems HAZards Subcommittee Meeting, 28-30 April 1993, Fort Lewis, WA.

**SOLVENTLESS, CURABLE FLUID OLIGOMERIC SYSTEMS
FOR HIGH PERFORMANCE MICROWAVE, ACOUSTICAL
AND MECHANICAL APPLICATIONS**

2474
P. 1

G.M. LeFave
Fluid Polymers, Inc.
Las Vegas, NV 89118

Leo Stanton
Fluid Polymers, Inc.
Las Vegas, NV 89118

Jim Foreman
Martin Marietta
Electronics, Information & Missiles Group
Orlando, FL 32855-5837

ABSTRACT

While establishing the basis for our "Technology 2000" product plan several years ago we plugged in the usual factors contributing toward product success.

- * Price/performance justifiable
- * Profitable, warranting high quality maintenance, enhancement and specific property improvement
- * Narrow inventory requirements
- * Raw material integrable backwards with easily variable properties (molecular weight, functionality, isomer control)

We resolved this by selecting radical functional, low molecular weight polybutadiene liquid polymers. Encouraged by the need for solid rocket binders several companies embarked on various perceptions of binder performance requirements over four decades ago. Initially dominated by progress of liquid polysulfides¹ soon a few settled primarily upon polybutadiene based binders.² Such an approach in a few instances was exploited quite viably with a series of functional group terminated liquid polybutadienes; hydroxyl, mercaptan, carboxyl, vinyl and amine. Our attention was directed to oligomers, liquid polymers and their hybrids. As you will see, the results have been spectacular. The only significant limits on compounded products has been solvent resistance and oxidative sensitivity, unless sufficient proportion of sulfide or nitrile moiety is incorporated. For convenience we have grouped them under the trademarks Nylane, Seamax, Oligomax, and Castomax all with a certain flair of acronymical significances.

GENERAL SYSTEM TECHNIQUES

The versatility of our complex oligomers may best be seen from the diverse summary of applications performance properties in Figure 1.

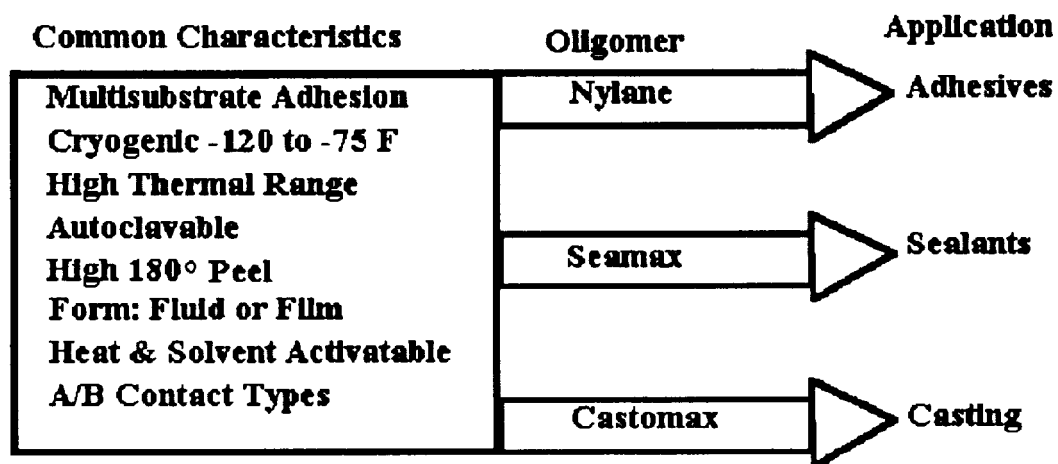


FIGURE 1

The abbreviated non-linear presentation in Figure 1 has proved quite useful in new product conception, development and improvement. Table 1 provides the functionality and process tools to arrive at targeted end product properties and performances for designed applications.

TABLE 1

RADICAL FUNCTIONALITIES	REACTION PROCESSES
Mercaptan	Vinyl addition, oxidation
Amine	Addition, Ionic, condensation
Unsaturation	Free radical, thermal/chemical
Silane	Hydrolysis, Addition
Isocyanate	Addition, Condensation Sterically, selective Isocyanurization
Ester	Transamination
Epoxide	Addition, auto polymerization

Exploratory work indicates a useful computer program is feasible using linear and random approaches.

APPLICATIONS

Foams, Sprayed-in-Place

The utilization of low density coatings is widespread in the aerospace industry. Historically, coatings of this type have been fabricated as syntactic foams in an attempt to meet the density, thermal conductivity, and/or electrical properties required. These coatings have significant deficiencies from many aspects including toughness, minimum density limits, cost and environmental problems. An alternative are blown foam coatings that match or exceed the mechanical, environmental, electrical and physical properties of the syntactic foam coatings.

Syntactic foam coatings consist of thermoset resin systems that have been loaded with fillers called microballoons to significantly lower the density of the coating. This in turn adjusts certain properties such as the dielectric constant and/or thermal conductivity of the coating to obtain a desired effect. The microballons utilized are typically either a hollow glass sphere or a hollow polymer sphere and by adding a specified quantity of these spheres to the thermoset resin a low density coating with the desired properties can be obtained.

The loading of large quantities of microballoons into thermoset resin systems severely degrades the mechanical properties and significantly increases the process problems associated with utilizing the thermoset resin system. To make low density coatings a high percentage of the system must be comprised of the microballons which tends to degrade the mechanical strength of the coating due to a resin starved scenario. Furthermore the effect of diminishing returns arises as more microballoons are added to the system which tends to bound the lower limit of the density of the coating at approximately 0.4 g/cc (25 lbs/ft³) for thermoset resin systems. In addition to the problems presented previously these systems typically require the use of significant quantities of solvents to mix the microballons into the resin system and to carry the coatings during spray applications. The initiative to lower VOC emissions has seriously restricted the use of syntactic foam coatings for this reason.

Sprayable blown foam coatings are a viable alternative to the syntactic foam coatings mentioned previously. Coatings of this type have been fabricated that have composite densities of 0.1 g/cc (6 lbs/ft³). All of these coatings were sprayed without the use of a carrier solvents so the VOC content of the system was limited to the VOC content of the resin system and the blowing action taking place (if any).

A polyurethane based sprayable blown foam coating series was developed based on NYLANE casting resin⁵. This resin system was selected due to the excellent mechanical properties, durability, and availability. Nylane IV is comprised of an oligomeric polyol and in this case aliphatic isocyanurate. This isocyanate was selected for the sprayable blown foam applications due to the low viscosity and low vapor pressure which is advantageous for spraying applications. It is a slow reacting isomeric isocyanate, so numerous catalysts were obtained and screened to determine which system or systems would produce the desired cure rate(s) and coating densities desired. The blowing agent mechanism for this system is the reaction of the emerging isocyanate with water to produce carbon dioxide gas. By utilizing the water/isocyanate reaction, alternative blowing agents such as FREON based systems were not needed to produce the blown foam. Uniform application over large area metallic surfaces is possible while obtaining uniform bulk and surface mechanical - electrical properties.

Numerous applications have been identified for low density sprayable blown foam coatings. Some examples include low thermal conductivity coatings, low dielectric/low loss coatings, and lightweight abrasion resistant coatings.

Transparent Adhesives (Seamax)

By hydrogenation with Wilkinson type platinum catalysts one can obtain two component adhesives which are optically transparent and very oxidation resistant. They are used as an adhesive to bond transparent Kynar to glass. This composite is installed in glove boxes with the Kynar facing the inside. The boxes are used for cleaning stainless steel with HF/HNO₃. Breaks in the Kynar often occur with sharp edges of the parts or with cleaning tools. The adhesive resists acid penetration at the cut area for at least two weeks. Glass etching is thus avoided. Optical

integrity is maintained over much of the life of the boxes. Visibility from 60° sight angles are virtually undistorted. Yield per square foot is high affording low material costs. However, application costs tend to be a bit high due to the skill needed to apply the film with no trapped bubbles and uniform adhesive thickness to assure clarity. There are obviously associated applications in the chemical industry.

Antenna Cover Bonding (Seamax 9-27C-1)

Seamax 9-27C-1 liquid adhesive was chosen for an antenna cover bonding because of its low dielectric constant and loss tangent combined with its retention of mechanical characteristics at low temperature and high humidity. Seamax is a two part polyurea-urethane hybrid adhesive. The Seamax film adhesive was evaluated for mechanical properties. Three types of tests were performed:

- (1) Climbing Drum Peel Test per ASTM D1781 (indicates quantitative resistance of adhesive to combined tensile and shear loads in a honeycomb sandwich with one Duroid 5880 face sheet).
- (2) Flatwise Tensile Test per ASTM C297 (indicates tensile strength of the adhesive normal to the plane of a honeycomb sandwich).
- (3) Lap Shear Test per ASTM D1002 (indicates shear strength) Modifications: This test was modified to find the effect of humidity on the adhesive. One side of each of the lap shear coupons was Duroid 5880, instead of aluminum, to simulate the application.

Climbing Drum Peel Tests

Acceptable peel strength: 8 pounds per linear inch
Goal peel strength: 20 pounds per linear inch
Results: 21 pounds/inch width
Note: Honeycomb failed

Conclusion - Climbing Drum Peel

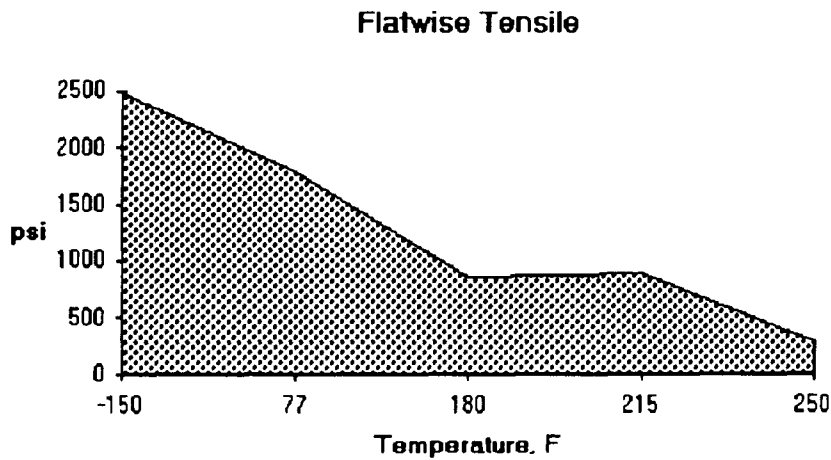
The average value was higher than the goal value chosen prior to testing. This fact, coupled with the honeycomb failure, is an indication that Seamax film's resistance to peel is exceptional in the given sandwich construction. Since some of the tests resulted in honeycomb failure rather than bond failure, higher peel strength should be anticipated if denser or tougher honeycomb were to be used.

Flatwise Tensile Test Data

Acceptable Tensile Strength: 200 pounds per square inch
Goal Tensile Strength: 1500 pounds per square inch

Note: Tensile strength criterion was based on flatwise tensile data from epoxy based adhesive tests performed with 3/16" cell aluminum honeycomb.

Figure 2



Conclusion - Flatwise Tensile

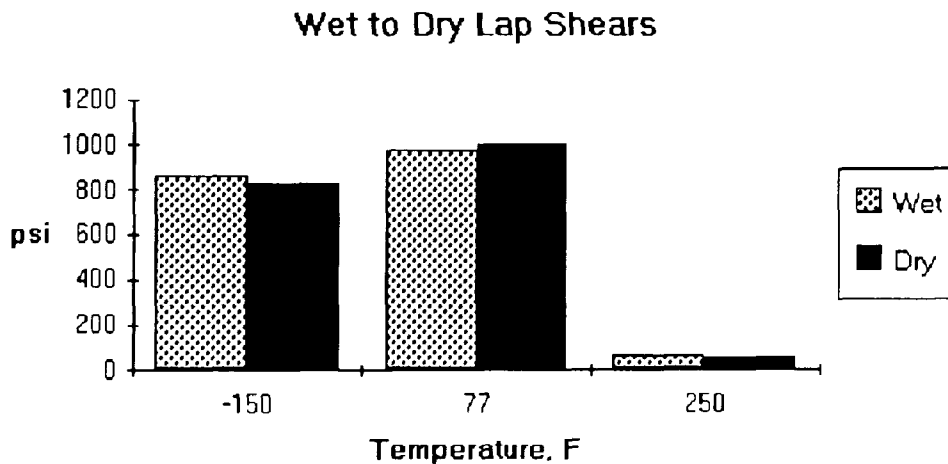
Figure 2 illustrates the excellent low temperature tensile strength of Seamax. The corrected bonding surface of the honeycomb in the 1" x 1" sandwich is 0.02925 square inches.

Lap Shear Test Data

Acceptable Ratio of Strength: Wet: Dry = 0.75:1
Goal Ratio of Strength: Wet: Dry = 0.95:1

Note: Samples out of humidity chamber 24 hours before testing.

Figure 3



Conclusion - Lap Shear, Wet vs Dry

The wet samples at ambient temperatures for Set One and Set Two had average strengths per inch width of 234# and 239# respectfully. This means that the failure point for the adhesive, in pounds per square inch, could not be reached before the 0.060" Duroid's failure point, in pounds per inch width. With the dry samples, Duroid's failure point was only reached in Set One. The failure point for the dry Duroid is approximately 317 pounds per inch width. For Set Two the force in pounds per inch width averaged 221, so the failure point of the Duroid was never reached and data on the shear strength of the adhesive was recorded.

Because the bondline for the wet samples could not be broken, the ambient temperature tests were not conclusive. The difference in average strength at ambient temperature between the wet and the dry is only 33 psi; this number is much lower than the standard deviation for either set. The ratio of the average strength values at 77°F for the wet samples to the dry samples is 0.967:1; this ratio is higher than the goal set prior to testing. Therefore, it can be assumed that at ambient temperature, humidity does not have a large effect. At cryogenic and elevated temperatures, the average bond strength is actually greater for the wet samples.

"7 Minute" Elastomeric Adhesive (Seamax)

A very favorable comparison may be made with mercaptan promoted "5 minute" epoxies! A Seamax type elastomer may be compounded that is very forgiving in its ability to bond to a wide variety of unprepared surfaces.

A typical application has the two component adhesive packaged in a "split" or "bi" pack for convenient containment and dispensing. The Baja 1000 served a number of years ago as an ideal field test.

One of the drivers of a dune buggy class was supplied with a few kits consisting of a hundred gram bi-pak, an application spatula, a metal brush, and a roll of polyester scrim. Fortunately (!) the driver blew a tire at forty miles out and again at 120 miles. A repair was necessary. The tear was about ten inches long and roughly followed the outside circumference of the tire. The rip was jagged. The surface was scrapped randomly for a minute, the mixed adhesive was applied to the surface and adjacent to the tear was coated generously with adhesive (slump grade). The scrim was applied over the coated area (about two inches in all direction of the tear) and pressed lightly. The remaining adhesive was then applied over the entire area. At 7 minutes the spread life was gone. At ten minutes the tire was mounted and at fifteen minutes the buggy was underway to complete the race!

Severe Adhesive Exposure, Oligomax

Cyclic harsh laundering and autoclaving at 270°F. for 1/2 hour periods is common in health care facilities. For example, bar graphing for loss prevention of a variety of nylon, polyester, and fabric supplies such as bedding and specialized apparel as breathable surgeons gowns is laundered and often autoclaved. Also, included are many instruments autoclaved for sanitary purposes. Oligomax adhesives functioning as the adhesive in composite tapes consisting of an imprinted fabric or metal tape, adhesive, and release film in the usual roll form is easily steam or heat activated for permanent application.

Breathable composite apparel has been assembled by B-stage preforms, steam activated, fully or partially cured for additional down-stream processing. Currently, this B-staging shows exceptional promise for continuous belt fabrication because of its bonding strength (Kevlar and steel) members.

Potting and Molding, Castomax

Commercial acceptance of a series of oligomers for acoustical sensor device protection. A number of desirable properties virtually assures their success.

Exceptional safety in handling and use
Excellent primerless adhesion
Excellent water resistance
User friendly, favorable Reynold's Number
Density close to water and variable
Rho C = $\sim 1597^6$ and tunable,
Variable work life from 10 to 90 minutes

SUMMARY

A collage of liquid polymers has been developed with wide-ranging applications. The products are variations of polybutadiene oligomers involving free radical and addition cross-linking and chain extension via several different radical functionalities such as amine, silicone, isocyanate and others.

The mechanical properties of the resultant cured polymers cover a range from viscoelastic fluids through elastomers, elastoplastic fluids through elastomers, elastoplastics and plastics. They have in common unusual mechanical and electric properties with outstanding water resistance. Furthermore evidence was shown that the development of products with engineered features which were not possible to produce heretofore. For instance, microwave antennas may be assembled with efficiencies over 95% while maintaining or advancing all antenna functions. Nylane demonstrates similar broad versatility with plastic mechanical performance. They may be described as solventless, liquid curable engineering plastics. It may reasonably be anticipated that further commercial products will continue to flow from this fascinating area of materials.

REFERENCES

- (1) G.M. LeFave, F.Y. Hayashi and A.W. Fradkin,
U.S. Patent 3,138,573 (1966)
- (2) G.M. LeFave and F.Y. Hayashi
U.S. Patent 3,138,573 (1964)
- (3) G.M. LeFave IEEE Electrical
Insulation Conference, September 23, 1971
- (4) G.M. LeFave, D.J. Wulgart, 29th National SAMPE
Symposium, April 3, 1984
- (5) Contract No. N66001-93-M-1924, Naval Research and Development
- (6) E.W. Thomas, USRD Tech Note 11, Rho C Value, October, 1982

539-27
2475
P. 8

Plasma Treatment of Polymer Dielectric Films to Improve Capacitive Energy Storage.

A. Yializis,
Sigma Labs Inc.
10960 N. Stallard Place
Tucson, Arizona
Tel: 602-575-8013

M. Binder, R.J. Mammone
Army Research Lab
Fort Monmouth, New Jersey
Tel: 908-544-4795

ABSTRACT

Demand for compact instrumentation, portable field equipment and new electromagnetic weapons is creating a need for new dielectric materials with higher energy storage capabilities. Recognizing the need for higher energy storage capacitors, the Army Research Lab at Fort Monmouth NJ, initiated a program years ago to investigate potential methods for increasing the dielectric strength of polyvinylidene difluoride (PVDF) film, which is the highest energy density material commercially available today. Treatment of small area PVDF films in a CF_4/O_2 plasma showed that the dielectric strength of these films can be increased significantly. Sigma Labs continued this work using large area films that were plasma treated in production size equipment, and found that the dielectric strength of PVDF films can be increased by as much as 20% when treated in a 96%- CF_4 /4%- O_2 plasma. This 44% increase in energy storage of a PVDF capacitor, is significant considering that the treatment can be implemented in a conventional metallizing chamber, with minimum capital investment. The data shows that improved breakdown strength may be unique to PVDF film and the particular CF_4/O_2 gas mixture, because PVDF film treated with 100% CF_4 , 100% O_2 , Ar gas plasma, and electron irradiation, shows no improvement in breakdown strength. Other data presented includes dissipation factor, dielectric constant and surface tension measurements.

INTRODUCTION

Increasing requirement for device miniaturization, portable field equipment and new electromagnetic weapon systems, is creating a demand for new dielectric materials with improved electrostatic energy storage capabilities. There is a well defined need for new materials with higher dielectric constants and improved breakdown strength. New material development is driven by various commercial and military applications including flash lamps, copiers, implantable defibrillators, pulsed lasers, radar modulators, isotope separation lasers, directed energy weapons, electronic warfare and countermeasure pulse generators and a broad range of electronic equipment.

When designing high energy density capacitors polymer films are the materials of choice. Polymer films are used in most applications, because they can withstand higher electric stresses, are lightweight and relatively economical. Low loss materials such as polypropylene are used in high rep-rate, lower energy applications. For higher energy density and low rep-rate applications, polyvinylidene difluoride (PVDF) is used. Over the years refinements made in the overall quality of these films and the capacitor manufacturing process equipment has allowed small incremental improvements in capacitor energy

densities. Today the highest energy density commercial capacitors have densities of about 2.5J/cc and are made PVDF films. There is little evidence that new polymer chemistries may be available in the near future to surpass the energy density of PVDF film. Lately we have seen some new films with high temperature capabilities from 3M, Foster-Miller, Hoechst Celanese, Dow Chemical and Maxdem. Maldecorn et.al [1] have shown that all these new films have dielectric constants in the range of $k=2.8$ to 3.6. When fully developed, these films may satisfy some surface-mount needs for low voltage metallized capacitor products and some high temperature applications, but they will have no impact in high energy density applications.

Addressing the need for increased demand for higher energy density capacitors in military and commercial applications, the Army Research Laboratory at Fort Monmouth NJ, initiated a development program to explore potential improvements in breakdown strength of capacitor films by treating these films in various gas plasmas [2-8]. This work among other findings showed that breakdown strength of small area PVDF films can be improved by exposure to a CF_4/O_2 plasma. Sigma Labs was awarded an SBIR contract to investigate if this effect persists in larger area films, processed in a production size vacuum system under conditions that simulate a production environment.

This paper reports the results of plasma treatment of PVDF films in a full size metallizer, where the film is moved from one roll to another through a plasma zone. X-ray-Photoelectron-Spectroscopy (XPS) was used to study the surface chemistry of the films before and after the treatment. Small area capacitors were produced to measure breakdown strength and other electrical properties of the treated films. In order to explore the mechanism by which plasma treatment affects a bulk property such as the breakdown strength of the polymer, films are irradiated with electron radiation and the data compared to that of plasma treatment.

EXPERIMENTAL TECHNIQUE

The experimental apparatus is shown in Figure 1. A full size metallizer with a 22" long drum was used. The film was treated by passing through a plasma zone that is formed between a plasma reactor and the rotating drum. The plasma reactor was a low power system in which RF power was coupled both inductively and capacitively to the plasma. The cylindrical reactor shell was water cooled and it can take a significant amount of power, although for this experiment we drove it with only 500W of real power (Forward power - Reflected power) using a manually variable tuning network. The reactor cylinder had a window facing the film that is 35.5cm long and 3.8cm wide. Therefore, based on the speed of the drum and real RF power transferred to the load, we can calculate a plasma power density in $W/cm^2/sec$. This value is an equipment specific number because it reflects the power input into the plasma reactor and does not account for ionization efficiency.

DC Breakdown Measurement Technique

Breakdown measurements on the films, used a dry double-metallized non contact measurement technique, and were performed at high vacuum ($<10^{-4}$ torr), to eliminate partial discharges and surface flashover. The breakdown system was built in a turbomolecularly pumped stainless steel vacuum chamber. Metallization masks allowed us to metallize small area stamp capacitors for breakdown measurements. Electrode contact was made to metallized pads that are outside the active area in order to prevent film damage. The voltage was ramped at about 500V/sec. For every breakdown measurement reported, at least 18 stamp capacitors were tested. We chose not to employ the more commonly used liquid impregnation technique for measuring breakdown strength of films. Since neither the film nor the electrodes are perfectly flat, there is always thin liquid layers involved in the breakdown. This results in

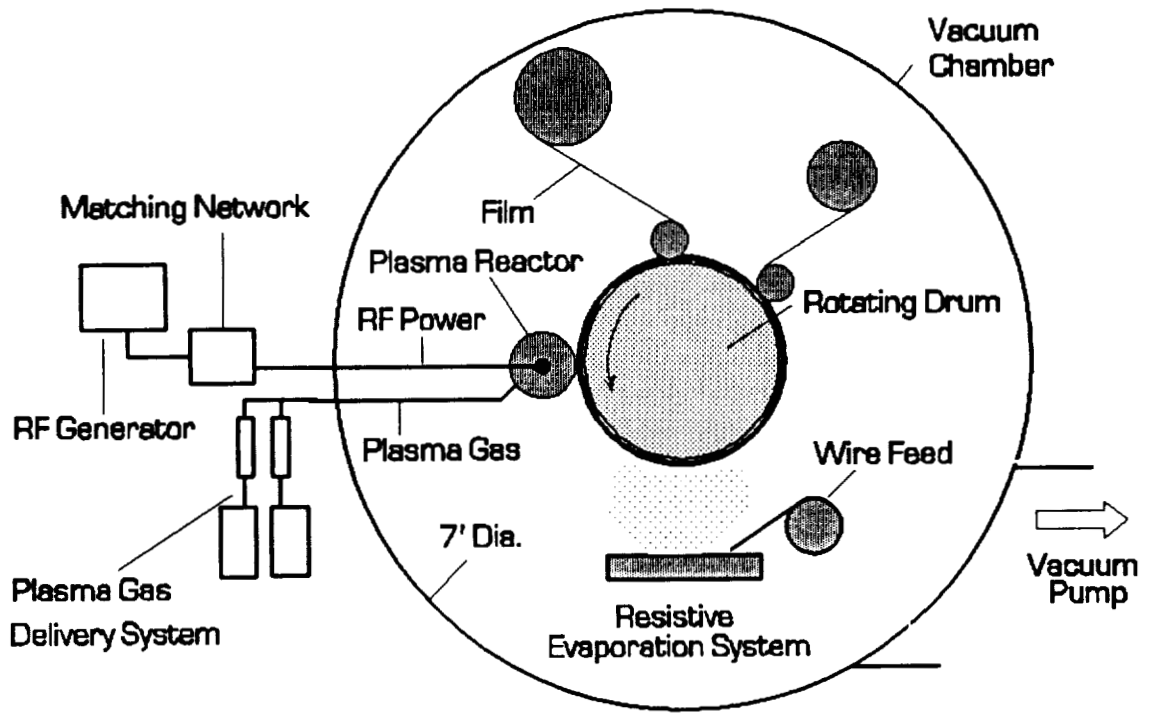


Figure 1. Schematic representation of the experimental set-up for plasma treating polymer films. The plasma reactor is placed against the rotating drum of a production size web coater, prior to the metallization station.

BREAKDOWN OF PLASMA TREATED PVDF FILM
 CF_4 vs. CF_4/O_2 vs. E-GUN

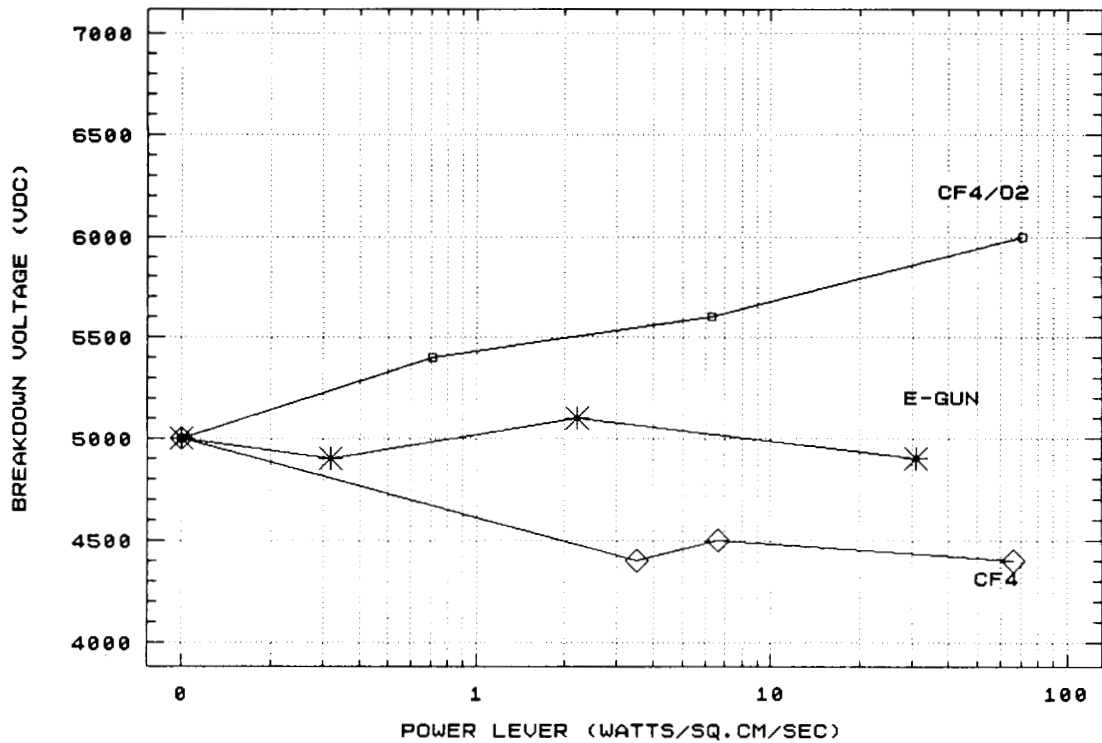


Figure 2. Breakdown voltage of $12\mu m$ PVDF film treated with a CF_4/O_2 plasma, electron radiation and a CF_4 plasma. Each breakdown point represents an average value derived from the breakdown of eighteen double metallized stamp capacitors. The maximum standard deviation of any of the above points is 500V.

slightly higher and more uniform breakdown values that often mask minor variations in film thickness that can result from film fibrils and microcrevices. The dry double metallized technique performed in a high vacuum environment produces results that depend strictly on the polymer film, and it eliminates any questions about the effects of the liquid impregnant.

TREATMENT OF PVDF FILMS

Plasma Treatment Using CF_4 Gas

Not knowing what effect a 100% CF_4 gas plasma will have on the PVDF films we started the study using pure CF_4 , to establish a baseline before proceeding to the CF_4/O_2 mixture. We first exposed PVDF film to a plasma density of 0.3 W/cm²/sec. DC breakdown values of the CF_4 plasma treated PVDF film were slightly lower than the control film (see Figure 2). When the plasma density was increased to 2.2 and 31.0 W/cm²/sec, and as shown in Figure 2, there was no significant effect on the breakdown strength of the film.

Plasma Treatment Using a CF_4/O_2 Plasma Gas

Implementing the process developed by Mammone et-al [4], a gas mixture of 96% CF_4 /4% O_2 was used for plasma treatment. As shown in Figure 2, this particular gas mixture at plasma densities as low as 0.71 W/cm²/sec has a significant effect in the DC breakdown values of the treated PVDF films. Following the CF_4 plasma treatment results, we did not expect the addition of a small amount of O_2 to have such a significant effect in the breakdown values under the same plasma conditions. This data supports the small area data derived by the Army ETDL group and illustrates that breakdown strength of large area PVDF film can be improved using a plasma treatment arrangement that simulates a production process. It should also be noted that the small area samples were immersed in the plasma whereas in our work only one side of the moving film was exposed to the "hot plasma", while the other side of the film was maintained at 25°C (water cooled drum).

Electron Beam Treatment of PVDF Films

Breakdown strength of a polymer film is considered to be a bulk property and one would not expect that a surface treatment would effect it. Given the high plasma power level and breakdown results, it is possible that the thermochemical treatment extends beyond the film surface. One postulation is that layers of the film close to the surface (up to 1-2 μm deep) are cross linked by the plasma radiation. Such modification of the polymer film results in a segment of the film that has superior breakdown strength. In order to separate the cross linking effect from the chemical effects of the plasma gas, an electron beam was used to irradiate PVDF film. Based on our experience with electron beam curable dielectrics [9,10], we used a 15kV accelerating voltage to penetrate 1.5 μm to 2.5 μm into the film and varied the beam current to obtain power densities similar to those used in the plasma treatment. The results of this experiment shown in Figure 2, show that the breakdown strength of PVDF film is virtually unchanged. This observation suggests that if PVDF film can be radiation cross linked, this effect alone may not be responsible for the increased breakdown strength. In fact the data suggests that the film may be damaged by electron irradiation. The results of the pure CF_4 and O_2 plasma treatments also support this view, because cross linking radiation derived from different plasmas (mostly electrons and energetic photons) is not expected to differ much from that of CF_4/O_2 plasma.

Dissipation Factor and Dielectric Constant Measurements

The data in Table 1 show that there are fluctuations in the DF and k values of treated films. Films treated with CF_4/O_2 have measurably lower values of DF at lower temperatures and at 100Hz and 1kHz, while at higher temperatures and 10kHz, the DF values are somewhat higher. At this point we do not have an explanation for this behavior. It is interesting to note that we do not see a reduction in the value of k at higher plasma densities as observed by Mammone et-al [4]. There are some key differences between the present experimental set-up and the one used by Mammone et-al [4]. PVDF used in this work had a higher dielectric constant ($k=13$ versus $k=10$), and in this investigation films were treated only on one side. It should also be noted that in the previous work, the k was lowered only during long exposure to the plasma. Under those conditions films could heat-up enough to recrystallize and affect the value of the dielectric constant.

XPS Analysis of the Treated Films

XPS analysis conducted on control and CF_4/O_2 plasma treated PVDF films shows that the F/C ratio increased as a function of the level of plasma treatment. We also found that aluminum is sputtered onto the PVDF film surface from the plasma reactor, which is fabricated from aluminum metal. High resolution spectra in the C1s region are shown in Figure 3. Analysis of these peaks indicates that as the level of plasma treatment increases, the ratio of C-N, C-O and C-C to C=O increases. One could also suggest that the effect of the peroxy and carboxylate peaks may also be visible. Using high resolution spectra of the C1s, F1s, O1s and Al2p peaks, elemental ratios can be calculated for each of the spectra. The F/C, O/C and Al/C ratios are shown in Figure 4, as a function of CF_4/O_2 plasma treatment level. The most significant observation that can be made from this data, is that additional fluorine is incorporated in the polymer as a function of plasma treatment.

Wetting Angle Measurements

Contact angle measurements made with a system that has a 35:1 magnification with an adjustable focus allowed us to make wetting angle measurements with an accuracy of better than 5 degrees. A pipet was used to dispense a controlled size droplet of deionized water. Contact angle measurements were made for both control films and films treated with CF_4 , CF_4/O_2 as well as electron radiation. Control films have a contact angle of about 65-70°. This angle remains very much unchanged for all treatments and power levels except for the higher power CF_4/O_2 plasma treatment, where it drops to about 35-40°. Since PVDF is highly polar, we did not expect to measure significant changes in the contact angle, unless there are major changes in the polarity and/or morphology of the film surface. Lowering of the contact angle at higher plasma levels suggests that there are significant changes on the surface of the film. If we also consider the DF data in Table 1, we may conclude that chemical changes extend into the bulk. Our experience in corona and plasma treating films is that even in less polar films such as polypropylene, a conventional surface treatment that is used to promote metal adhesion does not affect the DF of the film. This data supports the conclusion drawn from breakdown voltage measurements, that plasma treatment can alter chemical and physical properties of films beyond the surface layers.

SUMMARY

CF_4/O_2 plasma treatment results in a significant increase in the breakdown voltage of the PVDF film. When considering a common PVDF capacitor design that utilizes double metallized paper electrodes and

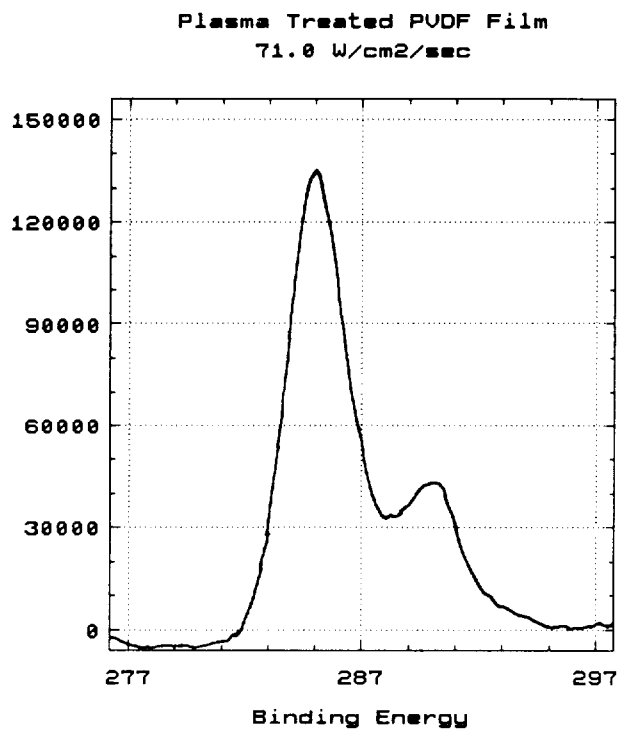
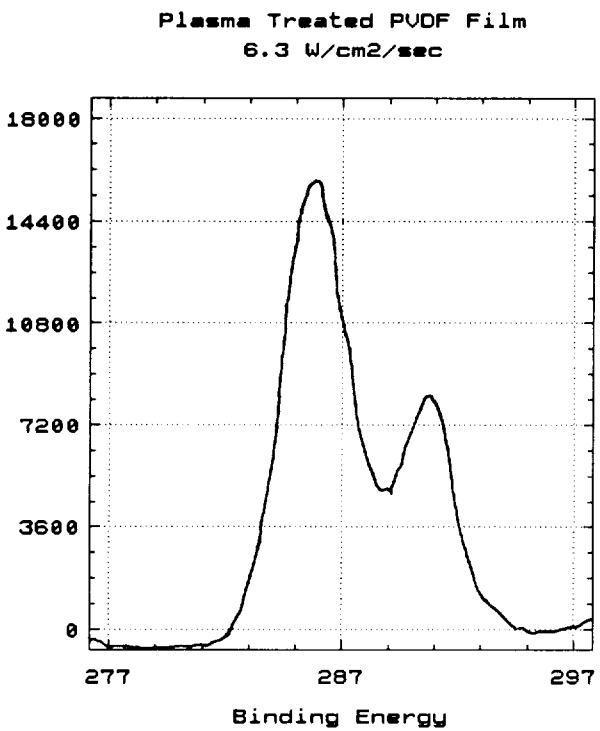
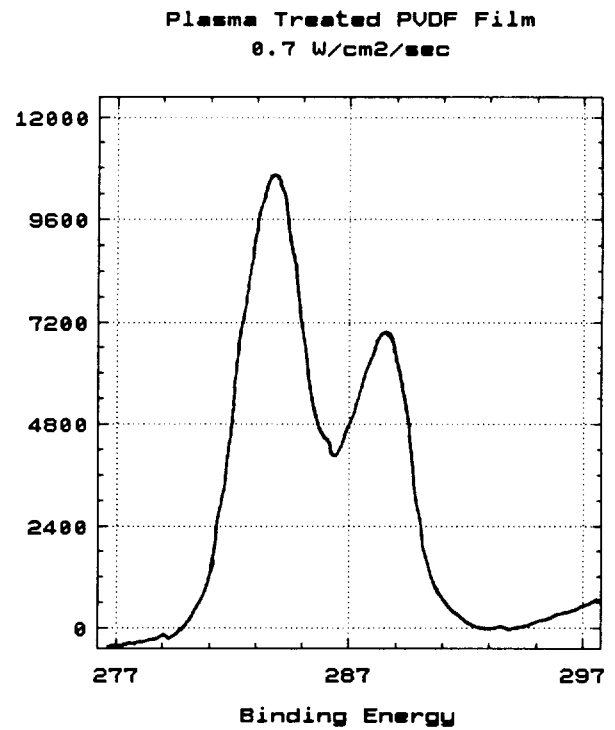
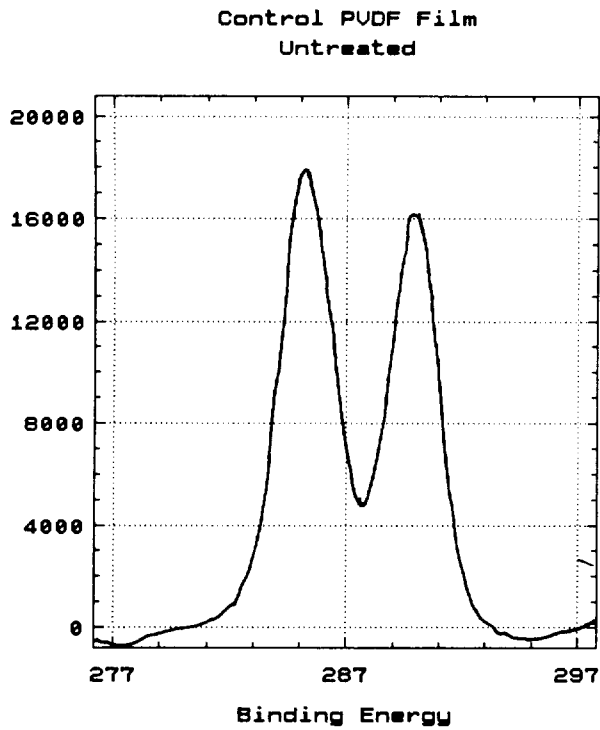


Figure 3. High resolution XPS spectra in the region of the C1s peak for control and CF₄/O₂ plasma treated 12 μm PVDF film, at different plasma power densities. The binding energy scale is approximate and measurements are made after a calibration is performed on the individual spectra.

TABLE 1. Dielectric measurements of 12um PVDF film, treated in a CF₄/O₂ plasma.

Plasma Density (W/cm ² /sec)	Test Temp. C	Dissipation Factor (%)			Dielectric Constant (k)			DC Break Voltage (KV)
		100Hz	1kHz	10kHz	100Hz	1kHz	10kHz	
0.0	30	1.48	1.73	3.28	12.9	12.7	12.3	5.0
	50	1.59	1.66	2.68	13.2	13.0	12.6	
	70	1.95	1.81	2.30	13.8	13.5	13.2	
	90	2.37	2.07	2.21	14.5	14.0	13.6	
	90	2.37	2.07	2.21	14.5	14.0	13.6	
0.7	30	1.20	1.57	3.48	12.4	12.2	11.8	5.4
	50	1.20	1.42	2.91	12.6	12.4	12.1	
	70	1.37	1.41	2.33	13.0	12.8	12.5	
	90	2.24	2.00	2.54	14.3	13.9	13.5	
6.3	30	1.20	1.52	3.30	12.4	12.2	11.9	5.6
	50	1.23	1.39	2.69	12.7	12.5	12.2	
	70	1.48	1.46	2.25	13.2	13.0	12.7	
	90	2.56	2.21	2.45	14.7	14.2	13.8	
71.0	30	1.27	1.48	2.95	12.5	12.2	12.0	6.0
	50	1.30	1.43	2.67	12.6	12.4	12.1	
	70	1.54	1.52	2.47	12.1	12.8	12.5	
	90	2.46	2.16	2.70	14.3	13.9	13.5	

XPS ANALYSIS OF PLASMA TREATED PVDF FILM
CF₄/O₂ PLASMA - 3 LEVELS

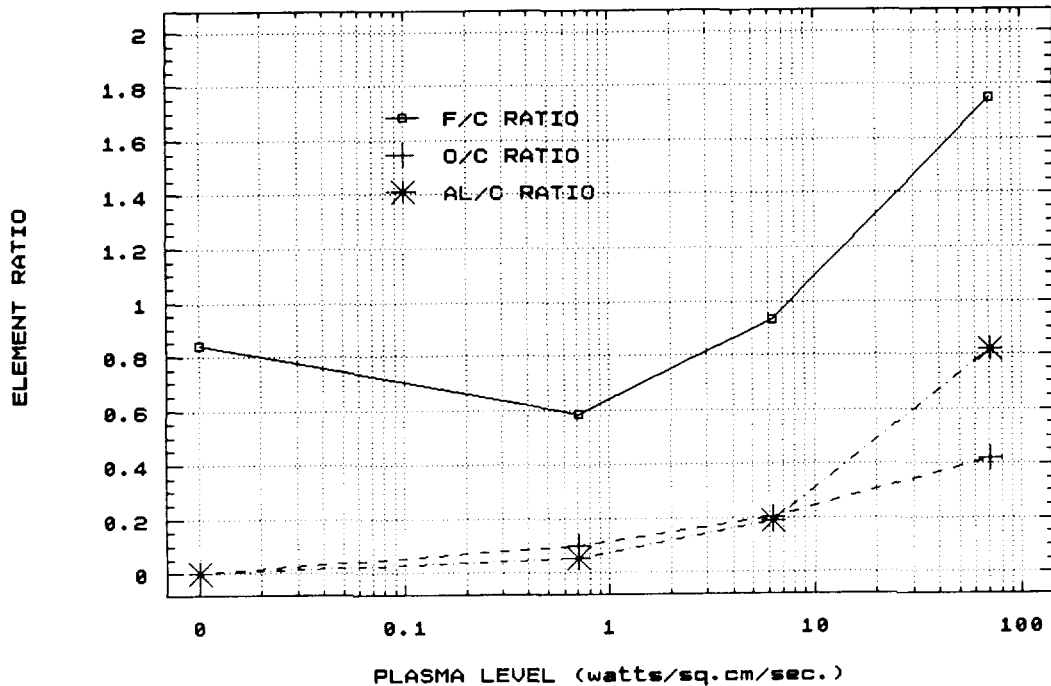


Figure 4. Fluorine, oxygen and aluminum / carbon ratios as a function of plasma power density, derived from high resolution XPS analysis of control and CF₄/O₂ plasma treated 12µm PVDF films.

has a delivered energy density of 2.44J/cc (current design by a major capacitor manufacturer), plasma treated PVDF film can raise this value to 3.51J/cc. What is even more significant is that the additional cost for this benefit may be minimal because process and equipment are relatively simple, and if the film is to be metallized, the treatment can be performed inline with the metallization process in the same chamber. Furthermore, the lower wetting angle of the surface of the treated film will improve the capacitor impregnation process and thus reduce air voids that can lead to partial discharges during the operation of the capacitor. Minimization of the partial discharge activity can lead to improved performance and reliability under a broad range of operating conditions.

Although such an increase in energy density and reliability may not satisfy the longer term objectives of several government programs that require capacitor energy densities as high as 10J/cc, plasma treated PVDF represents a significant step in this direction that is relatively easy to attain. In the short term this improvement can benefit several electromagnetic weapon programs, and it can have an impact on commercial capacitor products for applications such as portable defibrillators, flash lamps, and pulse generators.

REFERENCES

1. L. Maldecorn and R. L. Miller, "High Temperature, >200°C Polymer Film Capacitors", IEEE Power Sources Conf. Cherry Hill, NJ, June 25,1992
2. W.L. Wade Jr., R.J. Mammone and M. Binder, J. Applied Polymer Science, 43, 1989
3. M. Binder, W.L. Wade Jr., P. Cygan, T.R.Jow and R.J. Mammone¹², IEEE Transactions on Electrical Insulation, 27, 399 (1992).
4. R.J. Mammone, W.L. Wade Jr. and M. Binder, Proceedings of the 12th Capacitor and Resistor Technology Symposium, Tucson, AZ, March 16-19, 1992.
5. R.J. Mammone, W.L. Wade Jr. and M. Binder, Polymers for Advanced Technologies, 2 209 (1991).
6. M. Binder, R.J. Mammone, B.Lavene and E. Rondeau, 27th Int. Energy Conv. Eng. Conf. San Diego, Ca, Aug. 1992.
7. M. Binber, R.J. Mammone, E. Rondeau and B. Cavene, Proceedings of the 35th Power Sources Symposium, Cherry Hill NJ, June 22-25 1992.
8. M. Binder, R.J. Mammone, W.L. Wade Jr, E. Rondeau and B. Cavene, IEEE Electrical Insulation Magazine, July/August 1992.
9. A. Yializis, G. L. Powers & D. G. Shaw "A New High Temperature Multilayer Capacitor with Acrylate Dielectrics" IEEE Trans. on Components, Hybrids, and Manuf. Technology, V13, No. 4, pp 611-616, 1990
10. A. Yializis, D.G. Shaw, D.S. Strycker & M. Ham, "High Speed Process for Coating Substrates", US Patent No. 4,842,893, 1989
"Miniaturized Monolithic Multilayer Capacitor", US Patent No. 5,018,048, 1991

Development of Radiation Resistant Electrical Cable Insulations¹

B. S. Lee, P. Soo and D. R. MacKenzie

Department of Advanced Technology,
Brookhaven National Laboratory, Upton, NY 11973

ABSTRACT

Two new polyethylene cable insulations have been formulated for nuclear applications, and have been tested under gamma radiation. Both insulations are based on low density polyethylene, one with PbO and the other with Sb₂O₃ as additives. The test results show that the concept of using inorganic antioxidants to retard radiation initiated oxidation (RIO) is viable. PbO is more effective than Sb₂O₃ in minimizing RIO.

INTRODUCTION

The first comprehensive study of gamma radiation damage to insulation and jackets for electrical cables in nuclear reactor systems was conducted by Blodgett[1] two decades ago. In this study, thirteen different kinds of polymer were evaluated up to a total dose of 5×10^5 Gy (5×10^7 rads) at a dose rate of 5×10^3 Gy/h (5×10^5 rads/h). It was estimated that the total radiation dose absorbed by a cable within the commercial nuclear reactor containment area may approach 5×10^5 Gy during an assumed reactor lifetime of 40 years if there were no abnormal bursts of radiation. One of the conclusions drawn from this study was that CSPE (chlorosulfonated polyethylene) or CPE (chlorinated polyethylene) jacketed insulation based on nonfilled CLPE (cross-linked polyethylene) or carbon filled CLPE should last at least 40 years when exposed to a total radiation dose up to 5×10^5 Gy and would still be serviceable after exposure up to 10^6 Gy.

However, in November 1976 an inspection of a pump suction valve motor assembly in the Savannah River K-reactor at Aiken, South Carolina, revealed badly embrittled polyethylene (PE) insulation on the power control wiring. The maximum dose experienced by the cable materials was only 2.5×10^4 Gy during the 12 years of operating life. The subsequent checking of other cables in the C- and P- reactors disclosed additional embrittled cables[2]. This degradation of the cables was faster-than-expected, so Clough and Gillen[2] conducted an extensive investigation of cable degradation by radiation.

The most important finding from the study of Clough and Gillen was that, when oxygen is present, dose rate is another important parameter to consider in addition to total dose in the polymer degradation processes. It was also shown that a strong synergism of radiation and elevated temperature, as well as dose rate, led to unexpectedly rapid degradation of the Savannah River reactor cables. These findings can be explained by the effects of diffusion of oxygen into the cable materials during service which resulted in oxidation processes. Thus, the degradation process for the cable insulation and jacket under radiation can be termed radiation initiated oxidation (RIO).

1. This work was performed under the auspices of the U.S. Department of Energy. By acceptance of this article, the publisher and/or recipient acknowledges the U.S. Government's right to retain a nonexclusive, royalty-free license in and to any copyright covering this paper.

- a) Low valence states of the transition elements, e.g., Fe^{2+} , Mn^{2+} , Cr^{2+} , Co^{2+} . They might be used as oxides or as salts such as sulfates, phosphates, or possibly chlorides.
- b) Group V cations in the reduced state, e.g., As^{3+} , Sb^{3+} and Bi^{3+} . (Arsenic, however, is not recommended).
- c) Group IV cations in the reduced state, e.g., Pb^{2+} .
- d) Reducing anions which might be useful are sulfite, selenite, and phosphite.
- e) The reduced form of a cation could possibly be used as a salt with a reducing anion.

Choice of Additives

Among the cations listed above, the transition elements in a) may not be a good choice, since it was reported that some of these ions operate as catalysts in the autoxidation of certain polymer systems[9,10,11]. As shown in the above list, several other additives could have been tried for this study. However due to the limitation on resources, only two additives were selected, Sb_2O_3 and PbO . Rockbestos Company in Connecticut agreed to assist us in our work primarily by preparing the new polymer formulations.

Choice of Polymer

Currently, PVC and low density polyethylene (LDPE) are widely used for cable insulation and jackets due to their good extrudability combined with good insulation properties. These materials also show acceptable radiation resistance, and a fair amount of data on radiation effects on these is available. High density polyethylene (HDPE) is less radiation resistant than LDPE at both high and low dose rates; PVC is more sensitive to dose rate effects than LDPE[6]. Thus, LDPE was chosen as the base polymer for this study.

EXPERIMENTAL

As shown in Table 1, LDPE with seven different compositions were molded into sheets of 15 cm x 15 cm x 0.17 cm. The seven compositions are a LDPE control without additives, and LDPE with two different additives at three different concentrations.

Dogbone shaped samples (gauge length: 3.4 cm, width: 0.6 cm, thickness: 0.17 cm) were stamped from the sheets using a hydraulic press and an ASTM recommended die. A batch of 14 samples (two for each composition) were stacked together with spacers between them. The samples were degreased with alcohol before irradiation.

The gamma irradiation facility at Brookhaven National Laboratory (BNL) was used to irradiate the specimens in air at 10°C. Three different dose rates were used for this study: 3.31×10^3 , 6.26×10^3 and 1.1×10^4 Gy/h. The total doses used ranged from 1.3×10^6 Gy and 5.37×10^6 Gy.

An Instron tensile testing machine was used to measure elongation and tensile strength. A displacement rate of 5 cm/minute was used. A 2.5 cm gauge was marked at the center of the sample, and the distance between the gauge marks was followed until the sample broke.

TABLE I
Compositions of Test Samples

Sample ID	Composition (weight %)
A	LDPE homopolymer + 1% PbO
B	" + 1% Sb ₂ O ₃
C	" + 3% PbO
D	" + 3% Sb ₂ O ₃
E	" + 10% PbO
F	" + 10% Sb ₂ O ₃
Z (Control)	"

RESULTS

At the highest dose rate used, 1.1×10^4 Gy/h, samples A - D behaved very similarly to the control sample. Samples E and F seem to have slightly higher elongations compared to the control samples up to the total dose of 5×10^5 Gy, but the differences may not be significant.

At a dose rate of 6.26×10^3 Gy/h, all six samples showed improvements in elongation over control samples up to a total dose of 3×10^5 Gy, with the PbO containing samples, A, C and E outperforming the Sb₂O₃ added samples, B, D and F. At total doses higher than 5×10^5 Gy, all six samples behaved similarly to the control samples. Among the samples with the same kind of additive, the higher the concentration, the more distinct the improvement.

At a dose rate of 3.31×10^3 Gy/h, for the PbO containing samples, only sample E (10% PbO) showed improved elongations compared with the control sample up to the total dose of 1.6×10^5 Gy. It seems that all three Sb₂O₃ containing samples, B, D and F showed slight improvements in elongation over the control samples up to a dose of 1.6×10^5 Gy.

It should be mentioned that the addition of PbO to PE reduces the ductilities, i.e., elongations of the unirradiated samples decrease significantly as shown in Fig. 1. Thus, the real effects of the additives as antioxidants may be shown better if the elongation data are normalized to the elongations of the unirradiated samples. In Figures 2 - 5, the elongation values were averaged, and normalized to those of unirradiated samples. The same trends as discussed earlier can be seen in these plots except that the rankings of performance are switched in some cases. Again, more data are needed to draw firmer conclusions regarding the optimum composition.

From these plots, the effects of the additives may be roughly estimated in terms of total dose at which the elongation is reduced to half of its original value. For PbO added samples (Fig. 2), at a dose rate of 6.26×10^3 Gy/h, it takes about 40 % more total dose for the elongation to be reduced to half of its original value. In other words, at this dose rate, it takes 40 % longer time for the PbO added samples to reach half of the original elongation. At dose rates of 1.1×10^4 Gy/h and 3.31×10^3 Gy/h (Fig. 3 and 4), it takes 39 % and 30 % more time for the PbO added samples to reach half of the original elongations, respectively. As discussed earlier, for Sb₂O₃ added samples the effects are not as significant. For instance, at 3.31×10^3 Gy/h (Fig. 5), it takes 7 % more time for the elongations of Sb₂O₃ added samples to be reduced to their original values.

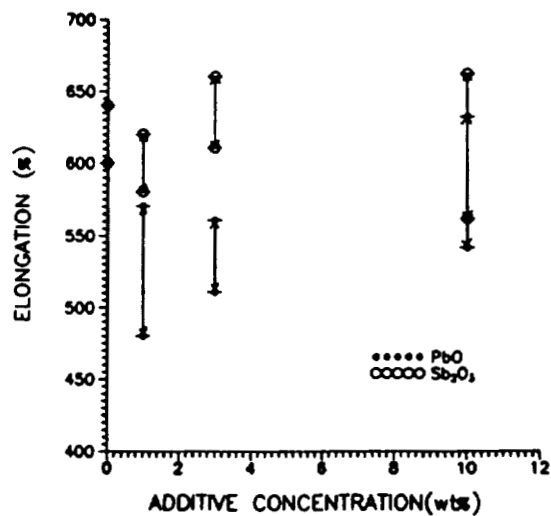


Figure 1. Elongation for unirradiated samples with different additive concentrations.

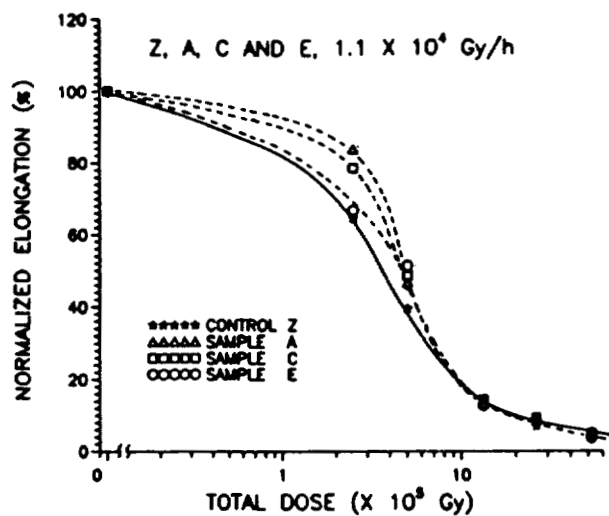


Figure 2. Normalized elongation for samples Z, A, C, and E irradiated at a dose rate of 1.1×10^4 Gy/hour.

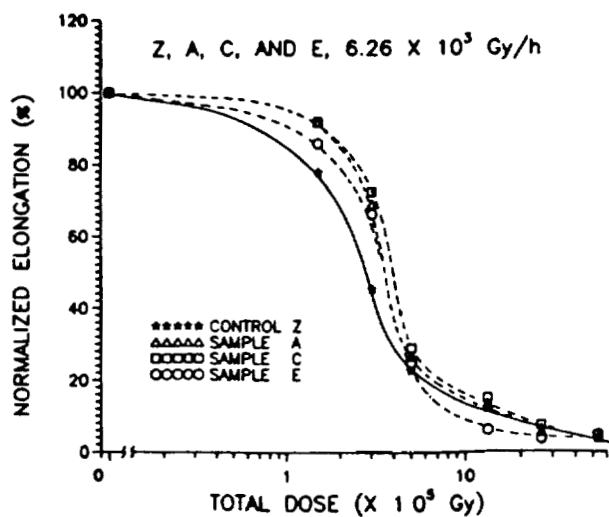


Figure 3. Normalized elongation for samples Z, A, C, and E irradiated at a dose rate of 6.26×10^3 Gy/hour.

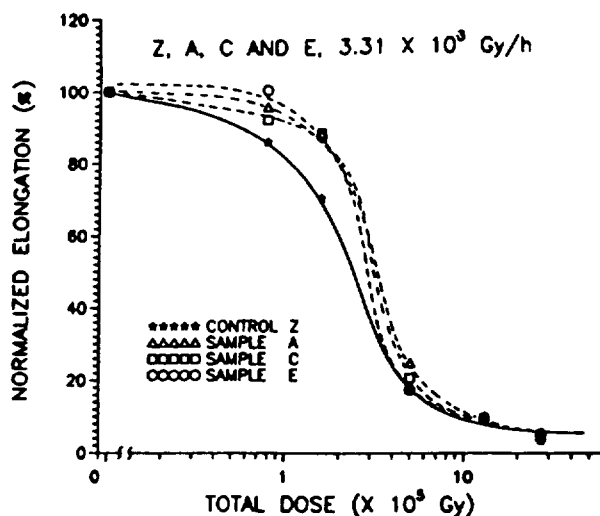


Figure 4. Normalized elongation for samples Z, A, C, and E irradiated at a dose rate of 3.31×10^3 Gy/hour.

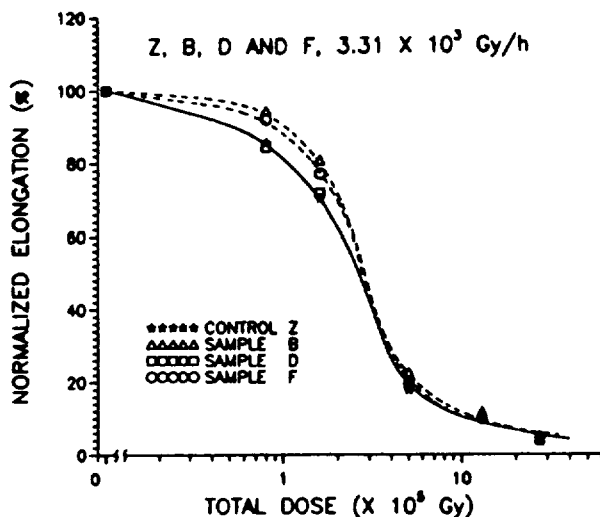


Figure 5. Normalized elongation for samples Z, B, D, and F irradiated at a dose rate of 3.31×10^3 Gy/hour.

Based on these results, it is believed that PbO works effectively as an antioxidant until the total dose reaches a certain level which is determined by the dose rate used and the amount of additive. For instance, at 6.26×10^3 Gy/h, for total doses higher than 3×10^5 Gy, the addition of PbO did not make much difference. For a dose rate of 3.31×10^3 Gy/h, the PbO addition to the samples A (1%) and C (3%) does not seem to be effective in slowing down RIO for the range of total doses used in this study, and only the sample E showed improved elongations up to a dose of 1.6×10^5 Gy.

Addition of Sb_2O_3 seems to improve the elongation slightly for all the three dose rates used. However, the degree of improvement is not as much as that for PbO.

DISCUSSION

These observed improvements of elongation properties may be attributed to one of the following mechanisms:

- a) the inorganic additives reacted with oxygen-containing free radicals and retarded RIO.
- b) the inorganic additives reacted with free radicals and retarded RIO.
- c) the inorganic additives worked as energy sinks.

It may also be possible that the additives, which in the ground state do not react with oxygen, became electronically excited and reacted with oxygen. Within the scope of this study, it is not possible to provide information which can determine exactly how the additives worked. However, due to the reduced state of the cations of the additives, it is believed that these additives retarded RIO by reacting with oxygen-containing free radicals.

Based on the RIO mechanisms discussed earlier and an assumption that the inorganic additives improved elongation properties by reacting with oxygen in polyethylene (PE), what follows is an attempt to explain the experimental results.

It is generally believed that the degradation inside a polymer is not homogeneous when oxygen diffusion is involved. Clough and Gillen[12] reasoned that, after the initially-dissolved O_2 is used up, a steady-state situation will result in which strong oxidation occurs near the edges and degradation may proceed in the absence of oxygen or at reduced oxygen concentrations in the interior regions.

As oxygen molecules diffuse in from the surface, they react with free radicals generated by radiation, and the oxygen concentration in the polymer will decrease with depth from the specimen surface. Also, there may be a certain distance from the surface beyond which the oxygen concentration is negligible. For a polymer exposed to a high dose rate radiation in air, oxygen diffusion depth, L , should be shallow since the free radical concentration in the polymer should be high. In other words, oxygen molecules are consumed by free radicals before they diffuse to an appreciable depth. On the other hand, for the case of a low dose rate radiation, L should be large. Thus, the oxygen profiles as a function of the distance from the polymer surface may be represented schematically as shown in Fig. 6 (a) for polymer samples exposed to high, medium and low dose rate radiations in air.

RIO will proceed mainly in the area where oxygen is available, which will result in different oxygen diffusion depths for different dose rates for the same total dose: L_1 , L_2 and L_3 for low, medium and high dose rate, respectively. Assuming that ductility, i.e., elongation is determined primarily by the amount of unoxidized polymer, these oxygen profiles (or oxidation profiles) may explain why the polymer irradiated at higher dose rate shows higher elongation (less radiation damage) than that irradiated at lower dose rate when the total doses absorbed are the same (dose rate effect).

The above argument on heterogeneous oxidation may be used to explain the effects of additives used in this study. The role of an additive is to reduce the oxygen concentration, so the effects of an additive on the oxidation profile of a polymer should be similar to those of free radicals. In other words, the difference between the profiles of a polymer with an additive and the one without should be similar to those between polymers irradiated at a high dose rate and a low one as shown in Fig. 6 (b).

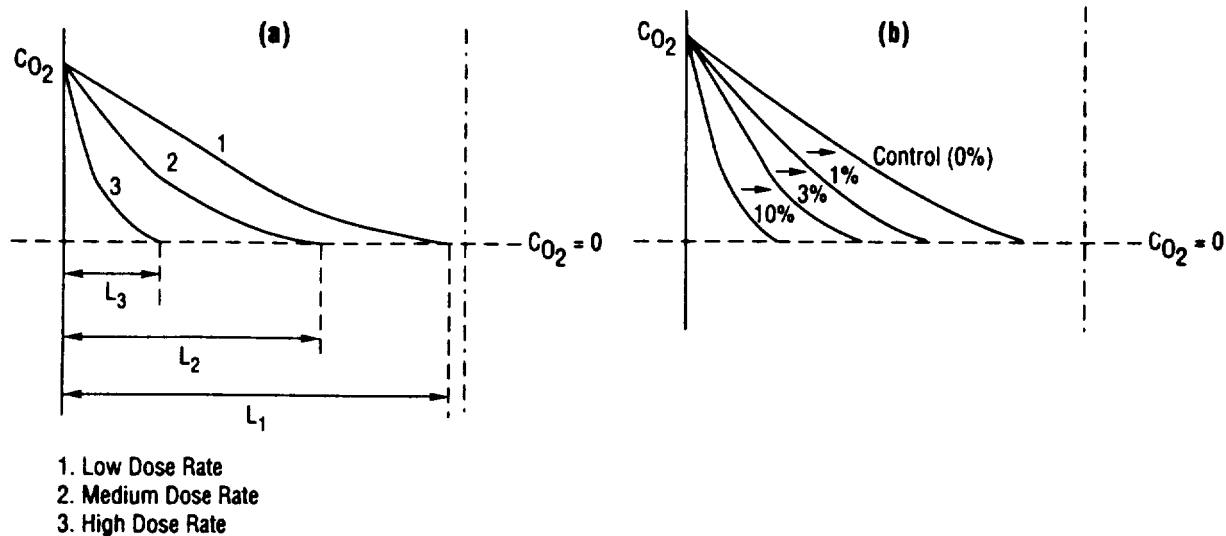


Figure 6. (a) Oxygen concentration profiles for different dose rates.
(b) Oxygen concentration profiles for different amount of additives.

After a certain period of time (or total dose) the additives within the oxidation layer will be consumed or their effectiveness will decrease, and the oxygen concentration profile will move in the direction shown by the arrows in Fig. 6 (b). Thus, the polymer samples with smaller amount of additives, for example, 1% and 3% PbO, will show improvements in elongation over the control sample up to a certain total dose (which is less than 8×10^4 Gy for dose rate of 3.31×10^3 Gy/h), after which these polymers will behave the same as the control sample. For the 10% PbO sample, a higher total dose is needed for the additives to lose effectiveness. The oxidation profile for 10% PbO shown in Fig. 6 (b) should move in the direction shown by the arrow as the total dose absorbed by the sample increases, until the sample behaves similarly to the control sample. Figure 3 shows that the additives were effective for the 10% PbO sample at least until the total dose reached 2×10^5 Gy at a dose rate of 3.31×10^3 Gy/h.

SUMMARY AND CONCLUSIONS

Two new polyethylene cable insulations have been formulated for nuclear applications, and preliminary tests have been completed under gamma radiation. Both insulations are based on low density polyethylene, one with PbO and the other with Sb_2O_3 as additives.

The following conclusions may be drawn from this study:

- a) The concept of using inorganic antioxidants to retard radiation initiated oxidation (RIO) is viable.
- b) PbO is more effective than Sb_2O_3 in retarding radiation initiated oxidation.
- c) Further comprehensive testing will be needed, if such formulations are to be fully qualified for nuclear applications.

REFERENCES

1. R. B. Blodgett and R. G. Fisher, "Insulations and Jackets for Control and Power Cables in Thermal Nuclear Reactor Generating Stations," *IEEE Trans. Power Apparatus and Sys.*, V. PAS-88, 529, (1969).
2. R. L. Clough and K. T. Gillen, "Investigation of Cable Deterioration Inside Reactor Containment," *Nucle. Technology*, 59, 344-54, (1982).
3. M. Dole, "Radiation Chemistry of Polyethylene," In M. Burton and J. Magee (Eds.), Advances in Radiation Chemistry, p. 307, V. 4, Wiley, New York, (1974).
4. J. Rabek, "Oxidative Degradation of Polymers," in C. Bamford and C. Tipper (Eds.), Comprehensive Chemical Kinetics, p. 425, V.14, Degradation of Polymers, Elsevier, Amsterdam, (1975).
5. L. Reich and S. Stivala, Elements of Polymer Degradation, McGraw-Hill, New York, (1971).
6. R. L. Clough, "Radiation Resistant Polymers," SAND 7-1, 1988, to appear as a chapter in Encyclopedia of Polymer Science and Engineering, John Wiley and Sons, Inc.
7. R. L. Clough and K. T. Gillen, "Radiation-Thermal Degradation of PE and PVC: Mechanism of Synergism and Dose Rate Effects," Sandia National Laboratory, NUREG/CR-2156, SAND-2149, (1981).
8. B. S. Lee et al., "Studies on Electrical Cable Insulation for Nuclear Applications", BNL-43813, Brookhaven National Laboratory, December 1989.
9. W. Schnabel, Polymer Degradation, p. 143 Hanser International, Munchen, (1981).
10. Z. Osawa and T. Saito, "The Effect of Transition Metal Compounds on the Thermal Oxidative Degradation of Polypropylene in Solution, p. 159 in "Stabilization and Degradation of Polymers", Advances in Chemistry Series 169, D. L. Allara and W. L. Hawkins (eds.), American Chemical Society, Washington, (1978).
11. L. Reich and S. S. Stivala, "Autooxidation of Hydrocarbons and polyolefins", Dekker, New York (1965).
12. R. L. Clough and K. T. Gillen, "Physical Techniques for Profiling Heterogeneous Polymer Degradation", Chap 28 in P. Klemcheck, ed., Polymer Stabilization and Degradation, American Chemical Society, Washington, D.C. (1985).

FOUR ADVANCES IN CARBON-CARBON MATERIALS TECHNOLOGY

Howard G. Maahs and Wallace L. Vaughn
NASA Langley Research Center
Hampton, Virginia 23681-0001

2477
p 10

Witold Kowbel
Materials & Electrochemical Research Corporation
Tucson, Arizona 85706

ABSTRACT

Carbon-carbon composites are a specialty class of materials having many unique properties making these composites attractive for a variety of demanding engineering applications. Chief among these properties are exceptional retention of mechanical properties at temperatures as high as 4000°F, excellent creep resistance, and low density (1.6 - 1.8 g/cm³). Although carbon-carbon composites are currently in service in a variety of applications much development work remains to be accomplished before these materials can be considered to be fully mature, realizing their full potential. This paper describes four recent technology advances holding particular promise for overcoming current barriers to the wide-spread commercialization of carbon-carbon composites. These advances are: markedly improved interlaminar strengths (more than doubled) of 2-D composites achieved by whiskerization of the fabric reinforcing plies, simultaneously improved oxidation resistance and mechanical properties achieved by the incorporation of matrix-phase oxidation inhibitors based on carborane chemistry, improved oxidation resistance achieved by compositionally graded oxidation protective coatings, and markedly reduced processing times (hours as opposed to weeks or months) accomplished through a novel process of carbon infiltration and coatings deposition based on the use of liquid-phase precursor materials.

INTRODUCTION

Carbon-carbon (C-C) composites are a specialty class of materials having many unique properties making them attractive for a variety of demanding engineering applications. Similar to other high-performance composites, C-C composites consist of a continuous fiber reinforcement phase held within a matrix phase. Unlike other composites, however, both the reinforcement and matrix phases consist of essentially pure carbon. The unique properties of C-C composites derive from their all-carbon composition coupled with the unique properties of carbonaceous materials.

Desirable properties of C-C composites relate to their low density (1.6 - 1.8 g/cm³), high strength, and excellent retention of mechanical properties at very high temperatures. At typically encountered service pressures, carbon does not melt or soften, and it retains good strength and stiffness to temperatures as high as 4000°F [1-3]. Figure 1 illustrates the mechanical property advantages of C-C composites relative to other high-temperature materials [3,4]. Other useful engineering properties include good fatigue and shock resistance, low coefficient of thermal expansion, good frictional characteristics, zero moisture expansion, no outgassing, and insensitivity to natural space radiation. Carbon-carbon composite materials have also been demonstrated to have excellent biocompatibility and are of interest for dental and bone implant applications [5,6].

Because of these many desirable properties, C-C composite materials have found use in several applications and are under consideration for many more (fig. 2). Current applications include the thermal protection system for the wing leading edges and nose cap of the Space Shuttle, friction applications such as aircraft brake disks, and ablative applications such as missile nose tips and rocket nozzle throats. Selected additional potential applications are also illustrated in figure 2.

In spite of current successes, however, several technology issues are still in need of resolution to exploit fully the engineering potential of these materials. Among these technology issues are the susceptibility of C-C composites to oxidation, lower than desired interlaminar (IL) strengths of 2-directional (2-D) reinforcement constructions, long manufacturing times (and associated high cost), low strain to failure, and inadequate reproducibility in a production environment. Four recent advances holding particular promise for overcoming the first three of these technology barriers are described in the present paper. Specifically, these advances are whiskerization of the reinforcing fabric plies for improving IL properties, incorporation of molecular-level matrix-phase additives (carboranes) to improve both oxidation resistance and IL properties, compositionally graded oxidation-protective coatings, and markedly reduced processing times (hours as opposed to weeks or months) accomplished by a novel process of carbon infiltration and coatings deposition based on the use of liquid-phase precursor materials.

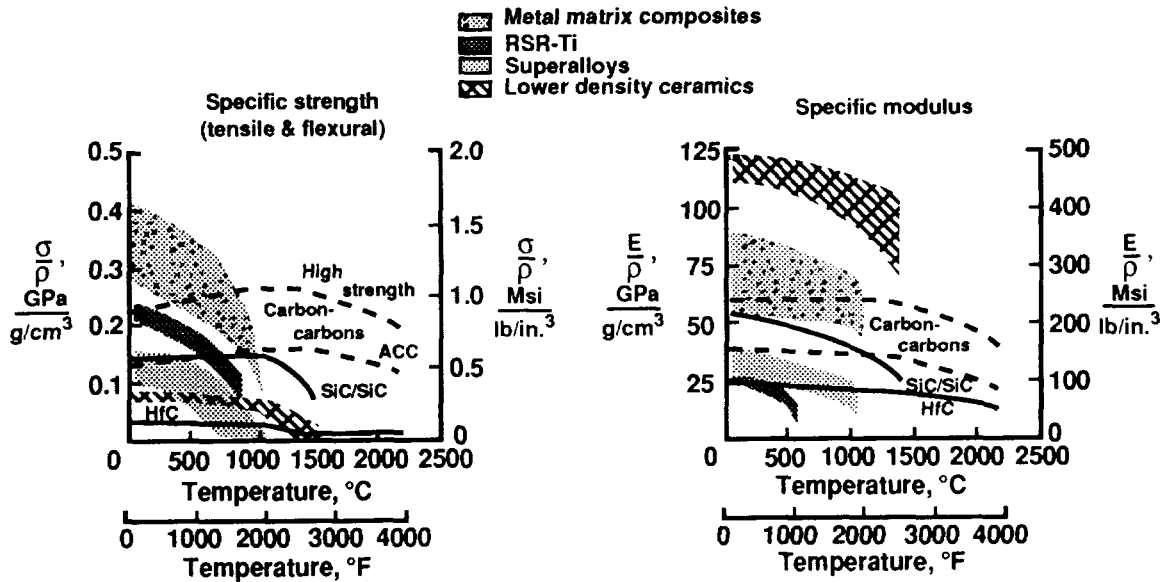


Figure 1. Specific strength and modulus for selected high-temperature materials [3,4].

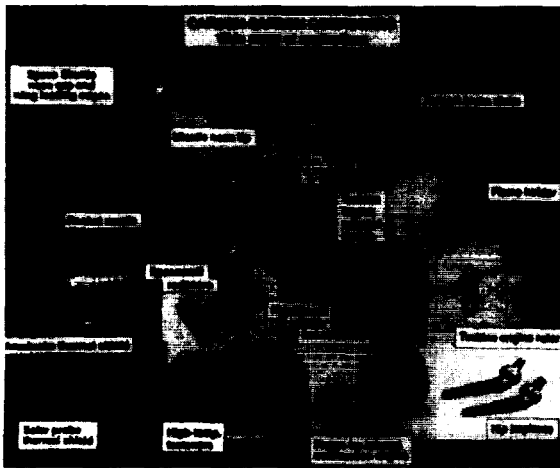


Figure 2. Current and projected applications for C-C composite materials.

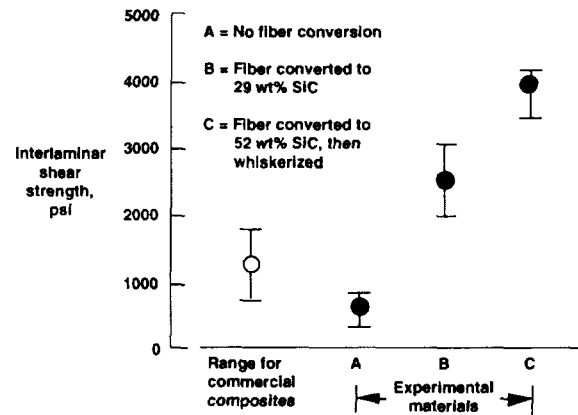


Figure 3. ILS strengths for composites with partially converted and whiskerized carbon fibers.

FABRIC PLY WHISKERIZATION

Thin structural C-C composites are typically reinforced with layers of woven fabric. This 2-D reinforcement construction affords good in-plane properties but IL properties are often lower than desired for many structural applications. Typically, interlaminar shear (ILS) strengths are on the order of 1.5 ksi and interlaminar tensile (ILT) strengths (cross-ply tension) less than 1 ksi. In some applications, the skillful structural designer can “design around” these low IL properties, but often they impose an undesirable design constraint.

Interlaminar properties in 2-D composites depend on the degree of fiber-matrix interaction, which, in turn, is controlled by various mechanical, chemical, and physical forces. Mechanical forces are influenced by fiber surface roughness, porosity, surface morphology and pore-filling capability of the carbon matrix. Chemical interactions depend on fiber surface activity and the nature of the functional groups on the carbon fiber surface. This chemical bonding can be increased to effect significant increases in the IL strengths of C-C composites, but too large an increase in bonding leads to brittle fracture and serious strength reductions [7-9]. Physical bonding is controlled by the wetting capabilities of the fiber and the Van der Waals interactions between the graphite crystallites on the fiber and matrix phases.

The use of through-the-thickness (3-directional, or 3-D) reinforcements is an obvious approach for increasing ILS strengths [10,11]. This 3-D reinforcement can be based on a variety of woven or braided constructions, or 2-D fabric plies stitched together. However, 3-D constructions are often boardy, difficult to densify, and have low fiber volume fractions (hence, low in-plane moduli). One attractive method being explored is to provide through-the-thickness reinforcement in just the right amount and at the micro-level by whiskers grown on the fibers in the reinforcing fabric plies of 2-D constructions. Although Fitzer [12] has shown that carbon whiskers grown on carbon fibers can significantly increase the ILS strengths in polymeric matrix composites, the application of whiskers in C-C composites is limited but encouraging [13]. In this section, initial results from a new whiskerization approach currently under development are described.



Figure 4. As-received T-300 fiber.



Figure 5. T-300 fibers partially converted to SiC; the carbon core has been oxidized away.

A chemical vapor reaction (CVR) process was developed to convert carbon fibers in a fabric ply either partially or completely to silicon carbide (SiC) as well as to grow strong, adherent SiC whiskers on the converted fibers. Figure 3 shows the very large (four-fold) increase in ILS strength achieved with this process. The range of ILS strengths for typical commercially available 2-D C-C composites is shown for comparison. (The relatively low value of 0.7 ksi for the experimental composite is due to the low density (1.39 g/cm^3) to which this composite was processed.) Figures 4-6 are scanning electron micrographs showing reinforcing fiber at the various stages in this whiskerization process. Figure 4 shows the as-received fibers (Amoco Performance Products T-300), and figure 5 the partially converted fiber (the carbon core has been oxidized away to enhance visualization). The increase in ILS strength observed for the partially converted but not whiskerized fiber is believed to be related, at least in part, to the significant increase in crenulation of the fiber surface following conversion. The fine network of whiskers produced by the CVR process is shown in figure 6; prospects for interlocking with adjacent plies is apparent. Certain advantages associated with this whiskerization include avoidance of brittle fracture because of too strong a fiber-matrix bond, controlled levels of whiskerization to provide optimum balance of properties, and flexibility to tailor the process for curved and complex shapes. An additional benefit is afforded by the SiC sheath, which sheath has been shown not to degrade fiber tensile properties but is expected to provide desirable oxidation resistance. Present research is exploring the range of processing conditions to optimize the CVR process and to establish the effect of ply whiskerization on a wide range of composite properties. Additional details on this process and property measurements are available in ref. [14].

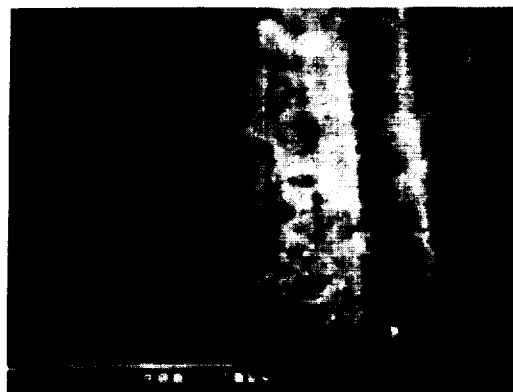


Figure 6. T-300 fibers partially converted and whiskerized.

CARBORANE-BASED MATRIX ADDITIVES

The primary approach for protecting C-C composites from oxidation at high temperatures is to apply an oxidation-protective coating. However, conventional coatings typically develop microcracks and often suffer from other defects such as thin areas, pinholes, etc., making additional protection of the C-C substrate desirable. This additional protection can be afforded by adding inhibitor materials to the matrix phase of the substrate during its fabrication. Previous studies have shown that glasses based on boria perform well in this role [15,16]. Specifically, the borate glasses block the cracks in the exterior silicon-based coatings and coat the pores within the C-C substrate to reduce its oxidation. McCormick [17] estimated a four-order-of-magnitude decrease in the oxidation rate for C-C composites protected with SiC coatings when the coating cracks were filled with boria as compared to those with unfilled cracks. Boria affords such protection because it has a desirably low viscosity between 1300°F and 2200°F, which varies only modestly over this temperature range; it is chemically compatible with SiC and carbon at moderate temperatures; and, because of its low surface energies, it wets carbon well [18], a necessary property for effective oxidation protection.

The drawback to most boria-based inhibitors is that they rely on the use of boron or boron carbide powders to provide the source of boron. These powders are added to the composite at the prepreg stage. It is difficult to infiltrate the powders within the tow bundles of the fabric and, due to their hardness, they can physically damage the fibers during the molding operation. In addition, the powders cannot be added to the infiltration resins. This leaves the carbon matrix applied last during processing as being the most exposed to oxidation. One attractive approach to avoiding the effects of particulates is to use molecular inhibitors.

Carborane (dicarbododecaborane) and its derivatives provide an excellent source of molecular boron. The carboranes are soluble in phenolic resin and furfural alcohol and can be used to produce oxidation-resistant carbons [19,20]. They also have been used in conjunction with polyarylacetylene-derived matrix systems for carbon-carbon composites, in low levels, as a graphitization aid [21]. However, their use as oxidation inhibitors in C-C composites has not been previously reported.

In this study, the effects of carborane and several of its derivatives were first investigated in phenolic resin chars. After down-selecting to a single carborane (vinyl-o-carborane), a series of composites was produced to determine its effectiveness in carbon-carbon composites and its influence on mechanical properties. Composites were also fabricated containing boron carbide particles as a reference inhibitor. The composites produced included uninhibited, inhibited with vinyl-o-carborane, inhibited with boron carbide, and inhibited with mixtures of the two. In addition, one-half of each composite panel was densified using vinyl-o-carborane in the densification resin whereas the other half was densified only with neat phenolic resin. Processing information and other details can be found in ref. [22].

Composite Mechanical Properties

The subpanels were machined into compression, ILT, and oxidation specimens. The ILT strengths of the composites are shown in figure 7. (In the figures and the following text the composites are designated by a two part nomenclature: the first half gives the amount and type of inhibitor added during initial pre-pregging and molding operations and the second half the amount and type of inhibitor added to the infiltration resin for densification; quantities are in percent, with "V-C" designating vinyl-o-carborane.) The none/none composite average strength of 550 psi is low for a phenolic densified material. However, the materials were only processed through three densifications (1.54 g/cm^3) instead of the normal four or five (1.65 g/cm^3) and this would give a lower ILT strength. Note that the use of inhibitors increases the ILT strength of the composites up to 35 percent for the 20 V-C/none composite. Even larger increases were observed when the vinyl-o-carborane was used in the infiltration resin, with a 50-percent increase between none/none and none/10 V-C. The greatest overall strength was in the 20 B₄C/10 V-C composite; it is postulated that the increase in strength is primarily due to the increased matrix density of these composites.

The compression strengths of the composites show a trend similar to the ILT strength although the strength increase is not as large (fig. 8). The 20 V-C/none composite once again has the highest strength (29.5 ksi) of the composites infiltrated with just the neat resin. Clearly, the presence of vinyl-o-carborane in the infiltrants raises the strength of the composites. The none/10 V-C composite is 30-percent stronger than the none/none composite. The 10 B₄C + 10 V-C/10V-C composite has the highest strength (33 ksi), a 35 percent improvement over the none/none composite. Since compression strength is influenced strongly by the matrix strength, it is not surprising that the trends are similar to the ILT strength results.

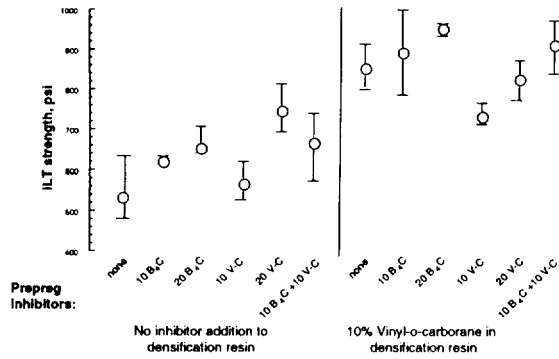


Figure 7. ILT strength of inhibited composites. Bars show total range of the data.

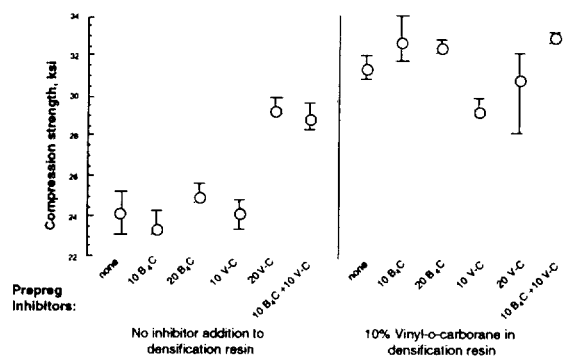


Figure 8. Compression strength of inhibited composites. Bars show total range of the data

Composite Oxidation Resistance

The oxidation performance of the composites was measured at 990°F and 1540°F at a pressure of 20 torr and a flow rate of 100 scfm in dry air, and the best two performing materials were also tested at 1271°F and 1820°F to enable a comparison with commercial materials over a range of temperatures. The oxidation results at 990°F are shown in figure 9. For the composites densified with neat phenolic resin, the 20 V-C/none composites had the best oxidation performance. The use of the vinyl-o-carborane in the densification resin gave improved results; even the none/10 V-C composite had the same oxidation performance as the 20 V-C /none composite. The use of prepreg inhibitors further decreased the oxidation rate, with the 20V-C/10 V-C composites (0.02 g/m²-min) showing one tenth the oxidation rate of the none/none composite. Comparison of the straight B₄C inhibited panels with the vinyl-o-carborane panels shows the advantages of the vinyl-o-carborane for oxidation protection.

The oxidation performance of the two best inhibited composites (20 V-C/10 V-C and 10 B₄C + 10 V-C/10 V-C) and the none/none composite was compared to commercially available inhibited C-C composites that were oxidized under identical conditions (fig. 10). At temperatures above 1700°F no advantage is gained by inhibitors since the rate of oxidation is controlled by diffusion rather than by chemical kinetics. As the temperature is lowered, the use of inhibitors becomes more important. The in-house composites perform comparably to the commercial systems down to temperatures of 1200°F, but below these temperatures the commercial systems have lower oxidation rates. The difference at low temperatures could be due to the overall higher loading of commercial inhibitors or the higher processing temperatures used in the commercial composites, since higher process temperatures tend to yield more oxidation resistant carbons, especially at lower temperatures [23].

The carborane systems reported here are at a very preliminary stage of development. Substantial work still needs to be done with respect to optimum loading and heat treatment. Based on the results to date, however, including the good mechanical properties achieved, this approach of using carboranes as molecular-level inhibitors is considered to have excellent potential for improving the oxidation resistance of structurally efficient C-C composites.

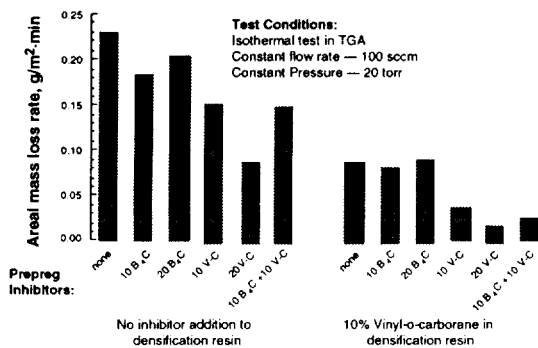


Figure 9. Oxidation rate of inhibited composites at 990°F.

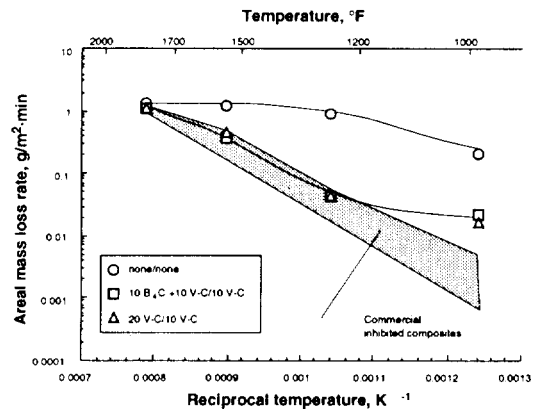


Figure 10. Comparison of oxidation rates for commercial and in-house inhibited composites.

FUNCTIONALLY GRADIENT COATINGS

As noted in the previous section, conventional oxidation-protective coatings typically develop microcracks, making substrate inhibitors desirable. Far preferable, however, would be totally crack-free coatings, but these are not easily produced because of the mismatch in coefficients of thermal expansion (CTE) of C-C substrates ($<1 \times 10^{-6}/^{\circ}\text{F}$) and typical coating materials, SiC ($2.8 \times 10^{-6}/^{\circ}\text{F}$), and silicon nitride ($1.7 \times 10^{-6}/^{\circ}\text{F}$). However, methods are presently emerging that hold particular hope for improving the situation and these methods are discussed in this section.

Two of the most widely used methods for coating C-C parts are chemical conversion of the outer layers of the part to SiC, and deposition of silicon-based coatings on the surface of the part by chemical vapor deposition (CVD). Both methods produce a relatively sharp substrate-coating interface and high thermal stresses develop at this interface. One way of minimizing these concentrated thermal stresses is to avoid formation of the sharp interface. This can be accomplished by effecting a gradual change in chemical composition and microstructure from the substrate to the coating. This deliberate grading of the coating to achieve a desired benefit falls within the rapidly growing technology area referred to as functionally gradient materials [24,25].

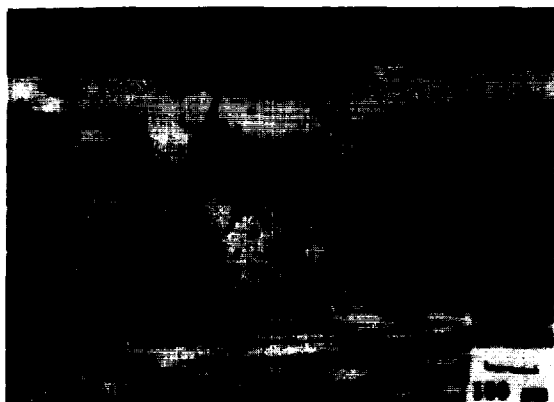


Figure 11. Two-layer CVD SiC, Si₃N₄ coating; after 20 oxidation cycles (see text).



Figure 12. Functionally gradient CVD C-SiC-Si₃N₄ coating; after 20 oxidation cycles (see text).

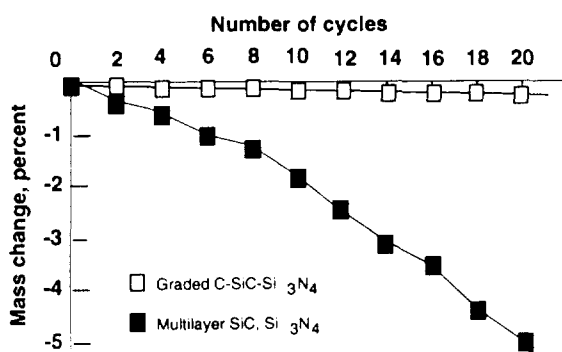


Figure 13. Oxidation results for coating systems in figs. 11 and 12.

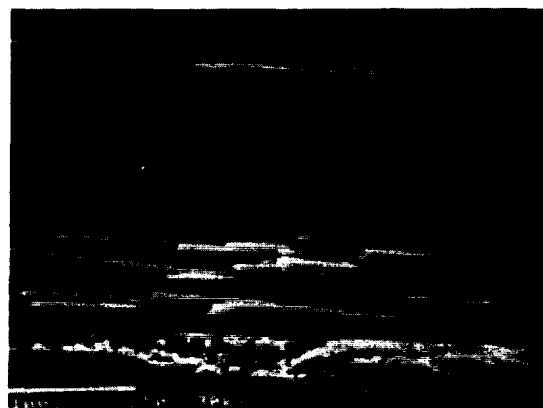


Figure 14. Functionally gradient CVR/CVD SiC-Si-Si₃N₄ coating.

Although the use of functionally gradient coatings on C-C composites is still very much in its infancy, these coatings are already showing high potential for reducing microcracks and achieving significant improvements in oxidation resistance. Figures 11 and 12 show sections of post-oxidized specimens illustrating the extent of improvements possible. Oxidation conditions consisted of 20 thermal cycles of: room temperature, rapid increase to 3000°F for 10 minutes, 1110°F for 20 minutes, and rapid decrease back to room temperature. This cycle, because of its high- and low-temperature holds and rapid temperature changes, constitutes a particularly severe test for coating

effectiveness. Figure 11 shows a section through a specimen protected with a state-of-the-art two-layer CVD-applied coating consisting of a SiC inner layer and silicon nitride (Si₃N₄) outer layer. Note the cracks in the coating and the large carbon loss within the substrate just below the coating. In contrast, figure 12 is for a similarly oxidatively exposed specimen (same substrate) protected with a functionally gradient CVD coating consisting of a layer of carbon-rich SiC adjacent to the substrate slowly graded to pure SiC and further graded to a pure Si₃N₄ outer layer. No cracks appear in the coating and no carbon loss occurred (the dark line in fig. 12 between the coating and the substrate is a polishing artifact and does not represent carbon loss or debonding). Mass change data for these materials as a function of the number of exposure cycles are shown in figure 13, clearly illustrating the much greater oxidation protection provided by the functionally gradient coating concept. Additional data and information concerning CVD functionally gradient coatings on C-C composites can be found in ref. [25].

Even more experimental are functionally gradient coatings produced by chemical conversion processes. A particularly convenient method here is the CVR process mentioned earlier. In this process, a reactive gas is brought into contact with the part to be coated, reacting with it and producing a layer of the new desired composition (e.g., SiC). The CVR process can be readily transitioned into a conventional CVD process by gradually changing the reactant gas composition and reactor conditions. This approach provides great flexibility for depositing coatings and grading compositions. Recently, C-C test materials have been successfully coated in the following manner: A thin outer layer of the C-C substrate was first converted to SiC by the CVR process; this SiC layer was then graded into a pure silicon (Si) overlayer using a combination of CVR and CVD. This was then followed by a controlled CVR conversion of the Si layer to Si₃N₄ giving a coating of the final composition: SiC graded to Si graded to Si₃N₄ (SiC-Si-Si₃N₄). Crack-free coatings have been successfully produced by this process (fig. 14) and preliminary oxidation tests are encouraging, but comparative oxidation data with conventional coatings are not yet available.

RAPID PROCESSING AND REDUCED COST

Compared to the costs for other more conventional engineering materials, C-C composites are relatively expensive. Depending on such factors as production volume, part complexity, geometric tolerances, property requirements, whether oxidatively protected, etc., costs can range from approximately \$80/lb to as much as \$15,000/lb. Table 1 [3,26] shows a cost comparison. Because of their relatively high cost, C-C composites have been employed only in those applications where their unique properties are necessary to meet demanding service requirements. One notable exception to this statement, however, relates to aircraft brake disks, where the durability and performance afforded by C-C composites have led to their supplanting steel brakes in transport aircraft for economic reasons.

Material	Cost, \$/lb
Aluminum alloys ^a	2-3
Titanium alloys ^a	20-60
Superalloys ^a	15-70
Refractory metals ^a	25-250
Organic matrix composites ^b	40-750
Carbon/carbon composites ^b :	
- Brakes	80-120
- Nozzles, exit cones, nose cones	600-1500
- Shuttle RCC	6000
- Advanced, oxidatively protected (in non-production environment)	2000-15,000

^a Approximate ranges for simple product forms

^b Approximate ranges for a mix of product shapes

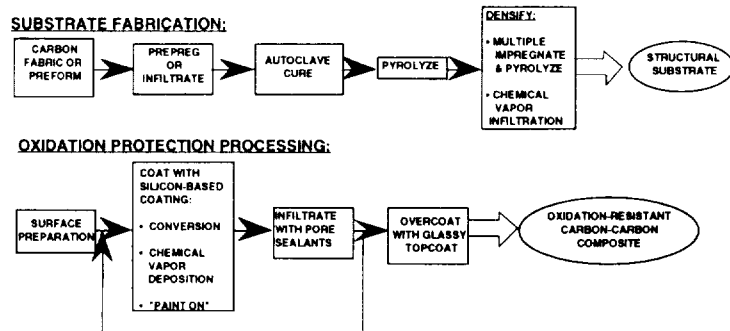


Figure 15. Process diagram for C-C composites. After refs. [3,26].

Table 1. Comparative costs of selected engineering materials [3,26].

For C-C composites to successfully compete with other engineering materials, their cost must be substantially reduced. These costs are strongly influenced by the lengthy processing times required by conventional fabrication methods, depicted schematically in figure 15. Although raw materials costs are generally relatively low (depending to a large extent on the particular fiber type selected), the large number of processing steps involved is responsible for long production times and, thus, high cost.

Referring to figure 15, one of the very time consuming steps in substrate fabrication is densification processing. Densification typically requires multiple cycles of resin or pitch impregnation, followed by cure, pyrolysis, and heat treatment. This cycle is repeated often four times and in some cases, many more. Another widely used densification method is that of chemical vapor infiltration (CVI), which is equally slow because of low mass transport rates in the

gas phase required to obtain full in-depth densification. To overcome these long processing times, a promising high-rate alternative densification process is being explored under a NASA contract with Lockheed Missiles and Space Company and their subcontractor Textron Specialty Materials [27]. This process is believed to offer the potential to reduce processing times from the order of weeks or months to only several hours.

The basic features of this high-rate densification process are described schematically in figure 16. An inductively heated porous carbon preform (the part to be densified) is immersed in a high-carbon-yield hydrocarbon liquid and the part is raised to a temperature sufficiently high so that the hydrocarbon liquid thermally cracks, depositing carbon within the porous part. By appropriate temperature control, the part can be densified from the interior to the surface, thus avoiding the development of a surface "skin," often encountered with gas-phase CVI. The heating also causes vigorous agitation of the liquid hydrocarbon, promoting excellent mass transport. By this process, thin-walled 1.5-in. dia. by 7-in. long tubes have been densified in as little as 4 hours (fig. 17). Densities and mechanical properties achieved are excellent: 1.75 g/cm³, with 28 ksi compression strength and 46 Msi compression modulus. In addition to tubes, other generic structural shapes including flat, curved, and stiffened structures are being investigated to explore the limits of the process. To date, flat panels having dimensions up to 6 in. by 12 in. have also been successfully densified.

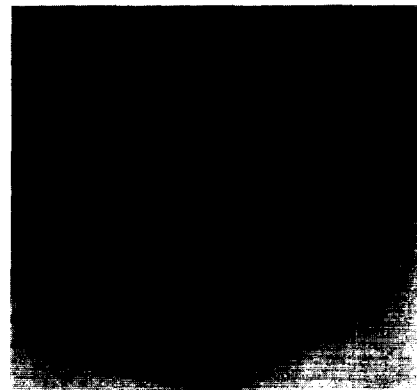
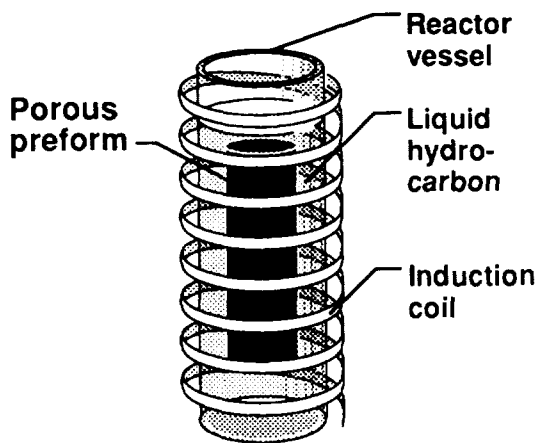


Figure 16. Schematic of rapid liquid-phase process for densification and applying coatings.

Figure 17. Carbon-carbon tubes densified in 4 hours.

Referring once again to figure 15, another step contributing significantly to overall part fabrication time is coating application, generally for oxidation protection. Two coating methods discussed previously are chemical conversion of the outer layers of the C-C part to SiC, and CVD of various silicon-based coatings and other interlayer materials. Yet a third method involves ceramic-based slurries which are painted on and fired in multiple steps. All these coating approaches are complex and time consuming. A modification of the rapid liquid-phase densification process described above holds significant promise for applying coatings at a much increased rate. This modification depends on the availability of suitable metal-organic liquid precursors which, when thermally decomposed, deposit a coating of the desired composition, whether it be SiC, hafnium carbide, or other desired chemistry. In addition to the high rates at which coatings can be applied, an additional advantage of this approach is that, at least conceptually, the hydrocarbon liquid employed for densification processing can gradually be replaced with the metal-organic liquid precursor for coating deposition. This approach enables processing to be accomplished in the same reactor without having to remove or handle the part, and also enables the coating to be graded in composition, thus eliminating sharp interfaces and reducing thermal stresses. To date, several organochlorosilane compounds have been identified and experiments run successfully demonstrating that SiC coatings can be deposited with compositions ranging from silicon-rich to stoichiometric to carbon-rich. Coating deposition rates approaching 1 mil/hr have been shown to be possible. Detailed technical discussions of the process are available in refs. [27,28].

Although process feasibility has been demonstrated both for densifying C-C components and for depositing coatings, considerable development work remains before the process can be considered economically viable and ready for factory production. One key technology issue needing resolution is improving uniformity of density. Scale-up and reproducibility issues must also be addressed, and the feasibility for continuous processing, especially for tubes, is worth pursuing. Studies are also planned to explore the feasibility of depositing coatings other than SiC—in particular, hafnium carbide and silicon. Nevertheless, no matter how technically viable the process, the ultimate measure of success will be cost savings relative to traditional methods. Once the process moves out of the

experimental stage and process parameters are better established, an economic analysis of the process will be conducted to establish its cost benefits relative to traditional current processes.

SUMMARIZING REMARKS

Current primary applications for carbon-carbon composites are aircraft brakes, missile nose tips, rocket nozzles and exit cones, and the nose cap and wing leading edge of the Space Shuttle Orbiter. Numerous additional engineering applications are envisioned for this material, however, provided important technology issues relating to improved oxidation resistance, increased interlaminar strengths, cost effective manufacturing, and production reproducibility are properly addressed. The authors are confident that many of these barriers will be overcome, and that this unique material will be exploited to an increasing extent in the future.

The present paper has described four recent technology advances that contribute to overcoming some of these barriers. These include fabric ply whiskerization for increased interlaminar properties, carborane-based molecular level inhibitors providing both improved oxidation resistance and interlaminar properties, functionally gradient coatings to minimize coating cracks and improve oxidation resistance, and a novel liquid-phase process for carbon infiltration and coatings deposition holding considerable promise for reducing fabrication costs. Clearly, extensive research and development remains yet to be accomplished in these areas, and others as well. However, these advances afford the optimism that continued improvements can and will be made in those key technology areas that advance the maturity of this class of materials and provide a sound basis for design engineers to include them more frequently in their range of materials options.

REFERENCES

1. Fitzer, E.; and Heym, M.: High-Temperature Mechanical Properties of Carbon and Graphite—A Review. *High Temperature-High Pressure*, Vol. 10, 1978, pp. 29-66.
2. Fitzer, E.: Carbon-Based Composites. *J. Chim. Phys.-Chim. Biol.*, Vol. 81, 1984, pp. 717-733.
3. Maahs, Howard G.: Carbon-Carbon Composites. Chapter 16 in *Ceramics and Ceramic Matrix Composites*, S. R. Levine, ed., in *Flight-Vehicle Materials, Structures and Dynamics—Assessment and Future Directions*, Vol. 3, A. K. Noor and S. L. Venneri, eds., American Society of Mechanical Engineers, New York, 1992, pp. 307-332.
4. Stein, B. A.; Maahs, H. G.; and Brewer, W. D.: Airframe Materials for Hypersonic Vehicles. *Metal Matrix, Carbon, and Ceramic Composites 1987*, J. D. Buckley, ed.; NASA CP-2482, 1987, pp. 1-24.
5. Louis, Jean-Paul: Immediate Complete Prostheses With Fibrous Carbon Artificial Roots. *Am. J. Dentistry.*, Vol. 3, No. 3, 1990, pp. 125-132.
6. Adams, D.; and Williams, D. F.: The Response of Bone to Carbon-Carbon Composites. *Biomaterials*, Vol. 5, 1984, pp. 59-64.
7. Kowbel, W.; and Shan, S. H.: The Mechanism of Fiber-Matrix Interactions in C-C Composites. *Carbon*, Vol. 28, 1990, pp. 287-299.
8. Maahs, H. G.; and Yamaki, Y. R.: Effects of Fiber Surface Treatment and Sizing on Fiber-Matrix Interactions in Carbon-Carbon Composites. 16th Conference on Metal Matrix, Carbon, and Ceramic Matrix Composites. NASA CP-3175, 1992, pp. 305-318.
9. Ransone, P. O.; and Spivack, B. D.: Effect of Fabric Thickness, Fiber Type, and Densification Process on Mechanical Properties of Thin 2-D Carbon-Carbon Composites. Presented at the 17th Annual Conference on Composites, Materials, and Structures. United States Advanced Ceramics Association, Cocoa Beach, FL, Jan. 10-15, 1993. (To appear in NASA CP)
10. Ransone, P. O.; Spivack, Bruce D.; and Maahs, H. G.: Mechanical Properties of Thin 3-D Reinforced Carbon-Carbon Composites Densified with Different Matrices. The 16th Annual Conference on Composites, Materials, and Structures. NASA CP-3175, 1992, pp. 347-366.
11. Yamaki, Y. R.; Ransone, P. O.; and Maahs, H. G.: Investigation of Stitching as a Method of Interlaminar Reinforcement in Thin Carbon-Carbon Composites. The 16th Conference on Metal Matrix, Carbon, and Ceramic Matrix Composites. NASA CP-3175, 1992, pp. 367-386.
12. Fitzer, E.: R-F Sputtered SiC Coatings on Carbon Fibers. *Thin Solid Films*, Vol. 170, 1987, pp. 93-108.
13. Munoz, C.; Ngai, T. T.; and Shyne, J. J.: Shear Property Enhancement of 2D Carbon-Carbon (C/C) Composites. Presented at the 15th Annual Conference on Composite Materials and Structures. United States Advanced Ceramics Association, Cocoa Beach, FL, January 16-18, 1991. (Unpublished)

14. Withers, J. C.: The Optimization of an Advanced Carbon-Carbon Composite with Improved Interlaminar and Flexure Properties and Oxidation Resistance. Materials and Electrochemical Research (MER) Corporation. Final report for NASA Contract NAS1-19528, Oct. 1992.
15. McKee, D. W.: Oxidation Behavior and Protection of Carbon/Carbon Composites. *Carbon*, Vol. 25, No. 4, 1987, pp. 551-557.
16. Ehrburger, P.; Baranne, P.; and Lahaye, J.: Inhibition of the Oxidation of Carbon-Carbon Composites by Boron Oxide. *Carbon*, Vol. 24, No. 4, 1986, pp. 495-499.
17. McCormick, E. Scott: Factors Influencing the Oxidation Performance of Carbon-Carbon Composites. Proceedings—Air Force Workshop on Oxidation-Resistant Carbon-Carbon Composites, AFWAL-TR-88-4071, U.S. Air Force, Mar. 1988, pp. 113-129.
18. Gray, Paul E.; and Sheehan, James E.: Oxidation Protected Carbon-Carbon Composite Development. Metal Matrix, Carbon, and Ceramic Matrix Composites 1986, Proceedings of a Joint NASA/DOD Conference, Cocoa Beach, FL, Jan. 21-24, 1986, NASA CP-2445, 1986, pp. 197-209.
19. Baicher, L. A.; Valetskil, P. M.; Vinogradova, S. V.; Zlatkis, A. M.; and Korshak, V. V.: Influence of Carborane-Containing Compounds on the Oxidative Stability of Products of Pyrolysis of Network Polymers. *Polymer Science U.S.S.R.*, Vol. 23, No. 10, 1981, pp. 2453-2459. Originally appeared in *Vysokomol, Soedin., Ser A.*, 23(10), 2257-62, 1981.
20. Chen, Philip S. H.; and Stevens, Ward C.: Novel Molecular Sources for Dispersing Boron in Carbon-Carbon Composites. AFSOR Report FQ8671-9101273, December, 1991.
21. Zaldivar, R. J.; Kobayashi, R. W.; and Rellick, G. S.: Carborane-Catalyzed Graphitization in Polyarylacetylene-Derived Carbon-Carbon Composites. *Carbon*, Vol. 29, No. 8, 1991, pp. 1145-1153.
22. Vaughn, Wallace. L.; and Petty, John T.: Carborane Based Inhibitors for Carbon-Carbon Composites. Proceedings of the 17th Annual Conference on Composites, Materials, and Structures (Restricted Sessions), NASA/DOD Conference, Cocoa Beach, FL, Jan. 10-15, 1993, Paper No. 84, to be published as NASA CP.
23. Ragan, S.; and Emmerson, G. T.: The Effect of Heat-treatment Temperature Upon the Properties of Matrix-Inhibited Carbon-Carbon Composites. *Carbon*, Vol. 30, No. 3, 1992, pp. 339-344.
24. Hirai, T.: Design of SiC-C Functionally Gradient Material and Its Preparation by Chemical Vapor Deposition. Proceedings of Japan Ceramic Soc. in Tohoku-Hokkaido Branch, 1987, p.37-48.
25. Kowbel, W.: The Mechanism of Oxidation of Oxidation Protection of C-C Composites Coated With Graded Codeposited Carbides and Nitrides. *Ceramic Transactions*, Vol. 34, 1993, pp. 237-244.
26. National Center for Advanced Technologies (NCAT): Carbon-Carbon Composites, in National Advanced Composites Strategic Plan, Symposium Draft. National Center for Advanced Technologies (NCAT), 1250 Eye Street, N.W., Washington DC, December 1990, pp. 253-301.
27. Finley, J. W.; Klavins, A.; Baker, D. F.; Carroll, T.; Thurston, G.; and O'Connor, T.: Efficient Processing of Carbon-Carbon Composites. Lockheed Missiles & Space Company Report LMSC/F109055, for the period March-Dec. 1992. To appear as NASA Contractor Report.
28. Thurston, G. S.; Carroll, T. J.; and Rawal, S. P.: Advanced Understanding of the Rapid Densification RDTM Process. Final Report to Office of Naval Research for the Period July 1991 to Sept. 1992, contract #N00014-91-C-0285, Dec. 1992.

**CASTING OF WELDABLE GRAPHITE/MAGNESIUM METAL MATRIX
COMPOSITES WITH BUILT-IN METALLIC INSERTS**

Jonathan A. Lee
Marshall Space Flight Center
Huntsville, AL 35812

Uday Kashalikar and Patricia Majkowski
Foster-Miller, Inc.
Waltham, MA 02154-1196

2478
P 6

ABSTRACT

This paper describes technology innovations directed at the advanced development of a potentially low cost and weldable graphite/magnesium metal matrix composites (MMC) through near net shape pressure casting. These MMC components uniquely have built-in metallic inserts to provide an innovative approach for joining or connecting other MMC components through conventional joining techniques such as welding, brazing, mechanical fasteners, etc. Moreover, the metallic inserts trapped within the MMC components can be made to transfer the imposed load efficiently to the continuous graphite fiber reinforcement thus producing stronger, stiffer and more reliable MMC components. The use of low pressure near net shape casting will be economical compared to other MMC fabrication processes. These castable and potentially weldable MMC components would provide great payoffs in terms of high strength, high stiffness, low thermal expansion, lightweight, and easily joinable MMC components for several future NASA space structural, industrial and commercial applications.

INTRODUCTION

Graphite fibers reinforced magnesium and aluminum are becoming more valuable metal matrix composite materials for aerospace and automotive applications because of their lightweight and high strength properties (1). The current candidate materials for advanced space structural component applications can be listed as beryllium, graphite/epoxy polymer composites, particulate SiC/aluminum MMC, and continuous graphite fiber reinforced aluminum and magnesium MMC. Table 1 presents a qualitative tradeoff analysis on these candidate materials for NASA space structural applications. Beryllium is a very lightweight metal of high specific stiffness but it has safety, cost, fabrication and handling problems. Graphite fibers reinforced polymeric composites are not suited for long exposure in space environment due to chemical reaction with atomic oxygen and deep space radiation. To overcome this problem, an aluminum protective coating can be applied onto the outside surface of these polymeric composites. However, this method not only adds significant processing cost, but it also reduces the component effective stiffness and resistance properties to thermal cycling.

Discontinuous fibers or particulates reinforced aluminum MMC has good resistance to space environment. However, they only provide a small to moderate increase in stiffness and strength performance over the conventional aluminum alloys. Finally, continuous graphite reinforced aluminum or magnesium offers the best material properties for space structural applications. Unfortunately, most graphite reinforced MMC components are prohibitively expensive for most applications due to high cost fabrication techniques such as powder metallurgy, thermal-arc plasma spray and diffusion bonding. These fabrication processes often yield MMC products in simple forms such as metal ingots, wires, thin metal sheets or cylindrical tubes as basic building blocks. The final component applications fabricated from these basic building blocks are often expensive and have limited shape complexity.

The present investigation is concerned with MMC components that can be cast with near net shape dimensional tolerance and at relatively low cost. The casting process can be performed with continuous, chopped or particulate reinforcements infiltrated with molten liquid aluminum or magnesium alloys. The significant advantage of such casting process is that it can produce MMC components with very complex body shapes with little or no requirements for final machining. This paper will focus on the casting of graphite P-100 continuous fibers reinforced magnesium AZ91E alloy.

Table 1. Candidate material systems for advanced NASA space structural applications.

MATERIALS	ADVANTAGES	DISADVANTAGES
Beryllium	<ul style="list-style-type: none"> • High specific stiffness • No outgassing problems • Very lightweight metal • Low CTE values 	<ul style="list-style-type: none"> • Toxic material • Very difficult to machine • Extremely Notch-Sensitive • High material & fabri. cost
Graphite/Epoxy Composites	<ul style="list-style-type: none"> • High specific stiffness • Relatively low material cost • Mature technology • Near Zero-CTE value 	<ul style="list-style-type: none"> • Attacked by atomic oxygen • Outgassing problems for optics • Low temperature applications
Particulate SiC/Al MMC	<ul style="list-style-type: none"> • Moderate specific stiffness over unreinforced metals • Relatively mature MMC tech. • No outgassing problems • Resistance to space environ. • Cast to near net shape parts 	<ul style="list-style-type: none"> • Inadequate specific stiffness & strength for some applica. • Low welding/brazing strength • Relatively high fabrica. cost
Continuous Graphite/Al and Magnesium MMC	<ul style="list-style-type: none"> • Outstanding specific stiffness • Excellent tailorable CTE values • Cast to near net shape parts • Resistance to space environ. • No outgassing problems • High thermal conductivity 	<ul style="list-style-type: none"> • Poor welding/brazing strength • Relatively high fabrica. cost

As seen in Table 1, in addition to the high cost problems associated with using MMC materials, another major disadvantage is that they can not be joined together easily through conventional joining methods such as welding, brazing or solder. The demand for a standardized and reliable joining method for graphite MMC components has become one of the critical MMC technology requirements. In the past, several MMC joining methods have been evaluated and most of these techniques were concluded as unsuccessful (2). In most cases, the MMC component joint strengths were limited by their low graphite-to-face sheet peel strengths. Under the extreme heat of arc welding, the joint strength can further decrease due to the graphite reinforcement migration into the weld nuggets. To overcome this joining problem, NASA and Foster-Miller, Inc. have developed a joinable graphite MMC through the innovative use of metallic inserts that are made to be permanently trapped within the cast composite components. In this way the metallic inserts can provide a site so that a conventional joining method can be applied directly onto them. The idea presented here is that welding can be done from one metallic insert connected with a metallic insert from another MMC component. Another advantage of using trapped metallic inserts is that they can transfer the imposed load efficiently to the graphite fibers. For example, in the design of a typical clevis joint, metallic inserts can be placed at a specific location within the MMC component to resist the bearing load exerted by the connecting pin and to distribute this axial load over a larger area of the component. Additionally, a certain type of insert materials can be used to greatly enhance the wear resistance of graphite MMC components subjected to unique bearing load applications.

MMC PRESSURE CASTING PROCEDURE

Although MMC pressure casting has been used in various forms over the years, its application to the production of practical components is rapidly growing just within the last 5 years (3,4). The typical equipment used to pressure cast graphite/magnesium MMC components is shown in Figure 1. The device consists of two main components: the pressure vessel and the water-cooled lid. The pressure vessel contains the crucible heater bank and the molten matrix alloy crucible. The water-cooled lid is positioned on top of the pressure vessel and attached to it is the die, its heater bank and the molten matrix transfer tube. There are also feedthroughs for thermocouple wires, power leads, and pressure sensors to this lid. The operating principle of the device is to use an inert pressurized gas to force the molten metal into an evacuated die. Dies can be made from common materials such as ceramics, graphite, quartz glass, and sheetmetals which hold advantages in terms of low cost and easy machinability.

In this study the die for the cast MMC component was machined out of a fine grained low porosity graphite block. Graphite was chosen because of its relatively low cost, easy to machine into complex shapes, low thermal mass and has potential for reusability. Low thermal mass die will allow a close control on the graphite fiber reinforcement temperature prior to molten metal infiltration within the die. A thin boron-nitride coating was applied onto the inside of the graphite die to ease the removal of the cast MMC component after infiltration by molten metal.

To operate the device the water-cooled lid is placed on top of the pressure vessel so that the end of the molten matrix transfer tube is immersed in the molten matrix crucible. Prior to heating the fiber preform and melting the metal alloy contained in the crucible, a vacuum must be drawn within the pressure vessel. This vacuum will help in preventing the molten liquid metal and the fiber preform from oxidizing at high temperature. When the molten metal and the fiber preform have reached the optimum processing temperatures, the vessel is then pressurized with argon gas to force the molten magnesium alloy into the die cavity. When the molten metal reaches the top of the die here it will come in contact with the water-cooled lid. The molten metal becomes solidified immediately and thereby creating a pressure seal for the vessel. With this seal on top of the die the pressure vessel can now be pressurized up to 800 psi with argon gas to force the molten magnesium into the die cavity for a complete infiltration of the graphite fiber reinforcements. Temperature and pressure are the two most important casting process parameters. Therefore, the crucible molten metal and the die cavity heater banks must be interactively controlled so that one can achieve a unique casting process condition. These parameters are critical to the quality and reproducibility of the cast MMC parts. Failure to optimize these parameters can result in many cast defects such as porosity, incomplete infiltration, oxide inclusions, excessive reaction of graphite fibers with matrix alloy, etc.

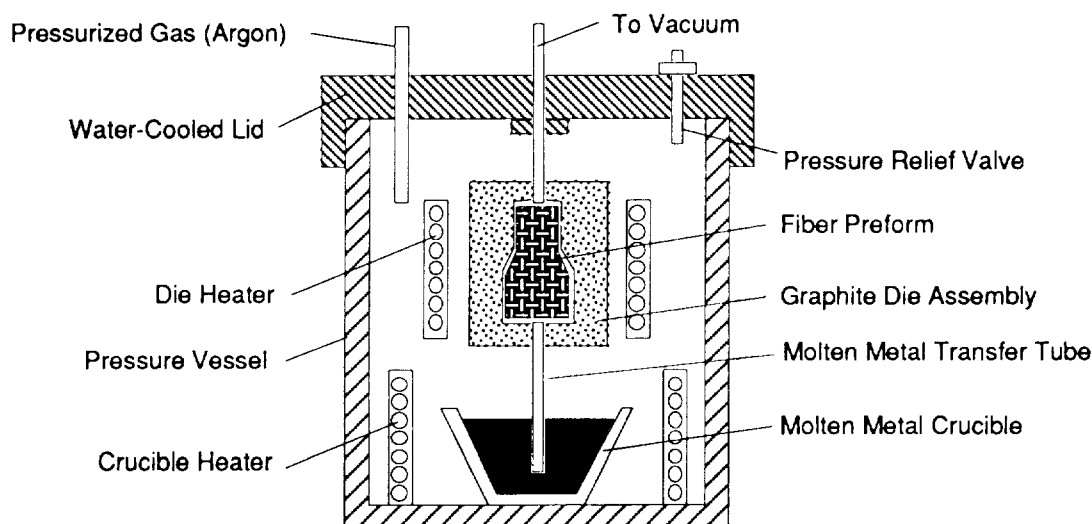


Figure 1. Schematic diagram for a typical MMC pressure casting apparatus.

COMPONENT SELECTION AND INSERT DEVELOPMENT

A representative clevis tube end-fitting component was selected as the demonstration article for this effort. This design was selected after performing a quantitative tradeoff analysis of various joint component candidates for potential use in NASA future space truss and commercial applications. Figure 2 shows a typical clevis joint of 4.5 in. long by 2.0 in. diameter and 0.25 in. wall thickness. This component has a moderately complex shaped body for a near net shape casting demonstration. In this design a continuous fiber preform was needed to provide a high axial stiffness in the clevis region and a high torsional stiffness in the tube region. To achieve the optimum fibers alignment within the cast a continuous fiber preform was developed using P-100 graphite fibers that were wound at plus and minus 45 degrees over a salt mandrel. These fibers come from a 0.25 in. wide by 0.005 in. thick graphite fiber tape with a polyethylene binder. This binder was used to hold the graphite fibers together during the casting process and it will decompose during the die heat up and leave no discernible residue within the cast component. The mandrel was machined from a cold isostatically pressed (CIPed) sodium chloride powder. From the previous experimental works this salt mandrel design was proven to be impervious to pressurized molten magnesium or aluminum alloys and washes out easily after casting (5).

To make such cast MMC components weldable, for easily joining through conventional welding or brazing technique, we incorporated metallic inserts that are made to be permanently trapped within the cast composite components. In this way the metallic inserts can provide a site so that conventional joining method can be applied directly onto them. The idea presented here is that welding can be done from one metallic insert connected with a metallic insert from another MMC component. As shown in Figure 2, this clevis joint has two different types of built-in metallic inserts. One type was used to facilitate easy joining while the other type of insert was used to enhance the load carrying capability of the cast component. At the tube end, the "joining insert" provided a metallic surface for joining to the neighboring component (not shown) by conventional metal joining techniques. At the clevis end, the "load transfer insert" was positioned at a specific location to resist the bearing load exerted by the connecting pin and to distribute this axial load over a larger area of the component.

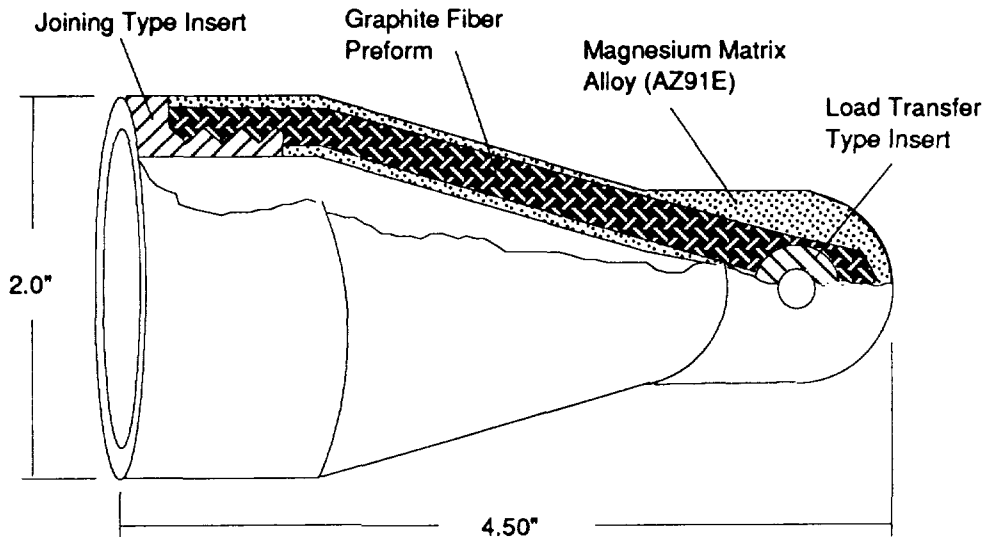


Figure 2. A clevis-joint component with moderately complex shaped body was selected for a near net shape casting demonstration. Note that this joint has two different types of built-in metallic inserts. One type is used to facilitate easy joining while the other insert is used to enhance the load carrying capability.

In the development of metallic inserts the selection of insert materials and their machined profile shapes are the two most important design parameters. To create a strong bond between the insert and the matrix metal the insert materials must be selected such that their liquidus and solidus temperatures are close to the infiltration temperature from the molten magnesium. Various candidate materials for inserts were selected and tested during casting trials. For instance, if one uses an aluminum alloy insert, due to its low melting temperature, this insert may completely melt during the infiltration process. On the other hand, the major concern regarding the use of titanium insert is the propensity to form unwanted brittle intermetallic phases and thereby degrading the load transfer capability of the MMC component.

The second design parameter for the metallic inserts is the cross sectional profile shape in which the insert is expected to fit and anchor firmly in the MMC component and to transfer the load evenly across the insert/MMC interfaces. A typical profile of the insert consists of a rippled outer surface such that the continuous graphite fiber reinforcements can wrap around it prior to infiltration. The higher the ripple surface angle the more area will be made available for the fiber bundles to anchor themselves firmly into the insert. However, such high ripple surface contour will result in minimum bending radius for the graphite fibers to bend around a typical anchoring corner which thereby can cause an unacceptable amount of fiber breakage within the fiber bundles in the preform. Although there is an optimum height for the ripple surface contour, the depth of this surface curvature is limited by the overall thickness of the metallic insert. Usually, the insert thickness is kept very minimum so that its weight is relatively small when comparing to the total weight of the MMC component.

RESULTS AND DISCUSSION

Figure 3a is a photograph showing the result of the cast near net shape graphite/magnesium MMC component with built-in metallic inserts for easy joining and better load transfer. The photograph shows that low pressure process can produce net shape casting of complex shaped MMC components using low cost materials and toolings. Cast MMC components evaluation were performed by static tensile testing and followed by optical microscopic examination.

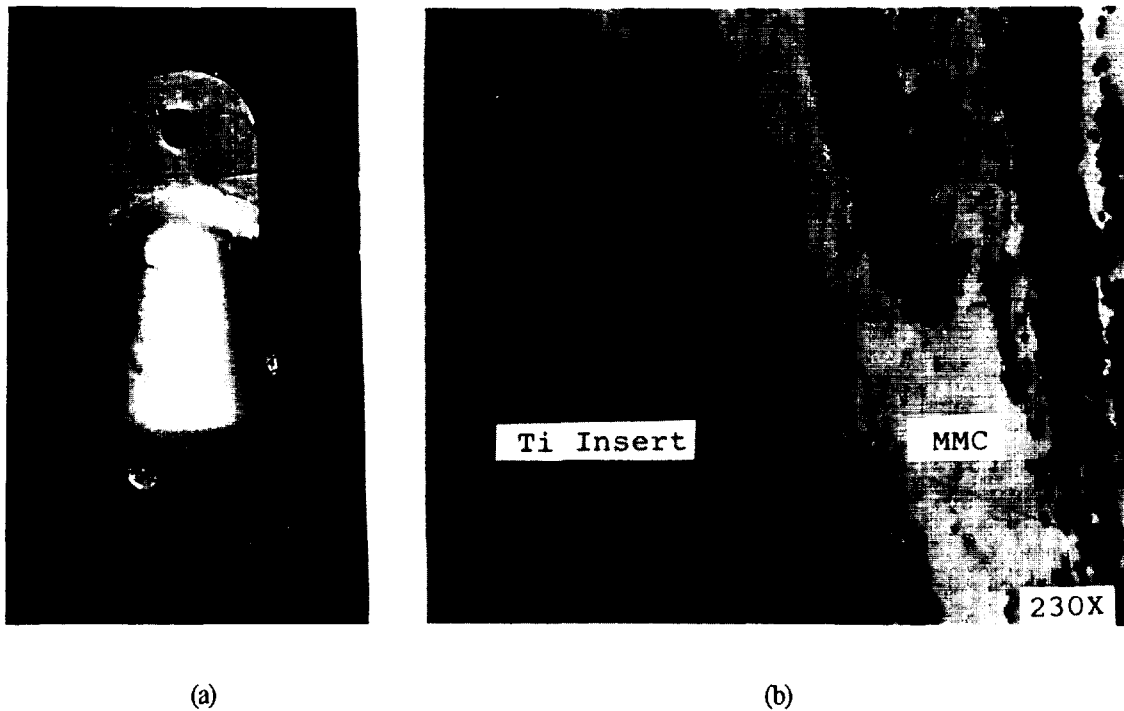


Figure 3. Photograph (a) shows the final result of the near net shape casting of graphite/magnesium MMC component with built-in titanium inserts. Photograph (b) at 230X magnification shows no cracks nor reaction zone at the interface between the titanium inserts and the MMC material.

Several graphite/magnesium cast components were subjected to static mechanical testing to assess the structural integrity of the MMC at the metallic insert interface. By using adhesive bonding, one end of the clevis component was connected to a cylindrical loading rod at the metallic insert interface. At the other end of the clevis joint, a loading pin was used by placing it through the clevis end loading hole. The tensile tests were conducted by attaching the cylindrical loading rod and the loading pin to the tensile testing machine so that the clevis component will be pulled away, under applied tensile stress, from the cylindrical loading rod. Test results showed that metallic inserts located at the tube end and at the clevis end region effectively transferred the axial load to the graphite fiber reinforcements because the MMC component failure mode occurred within the MMC material and away from the MMC/insert interface. The tensile test did demonstrate the feasibility of the cast MMC component with built-in metallic inserts since the failure site did not occur at or near the insert locations.

To perform microstructural analysis, sections of the component were cut and polished for observation under microscopic examination. Sections of MMC component around each metallic insert were evaluated for bonding strength, interactions with the insert materials, as well as fiber distribution, void content, and fiber damage, if any. Figure 3b shows the micrograph (at 230X magnification) of the interface between the titanium insert and the graphite/magnesium MMC material. This interface between titanium insert and magnesium matrix alloy did not show any formation of the intermetallic phases. These unwanted brittle phases would have degraded the mechanical properties of the component at the joint. Moreover, after the tensile tests were performed, as shown in figure 3b the interface between the insert and the magnesium matrix is also free of cracks, voids and fiber degradation. In summary, the cast MMC component exhibited excellent mechanical properties with complete molten metal infiltration under pressure casting technique as described in this investigation.

CONCLUSION

To encourage the widespread utilization of future MMC components in industrial and commercial markets, one must find a way to reduce the MMC component cost and develop better joining techniques. This paper describes a feasibility demonstration of a low cost pressure casting for a complex shaped MMC component with built-in metallic inserts to facilitate easy joining and better load transfer. The low cost factor was achieved through the use of near net shape casting in which the machining requirement to produce the component shape is significantly reduced or eliminated completely. From the microstructure analysis the cast MMC component exhibited complete molten metal infiltration of the fiber reinforcements and showed defect free at the interface between the metallic inserts and the MMC material. The component joint strength was tested through the use of adhesive bonding applied at the insert surfaces. The tensile test did demonstrate the feasibility of the cast MMC component with built-in metallic inserts since the failure site did not occur at or near the insert locations. In general, the tensile tests performed in this investigation proved that the joint strength at the insert/MMC interface is greater than the overall strength of the graphite/magnesium MMC materials within the cast component.

REFERENCES

1. Mortensen, A., Cornie, J.A., Flemings, M.C., "Solidification Processing of Metal Matrix Composites," *Journal of Metals*, February 1988.
2. Luhman, T.S., Williams, R.L., Das, K.B., "Development of Joint and Joining Techniques for Metal Matrix Composites," Final Report AMMRC TR 84-35, Boeing Company, August 1984.
3. Fishman, S.G., Dhingra, A.K., Cast Reinforced Metal Composites, Proceedings of the International Symposium on Advances in Cast Reinforced Metal Composites, Chicago, IL, Sept. 26-30, 1988.
4. Cook, A.J., Werner, P.S., "Pressure Infiltration Casting of Metal Matrix Composites," technical paper published by P-Cast Corporation, Pittsburgh, PA, July 17, 1990.
5. Majkowski, P., Kashalikar, U., "Continuous Fiber Graphite/Aluminum MMCs for Complex-Shaped Space Structural Joints," Foster-Miller Final Report, NASA Contract No. NAS9-17997, March 1991.

C11

DESIGN AND ANALYSIS OF COMPOSITE ISOGRID FOR BRIDGE CONSTRUCTION

James L. Koury

Advanced Isogrid Design Innovative Technology

11208 Cochiti, Albuquerque, NM 87123

and

Piyush K. Dutta

U.S.Army Cold Regions Research and Engineering Laboratory

Hanover, NH 03755-1290

ABSTRACT

This paper describes the use of continuous composite isogrid structures for potential applications in bridge decks. Preliminary design and analysis are presented showing the capability and reliability of this structure. Fabrication, and mechanical and thermal properties for the structure are presented. Low cost materials and fabrication techniques available are also discussed.

INTRODUCTION

Highly engineered composite structures for space and missile applications must meet a variety of properties depending upon their function. These structures also offer the potential of replacing traditional metallic structures due to their high strength to weight ratio, flexibility in design, custom tailoring of desired properties, the ability to perform reliably in different extreme environments, reduced thermal stress, and longer life.

The isogrid construction with continuous graphite fibers has proven to give exceptional stiffness and lighter weight to flat panels. They are immune to atmospheric corrosion. Recently serious concerns have been raised in the civil engineering community about the deterioration of thousands of bridges in our national highways because of severe corrosion of steel reinforcements in concrete decks. Carbon composite isogrid could be presented as a serious alternative to steel reinforcement with minimal use of concrete as filling and wear resistant material. Despite possibly a higher material cost fiber composite isogrids can offer a competing advantage of higher speed of construction. With increasing highway traffic, motorists are becoming more intolerent of delays during the building or replacement of bridge decks. Their impatience also increases the risk of accidents. Also the current bridge construction requires long lead time both in the design and manufacture. Metal bridges are heavy, expensive, require long lead times, susceptible to corrosion, and damage easily due to thermal stress within the main structure.

A methodology for designing composite isogrids has been developed. The methodology is based on optimizing the margins of safety for rib buckling, pocket buckling, and general instability. An

automated procedure was used to modify the isogrid geometrical parameters (rib height, weight, skin thickness, and triangle height) in the presence of multiple constraints (maximum rib height to width ratio, until the design criteria was satisfied. A nodal area was also included in the design and geometric patterns as shown in Figure 1.

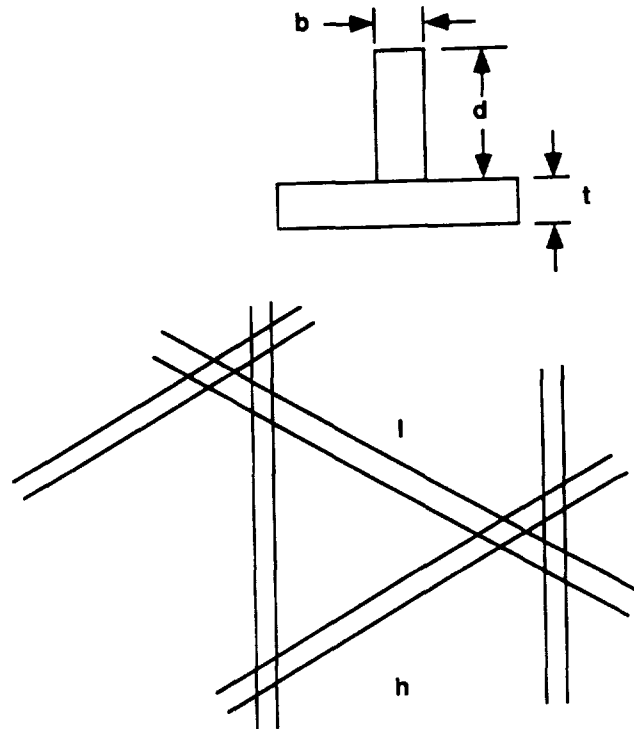


Figure 1 Isogrid schematic and dimensions

Several flat carbon/epoxy composite isogrid panels were fabricated and tested in axial compression to validate the design methodology. Multiple strain gages were used to measure the strain present in the skin and ribs at failure. Failure load levels agreed well with the pretest predictions.

TECHNICAL DISCUSSION

This effort was initiated in Jan 1990 at the US Air Force Phillips Laboratory under the direction of James L. Koury. A team consisting of technical personnel from the Air Force and Mc Donnell Douglas Space Systems Company conducted fundamental research into the processing science related to the automated fabrication of large composite isogrid structures [1]. This was followed by design development, fabrication, structural testing and evaluation.

Design and Analysis

A detailed cost and performance trade study was performed by Mc Donnell Douglas Space System Company, Huntington Beach Ca.,(MDSSC) in support of the Advanced Launch Vehicle System(ALVS) [2]. The study compared composite isogrid design to composite honeycomb, composite corrugated, composite monocoque, and traditional aluminum isogrid design [3]. A comparison of weight differences is shown in Table 1. These weight differences in various lengths of isogrids are shown in Figure 2.

Table 1 - ALVS fairing design - weight comparison

<u>Material Type</u>	<u>Weight (kg)</u>
1. Composite monocoque	15875
2. Aluminum isogrid	7821
3. Composite sandwich	5020
4. Composite corrugated	4850
5. Composite Isogrid	4428

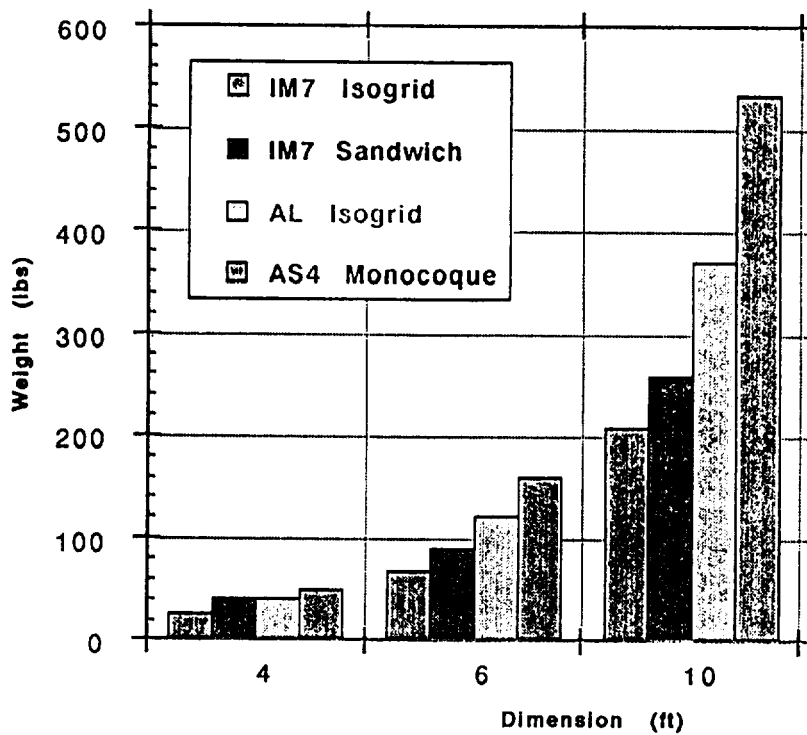


Figure 2. Weight comparisons of Isogrids of different materials

A design model was developed as part of this effort. The model has been validated by mechanical tests, plate equation prediction [4] and finite element analysis performed on composite isogrid panels [5]. Three point bend tests were also performed to validate the predicted effective modulus with the experimental effective modulus. The results of the tests results are shown in Table 2.

**TABLE 2
ISOGRID PANEL TEST RESULTS**

Compression Test

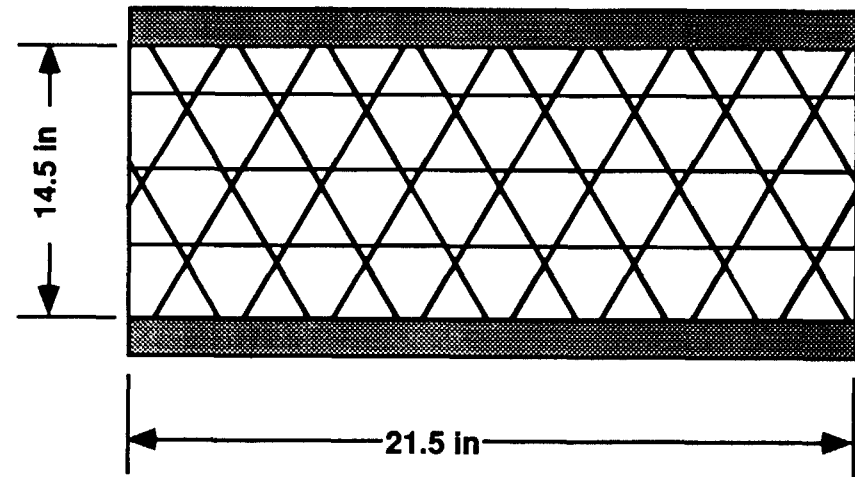
TEST #	MAX LOAD (lbf)
1	8556
2	8459
3	8101
4	8102

3 PT BEND TEST

Experimental Effective Modulus	Predictive Effective Modulus
1.1 Msi	1.28 Msi
1.21 Msi	

Natural Frequency (Hz)

Experimental Frequency	Finited Element Prediction	Plate Equation Prediction
309	326	305
296	323	



380

WEIGHT = 1.8125 lbs
RIB THICKNESS = 0.0534"
RIB HEIGHT = 0.6208"
SKIN THICKNESS = 0.694"

FABRICATION DEVELOPMENT

The several processes involved in manufacturing composite structures are shown in Figure 3.

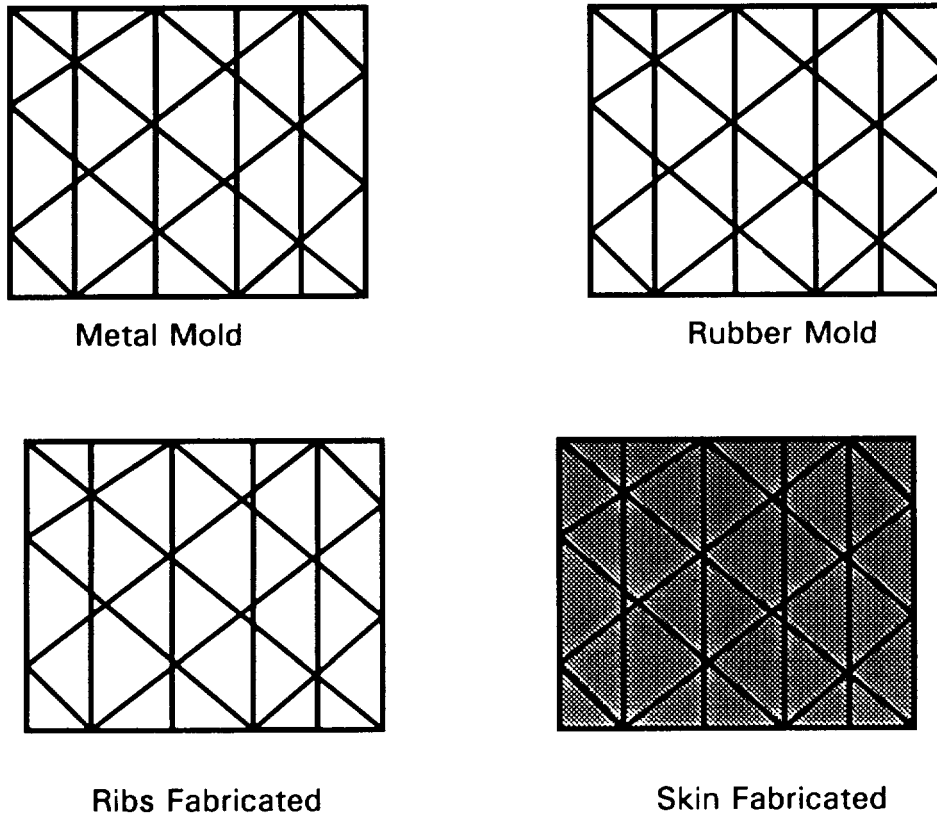


Figure 3. Fabrication of Composite Isogrid Panel

The fabrication of the composite isogrid panels starts with the development of the design for metallic isogrid mold. The pattern for the mold is generated using 2D cad design. A patterned metallic isogrid tool was first fabricated. Then silicone rubber was poured into the metal mold and formed the isogrid female rubber mold. Prepreg tow with various types of Graphite fiber and resins were fabricated into the mold followed by the skin, cured and tested. Panels with IM7/ 977-2 toughen epoxy IM7/ BYTE-1 Dicyanate resin have been fabricated, and tested. The results of the tests identified that the design for fairings, solar panels etc. are achievable. Excellent properties were validated as shown in Table 3. Mechanical tests were performed on the panels which demonstrated that the structures to have excellent strength and stiffness. The testing of the panels also demonstrated no global buckling. Damage was confined within the cell (s) thus not causing other cells to fail.

Table-3. Test data from Dicyanate ester/IM-7 panel

a. Compression Test Results

Layup	Width (in.)	Thickness (in.)	Modulus (psi x 10 ⁶)	Compressive Strength (psi x 10 ³)
0°	0.502	0.047	18.04 (0.25)*	-
0°/90°	0.500	0.061	11.14 (0.17)	-
0°/90°	0.502	0.062	-	98.1 (5.0)

b. Tensile Test Results

Layup	Test Type ASTM	Width (in.)	Thickness (in.)	Max. Load (lbf)	Tensile Modulus (psi x 10 ⁶)	Tensile Strength (psi x 10 ³)	Ultimate Strain (x 10 ⁻⁶)	Poisson's Ratio
[0°] ₈	D3039	0.502	0.047	8215	22.87 (0.53)	349 (15.2)	12151 (765)	0.281 (0.02)
[90°] ₁₆	D3039	1.002	0.092	502	-	5.49 (0.56)	5643 (303)	-
[45/135°] ₂₅	D3518	1.002	0.049	1184	1.82** (0.06)	23.8 (0.9)	-	0.88 (0.057)

* Figures in parenthesis show the standard the standard deviation.

** Shear modulus = 0.55 x 10⁶ psi. (Std. dev. = .016 x 10⁶ psi).

THERMAL STRESSES

The thermal environments that one would envision for bridges are considered minor as compared to Air Launch or National Aerospace Plane environments that are using composites. Composites cylinders have been known to survive the severe temperature for Air launch rocket motors (-65 F to + 300 F). The fabricated structures have been subjected to thermal shock and cycled 10 times within the above temperatures with minimum degradation to the structural performance. The major concern is the resin microcracking during the curing and thermal cycles.

Thermal stresses generated during the curing of the structure, high percent of voids and the high percent of water uptake must be understood and taken into account during the design of the structure. There is an extensive amount information in the literature on the types of resins that have been evaluated and can be used for the above applications [3][6][7]. The insertion of toughened epoxy and toughened dicyanate resins have expanded the resin's thermal capabilities. The National Aerospace Program (NASP) has developed and demonstrated the use of these types of resins for low (Liquid Hydrogen) temperatures for space applications. NASP Technology programs have successfully fabricated and tested composite cylinders, without metal liners, to contain liquid hydrogen. Cylinders were thermally cycled ten times to -423 F and Pressure cycles to limit pressure six times at -423 F with no hydrogen leakage and no structural distress. This technology has also identified that one must not only select the resin but must also design the composite structure in such a way to minimize and control the microcracking during the life of the structure.

As a result of this past effort the Phillips Laboratory is planning a program to design and fabricate two four foot cylinders and perform similar Liquid Hydrogen Leak Tests. This effort is in support of Single Stage To Orbit (SSTO) program. The resin that will be used on the above program has been tested by NASA and is the leading candidate for the SSTO program. B based allowables data have been performed for the resin material shown in Table 3.

TARGETED APPLICATIONS

The composite isogrid technology presented here has many other applications. However, the major concern is the materials and the fabrication costs. The materials cost for glass /epoxy and graphite/epoxy are high. In aerospace industry the major cost driver is the contractor/government control requirements. The number of test required for material validation i.e. A and B allowables performed by the manufacturer to validate the manufactures data drives the costs. A program is needed to assess the cost drivers, and determine if the requirements used by the government/contractors can be altered for use of the composite isogrid technology for civil engineering application, and thus reducing the costs. Also, the production rates for space and missiles is much lower than what would be for infrastructure applications, where much larger volume of materials will be needed. The increased demand and the high production rates should bring the overall cost down, thus making the composite very competitive with conventional bridge decking materials. The life cycle costs should also be evaluated for composites. The long life prediction for the composites should reduce the life cycle costs thus reducing the over all cost significantly.

CONCLUSIONS / RECOMMENDATIONS

The composite isogrid technology is ready for insertion into the commerical arena. The Technology developed by the Phillips Laboratory has validated the analytical models for panels. Low cost filament winding process has been demonstrated. Automation of the isogrid is just around the corner but needs government support. The design and resin technology has been demonstrated and is ready for commercialization. The only thing that one must be concerned with is the cost. We recommend that a program be generated to determine if the material and processing cost is ready for this area. In conclusions, I feel that this technology is ready for demonstration and implementation.

REFERENCES

1. Slysh, P. and Dyer, Et., Isogrid Structural Tests and Stability Analysis, Journal of Aircraft, Vol. 13, Oct. 1976.
2. Koury, J. and T. Kim, Phillips Laboratory, J. Tracy MDSSC, Continuous Fiber Composite Isogrid For Launch Vehicle Application, Ninth International Conference on Composites, Madrid, Spain, 12-16 July 93,
3. Meyer, R. , Isogrid Design Handbook, McDonnell Douglas, MDC G 4295A, Feb., 1973.
4. Timoshenko, S. and Gere, J.M., Theory of Elastic Stability, 2nd ed., McGraw-Hill Book Co., New York, 1961.
5. Rotz, C., and J. Koury, Mechanical Testing of Isogrid Structures, AFOSR Research Program, PL. International Sampe Symposium Anaheim CA. May 1992.
6. Koury, J., T. Kim, Continuous Filament Wound Composite Concept For Space Structures, Phillip Laboratory, Eight International Conference Symposium, July 91, Hawaii.
7. Koury, J., and T. Kim, J. Tracy, Continuous Fiber isogrid For Space Applications, ASM Internal Conference on Processing and Fabrication of Advanced Composites, Long Beach, CA. 9-11 August 93.

**IMPROVED CONSTRUCTION MATERIALS FOR POLAR REGIONS USING
MICROCELLULAR THERMOPLASTIC FOAMS**

Daniel J Cunningham
Axiomatics Corporation
3 G Gill St. Woburn, MA. 01801
617-932-0202
June 30, 1993

543-27
2479
p. 6

Abstract

Microcellular polymer foams (MCF) are thermoplastic foams with very small cell diameters, less than 10 microns, and very large cell densities, 10^9 to 10^{15} cells per cubic centimeter of unfoamed material. The concept of foaming polymers with microcellular voids was conceived by Dr. Nam P. Suh in 1979 to reduce the amount of material used for mass-produced items without compromising the mechanical properties. The reasoning behind this concept was that if voids smaller than the critical flaw size pre-existing in polymers were introduced into the matrix, they would not affect the overall strength of the product. MCF polycarbonate (PC), polystyrene (PS), and polyvinyl chloride (PVC) were examined to determine the effects of the micro-structure towards the mechanical properties of the materials at room and arctic temperatures. Batch process parameters were discovered for these materials and foamed samples of three densities were produced for each material. To quantify the toughness and strength of these polymers, the tensile yield strength, tensile toughness and impact resistance were measured at room and arctic temperatures. The feasibility of MCF polymers has been demonstrated by the consistent and repeatable MCF micro-structures formed, but the improvements in the mechanical properties were not conclusive. Therefore the usefulness of the MCF polymers to replace other materials in arctic environments is questionable.

Purpose and Scope

The purpose of this experimental research was to show that microcellular thermoplastic foams have similar or improved mechanical properties to solid thermoplastic materials at arctic temperatures. MCF thermoplastics have shown better fracture toughness, impact strength, and fatigue in previous tests performed at room temperatures for various materials.

This experimental research focused on three materials: polycarbonate (PC), polystyrene (PS), and polyvinyl chloride (PVC). These materials were foamed using the batch microcellular foaming process. This process creates a microcellular foam structure by inducing a thermodynamic instability in the materials with an inert gas (non-CFC). The resulting cell structure incorporates a 10^{10} to 10^{13} void per cm^3 , at an average size of 0.1 to 2.5 microns. The tensile strength and toughness and the impact resistance were examined to demonstrate the change in mechanical properties.

Background

Plastics have long been the material of choice in design due to the excellent combination of such advantages as low cost, ease of manufacturing, and outstanding properties as a function of weight. Many of the advancements in materials development over the past 50 years have been in the field of plastics, resulting in hundreds of different types and thousands of grades and alloys.

Thermoplastics are those polymers that have a melting point and solidify by cooling after processing. Thermoplastics have been characterized as having a dramatic reduction in their toughness at low temperatures. This is usually experienced in materials that are examined across their glass transition temperature (Tg). The glass transition temperature is where a polymer experiences a semi-phase change from a glassy state to a rubbery state. All of the polymers examined in this experiment were already

below their T_g, so a great reduction in toughness was not expected to come from crossing this phase. An increase in toughness per amount of material was expected to come from the microcellular foam structure. "The rationale is that if bubbles smaller than the flaws that naturally occur in polymers were created in sufficient numbers, then the material density could be reduced without compromising the mechanical properties." <Ref. 1>

Microcellular Foams (MCF) are polymers in which very small voids ranging in diameter from 0.1 to 25 microns, and are present in very large numbers, in the range of 10⁹ to 10¹⁵ voids per cubic centimeter (cc). The densities of these polymers have been reduced to as low as 0.04 g/cc in batch processing, which is an expansion of about 30 times the original volume. The invention of this foaming process that creates microcellular structures in polymers was pioneered by the Massachusetts Institute of Technology.

Nearly all polymers can be processed having a microcellular structure. It is accomplished by inducing a *thermodynamic instability after the polymer has been saturated with an inert gas through a sudden change in pressure and/or temperature*. In batch processing this is done by exposing solid samples to gaseous or super-critical fluid N₂ or CO₂, for example, under pressure until completely saturated, depressurizing them, and providing enough heat to allow the polymer matrix to deform and allow cell growth. Polymers may gain as much as 20% super-critical CO₂ fluid by weight. Process parameters have been established empirically and theoretically for many polymers. Continuous processing, such as extrusion, requires super-critical N₂ or CO₂ to form a homogeneous solution with the polymer melt and the pressure drop of the melt exiting the die allows cell growth.

Tensile elongation, tensile toughness, and tensile strength measurements are among the most important indications of strength in a material and are most widely specified properties of plastic materials. Tensile strength, in a broad sense, is a measurement of the ability of a material to withstand forces that tend to pull it apart and to determine to what extent the material stretches before breaking. Tensile modulus, an indication of the relative stiffness of a material, can be determined from a stress-strain diagram. Different types of plastic materials are often compared on the basis of tensile strength, elongation, and tensile modulus data. Many plastics are very sensitive to the rate of strain and environmental conditions. Therefore, the data obtained by a method cannot be considered valid for applications involving load-time scales or environments widely different from the method. The tensile property data are most useful in preferential selection of a particular type of plastic from a large group of plastic materials and such data are *of limited use in actual design in the product*. This is because the tensile test does not take into account the time-dependent behavior of plastic materials.

The impact properties of polymeric material are directly related to the toughness of the material as well. Impact resistance of a material is the ability to resist fracture under stress applied at high speed. That is to say, impact strength is a measure of the ability of a material or structure to withstand the application of a sudden load without failure, to prevent crack propagation through the sample. Furthermore, it is defined as the ability of a polymer to absorb applied energy that is related to the toughness of plastic materials. The toughness of a material is proportional to the area under the stress-strain curve, the tensile toughness. Impact is mathematically defined as $I = \text{Force} \times \text{Time}$. Thus, impact strength is related to the load as well as to the speed of the application.

In contrast to impact resistance, the fracture toughness of a solid polymer is much better defined for a given set of environmental conditions. Theoretically, the impact strength/brittleness of a material is related to micro-mechanical fracture in the matrix. Under shock loading, the matrix tries to readjust in a short time. Material will not fracture if energy applied is absorbed completely in this readjustment of molecules. For example, rigid polymers such as polystyrene and acrylics take a longer time to readjust than flexible polymers such as plasticized PVC. Flexibility of the molecules depends upon the chemical structure or molecule, type and amount of additives, temperature, time span of application (very short application time of load makes flexible polymers behave as solids), and possibly the cell structure. <Ref. 2>

The effects of the micro-cells in the polymer matrix were not expected to debilitate the tensile properties, because they were smaller than the critical flaw size to initiate a crack. Theoretically, the tensile strength and toughness of a MCF polymer should be the same as a solid polymer of equal weight. A small increase in impact strength was expected through the blunting of the crack tip primarily at open cell regions.

Experimental

Materials and Equipment

Materials:

Polystyrene (PS) GP crystal PS neat, Westlake Co.
Polyvinyl Chloride (PVC) Type I clear, Huls America
Polycarbonate (PC) Cryolan ZX 9034, Cylko Ind.
Polyamide (Nylon) Nylon 6/6 neat, EI DuPont
Carbon Dioxide gas

Equipment:

Hydropak gas intensifier
Autoclave Engineering 600 in³ pressure vessel
Heated water baths
Instron Tensile testing machine 6025
TMI Izod testing machine 43-1
Setra 100 Scale 150.000 grams

Procedure

The research plan consisted of examining the foaming parameters of microcellular foamed thermoplastic materials, discovering the micro-structure of these materials, and discovering the mechanical properties of these MCF polymers at room temperature and at an arctic temperature.

The first task of this research was to examine the gas absorption of the polymer materials to determine when they were completely saturated. These material specimens were saturated with super-critical CO₂ at 3500 psi and 40°C for different lengths of time to yield the data necessary to determine the gas absorption versus time curve for each material.

The second task of this experiment was to examine the foaming parameters. Each specimen after being completely saturated with super-critical CO₂ was submerged in glycerin oil at different temperatures, ranging from 30°C to 65°C, then measured to determine the void fraction. This data was used to correlate the void fraction with temperature in order to predetermine the foaming temperature to achieve a specific foam density.

The third task was to foam pre-cut specimens using the saturation and foaming conditions discovered in the previous tasks to achieve 10, 20, and 30% void fraction. The foamed test specimens were intended to be the same size as the unfoamed baseline ones.

The test specimens were foamed in heated water baths for more than 10 minutes to insure full cell growth. They were unrestrained and evenly heated to promote even cell growth. All of the test specimens were out-gassed in a vacuum chamber for 2 to 8 days to remove the residual CO₂.

The mechanical properties, namely the tensile strength and toughness and the impact resistance, were measured following ASTM D638-87b, "Standard Test Method for Tensile Properties of Plastics," and ASTM D256-84, "Impact Resistance of Plastics and Electrical Insulating Materials." Sample preparation and testing procedures followed the ASTM requirements. Tensile Type I samples were used for the

tensile testing and 0.125 inch wide by 0.5 inch thick, notched impact bars were used for the Izod impact testing.

The cell size and cell density were determined by examining the Scanning Electron micro-graphs taken. The cell size was measured using the scale present on the micro-graph. The cell density was determined by counting the cells in a measured area, calculating the area density, and taking the square root of that, and then cubing the result. This assumes isotropic bubble distribution.

Discussion of Results

The examination of the MCF specimen's micro-structure was done with an SEM. The cell sizes of the MCF PS and PVC specimens were remarkably small, 0.1 to 0.3 microns in diameter and the cell density was high, 10^{12} to 10^{13} cells per cubic centimeter of original material (See Charts). The skin thickness for the MCF PS specimens was approximately 2 microns and PVC specimen's skin thickness was less than 1 micron. MCF PC specimens had larger cells, 2 to 2.5 microns and consequently lower cell densities. The skin thickness for the PC specimens was about 25 microns. Both the MCF PVC and PS specimen's cells were spherical, but the PC specimen's cells were cavernous like, with numerous smaller cells throughout the larger cells. Cell densities were relatively uniform throughout the thickness of each specimen.

The mechanical property data was collected and analyzed for each material and foam density. The final testing specimens were all the same size to maintain uniformity, that is the 30% foamed specimens had 30% less material than the unfoamed ones.

The unfoamed sample data are presented in each chart to provide a base point for comparison. Since the unfoamed specimens were not processed with super-critical CO_2 and not put through the same processing procedures, it is biased to directly relate the foamed and unfoamed results. Gas saturation of the polymers caused annealing in the specimens and possible molecular and additive degradation. The effect of super-critical CO_2 to the polymers is not fully known, but visual inspection of some polymers shows evidence of degradation. It appeared that the MCF PS specimens that were saturated longer than 48 hours under went this degradation, the smooth surface features common to MCFs were destroyed and the material seemed to be very brittle. This could have been from the CO_2 reacting with the polymer matrix and possibly breaking the polymer chains.

In general, the foamed micro-structure of each sample did not debilitate the mechanical properties. While some properties improved for some materials, other properties decreased. Data taken from "Structural Design with Plastics," Ref. 3, for typical thermoplastic structural foams shows that MCFs have the same or better tensile strengths than structural foams.

The tensile yield strength of each MCF material significantly decreased from the unfoamed sample. This could be attributed to the effect of super-critical CO_2 towards the polymer. To provide a relevant unfoamed baseline, some specimens were saturated but not placed in the heated bath. Unfortunately, the chamber temperature during saturation provided enough heat to promote cell nucleation and foam growth. The yield strengths of the MCF samples show a decrease in strength roughly proportional to the decrease in the amount of material.

It was found that the cold temperature (-30°C) testing results were generally higher than the room temperature (21°C) results. This occurrence was expected for amorphous materials below their T_g , because the cold temperature constricts the polymer matrix. This constriction brings the polymer chains closer together creating a larger influence of the steric hindrances due to the interaction of the side chains elements. Close to 20% increases in tensile yield strength were observed in PC and PVC due to the cold temperature. PS specimens displayed slight increases in yield strength, probably from the fact that the benzene side molecules exhibit near their maximum steric hindrance even at room temperature.

Polycarbonate

Property	Units	Test Method		ASTM							
Density	kg/m ³	1200		1044		900		816			
Cell Size	microns	unfoamed		1		2		2.5			
Cell Density	voids/cm ³			1.12E+10		4.16E+10		6.4E+10			
				<u>21oC</u>		<u>-30oC</u>		<u>21oC</u>		<u>-30oC</u>	
Tensile Yield Strength	MPa	D 638	64	74	43	52	44	50	37	46	
Tensile Elongation	%	D 638	87	72	105	88	100	83	92	82	
Tensile Toughness	Joules	D 638	168	156	206	208	175	211	221	223	
Izod Impact Strength	Joules	D 256	6.85	5.71	7.12	2.68	4.99	2.3	2.79	1.9	

Polystyrene

Property	Units	Test Method		ASTM							
Density	kg/m ³	1050		914		809		735			
Cell Size	microns	unfoamed		0.2		0.3		0.3			
Cell Density	voids/cm ³			2.02E+12		2.33E+12		4.29E+12			
				<u>21oC</u>		<u>-30oC</u>		<u>21oC</u>		<u>-30oC</u>	
Tensile Yield Strength	MPa	D 638	46	48	29	29	29	29	15	18	
Tensile Elongation	%	D 638	2.4	2.6	2.2	1.7	2.2	2.1	1.4	1.2	
Tensile Toughness	Joules	D 638	2.44	2.81	1.71	1.29	2.00	1.88	0.69	0.72	
Izod Impact Strength	Joules	D 256	0.13	0.15	0.09	0.10	0.07	0.10	0.09	0.11	

Polyvinyl Chloride

Property	Units	Test Method		ASTM							
Density	kg/m ³	1400		1218		1148		980			
Cell Size	microns	unfoamed		0.1		0.2		0.2			
Cell Density	voids/cm ³			4.69E+13		1.85E+13		5.24E+13			
				<u>21oC</u>		<u>-30oC</u>		<u>21oC</u>		<u>-30oC</u>	
Tensile Yield Strength	MPa	D 638	79	99	37	53	32	42	32	43	
Tensile Elongation	%	D 638	5.4	7.1	10.5	3.8	5.3	3.4	9.4	4.3	
Tensile Toughness	Joules	D 638	10.6	18.2	13.6	5.5	6.0	4.2	13.0	6.2	
Izod Impact Strength	Joules	D 256	0.20	0.11	0.17	0.27	0.20	0.19	1.87	0.24	

The percent elongation was also examined. As expected, the cold temperature results were generally lower than the room temperature results. No significant increases were noticed for any of the MCF materials.

The tensile toughness value was generated through the software testing program. The area under the stress-strain curve was measured and recorded. The toughness measurement is a slow rate applied load. MCF PC specimens showed higher toughness values for all of the foam densities and displayed ductility until failure. The MCF PS and PVC specimens, on the other hand, displayed lower cold temperature toughness results and failed brittlely. The room temperature PVC specimen's toughness was generally the same. Since only MCF PC showed an increase in tensile toughness, it is thought that the foamed micro-structure improves the energy absorption of ductile materials, but not brittle materials.

The Izod impact test was also performed, which is the fast rate applied impact load. This provided the data to analyze the material for sudden impact or shock loading and energy absorption. MCF PC specimen's room temperature impact resistance decreased with a decrease in relative density. This represented PC losing its ductility as the void fraction increased. The cold temperature results initially decreased then remained constant. MCF PS and PVC specimen's impact resistance showed no substantial increase or decrease except for PVC at 30% void fraction at room temperature, which increased nearly 10 times. Instead of a brittle fracture, the PVC specimens exhibited ductile fracture. Since the arctic temperature specimens did not show the same results as the room temperature ones, this behavior is not strictly dependent on the cell size or cell density, but on overall molecular ductility.

Both tensile toughness and impact resistance measure the amount of energy a specimen can absorb before fracture. The results of these two tests should have correlated with each other. This was not the case. Since crack initiation and propagation were not examined in this work, it is difficult to understand how the very small closed celled matrix affects fracture mechanics.

Conclusion

Without examining the micro-mechanics of fracture for MCF, it is difficult to understand the assorted results obtained under this testing. Whereas some mechanical properties increased, others decreased. The micro-structure of the material appears to affect the ductility, and consequently the energy absorption of the samples. The largest effect to the mechanical properties came from the MCF batch processing of the materials. The effect of super-critical fluids on polymers is not well known and degradation was only visibly noticed with MCF PS, but could have affected the other materials.

In general, the cell size and foam densities did not affect the mechanical properties and maintained similar strengths throughout the samples of each material tested as expected. The most notable exception of this is the 30% void fraction MCF PVC specimens that displayed a tremendous increase in impact strength.

Bibliography and References Used

Bibliography:

1. K.A. Seeler, V. Kumar, 1992, "Tension-Tension Fatigue of Microcellular Polycarbonate: Initial Results", ANTEC '92, pp 1496.
2. J.C. Huang, S. Orroth, N.R. Schott, 1990, "Physical Properties of Polymers: A laboratory Syllabus", Plastics Composites and Development Center, Lowell, Ma., pp 21-25, 101-104.
3. Benjamin, B. S. "Structural Design with Plastics"; Van Nostrand Reinhold: New York, 1982.

References Used:

- D.F. Balswin, N.P. Suh, 1992, "Microcellular Poly(ethylene terephthalate) and Crystallizable Poly(ethylene terephthalate): Characterization of Process Variables", ANTEC '92, pp 1503-1507.
- S.W. Cha, N.P. Suh, 1992, "Room-Temperature Microcellular Foaming", ANTEC '92, pp 1527-1531.
- S. Cha, N.P. Suh, D.F. Baldwin, C.B. Park, 1992, "Microcellular Thermoplastic Foamed with Super-critical Fluid", U.S. Patent 5158986.
- R. D. Deanin, 1972, Polymer Structure, Properties and Applications, Cahners Books, Boston, MA.
- J. S. Huang, L. J. Gibson, 1990, "Fracture Toughness of Brittle Foams", Pergamon Press, Great Britian.
- J. S. Huang, L. J. Gibson, 1990, "Fracture Toughness of Brittle Honeycombs", Pergamon Press, Great Britian.
- L. J. Gibson, M. F. Ashby, 1988, Cellular Solids: Structure and Properties, Pergamon Press, Great Britian.
- Klempner, Frisch, 1991, Polymeric Foams, Hanser Publishers, Munich.
- V. Kumar, M.M. Vander Well, 1991, "Microcellular Polycarbonate-Part II: Characterization of Tension Modulus", ANTEC '91, pp 1406-1410.
- V. Kumar, J.E. Weller, H.Y. Hoffer, 1990, "Synthesis of Microcellular Polycarbonate: A Phenomenological Study of Bubble Nucleation and Growth", ASME Winter '90, Vol. MD-19, pp 197-212.
- V. Kumar, J.E. Weller, R. Montecillo, 1992, "Microcellular PVC", ANTEC '92, pp 1452-1456.
- J.A. Kweeder, N.S. Ramesh, G.A. Campbell, D.H. Rasmussen, 1991, "The Nucleation of Microcellular Polystyrene Foam", ANTEC '91, pp 1398-1400.
- N.S. Ramesh, J.A. Kweeder, D.H. Rasmussien, G.A. Campbell, 1992, "An Experimental Study on the Nucleation of Microcellular Foams in High Impact Polystyrene", ANTEC '92, pp 1078-1081.
- K.A. Seeler, V. Kumar, 1992, "Fatigue of Notched Microcellular Polycarbonate", ASME '92, MD-Vol. 38, pp 93-108.

This work was funded under NSF 91-20 III92-60553: Polar Regions Microcellular Foam

omit

POWER AND ENERGY

USE OF MAGNETIC COMPRESSION TO SUPPORT TURBINE ENGINE ROTORS

Squadron Leader Chris J Pomfret, Royal Air Force
Wright Laboratory
Wright-Patterson AFB OH 45433-7251

544-37

2480

p. 16

ABSTRACT

Ever since the advent of gas turbine engines, their rotating disks have had to be designed with sufficient size and weight to withstand the centrifugal forces generated when the engine is operating. Unfortunately, this requirement has always been a life and performance limiting feature of gas turbine engines and, as manufacturers strive to meet operator demands for more performance without increasing weight, the need for innovative technology has become more important. This has prompted engineers¹ to consider a fundamental and radical breakaway from the traditional design of turbine and compressor disks which have been in use since the first jet engine was flown 50 years ago. Magnetic compression aims to counteract, by direct opposition rather than restraint, the centrifugal forces generated within the engine. A magnetic coupling is created between a rotating disk and a stationary superconducting coil to create a massive inwardly-directed magnetic force. With the centrifugal forces opposed by an equal and opposite magnetic force, the large heavy disks could be dispensed with and replaced with a torque tube to hold the blades. The proof of this concept has been demonstrated and the thermal management of such a system studied in detail; this aspect, especially in the hot end of a gas turbine engine, remains a stiff but not impossible challenge. The potential payoffs in both military and commercial aviation and in the power generation industry are sufficient to warrant further serious studies for its application and optimization.

MECHANICS OF MAGNETIC COMPRESSED ROTORS (MCR)

Magnetic forces arise when electrical current flow is orthogonal to a magnetic field. Figure 1 shows the

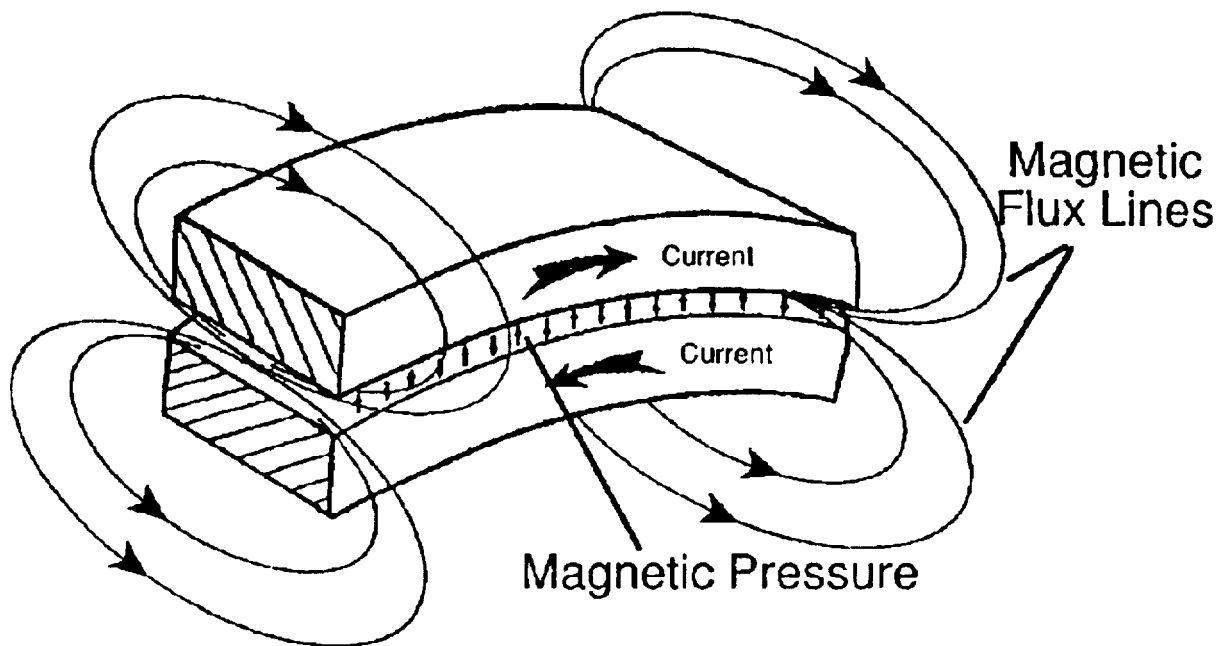


Figure 1: Opposing Currents Generate Repulsive Loads

¹Small Business Innovative Research program for Wright Laboratory, Wright-Patterson AFB OH by IAP Research Inc., Dayton OH. Technical Reports WRDC-TR-90-2088 "Magnetically Compressed Ring" and WL-TR-93-2014 "Magnetically Compressed Ring Thermal Management System Demonstration" refer.

principle for two conductors carrying oppositely directed currents. Each conductor generates its own magnetic flux and the interaction of the magnetic flux with the current in the opposite conductor creates a magnetic body force within each. As long as opposing currents flow in each conductor, the magnetic body force or "magnetic pressure" will repel the conductors from each other. If the conductors are rings then the inner ring will be in compression and the outer ring in tension. The concept of MCR has been founded on this principle.

Expanding the concept to gas turbine engines is depicted in Figure 2. The inner conducting ring, referred to as the armature conductor, rotates with the blades and supports the centrifugal loads. Magnetic pressure between the armature conductor and the stationary outer conductor (excitation conductor) transmits the centrifugal load to the outer conductor. A structural hoop wrapped around the outside of the excitation conductor ultimately supports the centrifugal loads.

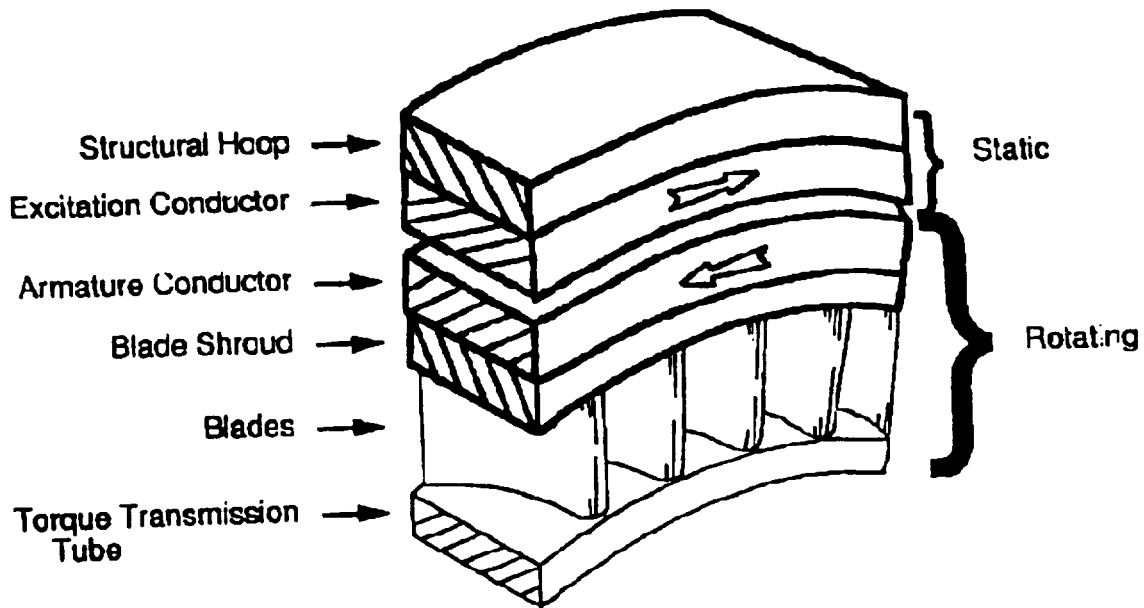


Figure 2: Centrifugal Loads are Transferred to a Static Structural Hoop

THE PERCEIVED BENEFITS OF MCR

There are clearly many challenges associated with a real-life, commercial, application of this concept and these will be addressed later. The many potential benefits are considered first.

Advanced Materials

We envision an increasing utilization of lighter weight materials such as ceramics and composites in future gas turbine engines. These advanced materials enjoy compressive rather than tensile forces. Using MCR, compressor and turbine blades would be in compression during operation.

Weight Savings

Although a detailed weight saving benefit analysis has not been carried out, there is an obvious potential for significant weight reductions. A turbine disk typically weighs 150 lbs; this would be dispensed with and replaced by a torque tube of much lighter weight. While the weight of the superconducting assembly would need to be added in, removal of obsolete bearing and lubrication equipment would provide further weight saving advantages. Based on rough approximations using the F110 engine, Figure 3 compares the weights of disks by

stage and the estimated weights of the MCR components which would be introduced. Savings in the region of 20% could be achieved for a HP Turbine first stage application (stage 13) whereas weight would be added if applied to a fan (stage 1). This assessment is very approximate and ongoing enhancements to superconductor technology would further increase the perceived benefits. The "MCR Dry" bar shows the complete system weight whereas the "MCR Rotating" bar is for the inner assembly only (torque tube, blades, insulation, armature etc.).

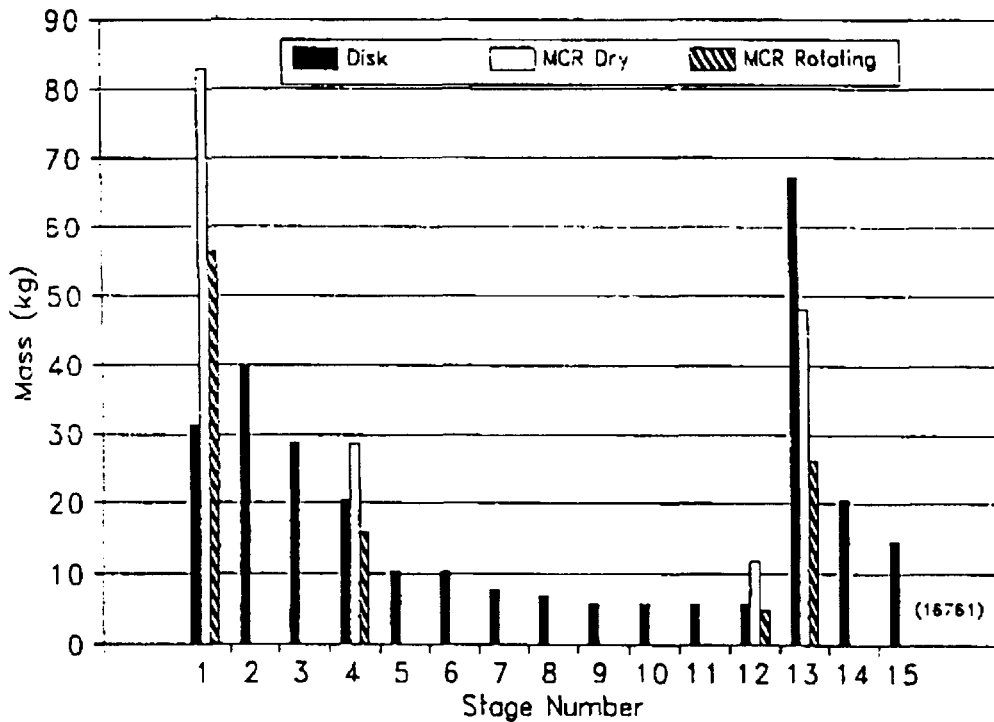


Figure 3: Comparison of Masses of MCR Components with Current F110 Disks

Performance Increases

Performance of gas turbine engines has always been limited by rotational speed constraints of compressor and turbine disks and the associated loads on bearings. Disposing of disks and bearings will permit increased rotational speeds and therefore increased performance. The perceived performance increases coupled with the weight reductions outlined above would make a significant impact on the Integrated High Performance Turbine Engine Technology (IHPTET) Initiative which aims to double the propulsive capability (thrust/weight ratio) of gas turbine engines in the next 10 years.

System Simplicity

Support features of a conventional gas turbine engine could be simplified or removed. There would no longer be a need for a bearing and lubrication system. The cost of design, purchase and upkeep of these features would thus be eliminated. Similarly, the significant design, manufacture and maintenance costs of disks would be zeroed. Currently, a great deal of cost and effort goes into life prediction, life measurement and inspection of disks so that their fatigue life is not exceeded. With the advent of two-level maintenance in the Air Force, equipment simplification and reduced maintenance activity are becoming more important and attractive. We believe that the simplifications cited above will be greater than the extra costs and upkeep created by the introduction of the superconducting equipment.

Life Availability

Currently, hot-end components are the major life limiting features of gas turbine engines. With MCR, increases in safe and useful life could be expected from the rotating components especially if metallic blades are replaced by advanced materials. The effects on life cycle costs would be significant; affordability would also be enhanced.

More Electric Aircraft (MEA) Initiative

Running in parallel with IHPTET is another initiative which, in its aim to increase aircraft reliability, supportability and maintainability, proposes fundamental changes to power subsystems. One such proposal is to remove the conventional hydraulic systems from aircraft and replace them with more reliance on electrical control and actuation. We have considered the interaction of MCR with the More Electric Aircraft (MEA) Initiative and found the two concepts to be, in theory, compatible. MEA would benefit from MCR by using the superconducting rings as an energy storage subsystem to prevent surges, ripples, and interruptions from the aircraft power supply. High temperature superconductor technology and cooling technology would be similar for the development of both concepts. Finally, the power requirements for spooling-up an MCR equipped engine (superconductor charge) would, at 300 kW, not exceed the perceived capacity of ground power units or aircraft APUs.

THE TECHNICAL CHALLENGES OF MCR

The foregoing advantages of MCR and its compatibility with ongoing initiatives for future gas turbine engines make the concept worthy of further study especially to specific areas in which the inherent benefits could be best applied. However, serious development of MCR presents many challenges.

Thermal Management

The MCR concept as applied to the hot end (the most difficult) of a gas turbine engine would require formidable thermal management; a superconductor operating at 50°K adjacent to an HP Turbine operating at 1700°K defines the challenge. Figure 4 shows a method of addressing the requirement.

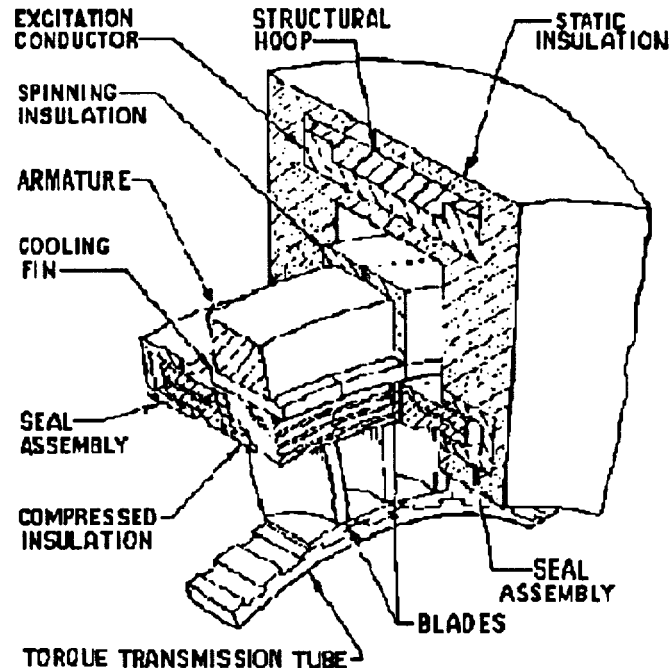


Figure 4: Schematic of Possible MCR Design

Compressed insulation would limit the amount of engine heat reaching the superconductor and would also need to transmit the centrifugal loads evenly to the cooling fin and armature. The material selected would need to be strong, (20 ksi compressive strength) lightweight, of small volume and with an extremely low thermal conductivity (0.5 W/mK). Clearly, these are conflicting properties. From a variety of potentially suitable materials studied, Zirconia Y-TZP, with a compressive strength of 1750 MPa and a thermal conductivity of 2.7 W/mK, was found to have the best combination of properties. It might be that increasing the porosity of Zirconia would reduce further the thermal conductivity without significant detriment to the compressive strength

The cooling fin helps to dissipate the heat which passes through the compressed insulation. Cryogenic fluid would be delivered to the cooling fin edges and the fluid then passes out from small holes to the spinning insulation. The spinning insulation protects the armature from heat generated by rotational drag. Coolant from the cooling fin passes between the armature and the spinning insulation, exiting at the rotor tip and removing heat passing through the spinning insulation. This is shown in Figure 5. The final insulation surrounds the excitation conductor, structural hoop and coolant seals. This insulation would protect the MCR system from environmental heat sources and heat generated by rotational drag.

Lastly, coolant seals would provide two functions. Engine gases would be prevented from entering the area between the armature and excitation conductors thus helping to keep coolant requirement to a minimum. The seals would also help to limit the amount of coolant leaked into the engine gas stream; again, excessive leakage would increase the coolant requirement and, ideally, seal leakage rates should be less than rotor coolant requirements. The seals would need to withstand rotor tip speeds of 2000 ft/sec, which are much greater speeds than currently fielded seals operate at, and would need to operate at close clearances (< 0.001 in) yet be efficient over a comparatively large range. Compliant foil seal technology shows the potential for meeting these high demands.

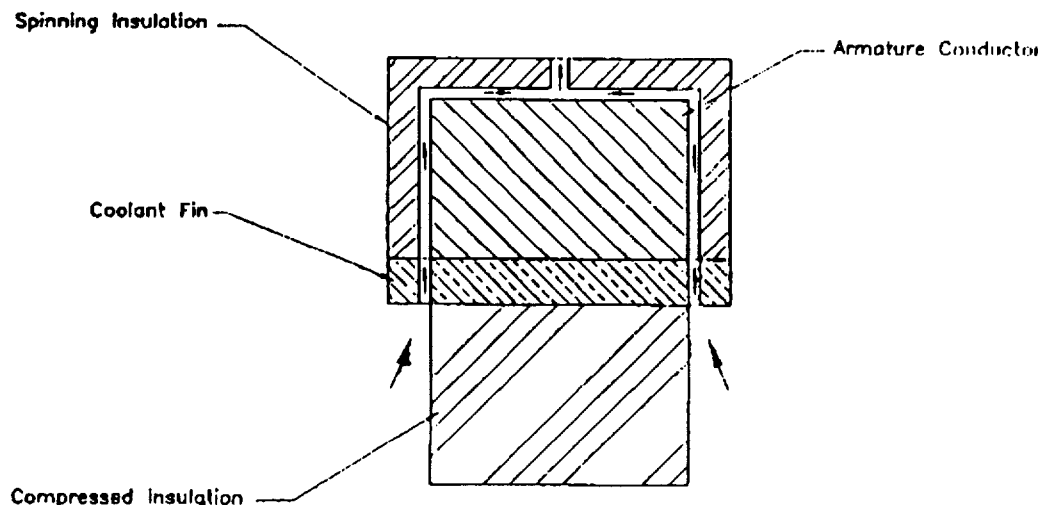


Figure 5: Flowpath of Coolant within Spinning Insulation

Other Potential Operating Difficulties.

The concept of a gas turbine engine operating without disks nor bearings is difficult to imagine. How does the rotating assembly sit when stationary; how does it spool up; and how does it remain axially stable when rotating? Similarly, what power does it consume in steady state; what happens in the event of power failure; and is there not a massive magnetic effect both for easy detection and to interfere with other systems in the aircraft? Finally, how is the superconductor temperature maintained at 50-100 K. These types of questions have been examined and most of them satisfactorily answered.

Electrical current is introduced into the outer (excitation) coil and the resulting opposing current in the inner (armature) coil is induced. During operation, changes in engine rotational speed would be accompanied by

Electrical current is introduced into the outer (excitation) coil and the resulting opposing current in the inner (armature) coil is induced. During operation, changes in engine rotational speed would be accompanied by an input or withdrawal of electrical power from the excitation coil so as to keep the magnetic pressure equal and opposite to the centrifugal force. The source of power for inputs to the excitation coil would be met from the MEA power capabilities; the electrical equivalent of an accumulator would meet this requirement. Similarly, withdrawal of power would be dissipated in some form of capacitor system. For initial start-up, the initial power into the excitation coil (100-300 kW for 4-5 secs) would lift and centralize the stationary rotor (armature) and then more power (probably as much again) would be introduced progressively as the rotational speed built up to ground idle rpm. This sequence would avoid crushing the rotor when it is not generating centrifugal force but a bigger concern is the structural integrity of the outer coil which ultimately has to withstand the centrifugal force. Superconductors currently tolerate around 0.5% strain which would, in the case of an MCR application with a 10 in radius, be 1/20 in increase. A strong, rigid structure in which to encase the outer coil would therefore be essential.

An envisioned large magnetic signature does not in practice occur. The flux density (T) decreases rapidly with distance both radially and axially from the armature as shown in Figure 6. Outside the MCR system, magnetic flux is less than that of stray fields from standard electric motors and appliances (0.05T). At a radial distance of less than 15 ft, the level is less than the world's background level (0.0001T). Therefore, neither detection by outside sources nor interference with engine controls is considered to be a problem.

Cooling of the superconductor is a more complex issue. Calculations based on the F110 engine suggest that approximately 50 kgs of liquid Hydrogen would be needed per hour to maintain the temperature. Hydrogen was chosen for the study because of its high cooling ability and its additional use as a fuel in the gas stream after it has cooled the superconductor. Clearly, the carriage of coolant for aircraft is a additional complexity and weight penalty and it might be that, in practice, a more efficient cooling method is used. Alternative methods include using fuel to first remove the "easy" heat followed by a cryocooler to remove the remaining "more difficult" heat.

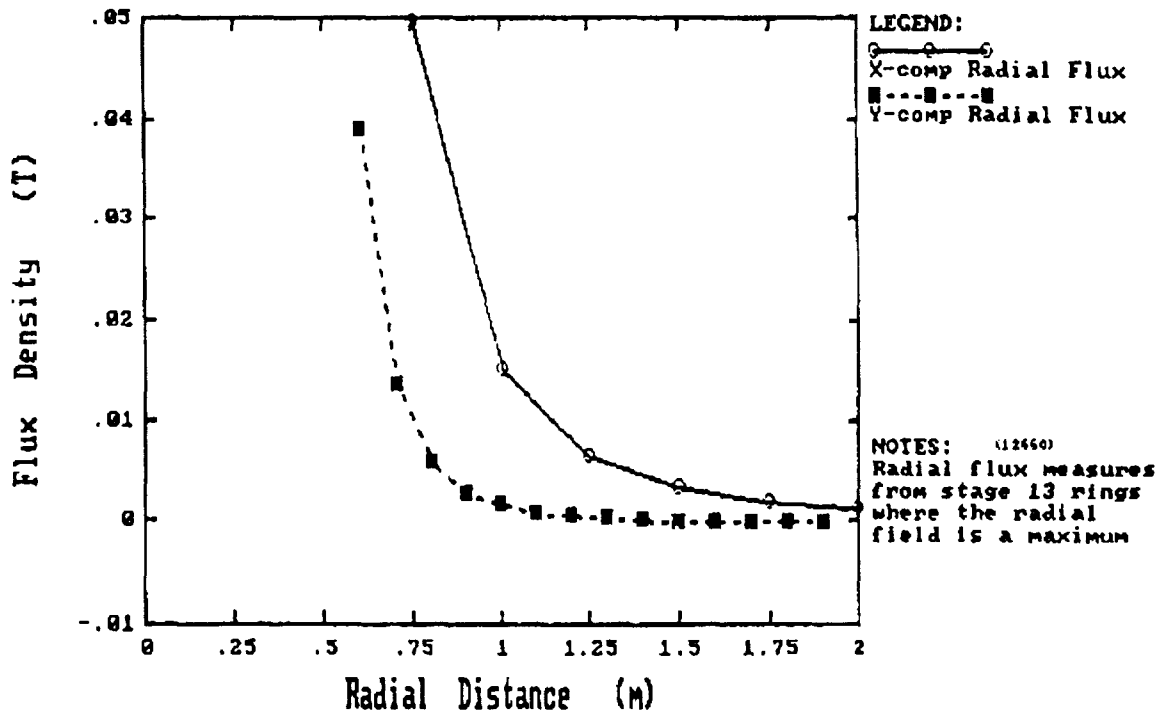


Figure 6: Magnetic Fields would be Low Outside a Gas Turbine Engine

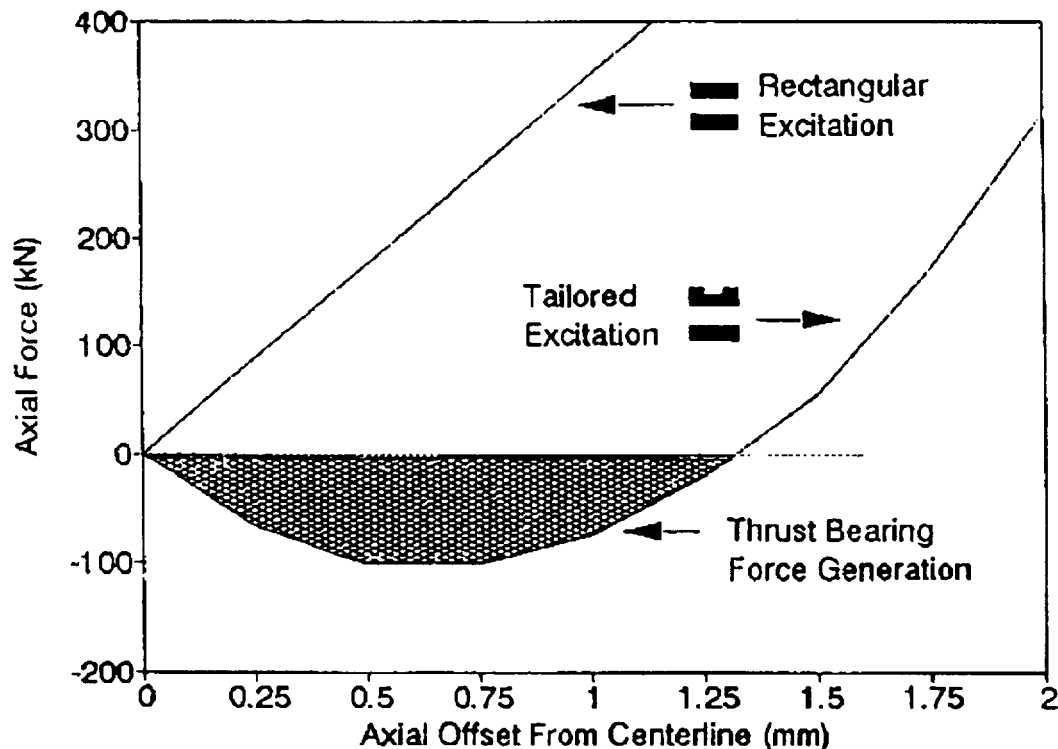


Figure 7: Shaping the Excitation Coil Creates a Magnetic Thrust Bearing

Stability is provided by the shapes of the excitation and armature conductors. Together the two conductors form a magnetic bearing. Radial stability occurs naturally as the MCR system is a radially stable magnetic bearing. Axial stability does not occur so readily but it can be achieved by concentrating excitation current on the outer edges of the excitation conductor. Figure 7 shows how shaping the excitation coil provides a specific magnetic thrust bearing capability.

TECHNOLOGY TRANSFER POTENTIAL OF MCR

While the MCR concept has been proven in laboratory tests and its merits applied theoretically to aircraft gas turbine engines, the way forward is not so clear. What is clear, however, is the relevance of the concept to other applications. For the airborne application the benefits of weight savings and system simplicity which are believed to be possible need to be assessed in more detail and quantified. An engine study, whereby an existing engine was redesigned using MCR, would be a next logical step. Additionally, the build of a mock up single stage turbine based on the schematics seen earlier would provide greater insight into the real-life workings of the concept. These initiatives could take place in parallel with other R&D efforts to improve the capabilities of compliant foil seals, superconductors, and high-strength insulation materials such as Zirconia.

The potential of MCR lends itself to a variety of commercial applications. One obvious example is civil air transport especially if the weight-saving benefits and reductions in life cycle costs were fulfilled. Similarly, industrial gas turbines could benefit significantly from the possible reductions in system size and complexity and the likely increases in operating life of the rotating components. Finally, but not so obviously, MCR could be considered as a potential replacement for conventional bearings in almost all applications. This paper has taken the first step by spreading the awareness of an innovative concept whose potential is far-reaching and wide ranging; those who will potentially benefit from the concept need to take it further.

Full Wave Analysis of Passive Microwave Monolithic Integrated Circuit Devices Using a Generalized Finite Difference Time Domain (GFDTD) Algorithm.

Faiza S. Lansing
California Institute of Technology
Jet Propulsion Laboratory
Pasadena, California

Daniel L. Rascoe
California Institute of Technology
Jet Propulsion Laboratory
Pasadena, California

ABSTRACT

This paper presents a modified Finite-Difference Time-Domain (FDTD) technique using a generalized conformed orthogonal grid. The use of the Conformed Orthogonal Grid, Finite Difference Time Domain (GFDTD) enables the designer to match all the circuit dimensions; hence eliminating a major source of error in the analysis. The method proves to be a powerful and efficient tool for modeling complicated microstrip circuits. From the time domain results, the frequency-dependent parameters of a millimeter-wave branch line coupler, a dual-stub filter, and a 3-dimensional package are computed. Accuracy verification of the model is further achieved by comparing the results with those obtained from measurements, when available, and other commercial software tools.

INTRODUCTION

Developing low-cost, compact, densely packed, and high-performance Monolithic Microwave Integrated Circuits (MMIC's) is a major technology thrust. To reduce the time and cost of the hardware iterative design cycle, and to increase the probability of first pass designs, rigorous analysis tools are needed to provide reliable predictions of the performance parameters.

Simple discontinuities, such as bends, tee- and cross-junctions, step in widths, etc., are basic components of any complex microstrip circuits [1 - 4]. To model such circuits, designers usually use the quasi-static analysis that is based on empirical low-frequency formulae. However, this quasi-static analysis does not accurately evaluate the characteristics of monolithic circuits at microwave or millimeter-wave frequencies since it does not account for radiation, coupling, fringing, and wave propagation effects. Some circuits, such as patch antennas, radial stubs, or spur filters, cannot be investigated using the quasi-static analysis because of the high radiation, and coupling effects. In such a case, more rigorous techniques, that provide an exact, or full-wave, solutions of Maxwell's equations are needed. One of the analysis tools, that is straight forward, versatile, and has acquired many new applications, is the Finite-Difference Time-Domain (FDTD), however the FDTD does not allow the designer to match all circuit dimensions. A new generalized 3-D conformed orthogonal grid, Finite Difference Time Domain (GFDTD) technique, presented in this paper, matches all circuit dimensions, and compensates for the deficiency in the FDTD technique. The GFDTD is designed to handle predominantly planar multilayered microstrip structures. Interlayer transitions such as striplines and vias can be easily simulated. The GFDTD proves to be flexible in handling a variety of complex circuit configurations.

Three sample structure are selected from a variety of test cases to demonstrate the versatility of the GFDTD technique and for the verification of the model. Three structures are modeled. A millimeter-wave branch line coupler fabricated on gallium arsenide (GaAs) substrate with $\epsilon=12.9$; a dual-stub low-pass filter fabricated on an Alumina substrate with $\epsilon=9.9$, and a 3-Dimensional package fabricated on a Alumina substrate with $\epsilon=9.9$. All the circuits represent resonant microstrip structures fabricated on an open substrate; hence, radiation and coupling effects dominate the performance significantly. The results of using the conformed orthogonal grid technique to the analysis of frequency-dependent scattering parameters and the performance of complex geometry printed microstrip circuits are presented. The GFDTD scattering parameters are further compared with the available measurements and computed results from a commercial software (nodal simulator) for the fabricated circuits.

GOVERNING EQUATIONS

The GFDTD method begins by considering the partial differential form of the two Maxwell's curl equations that govern the propagation of electric and magnetic fields in structures.

$$\mu \frac{\partial \vec{H}}{\partial t} = -\nabla \times \vec{E} \quad (1)$$

$$\epsilon \frac{\partial \vec{E}}{\partial t} = \nabla \times \vec{H} - \sigma \vec{E} \quad (2)$$

Where μ is permeability of the medium in henry/meter, ϵ is the permittivity of the medium in farad/meter, σ is conductivity of the medium in siemens/meter, E is electric field intensity in volt/meter, H is the magnetic field intensity in ampere/meter, and t is the time elapsed in seconds. To find an approximate solution to equations (1) and (2), the finite difference method is commonly used to discretize the three dimensional space and time domains and add the appropriate boundary conditions.

A. Finite-Difference Equations

In 1966, Yee [1] has developed a technique to solve the two Maxwell's curl equations. The six field components ($E_x, E_y, E_z, H_x, H_y, H_z$) are considered to be interleaved in space and are placed as shown in the elemental cell of Figure 1. The entire space domain no matter how complex it can be, is obtained by stacking these parallelepiped cells into a larger 3-D configuration. The $x, y,$ and z dimension of the elemental cell are $\Delta x, \Delta y,$ and $\Delta z,$ respectively.

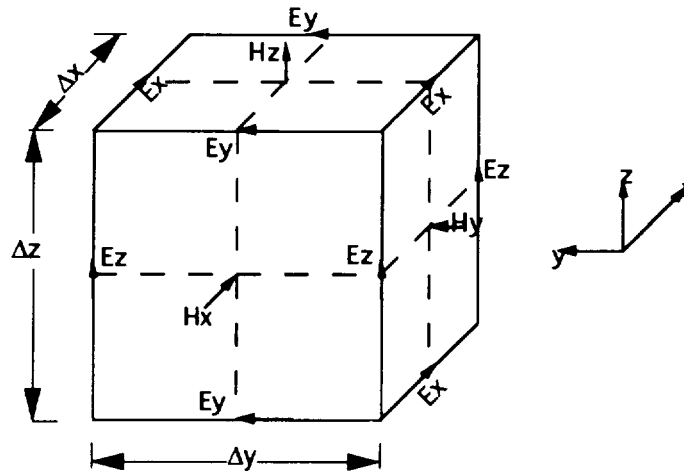


Figure 1. Field components placed in an FDTD elemental Cell (uniform grid)

Using the above arrangement notation for the E and H fields, the explicit finite difference forms of equations (1) and (2) for $E(\vec{r}, t)$ and $H(\vec{r}, t)$ are found [3].

B. Model Adaptation for Conformed Grids

The use of uniform grids, in most cases, contribute to errors [2]. To avoid such errors we adapted Yee's finite difference equations to suit conformed grids, producing the GFDTD technique, which offer a superior solution by avoiding errors resulting in mismatching the actual boundaries of the structure. As shown in Figure 2, electric field components (E white dots with black arrows, H in black dots) take new values at the boundaries between two consecutive non uniform spacing.

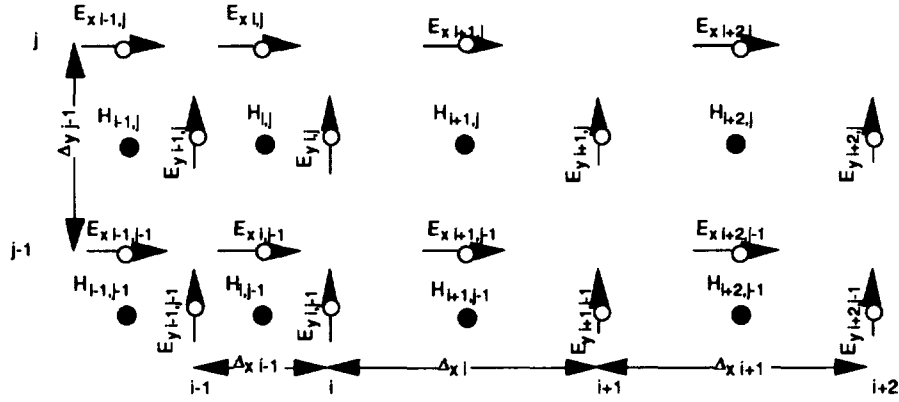


Figure 2. Field components in the x-y plane for a conformed grid

Hence, for conformed grids the finite difference equations for H_x , H_y , H_z remain unchanged while equations are:

$$H_{xi,j,k}^{n+\frac{1}{2}} = H_{xi,j,k}^{n-\frac{1}{2}} + \frac{\Delta t}{\mu\Delta z} (E_{yi,j,k}^n - E_{yi,j,k-1}^n) - \frac{\Delta t}{\mu\Delta y} (E_{zi,j,k}^n - E_{zi,j-1,k}^n) \quad (3)$$

$$H_{yi,j,k}^{n+\frac{1}{2}} = H_{yi,j,k}^{n-\frac{1}{2}} + \frac{\Delta t}{\mu\Delta x} (E_{zi,j,k}^n - E_{zi-1,j,k}^n) - \frac{\Delta t}{\mu\Delta z} (E_{xi,j,k}^n - E_{xi,j,k-1}^n) \quad (4)$$

$$H_{zi,j,k}^{n+\frac{1}{2}} = H_{zi,j,k}^{n-\frac{1}{2}} + \frac{\Delta t}{\mu\Delta y} (E_{xi,j,k}^n - E_{xi,j-1,k}^n) - \frac{\Delta t}{\mu\Delta x} (E_{yi,j,k}^n - E_{yi-1,j,k}^n) \quad (5)$$

$$E_{xi,j,k}^{n+1} = \left[\frac{1 - \frac{\sigma\Delta t}{2\epsilon}}{1 + \frac{\sigma\Delta t}{2\epsilon}} \right] E_{xi,j,k}^n + \frac{1}{1 + \frac{\sigma\Delta t}{2\epsilon}} \left\{ \frac{2\Delta t}{\epsilon(\Delta y_{j+1} + \Delta y_j)} \left[H_{xi,j+1,k}^{n+\frac{1}{2}} - H_{xi,j,k}^{n+\frac{1}{2}} \right] - \frac{2\Delta t}{\epsilon(\Delta z_{k+1} + \Delta z_k)} \left[H_{yi,j,k+1}^{n+\frac{1}{2}} - H_{yi,j,k}^{n+\frac{1}{2}} \right] \right\} \quad (6)$$

$$E_{yi,j,k}^{n+1} = \left[\frac{1 - \frac{\sigma\Delta t}{2\epsilon}}{1 + \frac{\sigma\Delta t}{2\epsilon}} \right] E_{yi,j,k}^n + \frac{1}{1 + \frac{\sigma\Delta t}{2\epsilon}} \left\{ \frac{2\Delta t}{\epsilon(\Delta z_{k+1} + \Delta z_k)} \left[H_{xi,j+1,k}^{n+\frac{1}{2}} - H_{xi,j,k}^{n+\frac{1}{2}} \right] - \frac{2\Delta t}{\epsilon(\Delta x_{i+1} + \Delta x_i)} \left[H_{zi+1,j,k}^{n+\frac{1}{2}} - H_{zi,j,k}^{n+\frac{1}{2}} \right] \right\} \quad (7)$$

$$E_{zi,j,k}^{n+1} = \left[\frac{1 - \frac{\sigma\Delta t}{2\epsilon}}{1 + \frac{\sigma\Delta t}{2\epsilon}} \right] E_{zi,j,k}^n + \frac{1}{1 + \frac{\sigma\Delta t}{2\epsilon}} \left\{ \frac{2\Delta t}{\epsilon(\Delta x_{i+1} + \Delta x_i)} \left[H_{yi+1,j,k}^{n+\frac{1}{2}} - H_{yi,j,k}^{n+\frac{1}{2}} \right] - \frac{2\Delta t}{\epsilon(\Delta y_{j+1} + \Delta y_j)} \left[H_{xi,j+1,k}^{n+\frac{1}{2}} - H_{xi,j,k}^{n+\frac{1}{2}} \right] \right\} \quad (8)$$

The GFDTD forward difference approximation is used to calculate the spatial partial derivatives instead of the centered difference used in equations [1-4]. The forward difference technique is first-order accurate, which may cause slight errors, when integrating for a large number of time steps. With this fact in mind, the GFDTD is only applied to determine the E fields at the boundaries of two consecutive layers of different spatial size, while Yee's equations [1] are used to compute the E fields within each layer. Also, the reader should be aware that the changes in spatial increment between layers is restricted to $\pm 30\%$. Better accuracy can be achieved if an interpolation technique is used, such as a spline to determine the spatial partial derivative of the magnetic field exactly at the interface between the two different layers.

C. Selection of size of Time Step

For the conformed grid, the size of the time step is based on modifying the stability criteria [2] to take into consideration the changing spatial steps. For l number of Δx 's, m number of Δy 's, and n number of Δz 's, the size of time step in a conformed grid computation, is determined from:

$$\Delta t \leq \min \left[\frac{1}{v_{\max}} \left(\frac{1}{\Delta x_i^2} + \frac{1}{\Delta y_j^2} + \frac{1}{\Delta z_k^2} \right)^{-\frac{1}{2}} \right] \quad (9)$$

Where $i=1, 2, \dots, l$; $j=1, 2, \dots, m$; $k=1, 2, \dots, n$ and Δt is chosen as the minimum of the permutation generated by varying i, j, k .

Equations (3) through (9) give an approximate solution of $E(\vec{r}, t)$ and $H(\vec{r}, t)$ in the computational domain (or grid). Special considerations are required, however, for the source and the mesh walls, as discussed in section D.

D. Treatment of the Source and Absorbing Boundary Conditions

1. Source Considerations

A Gaussian-shaped pulse is chosen as the source excitation at time $t=0$. This choice is advantageous because its frequency spectrum is also Gaussian. By adjusting the width of the pulse, the spectrum provides frequency-domain information ranging from dc to the desired cutoff frequency.

$$E_x = f_x(t) = e^{-\frac{(t-t_0)^2}{\tau^2}} \quad (10)$$

The Gaussian-shaped pulse excitation will result in the fundamental mode propagating down the microstrip in the frequency range of interest.

2. Absorbing Boundary Conditions

One of the six mesh boundaries is a ground plane and its tangential electric field values are set to be zero everywhere on the plane. The tangential electric field components on the remaining five mesh boundaries must be specified such that outgoing waves are not reflected, i.e., absorbed. Mur's [5] second-order approximate absorbing boundary condition is used to enforce the above non-reflection constraints, as shown below:

$$\begin{aligned} \Phi_0^{n+1} = & -\Phi_1^{n-1}(i, k) + \frac{c\Delta t - \Delta y}{c\Delta t + \Delta y} + \frac{2\Delta y}{c\Delta t + \Delta y} \left[\Phi_0^n(i, k) + \Phi_1^n(i, k) \right] \\ & + \frac{(c\Delta t)^2 \Delta y}{2\Delta x^2 (c\Delta t + \Delta y)} \left[\Phi_0^n(i+1, k) - \Phi_0^n(i, k) + \Phi_0^n(i-1, k) + \Phi_1^n(i+1, k) - \Phi_1^n(i, k) + \Phi_1^n(i-1, k) \right] \\ & + \frac{(c\Delta t)^2 \Delta y}{2\Delta z^2 (c\Delta t + \Delta y)} \left[\Phi_0^n(i, k+1) - \Phi_0^n(i, k) + \Phi_0^n(i, k-1) + \Phi_1^n(i, k+1) - \Phi_1^n(i, k) + \Phi_1^n(i, k-1) \right] \end{aligned} \quad (11)$$

Where c is the speed of light in vacuum, Φ is the desired parameter to be absorbed at the boundaries. Note that this expression is valid only for the x - z plane. Similar expressions can be derived for x - y and y - z planes.

E. Calculation of Frequency-Dependent Parameters

In addition to the time domain results (E, H , voltages, and currents), obtained by the GFDTD method, the frequency-dependent scattering parameters, characteristic impedance, and effective dielectric constant, which augment the analysis are calculated.

The scattering parameters provide a measure for the circuit performance. To calculate scattering parameters, the total vertical electric field underneath the center of each microstrip port is recorded at every time step and integrated along the z -direction as shown in figure 3-a. To obtain the scattering parameter $S_{11}(\omega)$, the incident and reflected voltage must be determined by calculating the incident and reflected voltages at the input port (port 1). The incident voltage, V_{1inc} is determined by assuming an infinite microstrip line, which extends from

source to the far absorbing wall. The same process is repeated using the actual microstrip structure, yielding the total voltage, V_{1t} at the input port. The reflected voltage, V_{1ref} is determined by subtracting the incident voltage from the total voltage at the input port. At the other ports only transient waveforms will be computed. The scattering parameters, S_{11} , S_{21} , and S_{12} are then obtained by simple Fourier transform of the voltages. The current $I(t)$ is computed at the port by integrating the magnetic field over the contour C as shown in Figure 3-b.

The characteristic impedance, $Z_0(\omega)$ of a microstrip line is defined at the fundamental mode of propagation, as the ratio of the voltage to the current in the frequency domain.

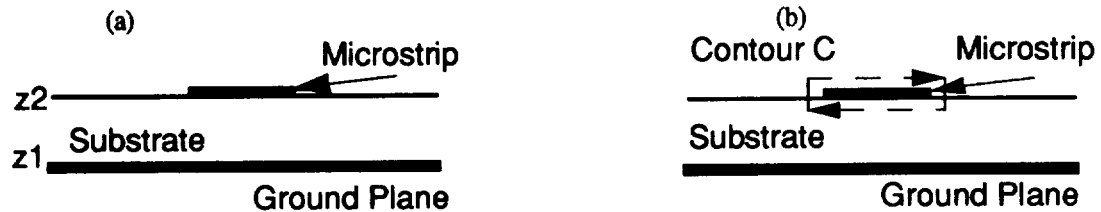


Figure 3 Configuration for computing the total voltage and current at the ports

RESULTS

The three structures used in testing the GFDTD model with conformed grid are as follows: a branch line coupler; a dual stub filter; and a 3-dimensional package. The first circuit is fabricated on gallium arsenide (GaAs) substrate with $\epsilon = 12.9$ and a thickness of $100 \mu\text{m}$. The dual stub filter is constructed on Alumina substrate with $\epsilon = 9.9$ and a thickness of 0.005 inch (0.127 mm), and a 3-dimensional package fabricated on an Alumina substrate with $\epsilon = 9.9$ and a thickness of 0.3 millimeters . The three circuits have dimensions of less than 1 cm , and the frequency range of interest is from dc to 50 GHz . Although the operating frequency of all circuits is less than 50 GHz ; the GFDTD is able to provide an insight to the performance of these circuits outside the operating range. Scattering matrix coefficients are measured for the dual stub filter, the using an HP 8510 network analyzer, which is calibrated between 2 to 45 GHz . Measurements for the millimeter-wave branch line coupler and the 3-D package are not available.

A. Millimeter-wave Branch Line Coupler

The selected branch line coupler, is shown in Figure 4, divides power equally between ports 2 and 4 from either ports 1 or 3. This occurs at the center frequency, where the center-to-center distance between the four lines is a quarter wavelength ($\lambda/4$). Also, at the center frequency, the phase difference between ports 2 and 4 is 90° . The total number of grid points is $49 \times 100 \times 16$. The thickness of the substrate is modeled as $3 \Delta z$, while the air space above is modeled as $13 \Delta z$.

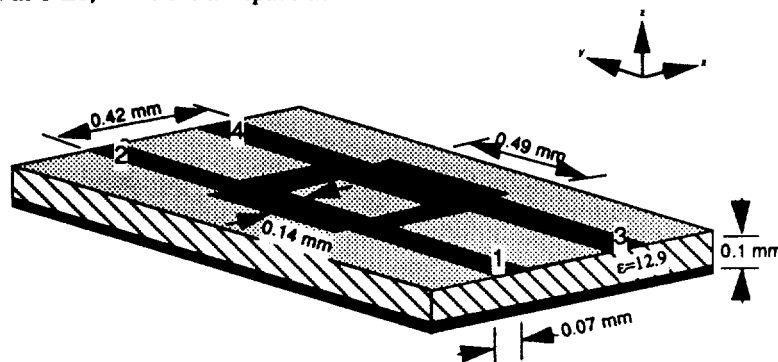


Figure 4. Millimeter-wave branch line coupler detail.

The center to center distance are $14 \Delta x$ and $14 \Delta y$. The distance from the source plane to the edge of the coupler is $40 \Delta y$, and the reference planes for ports 1 through 4 are $10 \Delta y$ from the edges of the coupler. The strip widths of ports 1 through 4 are modeled as $2 \Delta x$. The wide strips in the coupler are modeled as $4 \Delta x$ wide.

The time step Δt is 0.05 ps. The Gaussian half-width, T is 5 ps and the time delay, t_0 , is set to $3T$. The simulation is performed for 4000 time steps to allow the response on all four ports to reach zero. The computation time using the CRAY Y-MP2E/116 is less than 2 minutes for the conformed grid.

The scattering coefficient results, are shown in Figure 5. The desired branch line coupler performance is witnessed in the sharp S_{11} and S_{13} nulls which occur at approximately the same point (49 GHz) as the crossover in S_{12} , and S_{14} . At this crossover point S_{12} and S_{14} are both about -3 dB, indicating that the power is being evenly divided between ports 2 and 4. The nulls in S_{11} and S_{13} at the operating frequency indicate that little power is being transmitted by ports 2 and 4. The phase difference between S_{12} and S_{14} , is verified to be approximately 90° at the operating point (≈ 49 GHz). This behavior is also predicted by Compact Explorer software.

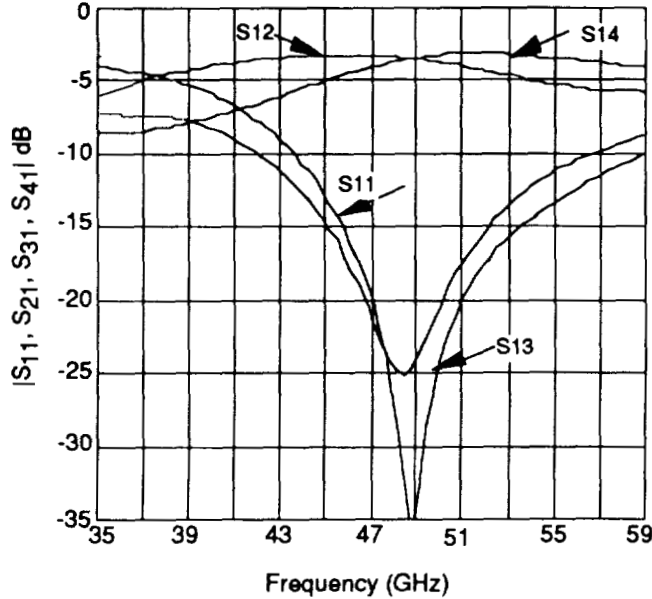


Figure 5 Scattering parameters for the millimeter-wave branch line coupler

B. Microstrip Dual-Stub filter

The dual stub filter analyzed is based on the design used by Texas Instrument and the University of Colorado, MIMICAD Center [6]. The dimensions are shown in Figure 6. The total number of grid points representing this filter is $120 \times 68 \times 16$. The operating resonance (≈ 10 GHz) corresponds to the frequency where $L = \lambda/4$, and $S = \lambda/16$ and the distance between the center of each stub and the ports is $\lambda/32$. For the GFDTD, $2 \Delta x$, $2 \Delta y$, and one Δz are carefully chosen to fit the dimensions of the circuit. The long rectangular patch is thus $2 \Delta x$'s by $68 \Delta y$'s. Each stub is modeled as $46 \Delta x$ by $2 \Delta y$. The thickness of the substrate is selected as $2 \Delta z$, the remaining $14 \Delta z$ represent the air space above the substrate.

$L = 2.921$ mm
 $S = 0.75692$ mm
 $\alpha = 0.44196$ mm

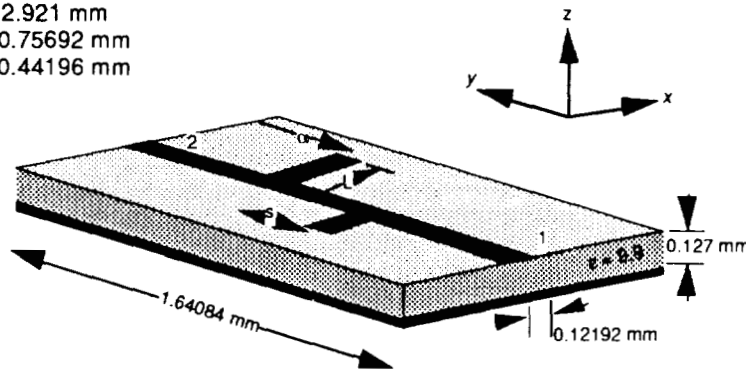


Figure 6 Double-stub filter detail

The time step, Δt used is 0.117 ps. The Gaussian half-width is $T = 10$ ps and the time delay t_0 is set to be $3T$. The simulation is performed for 15000 time steps to allow the response at both ports to become 0. Due to the circuit higher dielectric constant, the phase speed is lower and more samples, i.e., time steps, are needed to fully simulate the behavior of the circuit. The computation time for this circuit is approximately 18 minutes on the CRAY Y-MP2E/116 compared to 2 hours per each frequency for an HP workstation [6].

The resulting scattering coefficient $|S_{21}|$ is plotted in Figure 7-a for GFDTD, superimposed on the measured data. Good agreement is evident at the location of the response nulls. The desired low-pass filter performance is witnessed by the steep S_{21} roll-off beginning at approximately 8 GHz. The narrowing in the stopband determined from the GFDTD model, may be due to the approximation of using the forward difference technique for the conformed grid. In comparing the scattering parameters determined from measurements with the results determined from the nodal simulator, shown in figure 7-b it is obvious that the nodal simulator, lacks the capability to predict the performance of this filter. Additionally the nodal simulator is unable to predict the dual response nulls as expected from having dual stubs but is predicts correctly the location of one resonating frequency qualitatively and overestimates the depth of the response nulls.

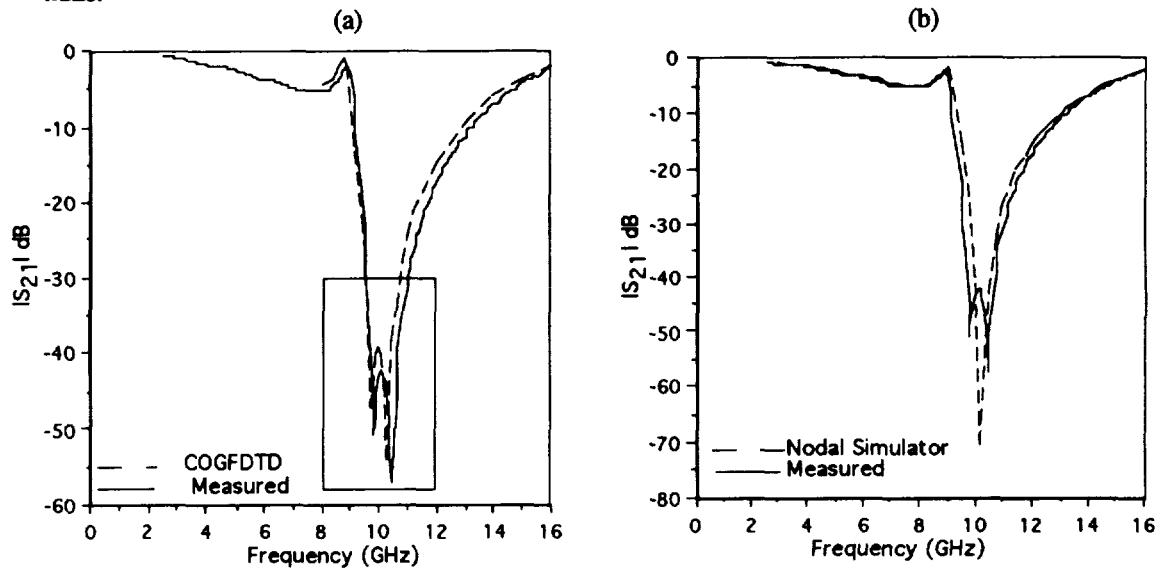


Figure 7 Insertion loss of a dual stub filter

C. 3-Dimensional Package

The 3-Dimensional Package is designed and fabricated on an Alumina substrate with $\epsilon = 9.9$. The 3-D package dimensions are shown in Figure 8. The space steps Δx , Δy , and Δz are chosen to match all circuit dimensions. This circuit is the most complicated, in all the cases treated in this paper, because it has multilayers. The total physical dimension of this package is 9 mm x 4.02 mm x 3 mm, which transferred 67x150x61 grid points. The thickness of the substrate is modeled as $10 \Delta z$ while the air spaces above and below the substrate are modeled as $25 \Delta z$ each.

The design procedure presented in [7] have been followed carefully for this circuit to yield the desired performance parameters.

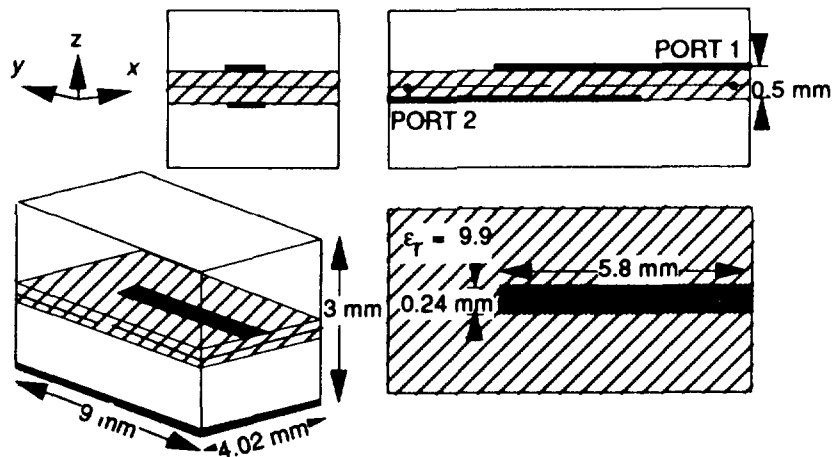


Figure 8. Detail of 3-Dimensional Package

The time step Δt is 0.1 ps. The Gaussian half-width, T is 15 ps and the time delay, t_0 , is set to $3T$. The simulation is performed for the GFDTD for 3000 time steps to allow the response on the two ports to reach zero. The computation time using the CRAY Y-MP2E/116, is less than 10 CPU minutes

The frequency response presented in figure 9, demonstrates the utility of this structure as an interconnect. The desired frequency response, i.e., center frequency, bandwidth, and shape is obtained by the proper selection of geometry. As shown in figure 9, the insertion loss at the center frequency is less than 0.2 dB and a very wide bandwidth is achievable, which makes this design versatile specially at higher frequencies.

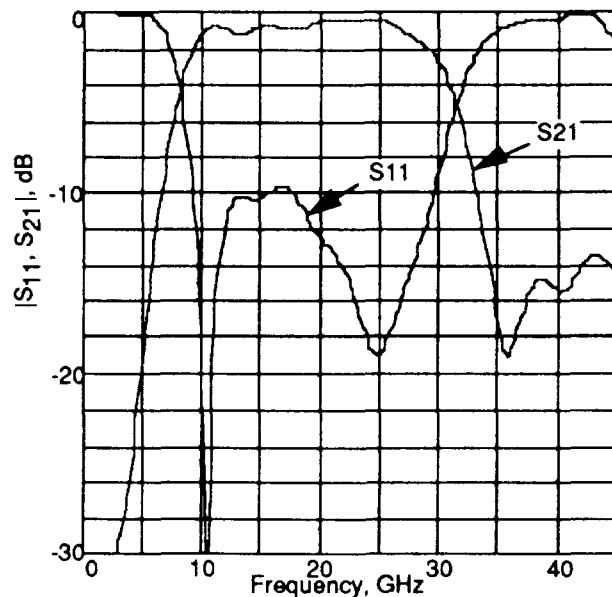


Figure 9. Scattering parameters for the 3-Dimensional Package

CONCLUSIONS

For the conformed orthogonal grid, the Generalized finite-difference time-domain method, GFDTD, has been used to perform time-domain simulations of pulse propagation in three printed microstrip circuits. Frequency-dependent scattering parameters, and characteristic impedance, have been calculated by Fourier transform of the time-domain results. The results are validated either by comparison with the results obtained from measured data taken from fabricated circuits, or results obtained from the nodal simulator. The versatility of the GFDTD method allows easy and accurate calculation of many complicated microstrip structures. It should be noted that simpler models, such as nodal simulator, are still highly useful for "first cut designs" of microstrip circuits since they allow

for quick solution and, in some cases, allow for intuition about devices being modeled. The GFDTD method can then be applied to determine the performance of the actual circuit more accurately.

The versatility of the GFDTD method allows for matching all circuit dimensions and for direct calculation of performance parameters for many complicated microstrip structures. The structures analyzed in this paper were selected so that comparisons could be made with other publications or measurements or methods of analysis. With the computational power of supercomputers increasing rapidly, such as the CRAY Y-MP2E/116, time savings in the order of 200 to 1 is achieved compared to the VAX workstation. The fast, accurate, GFDTD now lends itself as a computer aided design of many complex geometries of microstrip circuit components.

A video tape that visualizes the electric and magnetic fields as they evolve in time was produced.

ACKNOWLEDGMENT

This research was carried out in part by the Jet Propulsion Laboratory, California Institute of Technology, under a grant with the National Aeronautics and Space Administration. This research was also performed in part using the Jet Propulsion Laboratory/California Institute of technology CRAY Y-MP2E/116 Supercomputer. Access to this facility was provided by the Jet propulsion Laboratory Supercomputing project.

REFERENCES

- [1] K. S. Yee, "Numerical solution of initial boundary value problems in isotropic media," *IEEE Transactions on Antennas and Propagation*, vol. AP-14, pp. 302-307, May 1966.
- [2] D. Sheen, S. Ali, M. Abouzahra and J. A. Kong, "Application of the three-dimensional finite-difference time-domain method to the analysis of planar microstrip circuits," *IEEE Transactions on Microwave Theory and Techniques*, vol. 38, pp. 849-856, July 1990.
- [3] X. Zhang, J. Fang, K. Mei and Y. Lui, "Calculations of the dispersive characteristics of microstrips by the time-domain finite difference method," *IEEE Transactions on Microwave Theory and Techniques*, vol. 36, pp. 263-267, July 1988.
- [4] X. Zhang and K. Mei, "Time-domain finite difference approach to the calculation of the frequency-dependent characteristics of microstrip discontinuities," *IEEE Transactions on Microwave Theory and Techniques*, vol. 36, pp. 1775-1787, July 1988.
- [5] D. M. Sheen, "Numerical Modeling of Microstrip Circuits and Antennas". Ph.D. dissertation, Massachusetts Institute of Technology, June 1991.
- [6] Private communication with Dr. Doris Wu, MMICAD Center, University of Colorado, Boulder, Mars 1992.
- [7] Vandenberg, N. L., "Full-Wave Analysis of Microstrip-Fed Antennas and Couplers", Ph.D. dissertation, The University of Michigan, 1991.

A FUTURE, INTENSE SOURCE OF NEGATIVE HYDROGEN IONS

Hugh Siefken
 Greenville College Department of Physics
 Greenville, IL, 62246

545-72

Charles Stein
 Phillips Laboratory, Kirtland Air Force Base
 Albuquerque, NM 87117

2481

p. 10

ABSTRACT

By directly heating lithium hydride in a vacuum, up to $18 \mu\text{A}/\text{cm}^2$ of negative hydrogen has been obtained from the crystal lattice. The amount of ion current extracted and analyzed is closely related to the temperature of the sample and to the rate at which the temperature is changed. The ion current appears to be emission limited and saturates with extraction voltage. For a fixed extraction voltage, the ion current could be maximized by placing a grid between the sample surface and the extraction electrode. Electrons accompanying the negative ions were removed by a magnetic trap. A Wein velocity filter was designed and built to provide definitive mass analysis of the extracted ion species. This technique when applied to other alkali hydrides may produce even higher intensity beams possessing low values of emittance.

INTRODUCTION

As our high level of technology continues into the future, the basic assumption made by everyone is that sufficient electrical energy will be available. The method of producing the energy is the uncertain factor. The procedures¹ used to initially estimate future fossil fuel supplies have been remarkably accurate especially when applied to national resources of oil and natural gas. The use of coal has seen increased growth during the past decade but at a price. This is because the total cost of burning coal for the long term includes the damaging effects of the effluents on materials and the possible effects of loading the atmosphere with CO_2 .

An alternative is the process of nuclear fusion. This is a process which requires a machine to hold the reactants together long enough, and close enough, for the fusion of two nuclei into a product nucleus. One such machine is the TFTR at Princeton. The reactants are held within a strong magnetic field away from the vacuum chamber walls so losses are minimized. To supply the heat energy for the plasma at the place where it is needed, fast neutral atoms are used to penetrate the magnetic field which surrounds the reaction volume. In the TFTR positive ions are generated and then neutralized. However for the next

generation of Tokamak machines, planning is centered on the use of negative ions which can be more efficiently neutralized than the fast moving positive ion. Consequently, high current and high energy negative hydrogen (deuterium) ion beams are considered one of the best ways to achieve plasma heating and to provide for plasma diagnostics in these future machines^{2,3}. The negative ion can be accelerated to the desired energy (150 - 500 keV) and passed through a gas which removes the weakly bound ($\sim .75$ eV) electron resulting with neutral hydrogen which can penetrate the magnetic field used for confinement.

During the last decade, the development of ion sources has seen remarkable progress. Surface ionization, sputtering, and volume ion sources have each been developed so that the merits and drawbacks of each type are generally known. In some cases the precise physical mechanism for the ion production is not totally clear but enough is known in each of these cases to make a viable ion source for the respective application.

Figure 1 shows a schematic of a volume H^- ion source which has been developed at Lawrence Berkeley Laboratory⁴. It is representative of a larger group of H^- ion sources of this type produced in several laboratories. This ion source is attractive because it produces H^- at a low ion temperature ($\sim .3$ eV) which results in lower beam emittance than some other types. However, the tungsten or LaB_6 filaments have a finite lifetime that eventually terminate due to erosion or fatigue. Also an arrangement of strong permanent magnets must be used to confine the plasma which is needed for the eventual production of the H^- .

A variation of this is to replace the filament with an R-F discharge antenna. This produces the plasma effectively but typically a 50 kW power supply with a 2 MHz oscillator is required to produce the ions.

Various geometrical arrangements and operating conditions have increased the current obtainable from these sources, but they all require the production of a dense plasma with which is associated corresponding difficulties in maintaining the critical conditions required for optimum performance, especially in the pulsed, high arc current mode of operation.

In contrast to these present day H^- sources I now would like to present some of the initial work done at the Phillips Laboratory in which H^- was produced by a more elementary method. This method involves the formation of H^- ions simply by heating a compound, LiH , which is an alkali metal hydride. There are two important factors which converge to make this class of compounds the basis for a possible intense H^- (D^-) source.

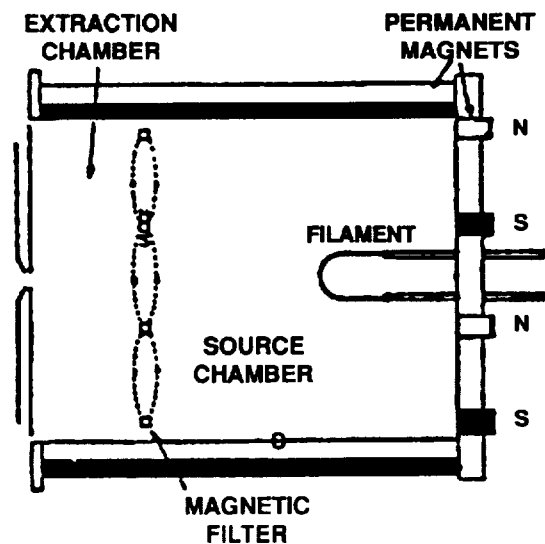


Figure 1. Schematic of LBL multicusp volume source. From Ref [4].

First, they store large volumes of hydrogen. It is been known for some time that metal hydrides permit the storage of hydrogen more efficiently with respect to volume than even liquid or solid hydrogen. Table 1 indicates some relative storage capacities of hydrogen.

Table 1. HYDROGEN DENSITIES IN SOME HYDROGEN-CONTAINING COMPOUNDS. FROM REFERENCE [5]

Compound	Number of Hydrogen Atoms per cm ³ X 10 ⁻²²
Liquid hydrogen (20°K)	4.2
Solid hydrogen (4.2°K)	5.3
LiH	5.9
TiH ₂	9.2
ZrH ₂	7.3
YH ₂	5.7
UH ₃	8.2

Formation of the hydride occurs when a given amount of hydrogen gas at a fixed temperature is brought into contact with the alkali metal. Some of the hydrogen is absorbed by the metal until a pressure equilibrium is reached at which time the hydrogen pressure becomes fixed. If more hydrogen is added, more is taken up by the metal until a new equilibrium pressure is reached. Thus for a given temperature an equilibrium pressure of hydrogen is reached. To reverse the hydrogen storage process the solid hydride is heated. As the temperature is increased higher equilibrium pressures of hydrogen are released. For LiH at 700° the equilibrium pressure is 28 mm.⁶

The second factor which makes this class of compounds feasible as a future source of negative ions is the strong ionic bonding between the constituent atoms. As hydrogen is taken into the metal, the metal lattice spacing decreases due to the strong attraction between the metal cation and hydrogen anion. The density of the hydride is thus much larger than the metal. The relatively large crystal lattice energies, defined as $MH-M^+ + H^-$, vary from 9.5 eV for LiH to 6.7 eV for CsH. Various experiments using LiH confirms the presence of a bond which is strongly ionic. Calder⁷ et al., using x-ray measurements, estimated the nature of the LiH bond to be between 80% and 100% ionic. Using electronegativity methods, Pretzel et al.⁸ estimated the LiH bond to be 87.5% ionic. Additional support is given to this ionic bond model by the fact that when molten LiH is electrolyzed, hydrogen appears at the positive electrode⁶ and the observation by Palmer⁹ of the breaking of LiH into H⁻ when impacted on heated tungsten.

EXPERIMENTAL SET-UP AND RESULTS

Due to the relative ease of handling compared to some of the other alkali metal hydrides we chose to use LiH. The experimental arrangement used to measure the electron and ion currents as the temperature of the LiH was changed is shown in Figure 2.

A small piece of solid LiH, mass ~ 0.4 g, was removed from a large block stored in a tight drum, crushed, put in the sample container of the apparatus, and immediately loaded into the vacuum system. Any small amount of water vapor absorbed from the low humidity of the environment or remaining from the manufacturing process was found to be released in the vacuum system several minutes prior to the production of H^- . A residual gas analyzer was used to monitor the presence of water vapor and other gases present in the vacuum system during each run as the temperature of the sample was increased. The crushed LiH was held in a stainless-steel container which also contained an iron-constantan thermocouple and tungsten heater. The heater and thermocouple were floated at the same (acceleration) potential as the sample holder. Electron and ion currents were measured with respect to ground potential.

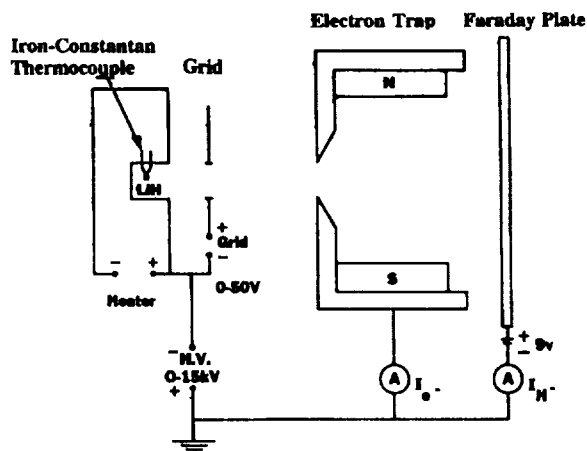


Figure 2. Experimental circuit used to measure electron and ion currents.

To separate the electrons from the negative ions an electron trap with a magnetic rigidity $\int Bdl = 3000$ G cm and average field of 600 G was used. A Faraday plate made of carbon to minimize the production of secondary electrons was used to collect the ions. A small positive bias voltage of 9 V on the plate made approximately an 8% effect on the magnitude of the H^- current by forcing secondaries back to the carbon plate.

Three different heater geometries were used. A flat heater, a helical coil, and a boat-shaped heater were each used to heat the sample. The results of heating a larger volume with a boat and helical coil did produce more stable currents but did not produce larger currents than the flat heater.

Hydrogen was removed from the sample by heating the sample over a range of temperatures up to 800°C . At a given temperature the hydrogen is removed from the sample at an equilibrium pressure in a reverse process by which the LiH was formed. Consequently, by increasing the temperature of the LiH sample, a higher equilibrium pressure is reached until the sample becomes depleted at that temperature and the pressure decreases. The sample decomposed very quickly above 688°C , the melting point of the two phase equilibrium pressure system, so for periods of extended data collection, the temperature was kept well below the melting temperature.

From the experimental results it becomes clear that the ion current collected depends not only on the temperature of the sample but also on the rate at which the temperature is changed. Figure 3 shows a typical DC ion current response to a rapid change in temperature. The current response to the rise in temperature is practically instantaneous.

For example, when the temperature of the LiH was changed by 56°C from a temperature of 587°C to a temperature of 643°C in ~ 60 s, an increase in H⁻ current of 17 μA was measured. The ratio of ion to electron currents, I_{H^-}/I_{e^-} , usually varied between 1/10 and 1/4 but occasionally would reach 1/100 when the rate of change of the temperature became small or static resulting in small amounts of H⁻ being produced. A static temperature usually produced an H⁻ current with a slow decay, most likely due to the depletion of the hydrogen from the sample. A test of the effectiveness of the electron trap was made with an empty sample holder using a red hot filament. No accelerated electrons were passed through the trap to the Faraday plate. The 1.2-cm-diam aperture at the entrance of the electron trap also served as the extractor electrode. The extractor was operated either as an open aperture or with a high transparency mesh across the opening. The maximum DC ion current density measured was 18 μA/cm². This result occurred during a moderate, positive rate of temperature change of about 1 °C/s.

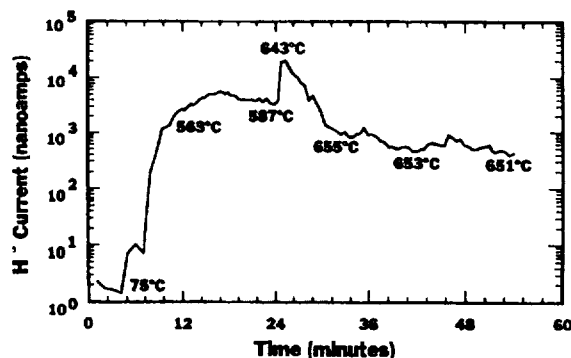


Figure 3. H⁻ current on Faraday plate vs time.

The results of placing an intermediate electrode between the sample and the anode (extractor) showed that it strongly affected the electron and ion currents. When a fine mesh was used as the intermediate electrode, a potential of ~ + 4 V with respect to the sample was used to maximize the H⁻ current. When no mesh was present on the aperture of the extractor electrode, ~ + 10 V was required on the intermediate grid electrode to maximize the electron and ion currents. When a negative potential with respect to the sample was placed on the grid or extractor electrodes, both the electron and H⁻ could be quenched. The variation of H⁻ current with extraction potential showed that the current saturated usually around 4 kV. For most of the work described here, a potential of 6 kV was used to ensure the measured currents were the maximum available.

As the temperature of the sample increased, the pressure in the vacuum system increased accordingly. In addition to H⁻ and electrons being emitted, hydrogen gas is released so the vacuum system must remove this unwanted gas load. Starting at a base pressure of 3 x 10⁻⁶ Torr, the pressure typically rose to 8 x 10⁻⁶ Torr during the run. Knowing the pumping speed of the vacuum pump and the conductance of the system, a gas load of approximately 4 x 10⁻² Torr ℓ/s = 3 scc/m was estimated to be produced.

MASS ANALYSIS

To conclusively determine the masses of the possible ion species coming off the hydride sample, a Wien filter was constructed following the approach of Selinger¹⁰. Under a balanced condition, a specific ion velocity will pass straight through the analyzer with the electric field force counterbalancing the Lorentz force. Since all ions are accelerated through the same potential difference, V_0 , the velocity of a given ion will depend directly on its mass. Figure 4 shows a schematic drawing of the filter. Those ions with velocity v_0 pass through the filter and a 3 mm aperture, en route to a cylindrical Faraday cup 7 cm in length. Those ions which do not possess the proper velocity are deflected as shown by the dashed line.

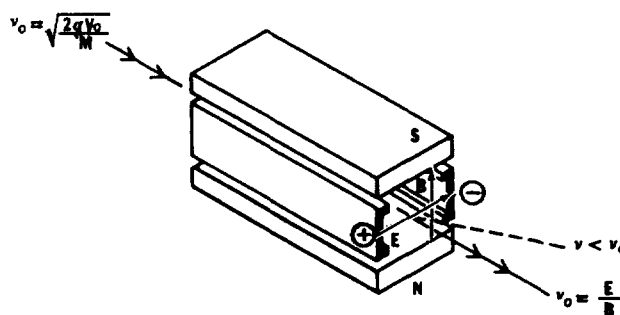


Figure 4. Schematic drawing of the velocity filter.

Two aluminum plates separated by 2.5 cm and machined with edge shims to reduce the fringing field were used as the electric field plates, marked + and - in Figure 4. The uniform magnetic field was provided by permanent ceramic magnets in a steel yoke with soft iron pole faces.

The magnetic field was mapped on four parallel axes within 1 cm of the principal axis. Figure 5 shows the strength and uniformity of the resulting field. At each end a copper plate with two sheets of mu-metal was used to terminate the E and B fields. It was found that the addition of a copper cylinder lined with mu-metal greatly reduced the B field at each end. The effective magnetic length of the mass filter was taken to be $L_m = 12$ cm. Upon exiting the filter, the ions drifted 9 cm to the aperture at the entrance of the Faraday cup. The overall resolution of the apparatus was calculated to be 10% ($\Delta m/m = 0.1$).

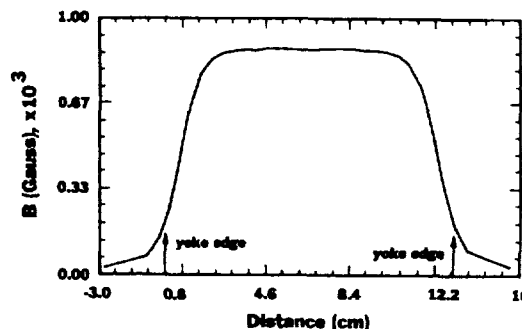


Figure 5. Mapping of magnetic field along $E \times B$ axis.

The optics used to form a beam prior to entering the mass analyzer were designed using a cylindrical Pierce geometry¹¹. This design is intended to give the ions parallel flow between the cathode and anode. Following the anode, the optics produced an ion beam with a focal length of $f = -3$ cm. The lithium hydride sample of was heated in the container below the Pierce electrode. The anode surface was formed from copper with a radius of 2.5 cm. For an aperture of $r_0 = 2$ mm, the half angle divergence of the beam is 3.8° . The entire anode-cathode assembly is housed in a steel yoke so that small Nd Fe magnets could be used to remove electrons generated in the emission

process if desired. The mapping of the magnetic field in this region produced a value of $\int Bdl = 450 \text{ G cm}$. with an average value of $B = 340 \text{ G}$ which is sufficient to remove 6 keV electrons. Due to the small temperature gradient applied to the sample during the mass analysis, small ion currents were produced, so an einzel lens was constructed to increase the intensity of the ions prior to entering the mass analyzer. This reduced the drift distance following the analyzer to 5 cm but did not significantly affect the resolution of the apparatus.

A series of potential difference readings across the electric field plates in the analyzer were made at each of four accelerating voltages, V_0 . Each series of potential differences placed across the analyzer plates required so much time to complete that the rate of temperature change of the sample had to be kept at a small value to keep the sample from releasing the stored hydrogen too quickly. Consequently, the amount of H^- produced at the source, as analyzed by the Wein filter and passed through the 3-mm-diam aperture to the Faraday cup, was small for the mass analysis measurements. As noted earlier, a positive rate of temperature change is required to produce a significant ion current. Therefore, it is not surprising that under the conditions of nearly static temperatures, the amount of collected ion current would be much reduced from the earlier experiments where larger rates of temperature change were maintained. A typical voltage sweep is shown in Figure 6.

Because the power supply providing the accelerating voltage was not regulated and tended to slowly drift, a slightly larger FWHM was produced on the peak than expected. When using the Wein filter for the mass analysis no electron trap was required since the electron experiences a much larger magnetic force compared to the ions and hence is promptly removed upon entering the crossed fields of the analyzer. The power supplies which provided the voltages for the crossed field analyzer handled the increased electron current loading without a significant drop in potential. Using the condition for the balance of forces in the analyzer and conservation of energy gives

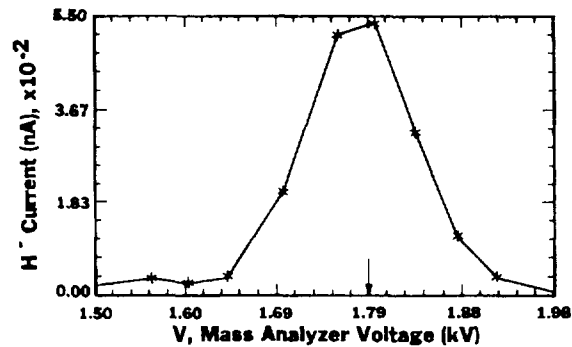


Figure 6. H^- current collected by Faraday cup as electric field is changed in E X B analyzer. Voltage uncertainties are $\pm 50 \text{ V}$.

$$V^2 = 2B^2 d^2 \frac{q}{m} V_0 \quad (1)$$

where V is the potential difference across the E -field plates, V_0 the accelerating potential of ion beam, B the magnetic field in analyzer, d the separation of E -field plates (2.54 cm), q/m the ionic charge to mass ratio, and where $2B^2 d^2 = 9.99 \times 10^{-6} \text{ T}^2 \text{m}^2$.

A plot of V^2 vs V_0 in Figure 7 shows the slope of the experimental data is best matched by ions with a charge to mass ratio, corresponding to H^- . This plot is produced from the analyzer peak voltages which result from the four voltage sweeps made on the Wein analyzer. The peak voltage was estimated as a centroid in the plane of each curve. A more accurate least square fitting of each sweep could generate a slightly different peak voltage but that would not alter the clear match to the data by ions with $M = 1$. The possibility of negative ions with mass $M = 2$ being produced and passed through the Wein analyzer would require a charge of $q = -2$ in order to maintain the same charge to mass ratio in Eq. (1). As part of the series of voltage sweeps on the analyzer, the possible presence of a $M = 2$ peak located several hundred volts away from the $M = 1$ peak was investigated. As expected, since H^{--} is not a stable ion, no peak was observed. Therefore, we conclude that H^- is the ion species observed as LiH is heated.

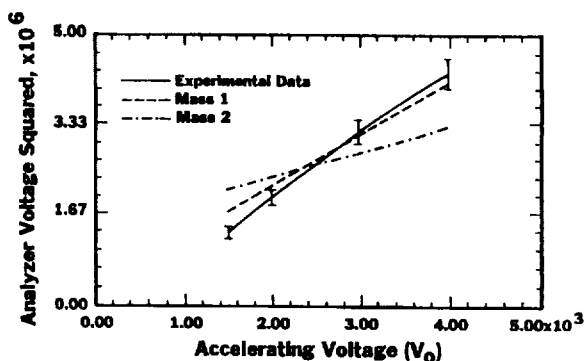


Figure 7. Graph of experimental data in Eq. (1). Accelerating voltage uncertainties are ± 75 V.

DISCUSSION AND FUTURE WORK

With the identity of the emitted negative ions confirmed, the logical next step is to understand the mechanism involved with the production of the H^- . It has been known for some time that above 250°C , LiH decomposes in a vacuum. At the temperatures used in this work, the lithium metal evaporates since it has an equilibrium pressure much larger than the surrounding vacuum.¹² Normally, when LiH is heated, the hydrogen is liberated to form molecular hydrogen. However, in this experiment, the H^- may actually be emitted directly from the LiH surface since the sample is connected to a power supply which delivers sufficient negative charge to neutralize the Li^+ prior to the Li being evaporated. This is consistent with low-energy electron diffraction (LEED) measurements made by Powell *et al.*¹³, which shows that as hydrogen is removed, the surface unit mesh increases relative to the bulk unit mesh and the stoichiometry of the LiH system changes so the surface becomes enriched in lithium.

An alternate view of the H^- emission involves a surface process in which the outgoing H atoms thermally liberated from the sample become ions by the tunneling of electrons from the conduction band of the metal to the affinity level of the H atom. In this model the frequency of tunneling depends strongly on the density of surface electrons and the work function of the surface. Several experiments^{14,16} have shown that low-energy (~ 1 eV) H atoms may reach an ionization probability greater than 0.1 when the work function of the converter material is less than 1.5 eV. In the case of LiH the value of the work function does not appear to be available in the scientific literature. However, on the basis of a model developed by Yamamoto *et al.*¹⁷ used to calculate the work function of a binary compound

involving gas absorption on a metal surface, the work function for the hydride is likely not much less than that of Li (2.4 eV). Consequently, it is not clear that the resonant charge transfer model should be used to interpret the H^- formation near the LiH surface.

Whatever the precise nature of the production mechanism, it is clear that this technique has the potential to achieve three important goals for future applications requiring sources of negative hydrogen ions. First, by using other saline hydrides such as NaH, which has a minimum equilibrium hydrogen pressure of 5800 mm at 500°C, the corresponding negative ion emission should be significantly increased. Increasing the temperature to 550°C raises the equilibrium pressure almost a factor of 3 beyond the 5800 mm value.⁶ Consequently, the prospect of developing a more elementary DC negative hydrogen ion source with an output current density at least comparable to those source already developed would appear to have possible commercial merits.

Secondly, the transport of the negative ions to the region in space where they are neutralized and eventually used requires a low value of transverse emittance. The present generation of H^- sources produce ion beams which possess emittance values much lower than those from a decade earlier. However the techniques described here involving a sample at ~ 700°C should result in an even smaller value. To operate at a temperature of only 500°C in the case of NaH would produce an even lower value of emittance for the ion/neutral beam being transported.

Thirdly, the lifetime of a saline hydride ion source would not be limited by the lifetime of a filament as is true for many present day sources. The hydride could be continuously fed into the heater or hydrogen gas could be used to resupply the metal hydride to keep it from being depleted of hydrogen. Either method should produce a long lifetime for the source. These are matters to be decided upon further technical development.

Ion sources usually require several years of study and advanced development before they become optimized. The technique described here is no exception. The work presented here notes the possibility of creating an advanced negative hydrogen ion source with many desirable features which may be of benefit as we face the energy needs of the next century.

References

1. M.K. Hubbert, Resources and Man, (W.H. Freeman, 1969).
2. H.P. Eubank et al., Phys. Rev. Lett. 43, 270 (1979).
3. D.J. Rej, I. Henins, R.J. Fonek, and Y.J. Kim, Rev. Sci. Instrum. 63, 4934(1992).
4. K.W. Ehlers, K.N. Leung, R.V. Pyle and W.B. Kunkel, Proceedings of the Fourth International Symposium on the Production and Neutralization of Negative Ions, AIP NO. 158, Brookhaven, 1986, p. 282.
5. G.G. Libowitz, in Critical Materials Problems in Energy Production, (Academic Press, New York, 1976).
6. W.M. Mueller, J.P. Blackledge and G.G. Libowitz, Metal Hydrides, (Academic Press, New York, 1986).
7. R.S. Calder, W. Cochran, D. Griffiths, and R.D. Lowde, J. Phys. Chem. Solids 23, 621 (1962).
8. F.E. Pretzel, G.N. Rupert, C.L. Mader, E.K. Storm, G.V. Gritton, and C.C. Rushing, J. Phys. Chem. Solids 16, 10 (1960).
9. R.L. Palmer, Proceedings of the Third International Symposium and Neutralization of Negative Ions, AIP NO. 111, Brookhaven, 1983, p. 281.
10. R.L. Seliger, J. Appl. Phys. 43, 2352 (1972).
11. A.T. Forrester, Large Ion Beams, (Wiley, New York, 1976).
12. C.E. Holcombe, G.L. Powell, and R.E. Clausing, Surf. Sci. 30, 561, (1972).
13. G.L. Powell, G.E. McGuire, D.S. Easton, and R.E. Clausing, Surf. Sci. 46, 345 (1974).
14. A. Pargellis and M. Seidl, Phys. Rev. B25, 4356 (1982).
15. J.N.M. Van Wernnik, J.J.C. Geerlings, and J. Los, Surf. Sci. 131, (1983).
16. J.P. Gauyacq and J.J. C. Geerlings, Surf. Sci. 182, 245 (1987).
17. S. Yamamoto, K. Susa, U. Kawage, and H. Okamo, Jpn. J. Appl. Phys. Suppl. 2, 209 (1974).

FIBER OPTICAL SOLAR SIMULATOR

Bhushan L. Sopori and Craig Marshall

National Renewable Energy Laboratory
1617 Cole Boulevard
Golden, CO 80401- 7 - 1 /
2482
p. 8**ABSTRACT**

This paper describes a new solar simulator whose output closely matches a desired solar spectrum for testing photovoltaic cells. The accurate simulation of the spectrum is attained by combining three light beams, each tailored to have suitable spectral content. The three light beams, derived from two sources, are filtered, and "mixed" by means of a trifurcated, randomized fiber cable so that when superimposed they add up to the desired solar spectrum. The Fiber Optic Solar Simulator (FOSS) simplifies solar cell testing by greatly reducing measurement time, obviating need for spectral mismatch corrections, and improving the accuracy of measurement. Other applications of FOSS are also described.

INTRODUCTION

During the past decade advances in the design and fabrication of solar cells have resulted in complex device designs capable of yielding very high efficiencies — approaching theoretical values. Today, an accurate measurement of the solar cell performance is a time-consuming, tedious, elaborate, and expensive process. The measurement problems arise because the solar simulators, based on a single xenon arc lamp, have an output spectrum that has significant deviations from a standard solar spectrum (1,2). These deviations are due to: mismatch in the envelopes of the standard and the actual output from a xenon lamp, presence of sharp emission lines from xenon lamp, and the absence of atmospheric absorption such as that arising from water vapor and CO₂. Although the current simulators employ some subtractive filtering, an accurate solar cell testing still requires elaborate procedures necessitating: (i) use of calibrated reference cells(s) fabricated on the same material and closely matching the performance of the test cell, (ii) measurement of the spectral response of the test cell, and (iii) measurement of the spectrum of the simulator and the current-voltage (I-V) characteristics of the test cell under this spectrum. After acquiring these data, a correction to the device short circuit current is made to compensate for the mismatch in the desired and the actual spectra. The current technique works well with single junction cells for which reference cells are available.

However, the technique for spectral mismatch corrections can only correct for the short circuit current; the cell parameters such as the open circuit voltage (V_{oc}) and the fill factor (FF) cannot be corrected. This can result in serious measurement errors in multijunction cells where a minor deviation in the current matching conditions between the design spectrum and the test spectrum can produce large effects on the FF of the cell (3). These problems can be circumvented if the measurements are done under a light source that can accurately reproduce the desired spectrum (4 - 8). Hence, we have developed the Fiber Optic Solar Simulator (FOSS), which produces an output beam that accurately replicates the solar spectra, Global AM1.5 or AM0, as desired (9,10). This paper describes the instrument and compares the results of test data on a variety of cells obtained by FOSS and conventional procedures used at NREL.

PRINCIPLE OF FOSS

Our approach is to synthesize a broad-band solar spectrum by superposing a number of light beams, each covering a different part of the spectrum. We have determined that a solar spectrum can be accurately synthesized by three broad-band beams covering UV, visible, and the IR regions of the solar spectrum. In order to ensure the lateral uniformity of the spectral content in the output beam, the intensity distribution of each individual beam must be uniform in the test plane. FOSS uses three suitably-filtered light beams which are superposed axially. This is accomplished by mixing the three optical beams by means of a randomized optical fiber. Each fiber acts as an element of an optical integrator. The randomized nature of the fiber cable and the large number of the elements of the optical integrator lead to a highly uniform spatial distribution of the intensity of each beam.

SYSTEM CONFIGURATION

Figure 1 is a schematic of the FOSS illustrating use of two light sources - a xenon arc lamp and a tungsten filament lamp. The xenon arc lamp is configured to produce two beams which serve as UV and visible (Vis) beams. The arrangement, shown in Figure 1, for extracting two beams from a single source can capture nearly all the light emanating from the xenon arc lamp and, hence, results in a much more efficient operation of the lamp as compared to the conventional use in a solar simulator. The output beams from the xenon arc lamp are modified by a suitable lens system and passed through low pass filters F1 and F2 that block the region of sharp emission lines and provide a smooth roll-off of the transmission beyond the cut-off wavelength. The tungsten lamp has no filter.

The output from the filters F1 and F2 and the direct output from the IR source are passed through individual apertures A1, A2, and A3, respectively. These apertures are used to control the power contained in each beam and hence allow adjustment of the ratio of three beam intensities in the output beam. The output from each aperture is focused by individual lenses, L1, L2, L3, onto the corresponding ends of the trifurcated optical fiber cable. Two legs of fiber cable, the Vis and the IR legs, are made of glass fibers, whereas the UV leg is made of quartz fibers. Each input leg of the fiber cable has about 2000 fibers, and the numerical apertures of the quartz and the glass fibers are about the same. The output beam is collimated by a quartz lens to produce a highly uniform beam whose spectrum can be adjusted by changing the intensity-ratio of the three beams. This allows an accurate production of the envelope of the solar spectrum.

The necessary characteristics of the various elements of FOSS are determined by a computer program that takes the spectrum of each source and determines the modified spectrum due to the transmittance of filters, lenses, and the optical fiber, and arrives at the combined spectrum at the output. This program can determine the optimum filter combination for the best fit to the spectrum required at the test plane. Although use of all-quartz optics can significantly reduce design effort, such a system would be quite expensive. Concomitantly, we have employed quartz optics only in the UV path. It should be pointed out that since our system can independently control power and the spectral distribution in each beam, there are many possible combinations of filters that can produce the same output spectrum.

One of the criterion for filter selection is to suppress the emission lines from the xenon arc in the UV and Visible beams; this establishes a cutoff around 0.7-0.8 μm for these filters. The fiber cable is designed to achieve the following features:

1. High coupling efficiency at each input end to ensure a minimum loss of optical power. Clearly, this is related to the optical design of the source, the focusing optics, and the

numerical aperture of the optical fibers. In our current fiber, a coupling efficiency of 60%-65% can be achieved.

2. The loss within the fiber should be minimized to avoid undesired dissipation.
3. The effective output (optical) diameter of the cable and the size of each fiber should be compatible with the requirements of the size and the uniformity of the output beam in the test plane.
4. The distribution of fibers in the output end of the cable should be random in order to produce a spatially uniform superposition of each input beam.

It is instructive to track the spectral changes that each beam develops as they propagate, and produce the combined output. Figure 2a shows the spectral contents of the UV beam at the input and the output of filter F₁. The corresponding spectra for the Vis beam are shown in Figure 2b. Figure 3 shows the spectra of the individual UV, Vis and IR beams in the test plane; the total output spectrum corresponding to these individual beams is also shown. Figure 4 shows a comparison of the spectrum from the fiber optic simulator and the standard Global AM1.5 spectrum. It is clear that a very close match of AM1.5 envelope can be produced by the fiber optic simulator. Figure 5 shows the typical distributions of the intensities of each beam in the test plane for a 4-in diameter of the output beam. The uniformity within the central 3-in spot is better than ± 2%. This high degree of the spatial uniformity of each beam ensures a corresponding high degree of the spectral uniformity in the output beam.

Due to ease of adjusting the output spectrum of FOSS, we can also produce AM0 solar spectrum by simply changing the ratio of the beams. Figure 6 shows a comparison of standard AM0 and the corresponding spectrum from FOSS.

TEST RESULTS

As a result of its highly uniform beam, with a spectrum closely matched to the solar spectrum, a measurement of the solar cell performance can be done under FOSS in only about 5 minutes, even on a multijunction cell. We have made measurements on a variety of solar cells fabricated on different materials and with single and multijunction devices. Tables 1 and 2 summarize the test results of single and multijunction cells, respectively. Also shown in these tables are test results from conventional procedures. The test results are in very close agreement with standard cell test measurements done by the National Renewable Energy Laboratory.

Cell Type/ID	I _{sc} (mA)		V _{oc} (Volts)		Fill Factor (%)		Area (cm ²)
	A	B	A	B	A	B	
GaAs/G361-42	2.25	2.24	0.89	0.89	79.2	79.7	0.25
Si/S1	35.9	36.1	0.65	0.65	74.8	74.8	1.00
a-Si/L3574-10	3.84	3.92	0.91	0.91	60.0	61.2	0.25
InGaP/G433-4	1.32	1.40	1.35	1.35	86.1	87.8	0.25
CIS/I182-1	31.7	31.2	0.54	0.54	49.3	49.6	1.00

Table 1: Comparison of single junction solar cell parameters measured with the Fiber Optic Simulator and with NREL standard.

A: Fiber Optic Simulator
B: Standrad NREL measurement

Cell Type/ID	I _{sc} (mA)		V _{oc} (Volts)		Fill Factor (%)		Area (cm ²)
	A	B	A	B	A	B	
GaInP on GaAs/G423-4	2.10	2.0*	2.35	2.34*	82.2	84.0*	0.25
Tandem α-Si/α-Si/L3079-8	1.83	1.97	1.83	1.85	70.6	71.2	0.27

Table 2: Comparison of multijunction solar cell parameters measured with the Fiber Optic Simulator and with NREL standard.

A: Fiber Optic Simulator

B:Standrad NREL measurement

*:These values were not verified by NREL.

The other advantages of the FOSS are

- It is a compact, table-top system that is convenient to use at laboratory test facilities and is considerably less expensive than conventional systems
- It has a high optical throughput
- Each source is maintained at a constant color temperature, which minimizes the variations in the spectrum
- The output spectrum can be easily corrected to accommodate for changes in the optical elements, such as those due to aging of lamps and filters.

OTHER APPLICATIONS OF FOSS

Although FOSS was designed primarily for testing solar cells, this system can be easily modified for a number of other applications. These applications include:

- Reflectometer for accurate measurement of solar reflectance of solar materials, paints, and textiles.
- Medical applications that require a controlled broad-band spectrum
- A system for solar cell testing that includes measurement of the spectral response of the cell under actual operating conditions.

CONCLUSION/MARKET POTENTIAL

A fiber-optic solar simulator has been developed that can be adjusted to produce an output beam to match either AM0 or AM1.5. The initial tests on single- and multi-junction cells show a good agreement between the cell parameters measured with the fiber optic simulator and by standard procedures. The measurements made with the fiber optic simulator did not incorporate any spectral mismatch corrections and did not use a reference cell. Further improvements are being incorporated that will allow individual cells of a multijunction device to be characterized.

The market potential of FOSS appears to be quite high. Photovoltaic energy is one of the most promising energy technologies for the future. The market for photovoltaics has been growing at a rate of 25% per year over the last 4 years and is expected to grow at an accelerated pace in the future. With markets that may soon be topping several billions of dollars per year, and with an increasing number of PV products coming into the market, the need for measurement standards and quality control will be imperative. Researchers and the industry will need a quick, easy, and accurate method for testing devices. The FOSS and its progeny are the instruments that will provide that service. The FOSS offers the expanding number of researchers who are developing new complex solar cell designs a unique opportunity that no other instruments can match—experimental adjustment of the cell design parameters such as doping profiles, material

composition, antireflection coatings, and window layers. A fine-tuning of such design parameters on an experimental basis, using an accurate simulator spectrum, is essential for advanced devices that use spectral splitting and current matching to achieve very high conversion efficiencies.

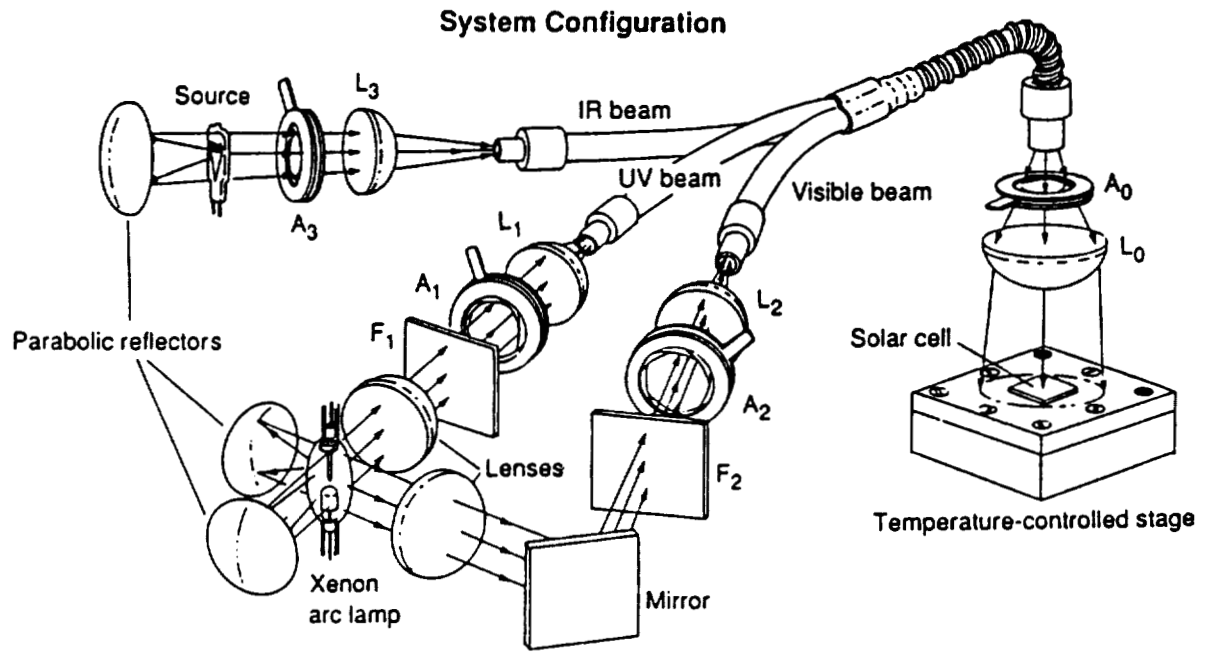
The FOSS can be used in other applications that require a tight control of the light spectrum. Such applications include measurement of the solar reflectance of materials for color matching, medical research, and characterization of solar materials and devices.

ACKNOWLEDGMENT

The authors are very grateful to Keith Emery of NREL for many valuable suggestions and the measurements he has made on the various devices we have used for comparison studies. They would like to thank Sarah Kurtz, Byron Stafford, and Harin Ullal for providing the cells used in this study. This work was supported by the NREL Director's Development Fund, Technology Maturation Fund, and by the U.S. Department of Energy under contract No. DE-AC02-83CH10093.

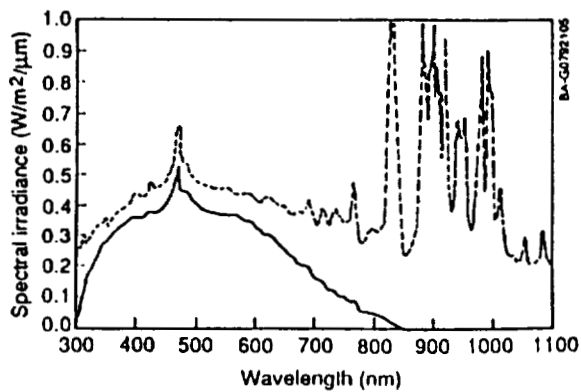
REFERENCES

1. XT-10 AND X-25 are manufactured by Spectrolab corporation.
2. Oriel Corporation, 250 Long beach Blvd., Stratford, CT 06497.
3. T. Glatfelter et. al. Proc. 19th IEEE PVSC, 1187(1987).
4. M.Kusuhara, US Patent Number 4,641,27, Feb. 1987.
5. M. Bennet et. al, Pros. 21st IEEE PVSC, 1438 (1990).
6. Wacom Co. Ltd., 3, Nihonbashi, Meromachi, 4-Chome, chuoku, Tokyo 103, Japan.
7. G. Virshup, Proc. 21st IEEE PVSC, 1249(1990).
8. K. Heidler et. al, Measurement of Multijunction Solar Cells, 10th PVSEC, Lisbon, 1990.
9. B. L. Sopori et. al, Proc. 21st IEEE PVSC, 1116(1990).
10. B. L. Sopori, US Patent Number 5,217,285, Jun. 1993.



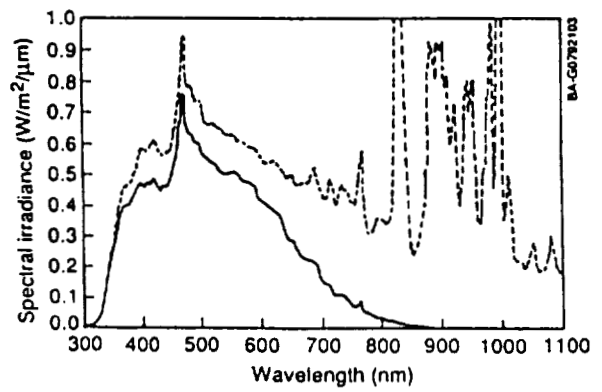
BA-G0792101

Figure 1. A schematic of the Fiber Optic solar simulator showing major elements of the system



---- UV beam before filter (F_1) — UV beam after filter (F_1)

Figure 2a. Comparison of the spectral contents of the UV beam before and after the filter F_1



---- Vis beam before filter (F_2) — Vis beam after filter (F_2)

Figure 2b. Comparison of the spectral contents of the Vis beam before and after filter F_2

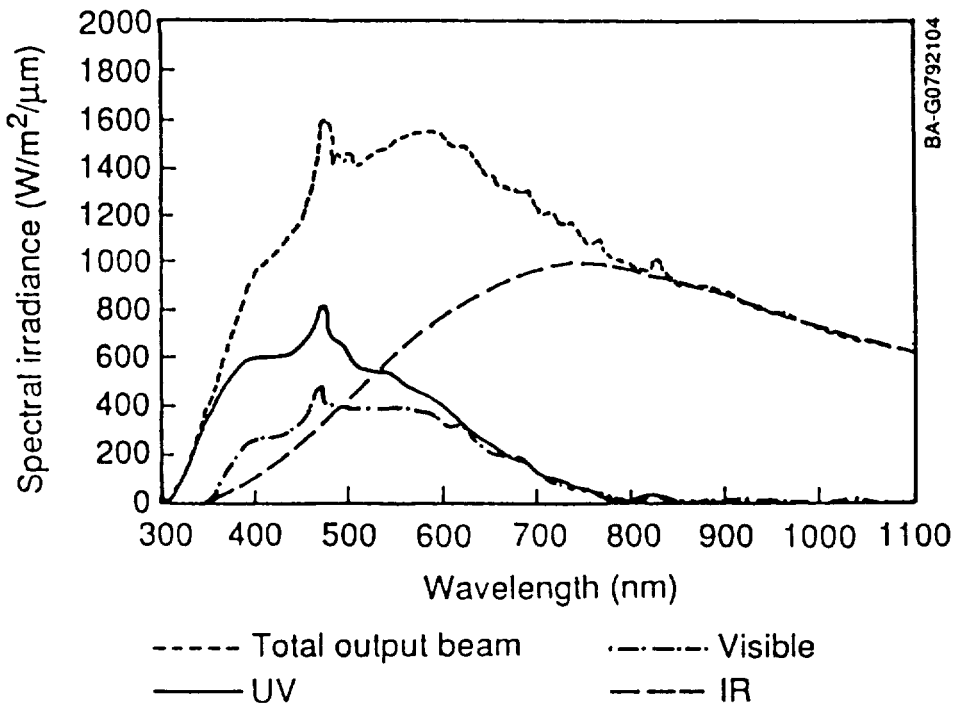


Figure 3. Spectra of individual UV, Vis and IR beams and the total output beam in the test plane

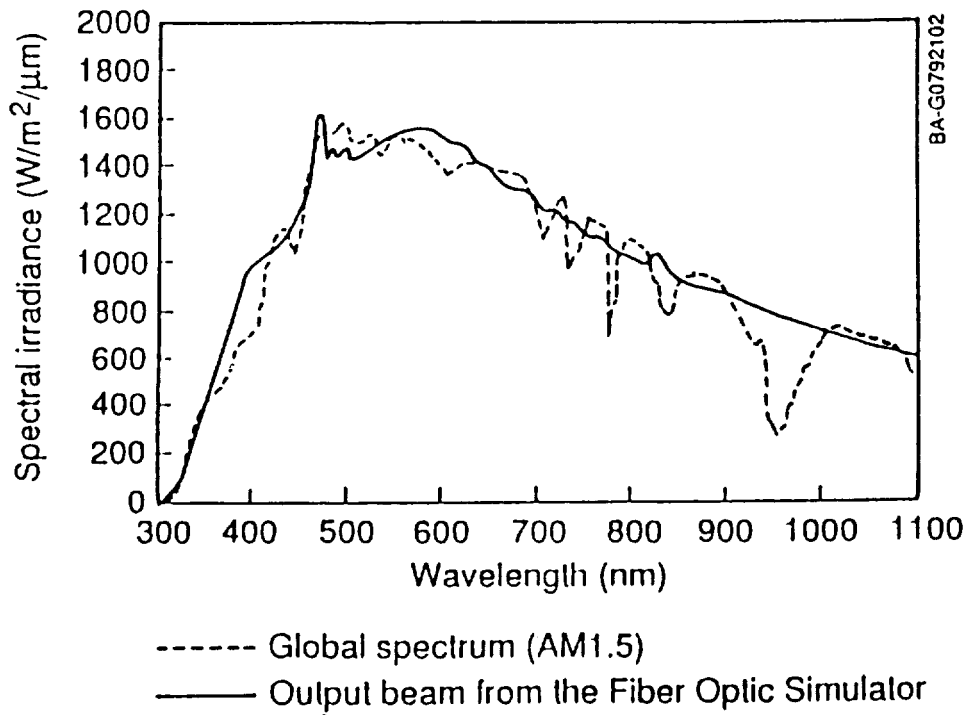


Figure 4. A comparison of the spectrum of the output beam from the fiber optic simulator with AM1.5 Global spectrum

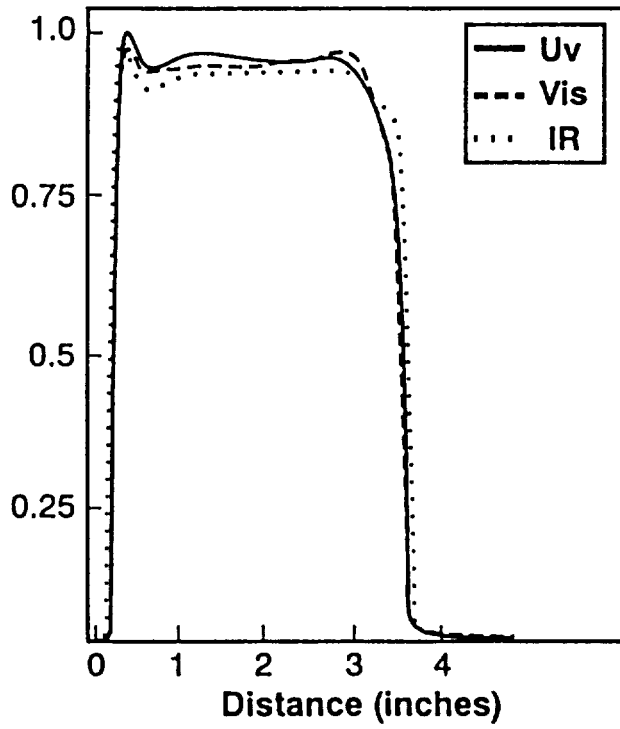


Figure 5. Normalized intensity distributions of UV, Vis, and IR beams in the test plane

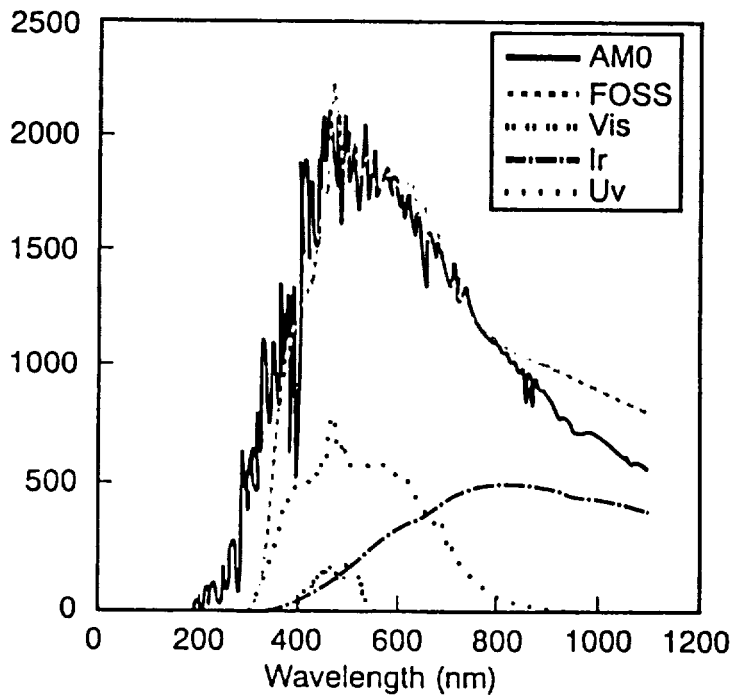


Figure 6. Comparison of the standard AM0 and the output from FOSS

CONF ID
END

ACKNOWLEDGMENTS

The Technology 2003 Conference Management would like to thank the following individuals who generously contributed their time to serve as session moderators:

Dr. Josephine Covino
Head, Applied Mechanics Branch
Naval Air Warfare Center
Weapons Division
China Lake, CA

Dr. Hamed M. El-Bisi
Chief Scientist
Army Research Laboratory
Materials Directorate
Watertown, MA

Donald G. Foster
Head, Mechanical Processes Dept.
Lawrence Berkeley Laboratory
Berkeley, CA

Linda Geissinger
Program Analyst
Environmental Management
McClellan Air Force Base
McClellan AFB, CA

Arif Husain
Technology Transfer Office
NASA Resident Office
Jet Propulsion Laboratory
Pasadena, CA

Anton L. Interbitzen
Deputy Assistant Director
for Research
U.S. Geological Survey
Reston, VA

Diana C. Jackson
Technology Transfer Representative
Naval Command, Control and Ocean
Surveillance Center
San Diego, CA

Geoffrey S. Lee
Technology Transfer Officer
NASA Ames Research Center
Office of Commercial and
Community Programs
Moffett Field, CA

Michael L. Mastracchi
Senior Environmental Engineer
U.S. Environmental Protection
Agency
Washington, DC

H. Dana Moran
Manager, Research and Technology
Applications
National Renewable Energy
Laboratory
Golden, CO

Dr. Mike Sullivan
Technology Transfer Manager
Naval Air Warfare Center
Point Migu, CA

Dr. R. Michael Templeton
President
Templeton and Associates, Inc.
San Diego, CA

Diana L. West
Associate Program Leader
Technology Transfer Initiatives
Program
Lawrence Livermore National
Laboratory
Livermore, CA

REPORT DOCUMENTATION PAGE			Form Approved OMB No. 0704-0188
1. AGENCY USE ONLY <i>(leave blank)</i>	2. REPORT DATE February 1994	3. REPORT TYPE AND DATES COVERED Conference Publication	
4. TITLE AND SUBTITLE Technology 2003, Volume 1		5. FUNDING NUMBERS	
6. AUTHOR(S) Michael Hackett, Compiler			
7. PERFORMING ORGANIZATION NAME(S) AND ADDRESS(ES) NASA Technology Transfer Program, Code CU		8. PERFORMING ORGANIZATION REPORT NUMBER	
9. SPONSORING / MONITORING AGENCY NAME(S) AND ADDRESS(ES) National Aeronautics and Space Administration Washington, DC 20546		10. SPONSORING / MONITORING AGENCY REPORT NUMBER NASA CP-3249, Vol. 1	
11. SUPPLEMENTARY NOTES			
12a. DISTRIBUTION / AVAILABILITY STATEMENT Unclassified/unlimited Subject Category 99		12b. DISTRIBUTION CODE	
13. ABSTRACT Proceedings from symposia of the Technology 2003 Conference and Exposition, December 7-9, 1993, Anaheim, CA. Volume 1 features the Plenary Session and the Plenary Workshop, plus papers presented in Advanced Manufacturing, Biotechnology/Medical Technology, Environmental Technology, Materials Science, and Power and Energy.			
14. SUBJECT TERMS Technology transfer, conferences, energy technology, medical science, defense program, environmental engineering, manufacturing		15. NUMBER OF PAGES 470	16. PRICE CODE
17. SECURITY CLASSIFICATION OF REPORT Unclassified	18. SECURITY CLASSIFICATION OF THIS PAGE Unclassified	19. SECURITY CLASSIFICATION OF ABSTRACT Unclassified	20. LIMITATION OF ABSTRACT Unlimited

Available from NASA Center for AeroSpace Information
800 Elkridge Landing Road
Linthicum Heights, MD 21090-2934
(301) 621-0390